Research Topics

Rising stars in virus and host: 2022

Edited by
Santiago Guerrero, Andrés López-Cortés, Laura Patricia Mendoza,
Danielle Malta Lima, Rameez Raja, Jian Chen, Zhenlong Liu and Song Yang

Published in
Frontiers in Cellular and Infection Microbiology

ISSN 1664-8714
ISBN 978-2-83251-060-5
DOI 10.3389/978-2-83251-060-5

About Frontiers

Frontiers is more than just an open access publisher of scholarly articles: it is a pioneering approach to the world of academia, radically improving the way scholarly research is managed. The grand vision of Frontiers is a world where all people have an equal opportunity to seek, share and generate knowledge. Frontiers provides immediate and permanent online open access to all its publications, but this alone is not enough to realize our grand goals.

Frontiers journal series

The Frontiers journal series is a multi-tier and interdisciplinary set of open-access, online journals, promising a paradigm shift from the current review, selection and dissemination processes in academic publishing. All Frontiers journals are driven by researchers for researchers; therefore, they constitute a service to the scholarly community. At the same time, the *Frontiers journal series* operates on a revolutionary invention, the tiered publishing system, initially addressing specific communities of scholars, and gradually climbing up to broader public understanding, thus serving the interests of the lay society, too.

Dedication to quality

Each Frontiers article is a landmark of the highest quality, thanks to genuinely collaborative interactions between authors and review editors, who include some of the world's best academicians. Research must be certified by peers before entering a stream of knowledge that may eventually reach the public - and shape society; therefore, Frontiers only applies the most rigorous and unbiased reviews. Frontiers revolutionizes research publishing by freely delivering the most outstanding research, evaluated with no bias from both the academic and social point of view. By applying the most advanced information technologies, Frontiers is catapulting scholarly publishing into a new generation.

What are Frontiers Research Topics?

Frontiers Research Topics are very popular trademarks of the *Frontiers journals series*: they are collections of at least ten articles, all centered on a particular subject. With their unique mix of varied contributions from Original Research to Review Articles, Frontiers Research Topics unify the most influential researchers, the latest key findings and historical advances in a hot research area.

Find out more on how to host your own Frontiers Research Topic or contribute to one as an author by contacting the Frontiers editorial office: frontiersin.org/about/contact

Rising stars in virus and host: 2022

Topic editors
Santiago Guerrero — Universidad Internacional del Ecuador., Ecuador
Andrés López-Cortés — Universidad de las Américas, Ecuador
Laura Patricia Mendoza — Universidad Nacional de Asunción, Paraguay
Danielle Malta Lima — University of Fortaleza, Brazil
Rameez Raja — Cleveland Clinic, United States
Jian Chen — Fudan University, China
Zhenlong Liu — McGill University, Canada
Song Yang — Capital Medical University, China

Citation
Guerrero, S., López-Cortés, A., Mendoza, L. P., Lima, D. M., Raja, R., Chen, J., Liu, Z., Yang, S., eds. (2022). *Rising stars in virus and host: 2022*.
Lausanne: Frontiers Media SA. doi: 10.3389/978-2-83251-060-5

Table of contents

frontiers | Frontiers in Cellular and Infection Microbiology

TYPE Editorial
PUBLISHED 01 December 2022
DOI 10.3389/fcimb.2022.1100695

Check for updates

OPEN ACCESS

EDITED AND REVIEWED BY
Curtis Brandt,
University of Wisconsin-Madison,
United States

*CORRESPONDENCE
Andres López-Cortés
aalc84@gmail.com

SPECIALTY SECTION
This article was submitted to
Virus and Host,
a section of the journal
Frontiers in Cellular and
Infection Microbiology

RECEIVED 17 November 2022
ACCEPTED 21 November 2022
PUBLISHED 01 December 2022

CITATION
López-Cortés A and
Guerrero S (2022) Editorial: Rising
stars in virus and host: 2022.
Front. Cell. Infect. Microbiol.
12:1100695.
doi: 10.3389/fcimb.2022.1100695

Editorial: Rising stars in virus and host: 2022

Andres López-Cortés[1,2]* and Santiago Guerrero[2,3]

[1]Cancer Research Group (CRG), Faculty of Medicine, Universidad de Las Américas, Quito, Ecuador, [2]Latin American Network for the Implementation and Validation of Clinical Pharmacogenomics Guidelines (RELIVAF-CYTED), Madrid, Spain, [3]Laboratorio de Ciencia de Datos Biomédicos, Escuela de Medicina, Facultad de Ciencias Médicas de la Salud y de la Vida, Universidad Internacional del Ecuador, Quito, Ecuador

KEYWORDS

SARS-CoV-2, COVID-19, reinfection, H7N9, leishmania, herpes simplex virus type 1, phage therapy, *Enterovirus A (normal)*

Editorial on the Research Topic
Rising stars in virus and host: 2022

Recognizing the future leaders of virology is fundamental to safeguard tomorrow's driving force in innovation for this fundamental research field. In this context, the objective of the Rising Stars in Virus and Host: 2022 article collection was to highlight high-quality research across the entire breadth of virology focusing on pending issues, new challenges, and future innovations. The research presented in this collection highlights worldwide effort to understand the complexity of virus concerning their infection mechanisms, immunological responses or even for phage-based therapies against multidrug-resistant bacteria.

Coronavirus disease 2019 (COVID-2019) and its causative agent, severe acute respiratory syndrome coronavirus 2 (SARS-CoV-2) continue to be the focus of intensive research. Indeed, this Research Topic contains three scientific articles related to multiple aspects of the disease. Firstly, Wang et al. have reviewed the immune responses of SARS-CoV-2 infection. This study summarizes the molecular underpinnings of innate immune mechanisms behind virus-host interactions, which can contribute to the development of effective therapeutic avenues. Secondly, Guevara et al. have provided epidemiological data concerning SARS-CoV-2 reinfection in Ecuador. Their study showed, by a 22 months-long surveillance strategy, that reinfection frequency has increased 10-fold following the introduction of the Omicron variant. Interestingly, this study performed the longest monitoring of reinfection events, showing an occurrence at regular intervals of 4-5 months, and confirming Omicron as the main cause of reinfection. Lastly, Wang et al. have discussed the current understanding of early differentiation of virus-specific effector follicular helper T-cells (TFH) and long-term maintenance of virus-specific memory cells in mouse models and patients with SARS-CoV-2 infection.

To shed light on the interaction between host immunity and influenza evasion, Zhu et al. studied the mechanisms underlying the virulence, pathogenicity, and immune response between H9N2 and H7N9 virus infections that cause influenza A. They used a mouse infection model to dissect the difference in the host response between both viruses through transcriptomic analyses of infected lungs. Consequently, they discovered that the H9N2-infected lungs elicited an earlier induction of innate immune response and earlier recruitment of macrophages than the H7N9-infected lungs. Finally, the different patterns of immune response may underlie more severe lung pathology caused by H7N9 infection compared to H9N2 infection.

Type I interferons (IFNs) are the first line of defense against viral infections, promoting antiviral, immunomodulatory, and antiproliferative effects. The IFN family contains 12 INF-α subtypes and IFN-β. However, the biological impact of individual subtypes remains controversial and drug-resistant infections with herpes simplex virus type 1 (HSV-1) are still lacking a protective or curing therapy in recurrent orogenital lesions. In this context, Schmitz et al. evaluated selective INF-α subtypes and IFN-β for their therapeutic potential in genital HSV-1 infections. Their results provided further insights into the diversity of IFN effector functions and their impact on the immunological control of HSV-1 infections.

Leishmania RNA virus 1 (LRV1) is a double-stranded RNA (dsRNA) virus found in some strains of the human protozoan parasite Leishmania, the causative agent of leishmaniasis, a neglected tropical disease. Jha et al. have explained the crucial role that the lymphatic system plays in infectious metastasis caused by Leishmania. Their results demonstrated that when infection in mucocutaneous leishmaniasis is associated with inflammation and LRV1, lymphatic vessels could serve as efficient routes of dissemination for infected cells to colonize distant organs from primary sites. On the other hand, the presence of LRV1 inside Leishmania constitutes an important virulence factor that worsens the leishmaniasis outcome in an IFN–dependent manner and contributes to treatment failure. Bekkar et al. contributed to shed light and dissect the intricate macrophage response toward infection by the Leishmania-LRV1 duo, providing new therapeutic strategies.

Bai et al. discovered promising prospects in the treatment of Carbapenem-Resistant *Klebsiella pneumoniae* (CRKP) infections by using phages and phage-encoded proteins. They isolated and identified a novel *Klebsiella pneumoniae* phage (vB_kpnM_17-11) using a CRKP host. vB_kpnM_17-11 belongs to the family of Myoviridae, order Caudovirales, and its genome is a double-stranded DNA (dsDNA) containing 165,894 base pairs and 275 Open Reading Frames (ORFs). Lastly, their results showed excellent *in vitro* and *in vivo* performance against *Klebsiella pneumoniae* infection and constitutes a promising candidate for the development of phage therapy against CRKP.

Enterovirus A (EV-A) species cause hand, foot, and mouth disease (HFMD) in young children. To better understand EV-A evolution and adaptation, Zeng et al. have examined multiple codon usage parameters finding that the codon usage bias among EV-A strains varies and is clade-specific. Additionally, they revealed that the codon usage patterns of EV-A strains were shaped by mutation pressure and natural selection. These findings have allowed them to identify novel characteristics of codon usage bias in distinct EV-A clades associated with their host range, transmission, and pathogenicity.

Finally, Chandra et al. have written an interesting review on the implications of host components in regulating integrity and dynamics of a dsRNA rotavirus (RV) replication factories. Their article focused on the interaction between the replication bodies (viroplasms) of a dsRNA RV and the host cellular determinants of infection to provide a platform for designing host-directed antiviral therapeutic interventions in the future.

Author contributions

All authors confirm being contributors of this work and have approved it for publication.

Conflict of interest

The authors declare that the research was conducted in the absence of any commercial or financial relationships that could be construed as a potential conflict of interest.

Publisher's note

frontiers | Frontiers in Cellular and Infection Microbiology

REVIEW
published: 29 June 2022
doi: 10.3389/fcimb.2022.937460

A Game of Infection – Song of Respiratory Viruses and Interferons

Guo Qiang Wang[1], Yinuo Gu[1], Chao Wang[1], Fang Wang[1]* and Alan Chen-Yu Hsu[2,3,4]*

[1] Department of Pathogeny Biology, College of Basic Medical Sciences, Jilin University, Changchun, China, [2] Signature Research Program in Emerging Infectious Diseases, Duke – National University of Singapore (NUS) Graduate Medical School, Singapore, Singapore, [3] School of Medicine and Public Health, The University of Newcastle, Newcastle, NSW, Australia, [4] Viruses, Infections/Immunity, Vaccines and Asthma, Hunter Medical Research Institute, Newcastle, NSW, Australia

Humanity has experienced four major pandemics since the twentieth century, with the 1918 Spanish flu, the 2002 severe acute respiratory syndrome (SARS), the 2009 swine flu, and the 2019 coronavirus disease (COVID)-19 pandemics having the most important impact in human health. The 1918 Spanish flu caused unprecedented catastrophes in the recorded human history, with an estimated death toll between 50 – 100 million. While the 2002 SARS and 2009 swine flu pandemics caused approximately 780 and 280,000 deaths, respectively, the current COVID-19 pandemic has resulted in > 6 million deaths globally at the time of writing. COVID-19, instigated by the SARS – coronavirus-2 (SARS-CoV-2), causes unprecedented challenges in all facets of our lives, and never before brought scientists of all fields together to focus on this singular topic. While for the past 50 years research have been heavily focused on viruses themselves, we now understand that the host immune responses are just as important in determining the pathogenesis and outcomes of infection. Research in innate immune mechanisms is crucial in understanding all aspects of host antiviral programmes and the mechanisms underpinning virus-host interactions, which can be translated to the development of effective therapeutic avenues. This review summarizes what is known and what remains to be explored in the innate immune responses to influenza viruses and SARS-CoVs, and virus-host interactions in driving disease pathogenesis. This hopefully will encourage discussions and research on the unanswered questions, new paradigms, and antiviral strategies against these emerging infectious pathogens before the next pandemic occurs.

Keywords: influenza A virus, coronavirus, coronavirus – COVID-19, virus infection, innate immunity, innate immune system

Edited by:
Rameez Raja,
Cleveland Clinic, United States

Reviewed by:
Showkat A. Dar,
National Institutes of Health (NIH),
United States
Reyaz Ur Rasool,
University of Pennsylvania,
United States

***Correspondence:**
Fang Wang
wf@jlu.edu.cn
Alan Chen-Yu Hsu
Alan.Hsu@duke-nus.edu.sg

Specialty section:
This article was submitted to
Virus and Host,
a section of the journal
Frontiers in Cellular and
Infection Microbiology

Received: *06 May 2022*
Accepted: *25 May 2022*
Published: *29 June 2022*

Citation:
Wang GQ, Gu Y, Wang C, Wang F and Hsu AC-Y (2022) A Game of Infection – Song of Respiratory Viruses and Interferons.
Front. Cell. Infect. Microbiol. 12:937460.
doi: 10.3389/fcimb.2022.937460

INTRODUCTION

Influenza A viruses (IAVs) and severe acute respiratory syndrome – coronaviruses (SARS-CoVs) are both regarded as the most important respiratory infectious pathogens in human population. Their ever-changing nature constantly escapes from our current therapeutics, while emerging into novel viruses with unpredictable lethality. We have little immunity to these new viruses, and when they evolve and if they become pandemic, the consequences would be unthinkable. The 2009 H1N1 pandemic caused devastating effects, although by sheer luck the virus was not a lethal virus. The International Health Regulations Committee (World Health Organization) concluded in their 2010 report that “the world is ill-prepared to respond to a severe influenza pandemic or to any similarly global, sustained and threatening public health emergency.” (WHO, 2011). Ten years later, the unexpected appearance of the novel SARS-CoV-2 and CoV disease 2019 (COVID-19) pandemic has again emphasised our lack of preparedness and apart from costly public health measures a complete absence of effective antiviral therapeutics. Despite serious concerns of vaccine mismatch and escape mutants (Australian Government, D.o.H., 2017; Paules et al., 2018), vaccination remains the most important preventative measure against IAVs and SARS-CoV-2. Nevertheless, there is also a need to develop immune-targeting therapeutics that can be immediately deployed at the initial phase of the pandemic before vaccines become available and accessible to all nations.

Human innate immunity is an ancient immune architecture that has evolved to protect the host from microbial insults. The host pattern recognition receptors (PRRs) recognise specific genetic features common to viruses, and these factors are essential barriers to most respiratory viruses and cross-species viral transmission.

IAVs and SARS-CoVs, in agreement with the Red Queen Hypothesis, have also evolved to withstand the selective pressure from the host immune responses (Brockhurst et al., 2014). These viruses produce not only essential proteins for viral replication but also factors that effectively weaken the host antiviral responses and enhances their virulence and survival. These virus-host interactions are the primary drivers of severe diseases in the host. While rapid advances in knowledge in the host innate antiviral responses and viral infections has been achieved by fundamental discoveries, how virus-host interactions mediate dysregulated immune responses and severe diseases remain to be further defined. Understanding these mechanisms will provide important insights in the development of effective antiviral therapeutics against these infectious pathogens.

In this Review, we summarize what the host antiviral networks have taught us, how the viruses compromise our defensive responses, and current unsolved mysteries in infection and innate immunity.

Intracellular Sentinels and the Enablers of the Antiviral Responses

IAVs and CoVs primarily infect human airway epithelial cells for viral replication. Human IAVs specifically bind with host cell surface glycoproteins carrying terminal α2,6 linked sialic acid residues, whereas avian IAVs bind to that with α2,3 linked sialic acid residues (Ito et al., 1997; Matrosovich et al., 2004). In contrast, SARS-CoVs gain cell entry by binding to angiotensin-converting enzyme (ACE)2 on airways epithelial cells (Wang Q et al., 2020; Scialo et al., 2020). IAVs and SARS-CoVs also infect alveolar type II pneumocytes and cause viral pneumonia that often requires hospitalization (Weinheimer et al., 2012; Wahl et al., 2021). Host innate immune responses initiated by these airway epithelial cells provide critical first line of defence against viral infections.

Human innate immune system has developed a suite of intracellular PRRs to detect viral RNAs and trigger innate immune responses that restrict viral replication (**Figure 1**). There are two major classes of PRRs that facilitate the host antiviral responses, retinoic acid-inducible gene I (RIG-I)-like receptors (RLRs), endosomal Toll-like receptors (TLRs). RLRs include RIG-I and melanoma differentiation–associated gene 5 (MDA5). RIG-I specifically recognises 5′ triphosphate RNAs (5′pppRNAs) that are produced by the IAVs, whereas MDA5 and TLR3/7 binds with virus double stranded (ds)RNAs. Two recent studies independently showed that RIG-I (Thorne et al., 2021) and MDA5 (Yin et al., 2021) was crucial in inducing antiviral responses to SARS-CoV-2, however the importance of the former remains controversial as SARS-CoV-2 has not been shown to produce 5′pppRNAs. Endosomal TLR3/7 also recognise IAV RNAs and are predicted to also detect that of SARS-CoVs, and mediate both antiviral and inflammatory responses.

Once engaged with viral RNAs, RIG-I is activated by adaptor proteins RING Finger (RNF)135 (also known as RIPLET) and Tripartite Motif Containing 5 (TRIM25) (Gack et al., 2007; Hayman et al., 2019), and MDA-5 activation is dependent on interferon-inducible gene (ISG)15 (Liu et al., 2021). Activated RIG-I and MDA-5 interacts with mitochondrial antiviral signalling (MAVS) adaptor protein. MAVS forms fibrillar oligomeric complexes when activated and drives downstream antiviral cytokine production. MAVS recruits tumor-necrosis-factor (TNF)-receptor associated factor (TRAF)3, which activates TANK binding kinase (TBK1) – IκB kinase (IKK)ϵ – IKKγ complex and mediates activations of interferon (IFN) regulatory factor 3/7 (Paz et al., 2011). Activated IRFs then translocate into nucleus where they facilitate the production of antiviral proteins including type I IFNs [IFN-α/-β/-κ/-ϵ (epsilon)/-ω (omega)] and type III IFNs IFN-λ1 [interleukin-29 (IL-29)], IFN-λ2 (IL-28A), IFN-λ3 (IL-28B), and IFN-λ4. The released IFNs act on the same/neighbouring cells to induce the expression of over 300 IFN-stimulated genes (ISGs) *via* the transcription factor signal transducer and activator of transcription (STAT)1. Notable ISGs that have been well characterised include protein kinase R (PKR) that inhibits viral replication and induces apoptosis (Stark et al., 1998; Fitzgerald et al., 2003; Seth et al., 2005; Hsu et al., 2012; Hsu et al., 2016), and IFN-inducible transmembrane (IFITM) 1, 2, and 3 proteins that entrap infecting virions within endosome and subsequent elimination in the endolysomes (Brass et al., 2009; Feeley et al., 2011; Compton et al., 2016).

In addition to RLRs and TLR3/, Asp-Glu-Ala-Asp (DEAD) box (DDX)1 protein is another PRR that has been shown to be important in IFN responses. Both RIG-I (aka. DDX58) and DD1 belongs to the same DEAD protein family. DDX1 forms a biomolecular condensate with DDX21 and Asp-Glu-Ala-His (DEAH) box (DHX)36 proteins (**Figure 1**) and induces type I IFNs *via* the adaptor toll-interleukin receptor (TIR)-containing adaptor molecule-1 (TICAM-1)/TIR domain-containing

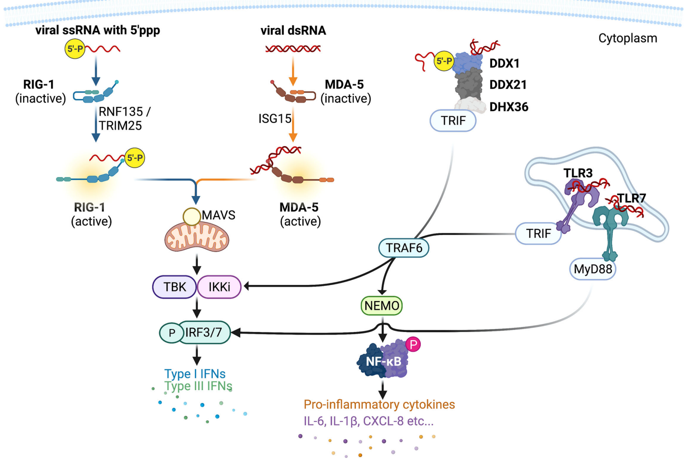

FIGURE 1 | Host intracellular viral RNA recognition and innate immune signalling network. Pattern recognition receptor RIG-I recognises influenza virus ssRNAs with 5` triphosphate group, whereas MDA5, DDX1-DDX21-DHX36 complex, and TLR3 recognises viral dsRNAs. Once engaged with viral RNAs, RIG-I and MDA5 are activated by adaptor proteins RIPLET and TRIM25 and ISG15, respectively, and then initiates the production of type I and III interferons (IFNs) *via* the mitochondrial antiviral (MAVS) adaptor protein and transcription factor IFN-regulatory factor (IRF)3. DDX1-DDX21-DHX36 complex and TLR3 induces the expression of both type I and III IFNs and pro-inflammatory cytokines [interleukin (IL)-6, IL-1β, etc…] *via* the adaptor TRIF and the transcription factors IRF3/7 and nuclear factor kappa-light-chain-enhancer of activated B cells (NF-κB). This figure was created with BioRender.com.

adaptor-induced IFN-β (TRIF) (Fuller-Pace, 2006; Zhang et al., 2011).

Endosomal TLR3 also employs TRIF as its adaptor protein and facilitates the activation of IKKα/β/γ complex (aka. NEMO) and nuclear factor kappa-light-chain-enhancer of activated B cells (NF-κB). NF-κB then drives the production of type I IFNs and pro-inflammatory cytokines and chemokines including interleukin (IL)-6, IL-1β, CXCL-8, and TNF-α (Vallabhapurapu and Karin, 2009). These cytokines recruit immune cells such as macrophages, neutrophils, and natural killer (NK) cells to the site of infection and remove virus-infected cells (Biron et al., 1999; Mandelboim et al., 2001; Hsu et al., 2016). TLR7 and its adaptor myeloid differentiation primary response (MyD)88 mediates activation of IRF7 and subsequent transcription of type I IFNs.

IAV infection can lead to heightened inflammation (aka. cytokine storm) that promotes tissue destruction and pneumonia (Hsu et al., 2017; Scharenberg et al., 2019; Vanders et al., 2019; Gu et al., 2019). Excessive IL-6, IL-1β, and TNFα levels along with increased recruitment of immune cells in the airways contribute to epithelial damage and acute lung injury, driving the development of acute respiratory distress syndrome (ARDS), leading to severe vascular leakage and pulmonary edema (Short et al., 2014). Local inflammation can spill over into the systemic circulation, causing systemic inflammation, sepsis, and death.

Similar to IAV infection, excessive airway inflammation and epithelial damage also occurs in severe COVID-19. In addition to elevated IL-1β and TNF-α productions (Sheridan et al., 1997; Kolb et al., 2001; Kimura et al., 2009; Al-Sadi et al., 2013; Kimura et al., 2013), chemokine CCL2 that is typically released by damaged cells and recruits monocytes has also been shown to be increased in COVID-19 patients (Huang et al., 2020; Li et al., 2020). These uncontrolled inflammation and tissue damage compromises the integrity of epithelial-endothelial (air-blood) barrier, leading to ARDS that is evident in severe COVID-19 (Huang et al., 2020; McGonagle et al., 2020; Mehta et al., 2020) as well as in highly pathogenic avian IAV H5N1 infection (Chotpitayasunondh et al., 2005; Tisoncik et al., 2012; Gu et al., 2019).

Constitutively Protective or Pathogenic IFNs

Protective, constitutive, and Inducible IFNs

The innate immune cytokines are thought to be only induced upon virus infection, reports have demonstrated that type I IFNs were constitutively expressed at low levels at resting state and primed the epithelial cells for a more robust antiviral responses to infection (**Figure 2**). This "revving-up" model has been observed with both IFN-α and IFN-β in IAV and hepatitis C virus (HCV) infection (Hsu et al., 2012; Tsugawa et al., 2014), and may be driven by the constitutive expression of IRF3. This however is unlikely as IRF3 dimerization is not evident at resting state (Yoo et al., 2014; Liu et al., 2015), and IRF3 deficiency had no effect on the production of constitutive IFN-β (Hata et al., 2001). Alternative mechanisms are possibly involved in the constitutive IFN responses. Indeed, transcriptional factors NF-κB and activating protein-1 (AP-1) appears to be essential in constitutive IFN-β production (Gough et al., 2010; Balachandran and Beg, 2011; Basagoudanavar et al., 2011), as subunits of these factors (RelA and c-Jun, respectively) have been reported to bind to the IFN-β promoter region at resting state, although they have been shown to be dispensable in virus-induced IFN-β expression

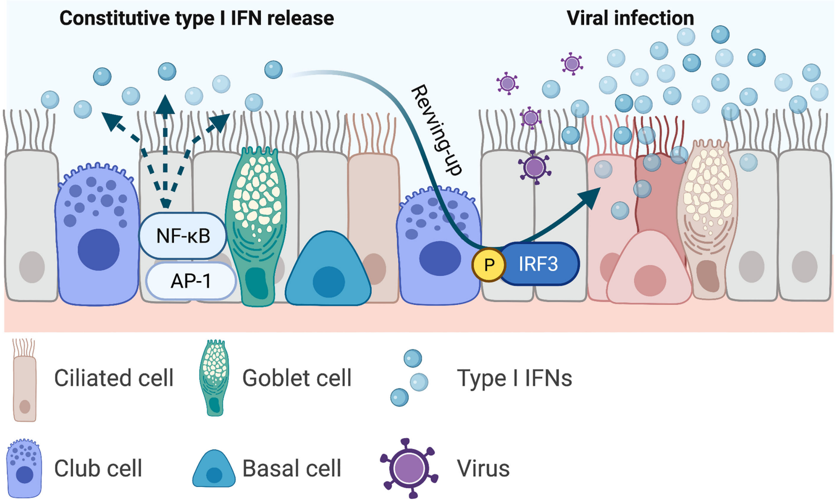

FIGURE 2 | Constitutive type I interferons and the revving-up model. Airway epithelial-derived type I interferons (IFNs) are constitutively expressed and primes the local microenvironment at resting state. This priming mediates a more robust antiviral responses upon viral infection. Current evidence shows that the constitutively expressed type I IFNs are driven by the transcription factors nuclear factor kappa-light-chain-enhancer of activated B cells (NF-κB) and activating protein (AP)1. Infection induced type I IFNs are mediated by the transcription factor IFN regulatory factor (IRF)3. Increased production of type I IFNs restrict viral replication. This figure was created with BioRender.com.

in airway epithelial cells. Deeper elucidation is needed to decipher the exact mechanisms by which constitutive IFNs and ISGs are maintained, particularly the interactions amongst transcriptional factors such as IRFs, NF-κB, AP-1, and other factors.

Pathogenic IFNs

Type I and III IFNs have consistently been reported to inhibit IAV viral replication in both *in vitro* (Hsu et al., 2011), *in vivo* animal models (Mordstein et al., 2008; Davidson et al., 2015), and human clinical trials (Bennett et al., 2013). However, the same protective force appears to be detrimental in severe SARS-CoV infections. Longitudinal studies revealed that while most patients with SARS-CoV infection had early IFN expression and the disease was resolved as the SARS-CoV-specific antibodies increased, those with severe diseases had initially delayed but later persistent IFN responses that were associated with reduced levels of SARS-CoV-specific antibodies and poor clinical outcomes (Cameron et al., 2007). Similarly, patients with mild-to-moderate COVID-19 also showed early IFN responses (Galani et al., 2021) (**Figure 3A**), and those with severe diseases and those deceased had increased and prolonged IFN expressions in the blood (Lucas et al., 2020) (**Figure 3B**). Interestingly, human seasonal CoV OC43 has also been shown to induce a delayed but productive viral replication with minimal type I and III IFNs as well as ISGs expressions in differentiated human primary bronchial epithelial cell model (Loo et al., 2020). The same pathological roles of IFNs have also been recapitulated in *in vivo* models. Infection with SARS-CoV or with SARS-CoV-2 showed delayed but enhanced levels of type I IFN expressions (after peak viral replication) and increased infiltration of inflammatory cytokines and macrophages, vascular leakage, and increased disease severity (Channappanavar et al., 2016; Bessiere et al., 2021). Prophylactic IFN-α treatment (1 day before infection) or early treatment post infection (1 day post inoculation) in experimental SARS-CoV-2 infection in hamster led to reduced mortality. Late IFN-α treatment (3 days post inoculation) had no protective effects (Bessiere et al., 2021) (**Figure 3C**). The protracted type I and possibly type III IFNs may be a common innate immunological feature in beta-CoV infections (including OC43 and SARS-CoVs), and this may be driven by continuous stimulation of ISG expressions. ISGs including STATs, RLRs, and IRFs further amplify type I IFN productions, which increases the recruitment and activation of immune cells into the lung. IFN-β-treated, and SARS-CoV-infected mice showed increased infiltration of macrophages in the lung compared with non-IFN treated and infected group, and IFN-β-mediated pathogenesis was reduced when monocytes were depleted (Channappanavar et al., 2016).

Possible Pathogenic Mechanisms by Late IFN Productions

Severe SARS-CoV-2 infection has been characterized with high levels of circulating mitochondrial (mt)DNA in the peripheral blood (Scozzi et al., 2021), strongly indicating compromised mitochondrial membrane integrity and function. mtDNAs stimulate the productions of type I IFNs expressions *via* cGAS-cGAMP-mediated STING pathway (Yang et al., 2018; Yu et al., 2020). Viral RNAs and host mtDNAs may likely trigger excessive expression of type I and III IFNs (**Table 1**).

In addition to enhanced clearance of virus-infected epithelial cells by macrophages and NK cells, exaggerated IFN levels may directly instigate sudden epithelial death. IAV infections have been shown to induce epithelial cell necroptosis (Shubina et al.,

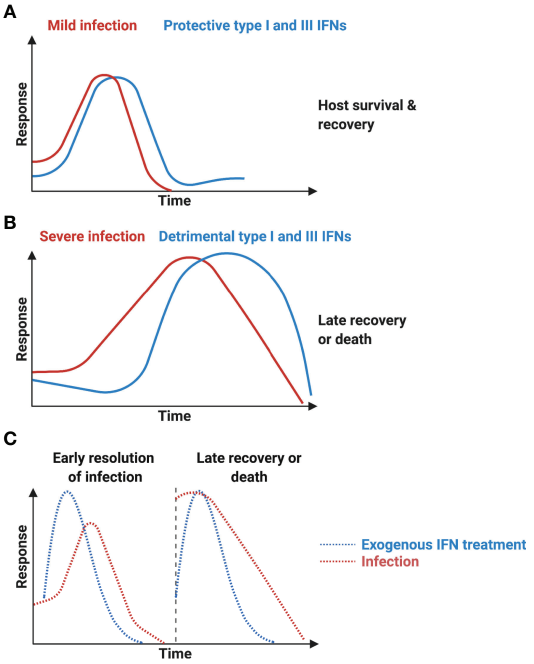

FIGURE 3 | Protective interferons and interferonopathy. **(A)** Mild SARS-CoV infection is associated with early productions of type I interferons (IFNs) and resolution of viral infection. **(B)** Severe infection is accompanied with delayed but sustained type I IFN expressions and is associated with more severe diseases with increased mortality. **(C)** Early exogenous type I IFN treatment results in early resolution of COVID-19, whereas late treatment fails to show protective effects. This figure was created with BioRender.com.

2020), and constitutive type I IFNs have recently been implicated in the induction of necroptosis *via* a key effector Mixed Lineage Kinase Domain Like Pseudokinase (MLKL) (Sarhan et al., 2019). ISGs including PKR, 2'5'A oligoadenylate synthetase (OAS), TNF-alpha related apoptosis inducing ligand (TRAIL), and galectin 9 have also been implicated in apoptosis induction (Chawla-Sarkar et al., 2003; Haw et al., 2016). While the exact ISGs and mechanisms that participate in IFN-mediated pathogenesis require further investigation, these signals enable an extensive suicidal response that clears virus-infected cells but at the expense of lung tissue integrity.

This late persistent IFN signature appears to be unique to severe COVID-19 and have not been observed with severe IAV infections (Wong et al., 2018; Turianova et al., 2019). This "interferonopathy" in COVID-19 may not be solely driven by type I IFNs. Type I and III IFNs have distinct homology and receptor utilisation but appear to induce similar ISG profiles (Kotenko et al., 2003; Sheppard et al., 2003; Prokunina-Olsson et al., 2013). While their functional differences and redundancies remain to be further defined, type I IFN-β has been reported to mediate acute ISG signatures, while type III IFN-λ induced more sustained ISG responses (Levy et al., 2011; Lin et al., 2016). IFN-λ has also been shown to be the primary effector of the antiviral defences against viral infection at the musical barrier such as the gastrointestinal tract (Pott et al., 2011; Li et al., 2019). Surprisingly, IFN-λ4, a member of the type III IFNs, was recently demonstrated to be expressed but mostly retained intracellularly in HCV and Sendai virus infection, instead of

TABLE 1 | Protective early IFNs and late pathogenic IFNs in severe COVID-19.

IFN timing	Early IFNs	Late IFNs
Role	**Protective**	**Pathogenic**
Mechanisms	O Viral RNA stimulation of IFNs and ISGs O Early IFN- and ISG-mediated inhibition of virus replication O Minimal removal of virus-infected epithelial cells by macrophages and NK cells O Increased specific antibody levels	O Viral RNA and mitochondrial RNA stimulation of IFNs and ISGs O Excessive IFN- and ISG-induced cell death O ER-retained IFN-λ4, ER stress, and UPR-induced cell death

IFN production induced by viral RNAs early in infection results in successful restriction of viral replication and elimination of virus-infected cells within the airways. Late IFN inductions observed in severe COVID-19 may be the result of viral RNAs and mitochondrial (mt)DNAs released from damaged mitochondrial during infection. Enhanced expressions of IFNs, mitochondrial dysfunction and ER stress and unfolded protein response (UPR) then lead to excessive cell death.

being secreted like other IFNs (Obajemu et al., 2017; Onabajo et al., 2021). Intracellular IFN-λ4 caused endoplasmic reticulum (ER) stress and the associated unfolded protein response (UPR), indicating that the translated IFN-λ4 were likely misfolded, and that the prolonged ER stress and UPR could lead to apoptotic death and tissue damage. It remains to be defined if IAV and CoV infections also cause accumulation of misfolded IFN-λ4, albeit ER stress and UPR has been demonstrated in SARS-CoV-2 infection (Koseler et al., 2020; Pathinayake et al., 2020; Bartolini et al., 2022).

The timing and magnitudes of IFN inductions, as well as the mechanisms of action of ISGs is therefore crucial in determining the molecular equipoise of protective and pathogenic IFNs. While the precise mechanisms require further investigation, it is tempting to speculate that IFN-mediated pathogenesis in COVID-19 is also attributed to viral factors.

Counterstrike by the IAVs and SARS-CoVs

Both IAVs and CoVs encode virulence factors that subvert host innate antiviral systems. IAV produces non-structural (NS)1 and polymerase basic (PB)1-F2 proteins that target multiple components of the IFN system (Hsu, 2018). NS1 is a small multifunctional protein that provides stealth within the cells and impairs the host antiviral responses. The RNA-binding domain of the NS1 recognises and shields viral nucleic acids from the host PRR system (Hatada and Fukuda, 1992; Qian et al., 1995; Chien et al., 2004). The non-structured effector domain stabilizes the RNA-binding domain but also interacts and interferes with host proteins including RIPLET, TRIM25, and PKR (**Figure 4**). RIPLET and TRIM25 facilitates activation of RIG-I and NS1 directly binds with these adaptors and inhibits RIG-I-mediated type I and III IFN expression (Wang et al., 2002; Bornholdt and Prasad, 2008; Rajsbaum et al., 2012). NS1 also impedes PKR from binding to viral RNAs and prevents PKR-mediated apoptosis. NS1 inhibits viral RNA recognition by PKR *via* the NS1 RNA-binding domain, and also directly interacts with PKR and suppresses PKR-mediated apoptosis through its effector domain (Bergmann et al., 2000; Dauber et al., 2006; Li et al., 2006; Min et al., 2007). Host PI3K signalling pathway is an important modulator of cellular proliferation and apoptosis. IAV has been shown to utilize this pathway as an alternative entry into cells in addition to the sialic acid residues-bearing glycoproteins (Hsu et al., 2011; Hsu et al., 2015). NS1 effector domain directly interacts with PI3K subunit p85β, further enhancing the rate of virus internalization, and this interaction also led to inhibition of PI3K-induced apoptosis (Hale et al., 2006; Shin et al., 2007; Li et al., 2008; Kedzierski et al., 2017). In addition to subverting host antiviral responses, NS1 also stalls

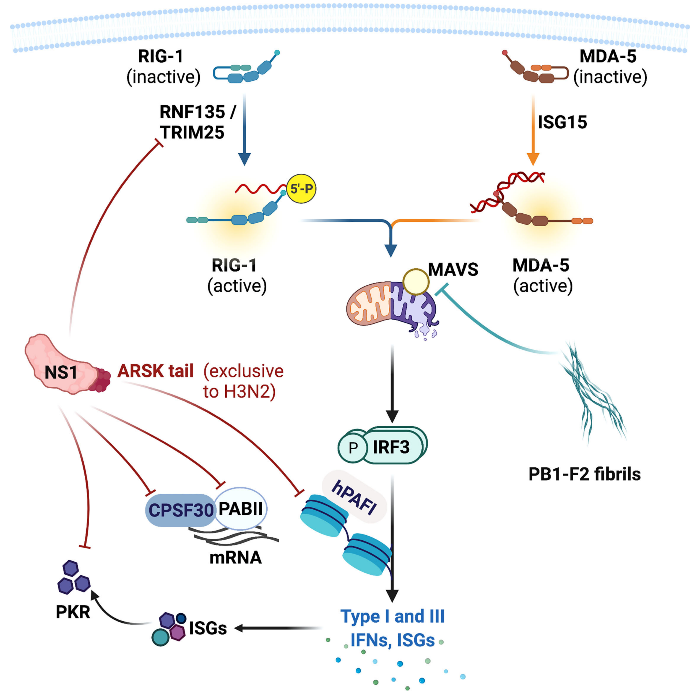

FIGURE 4 | Influenza A virus virulence factors and their targets in the host. Influenza A viruses produce non-structural (NS)1 and polymerase basic 1 (PB1)-F2 proteins that inhibit host antiviral signalling and responses. NS1 protein impairs the production of type I and III IFNs by directly targeting RIG-I activators RIPLET and TRIM25, and many IFN-stimulated genes (ISGs) including protein kinase R (PKR). NS1 also inhibits host protein synthesis by targeting pre-mRNA cleavage and polyadenylation specificity factor 30 (CPSF30) and poly A binding II (PABII) proteins. NS1 also possesses a ARSK tail that inhibits human polymerase II-associated factor 1 (hPAFI) function and host protein transcription. PB1-F2 forms a fibrillar higher-molecular weight aggregate that mainly targets mitochondria and its proteins. PB1-F2 binds with mitochondrial antiviral (MAVS) protein and other mitochondrial membrane proteins, leading to inhibition of type I and III IFN productions and mitochondrial dysfunction. This also results in apoptotic cell death. This figure was created with BioRender.com.

host mRNA processing. NS1 binds with the pre-mRNA cleavage and polyadenylation specificity factor 30 (CPSF30) and poly A binding II (PABII) proteins, shutting down the host protein synthesis during infection (Nemeroff et al., 1998; Chen et al., 1999; Noah et al., 2003) (**Figure 4**).

Human H3N2 NS1 possesses a Ala-Arg-Ser-Lys (ARSK) tail at the carboxyl terminus (amino acid residues 226 – 229), which is analogous to the ART(Thr)K motif found on the lysine 4 of histone H3 (H3K4) in the host cell nucleus (Marazzi et al., 2012). Like H3K4 ARTK, NS1 ARSK tail acts as a molecular mimic that directly interacts with human polymerase II-associated factor 1 (hPAFI) and inhibits host protein synthesis (**Figure 4**). Interestingly, this ARSK tail is exclusively found in the human H3N2 and appears to be lost in other IAV subtypes, including highly pathogenic viruses H5N1, H7N9, and the pandemic H1N1 2009. The reason for this loss of a seemingly beneficial motif in other subtypes remains a mystery.

PB1-F2 is an accessory protein translated from an alternative open reading frame of PB1. PB1-F2 promotes inflammatory cytokine storm during IAV infection (McAuley et al., 2013) and also modulate antiviral responses. PB1-F2 contains a carboxyl-terminal mitochondrial targeting sequence and directly binds with MAVS and disrupts RIG-I docking (Varga et al., 2011; Varga et al., 2012) (**Figure 5A**). PB1-F2 also targets inner and outer mitochondrial membrane transport proteins adenine nucleotide translocator 3 (ANT3) and voltage-dependent anion channel 1 (VDAC1), impairing mitochondrial membrane integrity and inducing apoptosis (Yoshizumi et al., 2014). Remarkably PB1-F2 has been shown to form a fibrillar aggregate structure that is dependent on the α-helical oligomerization domain at the carboxyl-terminus. This amyloid-like fibres have been hypothesized to form membrane pores, indicating that the PB1-F2 fibrillar structure may directly impair mitochondrial function (Chanturiya et al., 2004; Bruns et al., 2007; McAuley et al., 2013). Indeed, PB1-F2 has been demonstrated to translocate into the innate mitochondrial space *via* mitochondrial import receptor TOM40 protein (Yoshizumi et al., 2014), and avian IAV H7N9 PB1-F2 enhanced production of mitochondrial reactive oxygen species and calcium efflux, leading to mitochondrial dysfunction, inflammation and apoptosis (Pinar et al., 2017). Interestingly, full length PB1-F2 is mostly expressed by the highly pathogenic viruses including H5N1 and 1918 H1N1, as well as the human seasonal H3N2 virus. In contrast most seasonal H1N1 viruses express PB1-F2 without the carboxyl-terminus, which did not translocate into mitochondrial membrane (Yoshizumi et al., 2014). The truncated PB1-F2 of the 2009 pandemic H1N1 is thought to contribute to the reduced severity of the 2009 pandemic H1N1. This then raises an interesting question. Have the PB1-F2 of seasonal human IAVs lost all of its IFN antagonistic, inflammation- and death-inducing capabilities and what evolutionary advantages do this loss serve for the IAVs that adapt in humans? What does the truncated PB1-F2 do in the host cells? It is possible that PB1-F2 progressively loses the

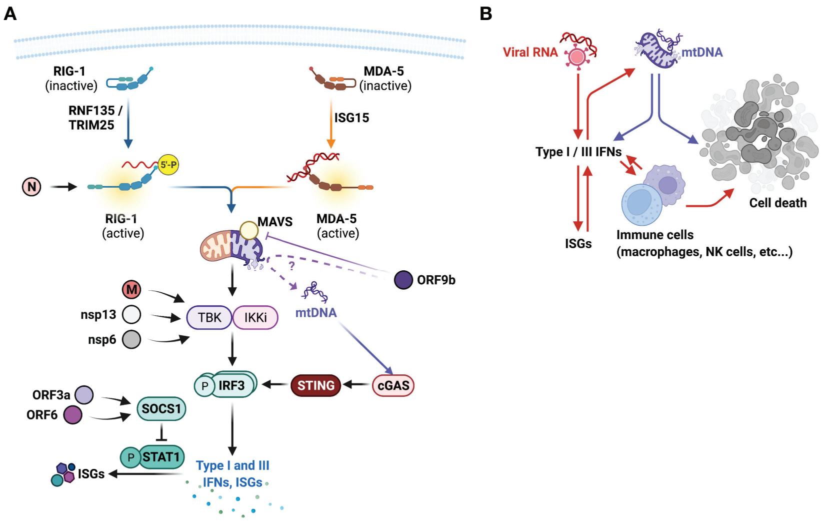

FIGURE 5 | SARS-CoV virulence factors, their targets in the host and type I interferonopathies. **(A)** SARS-CoVs encode numerous viral factors that directly reduce the hosts antiviral responses. Nucleocapsid (N) protein inhibits RIG-I activation, matrix (M), non-structural protein (nsp)13, and nsp6 impairs TANK binding kinase (TBK1) activation, thus impairing the production of type I and III IFN expressions. Open-reading frame (ORF)3a and ORF6 targets suppressor of cytokine signalling (SOCS)1 that negatively regulates signal transducer and activator of transcription (STAT)1 activation. ORF9b inhibits MAVS activity, suppressing RIG-I signal transduction. Does ORF9b compromise mitochondrial membrane integrity and promote mitochondrial (mt)DNAs escape? mtDNAs further drive the production of type I IFNs *via* cytoplasmic DNA sensor cGAS and STING and contribute to the type I interferonopathies observed in severe COVID-19. **(B)** Type I interferonopathies is initially facilitated by viral RNAs that induce the expression of type I and III IFNs and IFN-stimulated genes (ISGs), which further promote the productions of these IFNs. Excessive IFNs also promote the recruitment and activation of innate immune cells including macrophages and natural killer (NK) cells that destroy virus-infected epithelial cells. Intrinsically viral proteins cause mitochondrial membrane rupture, leading to the release of mtDNAs that not only further promote IFN productions, but also cell death. This figure was created with BioRender.com.

carboxyl-terminus as newly emerged viruses adapt in human, evolving into variants that replicate efficiently in human hosts without extensive apoptosis.

There also appears to be two opposing signals by the two most important IAV virulence factors, NS1 (anti-apoptotic) and PB1-F2 (pro-apoptotic). The molecular equipoise of apoptosis is currently unknown, although for human viruses the lost PB1-F2 carboxyl-terminus may indicate a more anti-apoptotic signals for the host cells. An inefficient virus kills it host, and a clever virus stays with it.

For SARS-CoVs, despite the protracted type I IFN signatures observed in severe COVID-19, SARS-CoVs express numerous molecules that inhibit host antiviral responses. Recent *in vitro* screening assays have indicated several SARS-CoV-2 factors that appeared to modulate host IFN responses, including structural N and M proteins, open reading frames (ORFs) 3a, 6, 7b, and 9b, and non-structural proteins (nsp) 1, 6, and 13 (Lei et al., 2020; Xia et al., 2020) (**Figure 5A**). Ectopically expressed SARS-CoV-2 N protein has been shown to bind and impede RIG-I-mediated IFN responses upon sendai virus infection (Chen et al., 2020). Whether this indicates SARS-CoV-2 viral RNA recognition by RIG-I require further investigation, but this demonstrates an interesting targeting choice by the N protein, and may indicate non-viral RNA binding functions of RIG-I.

M protein, nsp6 and nsp13 has been shown to directly interfere with TBK1 activation and inhibit IRF3 activation and IFN productions (Xia et al., 2020; Sui et al., 2021; Sui et al., 2022). ORF3a and ORF6 inhibits type I IFN responses by upregulating the suppressor of cytokine signalling (SOCS) 1 expression, a negative regulator of signal transducer and activator of transcription (STAT) 1 activation (Lei et al., 2020; Wang et al., 2021) (**Figure 5A**). ORF9b has been shown to localize to the mitochondria and impair type I IFN productions *via* its interactions with MAVS and TOM70 (Shi et al., 2014; Bojkova et al., 2020; Jiang et al., 2020). This may thus explain the presence of high circulating mtDNAs in those with severe COVID-19 (Scozzi et al., 2021) and COVID-19 interferonopathies (**Figure 5A**).

It is remarkable for SARS-CoVs to encode multiple IFN-antagonistic factors, could this, along with higher levels of initial exposure to virus and viral replication, explain the delayed type I IFN and type III IFN responses in those with severe COVID-19? Expression of these viral antagonistic factors in the early phase of infection restricts early IFN responses and maximize viral replication, whilst eliciting strong pro-inflammatory responses in the airways. High levels of viral RNAs and mtDNAs from damaged mitochondria then continuously drive excessive production of IFNs, which potentially become self-sustained through positive feed-back loops (**Figure 5B**). Integrated spatial and temporal transcriptomic, proteomic, and interactomic analyses of viral and host proteins will thus provide critical insights in the dynamic expressions and interactions of viral proteins and host antiviral responses, and to reveal optimal intervention strategies.

CONCLUDING PERSPECTIVES

The arms race between the host and the virus dictates the outcomes of the infection. While advanced genetic screening technologies have accelerated the discovery of host intrinsic restriction factors involved in host antiviral immunity and viral infection, their detailed molecular mechanisms of actions require further investigation. This includes constitutive IFN revving-up system and how they are produced and maintained at the mucosal sites and the transcription mechanisms involved. Are they constitutively expressed at low levels and released or are they stored within the cells such as IFN-λ4 in the ER? Despite the shared Jak-STAT pathway activated by type I and III IFNs, how are they differentially and transcriptionally tuned and whether they induce unique ISG signatures also deserve further clarification. These are fundamental but underexplored areas in innate antiviral immunity, identifying the diversity and functional insights into IFN and ISG biology will provide a wealth of advances in conserved and novel mechanisms of protection from viral pathogens.

Furthermore, there are many important but unanswered questions central to the inception of interferonopathies. This includes the identities of the stimulating moieties (viral RNAs, self-DNAs (mtDNAs), and/or other unidentified molecules) that induce exaggerated type I and perhaps type III IFNs, their signalling kinetics and specific ISG repertoires and precise mechanisms that control viral infection or drive interferonopathies.

The continuous viral mutations give the viruses a huge evolutionary advantage in subverting host innate antiviral systems for survival. IAVs and SARS-CoVs virulence factors strategically compromise key PRR and IFN signalling transduction, host gene transcription, as well as ISG effector functions. As more intrinsic antiviral and cell biological factors are continually being characterised, more of which have been shown to be targeted by viral virulence factors. It is critical that we understand the full spectrum of interacting partners of the IAV and CoV virulence factors and the mutations that render the viruses more infectious or virulent. This may contribute to the surveillance of not just emerging viruses but also their virulence potentials in human.

As we head into the third year of the COVID-19 pandemic and eased restrictions, SARS-CoV-2 is likely to become epidemic and co-circulate with seasonal IAVs in the community. Several studies have reported incidences of IAV and SARS-CoV-2 co-infection amongst those recovered from severe COVID-19 and in those deceased (Wang D et al., 2020; Khodamoradi et al., 2020; Konala et al., 2020; Wu et al., 2020; Cuadrado-Payan et al., 2020; Khorramdelazad et al., 2021). Whether and how co-infection leads to worsened clinical outcomes need to be elucidated, although a recent study showed IAV and SARS-CoV-2 co-infection was significantly associated with increased risk of death (Swets et al., 2022). More importantly, IAV infection has also been shown to increase angiotensin-converting enzyme (ACE)2 expression, the host surface receptor required for SARS-CoV-2 entry into host cells, which may lead to enhanced diseases (Schweitzer et al., 2021). Is SARS-influenza or "flurona" winter coming or is it here already?

It is also important to understand how inborn error of type I IFN signalling impacts overall antiviral responses in severe viral infections and immune-targeted therapeutics such as inhaled IFN-β (Djukanović et al., 2014). In particular, autosomalrecessive deficiencies in *IRF7* and *IFNAR1* and autosomal-dominant deficiencies in *TLR3*, *TBK1*, *IRF3*, *IRF7*, *IFNAR1* and *IFNAR2* genes have been found in a small percentage of patients with severe influenza and COVID-19 (Ciancanelli et al., 2015; Lim et al., 2019; Thomsen et al., 2019). This indicates that not all would benefit from IFN treatment and alternative immune-targeting therapeutic options need to be developed. Regardless, emerging respiratory infectious viruses will always pose a threat to human and our way of life, we need to continually invest in and support research in virology, immunology, and therapeutic strategies before the next pandemic occurs.

In summary, there has been a major explosion of knowledge in PRRs and IFNs, and this will provide important understandings in critical antiviral elements in controlling viral infection. We look forward to further exciting fundamental discoveries and translational research, and how these fields might develop into potential therapeutics against emerging respiratory infectious viruses in the future.

AUTHOR CONTRIBUTIONS

A-YH conceptualized and wrote the manuscript with GW, YG, CW, and FW. All authors contributed to the article and approved the submitted version.

REFERENCES

Al-Sadi, R., Guo, S., Ye, D., Dokladny, K., Alhmoud, T., Ereifej, L., et al. (2013). Mechanism of IL-1beta Modulation of Intestinal Epithelial Barrier Involves P38 Kinase and Activating Transcription Factor-2 Activation. *J. Immunol.* 190 (12), 6596–6606. doi: 10.4049/jimmunol.1201876

Australian Government, D.o.H (2017). *Australian Influenza Surveillance Report and Activity Updates*. (Victoria, Australia: D.o. Health)

Balachandran, S., and Beg, A. A. (2011). Defining Emerging Roles for NF-kappaB in Antivirus Responses: Revisiting the Interferon-Beta Enhanceosome Paradigm. *PLoS Pathog.* 7 (10), e1002165. doi: 10.1371/journal.ppat.1002165

Bartolini, D., Stabile, A. M., Vacca, C., Pistilli, A., Rende, M., Gioiello, A., et al. (2022). Endoplasmic Reticulum Stress and NF-kB Activation in SARS-CoV-2 Infected Cells and Their Response to Antiviral Therapy. *IUBMB Life* 74 (1), 93–100. doi: 10.1002/iub.2537

Basagoudanavar, S. H., Thapa, R. J., Nogusa, S., Wang, J., Beg, A. A., and Balachandran, S. (2011). Distinct Roles for the NF-Kappa B RelA Subunit During Antiviral Innate Immune Responses. *J. Virol.* 85 (6), 2599–610. doi: 10.1128/JVI.02213-10

Bennett, A. L., Smith, D. W., Cummins, M. J., Jacoby, P. A., Cummins, J. M., and Beilharz, M. W. (2013). Low-Dose Oral Interferon Alpha as Prophylaxis Against Viral Respiratory Illness: A Double-Blind, Parallel Controlled Trial During an Influenza Pandemic Year. *Influenza Other Respir. Viruses* 7 (5), 854–862. doi: 10.1111/irv.12094

Bergmann, M., Garcia-Sastre, A., Carnero, E., Pehamberger, H., Wolff, K., Palese, P., et al. (2000). Influenza Virus NS1 Protein Counteracts PKR-Mediated Inhibition of Replication. *J. Virol.* 74 (13), 6203–6. doi: 10.1128/JVI.74.13.6203-6206.2000

Bessiere, P., Wasniewski, M., Picard-Meyer, E., Servat, A., Figueroa, T., Foret-Lucas, C., et al. (2021). Intranasal Type I Interferon Treatment is Beneficial Only When Administered Before Clinical Signs Onset in the SARS-CoV-2 Hamster Model. *PLoS Pathog.* 17 (8), e1009427. doi: 10.1371/journal.ppat.1009427

Biron, C. A., Nguyen, K. B., Pien, G. C., Cousens, L. P., and Salazar-Mather, T. P. (1999). Natural Killer Cells in Antiviral Defense: Function and Regulation by Innate Cytokines. *Annu. Rev. Immunol.* 17, 189–220. doi: 10.1146/annurev.immunol.17.1.189

Bojkova, D., Klann, K., Koch, B., Widera, M., Krause, D., Ciesek, S., et al. (2020). Proteomics of SARS-CoV-2-Infected Host Cells Reveals Therapy Targets. *Nature* 583 (7816), 469–472. doi: 10.1038/s41586- 020-233207

Bornholdt, Z. A., and Prasad, B. V. (2008). X-Ray Structure of NS1 From a Highly Pathogenic H5N1 Influenza Virus. *Nature* 456 (7224), 985–8. doi: 10.1038/nature07444

Brass, A. L., Huang, I. C., Benita, Y., John, S. P., Krishnan, M. N., Feeley, E. M., et al. (2009). The IFITM Proteins Mediate Cellular Resistance to Influenza A H1N1 Virus, West Nile Virus, and Dengue Virus. *Cell* 139 (7), 1243–54. doi: 10.1016/j.cell.2009.12.017

Brockhurst, M. A., Chapman, T., King, K. C., Mank, J. E., Paterson, S., and Hurst, G. D. (2014). Running With the Red Queen: The Role of Biotic Conflicts in Evolution. *Proc. Biol. Sci.* 281 (1797). doi: 10.1098/rspb.2014.1382

Bruns, K., Studtrucker, N., Sharma, A., Fossen, T., Mitzner, D., Eissmann, A., et al. (2007). Structural Characterization and Oligomerization of PB1-F2, a Proapoptotic Influenza A Virus Protein. *J. Biol. Chem.* 282 (1), 353–363. doi: 10.1074/jbc.M606494200

Cameron, M. J., Ran, L., Xu, L., Danesh, A., Bermejo-Martin, J. F., Cameron, C. M., et al. (2007). Interferon-Mediated Immunopathological Events are Associated With Atypical Innate and Adaptive Immune Responses in Patients With Severe Acute Respiratory Syndrome. *J. Virol.* 81 (16), 8692–8706. doi: 10.1128/JVI.00527-07

Channappanavar, R., Fehr, A. R., Vijay, R., Mack, M., Zhao, J., Meyerholz, D. K., et al. (2016). Dysregulated Type I Interferon and Inflammatory Monocyte-Macrophage Responses Cause Lethal Pneumonia in SARS-CoV-Infected Mice. *Cell Host Microbe* 19 (2), 181–193. doi: 10.1016/j.chom.2016.01.007

Chanturiya, A. N., Basanez, G., Schubert, U., Henklein, P., Yewdell, J. W., and Zimmerberg, J. (2004). PB1-F2, an Influenza A Virus-Encoded Proapoptotic Mitochondrial Protein, Creates Variably Sized Pores in Planar Lipid Membranes. *J. Virol.* 78 (12), 6304–12. doi: 10.1128/JVI.78.12.6304-6312.2004

Chawla-Sarkar, M., Lindner, D. J., Liu, Y. F., Williams, B. R., Sen, G. C., Silverman, R. H., et al. (2003). Apoptosis and Interferons: Role of Interferon-Stimulated Genes as Mediators of Apoptosis. *Apoptosis* 8 (3), 237–249. doi: 10.1023/A:1023668705040

Chen, K., Xiao, F., Hu, D., Ge, W., Tian, M., Wang, W., et al. (2020). SARS-CoV-2 Nucleocapsid Protein Interacts With RIG-I and Represses RIG-Mediated IFN-Beta Production. *Viruses* 13 (1), 47. doi: 10.3390/v13010047

Chen, Z., Li, Y., and Krug, R. M. (1999). Influenza A Virus NS1 Protein Targets Poly(A)-Binding Protein II of the Cellular 3'-End Processing Machinery. *EMBO J.* 18 (8), 2273–83. doi: 10.1093/emboj/18.8.2273

Chien, C. Y., Xu, Y., Xiao, R., Aramini, J. M., Sahasrabudhe, P. V., Krug, R. M., et al. (2004). Biophysical Characterization of the Complex Between Double-Stranded RNA and the N-Terminal Domain of the NS1 Protein From Influenza A Virus: Evidence for a Novel RNA-Binding Mode. *Biochemistry* 43 (7), 1950–62. doi: 10.1021/bi030176o

Chotpitayasunondh, T., Ungchusak, K., Hanshaoworakul, W., Chunsuthiwat, S., Sawanpanyalert, P., Kijphati, R., et al. (2005). Human Disease From Influenza A (H5N1), Thailand, 2004. *Emerg. Infect. Dis.* 11 (2), 201–9. doi: 10.3201/eid1102.041061

Ciancanelli, M. J., Huang, S.X., Luthra, P., Garner, H., Itan, Y., Volpi, S., et al. (2015). Infectious Disease. Life-Threatening Influenza and Impaired Interferon Amplification in Human IRF7 Deficiency. *Science* 348 (6233), 448–453. doi: 10.1126/science.aaa1578

Compton, A. A., Roy, N., Porrot, F., Billet, A., Casartelli, N., Yount, J. S., et al. (2016). Natural Mutations in IFITM3 Modulate Post-Translational Regulation and Toggle Antiviral Specificity. *EMBO Rep.* 17 (11), 1657–1671. doi: 10.15252/embr.201642771

Cuadrado-Payan, E., Montagud-Marrahi, E., Torres-Elorza, M., Bodro, M., Blasco, M., Poch, E., et al. (2020). SARS-CoV-2 and Influenza Virus Co-Infection. *Lancet* 395 (10236), e84. doi: 10.1016/S0140-6736(20)31052-7

Dauber, B., Schneider, J., and Wolff, T. (2006). Double-Stranded RNA Binding of Influenza B Virus Nonstructural NS1 Protein Inhibits Protein Kinase R But is Not Essential to Antagonize Production of Alpha/Beta Interferon. *J. Virol.* 80 (23), 11667–77. doi: 10.1128/JVI.01142-06

Davidson, S., Maini, M. K., and Wack, A. (2015). Disease-Promoting Effects of Type I Interferons in Viral, Bacterial, and Coinfections. *J. Interferon Cytokine Res.* 35 (4), 252–264. doi: 10.1089/jir.2014.0227

Djukanović, R., Harrison, T., Johnston, S. L., Gabbay, F., Wark, P., Thomson, N. C., et al. (2014). The Effect of Inhaled IFN-β on Worsening of Asthma Symptoms Caused by Viral Infections. A Randomized Trial. *Am. J. Respir. Crit. Care Med.* 190 (2), 145–154. doi: 10.1164/rccm.201312-2235OC

Feeley, E. M., Sims, J. S., John, S. P., Chin, C. R., Pertel, T., Chen, L. M., et al. (2011). IFITM3 Inhibits Influenza A Virus Infection by Preventing Cytosolic Entry. *PLoS Pathog.* 7 (10), e1002337. doi: 10.1371/journal.ppat.1002337

Fitzgerald, K. A., McWhirter, S. M., Faia, K. L., Rowe, D. C., Latz, E., Golenbock, D. T., et al. (2003). IKKepsilon and TBK1 are Essential Components of the IRF3 Signaling Pathway. *Nat. Immunol.* 4 (5), 491–6. doi: 10.1038/ni921

Fuller-Pace, F. V. (2006). DExD/H Box RNA Helicases: Multifunctional Proteins With Important Roles in Transcriptional Regulation. *Nucleic Acids Res.* 34 (15), 4206–15. doi: 10.1093/nar/gkl460

Gack, M. U., Shin, Y. C., Joo, C. H., Urano, T., Liang, C., Sun, L., et al. (2007). TRIM25 RING-Finger E3 Ubiquitin Ligase is Essential for RIG-I-Mediated Antiviral Activity. *Nature* 446 (7138), 916–20. doi: 10.1038/nature05732

Galani, I. E., Rovina, N., Lampropoulou, V., Triantafyllia, V., Manioudaki, M., Pavlos, E., et al. (2021). Untuned Antiviral Immunity in COVID-19 Revealed by Temporal Type I/III Interferon Patterns and Flu Comparison. *Nat. Immunol.* 22 (1), 32–40. doi: 10.1038/s41590-020-00840-x

Gough, D. J., Messina, N. L., Hii, L., Gould, J. A., Sabapathy, K., Robertson, A. P., et al. (2010). Functional Crosstalk Between Type I and II Interferon Through the Regulated Expression of STAT1. *PLoS Biol.* 8 (4), e1000361. doi: 10.1371/journal.pbio.1000361

Gu, Y., Hsu, A. C., Pang, Z., Pan, H., Zuo, X., Wang, G., et al. (2019). Role of the Innate Cytokine Storm Induced by the Influenza A Virus. *Viral Immunol.* 32 (6), 244–51. doi: 10.1089/vim.2019.0032

Hale, B. G., Jackson, D., Chen, Y. H., Lamb, R. A., and Randall, R. E. (2006). Influenza A Virus NS1 Protein Binds P85beta and Activates Phosphatidylinositol-3-Kinase Signaling. *Proc. Natl. Acad. Sci. U.S.A.* 103 (38), 14194–9. doi: 10.1073/pnas.0606109103

Hatada, E., and Fukuda, R. (1992). Binding of Influenza A Virus NS1 Protein to dsRNA *In Vitro*. *J. Gen. Virol.* 73 (Pt 12), 3325–29. doi: 10.1099/0022-1317-73-12-3325

Hata, N., Sato, M., Takaoka, A., Asagiri, M., Tanaka, N., Taniguchi, T., et al. (2001). Constitutive IFN-Alpha/Beta Signal for Efficient IFN-Alpha/Beta Gene Induction by Virus. *Biochem. Biophys. Res. Commun.* 285 (2), 518–525. doi: 10.1006/bbrc.2001.5159

Haw, T. J., Starkey, M. R., Nair, P. M., Pavlidis, S., Liu, G., Nguyen, D. H., et al. (2016). A Pathogenic Role for Tumor Necrosis Factor-Related Apoptosis-Inducing Ligand in Chronic Obstructive Pulmonary Disease. *Mucosal Immunol.* 9 (4), 859–72. doi: 10.1038/mi.2015.111

Hayman, T. J., Hsu, A. C., Kolesnik, T. B., Dagley, L. F., Willemsen, J., Tate, M. D., et al. (2019). RIPLET, and Not TRIM25, is Required for Endogenous RIG-I-Dependent Antiviral Responses. *Immunol. Cell Biol.* 97 (9), 840–52. doi: 10.1111/imcb.12284

Hsu, A. C. (2018). Influenza Virus: A Master Tactician in Innate Immune Evasion and Novel Therapeutic Interventions. *Front. Immunol.* 9 (743), 743. doi: 10.3389/fimmu.2018.00743

Hsu, A. C. Y., Barr, I., Hansbro, P. M., and Wark, P. A. (2011). Human Influenza Is More Effective Than Avian Influenza at Antiviral Suppression in Airway Cells. *Am. J. Respir. Cell Mol. Biol.* 44 (6), 906–913. doi: 10.1165/rcmb.2010-0157OC

Hsu, A. C., Parsons, K., Barr, I., Lowther, S., Middleton, D., Hansbro, P. M., et al. (2012). Critical Role of Constitutive Type I Interferon Response in Bronchial Epithelial Cell to Influenza Infection. *PloS One* 7 (3), e32947. doi: 10.1371/journal.pone.0032947

Hsu, A. C., Starkey, M. R., Hanish, I., Parsons, K., Haw, T. J., Howland, L. J., et al. (2015). Targeting PI3K-P110alpha Suppresses Influenza Virus Infection in Chronic Obstructive Pulmonary Disease. *Am. J. Respir. Crit. Care Med.* 191 (9), 1012–1023. doi: 10.1164/rccm.201501-0188OC

Hsu, A. C., Parsons, K., Moheimani, F., Knight, D. A., Hansbro, P. M., Fujita, T., et al. (2016). Impaired Antiviral Stress Granule and IFN-Beta Enhanceosome Formation Enhances Susceptibility to Influenza Infection in Chronic Obstructive Pulmonary Disease Epithelium. *Am. J. Respir. Cell Mol. Biol.* 55 (1), 117–127. doi: 10.1165/rcmb.2015-0306OC

Hsu, A. C., Dua, K., Starkey, M. R., Haw, T. J., Nair, P. M., Nichol, K., et al. (2017). MicroRNA-125a and -B Inhibit A20 and MAVS to Promote Inflammation and Impair Antiviral Response in COPD. *JCI Insight* 2 (7), e90443. doi: 10.1172/jci.insight.90443

Huang, C., Wang, Y., Li, X., Ren, L., Zhao, J., Hu, Y., et al. (2020). Clinical Features of Patients Infected With 2019 Novel Coronavirus in Wuhan, China. *Lancet* 395 (10223), 497–506. doi: 10.1016/S0140-6736(20)30183-5

Ito, T., Suzuki, Y., Mitnaul, L., Vines, A., Kida, H., and Kawaoka, Y. (1997). Receptor Specificity of Influenza A Viruses Correlates With the Agglutination of Erythrocytes From Different Animal Species. *Virology* 227 (2), 493–499. doi: 10.1006/viro.1996.8323

Jiang, H. W., Zhang, H. N., Meng, Q. F., Xie, J., Li, Y., Chen, H., et al. (2020). SARS-CoV-2 Orf9b Suppresses Type I Interferon Responses by Targeting TOM70. *Cell Mol. Immunol.* 17 (9), 998–1000. doi: 10.1038/s41423-020-0514-8

Kedzierski, L., Tate, M. D., Hsu, A. C., Kolesnik, T. B., Linossi, E. M., Dagley, L., et al. (2017). Suppressor of Cytokine Signaling (SOCS)5 Ameliorates Influenza Infection *via* Inhibition of EGFR Signaling. *Elife* 6:e20444. doi: 10.7554/eLife.20444.025

Khodamoradi, Z., Moghadami, M., and Lotfi, M. (2020). Co-Infection of Coronavirus Disease 2019 and Influenza A: A Report From Iran. *Arch. Iran Med.* 23 (4), 239–43. doi: 10.34172/aim.2020.04

Khorramdelazad, H., Kazemi, M. H., Najafi, A., Keykhaee, M., Zolfaghari Emameh, R., and Falak, R (2021). Immunopathological Similarities Between COVID-19 and Influenza: Investigating the Consequences of Co-Infection. *Microb. Pathog.* 152, 104554. doi: 10.1016/j.micpath.2020.104554

Kimura, K., Morita, Y., Orita, T., Haruta, J., Takeji, Y., and Sonoda, K. H. (2013). Protection of Human Corneal Epithelial Cells From TNF-Alpha-Induced Disruption of Barrier Function by Rebamipide. *Invest. Ophthalmol. Vis. Sci.* 54 (4), 2572–2760.

Kimura, K., Teranishi, S., and Nishida, T. (2009). Interleukin-1beta-Induced Disruption of Barrier Function in Cultured Human Corneal Epithelial Cells. *Invest. Ophthalmol. Vis. Sci.* 50 (2), 597–603. doi: 10.1167/iovs.08-2606

Kolb, M., Margetts, P. J., Anthony, D. C., Pitossi, F., and Gauldie, J. (2001). Transient Expression of IL-1beta Induces Acute Lung Injury and Chronic Repair Leading to Pulmonary Fibrosis. *J. Clin. Invest.* 107 (12), 1529–36. doi: 10.1172/JCI12568

Konala, V. M., Adapa, S., Gayam, V., Naramala, S., Daggubati, S. R., Kammari, C. B., et al. (2020). Co-Infection With Influenza A and COVID-19. *Eur. J. Case Rep. Intern. Med.* 7 (5), 001656. doi: 10.12890/2020_001656

Koseler, A., Sabirli, R., Goren, T., Turkcuer, I., and Kurt, O. (2020). Endoplasmic Reticulum Stress Markers in SARS-COV-2 Infection and Pneumonia: Case-Control Study. *In Vivo* 34 (3 Suppl), 1645–1650. doi: 10.21873/invivo.11956

Kotenko, S. V., Gallagher, G., Baurin, V. V., Lewis-Antes, A., Shen, M., Shah, N. K., et al. (2003). IFN-Lambdas Mediate Antiviral Protection Through a Distinct Class II Cytokine Receptor Complex. *Nat. Immunol.* 4 (1), 69–77. doi: 10.1038/ni875

Lei, X., Dong, X., Ma, R., Wang, W., Xiao, X., Tian, Z., et al. (2020). Activation and Evasion of Type I Interferon Responses by SARS-CoV-2. *Nat. Commun.* 11 (1), 3810. doi: 10.1038/s41467-020-17665-9

Levy, D. E., Marie, I. J., and Durbin, J. E. (2011). Induction and Function of Type I and III Interferon in Response to Viral Infection. *Curr. Opin. Virol.* 1 (6), 476–86. doi: 10.1016/j.coviro.2011.11.001

Li, S., Min, J. Y., Krug, R. M., and Sen, G. C. (2006). Binding of the Influenza A Virus NS1 Protein to PKR Mediates the Inhibition of its Activation by Either PACT or Double-Stranded RNA. *Virology* 349 (1), 13–21. doi: 10.1016/j.virol.2006.01.005

Li, Y., Anderson, D. H., Liu, Q., and Zhou, Y. (2008). Mechanism of Influenza A Virus NS1 Protein Interaction With the P85beta, But Not the P85alpha, Subunit of Phosphatidylinositol 3-Kinase (PI3K) and Up-Regulation of PI3K Activity. *J. Biol. Chem.* 283 (34), 23397–409. doi: 10.1074/jbc.M802737200

Li, L., Xue, M., Fu, F., Yin, L., Feng, L., and Liu, P. (2019). IFN-Lambda 3 Mediates Antiviral Protection Against Porcine Epidemic Diarrhea Virus by Inducing a

Distinct Antiviral Transcript Profile in Porcine Intestinal Epithelia. *Front. Immunol.* 10, 2394. doi: 10.3389/fimmu.2019.02394

Li, H., Liu, L., Zhang, D., Xu, J., Dai, H., Tang, N., et al. (2020). SARS-CoV-2 and Viral Sepsis: Observations and Hypotheses. *Lancet* 395 (10235), 1517–20. doi: 10.1016/S0140-6736(20)30920-X

Lim, H. K., Huang, S. X. L., Chen, J., Kerner, G., Gilliaux, O., Bastard, P., et al. (2019). Severe Influenza Pneumonitis in Children With Inherited TLR3 Deficiency. *J. Exp. Med.* 216 (9), 2038–56. doi: 10.1084/jem.20181621

Lin, J. D., Feng, N., Sen, A., Balan, M., Tseng, H. C., McElrath, C., et al. (2016). Distinct Roles of Type I and Type III Interferons in Intestinal Immunity to Homologous and Heterologous Rotavirus Infections. *PLoS Pathog.* 12 (4), e1005600. doi: 10.1371/journal.ppat.1005600

Liu, S., Cai, X., Wu, J., Cong, Q., Chen, X., Li, T., et al. (2015). Phosphorylation of Innate Immune Adaptor Proteins MAVS, STING, and TRIF Induces IRF3 Activation. *Science* 347 (6227), aaa2630. doi: 10.1126/science.aaa2630

Liu, G., Lee, J. H., Parker, Z. M., Acharya, D., Chiang, J. J., van Gent, M., et al. (2021). ISG15-Dependent Activation of the Sensor MDA5 is Antagonized by the SARS-CoV-2 Papain-Like Protease to Evade Host Innate Immunity. *Nat. Microbiol.* 6 (4), 467–478. doi: 10.1038/s41564-021-00884-1

Loo, S. L., Wark, P. A. B., Esneau, C., Nichol, K. S., Hsu, A. C., and Bartlett, N. W. (2020). Human Coronaviruses 229E and OC43 Replicate and Induce Distinct Anti-Viral Responses in Differentiated Primary Human Bronchial Epithelial Cells. *Am. J. Physiol. Lung Cell Mol. Physiol.* 319(6):L926–L931. doi: 10.1152/ajplung.00374.2020

Lucas, C., Wong, P., Klein, J., Castro, T. B. R., Silva, J., Sundaram, M., et al. (2020). Longitudinal Analyses Reveal Immunological Misfiring in Severe COVID-19. *Nature* 584 (7821), 463–469. doi: 10.1038/s41586-020-2588-y

Mandelboim, O., Lieberman, N., Lev, M., Paul, L., Arnon, T. I., Bushkin, Y., et al. (2001). Recognition of Haemagglutinins on Virus-Infected Cells by NKp46 Activates Lysis by Human NK Cells. *Nature* 409 (6823), 1055–1060.

Marazzi, I., Ho, J. S., Kim, J., Manicassamy, B., Dewell, S., Albrecht, R. A., et al. (2012). Suppression of the Antiviral Response by an Influenza Histone Mimic. *Nature* 483 (7390), 428–433. doi: 10.1038/nature10892

Matrosovich, M. N., Matrosovich, T. Y., Gray, T., Roberts, N. A., and Klenk, H. D. (2004). Human and Avian Influenza Viruses Target Different Cell Types in Cultures of Human Airway Epithelium. *Proc. Natl. Acad. Sci. U.S.A.* 101 (13), 4620–24. doi: 10.1073/pnas.0308001101

McAuley, J. L., Tate, M. D., MacKenzie-Kludas, C. J., Pinar, A., Zeng, W., Stutz, A., et al. (2013). Activation of the NLRP3 Inflammasome by IAV Virulence Protein PB1-F2 Contributes to Severe Pathophysiology and Disease. *PLoS Pathog.* 9 (5), e1003392. doi: 10.1371/journal.ppat.1003392

McGonagle, D., Sharif, K., O'Regan, A., and Bridgewood, C. (2020). The Role of Cytokines Including Interleukin-6 in COVID-19 Induced Pneumonia and Macrophage Activation Syndrome-Like Disease. *Autoimmun Rev.*, 102537. doi: 10.1016/j.autrev.2020.102537

Mehta, P., McAuley, D. F., Brown, M., Sanchez, E., Tattersall, R. S., Manson, J. J., et al. (2020). COVID-19: Consider Cytokine Storm Syndromes and Immunosuppression. *Lancet* 395 (10229), 1033–1034. doi: 10.1016/S0140-6736(20)30628-0

Min, J. Y., Li, S., Sen, G. C., and Krug, R. M. (2007). A Site on the Influenza A Virus NS1 Protein Mediates Both Inhibition of PKR Activation and Temporal Regulation of Viral RNA Synthesis. *Virology* 363 (1), 236–43. doi: 10.1016/j.virol.2007.01.038

Mordstein, M., Kochs, G., Dumoutier, L., Renauld, J. C., Paludan, S. R., Klucher, K., et al. (2008). Interferon-Lambda Contributes to Innate Immunity of Mice Against Influenza A Virus But Not Against Hepatotropic Viruses. *PLoS Pathog.* 4 (9), e1000151. doi: 10.1371/journal.ppat.1000151

Nemeroff, M. E., Barabino, S. M., Li, Y., Keller, W., and Krug, R. M. (1998). Influenza Virus NS1 Protein Interacts With the Cellular 30 kDa Subunit of CPSF and Inhibits 3'end Formation of Cellular pre-mRNAs. *Mol. Cell* 1 (7), 991–1000. doi: 10.1016/S1097-2765(00)80099-4

Noah, D. L., Twu, K. Y., and Krug, R. M. (2003). Cellular Antiviral Responses Against Influenza A Virus are Countered at the Posttranscriptional Level by the Viral NS1A Protein *via* its Binding to a Cellular Protein Required for the 3' End Processing of Cellular pre-mRNAS. *Virology* 307 (2), 386–395. doi: 10.1016/S0042-6822(02)00127-7

Obajemu, A. A., Rao, N., Dilley, K. A., Vargas, J. M., Sheikh, F., Donnelly, R. P., et al. (2017). IFN-Lambda4 Attenuates Antiviral Responses by Enhancing Negative Regulation of IFN Signaling. *J. Immunol.* 199 (11), 3808–20. doi: 10.4049/jimmunol.1700807

Onabajo, O. O., Wang, F., Lee, M. H., Florez-Vargas, O., Obajemu, A., Tanikawa, C., et al. (2021). Intracellular Accumulation of IFN-Lambda4 Induces ER Stress and Results in Anti-Cirrhotic But Pro-HCV Effects. *Front. Immunol.* 12, 692263. doi: 10.3389/fimmu.2021.692263

Pathinayake, P. S., Hsu, A. C., and Wark, P. A. B. (2020). PAT in the ER for Transmembrane Protein Folding. *Trends Biochem. Sci.* 45 (12), 1007–8. doi: 10.1016/j.tibs.2020.10.001

Paules, C. I., Sullivan, S. G., Subbarao, K., and Fauci, A. S. (2018). Chasing Seasonal Influenza - The Need for a Universal Influenza Vaccine. *N Engl. J. Med.* 378 (1), 7–9. doi: 10.1056/NEJMp1714916

Paz, S., Vilasco, M., Werden, S. J., Arguello, M., Joseph-Pillai, D., Zhao, T., et al. (2011). A Functional C-Terminal TRAF3-Binding Site in MAVS Participates in Positive and Negative Regulation of the IFN Antiviral Response. *Cell Res.* 21 (6), 895–910. doi: 10.1038/cr.2011.2

Pinar, A., Dowling, J. K., Bitto, N. J., Robertson, A. A., Latz, E., Stewart, C. R., et al. (2017). PB1-F2 Peptide Derived From Avian Influenza A Virus H7N9 Induces Inflammation *via* Activation of the NLRP3 Inflammasome. *J. Biol. Chem.* 292 (3), 826–36. doi: 10.1074/jbc.M116.756379

Pott, J., Mahlakoiv, T., Mordstein, M., Duerr, C. U., Michiels, T., Stockinger, S., et al. (2011). IFN-Lambda Determines the Intestinal Epithelial Antiviral Host Defense. *Proc. Natl. Acad. Sci. U.S.A.* 108 (19), 7944–9. doi: 10.1073/pnas.1100552108

Prokunina-Olsson, L., Muchmore, B., Tang, W., Pfeiffer, R. M., Park, H., Dickensheets, H., et al. (2013). A Variant Upstream of IFNL3 (IL28B) Creating a New Interferon Gene IFNL4 is Associated With Impaired Clearance of Hepatitis C Virus. *Nat. Genet.* 45 (2), 164–171. doi: 10.1038/ng.2521

Qian, X. Y., Chien, C. Y., Lu, Y., Montelione, G. T., and Krug, R. M. (1995). An Amino-Terminal Polypeptide Fragment of the Influenza Virus NS1 Protein Possesses Specific RNA-Binding Activity and Largely Helical Backbone Structure. *RNA* 1 (9), 948–56.

Rajsbaum, R., Albrecht, R. A., Wang, M. K., Maharaj, N. P., Versteeg, G. A., Nistal-Villan, E., et al. (2012). Species-Specific Inhibition of RIG-I Ubiquitination and IFN Induction by the Influenza A Virus NS1 Protein. *PLoS Pathog.* 8 (11), e1003059. doi: 10.1371/journal.ppat.1003059

Sarhan, J., Liu, B. C., Muendlein, H. I., Weindel, C. G., Smirnova, I., Tang, A. Y., et al. (2019). Constitutive Interferon Signaling Maintains Critical Threshold of MLKL Expression to License Necroptosis. *Cell Death Differ* 26 (2), 332–47. doi: 10.1038/s41418-018-0122-7

Scharenberg, M., Vangeti, S., Kekalainen, E., Bergman, P., Al-Ameri, M., Johansson, N., et al. (2019). Influenza A Virus Infection Induces Hyperresponsiveness in Human Lung Tissue-Resident and Peripheral Blood NK Cells. *Front. Immunol.* 10, 1116. doi: 10.3389/fimmu.2019.01116

Schweitzer, K. S., Crue, T., Nall, J. M., Foster, D., Sajuthi, S., Correll, K. A., et al. (2021). Influenza Virus Infection Increases ACE2 Expression and Shedding in Human Small Airway Epithelial Cells. *Eur. Respir. J.* 58 (1):2003988. doi: 10.1183/13993003.03988-2020

Scialo, F., Daniele, A., Amato, F., Pastore, L., Matera, M. G., Cazzola, M., et al. (2020). ACE2: The Major Cell Entry Receptor for SARS-CoV-2. *Lung* 198 (6), 867–77. doi: 10.1007/s00408-020-00408-4

Scozzi, D., Cano, M., Ma, L., Zhou, D., Zhu, J. H., O'Halloran, J. A., et al. (2021). Circulating Mitochondrial DNA is an Early Indicator of Severe Illness and Mortality From COVID-19. *JCI Insight* 6 (4):e143299. doi: 10.1172/jci.insight.143299

Seth, R. B., Sun, L., Ea, C. K., and Chen, Z. J. (2005). Identification and Characterization of MAVS, a Mitochondrial Antiviral Signaling Protein That Activates NF-kappaB and IRF 3. *Cell* 122 (5), 669–682. doi: 10.1016/j.cell.2005.08.012

Sheppard, P., Kindsvogel, W., Xu, W., Henderson, K., Schlutsmeyer, S., Whitmore, T. E., et al. (2003). IL-28, IL-29 and Their Class II Cytokine Receptor IL-28r. *Nat. Immunol.* 4 (1), 63–8. doi: 10.1038/ni873

Sheridan, B. C., McIntyre, R. C., Meldrum, D. R., and Fullerton, D. A. (1997). Pentoxifylline Treatment Attenuates Pulmonary Vasomotor Dysfunction in Acute Lung Injury. *J. Surg. Res.* 71 (2), 150–4. doi: 10.1006/jsre.1997.5144

Shi, C. S., Qi, H. Y., Boularan, C., Huang, N. N., Abu-Asab, M., Shelhamer, J. H., et al. (2014). SARS-Coronavirus Open Reading Frame-9b Suppresses Innate Immunity by Targeting Mitochondria and the MAVS/TRAF3/TRAF6 Signalosome. *J. Immunol.* 193 (6), 3080–9. doi: 10.4049/jimmunol.1303196

Shin, Y. K., Li, Y., Liu, Q., Anderson, D. H., Babiuk, L. A., and Zhou, Y. (2007). SH3 Binding Motif 1 in Influenza A Virus NS1 Protein is Essential for PI3K/Akt Signaling Pathway Activation. *J. Virol.* 81 (23), 12730–9. doi: 10.1128/JVI.01427-07

Short, K. R., Kroeze, E., Fouchier, R. A. M., and Kuiken, T. (2014). Pathogenesis of Influenza-Induced Acute Respiratory Distress Syndrome. *Lancet Infect. Dis.* 14 (1), 57–69. doi: 10.1016/S1473-3099(13)70286-X

Shubina, M., Tummers, B., Boyd, D. F., Zhang, T., Yin, C., Gautam, A., et al. (2020). Necroptosis Restricts Influenza A Virus as a Stand-Alone Cell Death Mechanism. *J. Exp. Med.* 217 (11):e20191259. doi: 10.1084/jem.20191259

Stark, G. R., Kerr, I. M., Williams, B. R., Silverman, R. H., and Schreiber, R. D. (1998). How Cells Respond to Interferons. *Annu. Rev. Biochem.* 67, 227–264. doi: 10.1146/annurev.biochem.67.1.227

Sui, L., Zhao, Y., Wang, W., Wu, P., Wang, Z., Yu, Y., et al. (2021). SARS-CoV-2 Membrane Protein Inhibits Type I Interferon Production Through Ubiquitin-Mediated Degradation of TBK1. *Front. Immunol.* 12, 662989. doi: 10.3389/fimmu.2021.662989

Sui, C., Xiao, T., Zhang, S., Zeng, H., Zheng, Y., Liu, B., et al. (2022). SARS-CoV-2 NSP13 Inhibits Type I IFN Production by Degradation of TBK1 *via* P62-Dependent Selective Autophagy. *J. Immunol.* 208 (3), 753–61. doi: 10.4049/jimmunol.2100684

Swets, M. C., Russell, C. D., Harrison, E. M., Docherty, A. B., Lone, N., Girvan, M., et al. (2022). SARS-CoV-2 Co-Infection With Influenza Viruses, Respiratory Syncytial Virus, or Adenoviruses. *Lancet*. 399(10334), 1463–64. doi: 10.1016/S0140-6736(22)00383-X

Thomsen, M. M., Jorgensen, S. E., Gad, H. H., Storgaard, M., Gjedsted, J., Christiansen, M., et al. (2019). Defective Interferon Priming and Impaired Antiviral Responses in a Patient With an IRF7 Variant and Severe Influenza. *Med. Microbiol. Immunol.* 208 (6), 869–76. doi: 10.1007/s00430-019-00623-8

Thorne, L. G., Reuschl, A. K., Zuliani-Alvarez, L., Whelan, M. V. X., Turner, J., Noursadeghi, M., et al. (2021). SARS-CoV-2 Sensing by RIG-I and MDA5 Links Epithelial Infection to Macrophage Inflammation. *EMBO J.* 40 (15), e107826. doi: 10.15252/embj.2021107826

Tisoncik, J. R., Korth, M. J., Simmons, C. P., Farrar, J., Martin, T. R., and Katze, M. G. (2012). Into the Eye of the Cytokine Storm. *Microbiol. Mol. Biol. Rev.* 76 (1), 16–32. doi: 10.1128/MMBR.05015-11

Tsugawa, Y., Kato, H., Fujita, T., Shimotohno, K., and Hijikata, M. (2014). Critical Role of Interferon-α Constitutively Produced in Human Hepatocytes in Response to RNA Virus Infection. *PLoS One* 9 (2), e89869. doi: 10.1371/journal.pone.0089869

Turianova, L., Lachova, V., Svetlikova, D., Kostrabova, A., and Betakova, T. (2019). Comparison of Cytokine Profiles Induced by Nonlethal and Lethal Doses of Influenza A Virus in Mice. *Exp. Ther. Med.* 18 (6), 4397–405. doi: 10.3892/etm.2019.8096

Vallabhapurapu, S., and Karin, M. (2009). Regulation and Function of NF-kappaB Transcription Factors in the Immune System. *Annu. Rev. Immunol.* 27, 693–733. doi: 10.1146/annurev.immunol.021908.132641

Vanders, R. L., Hsu, A., Gibson, P. G., Murphy, V. E., and Wark, P. A. B. (2019). Nasal Epithelial Cells to Assess *In Vitro* Immune Responses to Respiratory Virus Infection in Pregnant Women With Asthma. *Respir. Res.* 20 (1), 259. doi: 10.1186/s12931-019-1225-5

Varga, Z. T., Ramos, I., Hai, R., Schmolke, M., Garcia-Sastre, A., Fernandez-Sesma, A., et al. (2011). The Influenza Virus Protein PB1-F2 Inhibits the Induction of Type I Interferon at the Level of the MAVS Adaptor Protein. *PLoS Pathog.* 7 (6), e1002067. doi: 10.1371/journal.ppat.1002067

Varga, Z. T., Grant, A., Manicassamy, B., and Palese, P. (2012). Influenza Virus Protein PB1-F2 Inhibits the Induction of Type I Interferon by Binding to MAVS and Decreasing Mitochondrial Membrane Potential. *J. Virol.* 86 (16), 8359–66. doi: 10.1128/JVI.01122-12

Wahl, A., Gralinski, L. E., Johnson, C. E., Yao, W., Kovarova, M., Dinnon, K. H. 3rd, et al. (2021). SARS-CoV-2 Infection is Effectively Treated and Prevented by EIDD-2801. *Nature* 591 (7850), 451–457.

Wang, X., Basler, C. F., Williams, B. R., Silverman, R. H., Palese, P., and Garcia-Sastre, A. (2002). Functional Replacement of the Carboxy-Terminal Two-Thirds of the Influenza A Virus NS1 Protein With Short Heterologous Dimerization Domains. *J. Virol.* 76 (24), 12951–62. doi: 10.1128/JVI.76.24.12951-12962.2002

Wang, Q., Zhang, Y., Wu, L., Niu, S., Song, C., Zhang, Z., et al. (2020). Structural and Functional Basis of SARS-CoV-2 Entry by Using Human Ace2. *Cell* 181 (4), 894–904 e9. doi: 10.1016/j.cell.2020.03.045

Wang, D., Hu, B., Hu, C., Zhu, F., Liu, X., Zhang, J., et al. (2020). Clinical Characteristics of 138 Hospitalized Patients With 2019 Novel Coronavirus-Infected Pneumonia in Wuhan, China. *JAMA* 323 (11), 1061–69. doi: 10.1001/jama.2020.1585

Wang, R., Yang, X., Chang, M., Xue, Z., Wang, W., Bai, L., et al. (2021). ORF3a Protein of Severe Acute Respiratory Syndrome Coronavirus 2 Inhibits Interferon-Activated Janus Kinase/Signal Transducer and Activator of Transcription Signaling *via* Elevating Suppressor of Cytokine Signaling 1. *Front. Microbiol.* 12, 752597. doi: 10.3389/fmicb.2021.752597

Weinheimer, V. K., Becher, A., Tonnies, M., Holland, G., Knepper, J., Bauer, T. T., et al. (2012). Influenza A Viruses Target Type II Pneumocytes in the Human Lung. *J. Infect. Dis.* 206 (11), 1685–94. doi: 10.1093/infdis/jis455

WHO (2011). *Report of the Review Committee on the Functioning of the International Health Regulations (2005) in Relation to Pandemic (H1N1) 2009* (World Health Organization).

Wong, S. S., Oshansky, C. M., Guo, X. J., Ralston, J., Wood, T., Seeds, R., et al. (2018). Severe Influenza Is Characterized by Prolonged Immune Activation: Results From the SHIVERS Cohort Study. *J. Infect. Dis.* 217 (2), 245–256. doi: 10.1093/infdis/jix571

Wu, Q., Xing, Y., Shi, L., Li, W., Gao, Y., Pan, S., et al. (2020). Coinfection and Other Clinical Characteristics of COVID-19 in Children. *Pediatrics* 146 (1): e20200961. doi: 10.1542/peds.2020-0961

Xia, H., Cao, Z., Xie, X., Zhang, X., Chen, J. Y., Wang, H., et al. (2020). Evasion of Type I Interferon by SARS-CoV-2. *Cell Rep.* 33 (1), 108234. doi: 10.1016/j.celrep.2020.108234

Yang, K., Huang, R., Fujihira, H., Suzuki, T., and Yan, N. (2018). N-Glycanase NGLY1 Regulates Mitochondrial Homeostasis and Inflammation Through NRF1. *J. Exp. Med.* 215 (10), 2600–16. doi: 10.1084/jem.20180783

Yin, X., Riva, L., Pu, Y., Martin-Sancho, L., Kanamune, J., Yamamoto, Y., et al. (2021). MDA5 Governs the Innate Immune Response to SARS-CoV-2 in Lung Epithelial Cells. *Cell Rep.* 34 (2), 108628. doi: 10.1016/j.celrep.2020.108628

Yoo, J. S., Takahasi, K., Ng, C. S., Ouda, R., Onomoto, K., Yoneyama, M., et al. (2014). DHX36 Enhances RIG-I Signaling by Facilitating PKR-Mediated Antiviral Stress Granule Formation. *PLoS Pathog.* 10 (3), e1004012. doi: 10.1371/journal.ppat.1004012

Yoshizumi, T., Ichinohe, T., Sasaki, O., Otera, H., Kawabata, S., Mihara, K., et al. (2014). Influenza A Virus Protein PB1-F2 Translocates Into Mitochondria *via* Tom40 Channels and Impairs Innate Immunity. *Nat. Commun.* 5, 4713. doi: 10.1038/ncomms5713

Yu, C. H., Davidson, S., Harapas, C. R., Hilton, J. B., Mlodzianoski, M. J., Laohamonthonkul, P., et al. (2020). TDP-43 Triggers Mitochondrial DNA Release *via* mPTP to Activate cGAS/STING in ALS. *Cell* 183 (3), 636–649 e18. doi: 10.1016/j.cell.2020.09.020

Zhang, Z., Kim, T., Bao, M., Facchinetti, V., Jung, S. Y., Ghaffari, A. A., et al. (2011). DDX1, DDX21, and DHX36 Helicases Form a Complex With the Adaptor Molecule TRIF to Sense dsRNA in Dendritic Cells. *Immunity* 34 (6), 866–78. doi: 10.1016/j.immuni.2011.03.027

Conflict of Interest: The authors declare that the research was conducted in the absence of any commercial or financial relationships that could be construed as a potential conflict of interest.

frontiers | Frontiers in Cellular and Infection Microbiology

ORIGINAL RESEARCH
published: 05 July 2022
doi: 10.3389/fcimb.2022.897531

Isolation and Characterization of vB_kpnM_17-11, a Novel Phage Efficient Against Carbapenem-Resistant *Klebsiella pneumoniae*

Jiawei Bai*[1], *Feiyang Zhang*[1], *Shuang Liang*[1], *Qiao Chen*[1], *Wei Wang*[1], *Ying Wang*[1], *Alberto J. Martín-Rodríguez*[2], *Åsa Sjöling*[2], *Renjing Hu*[3]* and *Yingshun Zhou*[1]

[1] Department of Pathogen Biology, School of Basic Medicine, Public Center Experimental Technology of Pathogen Biology, Southwest Medical University, Luzhou, China, [2] Department of Microbiology, Tumor and Cell Biology, Karolinska Institutet, Solna, Sweden, [3] Department of Laboratory Medicine, The Affiliated Wuxi No.2 People's Hospital of Nanjing Medical University, Wuxi, China

Edited by:
Rameez Raja,
Cleveland Clinic, United States

Reviewed by:
Amjad Ali,
University of Massachusetts Medical School, United States
Kasturi Banerjee,
Stony Brook University, United States

***Correspondence:**
Renjing Hu
weiweihuhu112@163.com
Yingshun Zhou
yingshunzhou@swmu.edu.cn

Specialty section:
This article was submitted to Virus and Host, a section of the journal Frontiers in Cellular and Infection Microbiology

Received: *16 March 2022*
Accepted: *03 June 2022*
Published: *05 July 2022*

Citation:
Bai J, Zhang F, Liang S, Chen Q, Wang W, Wang Y, Martín-Rodríguez AJ, Sjöling Å, Hu R and Zhou Y (2022) Isolation and Characterization of vB_kpnM_17-11, a Novel Phage Efficient Against Carbapenem-Resistant Klebsiella pneumoniae.
Front. Cell. Infect. Microbiol. 12:897531.
doi: 10.3389/fcimb.2022.897531

Phages and phage-encoded proteins exhibit promising prospects in the treatment of Carbapenem-Resistant *Klebsiella pneumoniae* (CRKP) infections. In this study, a novel *Klebsiella pneumoniae* phage vB_kpnM_17-11 was isolated and identified by using a CRKP host. vB_kpnM_17-11 has an icosahedral head and a retractable tail. The latent and exponential phases were 30 and 60 minutes, respectively; the burst size was 31.7 PFU/cell and the optimal MOI was 0.001. vB_kpnM_17-11 remained stable in a wide range of pH (4-8) and temperature (4-40°C). The genome of vB_kpnM_17-11 is 165,894 bp, double-stranded DNA (dsDNA), containing 275 Open Reading Frames (ORFs). It belongs to the family of *Myoviridae*, order Caudovirales, and has a close evolutionary relationship with *Klebsiella* phage PKO111. Sequence analysis showed that the 4530 bp *orf022* of vB_kpnM_17-11 encodes a putative depolymerase. *In vitro* testing demonstrated that vB_kpnM_17-11 can decrease the number of *K. pneumoniae* by 10^5-fold. In a mouse model of infection, phage administration improved survival and reduced the number of *K. pneumoniae* in the abdominal cavity by 10^4-fold. In conclusion, vB_kpnM_17-11 showed excellent *in vitro* and *in vivo* performance against *K. pneumoniae* infection and constitutes a promising candidate for the development of phage therapy against CRKP.

Keywords: phage, *Klebsiella pneumonia*, depolymerase, phage therapy, animal model

INTRODUCTION

K. pneumoniae is an opportunistic pathogen which often causes pneumonia, pyogenic liver abscess (PLA), necrotizing fasciitis and urinary tract infections (UTIs) (Fu et al., 2018). In recent years, multidrug-resistant bacteria especially Carbapenem-Resistant *Klebsiella pneumoniae* (CRKP), had posed a huge challenge to public health, with the emergence of a growing number of CRKP isolates worldwide (Zhang et al., 2021b; Zhang et al., 2021a). Thus, it is an urgent need to find novel ways to prevent and control CRKP infections.

As a potential antibacterial agent, phages can effectively and specifically infect host bacteria (Onsea et al., 2021). Nonetheless, phages often have distinct biological characteristics such as host range, proliferation rates, temperature and pH stability, which altogether limit the industrial production of phage preparations (Cai et al., 2019). Therefore, the isolation and characterization of phages with appropriate characteristics is of great significance.

In addition to their biological properties, advancing knowledge on phage genomics has intrinsic fundamental importance. By exploring the phage genome, we can analyze the genetic characteristics of phages and develop new phage-based antibacterial agents. Researchers often modularize phage genes to analyze the differences between the same functional modules, it is helpful to explore genetic and functional similarities in different phage genomes (Zhou et al., 2018). Phage genes can mutate during the proliferation process. The mutation rate of the individual phage genes differ depending on the evolutionary pressures they are subjected to (Comeau et al., 2007). For example, the gene encoding the phage head structure has a low probability to mutate. As a conserved protein, the phage major capsid protein (MCP) is often used to reconstruct the evolutionary relationships of phages (Zhao et al., 2019). In addition, phage tail genes coding products may have antibacterial potential, such as the depolymerase (Chen et al., 2020). The phage depolymerase is a protein that can specifically degrade bacterial surface capsular polysaccharides (CPS). While degrading CPS, the depolymerase simultaneously pulls the phage particles closer to the host surface and eventually binds to the outer membrane receptor (Michaud et al., 2003). Recent studies have shown that phage depolymerase can specifically recognize bacterial capsular types, remove bacterial biofilms, and effectively reduce bacterial virulence. Therapies based on phages and phage depolymerase brings new hope for the treatment of drug-resistant bacterial infections.

In previous studies, phage therapy was effectively employed in the treatment of prosthetic joint infection caused by *Staphylococcus aureus* (Ferry et al., 2020). In the context of COVID-19, phage therapy was successfully applied on secondary *Acinetobacter baumannii* infection in COVID-19 patients (Wu et al., 2021). However, the clinical application of phages has been limited due to a number of shortcomings including the narrow host range of phages or the development of resistance against phage infection by bacteria, among other factors (Labrie et al., 2010). Therefore, the isolation of new phages and the characterization of their application prospects for the treatment of pernicious infections is currently a preclinical research need. With these premises, in this study we set to isolate new phages efficient against the treatment of CRKP, identify the main genomic characteristics through genome sequencing and bioinformatic analysis, and explore their therapeutic efficacy in a mouse model of infection.

MATERIALS AND METHODS

Bacterial Strain, Phage Isolation and Identification

K. pneumoniae 17-11 carrying *bla*$_{\text{KPC-2}}$ (WGS accession: KZ984141) was used as a host for phage isolation. *K. pneumoniae* 17-11 is resistant to an array of antibiotics (**Supplementary Table 1**). A wastewater sample was collected from Affiliated Hospital of Southwest Medical University in Luzhou, Sichuan Province, China. One mL exponential phase *K. pneumoniae* 17-11 and 10 mL Luria-Bertani (LB) medium were added into 100 mL wastewater sample. This mixture was incubated at room temperature overnight, followed by centrifugation at 12,000 rpm for 10 min. The supernatant was filtered through a 0.22 μm filter to obtain acrude phage solution, which was subsequently serially diluted ten-fold from 10^{-1} to 10^{-5}. One-hundred μL of phage crude solution of each dilution gradient was mixed with an equal volume of logarithmic phase 17-11 solution, and incubated at room temperature for 15 min. The mixture was added to 4 mL semi-solid medium (agar 0.5%), poured over an LB broth agar plate, and cultured overnight at 37°C (double-layer plate method). Single phage plaques were picked with an inoculation needle and inoculated into a logarithmic phase 17-11 bacterial solution. When the solution was clear, indicating full bacterial lysis, it was centrifuged and filtered, and the phage titer was detected by the double-layer plate method. The procedure above was repeated 5 times (Kropinski et al., 2009). The phage solution was dripped onto a copper mesh and stained with 2% phosphotungstic acid (PTA). An HT 7800 transmission electron microscope was used to image virions at 80 kV (Hitachi, Tokyo, Japan) in FuXin (Shanghai, China) to analyze the morphological features of individual phage particles.

Optimal Multiplicity of Infection and One-Step Growth Curve Estimation

Five-hundred μL of a bacterial solution (10^6 CFU/mL) were mixed with phages (10^8, 10^7, 10^6, 10^5, 10^4, 10^3, or 10^2 PFU/mL) and incubated at room temperature for 15 min. Nine mL of LB medium was added to each group, and cultured at 37°C, 220 rpm, for 2 h. The mixture was centrifuged at 8,000 rpm for 10 min at 4°C, leaving the supernatant. The double-layer plate method was used to determine the phage titers of the mixture and the highest production was defined as the optimal MOI.

The one-step growth curve determination method was improved based on a previous study (Peng and Yuan, 2018). Phages and *K. pneumoniae* 17-11 were mixed at the optimal MOI and incubated for 10 min at 37°C. The mixture was then centrifuged at 4°C, 12,000 rpm for 2 min to remove free phages. The sediment was resuspended in 10 mL of LB broth. Aliquots (100 μL) were taken every 10 min from 0 min to 120 min to determine the phage titers. The burst size was defined as the number of phage progeny/number of latent infected cells.

Host Range Evaluation, Thermal and pH Stability

The host range of phage was defined based on 92 bacterial strains. 76 strains of *K. pneumoniae*, 1 staphylococcus aureus strain, and 5 strains of *Pseudomonas aeruginosa*, *Escherichia coli* and *Salmonella*, respectively. One-hundred μL of a phage suspension containing 10^5 PFU/mL was mixed with 100 μL 10^8 CFU/mL bacterial solution. The double-layer plate method was used to observe the development of plaques. Samples that produced a plaque were assumed to be lysed by phages. The lysed strains were serotyped by amplification and sequencing of the

CD1-VR2-CD2 region, a variable sequence coding region of the *wzc* gene (Primer: F: 5'- 3' GGGTTTTTATCGGGTTGTAC, R: 5'-3' TTCAGCTGGATTTGGTGG) (Pan et al., 2013).

To determine phage stability in the cold, seven mL of a phage suspension (10^8 PFU/mL) were divided into 7 microcentrifuge tubes, and all tubes were placed in a refrigerator at 4°C. Starting from 0 min, one tube was taken out every 10 min and the phage titer was detected by the double-layer plate method. The phage thermal stability tests at 25°C, 37°C, 40°C, 50°C, 60°C and 70°C were performed in an analogous way using a water bath at the appropriate temperature.

Phage stability at different pH values was determined using Saline-Magnesium (SM) buffer, pH 1-14, in individual 15 mL centrifuge tubes. One mL of phage suspension containing 10^9 PFU were added to each tube, incubated at room temperature for 1 h, and the phage titers counted by the double-layer plate method.

Phage DNA Extraction, Genome Sequence, and Bioinformatic Analysis

Phage DNA was extracted using the virus DNA\RNA Extraction Kit (TaKaRa Mini BEST Viral RNA/DNA Extraction Kit Ver.5.0) according to the manufacturer's protocol. The phage genome was sequenced at Majorbio (Shanghai, China). RAST was used to predict and annotate the ORFs. tRNAscan-SE (Chan and Lowe, 2019) was used to analyze viral tRNA genes. BLAST Ring Image Generator v0.95 (BRIG) (Alikhan et al., 2011) was used to map the whole genome and analyze the distribution of phage genes. BLAST+ (version 2.11.0) and Artemis Comparison Tool (ACT, version 18.1.0) (Carver et al., 2005) were used to carry out multiple genome comparisons to study differences in gene arrangement between phages. Phylogenies were reconstructed with MEGA-X by the Neighbor-Joining method with 1000 bootstrap replicates (Kumar et al., 2018). HHpred (Söding et al., 2005) software was used to predict depolymerase.

Bactericidal Effect of the Phage *in Vitro* and *in Vivo*

To determine the bactericidal effect of the phage *in vitro*, *K. pneumoniae* 17-11 was cultured to exponential phase in 150 mL LB medium. The bacterial culture was then divided into 3 conical bottles. Add 1 mL Phosphate Buffer Solution (PBS), 1 mL phage, 1 mL polymycin B (PB, Final concentration 2 μg/mL) to three conical bottles, respectively (Li et al., 2020). Samples (200 μL) were taken every 30 min for a total of 150 min, and the OD_{595} was measured at each time point.

Two experiments were designed to investigate the bacteriostatic effect of the phage *in vivo*. First, 20 mice were given cyclophosphamide (CTX) 300 mg/kg for 3 days in advance to construct the immunodeficient mouse models (Manepalli et al., 2013). Ten immunodeficient mice were injected with 500 μL PBS containing 10^7 CFU *K. pneumoniae* 17-11 and randomly divided into two groups: one group was treated with 500 μL of a phage suspension of 10^9 PFU/mL, and the other group was injected with 500 μL PBS as a control. The survival curves of the mice were recorded every 12 h up to 148 h. Other 10 immunodeficient mice were injected with 500 μL PBS containing 5 × 10^6 CFU *K. pneumoniae* 17-11 and also randomly divided into two groups: one group was treated with 500 μL phage suspension (10^9 PFU/mL) and the other group was injected with 500 μL PBS. Ten mice were sacrificed by cervical dislocation at 24 h post infection and peritoneal lavages were collected with 1 mL of sterile PBS, then plated on LB plates for colony enumeration. A summary of the *in vivo* experimental design is shown in **Supplementary Figure 1**. All experiments were conducted in compliance with approved protocols and guidelines of the Southwest Medical University Animal Care and Use Committee (20211124-002).

Statistical Analysis

All analyses were performed using Prism 8 software (GraphPad Software, CA, USA). All experimental data were expressed as mean ± SD. Differences in survival curves were tested with the Gehan-Breslow-Wilcoxon test. The two groups were compared using the Mann–Whitney test. $P < 0.05$ was deemed to be statistically significant.

RESULTS

Isolation and Morphology of Phage

A novel *K. pneumoniae* phage was isolated and named it vB_kpnM_17-11. vB_kpnM_17-11 can form transparent plaques of 3 mm in diameter on a double agar plate. The halo surrounding the plaque indicates that the phage has depolymerase activity (**Figure 1A**). Transmission electron microscopy showed that the length of vB_kpnM_17-11 was 250 nm (**Figure 1B**). The phage capsid is an icosahedron with a length and width of 120 nm and 90 nm, respectively. The retractable tail structure of vB_kpnM_17-11 is a typical feature of the *Myoviridae* phage family (**Figure 1C**).

The MOI and One-Step Growth Curve of vB_kpnM_17-11

To determine the optimal MOI, suspensions of vB_kpnM_17-11 phage particles containing 10^2-10^8 PFU/mL were mixed with *K. pneumoniae* 11-17 cells (10^6 CFU/mL). The optimal MOI giving the highest titer of progeny phages was determined to be 0.001 (**Table 1**).

To analyze phage proliferation *in vitro*, a one-step growth curve was performed (**Figure 2**). From this analysis, the latent phase of vB_kpnM_17-11 was determined to be 30 min, in which phage proliferation was negligible. Between 30 min and 90 min post inoculation, phage titers increased exponentially, reaching a plateau after 90 min. The burst size was 31.7 PFU/cell after the exponential phase.

Host Range, Thermal and pH Stability

vB_kpnM_17-11 was able to infect 4.35% (4/92) of the tested strains (**Supplementary Table 2**). Serotyping experiments upon sequencing of the *wzc* gene CD1-VR2-CD2 region of the 4 strains of *K. pneumoniae* lysed by vB_kpnM_17-11

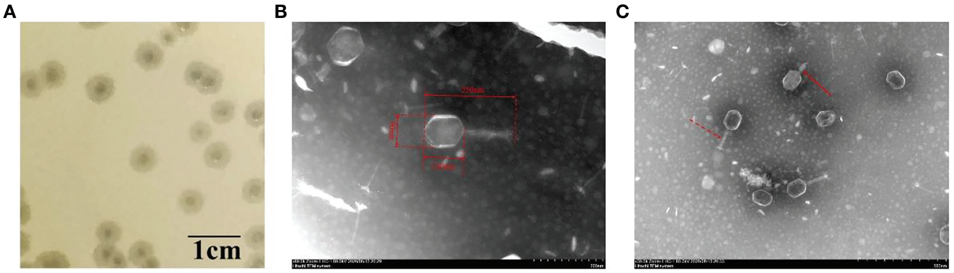

FIGURE 1 | Plaques and transmission electron microscopy of phage vB_kpnM_17-11. **(A)** Plaque morphology of phage vB_kpnM_17-11 on a bacterial lawn of *K. pneumoniae* 17-11 in nutrient broth with 0.5% agar (scale bar = 1 cm). **(B)** Transmission electron microscopy of phage vB_kpnM_17-11. **(C)** Contractive and non-contractive tails. Dashed arrow for non-contractile tail; Solid arrow for contractile tail.

demonstrated the 4 strains to belong to the K19 serotype (**Figure 3**). The phage titer remained stable at ambient temperatures from 4°C to 40°C. At 50°C, phage titers decreased by 79% after 60 min. Complete loss of viability after 10 min was recorded when the temperature was ≥ 60°C (**Figure 4A**). The titer of vB_kpnM_17-11 was relatively stable at pH 4 - 10 (> 50%). The phage titer decreased significantly in acidic (pH 2-3) or alkaline (pH 11-13) conditions. Phage titers could not be detected at pH 1 and 14 (**Figure 4B**).

Genomic Analysis of the Phage vB_kpnM_17-11

The genome sequence of phage vB_kpnM_17-11 is available from GenBank under accession MW239157. vB_kpnM_17-11 has dsDNA with a genome size of 165,894 bp, a G + C content of 39.5%, and a gene density of 1.66 (Gene density: Gene number/ 1000 bp). The coding density of vB_kpnM_17-11 genome was 93.0%, therefore only 7% of the genome represented non-coding sequences. A total of 16 tRNA genes were predicted. The absence of lysogen-formation genes in the vB_kpnM_17-11 indicates that vB_kpnM_17-11 is a lytic phage.

The vB_kpnM_17-11 genome encodes 275 ORFs (**Supplementary Table 3**) ranging from 30 to 1510 codons. 39.6% (109/275) of the ORFs encoded functional genes and were divided into four functional modules (**Figure 5**). First, 49.1% (54/109) of the functional ORFs are predicted to be involved in nucleotide metabolism and replication in association with a host, covering most processes of phage replication, regulation, transcription, and translation. Second, 41.3% (45/109) of the functional ORFs encode structural products such as phage head and tail morphology. Third, 3.67% (4/109) of the functional ORFs are predicted to be used to form packaging module. ORF96 encoded a portal vertex protein; ORF104 and ORF105 encoded a terminase; and ORF121 encoded a DNA ended protector protein. Fourth, vB_kpnM_17-11 has 5.5% (6/109) functional ORFs involved in host lysis, including a putative holin (ORF020), a Rz1 protein (ORF047), a lysis inhibition accessory protein (ORF058), a phage baseplate hub structural protein/Phage lysozyme R (ORF119), a phage lysozyme R (ORF147) and a rI lysis inhibition regulator membrane protein (ORF166).

The genome of vB_kpnM_17-11 shows high identity (> 90%) with the genomes of other 18 *Klebsiella* phages (**Table 2**). *Klebsiella* phages PKO111 and KP1 were used for multiple sequence alignment with vB_kpnM_17-11. Thus, vB_kpnM_17-11 has similar genome sequence and gene module arrangement as *Klebsiella* phages PKO111 and KP1. However, each phage has a distinct genomic organization (**Figure 6**). To determine the evolutionary relationships of phage vB_kpnM_17-11 with respect to other *Klebsiella* phages, a phylogenetic tree based on MCP was constructed. The phylogenetic reconstruction demonstrated that phage vB_kpnM_17-11 has a close evolutionary relationship with a variety of *Klebsiella* phage, such as PKO111, vB_kpnP_TU02, JD18, JIPh Kp122 and Mineola (**Figure 7**). Phage morphology and whole genome indicate that vB_kpnM_17-11 belongs to the family of *Myoviridae*, order *Caudovirales*.

TABLE 1 | Optimal MOI for phage.

MOI	Phage (PFU/mL)	Host (CFU/mL)	Product (PFU/mL)
100	10^8	10^6	1.41×10^7
10	10^7	10^6	2.63×10^7
1	10^6	10^6	1.57×10^8
0.1	10^5	10^6	2.80×10^8
0.01	10^4	10^6	5.05×10^8
0.001	10^3	10^6	2.00×10^9
0.0001	10^2	10^6	1.15×10^9

Phages and bacteria were mixed according to different MOI and the titer of the progeny phages was measured.

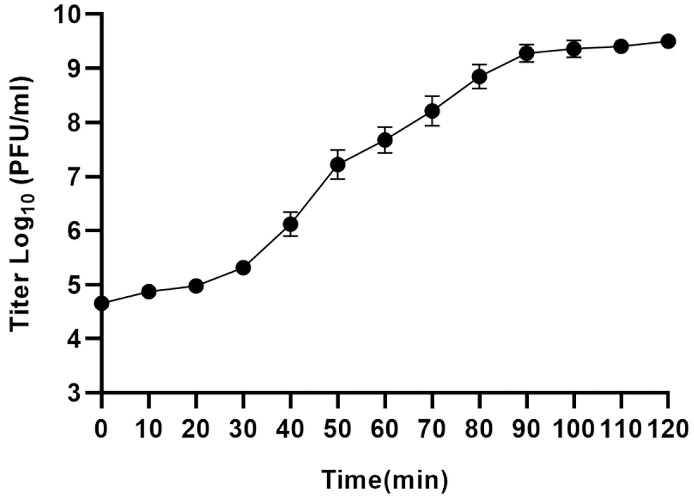

FIGURE 2 | One-step growth curve of vB_kpnM_17-11. The PFU of each infected cell is shown at different time points. Each data point represents the mean of three independent experiments, and the error bar represents the standard deviation.

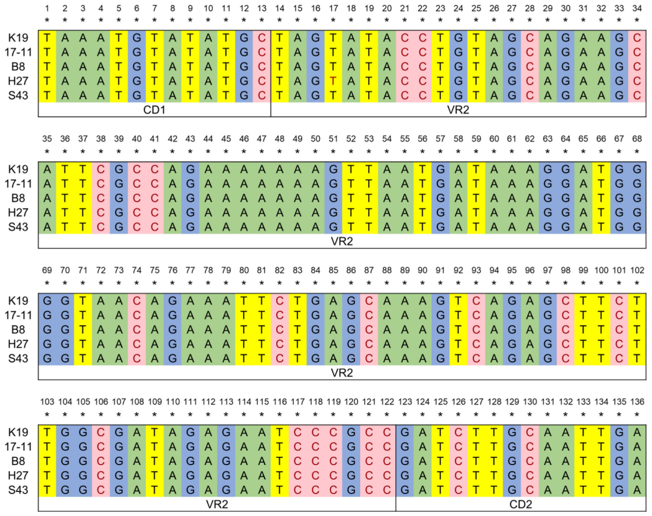

FIGURE 3 | Serotype identification of *k. pneumoniae*. The CD1-VR2-CD2 region of the *wzc* gene was amplified by PCR, sequenced and compared to determine the serotype of *k. pneumoniae* lysed by vB_kpnM_17-11. K19 represents the inherent sequence of CD1-VR2-CD2 region of *wzc* gene of *k. pneumoniae* serotype K19, and 17-11, B8, H27, and S43 are four strains that can be lysed by vB_kpnM_17-11 respectively.

Analysis of Depolymerase Dep022 Coding Gene

BLAST results showed that 99.08% (108/109) of vB_kpnM_17-11 functional genes had more than 95% similarity to known homologues in other phages. However, *orf022* had only 85.97% similarity with the L-shaped tail fiber protein of *Klebsiella* Phage vB_KpnM_311F. This suggests that this protein of phage vB_kpnM_17-11 is rather distinct. The size of *orf022* is 4530 bp and encodes a 1509 aa protein, annotated as a L-shaped tail fiber protein. HHpred software predicted this protein to contain two domains of depolymerase activity, namely a domain with a hyaluronidase function (PDB ID: 2WH7_A, probability = 72.83%) and a domain with Endo-N-acetylneuraminidase function (PDB ID: 3GW6_C, probability = 98.95%) analogous to those of *Escherichia coli* phage K1F (**Figure 8A**). Thus, *orf022* may encode a depolymerase protein, which we named Dep022. Dep022 has the closest evolutionary relationship with the proteins encoded by *Klebsiella* phage KPO111, vB_KpnM_311F, KPN6 and KPN5 (**Figure 8B**).

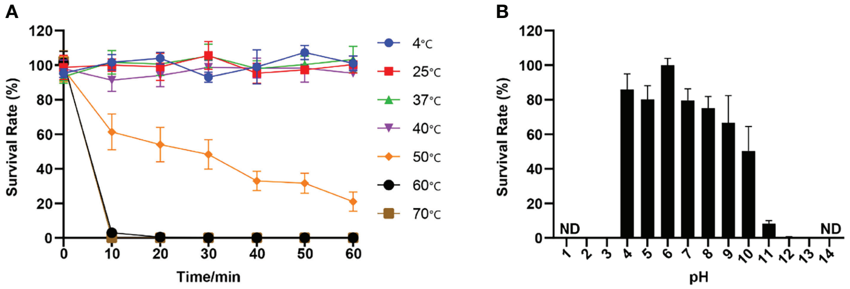

FIGURE 4 | Thermal and pH stability of vB_kpnM_17-11. **(A)** Temperature stability of phages vB_kpnM_17-11. When incubated at different temperatures for 60 min, the phages could survive at 4°C, 25°C, 37°C and 40°C. At 50°C, the phage concentration decreased by 80%. Phages could not survive at 60°C and 70°C. Data were obtained from three independent experiments and are shown as mean ± standard deviation. **(B)** PH stability of phages vB_kpnM_17-11. vB_kpnM_17-11 was incubated at the indicated pH conditions for 60 min. vB_kpnM_17-11 is relatively stable under neutral condition. The phage titer decreased significantly under acidic or alkaline conditions. vB_kpnM_17-11 titer extreme acid-base conditions cannot be detected (ND, Not Detected). Data were obtained from three independent experiments and are shown as mean ± standard deviation.

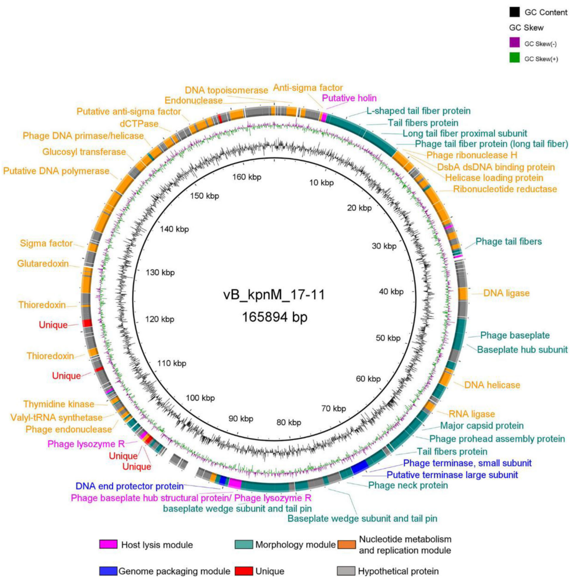

FIGURE 5 | Genome map of phage vB_kpnM_17-11. The black circle in the middle represents the GC content; the violet circle represents GC skew. Different colors represent genes with different functions: peach for host lysis module, green for morphology module, orange for nucleotide metabolism and replication, blue for packaging module, red for specific protein, gray for hypothetical protein.

Antibacterial Activity *in Vitro* and *in Vivo*

vB_kpnM_17-11 was able to effectively inhibit the growth of 17-11 (**Figure 9A**). Bacterial growth in the 17-11+PBS control group was not inhibited as determined by OD_{595} recording. The OD_{595} values in the 17-11+vB_kpnM_17-11 group decreased with time, dropping to baseline levels after 60 min. Bacterial growth in the presence of PB was notably inhibited for 120 min, but a trend towards a steep increase in bacterial numbers was recorded at the last time point (150 min), suggesting that bacteria were able to overcome the action of the antibiotic. The content of bacteria in 17-11+PBS group, 17-11+vB_kpnM_17-11 group and 17-11+PB group was 2.44×10^9 CFU/mL, 3.10×10^4 CFU/mL and 7.07×10^8 CFU/mL, respectively. The bacterial count of the 17-11+vB_kpnM_17-11 group was significantly lower than that of 17-11+PBS group and 17-11+PB group. At the later stage of the experiment, bacterial counts in the 17-11+PB group began to increase, but the count was significantly lower than of the 17-11+PBS group (**Figure 9B**). Compared with the 17-11+PBS group, vB_kpnM_17-11 *in vitro* reduced bacteria by 10^5 times from 10^9 to 10^4 CFU/mL.

To test the performance of vB_kpnM_17-11 *in vivo*, experiments were performed in a mouse infection model. The

TABLE 2 | Global genome comparison of vB_kpnM_17-11 with homologous phages.

	Host strain type	GenBank number	Genome size (bp)	Query coverage with vB_kpnM_17-11	Identity with vB_kpnM_17-11
vB_kpnM_17-11	*K. pneumoniae*	MW239157	165894 bp	100%	100%
PKO111	*K. oxytoca*	KR269720	168758 bp	94%	96.60%
KP1	*K. pneumoniae*	MG751100	167989 bp	94%	96.70%
KPV15	*K. pneumoniae*	NC_055715	167034 bp	93%	96.79%
vB_KpnM_311F	*Klebsiella*	LR877331	166710 bp	96%	95.17%
KPN6	*K. pneumoniae* *K. oxytoca*	MN101230		94%	95.08%
KPN5	*K. pneumoniae* *K. oxytoca*	MN101229	158756 bp	91%	95.04%
vB_KpnM_BovinicusUrsus	*K. pneumoniae*	MW021752	166829 bp	95%	94.52%
Mineola	*K. pneumoniae*	NC_055748	166130 bp	93%	94.24%
KP179	*K. pneumoniae*	NC_055768	162630 bp	91%	96.55%
KPN2 HKu-2019	*K. pneumoniae* *K. oxytoca*	MN101226	122724 bp	67%	95.00%
JD18	*K. pneumoniae*	KT239446	166313 bp	95%	96.03%
JIPh_Kp122	*K. pneumoniae*	MN434095	166475 bp	95%	95.99%
KpnM6E1	*K. pneumoniae*	MT580897	167920 bp	94%	96.56%
AShe-2020a	*K. pneumoniae*	CP062992	168979 bp	93%	96.10%
KPN1	*K. pneumoniae* *K. oxytoca*	MN101225	98975 bp	56%	95.71%
vB_KpnM_KpV477	*K. pneumoniae*	KX258185	168272 bp	93%	94.13%
vB_KpnP_TU02	*K. pneumoniae*	MZ560702	166230 bp	93%	97.53%
Metamorpho	*K. aerogenes*	MT701588	171475 bp	77%	91.18%

survival rate of mice in the CTX+17-11+PBS group was 20% within 24 h, and all mice died within 36 h. However, all mice in the CTX+17-11+vB_kpnM_17-11 group survived (**Figure 9C**). Bacterial cell counts in mice peritoneal lavage fluids were 2.27 × 10^8 CFU/mL for the CTX+17-11+PBS group, and 2.89 × 10^4 CFU/mL for the CTX+17-11+vB_kpnM_17-11 group. Therefore, vB_kpnM_17-11 reduced the bacterial content of peritoneal lavage fluid by 10^4 times in immunodeficient mice (**Figure 9D**).

DISCUSSION

An increasing number of CRKP isolates poses a significant challenge to public health worldwide (Cai et al., 2019; Zhang et al., 2022). The safety and effectiveness of phages and their coding products in the treatment of drug-resistant bacterial infections have been extensively demonstrated (Majkowska-Skrobek et al., 2018). Therefore, research and development of novel therapies based on phages and their coding products may help treat infections caused by drug-resistant bacteria, which are on the rise and expected to increase in the coming years. In this study, we isolated a phage vB_kpnM_17-11 that can lyse CRKP, studied its biological characteristics, analyzed its whole genome and coding products, and studied its efficacy *in vitro* and *in vivo*.

vB_kpnM_17-11 can form transparent plaques with a halo of around of 3 mm in diameter, and the plaque indicates that vB_kpnM_17-11 is a lytic phage (Peng et al., 2020). As a lytic phage, vB_kpnM_17-11 has promising potential prospects in clinical therapy and production of phage preparations. When bacterial growth on the plate reaches a plateau, phage proliferation usually stops or slows down dramatically, resulting in no increase in the plaque area. However, the tails of some phages can still depolymerize bacterial exopolysaccharides, resulting in translucence regions of varying sizes on the outside of the phage plaque, called halos (Cornelissen et al., 2011). The presence of a halo indicates that the phage has depolymerase activity, and depolymerase is a potential choice for treating antibiotic-resistant bacterial infections (Dunstan et al., 2021). Compared to literature data, the plaque size of vB_kpnM_17-11 and TSK1 were similar, but the halo of *Klebsiella* phage TSK1 and *Klebsiella* phage π VLC6 were larger than that vB_kpnM_17-11, suggesting that TSK1 (Tabassum

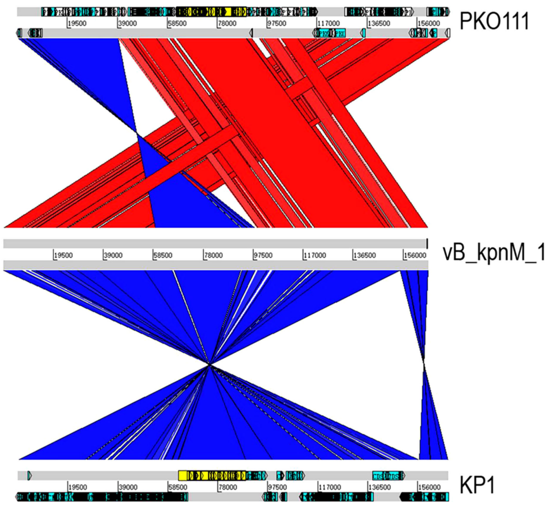

FIGURE 6 | Multiple genome alignments of phage vB_kpnM_17-11, PKO111 and KP1. Red and blue represent the forward and reverse matches, respectively. The darker the color, the higher similarity.

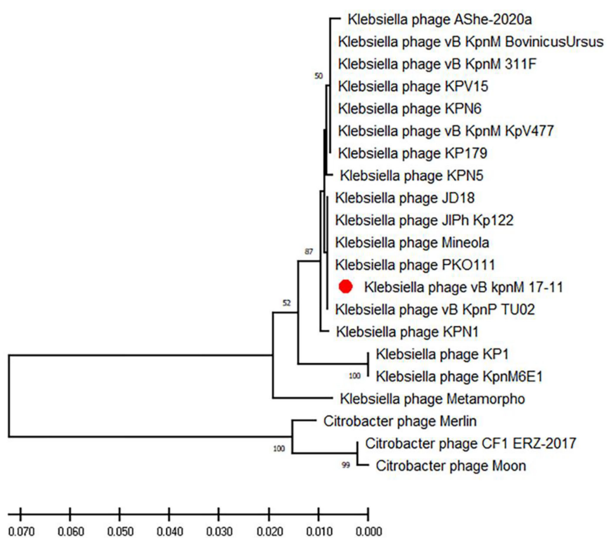

FIGURE 7 | Phylogenetic tree of vB_kpnM_17-11 based on MCP. Phylogenetic tree of phages established using MEGA-X software by the neighbor-joining method with 1000 bootstrap replicates. The red dot highlights the vB_kpnM_17-11.

et al., 2018) and π VLC6 (Domingo-Calap et al., 2020) might have more powerful depolymerase activity. Genome sequence analysis in combination with the study of morphological features such as the retractable tail structure of vB_kpnM_17-11 indicate that the phage belongs to the *Myoviridae* family, order *Caudovirales*.

The optimal MOI for phages varies, and the smaller the optimal MOI, the fewer phages required to lyse the same number of bacteria. The optimal MOI of vB_kpnM_17-11 was 0.001, which was similar to that reported for *Klebsiella* phage vB_KpnP_IME337 (Gao et al., 2020), indicating that when their MOI was 0.001, the unit phage produced the most progeny and had the highest proliferation efficiency. In the industrial preparation of phages, to obtain a higher titer, researchers often culture phages based on the optimal MOI, which reduces production costs and increases profits. The growth curve of phage is divided into latency phase, logarithmic phase and stationary phase. The incubation period of vB_kpnM_17-11 was 30 min, in contrast with that of the *Klebsiella* phage vB_KleS-HSE3 which was 40 min (Peng et al., 2020). Phages with shorter incubation periods can produce progeny faster and increase the number of phages in a shorter time. Furthermore, the long logarithmic period of the vB_kpnM_17-11 may be related to its larger whole genome and longer gene replication time.

The titer of vB_kpnM_17-11 remains stable at temperature between 4°C and 40°C and pH between 4 - 10. This temperature and pH range are just the common environment for phage preparation production, transportation, storage and treatment, indicating that the phage has the potential for further industrial application (Jończyk et al., 2011). Furthermore, phage with versatile temperature and pH adaptability are more suitable for various infection models, such as skin infections that become more alkaline due to bacterial colonization, or urinary tract infections that have highly variable microenvironments (Martín-Rodríguez et al., 2020).

The loss of viability of t vB_kpnM_17-11 at pH = 1 prevents its oral administration because of the acidic conditions of the gastric environment (Beasley et al., 2015). To overcome this drawback, vB_kpnM_17-11 can be protected by alginate and chitosan to avoid inactivation by gastric juices (Silva Batalha et al., 2021). A limitation of vB_kpnM_17-11 is its narrow range, being able to lyse only 4 out of 96 tested strains of *K. pneumoniae*. Lysed strains belonged to serotype K19. In this sense, phages with a wider host range are desirable. In addition, bacteria are more likely to develop phage resistance to narrow host spectrum phages. These limitations should be acknowledged when considering future applications of vB_kpnM_17-11. On the other hand, however, phages that lyse single bacterial serotypes may prove useful in bacterial serotyping (Song et al., 2021). Differences in host range are often related to the phage tail structure responsible for recognition and adsorption. However, the specific mechanism of host range of vB_kpnM_17-11 needs to be further studied.

The basic characteristics of the vB_kpnM_17-11 genome are similar to those of other published *Myoviridae* phages. Their genomes are all dsDNA and the genes encoding the same function are arranged in clusters (Dion et al., 2020). The

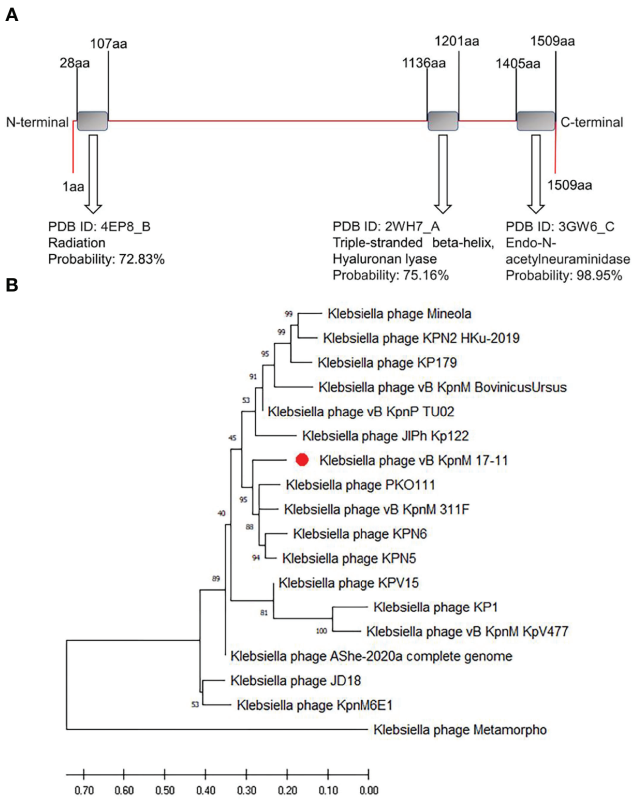

FIGURE 8 | The prediction domines and phylogenetic tree of depolymerase Dep022. **(A)** Domains of depolymerase Dep022 predicted using HHpred software. HHpred prediction results show that DEP022 has three different domains. **(B)** Phylogenetic tree of depolymerase. Phylogenic tree of depolymerases established using MEGA-X software by the neighbor-joining method with 1000 bootstrap replicates. The red dot highlights the Dep022 depolymerase of vB_kpnM_17-11.

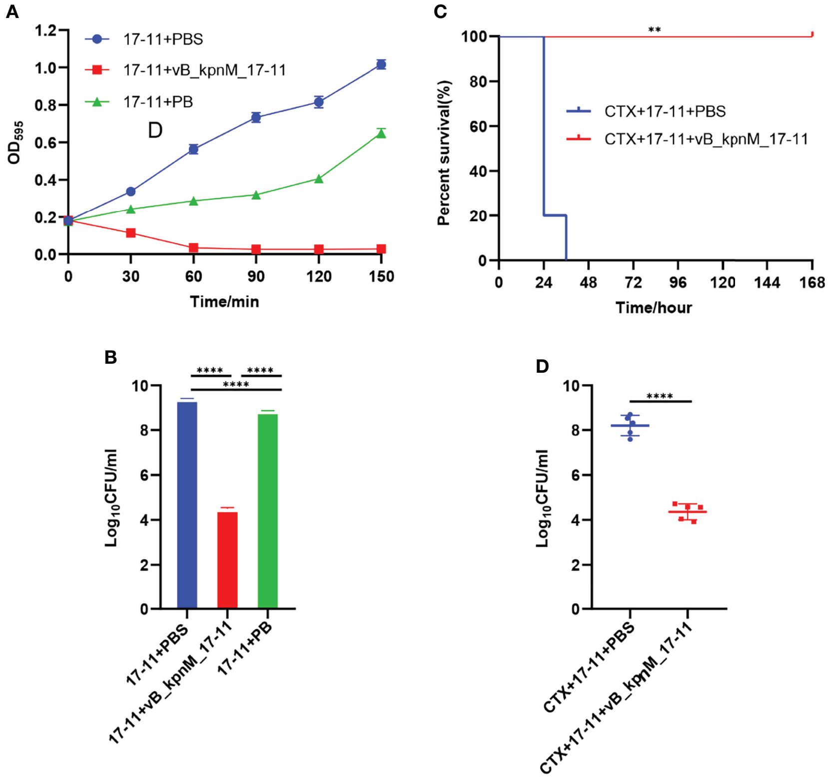

FIGURE 9 | Sterilization experiment *in vitro* and *in vivo*. **(A)** Bacteriostatic curve of phage *in vitro*. PBS, vB_kpnM_17-11 or PB were added to 50 mL exponential phase *K. pneumoniae* 17-11. The value of OD_{595} was measured every 30 min from 0 min to 180 min. **(B)** Bactericidal efficiency of phage *in vitro*. ****$P < 0.0001$, two-sided Mann–Whitney test. **(C)** Survival of mice after infection by *K. pneumoniae* 17-11. **$P < 0.01$ (Gehan-Breslow-Wilcoxon test). **(D)** Abdominal lavage fluid bacterial load. Mice were infected with *K. pneumoniae* 17-11 intraperitoneally and treated with phage. Peritoneal lavage was harvested at 24 h post infection and CFU were quantified. ****$P < 0.0001$, two-sided Mann–Whitney test.

proportion of non-coding regions of vB_kpnM_17-11 is only 3%. The coding genes for vB_kpnM_17-11 are tightly packed, with overlapping ORFs. This phenomenon allows phages to encode enough functional genes in a small genome; the smaller the genome, the lower the cost of replication.

vB_kpnM_17-11 genome was modularized in this study. The nucleotide metabolism and replication module is mainly responsible for the replication and regulation of phage genome. Usually, dsDNA phage genomes encode their own RNA polymerase (RNAP) (Zhao et al., 2019), but the phage vB_kpnM_17-11 does not encode RNAP. In addition, we found sigma factors and RNA polymerase binding proteins in the vB_kpnM_17-11 genome, which can modify host RNAP to recognize the promoter region of phage genes to complete the expression of phage genes (Yuan et al., 2020). In the packaging module, a putative portal vertex protein is predicted to form phage DNA channels into empty capsid proteins located at the tip of the phage head. The terminal enzyme large subunit transfers the phage DNA to the empty capsid and modifies it to complete the packaging process. The small subunit of the terminal enzyme binds to the packaging initiation site and regulates the ATP activity of the large subunit of the terminal enzyme (Feiss and Rao, 2012). In the host lysis module, the RZ/RZ1 protein widely present in Gram-negative phages was also found in vB_kpnM_17-11. This protein has certain peptidase activity, which can degrade the oligopeptide bond between the cell wall and the cell membrane, and promote the rapid release of daughter phages. dsDNA phages are mostly Holin-Endolysin systems, but vB_kpnM_17-11 has only holin (Young et al., 2000); endolysin is not found. This suggests that the phage may encode a new endolysin or have other lysing systems, which need to be further studied. The genes in the morphological module can be divided into two parts, the head morphological genes and the tail morphological genes. The genes responsible for phage head formation tend to be highly conserved to ensure the life process of the phage, but the phage tail genes experience frequent mutations to change their structure to recognize more diverse bacteria (Dion et al., 2020).

Multiple sequence alignment and BLAST highlighted the similarity between vB_kpnM_17-11 and related phages such as PKO111 and KP1. The genes with lower similarity were mainly phage tail genes. The tail gene of the phage is most prone to mutation and evolution (Comeau et al., 2007). The tail genes are often related to recognition and adsorption, so the phage gene rearrangement and mutation may affect the host range of the phage. This may be the reason why vB_kpnM_17-11 has a high similarity with PKO111 and KP1 genes, but the host range is completely different. Phylogenetic analysis showed that vB_kpnM_17-11 was closely related to *Klebsiella* phages PKO111, vB_kpnP_TU02, JD18, JIPh Kp122 and Mineola. Genomic comparisons also showed that these phages were similar and evolutionarily close to vB_kpnM_17-11.

Depolymerase was first reported in the 1956s (Adams and Park, 1956). Specifically, the depolymerase encoded by *Pseudomonas aeruginosa* phage IME180 (Mi et al., 2019), *Escherichia coli* phage vB_EcoM_ECOO78 (Guo et al., 2017) and *K. pneumoniae* phage KP36 (Majkowska-Skrobek et al., 2016) showed great biofilm elimination and antibacterial ability *in vitro*. In our study, we found a phage depolymerase Dep022. Dep022 contains two depolymerase domains and shares an ORF with the phage structural protein. The Endo-N-acetylneuraminidase domain of Dep022 belongs to the hydrolytic depolymerase domain, which acts by hydrolyzing the side chain of the O-antigen of lipopolysaccharide (LPS) or the oxyglycoside bond in the capsular polysaccharide (Kim et al., 2011). Neuraminidase is the most common structural protein depolymerase in phages and is widely distributed in the tail fiber and tail plate of *Myoviridae* phages (Pires et al., 2016). The hyaluronidase domain belongs to the lytic depolymerase domain, which cleaves polysaccharides into monosaccharides by directly severing the chemical bond between monosaccharides and C4 uronic acids and introducing unsaturated bonds between the aldehyde acid ends of C4 and C5. However, the related domain of hyaluronidase is relatively rare in phages (Pires et al., 2016). At the same time, the two depolymerase domains presented us with a problem: we were unable to determine the type of Dep022. The resolution of this problem depends on the subsequent study of Dep022. In addition, DepoKP36 (Majkowska-Skrobek et al., 2016), a depolymerase encoded by *K. pneumoniae* phage KP36 with a similar Endo-N-acetylneuraminidase domain, has been confirmed to have depolymerase activity. This finding further raises the possibility that Dep022 has depolymerase activity. Phylogenetic tree analysis showed that Dep022 had a close genetic relationship with other similar phage genes that might encode depolymerases. Nonetheless, these phages have not been reported to have depolymerase activity, which may be related to gene point mutations in the phage genes.

PB and vB_kpnM_17-11 were used in *in vitro* sterilization tests. We found that vB_kpnM_17-11 is more effective than PB in terms of bactericidal ability, which may be associated with the continuous reproduction of vB_kpnM_17-11 (Taati Moghadam et al., 2020). vB_kpnM_17-11 reduced the number of bacteria *in vitro* from 10^9 CFU/mL to 10^4 CFU/mL, a 10^5-fold reduction. In comparison, phage phiLLS could only lyse 94% of *Escherichia coli in vitro* at MOI of 10 and 100 (Amarillas et al., 2017), indicating that the lytic efficiency of vB_kpnM_17-11 was higher than that of phiLLS. vB_kpnM_17-11 was able to increase the 24 hours survival rate of systemic-infected mice from 20% to 100%, and the therapeutic effect was comparatively better than that reported for *Klebsiella* phage 1513 (Cao et al., 2015) which can improve the 24 hours survival rate of mice with pneumonia by 70%. vB_kpnM_17-11 reduced the number of bacteria in peritoneal lavage fluid by 10^4 times, while *Klebsiella* phage 1513 only reduced bacterial load in the lungs of mice by 10^2 times (Cao et al., 2015). However, the phage cocktail VBSM-A1/VBSP-A2 (Geng et al., 2020) reduced bacterial load in the breast of mice about 10^5 times, which was superior to vB_kpnM_17-11. Frequently, phage cocktails work better than therapies based on a single phage. Furthermore, phage treatment has also shown great therapeutic effects in human. Recently, researchers cleared CRKP from the patients' intestines using oral and rectal administration of phage preparations (Corbellino et al., 2020). In addition to clinical treatment, phage preparations are also expected to play a key role in environmental disinfection, fisheries, animal husbandry, and industrial fermentation. Phages show good antibacterial effects as potential antibacterial agents, and their effects on bacteria deserve further study.

Previous studies have also isolated phages that lyse CRKP, such as kpssk3 (Shi et al., 2020), vB_KpnP_IME337 (Gao et al., 2020), and TSK1 (Tabassum et al., 2018). The biological characteristics of vB_kpnM_17-11 were not significantly different from those of these phages in terms of the one-step growth curve, temperature, and pH stability. In terms of genetic characteristics, their genome size and ORF number vary greatly, which is related to the large difference in phage genome among different species. The biggest difference was in the host range, kPSSK3 could lyse 25 of 77 strains, vB_KpnP_IME337 had no sensitivity to other 29 strains except host bacteria, and vB_kpnM_17-11 could lyse the only 4 of 92 strains. The difference in host range is related to the difference in phage tail structure, and the specific mechanism remains to be further explored. But vB_kpnM_17-11 has two potential advantages over other phages that can lyse CRKP. One advantage is that we can develop new antibacterial agents based on the predicted depolymerase Dep022, which is expected to ameliorate the increasingly serious bacterial resistance phenomenon. Another advantage is that we can use more *K. pneumoniae* to explore the host range of vB_kpnM_17-11. If vB_kpnM_17-11 is specific for *K. pneumoniae* serotype K19, then vB_kpnM_17-11 has potential application in the identification of *K. pneumoniae* serotype.

Although phages have broad clinical application prospects for the treatment of infections caused by drug-resistant bacteria, phages still have limitations in practical clinical application. First, the *in vivo* pharmacokinetics and pharmacodynamics of different phage preparations vary compared to antibiotic therapy. Preparations containing different phages have different biological properties, so there are many differences in practical clinical applications (Nilsson, 2019). In addition, there are no standard treatment guidelines for phage therapy, and there are no effective guidelines for how much phage should be used during treatment, how long it should be administered, and how it should be administered. Furthermore, certain endotoxins are produced during the production of phage preparations, which may be cytotoxic and immunogenic. According to the upper limit of endotoxin content of existing clinical preparations of 5 EU/(kg·h), most phage preparations do not meet the standards for clinical use (Henein, 2013). Finally, phage therapy may not be accepted by some people due to the lack of awareness of phages among medical personnel and the public. Although there are still many problems in the large-scale clinical application of phages, more and more researchers have paid attention to the value of phage therapy. It is important to note that the use of phages is not only the use of phages to treat bacterial infections, but also includes the use of phage antibiotic combinations, phage-derived enzymes and phage disinfection in hospital environments (Gordillo Altamirano and Barr, 2019). It is believed that with the further development of phage research, the clinical application of phage will usher in a bright future (Sharma et al., 2017).

DATA AVAILABILITY STATEMENT

The datasets presented in this study can be found in online repositories. The names of the repository/repositories and accession number(s) can be found below: https://www.ncbi.nlm.nih.gov/nuccore/MW239157.

ETHICS STATEMENT

The animal study was reviewed and approved by Ethics Committee of Experimental Animals, Southwest Medical University 20211124-002.

AUTHOR CONTRIBUTIONS

JB, RH and YZ conceived and designed this study. JB performed the experiments and drafted the manuscript. FZ, SL, QC, WW and RH contributed reagents/materials/analysis tools. YW, AM-R, ÅS and YZ critically revised the manuscript. All authors read and approved the final manuscript. All authors contributed to the article and approved the submitted version.

FUNDING

This research was funded by the National Natural Science Foundation of China [31500114], the Sichuan Province Science and Technology project [2020YJ0338], Natural Science Foundation of Luzhou (2021-NYF-20) and Southwest Medical University project [21YYJC0529].

SUPPLEMENTARY MATERIAL

The Supplementary Material for this article can be found online at: https://www.frontiersin.org/articles/10.3389/fcimb.2022.897531/full#supplementary-material

REFERENCES

Adams, M. H., and Park, B. H. (1956). An Enzyme Produced by a Phage-Host Cell System. II. The Properties of the Polysaccharide Depolymerase. *Virology* 2, 719–736. doi: 10.1016/0042-6822(56)90054-X

Alikhan, N. F., Petty, N. K., Ben Zakour, N. L., and Beatson, S. A. (2011). BLAST Ring Image Generator (BRIG): Simple Prokaryote Genome Comparisons. *BMC Genomics* 12, 402. doi: 10.1186/1471-2164-12-402

Amarillas, L., Rubí-Rangel, L., Chaidez, C., González-Robles, A., Lightbourn-Rojas, L., and León-Félix, J. (2017). Isolation and Characterization of phiLLS, a Novel Phage With Potential Biocontrol Agent Against Multidrug-Resistant Escherichia Coli. *Front. Microbiol.* 8. doi: 10.3389/fmicb.2017.01355

Beasley, D. E., Koltz, A. M., Lambert, J. E., Fierer, N., and Dunn, R. R. (2015). The Evolution of Stomach Acidity and Its Relevance to the Human Microbiome. *PloS One* 10, e0134116. doi: 10.1371/journal.pone.0134116

Cai, R., Wang, Z., Wang, G., Zhang, H., Cheng, M., Guo, Z., et al. (2019). Biological Properties and Genomics Analysis of Vb_KpnS_GH-K3, a Klebsiella Phage With a Putative Depolymerase-Like Protein. *Virus Genes* 55, 696–706. doi: 10.1007/s11262-019-01681-z

Cao, F., Wang, X., Wang, L., Li, Z., Che, J., Wang, L., et al. (2015). Evaluation of the Efficacy of a Bacteriophage in the Treatment of Pneumonia Induced by Multidrug Resistance Klebsiella Pneumoniae in Mice. *BioMed. Res. Int.* 2015, 752930. doi: 10.1155/2015/752930

Carver, T. J., Rutherford, K. M., Berriman, M., Rajandream, M. A., Barrell, B. G., and Parkhill, J. (2005). ACT: The Artemis Comparison Tool. *Bioinformatics* 21, 3422–3423. doi: 10.1093/bioinformatics/bti553

Chan, P. P., and Lowe, T. M. (2019). Trnascan-SE: Searching for tRNA Genes in Genomic Sequences. *Methods Mol. Biol.* 1962, 1–14. doi: 10.1007/978-1-4939-9173-0_1

Chen, Y., Li, X., Wang, S., Guan, L., Li, X., Hu, D., et al. (2020). A Novel Tail-Associated O91-Specific Polysaccharide Depolymerase From a Podophage Reveals Lytic Efficacy of Shiga Toxin-Producing Escherichia Coli. *Appl. Environ. Microbiol.* 86 (9), e00145–20. doi: 10.1128/AEM.00145-20

Comeau, A. M., Bertrand, C., Letarov, A., Tétart, F., and Krisch, H. M. (2007). Modular Architecture of the T4 Phage Superfamily: A Conserved Core Genome and a Plastic Periphery. *Virology* 362, 384–396. doi: 10.1016/j.virol.2006.12.031

Corbellino, M., Kieffer, N., Kutateladze, M., Balarjishvili, N., Leshkasheli, L., Askilashvili, L., et al. (2020). Eradication Of A Multidrug-Resistant, Carbapenemase-Producing Klebsiella Pneumoniae Isolate Following Oral And Intra-Rectal Therapy With A Custom Made, Lytic Bacteriophage Preparation. *Clin. Infect. Dis.* 70, 1998–2001. doi: 10.1093/cid/ciz782

Cornelissen, A., Ceyssens, P. J., T'syen, J., Van Praet, H., Noben, J. P., Shaburova, O. V., et al. (2011). The T7-Related Pseudomonas Putida Phage Φ15 Displays Virion-Associated Biofilm Degradation Properties. *PloS One* 6, E18597. doi: 10.1371/journal.pone.0018597

Dion, M. B., Oechslin, F., and Moineau, S. (2020). Phage Diversity, Genomics And Phylogeny. *Nat. Rev. Microbiol.* 18, 125–138. doi: 10.1038/s41579-019-0311-5

Domingo-Calap, P., Beamud, B., Mora-Quilis, L., González-Candelas, F., and Sanjuán, R. (2020). Isolation And Characterization Of Two Klebsiella Pneumoniae Phages Encoding Divergent Depolymerases. *Int. J. Mol. Sci.* 21 (9), 3160. doi: 10.3390/ijms21093160

Dunstan, R. A., Bamert, R. S., Belousoff, M. J., Short, F. L., Barlow, C. K., Pickard, D. J., et al. (2021). Mechanistic Insights Into The Capsule-Targeting Depolymerase From A Klebsiella Pneumoniae Bacteriophage. *Microbiol. Spectr.* 9, E0102321. doi: 10.1128/Spectrum.01023-21

Feiss, M., and Rao, V. B. (2012). The Bacteriophage Dna Packaging Machine. *Adv. Exp. Med. Biol.* 726, 489–509. doi: 10.1007/978-1-4614-0980-9_22

Ferry, T., Kolenda, C., Batailler, C., Gustave, C. A., Lustig, S., Malatray, M., et al. (2020). Phage Therapy As Adjuvant To Conservative Surgery And Antibiotics To Salvage Patients With Relapsing S. Aureus Prosthetic Knee Infection. *Front. Med. (Lausanne)* 7. doi: 10.3389/fmed.2020.570572

Fu, L., Huang, M., Zhang, X., Yang, X., Liu, Y., Zhang, L., et al. (2018). Frequency of Virulence Factors in High Biofilm Formation Bla(KPC-2) Producing Klebsiella Pneumoniae Strains From Hospitals. *Microb. Pathog.* 116, 168–172. doi: 10.1016/j.micpath.2018.01.030

Gao, M., Wang, C., Qiang, X., Liu, H., Li, P., Pei, G., et al. (2020). Isolation and Characterization of a Novel Bacteriophage Infecting Carbapenem-Resistant Klebsiella Pneumoniae. *Curr. Microbiol.* 77, 722–729. doi: 10.1007/s00284-019-01849-8

Geng, H., Zou, W., Zhang, M., Xu, L., Liu, F., Li, X., et al. (2020). Evaluation Of Phage Therapy In The Treatment Of Staphylococcus Aureus-Induced Mastitis In Mice. *Folia Microbiol. (Praha)* 65, 339–351. doi: 10.1007/s12223-019-00729-9

Gordillo Altamirano, F. L., and Barr, J. J. (2019). Phage Therapy In The Postantibiotic Era. *Clin. Microbiol. Rev.* 32 (2), e00066–18. doi: 10.1128/CMR.00066-18

Guo, Z., Huang, J., Yan, G., Lei, L., Wang, S., Yu, L., et al. (2017). Identification And Characterization Of Dpo42, A Novel Depolymerase Derived From The Escherichia Coli Phage Vb_Ecom_Ecoo78. *Front. Microbiol.* 8. doi: 10.3389/fmicb.2017.01460

Henein, A. (2013). What Are The Limitations On The Wider Therapeutic Use Of Phage? *Bacteriophage* 3, E24872. doi: 10.4161/bact.24872

Jończyk, E., Kłak, M., Międzybrodzki, R., and Górski, A. (2011). The Influence Of External Factors On Bacteriophages–Review. *Folia Microbiol. (Praha)* 56, 191–200. doi: 10.1007/s12223-011-0039-8

Kim, S., Oh, D. B., Kang, H. A., and Kwon, O. (2011). Features And Applications Of Bacterial Sialidases. *Appl. Microbiol. Biotechnol.* 91, 1–15. doi: 10.1007/s00253-011-3307-2

Kropinski, A. M., Mazzocco, A., Waddell, T. E., Lingohr, E., and Johnson, R. P. (2009). Enumeration Of Bacteriophages By Double Agar Overlay Plaque Assay. *Methods Mol. Biol.* 501, 69–76. doi: 10.1007/978-1-60327-164-6_7

Kumar, S., Stecher, G., Li, M., Knyaz, C., and Tamura, K. (2018). Mega X: Molecular Evolutionary Genetics Analysis Across Computing Platforms. *Mol. Biol. Evol.* 35, 1547–1549. doi: 10.1093/molbev/msy096

Labrie, S. J., Samson, J. E., and Moineau, S. (2010). Bacteriophage Resistance Mechanisms. *Nat. Rev. Microbiol.* 8, 317–327. doi: 10.1038/nrmicro2315

Li, M., Xiao, Y., Li, P., Wang, Z., Qi, W., Qi, Z., et al. (2020). Characterization And Genome Analysis Of Klebsiella Phage P509, With Lytic Activity Against Clinical Carbapenem-Resistant Klebsiella Pneumoniae Of The Kl64 Capsular Type. *Arch. Virol.* 165, 2799–2806. doi: 10.1007/s00705-020-04822-0

Majkowska-Skrobek, G., Łątka, A., Berisio, R., Maciejewska, B., Squeglia, F., Romano, M., et al. (2016). Capsule-Targeting Depolymerase, Derived From Klebsiella Kp36 Phage, As A Tool For The Development Of Anti-Virulent Strategy. *Viruses* 8 (12):324. doi: 10.3390/v8120324

Majkowska-Skrobek, G., Latka, A., Berisio, R., Squeglia, F., Maciejewska, B., Briers, Y., et al. (2018). Phage-Borne Depolymerases Decrease Klebsiella Pneumoniae Resistance To Innate Defense Mechanisms. *Front. Microbiol.* 9. doi: 10.3389/fmicb.2018.02517

Manepalli, S., Gandhi, J. A., Ekhar, V. V., Asplund, M. B., Coelho, C., and Martinez, L. R. (2013). Characterization Of A Cyclophosphamide-Induced Murine Model Of Immunosuppression To Study Acinetobacter Baumannii Pathogenesis. *J. Med. Microbiol.* 62, 1747–1754. doi: 10.1099/jmm.0.060004-0

Martín-Rodríguez, A. J., Rhen, M., Melican, K., and Richter-Dahlfors, A. (2020). Nitrate Metabolism Modulates Biosynthesis Of Biofilm Components In Uropathogenic Escherichia Coli And Acts As A Fitness Factor During Experimental Urinary Tract Infection. *Front. Microbiol.* 11, 26. doi: 10.3389/fmicb.2020.00026

Michaud, P., Da Costa, A., Courtois, B., and Courtois, J. (2003). Polysaccharide Lyases: Recent Developments As Biotechnological Tools. *Crit. Rev. Biotechnol.* 23, 233–266. doi: 10.1080/07388550390447043

Mi, L., Liu, Y., Wang, C., He, T., Gao, S., Xing, S., et al. (2019). Identification Of A Lytic Pseudomonas Aeruginosa Phage Depolymerase And Its Anti-Biofilm Effect And Bactericidal Contribution To Serum. *Virus Genes* 55, 394–405. doi: 10.1007/s11262-019-01660-4

Nilsson, A. S. (2019). Pharmacological Limitations Of Phage Therapy. *Ups J. Med. Sci.* 124, 218–227. doi: 10.1080/03009734.2019.1688433

Onsea, J., Post, V., Buchholz, T., Schwegler, H., Zeiter, S., Wagemans, J., et al. (2021). Bacteriophage Therapy For The Prevention And Treatment Of Fracture-Related Infection Caused By Staphylococcus Aureus: A Preclinical Study. *Microbiol. Spectr.* 9, E0173621. doi: 10.1128/spectrum.01736-21

Pan, Y. J., Lin, T. L., Chen, Y. H., Hsu, C. R., Hsieh, P. F., Wu, M. C., et al. (2013). Capsular Types Of Klebsiella Pneumoniae Revisited By Wzc Sequencing. *PloS One* 8, E80670. doi: 10.1371/journal.pone.0080670

Peng, Q., Fang, M., Liu, X., Zhang, C., Liu, Y., and Yuan, Y. (2020). Isolation And Characterization Of A Novel Phage For Controlling Multidrug-Resistant Klebsiella Pneumoniae. *Microorganisms* 8 (4):542. doi: 10.3390/microorganisms8040542

Peng, Q., and Yuan, Y. (2018). Characterization Of A Novel Phage Infecting The Pathogenic Multidrug-Resistant Bacillus Cereus And Functional Analysis Of Its Endolysin. *Appl. Microbiol. Biotechnol.* 102, 7901–7912. doi: 10.1007/s00253-018-9219-7

Pires, D. P., Oliveira, H., Melo, L. D., Sillankorva, S., and Azeredo, J. (2016). Bacteriophage-Encoded Depolymerases: Their Diversity And Biotechnological Applications. *Appl. Microbiol. Biotechnol.* 100, 2141–2151. doi: 10.1007/s00253-015-7247-0

Sharma, S., Chatterjee, S., Datta, S., Prasad, R., Dubey, D., Prasad, R. K., et al. (2017). Bacteriophages And Its Applications: An Overview. *Folia Microbiol. (Praha)* 62, 17–55. doi: 10.1007/s12223-016-0471-x

Shi, Y., Chen, Y., Yang, Z., Zhang, Y., You, B., Liu, X., et al. (2020). Characterization And Genome Sequencing Of A Novel T7-Like Lytic Phage, Kpssk3, Infecting Carbapenem-Resistant Klebsiella Pneumoniae. *Arch. Virol.* 165, 97–104. doi: 10.1007/s00705-019-04447-y

Silva Batalha, L., Pardini Gontijo, M. T., Vianna Novaes De Carvalho Teixeira, A., Meireles Gouvêa Boggione, D., Soto Lopez, M. E., Renon Eller, M., et al. (2021). Encapsulation In Alginate-Polymers Improves Stability And Allows Controlled Release Of The Ufv-Areg1 Bacteriophage. *Food Res. Int.* 139, 109947. doi: 10.1016/j.foodres.2020.109947

Söding, J., Biegert, A., and Lupas, A. N. (2005). The HHpred Interactive Server for Protein Homology Detection and Structure Prediction. *Nucleic Acids Res.* 33, W244–W248. doi: 10.1093/nar/gki408

Song, Y., Peters, T. L., Bryan, D. W., Hudson, L. K., and Denes, T. G. (2021). Characterization of a Novel Group of Listeria Phages That Target Serotype 4b Listeria Monocytogenes. *Viruses* 13 (4):671. doi: 10.3390/v13040671

Taati Moghadam, M., Amirmozafari, N., Shariati, A., Hallajzadeh, M., Mirkalantari, S., Khoshbayan, A., et al. (2020). How Phages Overcome the Challenges of Drug Resistant Bacteria in Clinical Infections. *Infect. Drug Resist.* 13, 45–61. doi: 10.2147/IDR.S234353

Tabassum, R., Shafique, M., Khawaja, K. A., Alvi, I. A., Rehman, Y., Sheik, C. S., et al. (2018). Complete Genome Analysis of a Siphoviridae Phage TSK1 Showing Biofilm Removal Potential Against Klebsiella Pneumoniae. *Sci. Rep.* 8, 17904. doi: 10.1038/s41598-018-36229-y

Wu, N., Dai, J., Guo, M., Li, J., Zhou, X., Li, F., et al. (2021). Pre-Optimized Phage Therapy on Secondary Acinetobacter Baumannii Infection in Four Critical COVID-19 Patients. *Emerg. Microbes Infect.* 10, 612–618. doi: 10.1080/22221751.2021.1902754

Young, I., Wang, I., and Roof, W. D. (2000). Phages Will Out: Strategies of Host Cell Lysis. *Trends Microbiol.* 8, 120–128. doi: 10.1016/S0966-842X(00)01705-4

Yuan, Y., Xi, H., Dai, J., Zhong, Y., Lu, S., Wang, T., et al. (2020). The Characteristics and Genome Analysis of the Novel Y. Pestis Phage JC221. *Virus Res.* 283, 197982. doi: 10.1016/j.virusres.2020.197982

Zhang, F., Ding, M., Yan, X., Bai, J., Li, Q., Zhang, B., et al. (2021a). Carbapenem-Resistant K. Pneumoniae Exhibiting Clinically Undetected Amikacin and Meropenem Heteroresistance Leads to Treatment Failure in a Murine Model of Infection. *Microb. Pathog.* 160, 105162. doi: 10.1016/j.micpath.2021.105162

Zhang, B., Hu, R., Liang, Q., Liang, S., Li, Q., Bai, J., et al. (2022). Comparison of Two Distinct Subpopulations of Klebsiella Pneumoniae ST16 Co-Occurring in a Single Patient. *Microbiol. Spectr.*, e0262421. doi: 10.1128/spectrum.02624-21

Zhang, F., Li, Q., Bai, J., Ding, M., Yan, X., Wang, G., et al. (2021b). Heteroresistance to Amikacin in Carbapenem-Resistant Klebsiella Pneumoniae Strains. *Front. Microbiol.* 12. doi: 10.3389/fmicb.2021.682239

Zhao, F., Sun, H., Zhou, X., Liu, G., Li, M., Wang, C., et al. (2019). Characterization and Genome Analysis of a Novel Bacteriophage Vb_SpuP_Spp16 That Infects Salmonella Enterica Serovar Pullorum. *Virus Genes* 55, 532–540. doi: 10.1007/s11262-019-01664-0

Zhou, W., Feng, Y., and Zong, Z. (2018). Two New Lytic Bacteriophages of the Myoviridae Family Against Carbapenem-Resistant Acinetobacter Baumannii. *Front. Microbiol.* 9, 850. doi: 10.3389/fmicb.2018.00850

Conflict of Interest: The authors declare that the research was conducted in the absence of any commercial or financial relationships that could be construed as a potential conflict of interest.

frontiers | Frontiers in Cellular and Infection Microbiology

ORIGINAL RESEARCH
published: 14 July 2022
doi: 10.3389/fcimb.2022.941325

Enterovirus A Shows Unique Patterns of Codon Usage Bias in Conventional Versus Unconventional Clade

Liyan Zeng[1†], Ming Chen[1†], Min Wang[1], Liuyao Zhu[1], Jingjing Yan[1], Xiaoyan Zhang[1*], Jianqing Xu[1*] and Shuye Zhang[2*]

[1] Shanghai Public Health Clinical center AND Institutes of Biomedical Sciences, Fudan University, Shanghai, China, [2] Clinical Center for BioTherapy & Institutes of Biomedical Sciences, Zhongshan Hospital, Fudan University, Shanghai, China

Edited by:
Zhenlong Liu,
McGill University, Canada

Reviewed by:
Yongfen Xu,
Chinese Academy of Sciences (CAS),
China
Xing-Yi Ge,
Hunan University, China
Robert Scarborough,
Lady Davis Institute (LDI), Canada

***Correspondence:**
Shuye Zhang
shuye_zhang@fudan.edu.cn
Xiaoyan Zhang
zhangxiaoyan@fudan.edu.cn
Jianqing Xu
xujianqing@fudan.edu.cn

†These authors have contributed equally to this work and share first authorship

Specialty section:
This article was submitted to
Virus and Host,
a section of the journal
Frontiers in Cellular and
Infection Microbiology

Received: 11 May 2022
Accepted: 21 June 2022
Published: 14 July 2022

Citation:
Zeng L, Chen M, Wang M, Zhu L, Yan J, Zhang X, Xu J and Zhang S (2022) Enterovirus A Shows Unique Patterns of Codon Usage Bias in Conventional Versus Unconventional Clade. Front. Cell. Infect. Microbiol. 12:941325. doi: 10.3389/fcimb.2022.941325

Enterovirus A (*EV-A*) species cause hand, foot and mouth disease (HFMD), threatening the health of young children. Understanding the mutual codon usage pattern of the virus and its host(s) has fundamental and applied values. Here, through examining multiple codon usage parameters, we found that the codon usage bias among *EV-A* strains varies and is clade-specific. EVA76, EVA89, EVA90, EVA91 and EVA92, the unconventional clade of *EV-A* strains, show unique codon usage pattern relative to the two conventional clades, including EVA71, CVA16, CVA6 and CVA10, *etc.* Analyses of Effective Number of Codon (ENC), Correspondence Analysis (COA) and Parity Rule 2 (PR2), *etc.*, revealed that the codon usage patterns of *EV-A* strains are shaped by mutation pressure and natural selection. Based on the neutrality analysis, we determined the dominant role of natural selection in the formation of the codon usage bias of *EV-A*. In addition, we have determined the codon usage compatibility of potential hosts for *EV-A* strains using codon adaptation index (CAI), relative codon deoptimization index (RCDI) and similarity index (SiD) analyses, and found that *EV-A* showed host-specific codon adaptation patterns in different clades. Finally, we confirmed that the unique codon usage pattern of the unconventional clade affected protein expression level in human cell lines. In conclusion, we identified novel characteristics of codon usage bias in distinct *EV-A* clades associated with their host range, transmission and pathogenicity.

Keywords: ***enterovirus A*, HFMD, codon usage, natural selection, evolution**

1 INTRODUCTION

Enterovirus (EV) is a small, non-enveloped RNA virus of the family *Picornaviridae*, consisting of a positive-sense single-stranded RNA genome of approximately 7.4 kb and a 30 nM icosahedral capsid. The EV genome has an open reading frame, and the encoded polyprotein consists of P1, P2 and P3 regions. The P1 region encodes the capsid proteins: VP1, VP2, VP3 and VP4, while the P2 and P3 regions (P2-P3) encode the non-structural proteins: 2A, 2B, 2C, 3A, 3B, 3C and 3D. Four species of EVs are known to infect humans: *EV-A, EV-B, EV-C* and *EV-D*. *EV-A* consists of at least

22 serotypes (Oberste and Gerber, 2014). EVA71, CVA6, CVA10 and CVA16 in *EV-A* are the major pathogens of HFMD, although other serotypes of *EV-A* and some *EV-B* strains are also less frequently identified (Zhuang et al., 2015). HFMD mainly affects children less than 5 years of age worldwide. Typical symptoms of HFMD include fever, nodular lesions and small ulcers or blisters in the hands, feet and mouth, *etc* (Organization, W.H., 2011). Most affected children can recover quickly while a small number of children can have serious complications such as myocarditis, pulmonary edema, aseptic meningoencephalitis and even death. It has been reported that CVA16 infection is benign and self-limited (Mao et al., 2014) while EVA71 infection can cause serious illnesses (Wang and Liu, 2014). Recently, CVA6 and CVA10 have increasingly caused outbreaks of HFMD around the world as emerging pathogens of HFMD (Bian et al., 2015; Zhang et al., 2017). The CVA6-related HFMD showed a higher incidence among adults (Bian et al., 2015). CVA10 is often co-epidemic with CVA6 (Blomqvist et al., 2010) and the co-infection of multiple pathogens increases the risk of virus recombination (Liu et al., 2014). EVA76, EVA89, EVA90 and EVA91 have been characterized as an unique phylogenetic clade of *EV-A* since 2005 (Oberste et al., 2005; Xu et al., 2011; Tao et al., 2013). Based on the phylogenetic and receptor usage, *EV-A* strains are currently divided into three unique clades. Clade 1 includes EVA71 and CVA16 using SCARB2 as receptor (Yamayoshi et al., 2009), clade 2 includes CVA6 and CVA10 using KREMEN1 as receptor (Staring et al., 2018), whereas clade 3 includes EVA76 and EVA89 with their receptor still unidentified. Recently, we further showed that the *EV-A* strains of EVA76 and EVA89 clade have virological properties distinct from other "conventional" *EV-A* strains (Wang et al., 2020), and are regarded as "unconventional" *EV-A* viruses. It is concerned that the application of EVA71 vaccine may alter the spectrum of the HFMD epidemic, and that co-circulating of *EV-A* viruses may results in new mutants or recombinants (Yip et al., 2013; Lukashev et al., 2014). Unconventional *EV-As* has the potential to spread and cause outbreaks in the future. Therefore, further investigation into the evolution and variability of the *EV-A* gene pools is required.

This codon usage bias has been observed in all branches of life and results in species-specific patterns of codon usage (Sharp et al., 1995). The cause of codon bias may be explained by mutation pressure and natural selection pressure (Bulmer, 1991). Mutation pressure theory explains codon bias through genomic mutation bias, where the composition of AU/GC nucleotides is uneven (Sueoka, 1988). Natural selection theory assumes that the codon usage bias comes mainly from translational pressure, due to the host tRNA pool and secondary RNA structure (Simmonds et al., 2004; Steil and Barton, 2009). The CpG and UpA composition of pathogens may also be classified as selective pressure as a result of immune defense recognition (Belalov and Lukashev, 2013). The codon usage bias are important for the fitness, evolution and virulence of viruses. Discovering codon usage patterns of viruses may provide insights into the drivers of virus evolution and adaptation.

Although there are previous reports regarding the codon usage patterns for some major pathogens of HFMD (Ma et al., 2014; Zhang et al., 2014), the patterns of the *EV-A* species are still unclear, especially for the unconventional strains (Liu et al., 2011; Su et al., 2017). The difference of codon bias between the structural and non-structural genetic regions of *EV-A* is also uncertain. Consequently, in this study, we conducted a wide range of analyses to investigate (i) the codon bias pattern of *EV-A*; (ii) the primary factors causing codon usage bias of *EV-A*; (iii) the adaptability of *EV-A* to the host; and (iv) the level of protein expression affected by the specific codon bias.

2 MATERIALS AND METHODS

2.1 Viral Sequence Data

The complete genomic sequences and coding sequence (CDS) of 1006 *EV-A* strains were obtained from the Virus Pathogen Resource (ViPR) database (Pickett et al., 2012).

2.2 Recombination and Phylogenetic Analyses

Phylogenetic analysis requires that the evolution of a serious of sequences may be properly delineated by a single phylogenetic tree, whereas recombination events in these sequences may severely compromise the accuracy of phylogenetic trees. Hence, non-recombinant datasets produced by recombination analysis are desirable prior to phylogenetic analysis. We have conducted the recombination analysis by Recombination Detection Program (version 4.95) using RDP methods (Martin et al., 2015). Phylogenetic analysis was then carried out on non-recombinant sequences in the MEGA software (version 7.0) using the maximum likelihood model (bootstrap value=1000) (Kumar et al., 2016).

2.3 Nucleotide Composition Analysis

The codon compositions in 3rd position (A3%, U3%, C3% and G3%) have been calculated with Codon W 1.4.2 (Peden and John, 2000). The frequencies of A, U, C and G (%), GC/AU and GC1, GC2, GC12, GC3 content (frequency of occurrence of GC-dinucleotides at each location) have also been calculated. Five codons were excluded from the codon usage bias analyses, including stop codons (UAA, UAG and UGA) and the only codon encoding for Met(AUG) and Trp(UGG).

2.4 Dinucleotide Analysis

The frequencies of dinucleotides are known to be influenced by corresponding individual nucleotide abundance. To avoid this bias, the odds ratio index (ρXY) is used (Karlin et al., 1997). X and Y stand for each nucleotide (A, U, G or C). F_X is the frequency of X while F_Y is the frequency of Y. F_{XY} is the frequency of dinucleotide XY. The calculation of ρXY is as follows:

$$\rho XY = F_{XY}/F_X F_Y$$

ρXY=1 indicates that the dinucleotide is present at the corresponding single nucleotide frequencies. Values of ρXY>1 indicate an over-representation of dinucleotide, and ρXY<1 indicates an under-representation.

2.5 Relative Synonymous Codon Usage Analysis

The relative synonymous codon usage (RSCU) values for all the *EV-A* CDS were calculated to determine the characteristics of synonymous codon usage. The RSCU values represent the ratio of the observed frequency of one codon to its expected frequency in the synonymous codon family, considering that all codons for an particular amino acid are equally used. Thus, the RSCU values may eliminate the influences from the amino acid compositions or the coding sequence sizes. When the RSCU value is 1.0, there is no bias for codon usage (Sharp and Li, 1986). Synonymous codons with RSCU values >1.0 display a positive codon usage bias while those with RSCU values <1.0 display a negative codon usage bias. Synonymous codons with RSCU values above 1.6 and below 0.6 were considered to be over-represented or under-represented codons, respectively (Wong et al., 2010). The RSCU of individual codons has been calculated by CodonW 1.4.2.

2.6 Effective Number of Codons Analysis

The effective number of codons (ENC) value describes the degree of unbalanced use of synonymous codons (Wright, 1990). ENC values range between 20 and 61. The lower ENC value indicates a greater extent of codon bias within a gene. Typically, an ENC value below 35 denotes a strong codon bias while an ENC value above 50 denotes a weak codon bias. ENC values were calculated through CodonW 1.4.2.

The ENC-GC3 may be used to explore the pattern for synonymous codon usage. Genes where the codon selection is limited only by the G&C mutation will be on or just below the the expected ENC curve (Comeron and Aguadé, 1998).

2.7 Correspondence Analysis

Correspondence analysis (COA) is a multivariate analysis that provides a geometrical representation of a contingency table, which is used to analyze the major trends of codon usage patterns among genes (Grantham et al., 1980). RSCU is used in COA to minimize the effect of amino acid composition on the analysis of codon usage. Each coding sequence is represented as a vector with 59 dimensions which correspond to the RSCU value of each codon except for Met, Trp and the stop codons. COA reduces the high-dimensional codon-frequency data to a limited number of variables, referred to as principal axes. The axes preserve much of the information about the variability of codon usage among the genes. COA plot selects the first two principal axes as X and Y axes and shows the viral strains as scatters in the two-dimensional diagram. COA analysis is conducted using CodonW 1.4.2.

2.8 Correlation Analysis

Correlation analyses were conducted to identify the relationships between the nucleotide composition and the first two COA principal axes using Spearman's rank correlation test, using the R package "Corrgrams" (Friendly, 2002).

2.9 Parity Rule 2 Analysis

Parity rule 2 (PR2) analysis, exploring the bias between A3/(A3 + U3) and G3/(G3 + C3) in the amino acid family with four-codon, was used to demonstrate the effects of mutation pressure and natural selection on the codon usage. The dots at the center of the plot (A=U, G=C) indicate equal effects of mutation and selection (Sueoka, 1995; Sueoka, 1999).

2.10 Neutrality Plot Analysis

In the neutrality plot analysis, the regression coefficient (CG12 against GC3) is considered to be the mutation-selection equilibrium coefficient. This analysis was performed to determine the effects of mutation pressure and natural selection on the codon usage patterns of the *EV-A* coding sequences (Sueoka, 1988). The slope of the regression lines (ϵ) may indicate the evolutionary rates of mutation pressure, whereas 1-ϵ represents selective pressure. If ϵ is close to 1, it means a strong correlation between GC12 and GC3, indicating that mutation pressure is dominant. While ϵ is near 0, it indicates a low mutation pressure.

2.11 Codon Adaptation Analysis

The codon adaptation index (CAI) is a common measure used to quantify the similarity of the synonymous codon usage between samples and reference. It may also be used to predict the gene expression level based on its codon sequence. The CAI values range from 0 through 1. The higher the CAI value, the higher the degree of gene expression and the higher the adaptation to specific hosts (Sharp and Li, 1987). We also borrowed two other indices reported in recent studies, the relative codon deoptimization index (RCDI) and the similarity index (SiD), to confirm the effects of *EV-A* codon usage patterns on hosts or vectors. When the RCDI value is closer to 1, the codon usage pattern between the virus and its hosts is more similar. When RCDI is greater than 1, the higher RCDI value indicates greater deoptimization of the virus codon usage patterns relative to hosts (Mueller et al., 2006). The SiD value ranges from 0 to 1. When the SiD value is closer to 1, the codon usage patterns between the virus and the hosts differ significantly, and the effect of host codon usage on the virus is stronger (Zhou et al., 2013).

The CAI and RCDI analysis of the *EV-A* coding sequences was carried out using the CAIcal server (Puigbò et al., 2008). Here, synonymous codon usage patterns of selected potential hosts were used as references and obtained from the Codon Usage database (Nakamura et al., 2000).

2.12 Codon Optimization Experiment

EV-A genomic sequences were obtained from the National Center for Biotechnology Information, including EV71 (KU936132), CVA6 (KX064292), CVA10 (AY421767), CVA16 (MG957117), EVA76 (AY697458.1) and EVA89 (KT277550.1). The viral capsid encoding segment was obtained through *in vitro* synthesis, and was cloned into the expression vector by a

Seamless Cloning Kit (D7010M, Beyotime, Shanghai, China) according to the manufacturer's instruction. The expression vector was derived from the previously reported "pcDNA6.0A-FY-capsid-GFP" (Chen et al., 2012). The vector is based on pcDNA6.0 backbone and contained a CMV promoter. A fused green fluorescent protein (EGFP) was introduced between the promoter and the viral capsid, and a EVA71 2A protease recognition site (-AITTL-) was inserted between EGFP and VP4. Thus, EGFP was fused to the capsid protein and co-expressed. The amount of green fluorescence could be employed to signal the production of capsid protein.

3 RESULTS

3.1 Recombination and Phylogenetic Analyses of EV-A Genomes

To avoid the interference by the recombination events in phylogenetic analysis, recombination analysis was first performed on 1006 *EV-A* genomes to obtain non-recombinant datasets. 878 sequences showing a recombinant signal and 3 containing several stop codons were excluded from the analysis. The P1 region of 125 *EV-A* genomes and three EVs as outgroup (EVD68, accession numbers: AY426531, CVB3, accession numbers: M33854, PV1, accession numbers: V01150) were subjected to a phylogenetic analysis. A maximum likehood (ML) tree was built, and verified with 1000 bootstrap replicates. *EV-A* clustered into three phylogenetic clades: clade 1 (n=36), clade 2 (n=80) and clade 3 (n=9). The clade 1 includes CVA7, CVA14, CVA16, EVA71 and EVA120. Clade 2 includes CVA2, CVA3, CVA4, CVA5, CVA6, CVA8, CVA10 and CVA12. Clade 3 comprises EVA76, EVA89, EVA90, EVA91 and EVA92. The descriptions of the 125 strains are given in **Supplementary Table S1** and the phylogenetic tree is shown in **Supplementary Figure S1**.

3.2 The Genomes of EV-A Are Rich in AU Nucleotides and Lack CpG Dinucleotide

To understand the common features and differences of the *EV-A* genomes, we determined the contents of nucleotides and dinucleotides (**Supplementary Table S2**). The composition for nucleotide A (28.44 ± 0.35%) is highest, followed by U (24.49 ± 0.32%), C (24.23 ± 0.32%), and G (22.84 ± 0.38%). The proportions of different nucleotides at the 3rd codon position (A3, U3, G3 and C3) show that U3 (29.04 ± 1.04%) and C3 (27.04 ± 0.86%) are higher than A3 (24.65 ± 0.72%) and G3 (19.26 ± 0.90%). Compositions for GC and AU are 47.07 ± 0.61% and 52.93 ± 0.61% respectively, while compositions for GC3 and AU3 are 46.31 ± 1.60% and 53.69 ± 1.59%. These data show that *EV-A* coding sequences are rich in AU. The Kruskal-Wallis test, one way ANOVA and multiple comparison by LSD test was performed on three EV-A clades for each nucleotide index (**Supplementary Table S3**). Three of the 15 nucleotide indices show significant differences across the three *EV-A* clades ($p<0.01$). Other comparisons show significant differences between clade 1 and clade 2 in 7 out of 15 indices ($p<0.05$), whereas clade 3 shows significant differences in 15 indices compared to clade 1 and clade 2 ($p<0.01$).

Analysis of dinucleotide shows that the relative frequency of CpG is significantly lower than other dinucleotides (**Figure 1A**), which explains in part why G and G3 are less frequent. The composition of UpA is also significantly lower than that of other dinucleotides. CpG levels for clade 3 are significantly lower than other clades ($p < 0.05$).

3.3 Codon Usage Bias Varies Among Different EV-A Clades

We found that clade 3 has a particular nucleotide composition that may affect codon bias. To estimate the extent of the codon usage bias in *EV-A* coding sequences, the ENC values were calculated (**Figure 1B**). The average ENC value of all *EV-A* strains is 55.97 ± 1.43, while those of clade 1, 2 and 3 are 56.44 ± 0.41, 56.30 ± 0.45, 51.16 ± 0.96. For the CDS of each gene, the ENC values of clade 3 were significantly lower than the other two clades ($p<0.01$), while the ENC values of clade 1 and clade 2 are similar. We also noticed that ENC values of P2P3 regions were significantly lower than P1 ($p<0.01$). Overall, ENC values indicated that the codon usage bias in *the EV-A* genomes varied in different clades.

3.4 EV-A Genomes Have Evolved Clade-Specific RSCU Patterns

RSCU was calculated to determine the synonymous codons usage in the *EV-A* coding sequences (**Table 1**) and the

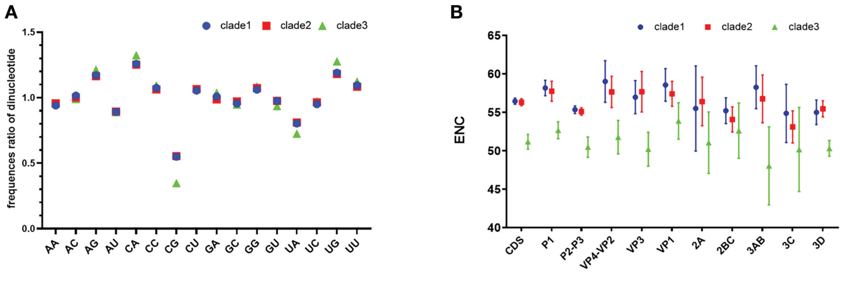

FIGURE 1 | Relative dinucleotide analysis and ENC plot. **(A)** Dinucleotide composition of EV-A clades. **(B)** Clade-level comparison of ENC values of *EV-A* CDS and individual gene segments. CDS is short for coding sequences.

TABLE 1 | The relative synonymous codon usage (RSCU) patterns of Enterovirus A.

Amino acid	Codon	*Enterovirus A*				Host
		Overall	**Clade 1**	**Clade 2**	**Clade 3**	**H. sapiens**
Phe	**UUU**	**1.06**	**1.06**	**1.06**	**1.02**	0.93
	UUC	0.94	0.94	0.94	0.98	**1.07**
Leu	UUA	0.77	0.96	0.66	0.98	0.46
	UUG	**1.30**	**1.28**	**1.34**	1.05	0.77
	CUU	1.08	0.97	1.12	**1.19**	0.79
	CUC	1.09	1.02	1.11	1.13	1.17
	CUA	0.87	0.83	0.89	0.89	0.43
	CUG	0.89	0.95	0.88	0.76	**2.37**
Ile	**AUU**	**1.15**	**1.19**	1.09	**1.41**	1.08
	AUC	1.14	1.03	**1.20**	1.09	**1.41**
	AUA	0.71	0.78	0.70	0.57	0.51
Val	GUU	0.91	0.86	0.90	1.20	0.73
	GUC	0.82	0.85	0.78	0.99	0.95
	GUA	0.69	0.67	0.70	0.59	0.47
	GUG	**1.58**	**1.61**	**1.61**	**1.22**	**1.85**
Pro	CCU	1.19	1.02	1.30	0.93	1.15
	CCC	0.90	1.01	0.86	0.82	**1.29**
	CCA	**1.52**	**1.46**	**1.49**	**2.00**	1.11
	CCG	0.39	0.51	0.35	0.25	0.45
Thr	**ACU**	**1.23**	**1.23**	1.21	**1.39**	0.99
	ACC	1.20	1.21	1.22	1.07	1.42
	ACA	1.23	1.19	**1.23**	1.38	**1.14**
	ACG	0.33	0.37	0.33	0.17	0.46
Ala	**GCU**	**1.36**	**1.36**	**1.35**	**1.49**	1.06
	GCC	0.95	1.07	0.91	0.87	**1.60**
	GCA	1.30	1.17	1.35	1.47	0.91
	GCG	0.39	0.40	0.40	0.19	0.42
Tyr	UAU	0.96	**1.03**	0.93	0.93	0.89
	UAC	**1.04**	0.97	**1.07**	**1.07**	**1.11**
Ser	UCU	1.09	1.06	1.10	1.18	1.13
	UCC	1.05	1.11	1.02	1.06	1.31
	UCA	**1.29**	**1.29**	**1.24**	**1.74**	0.90
	UCG	0.42	0.45	0.43	0.24	0.33
	AGU	1.19	1.17	1.21	1.16	0.90
	AGC	0.95	0.92	1.00	0.63	**1.44**
Arg	**AGA**	**2.00**	**2.16**	**1.80**	**3.24**	**1.29**
	CGU	0.44	0.45	0.45	0.34	0.48
	CGC	1.01	0.90	1.12	0.39	1.10
	CGA	0.57	0.52	0.63	0.21	0.65
	CGG	0.32	0.36	0.31	0.15	1.21
	AGG	1.66	1.61	1.68	1.68	1.27
Cys	UGU	0.99	0.90	**1.01**	**1.09**	0.91
	UGC	**1.01**	**1.10**	0.99	0.91	**1.09**
His	CAU	0.79	0.75	0.78	0.93	0.84
	CAC	**1.21**	**1.25**	**1.22**	**1.07**	**1.16**
Gln	**CAA**	**1.15**	**1.09**	**1.16**	**1.22**	0.53
	CAG	0.85	0.91	0.84	0.78	**1.47**
Asn	AAU	0.97	0.95	0.97	**1.03**	0.94
	AAC	**1.03**	**1.05**	**1.03**	0.97	**1.06**
Lys	AAA	0.88	0.94	0.82	**1.14**	0.87
	AAG	**1.12**	**1.06**	**1.18**	0.86	**1.13**
Asp	**GAU**	**1.13**	**1.06**	**1.16**	**1.19**	0.93
	GAC	0.87	0.94	0.84	0.81	**1.07**
Glu	GAA	0.95	0.88	0.97	**1.07**	0.84
	GAG	**1.05**	**1.12**	**1.03**	0.93	**1.16**
Gly	**GGU**	**1.12**	**1.14**	**1.09**	**1.32**	0.65
	GGC	0.83	0.85	0.81	0.82	**1.35**
	GGA	1.02	0.94	1.04	1.20	1.00
	GGG	1.03	1.06	1.05	0.65	1.00

Preferred codons of EV-A and H. sapiens are shown in bold.

preferred codon with the highest RSCU value for each animo acid was bolded. We noted that the commonly/uncommonly preferred codons ratios among *EV-A* clade 1:clade 2, clade 1: clade 3 and clade 2:clade 3 were 14:4, 12:6 and 12:6, respectively. By comparing the codon usage patterns of *Homo sapiens* and *EV-A*, the ratio of coincident/antagonistic preferred codons is 7/11 in clade 1, 9/9 in clade 2, while only 4/14 in clade 3 among the 18 preferred codons (**Table 1**). This clade-specific RSCU pattern highlights the distinct evolutionary dynamics of the *EV-A* clades.

Of the 18 preferred codons, eight are G/C-ended (four C-ended; four G-ended) and the remaining ten are A/U-ended (five A-ended; five U-ended) in the *EV-A* coding sequences. The findings show that *EV-As* prefer A/U at the end of codons rather than G/C. We have summarized the RSCU values of the preferred codons by each amino acid in **Figure 2**. It also shows that *EV-As* prefer A/U at the end of codons rather than G/C. We noted that *EV-A* clade 3 has a stronger AU3 bias than other clades, and the AU3 bias in the P2P3 region of *EV-As* is stronger than the P1 region.

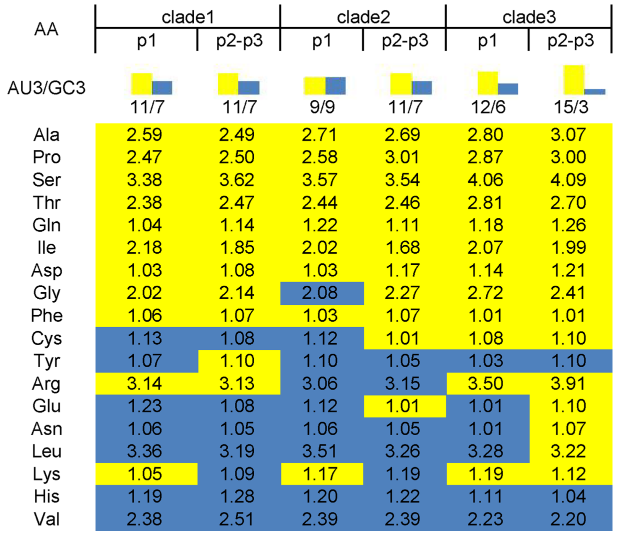

AA	clade1		clade2		clade3	
	p1	p2-p3	p1	p2-p3	p1	p2-p3
AU3/GC3	11/7	11/7	9/9	11/7	12/6	15/3
Ala	2.59	2.49	2.71	2.69	2.80	3.07
Pro	2.47	2.50	2.58	3.01	2.87	3.00
Ser	3.38	3.62	3.57	3.54	4.06	4.09
Thr	2.38	2.47	2.44	2.46	2.81	2.70
Gln	1.04	1.14	1.22	1.11	1.18	1.26
Ile	2.18	1.85	2.02	1.68	2.07	1.99
Asp	1.03	1.08	1.03	1.17	1.14	1.21
Gly	2.02	2.14	2.08	2.27	2.72	2.41
Phe	1.06	1.07	1.03	1.07	1.01	1.01
Cys	1.13	1.08	1.12	1.01	1.08	1.10
Tyr	1.07	1.10	1.10	1.05	1.03	1.10
Arg	3.14	3.13	3.06	3.15	3.50	3.91
Glu	1.23	1.08	1.12	1.01	1.01	1.10
Asn	1.06	1.05	1.06	1.05	1.01	1.07
Leu	3.36	3.19	3.51	3.26	3.28	3.22
Lys	1.05	1.09	1.17	1.19	1.19	1.12
His	1.19	1.28	1.20	1.22	1.11	1.04
Val	2.38	2.51	2.39	2.39	2.23	2.20

FIGURE 2 | AU3 and GC3 in codons of P1 and P2P3 regions of *EV-A* clade 1, clade 2 and clade 3. Numbers in the square array indicate the RSCU values of preferred codon by each amino acid. Yellow shade indicate AU3 and blue shade indicate GC3 for the codon ending.

3.5 Trends in Codon Usage Variation of EV-A

We built COA plots of CDS and each gene segment to show trends in codon usage variations among different EV-A strains (**Figure 3**). The first (f'1) and second (f'2) principal axes represent respectively 28.17% and 16.15% of the total variation of the *EV-A* coding sequences. The *EV-A* strains were grouped into three distinct clusters on the plot which were shown to be largely correlated with their phylogenetic relationships. Overall, clade 1 and clade 2 formed cluster I, except for CVA5 and CVA6, which formed cluster II; and cluster III comprised all clade 3 strains. These data further support that clade 3 has a unique codon usage pattern. At the level of the individual genes, the clade-specific clustering was also observed (**Supplementary Figure S2**). For genes encoding 3C, 3D and VP3, clade 3 strains were clustered independently, indicating the effect of divergence events on individual genes. For the genes encoding 2A, 2BC, 3AB, VP1, VP4 and VP2, overlapping patterns in codon usage were observed. Based on these data and together with ENC and RSCU, we confirm that clade 3 has a unique codon usage pattern and likely has an independent evolutionary origin. Conversely, the overlap between clade 1 and clade 2 indicates that they have similar codon usage patterns and a closer relationship. Together, clade 3 stands apart from other clades, which may be affected by unique evolutionary forces.

3.6 Codon Usage Patterns of EA-V Strains Are Influenced by Mutation Pressure and Natural Selection

Mutational pressure and translational selection were reported as the primary factors influencing the codon usage bias. Here, we examined whether they have affected the *EV-A* codon usage and which factor is dominant through correlation analysis, PR2 plot and ENC-GC3 plot analysis. In the correlation analysis, we compared the correlation between the nucleotide compositions and the principal axes of the COA plot, and noted a significant positive or negative correlation between nucleotide composition, such as A/A3 or A/G. We also observed that most nucleotide composition constraints were significantly correlated with f'1 and f'2 (**Figure 4**). Together, these results supports that mutation pressure from the nucleotide composition may have affected the *EV-A* codon biases.

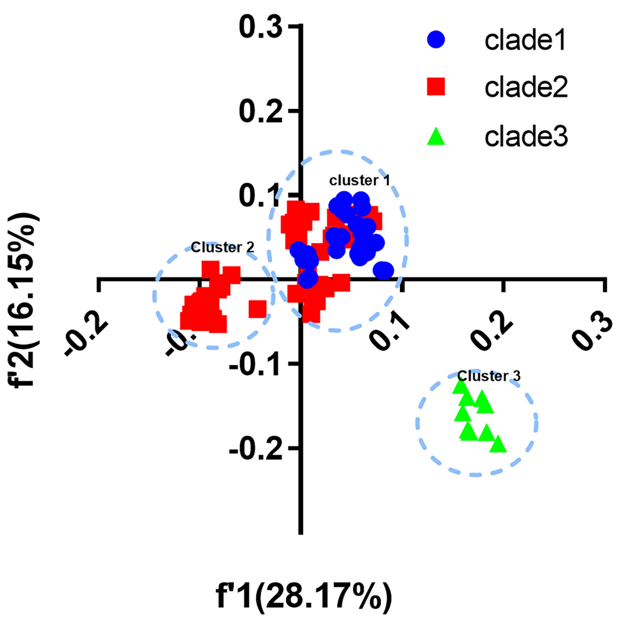

FIGURE 3 | Correspondence analysis (COA). COA plots were constructed for coding sequences of each *EV-A* strains.

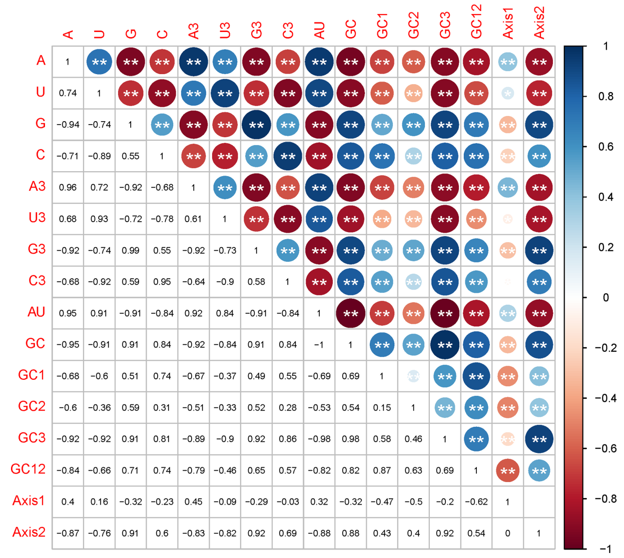

	A	U	G	C	A3	U3	G3	C3	AU	GC	GC1	GC2	GC3	GC12	Axis1	Axis2
A	1	**	**	**	**	**	**	**	**	**	**	**	**	**	**	**
U	0.74	1	**	**	**	**	**	**	**	**	**	**	**	**	*	**
G	−0.94	−0.74	1	**	**	**	**	**	**	**	**	**	**	**	**	**
C	−0.71	−0.89	0.55	1	**	**	**	**	**	**	**	**	**	**	**	**
A3	0.96	0.72	−0.92	−0.68	1	**	**	**	**	**	**	**	**	**	**	**
U3	0.68	0.93	−0.72	−0.78	0.61	1	**	**	**	**	**	**	**	**	*	**
G3	−0.92	−0.74	0.99	0.55	−0.92	−0.73	1	**	**	**	**	**	**	**	**	**
C3	−0.68	−0.92	0.59	0.95	−0.64	−0.9	0.58	1	**	**	**	**	**	**		**
AU	0.95	0.91	−0.91	−0.84	0.92	0.84	−0.91	−0.84	1	**	**	**	**	**	**	**
GC	−0.95	−0.91	0.91	0.84	−0.92	−0.84	0.91	0.84	−1	1	**	**	**	**	**	**
GC1	−0.68	−0.6	0.51	0.74	−0.67	−0.37	0.49	0.55	−0.69	0.69	1	**	**	**	**	**
GC2	−0.6	−0.36	0.59	0.31	−0.51	−0.33	0.52	0.28	−0.53	0.54	0.15	1	**	**	**	**
GC3	−0.92	−0.92	0.91	0.81	−0.89	−0.9	0.92	0.86	−0.98	0.98	0.58	0.46	1	**	**	**
GC12	−0.84	−0.66	0.71	0.74	−0.79	−0.46	0.65	0.57	−0.82	0.82	0.87	0.63	0.69	1	**	**
Axis1	0.4	0.16	−0.32	−0.23	0.45	−0.09	−0.29	−0.03	0.32	−0.32	−0.47	−0.5	−0.2	−0.62	1	
Axis2	−0.87	−0.76	0.91	0.6	−0.83	−0.82	0.92	0.69	−0.88	0.88	0.43	0.4	0.92	0.54	0	1

FIGURE 4 | Correlation analysis between nucleotide compositions and the two principal axes of COA plot. The numbers in lower triangle matrix show the slope of regression line. The upper triangle matrix shows the information by the color and size of circles; Dark blue means positive correlation and dark red means negative correlation; The bigger circle means more significant correlation; NS means non-significant (p > 0.05), * represents p < 0.05, ** represents p < 0.01.

In PR2 plot, the relationship between A/U and G/C composition on the 3rd codon position in four degenerated codon families (Ala, Arg, Gly, Leu, Pro, Ser, Thr, and Val) was analyzed. We observed that U3 was used more frequently than A3, while G3 is approximately equal to C3 in the entire coding sequences (**Figure 5**). G3 and U3 were more frequent in P1 regions, while C3 and U3 were more frequent in P2-P3 regions. The A3/U3 and G3/C3 bias denotes the influence of both selective pressure and mutation effect.

To understand whether pressure dominates in the *EV-A* codon usage bias, ENC–GC3 plots were constructed. We observed that all the *EV-A* strains clustered together under the expected ENC curve (**Figure 6A**). This suggests that natural selection may affect the genomic evolution of *EV-A* strains. The *EV-A* clades deviated from the expected curve differently and the clade 3 strains were lower below the curve, suggesting that clade 3 strains are subjected to higher selective pressure than other clades. The clade-specific difference can also be seen in P1 and P2P3 coding regions (**Figures 6B, C**). However, the effects of mutation pressure and natural selection on individual proteins varied (**Supplementary Figure S3**). All 2BC and 3D gene data points fell below the expected curve, while the 3AB, 3C, VP3 and VP4-VP2 coding sequences of some strains were aggregated on the curve, suggesting a dominant influence due to mutation pressure. It is noteworthy that clade 3 strains are the lower points under the curve in 3AB, 3D and VP3 plots, indicating a greater effect by natural selection in these coding regions.

3.7 Natural Selection Predominates in Shaping the Codon Usage Patterns in EV-A

Mutation pressure and natural selection help to shape the codon usage patterns. To study the magnitude of each force, we used the neutrality plot analysis. We observed a significant positive correlation between GC12 and GC3 values across the *EV-A* coding sequences (slope =0.113, r =0.695, p=0.007). The linear regression slope suggested that the relative neutrality (mutation pressure) was 11.31%, and the relative constraint on GC3 (natural selection) was 89.69%, indicating that the *EV-A* codon usage patterns were primarily shaped by natural selection. Regression slopes in clade 1 and clade 2 are 0.1461 and 0.0417, while the correlation is not significant in clade 3, consistently indicating high levels of influence on codon patterns by natural selection (**Figure 7A**). The results of the neutrality plot analysis in P1 and P2P3 regions were similar to the whole coding sequences (**Figures 7B, C**). We analyzed individual proteins in three clades, and observed significant correlations between the GC12 and GC3 values of the VP1, 2A, 3D sequences in clade 1 and the VP3, 2BC, 3D coding sequences in clade 2 strains. All slope values for each protein are below 0.5 (from 0.007 to 0.4076), which supports the stronger effects of selection pressure than mutation pressure (**Supplementary Figure S4**). Notably, the VP1 coding sequences in clade 1 showed an exceptional slope value= 0.8696, indicating a weak selection force in this region (**Figure 7D**). Overall, our data suggest that the influence of natural selection prevails over the coding sequences of *EV-A* strains.

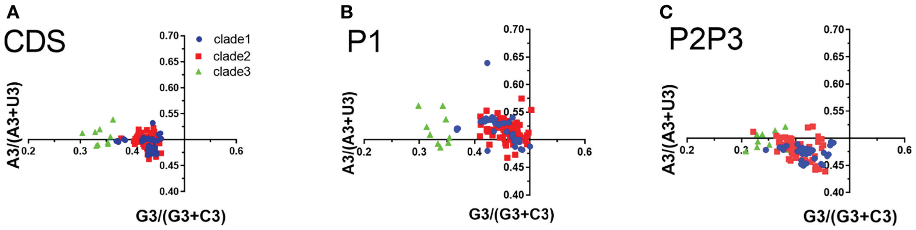

FIGURE 5 | Parity rule 2 (PR2) bias plots. PR2 plots were constructed for the coding sequences, P1 and P2P3 regions of *EV-A* strains respectively. **(A)** coding sequences, **(B)** P1 region, **(C)** P2P3 region. The blue dots, red squares, and green triangles indicate clade 1, clade 2 and clade 3 strains.

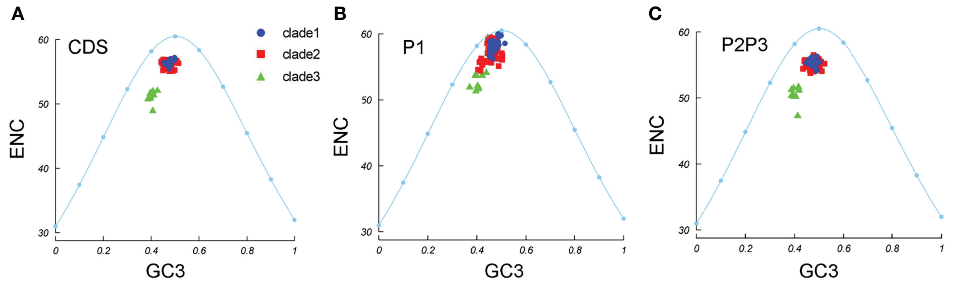

FIGURE 6 | ENC-GC3 plots. The curve indicates the expected codon usage if GC compositional constraints alone account for the codon usage bias. **(A)** coding sequences, **(B)** P1 region, **(C)** P2P3 region. The blue dots, red squares, and green triangles indicate clade 1, clade 2 and clade 3 strains.

3.8 EV-A Showed Host-Specific Codon Adaptation Patterns

The CAI analysis reflects the fitness of the viral gene for the host cell. The CAI values were calculated for each coding sequence against 38 model organisms based on the CUTG database. The six highest average CAI values obtained for the entire *EV-A* coding sequence were assigned to *Xenopus laevis* (0.82 ± 0.006), *Ciona intestinalis* (0.78 ± 0.009), *Gallus gallus* (0.77 ± 0.005), *Danio rerio* (0.76 ± 0.005), *Homo sapiens* (0.74 ± 0.005), and *Mus musculus* (0.74 ± 0.005) (**Figure 8** and **Supplementary Table S4A**). For all six matched species, the CAI analyses of the P1 and P2P3 regions are consistent with the entire coding sequence. We also observed that the CAI values of clade 3 is significantly higher than clade 1 and clade 2 in *Xenopus laevis and Ciona intestinalis* (p<0.01), indicating that *EV-A* strains show clade-specific codon adaptation patterns.

In addition, we also calculate the RCDI and SiD values to show the degree of unsuitability and potential impact of model organism codon usage patterns on *EV-A*. (**Supplementary Figure S5**, and **Supplementary Table S4**). The six lowest average RCDI values of the entire EV-A coding sequence include *Xenopus laevis* (1.06), *Ciona interstinals* (1.09), *Gallus gallus* (1.11), *Danio rerio* (1.11), *Mus musculus* (1.12), *Homo sapiens* (1.12). Among the 38 model animals, the six species with the lowest mean SiD values also matched the CAI and RCDI analysis, indicating that they have similar codon bias patterns and may be most appropriate hosts for *EV-A*. The data of the P1 and P2P3 regions are consistent with the entire coding sequence.

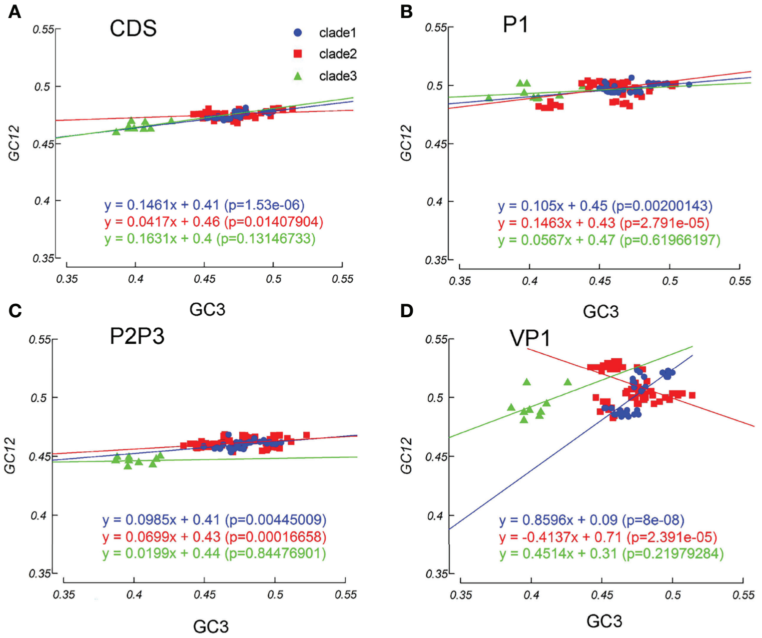

FIGURE 7 | Neutrality plot analysis. Neutrality plots (GC12 and GC3) was constructed for the coding sequences, P1 and P2P3 regions of *EV-A* strains. **(A)** coding sequences, **(B)** P1 region, **(C)** P2P3 region, **(D)** VP1 gene. The blue dots, red squares, and green triangles indicate clade 1, clade 2 and clade 3 strains.

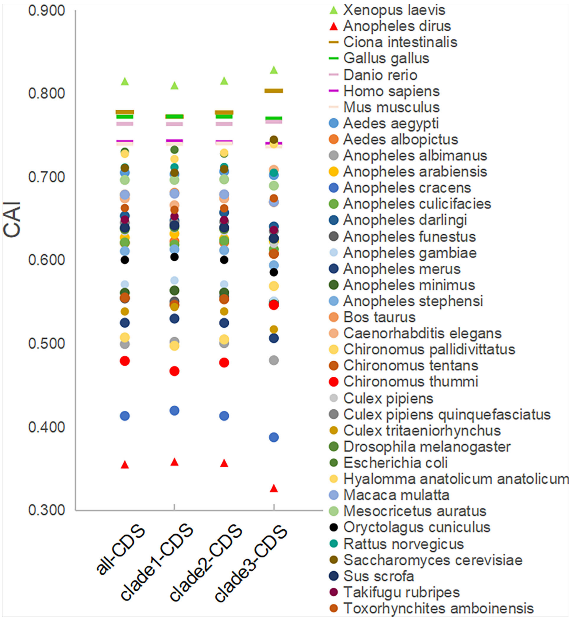

FIGURE 8 | CAI analysis of the *EV-A* coding sequences against model organisms. CDS stands for the coding sequences of *EV-A* strains.

3.9 Specific Codon Bias can Affect the Protein Expression Level of EV-A

As above, we concluded that there are significant differences in codon bias patterns between conventional and unconventional *EV-A* strains. To explore whether the codon bias can affect the protein translation of *EV-A*, we first tested if there are differences in protein translation between viruses representative of three clades. The expression of GFP-tagged viral capsid protein in HEK293T cells was examined by fluorescence microscopy (**Figures 9A, B**). It was found that EV71 and CVA16 of clade 1, CVA6 and CVA10 of clade 2 had similar levels of expression, significantly higher than EVA76 and EVA89 of clade 3. This result indicates that the expression levels of conventional *EV-A capsids* are substantially higher than those of unconventional *EV-A*.

To confirm if the lower expression levels of unconventional clades are caused by codon bias, we have optimized the codon of the capsid region of EVA89 and EVA76 according to *Homo sapiens*. The optimized fragments EVA76-Cap-opti and EVA89-Cap-opti were expressed in HEK293T and RD cell lines. Using immunofluorescence microscopy and Western blot, we found that the optimized capsid protein of EVA89 and EVA76 expressed at significantly higher levels (**Figure 9C**), showing that the codon bias of clade 3 does contribute to the lower protein expression.

4 DISCUSSION

This study analyzed the codon usage bias in the *EV-A* in order to understand its evolutionary patterns. It is known that recombination events can affect the codon usage patterns and the phylogenetic tree topology, which can lead to misinterpretations. Therefore, we excluded all possible recombinants and the remaining 125 complete *EV-A* genomes were analyzed. Based on phylogenetic analysis, *EV-A* is divided into three clades: clade 1, clade 2 and clade 3. The clade 1 comprises CVA7, CVA14, CVA16, EV71 and EV120, of which EV71 and CVA16 are principle pathogens of HFMD. Clade 2 includes CVA2, CVA3, CVA4, CVA5, CVA6, CVA8, CVA10 and CVA12, of which CVA6 and CVA10 are emerging recently. Clade 3 includes the unconventional strains, EVA76, 89, 90, 91 and 92.

Mutational pressure and natural selection are known to account for the codon usage bias, which has been reported in

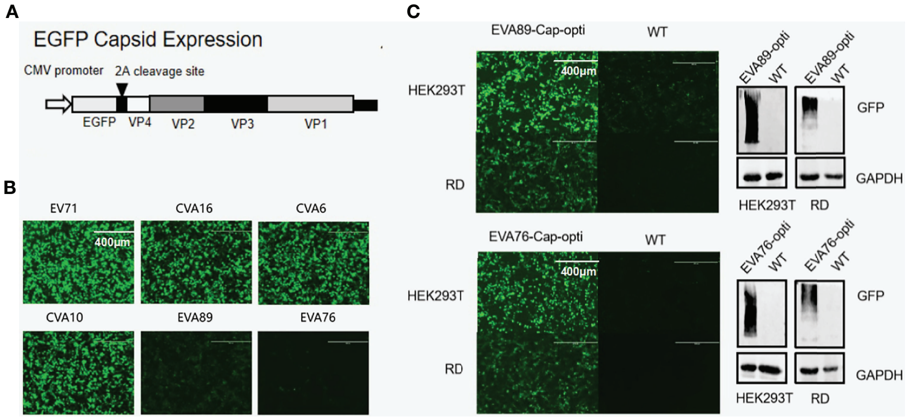

FIGURE 9 | Codon optimization and protein expression levels for *EV-A* strains. **(A)** Schematic map of P1 protein expression plasmid. **(B)** Post plasmid transfection, GFP-tagged P1 protein levels of different *EV-A* strains in HEK293T cells was monitored by fluorescence microscopy. **(C)** Comparison of EVA76 and EVA89 P1 protein levels before and after codon optimization. Expression of GFP-tagged P1 protein in the cell culture was monitored through fluorescence microscopy (left panel). Furthermore, the expression of GFP-tagged P1 proteins was examined by anti-GFP antibodies using Western Blot (right panel). Housekeeping gene GAPDH was used for loading control.

many species, including RNA virus. Here we use multiple methods to explore the codon bias of the *EV-A* strains and quantify the effect of mutation pressure and natural selection. First, ENC values of *EV-A* show a low overall codon usage bias, consistent with many RNA viruses (Jenkins and Holmes, 2003). Here we analyzed the RSCU pattern of *EV-A*, and found that *EV-A* evolved a mixed pattern of coincident and antagonistic codons relative to humans. This suggests that *EV-A* may have a complicated process of adapting to humans as host. When the codon usage between the virus and the host is consistent, the host can more effectively translate the corresponding virus amino acid codons and produce proteins faster, where the virus must compete with its host. In contrast, the use of antagonistic codons can avoid competition with the host and the virus protein can be folded better to get a more stable viral capsid, although this may reduce the translation effectiveness of the viral amino acid codons. Previous studies indicate that the codon bias pattern of poliovirus is very similar to that of humans, whereas the hepatitis A virus and EB virus have developed a codon usage pattern which is largely antagonistic to the host (Karlin et al., 1990; Pintó et al., 2018). Thus, different codon adaptation patterns may be related to the translation shutdown mechanism, virus life cycle and transmission pathway.

The codon usage bias may be strongly influenced by the overall nucleotide composition. For viruses, the GC- or AU-rich compositions tend to correlate with their RSCU patterns. In addition, GC- or AU-rich genomes tend to contain codons preferentially ending with either G/C or A/U, respectively. Such trends, if present, support the influence of mutation pressure. Here, we observed that *EV-A* genomes are AU-rich and prefer to end with A/U, which supports a mutation pressure effect. We also find a proportion of CpG and UpA dinucleotide in *EV-A* as seen in nearly all RNA viruses (Karlin et al., 1994), that is probably linked to evasion of antiviral immune responses (Sugiyama et al., 2005; Greenbaum et al., 2009). Microbial DNA sequences containing unmethylated CpG dinucleotides can trigger an immune response through the Toll-like receptor 9 (Latz et al., 2004). A similar sensor for CpG in RNA viruses was likely present, but it remains to be discovered (Greenbaum et al., 2009; Atkinson et al., 2014), while UpA is susceptible to cleavage by RNaseL (Steil and Barton, 2009). The importance of dinucleotide compositions has been demonstrated in attenuation of RNA virus by codon deoptimization after artificial increase of CpG/UpA (Atkinson et al., 2014).

The findings from ENC and nucleotide composition analysis suggest that both mutation and selection pressure may shape the *EV-A* genome. Then, by the neutrality plot, we conclude that the selection pressure is dominant in *EV-A* codon bias, due to the non-significant correlation or near-zero slope between the GC12 and GC3 values. This finding is not consistent with a previous EV71 report (Ma et al., 2014), probably because previous studies based only on nucleotide composition and the ENC-GC3 plot, which is inadequate (Wright, 1990). In contrast, we conducted neutrality plot analysis which provided a more robust support to the conclusion.

We also analyzed each protein sequence by ENC-GC3 plot and neutrality plot. It is worth noting that the effects of both forces on each protein are different. In the neutrality plots, natural selection is found to be the dominant factor in the formation of codon usage patterns. However, VP1 in clade 1 is mainly affected by mutation pressure, rather than by natural selection. For specific proteins of different strains, their ENC-GC3 plot is not always consistent. Some protein sequences of particular *EV-A* strains are distributed on the curve, indicating that they are primarily affected by mutation pressure.

In the COA analysis, clade 1 and clade 2 strains clustered together while clade 3 is in a separate cluster, suggesting that clade 3 strains have different codon usage patterns with clade 1 and clade 2. However, at the individual gene level, many clusters of all three clades overlap, indicating that *EV-A* strains likely originate from common ancestors and have undergone subsequent evolutionary divergence, especially for 3C, 3D and VP3. We also noticed that clustering is not entirely consistent in the COA plots with phylogenetic analysis. Clade 1 and clade 2 aggregate to form cluster 1, while CVA5 and CVA6 in clade 2 form cluster 2 separately, likely due to phylogenetic analysis algorithms ignoring differences in nucleotide differences at the 3rd codon position. These results indicate that CVA5 and CVA6 differ from other clade 2 viruses in codon usage patterns, in particular the 3rd codon position, whereas other clade 2 viruses have similar codon usage patterns with clade 1. Based on the RSCU, ENC and COA analyses, we also found that there were differences in codon bias between *EV-A* P1 and P2-P3 regions. The codon bias of P2-P3 region is higher than that of P1 region, and is subjected to more selective pressure and tends to use U and C more frequently.

The CAI, RCDI and SiD analyses suggest that the suitable host species in terms of codon adaptability for *EV-A* may include: *Xenopus laevis*, *Ciona intestinalis*, *Gallus gallus*, *Danio rerio*, *Homo sapiens* and *Mus musculus*, whereas the more suitable hosts for the clade 3 viruses are likely to be *Xenopus laevis*, *Ciona interstinals.* Given its unique codon bias, it is tempting to assume that the clade 3 viruses may circulate in different host species other than *EV-A* clade 1 and clade 2 viruses. However, human and non-human primates are the only known natural hosts for *EV-A (*Wang and Yu, 2014; Mombo et al., 2017*)*. In previous surveys, clade 3 viruses were also detected in mandrill, chimpanzee, rhesus macaque, baboon (Oberste et al., 2013). In the future, the verification at the cellular or animal level is required to determine whether the analyzed model organisms are indeed possible hosts for *EV-A*. Despite enterovirus have narrow host ranges, their SiD values are relatively low and similar to virus with broad host ranges. Otherwise, this may suggest that enterovirus do not need high codon compatibility with its host to replicate rapidly (Tian et al., 2018).

Clade 3 viruses have a unique phylogenetic relationship, low pathogenicity and epidemic features with respect to other *EV-A* strains (Fan et al., 2015). Here, we have found a unique codon usage pattern in clade 3 strains which may explain these differences. Indeed, our experiments have shown that codon optimization of the clade 3-P1 constructs increases their expressions to comparable levels to other clades. Following codon optimization, the CAI value of EVA76 over *homo sapiens* was also raised from 0.74 to 0.84. Since P2P3 regions have a higher codon bias and different function with P1 region, it is possible that optimization on P2P3 regions also improves the virus activity in human cell lines. Curiously, the codon deoptimization of conventional enteroviruses has made them less pathogenic and vaccine candidates (Tsai et al., 2019; Lee et al., 2021), one waits to see if codon optimization will now make clade 3 enteroviruses more virulent.

With low replication fidelity and frequent recombination, enteroviruses exhibit high genetic diversity and a potential for cross-species infection. Studies of *EV-A* infection in non-human primates provide increasing evidence of a risk of zoonotic transmission between animals and humans (Mombo et al., 2017). In fact, the pathogenic spectrum of *EV-A* is evolving rapidly, from EV71 and CVA16 previously to CVA10 and CVA6, which have caused many epidemics in recent years. It is unclear if the unconventional *EV-A* strains will cause epidemics over time, although we have recently reported that viable recombinants between conventional and unconventional *EV-A* types could be generated successfully (Wang et al., 2020). Thus, it is of great interest to study the evolutionary mechanism of viruses, especially these forthcoming unconventional viruses.

5 CONCLUSIONS

Our study shows that *EV-A* has developed clade-specific codon bias patterns. Both mutation pressure and natural selection affected the codon usage patterns in *EV-A*. These data have new implications for vaccine development and management of *EV-A* infection.

DATA AVAILABILITY STATEMENT

The original contributions presented in the study are included in the article/**Supplementary Material**. Further inquiries can be directed to the corresponding authors.

AUTHOR CONTRIBUTIONS

Conceptualization, LiYZ, JQX, XYZ and SYZ. Data curation, LiYZ and MC. Formal analysis, LiYZ and MC. Funding acquisition, LiYZ, SYZ and JJY. Investigation, LiYZ, MC, JJY and MW. Methodology, LiYZ and SYZ. Resources, JQX, XYZ and SYZ. Visualization, LiYZ, MC and LiuYZ. Writing—original draft preparation, LiYZ and MC. Writing—review and editing, LiYZ, JQX, XYZ and SYZ. Supervision, SYZ, JQX and XYZ. Project administration, LiYZ. and SYZ. All authors contributed to the article and approved the submitted version.

FUNDING

This research was supported by the Fundamental Research Funds for the Shanghai Public Health Clinical Center (grant number: KY-GW-2016-04 and KY-GW-2018-17) and National Natural Science Foundation of China (82002135).

SUPPLEMENTARY MATERIAL

The Supplementary Material for this article can be found online at: https://www.frontiersin.org/articles/10.3389/fcimb.2022.941325/full#supplementary-material

Supplementary Figure 1 | Phylogenetic analysis of the *EV-A* stains.

Supplementary Figure 2 | Genotype-specific of correspondence analysis plots were constructed for individual *EV-A* coding sequences.

Supplementary Figure 3 | ENC–GC3 plots.

Supplementary Figure 4 | Neutrality plot analysis.

Supplementary Figure 5 | RCDI and SiD analysis of the EV-A coding sequences against model organisms.

Supplementary Table 1 | Demographics of *Enterovirus A* genomes analyzed in present study.

Supplementary Table 2 | Nucleotide composition analysis of *EV-A* coding sequences.

Supplementary Table 3 | One way Anova analysis between three clades.

Supplementary Table 4 | Summary data of CAI, RCDI and SiD analysis.

REFERENCES

Atkinson, N. J., Jeroen, W., Evans, D. J., and Peter, S. (2014). The Influence of CpG and UpA Dinucleotide Frequencies on RNA Virus Replication and Characterization of the Innate Cellular Pathways Underlying Virus Attenuation and Enhanced Replication. *Nucleic Acids Res* 42 (7), 4527–4545. doi: 10.1093/nar/gku075

Belalov, I. S., and Lukashev, A. N. (2013). Causes and Implications of Codon Usage Bias in RNA Viruses. *PLoS One* 8 (2), e56642. doi: 10.1371/journal.pone.0056642

Bian, L., Wang, Y., Yao, X., Mao, Q., Xu, M., and Liang, Z. (2015). Coxsackievirus A6: A New Emerging Pathogen Causing Hand, Foot and Mouth Disease Outbreaks Worldwide. *Expert Rev. Anti-Infect. Ther.* 13 (9), 1061–1071. doi: 10.1586/14787210.2015.1058156

Blomqvist, S., Klemola, P., Kaijalainen, S., Paananen, A., Simonen, M.-L., Vuorinen, T., et al. (2010). Co-Circulation of Coxsackieviruses A6 and A10 in Hand, Foot and Mouth Disease Outbreak in Finland. *J. Clin. Virol.* 48 (1), 49–54. doi: 10.1016/j.jcv.2010.02.002

Bulmer, M. (1991). The Selection-Mutation-Drift Theory of Synonymous Codon Usage. *Genetics* 129 (3), 897–907. doi: 10.1093/genetics/129.3.897

Chen, P., Song, Z., Qi, Y., Feng, X., Xu, N., Sun, Y., et al. (2012). Molecular Determinants of Enterovirus 71 Viral Entry Cleft Around Gln-172 on VP1 Protein Interacts With Variable Region on Scavenge Receptor B 2. *J. Biol. Chem.* 287 (9), 6406–6420. doi: 10.1074/jbc.M111.301622

Comeron, J. M., and Aguadé, M. (1998). An Evaluation of Measures of Synonymous Codon Usage Bias. *J. Mol. Evol.* 47 (3), 268–274. doi: 10.1007/PL00006384

Fan, Q., Zhang, Y., Hu, L., Sun, Q., Cui, H., Yan, D., et al. (2015). A Novel Recombinant Enterovirus Type EV-A89 With Low Epidemic Strength in Xinjiang, China. *Sci. Rep.* 5, 18558. doi: 10.1038/srep18558

Friendly, M. (2002). Corrgrams: Exploratory Displays for Correlation Matrices. *Am. Stat.* 56 (4), 316–324. doi: 10.1198/000313002533

Grantham, R., Gautier, C., and Gouy, M. (1980). Codon Frequencies in 119 Individual Genes Confirm Corsistent Choices of Degenerate Bases According to Genome Type. *Nucleic Acids Res.* 8 (9), 1893–1912. doi: 10.1093/nar/8.9.1893

Greenbaum, B. D., Rabadan, R., and Levine, A. J. (2009). Patterns of Oligonucleotide Sequences in Viral and Host Cell RNA Identify Mediators of the Host Innate Immune System. *PloS One* 4 (6), e5969. doi: 10.1371/journal.pone.0005969

Jenkins, G. M., and Holmes, E. C. (2003). The Extent of Codon Usage Bias in Human RNA Viruses and its Evolutionary Origin. *Virus Res.* 92 (1), 1–7. doi: 10.1016/S0168-1702(02)00309-X

Karlin, S., Blaisdell, B. E., and Schachtel, G. A. (1990). Contrasts in Codon Usage of Latent Versus Productive Genes of Epstein-Barr Virus: Data and Hypotheses. *J. Virol.* 64 (9), 4264–4273. doi: 10.1128/jvi.64.9.4264-4273.1990

Karlin, S., Doerfler, W., and Cardon, L. (1994). Why is CpG Suppressed in the Genomes of Virtually All Small Eukaryotic Viruses But Not in Those of Large Eukaryotic Viruses? *J. Virol.* 68 (5), 2889–2897. doi: 10.1128/jvi.68.5.2889-2897.1994

Karlin, S., Mrazek, J., and Campbell, A. M. (1997). Compositional Biases of Bacterial Genomes and Evolutionary Implications. *J. Bacteriol.* 179 (12), 3899–3913. doi: 10.1128/jb.179.12.3899-3913.1997

Kumar, S., Stecher, G., and Tamura, K. (2016). MEGA7: Molecular Evolutionary Genetics Analysis Version 7.0 for Bigger Datasets. *Mol. Biol. Evol.* 33 (7), 1870–1874. doi: 10.1093/molbev/msw054

Latz, E., Schoenemeyer, A., Visintin, A., Fitzgerald, K. A., Monks, B. G., Knetter, C. F., et al. (2004). TLR9 Signals After Translocating From the ER to CpG DNA in the Lysosome. *Nat. Immunol.* 5 (2), 190–198. doi: 10.1038/ni1028

Lee, M. H. P., Tan, C. W., Tee, H. K., Ong, K. C., Sam, I. C., and Chan, Y. F. (2021). Vaccine Candidates Generated by Codon and Codon Pair Deoptimization of Enterovirus A71 Protect Against Lethal Challenge in Mice. *Vaccine* 39 (12), 1708–1720. doi: 10.1016/j.vaccine.2021.02.024

Liu, W., Wu, S., Xiong, Y., Li, T., Wen, Z., Yan, M., et al. (2014). Co-Circulation and Genomic Recombination of Coxsackievirus A16 and Enterovirus 71 During a Large Outbreak of Hand, Foot, and Mouth Disease in Central China. *PloS One* 9 (4), e96051. doi: 10.1371/journal.pone.0096051

Liu, Y.-S., Zhou, J.-H., Chen, H.-T., Ma, L.-N., Pejsak, Z., Ding, Y.-Z., et al. (2011). The Characteristics of the Synonymous Codon Usage in Enterovirus 71 Virus and the Effects of Host on the Virus in Codon Usage Pattern. *Infect. Genet. Evol.* 11 (5), 1168–1173. doi: 10.1016/j.meegid.2011.02.018

Lukashev, A. N., Shumilina, E. Y., Belalov, I. S., Ivanova, O. E., Eremeeva, T. P., Reznik, V. I., et al. (2014). Recombination Strategies and Evolutionary Dynamics of the Human Enterovirus A Global Gene Pool. *J. Gen. Virol* 95, 868–873. doi: 10.1099/vir.0.060004-0

Ma, M., Hui, L., Wang, M., Tang, Y., Chang, Y., and Jia, Q. (2014). Overall Codon Usage Pattern of Enterovirus 71. *Genet. Mol. Res.* 13 (1), 336–343. doi: 10.4238/2014.January.21.1

Mao, Q., Wang, Y., Yao, X., Bian, L., Wu, X., Xu, M., et al. (2014). Coxsackievirus A16: Epidemiology, Diagnosis, and Vaccine. *Hum. Vaccines Immunother.* 10 (2), 360–367. doi: 10.4161/hv.27087

Martin, D. P., Murrell, B., Golden, M., Khoosal, A., and Muhire, B. (2015). RDP4: Detection and Analysis of Recombination Patterns in Virus Genomes. *Virus Evol.* 1 (1), vev003. doi: 10.1093/ve/vev003

Mombo, I. M., Lukashev, A. N., Bleicker, T., Brünink, S., Berthet, N., Maganga, G. D., et al. (2017). African non-Human Primates Host Diverse Enteroviruses. *PLoS One* 12 (1), e0169067. doi: 10.1371/journal.pone.0169067

Mueller, S., Papamichail, D., Coleman, J. R., Skiena, S., and Wimmer, E. (2006). Reduction of the Rate of Poliovirus Protein Synthesis Through Large-Scale Codon Deoptimization Causes Attenuation of Viral Virulence by Lowering Specific Infectivity. *J. Virol.* 80 (19), 9687–9696. doi: 10.1128/JVI.00738-06

Nakamura, Y., Gojobori, T., and Ikemura, T. (2000). Codon Usage Tabulated From International DNA Sequence Databases: Status for the Year 2000. *Nucleic Acids Res.* 28 (1), 292–292. doi: 10.1093/nar/28.1.292

Oberste, M. S., Feeroz, M. M., Maher, K., Nix, W. A., Engel, G. A., Hasan, K. M., et al. (2013). Characterizing the Picornavirus Landscape Among Synanthropic Nonhuman Primates in Bangladesh 2007 to 2008. *J. Virol.* 87 (1), 558–571. doi: 10.1128/JVI.00837-12

Oberste, M. S., and Gerber, S. I. (2014). "Enteroviruses and Parechoviruses: Echoviruses, Coxsackieviruses, and Others" In:R. Kaslow, L. Stanberry and J. Le Duc(eds) *Viral Infections of Humans* (Springer, Boston, MA) 225–252. doi: 10.1007/978-1-4899-7448-8_11

Oberste, M. S., Maher, K., Michele, S. M., Belliot, G., Uddin, M., and Pallansch, M. A. (2005). Enteroviruses 76, 89, 90 and 91 Represent a Novel Group Within the Species Human Enterovirus A. *J. Gen. Virol.* 86 (2), 445–451. doi: 10.1099/vir.0.80475-0

Organization, W.H (2011). *"A Guide to Clinical Management and Public Health Response for Hand, Foot and Mouth Disease (HFMD)"* (Manila: WHO Regional Office for the Western Pacific).

Peden, J. F. (1999). Analysis of Codon Usage. (University of Nottingham, United Kingdom). doi: 10.1006/expr.1997.4185. Available at: https://sourceforge.net/projects/codonw/.

Pickett, B. E., Sadat, E. L., Zhang, Y., Noronha, J. M., Squires, R. B., Hunt, V., et al. (2012). ViPR: An Open Bioinformatics Database and Analysis Resource for Virology Research. *Nucleic Acids Res.* 40 (D1), D593–D598. doi: 10.1093/nar/gkr859

Pintó, R. M., Pérez-Rodríguez, F.-J., D'Andrea, L., de Castellarnau, M., Guix, S., and Bosch, A. (2018). Hepatitis A Virus Codon Usage: Implications for Translation Kinetics and Capsid Folding. *Cold Spring Harbor Perspect. Med.* 8 (10), a031781. doi: 10.1101/cshperspect.a031781

Puigbò, P., Bravo, I. G., and Garcia-Vallve, S. (2008). CAIcal: A Combined Set of Tools to Assess Codon Usage Adaptation. *Biol. Direct.* 3 (1), 1–8. doi: 10.1186/1745-6150-3-38

Sharp, P. M., Averof, M., Lloyd, A. T., Matassi, G., and Peden, J. F. (1995). DNA Sequence Evolution: The Sounds of Silence. *Philos. Trans. R. Soc. London. Ser. B.: Biol. Sci.* 349 (1329), 241–247. doi: 10.1098/rstb.1995.0108

Sharp, P. M., and Li, W.-H. (1986). Codon Usage in Regulatory Genes in Escherichia Coli Does Not Reflect Selection for 'Rare'codons. *Nucleic Acids Res.* 14 (19), 7737–7749. doi: 10.1093/nar/14.19.7737

Sharp, P. M., and Li, W.-H. (1987). The Codon Adaptation Index-a Measure of Directional Synonymous Codon Usage Bias, and its Potential Applications. *Nucleic Acids Res.* 15 (3), 1281–1295. doi: 10.1093/nar/15.3.1281

Simmonds, P., Tuplin, A., and Evans, D. J. (2004). Detection of Genome-Scale Ordered RNA Structure (GORS) in Genomes of Positive-Stranded RNA Viruses: Implications for Virus Evolution and Host Persistence. *Rna* 10 (9), 1337–1351. doi: 10.1261/rna.7640104

Staring, J., van den Hengel, L. G., Raaben, M., Blomen, V. A., Carette, J. E., and Brummelkamp, T. R. (2018). KREMEN1 Is a Host Entry Receptor for a Major Group of Enteroviruses. *Cell Host Microbe* 23 (5), 636–643.e635. doi: 10.1016/j.chom.2018.03.019

Steil, B. P., and Barton, D. J. (2009). Cis-Active RNA Elements (CREs) and Picornavirus RNA Replication. *Virus Res.* 139 (2), 240–252. doi: 10.1016/j.virusres.2008.07.027

Sueoka, N. (1988). Directional Mutation Pressure and Neutral Molecular Evolution. *Proc. Natl. Acad. Sci.* 85 (8), 2653–2657. doi: 10.1073/pnas.85.8.2653

Sueoka, N. (1995). Intrastrand Parity Rules of DNA Base Composition and Usage Biases of Synonymous Codons. *J. Mol. Evol.* 40 (3), 318–325. doi: 10.1007/BF00163236

Sueoka, N. (1999). Translation-Coupled Violation of Parity Rule 2 in Human Genes is Not the Cause of Heterogeneity of the DNA G+ C Content of Third Codon Position. *Gene* 238 (1), 53–58. doi: 10.1016/S0378-1119(99)00320-0

Sugiyama, T., Gursel, M., Takeshita, F., Coban, C., Conover, J., Kaisho, T., et al. (2005). CpG RNA: Identification of Novel Single-Stranded RNA That Stimulates Human CD14+ CD11c+ Monocytes. *J. Immunol.* 174 (4), 2273–2279. doi: 10.4049/jimmunol.174.4.2273

Su, W., Li, X., Chen, M., Dai, W., Sun, S., Wang, S., et al. (2017). Synonymous Codon Usage Analysis of Hand, Foot and Mouth Disease Viruses: A Comparative Study on Coxsackievirus A6, A10, A16, and Enterovirus 71 From 2008 to 2015. *Infect. Genet. Evol.: J. Mol. Epidemiol. Evol. Genet. Infect. Dis.* 53, 212–217. doi: 10.1016/j.meegid.2017.06.004

Tao, Z., Cui, N., Xu, A., Liu, Y., Song, L., Li, Y., et al. (2013). Isolation and Genomic Characterization of Three Enterovirus 90 Strains in Shandong, China. *Arch. Virol.* 158 (2), 479–483. doi: 10.1007/s00705-012-1517-2

Tian, L., Shen, X., Murphy, R. W., and Shen, Y. (2018). The Adaptation of Codon Usage of+ ssRNA Viruses to Their Hosts. *Infect. Genet. Evol.* 63, 175–179. doi: 10.1016/j.meegid.2018.05.034

Tsai, Y. H., Huang, S. W., Hsieh, W. S., Cheng, C. K., Chang, C. F., Wang, Y. F., et al. (2019). Enterovirus A71 Containing Codon-Deoptimized VP1 and High-

Fidelity Polymerase as Next-Generation Vaccine Candidate. *J. Virol.* 93 (13), e02308–18. doi: 10.1128/JVI.02308-18

Wang, S.-M., and Liu, C.-C. (2014). Update of Enterovirus 71 Infection: Epidemiology, Pathogenesis and Vaccine. *Expert Rev. Anti-infect. Ther.* 12 (4), 447–456. doi: 10.1586/14787210.2014.895666

Wang, Y.-F., and Yu, C.-K. (2014). Animal Models of Enterovirus 71 Infection: Applications and Limitations. *J. Biomed. Sci.* 21 (1), 31. doi: 10.1186/1423-0127-21-31

Wang, M., Zhu, L., Fan, J., Yan, J., Dun, Y., Yu, R., et al. (2020). Rules Governing Genetic Exchanges Among Viral Types From Different Enterovirus A Clusters. *J. Gen. Virol.* 101 (11), 1145–1155. doi: 10.1099/jgv.0.001479

Wong, E. H., Smith, D. K., Rabadan, R., Peiris, M., and Poon, L. L. (2010). Codon Usage Bias and the Evolution of Influenza A Viruses. Codon Usage Biases of Influenza Virus. *BMC Evol. Biol.* 10 (1), 253. doi: 10.1186/1471-2148-10-253

Wright, F. (1990). The 'Effective Number of Codons' Used in a Gene. *Gene* 87 (1), 23–29. doi: 10.1016/0378-1119(90)90491-9

Xu, A., Tao, Z., Lin, X., Liu, Y., Zhang, Y., Song, L., et al. (2011). The Complete Genome Sequence of an Enterovirus 76 Isolate in China Reveals a Recombination Event. *Arch. Virol.* 156 (9), 1685–1689. doi: 10.1007/s00705-011-1067-z

Yamayoshi, S., Yamashita, Y., Li, J., Hanagata, N., Minowa, T., Takemura, T., et al. (2009). Scavenger Receptor B2 is a Cellular Receptor for Enterovirus 71. *Nat. Med.* 15 (7), 798–801. doi: 10.1038/nm.1992

Yip, C., Lau, S., Woo, P., and Yuen, K. Y. (2013). Human Enterovirus 71 Epidemics: What's Next? *Emerg. Health Threat. J.* 6 (6), 19780. doi: 10.3402/ehtj.v6i0.19780

Zhang, H., Cao, H.-W., Li, F.-Q., Pan, Z.-Y., and Wu, Z.-J. (2014). Analysis of Synonymous Codon Usage in Enterovirus 71. *VirusDisease* 25 (2), 243–248. doi: 10.1007/s13337-014-0215-y

Zhang, Z., Dong, Z., Li, J., Carr, M. J., Zhuang, D., Wang, J., et al. (2017). Protective Efficacies of Formaldehyde-Inactivated Whole-Virus Vaccine and Antivirals in a Murine Model of Coxsackievirus A10 Infection. *J. Virol.* 91 (13), e00333–e00317. doi: 10.1128/JVI.00333-17

Zhou, J.-H., Zhang, J., Sun, D.-J., Ma, Q., Chen, H.-T., Ma, L.-N., et al. (2013). The Distribution of Synonymous Codon Choice in the Translation Initiation Region of Dengue Virus. *PLoS One* 8 (10), e77239. doi: 10.1371/journal.pone.0077239

Zhuang, Z.-C., Kou, Z.-Q., Bai, Y.-J., Cong, X., Wang, L.-H., Li, C., et al. (2015). Epidemiological Research on Hand, Foot, and Mouth Disease in Mainland China. *Viruses* 7 (12), 6400–6411. doi: 10.3390/v7122947

Conflict of Interest: The authors declare that the research was conducted in the absence of any commercial or financial relationships that could be construed as a potential conflict of interest.

frontiers | Frontiers in Cellular and Infection Microbiology

REVIEW
published: 14 July 2022
doi: 10.3389/fcimb.2022.953022

The Differentiation and Maintenance of SARS-CoV-2-Specific Follicular Helper T Cells

Yifei Wang[1†], *Qin Tian*[2,3†] and *Lilin Ye*[1,3*]

[1] Guangdong Provincial Key Laboratory of Immune Regulation and Immunotherapy, School of Laboratory Medicine and Biotechnology, Southern Medical University, Guangzhou, China, [2] Dermatology Hospital, Southern Medical University, Guangzhou, China, [3] Institute of Immunology, The People's Liberation Army (PLA), Third Military Medical University, Chongqing, China

Edited by:
Rameez Raja,
Cleveland Clinic, United States

Reviewed by:
Showkat A Dar,
National Institutes of Health (NIH), United States
Muhammad Bilal Latif,
Emory University, United States
Arundhoti Das,
National Institutes of Health (NIH), United States

***Correspondence:**
Lilin Ye
yelilinlcmv@tmmu.edu.cn

†*These authors have contributed equally to this work and share first authorship*

Specialty section:
This article was submitted to Virus and Host, a section of the journal Frontiers in Cellular and Infection Microbiology

Received: 25 May 2022
Accepted: 20 June 2022
Published: 14 July 2022

Citation:
Wang Y, Tian Q and Ye L (2022) The Differentiation and Maintenance of SARS-CoV-2-Specific Follicular Helper T Cells. Front. Cell. Infect. Microbiol. 12:953022. doi: 10.3389/fcimb.2022.953022

Upon acute viral infection, virus-specific $CD4^+$ T cells differentiate into either T_H1 cells or follicular helper T (T_{FH}) cells. The molecular pathways governing such bimodal cell fate commitment remain elusive. Additionally, effector virus-specific T_{FH} cells further differentiate into corresponding memory population, which confer long-term protection against re-infection of same viruses by providing immediate help to virus-specific memory B cells. Currently, the molecular mechanisms underlying the long-term maintenance of memory T_{FH} cells are largely unknown. In this review, we discuss current understanding of early differentiation of virus-specific effector T_{FH} cells and long-term maintenance of virus-specific memory T_{FH} cells in mouse models of viral infection and patients of the severe acute respiratory syndrome coronavirus 2 (SARS-CoV-2) infection.

Keywords: $CD4^+$ T cell, follicular helper T cell, Viral infection, COVID-19, SARS-CoV-2.

INTRODUCTION

During viral infection, the orchestration of $CD4^+$ T cells, $CD8^+$ T cells and B cells constitutes the core events of host adaptive immunity, which confers specialized and long-term cellular and humoral immune protection. As "helper" cells, $CD4^+$ T cells not only optimize the cytotoxic function and memory generation of $CD8^+$ T cells, but also play indispensable roles in both efficient neutralizing antibody production and antibody-producing long-lived plasma cells as well as memory B cells development (Seder and Ahmed, 2003; Kurosaki et al., 2015). Regulated by specific cytokine milieu and transcriptional factors, activated $CD4^+$ T cells have the potential to differentiate into various cellular subsets, including T_H1, T_H2, T_H9, T_H17, T_H22, T_H25, follicular helper T (T_{FH}), and induced regulatory T (iT_{REG}) cells (**Figure 1**), to deal with different types of infection or non-infection situations (O'Shea John and Paul William, 2010; Caza and Landas, 2015; Das et al., 2017; Umar et al., 2020). During viral infection, virus-specific $CD4^+$ T cells mainly differentiate into T helper type 1 (T_H1) cells and follicular helper T (T_{FH}) cells (Crotty, 2014; Xu et al., 2015; Huang et al., 2019). T_{FH} cell subset was first identified in human tonsils and peripheral blood, characterized by the expression of C-X-C chemokine receptor type 5 (CXCR5) and inducible costimulator (ICOS), in which the former facilitates T_{FH} cells to interact with cognate B cells and

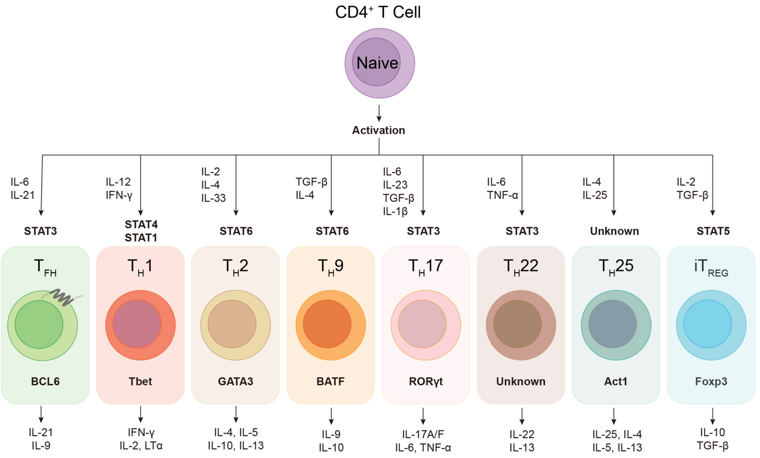

FIGURE 1 | The plasticity of helper CD4+ T cells. Upon activation, naïve $CD4^+$ T cell can differentiate into various subsets of T helper lineages, regulated by certain cytokines and activated signal transducers and activators of transcription (STATs). Each $CD4^+$ helper lineage has the specific lineage-defining transcription factors, e.g. BCL6 in T_{FH} cell, and the characteristic profile of cytokine production, e.g. IL-21 and IL-9 in T_{FH} cell.

further drives B cells homing to follicles and sustains T-B interaction (Breitfeld et al., 2000; Schaerli et al., 2000).

Canonical T_{FH} cells usually locate in the intra-follicle germinal center (GC) of secondary lymphoid organs (SLO), such as lymph nodes, spleen, and tonsils, in which T_{FH} cells frequently wander out and in different GC regions, keeping close interaction with the cognate B cells (Shulman et al., 2013). GC is a highly dynamic structure where the high-affinity mutants of B cells are generated *via* somatic hypermutation (SHM) and affinity-based selection implemented by T_{FH} cells (Victora and Nussenzweig, 2012). In addition, a fraction of T_{FH} cells lingering in T-B border helps cognate B cells ahead to the extrafollicular pathways of antibody generation, which provides immediate protection against invading viruses at the early time of infection (Lee et al., 2011; Di Niro et al., 2015). In addition to SLO, T_{FH} cells have also been witnessed functional in the inducible bronchus-associated lymphoid tissues (iBALT) in lung (Tan et al., 2019), and the tertiary lymphoid structures (TLS) in tumor (Garaud et al., 2022), and the periphery circulation (Morita et al., 2011).

T_{FH} cells are featured as the key players to facilitate high-affinity antibody production of B cells *via* guaranteeing efficient SHM of immunoglobulin genes and the selective processes in GC during viral infection. After primed by dendritic cells (DCs) through engagement of viral peptide-major histocompatibility complex class II molecules (p-MHCII) complex and virus-specific TCR, T_{FH}-committed $CD4^+$ helper T cells initiate GC responses by moving to the T-B border and interact with cognate B cells to elicit B cell proliferation. During this process, B cells circulate between the light zone (LZ), where follicular dendritic cells (FDCs) deposit antigens and T_{FH} cells recognize the p-MHCII complexes on cognate B cells, and the dark zone (DZ), where B cells extensively proliferate after receiving "help" signals from T_{FH} cells. In DZ, GC B cells undergo rapid proliferation accompanied by SHM, allowing generation of mutated BCRs with diverse affinities to antigens. When back into LZ, mutated GC B cells with higher affinity are selected by T_{FH} cells for another circulation of proliferation and mutation (Victora and Nussenzweig, 2012; Shulman et al., 2013; Crotty, 2014). In addition to directly providing costimulatory signaling to cognate B cells *via* ICOS, CD40L, and SAP (Qi et al., 2008; Crotty, 2014), T_{FH} cells produce high levels of IL-21, which is essential for B cell survival, proliferation, plasma cell differentiation, and isotype switching (Chtanova et al., 2004; Kuchen et al., 2007; Linterman et al., 2010). In addition to IL-21, T_{FH} cell-derived IL-9 also promotes the development of memory B cells in GC (Wang et al., 2017). It was long and widely believed that T_H1 cells rather than T_{FH} cells primarily contribute to promote killing function of $CD8^+$ T cells. Of late, however, Cui et al. revealed that IL-21 produced by tumor-specific T_{FH} cells directly promotes the anti-tumor capacity of $CD8^+$ T cell (Cui et al., 2021). Meanwhile, Zander et al. demonstrated that T_{FH}-derived IL-21 promotes the development and antiviral immunity of $CD8^+$ T cells during chronic viral infection (Zander et al., 2022). Since IL-21 promotes the formation of stem-like/memory $CD8^+$ T cells (Tian and Zajac, 2016), it is possible that the help from $CD4^+$ T cells to $CD8^+$ T cell memory may be mediated by T_{FH} cells. Moreover, $CXCR5^+$ $CD4^+$ T_{FH} cells locating in perifollicular areas of iBALT act to enhance the homing and fitness of $CD8^+$ T cells through IL-21 and IFN-γ production during influenza A virus infection (Pruner and Pepper, 2021).

Overall, T_{FH} cells bridge the cellular and humoral immunity in host, thus playing an essential role in adaptive immune responses. Here we firstly focus on the current understanding of the generation and longevity of virus-specific T_{FH} cells during viral infection, including the fate commitment, lineage differentiation, memory formation, and long-term maintenance (**Figure 2**). Then, we also discuss the role of SARS-CoV-2-specific T_{FH} cells during currently still ongoing pandemic coronavirus disease 2019 (COVID-19) **(Figure 3)**.

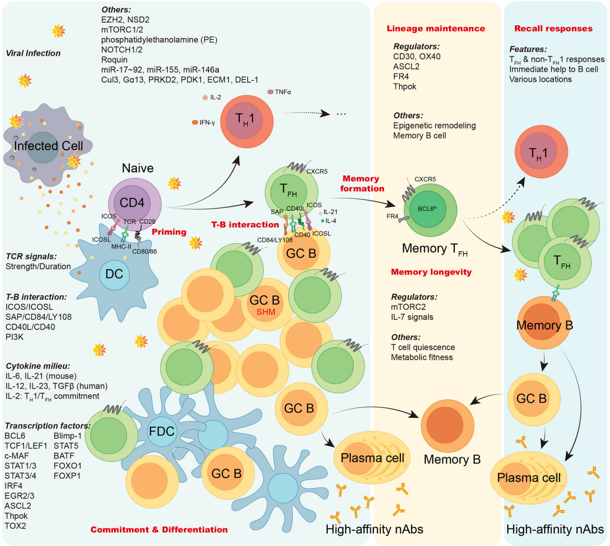

FIGURE 2 | The generation, maintenance, and functions of virus-specific TFH cells. In viral infection, antigen presenting cells like dendritic cells (DCs) conduct antigen uptake, processing, and presentation to prime naïve virus-specific CD4$^+$ T cells, inducing T cell activation. Upon activation, virus-specific CD4$^+$ T cells are mainly committed into either T_H1 cells or T_{FH} cells. The lineage commitment and differentiation of T_H1/T_{FH} cell are orchestrated under the regulation of TCR signals, T-B interaction, cytokine milieu, transcription factors, and other factors as illustrated. Virus-specific effector T_{FH} cells work on initiating GC responses, facilitating the cognate B cell maturation, promoting generation of long-lived memory B cells and high-affinity neutralizing antibodies. Memory virus-specific T_{FH} cells are developed and sustained after viral clearance under the regulation of a variety of regulators, epigenetic remodeling, and cognate memory B cells. The longevity of memory T_{FH} cells are guaranteed by T cell quiescence and viability conferred by mTORC2 signaling. Upon re-challenge of encountered viruses, memory virus-specific T_{FH} cells provide immediate help to cognate memory B cells, promoting robust cellular and humoral recall responses.

VIRUS-SPECIFIC T_{FH} CELL DIFFERENTIATION

Signals from T Cell Receptor Elicit T_{FH} Commitment

T_{FH} cell differentiation is a multistep and multifactorial process. Naïve CD4$^+$ T cells are primed by TCR recognition of p-MHCII presented on DCs to initiate the activation and lineage differentiation (Goenka et al., 2011). T_{FH} cell program starts at a very early stage after TCR activation. After immunization, antigen-specific CD4$^+$ T cells in draining lymph nodes upregulate expression of BCL6, which is the master transcriptional factor for T_{FH} cells, within 48 hours (Baumjohann et al., 2011). Meanwhile, using lymphocytic choriomeningitis virus- (LCMV) specific TCR transgenic CD4$^+$ T (SMARTA) cells, Choi et al. showed an early development of virus-specific T_{FH} cells at day 3 post-infection (Choi et al., 2011). Previous studies demonstrated that DCs are necessary and sufficient to induce CXCR5$^+$ BCL6$^+$ T_{FH} generation (Goenka et al., 2011), while the late B cell interactions are required for complete differentiation of T_{FH} cells (Barnett et al., 2014; Hao et al., 2018). However, in some scenarios, T_{FH} cells are generated in DC-depleted mice as long as cognate T-B interactions are available (Dahlgren et al., 2015; Arroyo and Pepper, 2019). The strength and duration of TCR signaling are considered to affect the bimodal fate commitment of T_{FH}/T_H1 cell during viral infection. By adoptive transfer of TCR transgenic T cells with different TCR affinities, Fazilleau et al. demonstrated that CD4$^+$ helper T cells with higher specific binding of p-MHCII and more restricted TCR junctional diversities tend to commit to T_{FH} cell differentiation (Fazilleau et al., 2009). Further investigations suggested that the interaction between TCR and p-MHCII with long duration favors T_{FH} cell commitment (Baumjohann et al., 2013b; Tubo et al., 2013). This mechanism of T_{FH} cell commitment echoes the observation of the accumulation of T_{FH} cells during chronic viral infection, in which persistent antigen induces sustained TCR stimulation with a long dwell time (Fahey et al., 2011; Vella et al., 2017). However, there are controversial views about the facilitation of stronger TCR signals in determining T_{FH} cell commitment and differentiation (Keck et al., 2014; Snook Jeremy et al., 2018; Kotov et al., 2019). Both Keck et al. and Kotov et al. utilized the *Listeria monocytogenes* expressing peptides with different TCR affinities and corresponding TCR transgenic mice to demonstrate that TCRs with higher affinity promote T_H1 cell formation, whereas TCRs with lower affinity poised to the T_{FH}-biased differentiation of naïve CD4$^+$ T cells (Keck et al., 2014; Kotov et al., 2019). In addition, Jeremy P. Snook et al. confirmed ectopically enhanced TCR signaling *via* knockdown SHP-1, which is a tyrosine phosphatase that suppresses early TCR signaling events, increases the differentiation of T_H1 cells rather than T_{FH} cells (Snook Jeremy et al., 2018). These discrepancies warrant to be reconciled by future studies.

ICOS, SAP, and CD40L Maintain T_{FH} Differentiation

In addition to the interaction of TCR and cognate p-MHCII on DCs, molecules associated with T-B cell conjugation, like ICOS, SAP and CD40L, are also important regulators of T_{FH} cell differentiation during viral infection (Crotty, 2011). With a high expression of CXCR5 and a low level of CCR7, T_{FH} cells are capable of migrating to the T-B border (Breitfeld et al., 2000; Schaerli et al., 2000), where the B cell-dependent T_{FH} cell differentiation occurs. ICOSL expressed on B cells is essential for the responses of T_{FH} cells (Akiba et al., 2005; Bossaller et al., 2006; Gigoux et al., 2009; Xu et al., 2013; Liu et al., 2015), in both CD28-dependent and CD28-independent pathways (Tan et al., 2006; Linterman et al., 2009). ICOSL expression on B cell is subject to the negative feedback regulation of ICOS-ICOSL interaction (Watanabe et al., 2008), while ICOS expression on T_{FH} cells seems under the negative regulation of transcriptional suppressor FOXP1 (Wang et al., 2014). ICOS signaling inactivates FOXO1, which strongly inhibits T_{FH} cell development *via* negatively regulating BCL6 expression (Stone et al., 2015). ICOS-ICOSL interaction is also required for the persistence of T_{FH} cells and GC responses by down-regulating

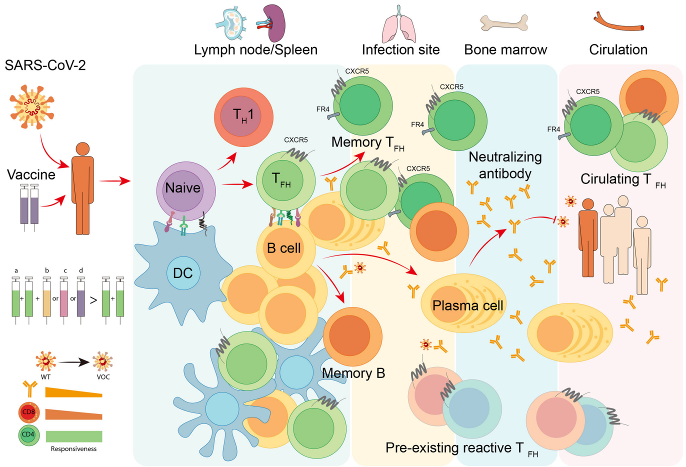

FIGURE 3 | TFH cell responses to COVID-19. Infection or vaccination of SARS-CoV-2 induces differentiation of virus-specific T_{FH} cells and activation of cognate B cells in secondary lymphoid organs like lymph nodes and spleen. With the help of T_{FH} cells, antigen-specific B cells develop into plasma cells to produce neutralizing antibodies with increased affinity, and meanwhile, generate long-lived plasma cells and memory B cells that traffic to the bone marrow and provide long-term protection. Neutralizing antibodies are capable of blocking the attachment and entry of SARS-CoV-2 to prevent COVID-19. In infection site and circulation, the pre-existing cross-reactive T_{FH} cells and circulating T_{FH} cells are proved to be beneficial for the immune protection of natural infection and vaccination. To date, multiple vaccine platforms are utilized to develop SARS-CoV-2 vaccines, including (a) inactivated virus vaccines, (b) adjuvanted recombinant protein vaccines, (c) adenoviral vector-based vaccines, and (d) mRNA vaccines. The heterologous sequential immunization provides a superior effectiveness to protect vaccines from variant of concern (VOC) of SARS-CoV-2 compared to homologous vaccination. The superiority of this vaccination strategy may attribute to the competent responsiveness of memory $CD4^+$ T cells to SARS-CoV-2 VOCs.

KLF2, which serves to inhibit T_{FH} cell differentiation (Weber et al., 2015). In addition to conduct TCR signaling, PI3K signaling acts to mediate the T_{FH}-promoting function of ICOS (Gigoux et al., 2009). Rolf et al. showed that the number of T_{FH} cells, GC B cells, and high-affinity antibody-secreting cells is correlated with the magnitude of PI3K signaling (Rolf et al., 2010). SAP expression on T_{FH} cell is critical for the formation of T-B interaction (Qi et al., 2008; Cannons et al., 2010a), which is indispensable for GC T_{FH} cell differentiation. Moreover, SAP actively participates in the modulation of TCR signaling in T_{FH} cells (Cannons et al., 2004; Cannons et al., 2010b). In addition, CD40L expressed on T_{FH} cells is essential for the GC B cells survival and GC maintenance as well as the function of T_{FH} cells (Elgueta et al., 2009; Crotty, 2011; Vinuesa et al., 2016).

Cytokines Shape T_{FH} Lineage Differentiation

Cytokine milieu is pivotal to the lineage fate determination of $CD4^+$ helper T cells. Unlike other subsets of $CD4^+$ T cells which have the default cytokine-driving paradigm of lineage differentiation, for examples, IFN-γ and IL-12 promote T_H1 differentiation, whereas IL-4 facilitates T_H2 generation, T_{FH} cells manifest no default cytokine-driving differentiation pathway. Though without determining cytokines, T_{FH} cells can be shaped by multiple cytokine types (Pawlak et al., 2020).

IL-6 and IL-21 are important cytokines for T_{FH} cell differentiation in mice (Karnowski et al., 2012), whereas IL-12, IL-23, and TGF-β play prominent roles in human T_{FH} cell differentiation (Ma et al., 2009; Sweet et al., 2012; Schmitt et al., 2014). IL-21 is also an essential effector molecular of T_{FH} cells, though it can be mainly expressed by both T_H17 and T_{FH} cells (Chtanova et al., 2004). It is generally acknowledged that IL-21 signaling is critical for the maintenance of GC in a B cell intrinsic mechanism (Linterman et al., 2010; Zotos et al., 2010). IL-6 produced by DCs induces early up-regulation of BCL6 in mouse T_{FH} cells (Eto et al., 2011), as well as promotes the maintenance of T_{FH} cells during chronic viral infection (Harker James et al., 2011). IL-21 also functions in an autocrine manner to support T_{FH} cell responses (Nurieva et al., 2008). In human, plasmacytes-derived IL-6 induces the differentiation of circulating T_{FH} cells (Chavele et al., 2015). Different with murine $CD4^+$ T cells, human $CD4^+$ T cells differentiate into IL-21 producing T_{FH} cells with increased expression of CXCR5, ICOS, and BCL6 under the regulation of IL-12 rather than IL-6 (Ma et al., 2009; Schmitt et al., 2009). Moreover, TGF-β, which substantially inhibits T_{FH} cell differentiation in mice, induces human T_{FH} cell development *via* activating STAT3-STAT4 signaling (Schmitt et al., 2014).

Recently, an important role of IL-2 in controlling T_{FH}/non-T_{FH} cell commitment was revealed. By using IL-2 reporter mice, DiToro et al. demonstrated that naïve $CD4^+$ T cells receiving highest TCR signals and producing IL-2 will differentiate into T_{FH} cells, whereas IL-2 non-producers will differentiate into non-T_{FH} cells (DiToro et al., 2018). Given abovementioned discrepant roles between certain human and mouse cytokines in regulating T_{FH} cell differentiation, whether IL-2 signaling exerts the same or similar function on mouse and human T_H1/T_{FH} commitment needs further investigation.

Transcription Factors Regulate T_{FH} Commitment and Differentiation

Intrinsic programs for T_{FH} cell commitment and differentiation initiate very early upon activation (Baumjohann et al., 2011; Choi et al., 2011). BCL6 is required for T_{FH} cell differentiation by inhibiting Blimp-1, which drives $CD4^+$ T cells developing into non-T_{FH} lineages (Johnston Robert et al., 2009; Nurieva Roza et al., 2009; Yu et al., 2009). BCL6 expression is associated with upregulation of CXCR5 and downregulation of CCR7 and PSGL1, allowing the migration of T_{FH} cells to T-B border and GC (Hatzi et al., 2015). KLF2, another target of BCL6, impedes T_{FH} cell differentiation *via* inducing expression of *Prdm1*. *Tbx21*, and *Gata3*, and meanwhile repressing *Cxcr5* transcription *via* directly binding to its genomic region (Hatzi et al., 2015; Lee et al., 2015; Weber et al., 2015). Recent studies further elucidated that BCL6 also negatively regulates ID2 to facilitate T_{FH} cell differentiation (Shaw et al., 2016) and positively regulates TOX2 to promote chromatin accessibility of T_{FH}-associated genes (Xu et al., 2019).

Since BCL6 was identified to be the master transcription factor in T_{FH} cell differentiation, plenty of transcription factors have been discovered to regulate T_{FH} cell differentiation *via* directly or indirectly affecting BCL6 expression and function (Vinuesa et al., 2016; Choi et al., 2020; Schroeder et al., 2021). TCF1 and LEF1 initiate and promote T_{FH} cell differentiation by ensuring the early expression of BCL6 and the repression of Blimp-1 (Choi et al., 2015; Wu et al., 2015; Xu et al., 2015). TCF1 is also involved in suppression of IL-2Rα (Wu et al., 2015), which together with Blimp-1 forms a negative feedback loop of TCF1/IL-2R/Blimp-1 regulating the T_{FH} responses during viral infection. In addition, signal transducers and activator (STAT) 1 and 3 both contribute to T_{FH} differentiation *via* IL-21 and IL-6 signaling (Nurieva et al., 2008). STAT3 and STAT4, in response to IL-12 and IL-23, cooperatively with TGF-β promote human but not mouse T_{FH} cell differentiation by promoting T_{FH} cell associated molecules (CXCR5, ICOS, IL-21, Bcl-6, etc.) expression and repressing Blimp-1 expression (Schmitt et al., 2014). IRF4 promotes T_{FH} cell differentiation also through signals mediated by STATs (Nurieva et al., 2008) or other transcription factors (Huber and Lohoff, 2014). However, STAT5, in collaboration with Blimp-1 and IL-2 signals, is a potent negative regulator of T_{FH} cell differentiation (Johnston et al., 2012). Also, BATF directly induces transcription of BCL6 and c-MAF in T_{FH} cell to promote the T_{FH} cell differentiation (Betz et al., 2010). Not surprisingly, absence of c-MAF decreases the amount of T_{FH} cells and IL-21 production (Bauquet et al., 2009; Andris et al., 2017). Transcription factors EGR2/3 are also required for T_{FH} cell differentiation and GC formation by regulating BCL6 (Ogbe et al., 2015). Moreover, ASCL2, which has multiple binding sites in *Cxcr5* locus, directs the migration of T_{FH} cells towards B cell follicles, and is essential for early T_{FH} cell differentiation (Liu et al., 2014). Recently, Vacchio et al. revealed that Thpok promotes BCL6 and MAF to facilitate virus-specific T_{FH} cell differentiation and GC formation in LCMV infection (Vacchio et al., 2019).

Two forkhead box proteins, FOXO1 and FOXP1, are demonstrated to negatively regulate T_{FH} cell differentiation (Wang et al., 2014; Stone et al., 2015). FOXO1 closely binds to the region of *Bcl6* locus, limiting the BCL6 expression and T_{FH} cell development (Stone et al., 2015). FOXP1 directly binds to the *Il21* promoter region to suppress IL-21 expression. In addition, FOXP1-deficient $CD4^+$ T cells upregulate expression of ICOS during T cell activation (Wang et al., 2014), indicating a repressive role of FOXP1 on ICOS. In addition, a recent investigation showed that TOX2 acts to bind to and facilitate the chromatin accessibility of gene loci associated with T_{FH} cell differentiation and function, including BCL6 (Xu et al., 2019).

Other Factors Regulating T_{FH} Cell Differentiation

Epigenetic modulation is also involved in T_{FH} cell differentiation. Besides abovementioned chromatin remodeling of T_{FH} cell associated genes *via* BCL6-TOX2 (Xu et al., 2019), the histone methyltransferase EZH2 also plays an important role in epigenetic regulation of T_{FH} cell differentiation. Using assay for transposase-accessible chromatin with high-throughput sequencing (ATAC-seq), Chen et al. demonstrated that EZH2 is essential for chromatin accessibility remodeling of T_{FH}-associated genes at the early commitment of T_{FH} cells (Chen et al., 2020a). Li et al. revealed that abundant EZH2 binding peaks overlapped with TCF1 peaks, explaining the defective differentiation of T_{FH} cell with EZH2 deficiency (Li et al., 2018). Another histone methyltransferase, NSD2, which is induced by CD28 stimulation and sustained by ICOS signaling, is also required for the early expression of BCL6 and late maintenance of T_{FH} cells (Long et al., 2020).

Moreover, T cell activation and differentiation always manifest substantial re-programming of cellular metabolism (MacIver et al., 2013; Chapman et al., 2020). The serine/threonine kinase mammalian target of rapamycin (mTOR) is a potent regulator of T cell response *via* sensing and integrating inputs from nutrients, growth factors, energy, and cellular stress (Chi, 2012; Yang and Chi, 2012; Huang et al., 2020). By down-regulating mTOR, Myr-Akt, and/or CD25 signals in LCMV-specific $CD4^+$ T cells, Ray et al. demonstrated that IL-2/mTORC1 axis orchestrates the reciprocal balance between T_{FH} and T_H1 cell differentiation during viral infection (Ray et al., 2015). Further studies revealed the discrete regulatory roles of two different mTOR complexes, mTORC1 and mTORC2 (Yang et al., 2016; Zeng et al., 2016; Hao et al., 2018). Deficiency of mTORC1 substantially impairs cell proliferation and T_{FH} cell differentiation, whereas mTORC2 is needed for T_{FH} cell differentiation by promoting Akt activation and TCF1 expression without impacting cell proliferation (Yang et al., 2016). Hao et al. further demonstrated that mTORC2 signals induced by TCR and ICOS stimulation participates in cell migration, late differentiation and maturation of T_{FH} cells (Hao et al., 2018). Recently, using *in vivo* CRISPR-Cas9 screening and functional validation in mice, Fu et al. revealed a direct regulatory function of *de novo* synthesis of phosphatidylethanolamine (PE) on T_{FH} cell development *via* controlling surface expression of CXCR5 (Fu et al., 2021). Taken together, those findings highlight the metabolic control of T_{FH} cell differentiation.

In addition, these are many other factors involved in regulating T_{FH} cell commitment and differentiation. For example, RNA-binding protein Roquin exerts negative post-transcriptional regulation on T_{FH} cells *via* binding to the T_{FH}-associated genes like *Icos*, *Ox40* (Vinuesa et al., 2005). Some microRNAs also play roles in post-transcriptional regulation of T_{FH} cell differentiation. miR-17~92 promotes T_{FH} cell differentiation by enhancing PI3K signaling as well as repressing non-T_{FH} genes (Baumjohann et al., 2013a). miR-155 promotes T_{FH} cell differentiation during chronic inflammation in which miR-155-knockout diminished the accumulation of T_{FH} cells (Hu et al., 2014). In addition, miR-146a acts as a post-transcriptional repressor to ICOS-ICOSL signaling and the subsequent T_{FH} cell differentiation and GC responses (Pratama et al., 2015). Also, NOTCH1/2 deficiency in $CD4^+$ T cell reduces the expression of BCL6, IL-21, and CXCR5, but increases Blimp-1 expression, resulting in impairment of the development and function of T_{FH} cells. Additional factors have been verified in regulating T_{FH} cell differentiation, including but not limited to the E3 ligase cullin 3 (Cul3) (Mathew et al., 2014), heterotrimeric G protein $G\alpha_{13}$ (Kuen et al., 2021), kinase PRKD2 (Misawa et al., 2020), kinase PDK1 (Sun et al., 2021), extracellular matrix protein 1 (ECM1) (He et al., 2018), and stromal cell-derived DEL-1 (Wang et al., 2021).

MEMORY VIRUS-SPECIFIC T_{FH} CELLS

Identification of Virus-Specific Memory T_{FH} Cells

In acute viral infection or vaccination, a small proportion of the antigen-experienced $CD4^+$ T cells survive after antigen clearance, subsequently become the memory $CD4^+$ helper T cells. In addition to survival capacity and homeostatic proliferation without antigenic stimulation, a memory $CD4^+$ helper T cell also need to preserve the lineage features during resting and recall responses (MacLeod et al., 2009; Hale and Ahmed, 2015). In the first report describing the existence of antigen-specific memory T_{FH} cells, Fazilleau et al. found a group of antigen-specific $CXCR5^+ICOS^{lo}$ T_{FH} cells in the memory phase of protein vaccination (Fazilleau et al., 2007). It is worth noting that those $CXCR5^+ICOS^{lo}$ cells were retained along with persistent peptide-MHCII (Fazilleau et al., 2007), which raises a question about the true memory property of T_{FH} cells. By adoptive transfer of TCR transgenic antigen-specific $CD4^+$ T cells or T_{FH}/non-T_{FH} cells into second recipients, MacLeod et al. further confirmed the existence of antigen-specific memory T_{FH} cells after protein immunization (MacLeod et al., 2011). Accumulating studies further demonstrated the validity and characteristics of virus-specific memory T_{FH} cells during viral infection and vaccination (Weber et al., 2012; Bentebibel et al., 2013; Hale et al., 2013; Locci et al., 2013).

Memory T_{FH} cells are usually marked by co-expression of CXCR5, CCR7, CD62L, and FR4, along with downregulated expression of PD1, ICOS, Ly6c, and BCL6 (Iyer et al., 2013; Hale and Ahmed, 2015). Memory T_{FH} cells exert a superior help function on naïve B cells than primary responding T_{FH} cells (MacLeod et al., 2011). In recall responses, virus-specific T_{FH} cells provide immediate help to virus-specific memory B cells (He et al., 2013; Locci et al., 2013; Phan and Tangye, 2017). In addition, local memory T_{FH} cells colocalized with B cells within the parenchymal lung tissues are critical for the production of virus-specific B cells and antibodies (Son Young et al., 2021).

Formation of Virus-Specific Memory T_{FH} Cells

A consensus is that virus-specific memory $CD4^+$ T cells are progenies of corresponding effector $CD4^+$ T cells, the so-called memory precursors generated during effector phase of acute viral infection (Hale and Ahmed, 2015). But the high plasticity (Zhou et al., 2009) and non-default differentiation pathway (Choi et al., 2020) of T_{FH} cells make it hard to track a destined memory precursor T_{FH} cell at early effector phase. Some studies suggest formation of memory T_{FH} cells can be prior to GC development (He et al., 2013; Tsai and Yu, 2014). However, given the antigen retention in follicle and a rather long time of persistent GC reaction, another view is that since T_{FH} cells can shuttle between different GCs, and when they emigrate into follicles where no presented antigens exist, they acquire less activated phenotypes, resultantly, these T_{FH} cells gradually differentiate into memory cells with a resting state (Kitano et al., 2011; Choi et al., 2013).

Since T_{FH} cells are prone to stay at GC while T_H1 cells migrate into infected location, T_{FH} cells are regarded to be more likely to differentiate into central memory T_{FH} cells (Zhu et al., 2010). Nevertheless, distribution of memory T_{FH} cells is not necessarily limited in GCs. Circulating HIV-specific effector memory T_{FH} cells are potent players for immune surveillance *in situ* (Locci et al., 2013). Moreover, iBALT-resident memory T_{FH} cells in lung are essential for the robust recall humoral responses and provide help to local $CD8^+$ T_{RM} cells (Pruner and Pepper, 2021; Son Young et al., 2021).

Early study showed that CD30 and OX40 signals are needed to form $CD4^+$ T cell memory (Gaspal et al., 2005). Further investigations revealed that memory T_{FH} cells down-regulate BCL6 while retain the surface expression of CXCR5 (Hale and Ahmed, 2015). ASCL2 may be important for the expression of CXCR5 in memory T_{FH} cells, because it binds to the conserved non-coding sequence regions of *Cxcr5* locus to promote *Cxcr5* transcription without inducing BCL6 expression (Liu et al., 2014). FR4, highly expressed by naïve $CD4^+$ T cells, is down-regulated upon activation and re-expressed on T_{FH} cells (Iyer et al., 2013), and is maintained on memory T_{FH} cells as CXCR5 does (Hale and Ahmed, 2015). What's more, recent study shows that long-lived T_{FH} cells persisted for over 400 days after infection are marked by high expression of FR4 (Künzli et al., 2020). Yet the mechanism driving the FR4 expression is still unknown. In addition, Ciucci et al. recently showed that Thpok is required for the signatures and emergence of memory $CD4^+$ T cell *via* antagonizing the expression of Blimp-1 and Runx3 (Ciucci et al., 2019). Overall, mechanisms underlying the formation of virus-specific memory T_{FH} cells remain largely unknown. The imprinting effects from effector phase, the various features induced by different niches (GC in SLO, peripheral residence, or circulation), and driving force of the continuous expression of CXCR5, are parts of the unsolved issues about T_{FH} cell memory formation.

Lineage Maintenance Versus Plasticity

$CD4^+$ helper T cells are featured with high plasticity. Several studies showed that adoptively transferred memory T_{FH} cells eventually differentiate into both T_{FH} and non-T_{FH} cells in second recipients upon rechallenge (Pepper et al., 2011; Lüthje et al., 2012; Künzli et al., 2020). The plasticity of T_{FH} cells is highlighted by the work of Lu et al, in which the authors found that T_{FH} cells harboring chromatin accessibility of *Tbx21*, *Gata3*, and *Rorc* genes that could drive $CD4^+$ Helper T cells to differentiate into T_H1, T_H2, and T_H17 cells under the respective polarizing conditions (Lu et al., 2011).

Given the extrinsic factors, like antigens and effector cytokine milieu (O'Shea John and Paul William, 2010), which promote T helper cell differentiation, are absent after viral clearance, it is reasonable to consider that intrinsic programs play a dominant role in sustaining memory virus-specific T_{FH} cell lineage during memory phase. However, the master transcription factor of T_{FH} cells like BCL6, and other factors constraining T helper cell lineages are down-regulated in memory $CD4^+$ T cells (Hale and Ahmed, 2015). How do memory T cells retain lineage commitment? It is still an unsolved question. Transcriptional and epigenetic profiling suggest that epigenetic remodeling during effector phase may play an important role in retaining lineage characteristics in memory T_{FH} cells (Wilson et al., 2009; Josefowicz, 2013; Youngblood et al., 2013). In addition, memory B cells conduct immediate antigen presentation to memory T_{FH} cells, inducing rapid re-expression of BCL6 in reactivated T_{FH} cells (Ise et al., 2014), which safeguards the T_{FH}-oriented recall responses.

Longevity of Virus-Specific Memory T_{FH} Cells

Following the clearance of virus in acute viral infection, virus-specific memory $CD8^+$ T cells can persist for a very long period at a stable level, whereas virus-specific memory $CD4^+$ T cells gradually decay over time (Homann et al., 2001). However, there is much less knowledge about how memory $CD4^+$ T cells sustain longevity compared to that of memory $CD8^+$ T cells. By transcriptional profiling, Song et al. reveal multiple genetic programs contributed to the longevity of antigen-specific memory $CD4^+$ T cells by maintaining T cell quiescence (Song et al., 2020). In a mouse model of acute infection with LCMV, Wang et al. demonstrated that the mTORC2-Akt-GSK3β axis is critical for the longevity of virus-specific memory T_{FH} and T_H1 cells by protecting these memory cells from ferroptosis, however this signaling axis seems to be non-essential for memory $CD8^+$ T cells (Wang et al., 2022c). The tonic mTORC2 activity in virus-specific memory $CD4^+$ T cells is sustained by the IL-7 signaling at memory phase, which suggests an important role of IL-7 signaling in memory T_{FH} cell maintenance (Wang et al., 2022c). Given the essential functions of mTOR signaling pathway in regulating cellular metabolism and the divergent role of mTORC2 in memory $CD4^+$ T cells and $CD8^+$ T cells (Pollizzi et al., 2015), it is reasonable to speculate that there are certain differences either in metabolic features or/and redox homeostasis between virus-specific memory $CD4^+$ and $CD8^+$ T cells. Paired comparison analysis of memory $CD4^+$ and $CD8^+$ T cells may provide valuable clues in further understanding memory $CD4^+$ T cell longevity.

VIRUS-SPECIFIC T_{FH} CELLS IN COVID-19

T_{FH} Cell Responses in SARS-CoV-2-Infection and Vaccination

Severe Acute Respiratory Syndrome Coronavirus (SARS-CoV-2) is an enveloped single-stranded positive-sense RNA virus accounting for the ongoing pandemic of COVID-19. SARS-CoV-2 genome encodes 4 structural proteins including surface spike (S) glycoprotein, membrane protein (M), envelop protein (E), and nucleoprotein (N). The S protein of SARS-CoV-2 facilitates viral attachment and entry through the engagement with its cognate receptor, angiotensin converting enzyme-2 (ACE2), which is mediated by the receptor binding domain (RBD) within the S1 subunit of S protein (V'Kovski et al., 2021). SARS-CoV-2 infection induces both humoral and cellular immune responses in hosts (Post et al., 2020; Sette and Crotty, 2021; Shrotri et al., 2021). Commonly, neutralizing antibodies are vital for sterilizing immunity of viral infection. Antibodies targeting S protein and RBD are capable of blocking the attachment and entry of SARS-CoV-2 into host cells to prevent COVID-19 infection (Robbiani et al., 2020; Gupta et al., 2021; Wang et al., 2022a; Wang et al., 2022b). The production of neutralizing antibodies targeting SARS-CoV-2 with high magnitude and durability requires potent B cell responses with the help from virus-specific T_{FH} cells. Evidences from non-human primate studies validated that natural infection of SARS-CoV-2 protects rhesus macaques from reinfection, indicating the occurrence of protective immunological memory post SARS-CoV-2 infection (Chandrashekar et al., 2020; Deng et al., 2020). Both two studies verified viral S protein-specific memory $CD4^+$ T cells in rhesus macaques after infection of SARS-CoV-2; moreover, Deng et al. further detected the increased viral S protein-specific central memory $CD4^+$ T cells in lymph nodes of rhesus macaques post rechallenge of SARS-CoV-2. Given the bimodal differentiation of virus-specific T_{FH} and T_H1 cells in acute infection, these studies highlight the importance of virus-specific T_{FH} cells in SARS-CoV-2 natural immunity and vaccine-induced immunological protection.

Vaccine candidates that can induce sufficient antibodies targeting S protein and RBD are reckoned to be protective against SARS-CoV-2 infection. Therefore, investigations on

SARS-CoV-2-specifc T cell responses, especially the virus-specific T_{FH} cell's help to cognate B cell, help to accelerate the vaccine testing pipeline and contribute to vaccine development under the pandemic COVID-19. Currently, a plethora of vaccines are applied to fight against COVID-19, including mRNA vaccines, adenoviral vector-based vaccines, recombinant protein vaccines, and inactivated virus vaccines (Grigoryan and Pulendran, 2020). According to the results from clinical trials, all vaccines induce detectable antibodies against SARS-CoV-2. To now, the most efficient vaccine platform is mRNA/LNP, which delivers mRNA encoding S protein of SARS-CoV-2 by lipid nanoparticle (LNP) to host cells and induces robust immune responses towards the S antigen (Laczkó et al., 2020; Painter et al., 2021; Mudd et al., 2022). Immunization with SARS-CoV-2 mRNA vaccines foster potent antigen-specific GC responses (Laczkó et al., 2020) and virus-specific $CD4^+$ T cells (Painter et al., 2021) to generate robust neutralizing antibody responses. By analyzing T cells from samples of lymph nodes acquired by fine-needle aspiration from donors who received mRNA vaccines, Mudd et al. further underscored the vital role of virus-specific T_{FH} cell responses in mRNA vaccine-induced robust and durable immunological protection against SARS-CoV-2 (Mudd et al., 2022).

The Functions of SARS-CoV-2-Specific T_{FH} Cells

In infected individuals, the durable neutralization and memory B cells can be predicted by prompt $CD4^+$ T cell responses, especially the strong circulating T_{FH} (cT_{FH}) cell responses (Gong et al., 2020; Boppana et al., 2021; Narowski et al., 2022). Nevertheless, the imbalanced humoral and cellular immunity were often observed in COVID-19 patients (Oja et al., 2020; Gao et al., 2021). Among convalescents, stronger antibody responses were observed in individuals experienced a severe COVID-19, compared to those got moderate symptoms or asymptomatic individuals (Chen et al., 2020b; Gudbjartsson et al., 2020; Röltgen et al., 2020). In some severe sick patients, remarkably strong virus-specific IgG responses were observed, along with decreased $CD4^+$ T cell responses (Oja et al., 2020). By sequencing the B cell receptor repertoires, Schultheiß et al. further found that individuals who have much severer clinical course got a markedly lower percentage of B cells carrying un-mutated BCRs (Schultheiß et al., 2020), which indicates a profound T_{FH} cell-mediated SHM-and-selection have occurred. Above data suggest a gradually compromise of $CD4^+$ T cell responses during COVID-19 progression. Impaired GC reaction was also observed in some cases, of which Naoki Kaneko et al. showed that GC and $BCL6^+$ T_{FH} and B cells were absent in lymph nodes and spleens from severely SARS-CoV-2 infected patients who eventually succumbed after admission (Kaneko et al., 2020). Altogether, these findings emphasize the essential role of virus-specific T_{FH} cells in natural immunity to control COVID-19.

Evidences of robust responses of SARS-CoV-2-specific T_{FH} cell responses upon administration of mRNA vaccines suggest that virus-specific T_{FH} cell responses contribute to the successful immunization of this preeminent vaccine platform (Painter et al., 2021; Mudd et al., 2022). Moreover, using T_{FH} cell-deletion (T_{FH}-DTR) mice, Cavazzoni et al. showed that reduction of T_{FH} cells results in compromised GC responses and decreased production of anti-S and anti-RBD IgG upon SARS-CoV-2 protein vaccination (Cavazzoni et al., 2022), suggesting that virus-specific T_{FH} cell response is also essential to establish an optimized immune protection in traditional immunization strategy.

On the other hand, T_{FH} cells may also play a pathogenic role in certain circumstances. Wang et al. showed that the hyper-functional $CD8^+$ and $CD4^+$ T cells were associated with the pathogenesis of extremely severe COVID-19 patients (Wang et al., 2020). In another study conducted by Meckiff et al., the authors found compared to non-hospitalized COVID-19 patients, increased cytotoxic T_{FH} cells which manifest high production of IFN-γ, IL-2, and TNF-α were observed in hospitalized patients with severe illness (Meckiff et al., 2020). In addition, Fenoglio et al. revealed the pathogenic roles of $CCR4^+$ and $CCR6^+$ T_{FH} cells in COVID-19 patients (Fenoglio et al., 2021). Moreover, it is necessary to pay additional attentions to COVID-19 patients who also suffer from other diseases associated with T_{FH} cell responses, like HIV-infection, autoimmune diseases and cancers treated with immune checkpoint blockade (ICB) therapies (Picchianti-Diamanti et al., 2021; Riou et al., 2021; Salomé and Horowitz, 2021).

Memory SARS-Cov-2-Specific T_{FH} Cells

Bacher et al. suggested that there are pre-existing memory T cells with low avidity and a cross-reactivity to SARS-CoV-2 in unexposed individuals (Bacher et al., 2020). Given the observation that excessive but low-avidity T cell response to SARS-CoV-2 features the severe COVID-19 but not the mild disease, Bacher et al. questions the protective role of pre-existing cross-reactive memory T cells in anti-SARS-CoV-2 immunity (Bacher et al., 2020). However, other investigations targeting T cell responses to SARS-CoV-2 in unexposed individuals revealed that cross-reactive memory T_{FH} cells could trigger a rapid and superior antibody response to SARS-CoV-2, which might exert better viral control in upper respiratory tract and lung (Grifoni et al., 2020; Lipsitch et al., 2020). The latter view was appreciated by Bonifacius et al., who showed that COVID-19 patients with pre-existing anti-human coronavirus $CD4^+$ and $CD8^+$ T cells with cross-reactivity of endemic coronaviruses manifested higher frequency of SARS-CoV-2 S protein-specific T cells (Bonifacius et al., 2021). In addition, Mateus et al. observed a significantly higher frequency of viral S protein-specific $CD4^+$ T cells and stronger neutralizing antibody responses in vaccinated individuals who present pre-existing SARS-CoV-2 S protein-specific $CD4^+$ T cells than subjects with no cross-reactive memory (Mateus et al., 2021). Therefore, besides the classical functions of virus-specific memory T_{FH} cells, the pre-existing virus-specific T_{FH} cells also function to favor T cell and antibody responses against SARS-CoV-2.

Following SARS-CoV-2 infection, substantial virus-specific T cell memory responses are induced in convalescent individuals, whereas the breadth and magnitude were positively correlated to the disease severity of COVID-19 (Peng et al., 2020). The longitude study of T/B cell and antibody responses to COVID-19 revealed a long duration of $CD8^+$ and $CD4^+$ T cell memory and neutralizing antibodies against SARS-CoV-2 (Dan et al., 2021). In general, accruing evidences suggest a profound protection of nature infection of COVID-19 and vaccination. The emerging incompetent immune protection from vaccination or immunological memory of convalescent individuals is more associated with the rapid evolution of SARS-CoV-2 variants (Thakur et al., 2022; Woldemeskel et al., 2022). SARS-CoV-2 continuously undergoes genetic mutations or viral recombination, resulting in variants with possible differences in transmissibility, clinical manifestation, and immunogenicity. To date, the variant of concern (VOC) is Omicron variant (B.1.1.529), which harbors as many as 36 substitutions in viral S protein and total 59 mutations in whole genome compared with SARS-CoV-2 ancestral strain, leading to immune evasion from neutralization by vaccination- and infection-induced antibodies (Woldemeskel et al., 2022). Although Omicron evade a large fraction of antibodies, its neutralizing antibodies are still represented in a portion of memory B cell repertoire induced by mRNA vaccines (Sokal et al., 2022).

Multiple studies revealed that despite the decay of protective serologic components and decreased effectiveness against infection, vaccines developed based on ancestral strains still efficiently protect individuals from SARS-CoV-2 variants-induced hospitalization and/or severe diseases (Nanduri et al., 2021; Rosenberg et al., 2021; Tenforde et al., 2021). This phenomenon highlights the relative impervious function of T cell immunity against SARS-CoV-2 variants, given that virus-specific T cells mainly act to eliminate infected cells ($CD8^+$ T cell) and help B/$CD8^+$ T cells responses after activation ($CD4^+$ T cell), rather than to directly prevent infection like neutralizing antibodies do. In addition, a recent study demonstrated that the preserved T cell reactivity to variant Omicron variant in most infected and vaccinated individuals can be enhanced shortly after booster vaccination (Naranbhai et al., 2022). In this study, Naranbhai et al. identified about 79% individuals with a preserved T cell reactivity to the viral S protein of Omicron. Moreover, the effector T cell responses to SARS-CoV-2, including both wild type and Omicron strain, were enhanced after additional booster vaccine, accompanied with proliferative memory viral S protein-specific $CD4^+$ T cell responses but reduced $CD8^+$ T cell responses to Omicron. This evidence indicates that virus-specific memory T cell, especially virus-specific memory $CD4^+$ T cell, is a silver lining to the plight of controlling circulating SARS-CoV-2 variants. Notably, heterologous vaccination was used in the abovementioned infection/vaccination-booster stratagem, providing corroborative evidence to the effectiveness of the heterologous sequential vaccination strategy against mutant VOCs of SARS-CoV-2. Compared to homologous vaccination, multiple kinds of heterologous sequential immunization were proved to be superior to induce broad neutralization against VOCs, including combination of inactivated vaccine followed by heterologous mutant RBD vaccine (Song et al., 2022), adenoviral vectored vaccine followed by mRNA vaccine (Pozzetto et al., 2021), inactivated vaccine followed by mRNA vaccine (Zuo et al., 2022), and inactivated vaccine followed by adenoviral vectored vaccine (Li et al., 2022). Given the barely affected memory $CD4^+$ T cell responses to peptide pool of Omicron S protein (Naranbhai et al., 2022), it is thus clear that virus-specific memory T_{FH} cells play an important role in the generation of potent and broad neutralizing antibodies to VOCs induced by the heterologous sequential vaccination strategy.

CONCLUDING REMARKS

Since the initial seminal description of T_{FH} cells in 2000 (Breitfeld et al., 2000; Schaerli et al., 2000), many characteristics, functions, and underlying mechanisms of T_{FH} cells have been uncovered over the past two decades. We illustrate the multiple lines and underpinnings of the T_{FH} cell differentiation and maintenance during viral infection in **Figure 1**. But still a lot of puzzles remain to be solved. For example, the extrinsic and intrinsic factors that determine the fate commitment of antigen-specific T_{FH} cells are still unknown. Maybe the differentiation of T_{FH} cells is not a "default" pathway (Choi et al., 2020), and deciphering the networks regulating T_{FH} cell differentiation needs more intense investigations. In addition, how memory T_{FH} cells retain lineage features and prolong over time is fascinating and merits further studies. Better understanding of virus-specific T_{FH} cells will be of great importance for optimizing anti-viral vaccine development, including SARS-CoV-2 vaccines.

AUTHOR CONTRIBUTIONS

YW and QT drafted and revised the manuscript with LY. All authors contributed to the article and approved the submitted version.

FUNDING

This work was supported by grants from the National Key Research Development Plan (2021YFC2300502), and the National Natural Science Foundation of China (No. 32030041 to LY, No. 31800748 to YW, and No. 31800742 to QT).

REFERENCES

Akiba, H., Takeda, K., Kojima, Y., Usui, Y., Harada, N., Yamazaki, T., et al. (2005). The Role of ICOS in the CXCR5+ Follicular B Helper T Cell Maintenance *In Vivo*. *J. Immunol.* 175 (4), 2340. doi: 10.4049/jimmunol.175.4.2340

Andris, F., Denanglaire, S., Anciaux, M., Hercor, M., Hussein, H., and Leo, O. (2017). The Transcription Factor C-Maf Promotes the Differentiation of Follicular Helper T Cells. *Front. Immunol.* 8. doi: 10.3389/fimmu.2017.00480

Arroyo, E. N., and Pepper, M. (2019). B Cells are Sufficient to Prime the Dominant CD4+ Tfh Response to Plasmodium Infection. *J. Exp. Med.* 217 (2), e20190849. doi: 10.1084/jem.20190849

Bacher, P., Rosati, E., Esser, D., Martini, G. R., Saggau, C., Schiminsky, E., et al. (2020). Low-Avidity CD4(+) T Cell Responses to SARS-CoV-2 in Unexposed

Individuals and Humans With Severe COVID-19. *Immunity* 53 (6), 1258–1271.e1255. doi: 10.1016/j.immuni.2020.11.016

Barnett, L. G., Simkins, H. M. A., Barnett, B. E., Korn, L. L., Johnson, A. L., Wherry, E. J., et al. (2014). B Cell Antigen Presentation in the Initiation of Follicular Helper T Cell and Germinal Center Differentiation. *J. Immunol. (Baltimore Md. 1950)* 192 (8), 3607–3617. doi: 10.4049/jimmunol.1301284

Baumjohann, D., Kageyama, R., Clingan, J. M., Morar, M. M., Patel, S., de Kouchkovsky, D., et al. (2013a). The microRNA Cluster miR-17∼92 Promotes TFH Cell Differentiation and Represses Subset-Inappropriate Gene Expression. *Nat. Immunol.* 14 (8), 840–848. doi: 10.1038/ni.2642

Baumjohann, D., Okada, T., and Ansel, K. M. (2011). Cutting Edge: Distinct Waves of BCL6 Expression During T Follicular Helper Cell Development. *J. Immunol.* 187 (5), 2089. doi: 10.4049/jimmunol.1101393

Baumjohann, D., Preite, S., Reboldi, A., Ronchi, F., Ansel, K. M., Lanzavecchia, A., et al. (2013b). Persistent Antigen and Germinal Center B Cells Sustain T Follicular Helper Cell Responses and Phenotype. *Immunity* 38 (3), 596–605. doi: 10.1016/j.immuni.2012.11.020

Bauquet, A. T., Jin, H., Paterson, A. M., Mitsdoerffer, M., Ho, I. C., Sharpe, A. H., et al. (2009). The Costimulatory Molecule ICOS Regulates the Expression of C-Maf and IL-21 in the Development of Follicular T Helper Cells and TH-17 Cells. *Nat. Immunol.* 10 (2), 167–175. doi: 10.1038/ni.1690

Bentebibel, S.-E., Lopez, S., Obermoser, G., Schmitt, N., Mueller, C., Harrod, C., et al. (2013). Induction of ICOS+CXCR3+CXCR5+ TH Cells Correlates With Antibody Responses to Influenza Vaccination. *Sci. Trans. Med.* 5 (176), 176ra132–176ra132. doi: 10.1126/scitranslmed.3005191

Betz, B. C., Jordan-Williams, K. L., Wang, C., Kang, S. G., Liao, J., Logan, M. R., et al. (2010). Batf Coordinates Multiple Aspects of B and T Cell Function Required for Normal Antibody Responses. *J. Exp. Med.* 207 (5), 933–942. doi: 10.1084/jem.20091548

Bonifacius, A., Tischer-Zimmermann, S., Dragon, A. C., Gussarow, D., Vogel, A., Krettek, U., et al. (2021). COVID-19 Immune Signatures Reveal Stable Antiviral T Cell Function Despite Declining Humoral Responses. *Immunity* 54 (2), 340–354.e346. doi: 10.1016/j.immuni.2021.01.008

Boppana, S., Qin, K., Files, J. K., Russell, R. M., Stoltz, R., Bibollet-Ruche, F., et al. (2021). SARS-CoV-2-Specific Circulating T Follicular Helper Cells Correlate With Neutralizing Antibodies and Increase During Early Convalescence. *PloS Pathog.* 17 (7), e1009761–e1009761. doi: 10.1371/journal.ppat.1009761

Bossaller, L., Burger, J., Draeger, R., Grimbacher, B., Knoth, R., Plebani, A., et al. (2006). ICOS Deficiency Is Associated With a Severe Reduction of CXCR5+ CD4 Germinal Center Th Cells. *J. Immunol.* 177 (7), 4927. doi: 10.4049/jimmunol.177.7.4927

Breitfeld, D., Ohl, L., Kremmer, E., Ellwart, J., Sallusto, F., Lipp, M., et al. (2000). Follicular B Helper T Cells Express Cxc Chemokine Receptor 5, Localize to B Cell Follicles, and Support Immunoglobulin Production. *J. Exp. Med.* 192 (11), 1545–1552. doi: 10.1084/jem.192.11.1545

Cannons, J. L., Qi, H., Lu, K. T., Dutta, M., Gomez-Rodriguez, J., Cheng, J., et al. (2010a). Optimal Germinal Center Responses Require a Multistage T Cell:B Cell Adhesion Process Involving Integrins, SLAM-Associated Protein, and CD84. *Immunity* 32 (2), 253–265. doi: 10.1016/j.immuni.2010.01.010

Cannons, J. L., Wu, J. Z., Gomez-Rodriguez, J., Zhang, J., Dong, B., Liu, Y., et al. (2010b). Biochemical and Genetic Evidence for a SAP-PKC-θ Interaction Contributing to IL-4 Regulation. *J. Immunol.* 185 (5), 2819. doi: 10.4049/jimmunol.0902182

Cannons, J. L., Yu, L. J., Hill, B., Mijares, L. A., Dombroski, D., Nichols, K. E., et al. (2004). SAP Regulates TH2 Differentiation and Pkcθ-Mediated Activation of NF-κb1. *Immunity* 21 (5), 693–706. doi: 10.1016/j.immuni.2004.09.012

Cavazzoni, C. B., Hanson, B. L., Podestà, M. A., Bechu, E. D., Clement, R. L., Zhang, H., et al. (2022). Follicular T Cells Optimize the Germinal Center Response to SARS-CoV-2 Protein Vaccination in Mice. *Cell Rep.* 38 (8), 110399–110399. doi: 10.1016/j.celrep.2022.110399

Caza, T., and Landas, S. (2015). Functional and Phenotypic Plasticity of CD4+ T Cell Subsets. *BioMed. Res. Int.* 2015, 521957. doi: 10.1155/2015/521957

Chandrashekar, A., Liu, J., Martinot, A. J., McMahan, K., Mercado, N. B., Peter, L., et al. (2020). SARS-CoV-2 Infection Protects Against Rechallenge in Rhesus Macaques. *Sci. (New York N.Y.)* 369 (6505), 812–817. doi: 10.1126/science.abc4776

Chapman, N. M., Boothby, M. R., and Chi, H. (2020). Metabolic Coordination of T Cell Quiescence and Activation. *Nat. Rev. Immunol.* 20 (1), 55–70. doi: 10.1038/s41577-019-0203-y

Chavele, K.-M., Merry, E., and Ehrenstein, M. R. (2015). Cutting Edge: Circulating Plasmablasts Induce the Differentiation of Human T Follicular Helper Cells *via* IL-6 Production. *J. Immunol.* 194 (6), 2482. doi: 10.4049/jimmunol.1401190

Chen, X., Cao, G., Wu, J., Wang, X., Pan, Z., Gao, J., et al. (2020a). The Histone Methyltransferase EZH2 Primes the Early Differentiation of Follicular Helper T Cells During Acute Viral Infection. *Cell. Mol. Immunol.* 17 (3), 247–260. doi: 10.1038/s41423-019-0219-z

Chen, X., Pan, Z., Yue, S., Yu, F., Zhang, J., Yang, Y., et al. (2020b). Disease Severity Dictates SARS-CoV-2-Specific Neutralizing Antibody Responses in COVID-19. *Signal Transduction Targeted Ther.* 5 (1), 180. doi: 10.1038/s41392-020-00301-9

Chi, H. (2012). Regulation and Function of mTOR Signalling in T Cell Fate Decisions. *Nat. Rev. Immunol.* 12 (5), 325–338. doi: 10.1038/nri3198

Choi, J., Diao, H., Faliti, C. E., Truong, J., Rossi, M., Bélanger, S., et al. (2020). Bcl-6 is the Nexus Transcription Factor of T Follicular Helper Cells *via* Repressor-of-Repressor Circuits. *Nat. Immunol.* 21 (7), 777–789. doi: 10.1038/s41590-020-0706-5

Choi, Y. S., Gullicksrud, J. A., Xing, S., Zeng, Z., Shan, Q., Li, F., et al. (2015). LEF-1 and TCF-1 Orchestrate T(FH) Differentiation by Regulating Differentiation Circuits Upstream of the Transcriptional Repressor Bcl6. *Nat. Immunol.* 16 (9), 980–990. doi: 10.1038/ni.3226

Choi, Y. S., Kageyama, R., Eto, D., Tania, C., Robert, J., Monticelli, L., et al. (2011). ICOS Receptor Instructs T Follicular Helper Cell Versus Effector Cell Differentiation *via* Induction of the Transcriptional Repressor Bcl6. *Immunity* 34 (6), 932–946. doi: 10.1016/j.immuni.2011.03.023

Choi, Y. S., Yang, J. A., Yusuf, I., Johnston, R. J., Greenbaum, J., Peters, B., et al. (2013). Bcl6 Expressing Follicular Helper CD4 T Cells are Fate Committed Early and Have the Capacity to Form Memory. *J. Immunol. (Baltimore Md. 1950)* 190 (8), 4014–4026. doi: 10.4049/jimmunol.1202963

Chtanova, T., Tangye, S. G., Newton, R., Frank, N., Hodge, M. R., Rolph, M. S., et al. (2004). T Follicular Helper Cells Express a Distinctive Transcriptional Profile, Reflecting Their Role as Non-Th1/Th2 Effector Cells That Provide Help for B Cells. *J. Immunol.* 173 (1), 68. doi: 10.4049/jimmunol.173.1.68

Ciucci, T., Vacchio, M. S., Gao, Y., Tomassoni Ardori, F., Candia, J., Mehta, M., et al. (2019). The Emergence and Functional Fitness of Memory CD4(+) T Cells Require the Transcription Factor Thpok. *Immunity* 50 (1), 91–105.e104. doi: 10.1016/j.immuni.2018.12.019

Crotty, S. (2011). Follicular Helper CD4 T Cells (TFH). *Annu. Rev. Immunol.* 29 (1), 621–663. doi: 10.1146/annurev-immunol-031210-101400

Crotty, S. (2014). T Follicular Helper Cell Differentiation, Function, and Roles in Disease. *Immunity* 41 (4), 529–542. doi: 10.1016/j.immuni.2014.10.004

Cui, C., Wang, J., Fagerberg, E., Chen, P.-M., Connolly, K. A., Damo, M., et al. (2021). Neoantigen-Driven B Cell and CD4 T Follicular Helper Cell Collaboration Promotes Anti-Tumor CD8 T Cell Responses. *Cell* 184 (25), 6101–6118.e6113. doi: 10.1016/j.cell.2021.11.007

Dahlgren, M. W., Gustafsson-Hedberg, T., Livingston, M., Cucak, H., Alsén, S., Yrlid, U., et al. (2015). T Follicular Helper, But Not Th1, Cell Differentiation in the Absence of Conventional Dendritic Cells. *J. Immunol.* 194 (11), 5187–5199. doi: 10.4049/jimmunol.1401938

Dan, J. M., Mateus, J., Kato, Y., Hastie, K. M., Yu, E. D., Faliti, C. E., et al. (2021). Immunological Memory to SARS-CoV-2 Assessed for Up to 8 Months After Infection. *Sci. (New York N.Y.)* 371 (6529), eabf4063. doi: 10.1126/science.abf4063

Das, A., Ranganathan, V., Umar, D., Thukral, S., George, A., Rath, S., et al. (2017). Effector/memory CD4 T Cells Making Either Th1 or Th2 Cytokines Commonly Co-Express T-Bet and GATA-3. *PloS One* 12 (10), e0185932–e0185932. doi: 10.1371/journal.pone.0185932

Deng, W., Bao, L., Liu, J., Xiao, C., Liu, J., Xue, J., et al. (2020). Primary Exposure to SARS-CoV-2 Protects Against Reinfection in Rhesus Macaques. *Sci. (New York N.Y.)* 369 (6505), 818–823. doi: 10.1126/science.abc5343

Di Niro, R., Lee, S.-J., Heiden, V., Jason, A., Rebecca, A., Trivedi, N., et al. (2015). Salmonella Infection Drives Promiscuous B Cell Activation Followed by Extrafollicular Affinity Maturation. *Immunity* 43 (1), 120–131. doi: 10.1016/j.immuni.2015.06.013

DiToro, D., Winstead Colleen, J., Pham, D., Witte, S., Andargachew, R., Singer Jeffrey, R., et al. (2018). Differential IL-2 Expression Defines Developmental Fates of Follicular Versus Nonfollicular Helper T Cells. *Science* 361 (6407), eaao2933. doi: 10.1126/science.aao2933

Elgueta, R., Benson, M. J., De Vries, V. C., Wasiuk, A., Guo, Y., and Noelle, R. J. (2009). Molecular Mechanism and Function of CD40/CD40L Engagement in the Immune System. *Immunol. Rev.* 229 (1), 152–172. doi: 10.1111/j.1600-065X.2009.00782.x

Eto, D., Lao, C., DiToro, D., Barnett, B., Escobar, T. C., Kageyama, R., et al. (2011). IL-21 and IL-6 are Critical for Different Aspects of B Cell Immunity and Redundantly Induce Optimal Follicular Helper CD4 T Cell (Tfh) Differentiation. *PloS One* 6 (3), e17739–e17739. doi: 10.1371/journal.pone.0017739

Fahey, L. M., Wilson, E. B., Elsaesser, H., Fistonich, C. D., McGavern, D. B., and Brooks, D. G. (2011). Viral Persistence Redirects CD4 T Cell Differentiation Toward T Follicular Helper Cells. *J. Exp. Med.* 208 (5), 987–999. doi: 10.1084/jem.20101773

Fazilleau, N., Eisenbraun, M. D., Malherbe, L., Ebright, J. N., Pogue-Caley, R. R., McHeyzer-Williams, L. J., et al. (2007). Lymphoid Reservoirs of Antigen-Specific Memory T Helper Cells. *Nat. Immunol.* 8 (7), 753–761. doi: 10.1038/ni1472

Fazilleau, N., McHeyzer-Williams, L. J., Rosen, H., and McHeyzer-Williams, M. G. (2009). The Function of Follicular Helper T Cells is Regulated by the Strength of T Cell Antigen Receptor Binding. *Nat. Immunol.* 10 (4), 375–384. doi: 10.1038/ni.1704

Fenoglio, D., Dentone, C., Parodi, A., Di Biagio, A., Bozzano, F., Vena, A., et al. (2021). Characterization of T Lymphocytes in Severe COVID-19 Patients. *J. Med. Virol.* 93 (9), 5608–5613. doi: 10.1002/jmv.27037

Fu, G., Guy, C. S., Chapman, N. M., Palacios, G., Wei, J., Zhou, P., et al. (2021). Metabolic Control of TFH Cells and Humoral Immunity by Phosphatidylethanolamine. *Nature* 595 (7869), 724–729. doi: 10.1038/s41586-021-03692-z

Gao, L., Zhou, J., Yang, S., Wang, L., Chen, X., Yang, Y., et al. (2021). The Dichotomous and Incomplete Adaptive Immunity in COVID-19 Patients With Different Disease Severity. *Signal Transduction Targeted Ther.* 6 (1), 113. doi: 10.1038/s41392-021-00525-3

Garaud, S., Dieu-Nosjean, M.-C., and Willard-Gallo, K. (2022). T Follicular Helper and B Cell Crosstalk in Tertiary Lymphoid Structures and Cancer Immunotherapy. *Nat. Commun.* 13 (1), 2259. doi: 10.1038/s41467-022-29753-z

Gaspal, F. M. C., Kim, M.-Y., McConnell, F. M., Raykundalia, C., Bekiaris, V., and Lane, P. J. L. (2005). Mice Deficient in OX40 and CD30 Signals Lack Memory Antibody Responses Because of Deficient CD4 T Cell Memory. *J. Immunol.* 174 (7), 3891–3896. doi: 10.4049/jimmunol.174.7.3891

Gigoux, M., Shang, J., Pak, Y., Xu, M., Choe, J., Mak Tak, W., et al. (2009). Inducible Costimulator Promotes Helper T-Cell Differentiation Through Phosphoinositide 3-Kinase. *Proc. Natl. Acad. Sci.* 106 (48), 20371–20376. doi: 10.1073/pnas.0911573106

Goenka, R., Barnett, L. G., Silver, J. S., O'Neill, P. J., Hunter, C. A., Cancro, M. P., et al. (2011). Cutting Edge: Dendritic Cell-Restricted Antigen Presentation Initiates the Follicular Helper T Cell Program But Cannot Complete Ultimate Effector Differentiation. *J. Immunol.* 187 (3), 1091. doi: 10.4049/jimmunol.1100853

Gong, F., Dai, Y., Zheng, T., Cheng, L., Zhao, D., Wang, H., et al. (2020). Peripheral CD4+ T Cell Subsets and Antibody Response in COVID-19 Convalescent Individuals. *J. Clin. Invest.* 130 (12), 6588–6599. doi: 10.1172/JCI141054

Grifoni, A., Weiskopf, D., Ramirez, S. I., Mateus, J., Dan, J. M., Moderbacher, C. R., et al. (2020). Targets of T Cell Responses to SARS-CoV-2 Coronavirus in Humans With COVID-19 Disease and Unexposed Individuals. *Cell* 181 (7), 1489–1501.e1415. doi: 10.1016/j.cell.2020.05.015

Grigoryan, L., and Pulendran, B. (2020). The Immunology of SARS-CoV-2 Infections and Vaccines. *Semin. Immunol.* 50, 101422–101422. doi: 10.1016/j.smim.2020.101422

Gudbjartsson, D. F., Norddahl, G. L., Melsted, P., Gunnarsdottir, K., Holm, H., Eythorsson, E., et al. (2020). Humoral Immune Response to SARS-CoV-2 in Iceland. *New Engl. J. Med.* 383 (18), 1724–1734. doi: 10.1056/NEJMoa2026116

Gupta, A., Gonzalez-Rojas, Y., Juarez, E., Crespo Casal, M., Moya, J., Falci, D. R., et al. (2021). Early Treatment for Covid-19 With SARS-CoV-2 Neutralizing Antibody Sotrovimab. *New Engl. J. Med.* 385 (21), 1941–1950. doi: 10.1056/NEJMoa2107934

Hale, J. S., and Ahmed, R. (2015). Memory T Follicular Helper CD4 T Cells. *Front. Immunol.* 6. doi: 10.3389/fimmu.2015.00016

Hale, J. S., Youngblood, B., Latner, D. R., Mohammed, A. U. R., Ye, L., Akondy, R. S., et al. (2013). Distinct Memory CD4+ T Cells With Commitment to T Follicular Helper- and T Helper 1-Cell Lineages are Generated After Acute Viral Infection. *Immunity* 38 (4), 805–817. doi: 10.1016/j.immuni.2013.02.020

Hao, Y., Wang, Y., Liu, X., Yang, X., Wang, P., Tian, Q., et al. (2018). The Kinase Complex mTOR Complex 2 Promotes the Follicular Migration and Functional Maturation of Differentiated Follicular Helper CD4(+) T Cells During Viral Infection. *Front. Immunol.* 9. doi: 10.3389/fimmu.2018.01127

Harker James, A., Lewis Gavin, M., Mack, L., and Zuniga Elina, I. (2011). Late Interleukin-6 Escalates T Follicular Helper Cell Responses and Controls a Chronic Viral Infection. *Science* 334 (6057), 825–829. doi: 10.1126/science.1208421

Hatzi, K., Nance, J. P., Kroenke, M. A., Bothwell, M., Haddad, E. K., Melnick, A., et al. (2015). BCL6 Orchestrates Tfh Cell Differentiation *via* Multiple Distinct Mechanisms. *J. Exp. Med.* 212 (4), 539–553. doi: 10.1084/jem.20141380

He, L., Gu, W., Wang, M., Chang, X., Sun, X., Zhang, Y., et al. (2018). Extracellular Matrix Protein 1 Promotes Follicular Helper T Cell Differentiation and Antibody Production. *Proc. Natl. Acad. Sci. U States America* 115 (34), 8621–8626. doi: 10.1073/pnas.1801196115

He, J., Louis, M., Yew, A., Hu, X., Cindy, S., Chevalier, N., et al. (2013). Circulating Precursor CCR7loPD-1hi CXCR5+ CD4+ T Cells Indicate Tfh Cell Activity and Promote Antibody Responses Upon Antigen Reexposure. *Immunity* 39 (4), 770–781. doi: 10.1016/j.immuni.2013.09.007

Homann, D., Teyton, L., and Oldstone, M. B. A. (2001). Differential Regulation of Antiviral T-Cell Immunity Results in Stable CD8+ But Declining CD4+ T-Cell Memory. *Nat. Med.* 7 (8), 913–919. doi: 10.1038/90950

Huang, Q., Hu, J., Tang, J., Xu, L., and Ye, L. (2019). Molecular Basis of the Differentiation and Function of Virus Specific Follicular Helper CD4+ T Cells. *Front. Immunol.* 10. doi: 10.3389/fimmu.2019.00249

Huang, H., Long, L., Zhou, P., Chapman, N. M., and Chi, H. (2020). mTOR Signaling at the Crossroads of Environmental Signals and T-Cell Fate Decisions. *Immunol. Rev.* 295 (1), 15–38. doi: 10.1111/imr.12845

Huber, M., and Lohoff, M. (2014). IRF4 at the Crossroads of Effector T-Cell Fate Decision. *Eur. J. Immunol.* 44 (7), 1886–1895. doi: 10.1002/eji.201344279

Hu, R., Kagele, D. A., Huffaker, T. B., Runtsch, M. C., Alexander, M., Liu, J., et al. (2014). miR-155 Promotes T Follicular Helper Cell Accumulation During Chronic, Low-Grade Inflammation. *Immunity* 41 (4), 605–619. doi: 10.1016/j.immuni.2014.09.015

Ise, W., Inoue, T., McLachlan James, B., Kometani, K., Kubo, M., Okada, T., et al. (2014). Memory B Cells Contribute to Rapid Bcl6 Expression by Memory Follicular Helper T Cells. *Proc. Natl. Acad. Sci.* 111 (32), 11792–11797. doi: 10.1073/pnas.1404671111

Iyer, S. S., Latner, D. R., Zilliox, M. J., McCausland, M., Akondy, R. S., Penaloza-Macmaster, P., et al. (2013). Identification of Novel Markers for Mouse CD4(+) T Follicular Helper Cells. *Eur. J. Immunol.* 43 (12), 3219–3232. doi: 10.1002/eji.201343469

Johnston, R. J., Choi, Y. S., Diamond, J. A., Yang, J. A., and Crotty, S. (2012). STAT5 is a Potent Negative Regulator of TFH Cell Differentiation. *J. Exp. Med.* 209 (2), 243–250. doi: 10.1084/jem.20111174

Johnston Robert, J., Poholek Amanda, C., DiToro, D., Yusuf, I., Eto, D., Barnett, B., et al. (2009). Bcl6 and Blimp-1 Are Reciprocal and Antagonistic Regulators of T Follicular Helper Cell Differentiation. *Science* 325 (5943), 1006–1010. doi: 10.1126/science.1175870

Josefowicz, S. Z. (2013). Regulators of Chromatin State and Transcription in CD4 T-Cell Polarization. *Immunology* 139 (3), 299–308. doi: 10.1111/imm.12115

Kaneko, N., Kuo, H.-H., Boucau, J., Farmer, J. R., Allard-Chamard, H., Mahajan, V. S., et al. (2020). Loss of Bcl-6-Expressing T Follicular Helper Cells and Germinal Centers in COVID-19. *Cell* 183 (1), 143–157.e113. doi: 10.1016/j.cell.2020.08.025

Karnowski, A., Chevrier, S., Belz, G. T., Mount, A., Emslie, D., D'Costa, K., et al. (2012). B and T Cells Collaborate in Antiviral Responses *via* IL-6, IL-21, and

Transcriptional Activator and Coactivator, Oct2 and OBF-1. *J. Exp. Med.* 209 (11), 2049–2064. doi: 10.1084/jem.20111504

Keck, S., Schmaler, M., Ganter, S., Wyss, L., Oberle, S., Huseby Eric, S., et al. (2014). Antigen Affinity and Antigen Dose Exert Distinct Influences on CD4 T-Cell Differentiation. *Proc. Natl. Acad. Sci.* 111 (41), 14852–14857. doi: 10.1073/pnas.1403271111

Kitano, M., Moriyama, S., Ando, Y., Hikida, M., Mori, Y., Kurosaki, T., et al. (2011). Bcl6 Protein Expression Shapes Pre-Germinal Center B Cell Dynamics and Follicular Helper T Cell Heterogeneity. *Immunity* 34 (6), 961–972. doi: 10.1016/j.immuni.2011.03.025

Kotov, D. I., Mitchell, J. S., Pengo, T., Ruedl, C., Way, S. S., Langlois, R. A., et al. (2019). TCR Affinity Biases Th Cell Differentiation by Regulating CD25, Eef1e1, and Gbp2. *J. Immunol.* 202 (9), 2535. doi: 10.4049/jimmunol.1801609

Kuchen, S., Robbins, R., Sims, G. P., Sheng, C., Phillips, T. M., Lipsky, P. E., et al. (2007). Essential Role of IL-21 in B Cell Activation, Expansion, and Plasma Cell Generation During $CD4^+$ T Cell-B Cell Collaboration. *J. Immunol.* 179 (9), 5886–5896. doi: 10.4049/jimmunol.179.9.5886

Kuen, D.-S., Park, M., Ryu, H., Choi, G., Moon, Y.-H., Kim, J.-O., et al. (2021). Critical Regulation of Follicular Helper T Cell Differentiation and Function by Gα13 Signaling. *Proc. Natl. Acad. Sci.* 118 (43), e2108376118. doi: 10.1073/pnas.2108376118

Künzli, M., Schreiner, D., Pereboom Tamara, C., Swarnalekha, N., Litzler Ludivine, C., Lötscher, J., et al. (2020). Long-Lived T Follicular Helper Cells Retain Plasticity and Help Sustain Humoral Immunity. *Sci. Immunol.* 5 (45), eaay5552. doi: 10.1126/sciimmunol.aay5552

Kurosaki, T., Kometani, K., and Ise, W. (2015). Memory B Cells. *Nat. Rev. Immunol.* 15 (3), 149–159. doi: 10.1038/nri3802

Laczkó, D., Hogan, M. J., Toulmin, S. A., Hicks, P., Lederer, K., Gaudette, B. T., et al. (2020). A Single Immunization With Nucleoside-Modified mRNA Vaccines Elicits Strong Cellular and Humoral Immune Responses Against SARS-CoV-2 in Mice. *Immunity* 53 (4), 724–732.e727. doi: 10.1016/j.immuni.2020.07.019

Lee, S. K., Rigby, R. J., Zotos, D., Tsai, L. M., Kawamoto, S., Marshall, J. L., et al. (2011). B Cell Priming for Extrafollicular Antibody Responses Requires Bcl-6 Expression by T Cells. *J. Exp. Med.* 208 (7), 1377–1388. doi: 10.1084/jem.20102065

Lee, J.-Y., Skon, C. N., Lee, Y. J., Oh, S., Taylor, J. J., Malhotra, D., et al. (2015). The Transcription Factor KLF2 Restrains $CD4^+$ T Follicular Helper Cell Differentiation. *Immunity* 42 (2), 252–264. doi: 10.1016/j.immuni.2015.01.013

Linterman, M. A., Beaton, L., Yu, D., Ramiscal, R. R., Srivastava, M., Hogan, J. J., et al. (2010). IL-21 Acts Directly on B Cells to Regulate Bcl-6 Expression and Germinal Center Responses. *J. Exp. Med.* 207 (2), 353–363. doi: 10.1084/jem.20091738

Linterman, M. A., Rigby, R. J., Wong, R., Silva, D., Withers, D., Anderson, G., et al. (2009). Roquin Differentiates the Specialized Functions of Duplicated T Cell Costimulatory Receptor Genes *Cd28* and *Icos*. *Immunity* 30 (2), 228–241. doi: 10.1016/j.immuni.2008.12.015

Lipsitch, M., Grad, Y. H., Sette, A., and Crotty, S. (2020). Cross-Reactive Memory T Cells and Herd Immunity to SARS-CoV-2. *Nat. Rev. Immunol.* 20 (11), 709–713. doi: 10.1038/s41577-020-00460-4

Liu, X., Chen, X., Zhong, B., Wang, A., Wang, X., Chu, F., et al. (2014). Transcription Factor Achaete-Scute Homologue 2 Initiates Follicular T-Helper-Cell Development. *Nature* 507 (7493), 513–518. doi: 10.1038/nature12910

Liu, D., Xu, H., Shih, C., Wan, Z., Ma, X., Ma, W., et al. (2015). T–B-Cell Entanglement and ICOSL-Driven Feed-Forward Regulation of Germinal Centre Reaction. *Nature* 517 (7533), 214–218. doi: 10.1038/nature13803

Li, J.-X., Wu, S.-P., Guo, X.-L., Tang, R., Huang, B.-Y., Chen, X.-Q., et al. (2022). Safety and Immunogenicity of Heterologous Boost Immunisation With an Orally Administered Aerosolised Ad5-Ncov After Two-Dose Priming With an Inactivated SARS-CoV-2 Vaccine in Chinese Adults: A Randomised, Open-Label, Single-Centre Trial. *Lancet Respir. Med.* S2213-2600 (22), 00087-X. doi: 10.1016/S2213-2600(22)00087-X

Li, F., Zeng, Z., Xing, S., Gullicksrud, J. A., Shan, Q., Choi, J., et al. (2018). Ezh2 Programs T(FH) Differentiation by Integrating Phosphorylation-Dependent Activation of Bcl6 and Polycomb-Dependent Repression of p19Arf. *Nat. Commun.* 9 (1), 5452–5452. doi: 10.1038/s41467-018-07853-z

Locci, M., Havenar-Daughton, C., Landais, E., Wu, J., Kroenke, M. A., Arlehamn, C. L., et al. (2013). Human Circulating PD-1+CXCR3-CXCR5+ Memory Tfh Cells are Highly Functional and Correlate With Broadly Neutralizing HIV Antibody Responses. *Immunity* 39 (4), 758–769. doi: 10.1016/j.immuni.2013.08.031

Long, X., Zhang, L., Zhang, Y., Min, M., Lin, B., Chen, J., et al. (2020). Histone Methyltransferase Nsd2 is Required for Follicular Helper T Cell Differentiation. *J. Exp. Med.* 217 (1), e20190832. doi: 10.1084/jem.20190832

Lu, K. T., Kanno, Y., Jennifer, L., Handon, R., Bible, P., Abdel, G., et al. (2011). Functional and Epigenetic Studies Reveal Multistep Differentiation and Plasticity of In Vitro-Generated and In Vivo-Derived Follicular T Helper Cells. *Immunity* 35 (4), 622–632. doi: 10.1016/j.immuni.2011.07.015

Lüthje, K., Kallies, A., Shimohakamada, Y., Belz, G. T., Light, A., Tarlinton, D. M., et al. (2012). The Development and Fate of Follicular Helper T Cells Defined by an IL-21 Reporter Mouse. *Nat. Immunol.* 13 (5), 491–498. doi: 10.1038/ni.2261

MacIver, N. J., Michalek, R. D., and Rathmell, J. C. (2013). Metabolic Regulation of T Lymphocytes. *Annu. Rev. Immunol.* 31, 259–283. doi: 10.1146/annurev-immunol-032712-095956

MacLeod, M. K. L., Clambey, E. T., Kappler, J. W., and Marrack, P. (2009). CD4 Memory T Cells: What are They and What can They do? *Semin. Immunol.* 21 (2), 53–61. doi: 10.1016/j.smim.2009.02.006

MacLeod, M. K. L., David, A., McKee, A. S., Crawford, F., Kappler, J. W., and Marrack, P. (2011). Memory CD4 T Cells That Express CXCR5 Provide Accelerated Help to B Cells. *J. Immunol. (Baltimore Md. 1950)* 186 (5), 2889–2896. doi: 10.4049/jimmunol.1002955

Ma, C. S., Suryani, S., Avery, D. T., Chan, A., Nanan, R., Santner-Nanan, B., et al. (2009). Early Commitment of Naïve Human CD4(+) T Cells to the T Follicular Helper (T(FH)) Cell Lineage is Induced by IL-12. *Immunol. Cell Biol.* 87 (8), 590–600. doi: 10.1038/icb.2009.64

Mateus, J., Dan, J. M., Zhang, Z., Rydyznski Moderbacher, C., Lammers, M., Goodwin, B., et al. (2021). Low-Dose mRNA-1273 COVID-19 Vaccine Generates Durable Memory Enhanced by Cross-Reactive T Cells. *Sci. (New York N.Y.)* 374 (6566), eabj9853–eabj9853. doi: 10.1126/science.abj9853

Mathew, R., Mao, A., Chiang, A. H., Bertozzi-Villa, C., Bunker, J. J., Scanlon, S. T., et al. (2014). A Negative Feedback Loop Mediated by the Bcl6–cullin 3 Complex Limits Tfh Cell Differentiation. *J. Exp. Med.* 211 (6), 1137–1151. doi: 10.1084/jem.20132267

Meckiff, B. J., Ramírez-Suástegui, C., Fajardo, V., Chee, S. J., Kusnadi, A., Simon, H., et al. (2020). Imbalance of Regulatory and Cytotoxic SARS-CoV-2-Reactive CD4+ T Cells in COVID-19. *Cell* 183 (5), 1340–1353.e1316. doi: 10.1016/j.cell.2020.10.001

Misawa, T., SoRelle, J. A., Choi, J. H., Yue, T., Wang, K.-W., McAlpine, W., et al. (2020). Mutual Inhibition Between Prkd2 and Bcl6 Controls T Follicular Helper Cell Differentiation. *Sci. Immunol.* 5 (43), eaaz0085. doi: 10.1126/sciimmunol.aaz0085

Morita, R., Schmitt, N., Bentebibel, S.-E., Ranganathan, R., Bourdery, L., Zurawski, G., et al. (2011). Human Blood CXCR5+CD4+ T Cells Are Counterparts of T Follicular Cells and Contain Specific Subsets That Differentially Support Antibody Secretion. *Immunity* 34 (1), 108–121. doi: 10.1016/j.immuni.2010.12.012

Mudd, P. A., Minervina, A. A., Pogorelyy, M. V., Turner, J. S., Kim, W., Kalaidina, E., et al. (2022). SARS-CoV-2 mRNA Vaccination Elicits a Robust and Persistent T Follicular Helper Cell Response in Humans. *Cell* 185 (4), 603–613.e615. doi: 10.1016/j.cell.2021.12.026

Nanduri, S., Pilishvili, T., Derado, G., Soe, M. M., Dollard, P., Wu, H., et al. (2021). Effectiveness of Pfizer-BioNTech and Moderna Vaccines in Preventing SARS-CoV-2 Infection Among Nursing Home Residents Before and During Widespread Circulation of the SARS-CoV-2 B.1.617.2 (Delta) Variant - National Healthcare Safety Network, March 1-August 1, 2021. *MMWR. Morbid mortal weekly Rep.* 70 (34), 1163–1166. doi: 10.15585/mmwr.mm7034e3

Naranbhai, V., Nathan, A., Kaseke, C., Berrios, C., Khatri, A., Choi, S., et al. (2022). T Cell Reactivity to the SARS-CoV-2 Omicron Variant is Preserved in Most But Not All Individuals. *Cell* 185 (6), 1041–1051.e1046. doi: 10.1016/j.cell.2022.01.029

Narowski, T. M., Raphel, K., Adams, L. E., Huang, J., Vielot, N. A., Jadi, R., et al. (2022). SARS-CoV-2 mRNA Vaccine Induces Robust Specific and Cross-Reactive IgG and Unequal Neutralizing Antibodies in Naive and Previously

Infected People. *Cell Rep.* 38 (5), 110336–110336. doi: 10.1016/j.celrep.2022.110336

Nurieva, R. I., Chung, Y., Hwang, D., Yang, X. O., Kang, H. S., Ma, L., et al. (2008). Generation of T Follicular Helper Cells Is Mediated by Interleukin-21 But Independent of T Helper 1, 2, or 17 Cell Lineages. *Immunity* 29 (1), 138–149. doi: 10.1016/j.immuni.2008.05.009

Nurieva Roza, I., Chung, Y., Martinez Gustavo, J., Yang Xuexian, O., Tanaka, S., Matskevitch Tatyana, D., et al. (2009). Bcl6 Mediates the Development of T Follicular Helper Cells. *Science* 325 (5943), 1001–1005. doi: 10.1126/science.1176676

Ogbe, A., Miao, T., Symonds, A. L. J., Omodho, B., Singh, R., Bhullar, P., et al. (2015). Early Growth Response Genes 2 and 3 Regulate the Expression of *Bcl6* and Differentiation of T Follicular Helper Cells *. *J. Biol. Chem.* 290 (33), 20455–20465. doi: 10.1074/jbc.M114.634816

Oja, A. E., Saris, A., Ghandour, C. A., Kragten, N. A. M., Hogema, B. M., Nossent, E. J., et al. (2020). Divergent SARS-CoV-2-Specific T- and B-Cell Responses in Severe But Not Mild COVID-19 Patients. *Eur. J. Immunol.* 50 (12), 1998–2012. doi: 10.1002/eji.202048908

O'Shea John, J., and Paul William, E. (2010). Mechanisms Underlying Lineage Commitment and Plasticity of Helper CD4+ T Cells. *Science* 327 (5969), 1098–1102. doi: 10.1126/science.1178334

Painter, M. M., Mathew, D., Goel, R. R., Apostolidis, S. A., Pattekar, A., Kuthuru, O., et al. (2021). Rapid Induction of Antigen-Specific CD4+ T Cells is Associated With Coordinated Humoral and Cellular Immunity to SARS-CoV-2 mRNA Vaccination. *Immunity* 54 (9), 2133–2142.e2133. doi: 10.1016/j.immuni.2021.08.001

Pawlak, M., Ho, A. W., and Kuchroo, V. K. (2020). Cytokines and Transcription Factors in the Differentiation of CD4+ T Helper Cell Subsets and Induction of Tissue Inflammation and Autoimmunity. *Curr. Opin. Immunol.* 67, 57–67. doi: 10.1016/j.coi.2020.09.001

Peng, Y., Mentzer, A. J., Liu, G., Yao, X., Yin, Z., Dong, D., et al. (2020). Broad and Strong Memory CD4(+) and CD8(+) T Cells Induced by SARS-CoV-2 in UK Convalescent Individuals Following COVID-19. *Nat. Immunol.* 21 (11), 1336–1345. doi: 10.1038/s41590-020-0782-6

Pepper, M., Pagán, Antonio, J., Igyártó, Botond, Z., Taylor, Justin, J., and Jenkins, Marc, K. (2011). Opposing Signals From the Bcl6 Transcription Factor and the Interleukin-2 Receptor Generate T Helper 1 Central and Effector Memory Cells. *Immunity* 35 (4), 583–595. doi: 10.1016/j.immuni.2011.09.009

Phan, T. G., and Tangye, S. G. (2017). Memory B Cells: Total Recall. *Curr. Opin. Immunol.* 45, 132–140. doi: 10.1016/j.coi.2017.03.005

Picchianti-Diamanti, A., Aiello, A., Laganà, B., Agrati, C., Castilletti, C., Meschi, S., et al. (2021). ImmunosuppressiveTherapies Differently Modulate Humoral- and T-Cell-Specific Responses to COVID-19 mRNA Vaccine in Rheumatoid Arthritis Patients. *Front. Immunol.* 12. doi: 10.3389/fimmu.2021.740249

Pollizzi, K. N., Patel, C. H., Sun, I.-H., Oh, M.-H., Waickman, A. T., Wen, J., et al. (2015). Mtorc1 and Mtorc2 Selectively Regulate CD8$^+$ T Cell Differentiation. *J. Clin. Invest.* 125 (5), 2090–2108. doi: 10.1172/JCI77746

Post, N., Eddy, D., Huntley, C., van Schalkwyk, M. C. I., Shrotri, M., Leeman, D., et al. (2020). Antibody Response to SARS-CoV-2 Infection in Humans: A Systematic Review. *PloS One* 15 (12), e0244126–e0244126. doi: 10.1371/journal.pone.0244126

Pozzetto, B., Legros, V., Djebali, S., Barateau, V., and Trouillet-Assant, S. (2021). Immunogenicity and Efficacy of Heterologous ChadOx1/BNT162b2 Vaccination. *Nature* 600 (7890), 6. doi: 10.1038/s41586-021-04120-y

Pratama, A., Srivastava, M., Williams, N. J., Papa, I., Lee, S. K., Dinh, X. T., et al. (2015). MicroRNA-146a Regulates ICOS–ICOSL Signalling to Limit Accumulation of T Follicular Helper Cells and Germinal Centres. *Nat. Commun.* 6 (1), 6436. doi: 10.1038/ncomms7436

Pruner, K. B., and Pepper, M. (2021). Local Memory CD4 T Cell Niches in Respiratory Viral Infection. *J. Exp. Med.* 218 (8), e20201733. doi: 10.1084/jem.20201733

Qi, H., Cannons, J. L., Klauschen, F., Schwartzberg, P. L., and Germain, R. N. (2008). SAP-Controlled T-B Cell Interactions Underlie Germinal Centre Formation. *Nature* 455 (7214), 764–769. doi: 10.1038/nature07345

Ray, J. P., Staron, Matthew, M., Shyer, Justin, A., Ho, P.-C., Marshall, Heather, D., Simon, M., et al. (2015). The Interleukin-2-Mtorc1 Kinase Axis Defines the Signaling, Differentiation, and Metabolism of T Helper 1 and Follicular B Helper T Cells. *Immunity* 43 (4), 690–702. doi: 10.1016/j.immuni.2015.08.017

Riou, C., du Bruyn, E., Stek, C., Daroowala, R., Goliath, R. T., Abrahams, F., et al. (2021). Relationship of SARS-CoV-2-Specific CD4 Response to COVID-19 Severity and Impact of HIV-1 and Tuberculosis Coinfection. *J. Clin. Invest.* 131 (12), e149125. doi: 10.1172/JCI149125

Robbiani, D. F., Gaebler, C., Muecksch, F., Lorenzi, J. C. C., Wang, Z., Cho, A., et al. (2020). Convergent Antibody Responses to SARS-CoV-2 in Convalescent Individuals. *Nature* 584 (7821), 437–442. doi: 10.1038/s41586-020-2456-9

Rolf, J., Bell, S. E., Kovesdi, D., Janas, M. L., Soond, D. R., Webb, L. M. C., et al. (2010). Phosphoinositide 3-Kinase Activity in T Cells Regulates the Magnitude of the Germinal Center Reaction. *J. Immunol.* 185 (7), 4042. doi: 10.4049/jimmunol.1001730

Röltgen, K., Powell, A. E., Wirz, O. F., Stevens, B. A., Hogan, C. A., Najeeb, J., et al. (2020). Defining the Features and Duration of Antibody Responses to SARS-CoV-2 Infection Associated With Disease Severity and Outcome. *Sci. Immunol.* 5 (54), eabe0240. doi: 10.1126/sciimmunol.abe0240

Rosenberg, E. S., Holtgrave, D., Dorabawila, V., et al. (2021). New COVID-19 Cases and Hospitalizations Among Adults, by Vaccination Status_New York, May 3-July 25. *MMWR Morb Mortal Wkly Rep.* 2021 (70), 6. doi: 10.15585/mmwr.mm7037a7

Salomé, B., and Horowitz, A. (2021). Impaired CD4 T-Cell Response to SARS-CoV-2: Rationale for PD-1 Blockade in Patients With Cancer and COVID-19? *Cancer Discovery* 11 (8), 1877–1878. doi: 10.1158/2159-8290.CD-21-0613

Schaerli, P., Willimann, K., Lang, A. B., Lipp, M., Loetscher, P., and Moser, B. (2000). Cxc Chemokine Receptor 5 Expression Defines Follicular Homing T Cells With B Cell Helper Function. *J. Exp. Med.* 192 (11), 1553–1562. doi: 10.1084/jem.192.11.1553

Schmitt, N., Liu, Y., Bentebibel, S.-E., Munagala, I., Bourdery, L., Venuprasad, K., et al. (2014). The Cytokine TGF-β Co-Opts Signaling *via* STAT3-STAT4 to Promote the Differentiation of Human TFH Cells. *Nat. Immunol.* 15 (9), 856–865. doi: 10.1038/ni.2947

Schmitt, N., Morita, R., Bourdery, L., Bentebibel, S. E., Zurawski, S. M., Banchereau, J., et al. (2009). Human Dendritic Cells Induce the Differentiation of Interleukin-21-Producing T Follicular Helper-Like Cells Through Interleukin-12. *Immunity* 31 (1), 158–169. doi: 10.1016/j.immuni.2009.04.016

Schroeder, A. R., Zhu, F., and Hu, H. (2021). Stepwise Tfh Cell Differentiation Revisited: New Advances and Long-Standing Questions. *Faculty Rev.* 10, 3. doi: 10.12703/r/10-3

Schultheiß, C., Paschold, L., Simnica, D., Mohme, M., Willscher, E., von Wenserski, L., et al. (2020). Next-Generation Sequencing of T and B Cell Receptor Repertoires From COVID-19 Patients Showed Signatures Associated With Severity of Disease. *Immunity* 53 (2), 442–455.e444. doi: 10.1016/j.immuni.2020.06.024

Seder, R. A., and Ahmed, R. (2003). Similarities and Differences in CD4+ and CD8+ Effector and Memory T Cell Generation. *Nat. Immunol.* 4 (9), 835–842. doi: 10.1038/ni969

Sette, A., and Crotty, S. (2021). Adaptive Immunity to SARS-CoV-2 and COVID-19. *Cell* 184 (4), 861–880. doi: 10.1016/j.cell.2021.01.007

Shaw, L. A., Bélanger, S., Omilusik, K. D., Cho, S., Scott-Browne, J. P., Nance, J. P., et al. (2016). Id2 Reinforces TH1 Differentiation and Inhibits E2A to Repress TFH Differentiation. *Nat. Immunol.* 17 (7), 834–843. doi: 10.1038/ni.3461

Shrotri, M., van Schalkwyk, M. C. I., Post, N., Eddy, D., Huntley, C., Leeman, D., et al. (2021). T Cell Response to SARS-CoV-2 Infection in Humans: A Systematic Review. *PloS One* 16 (1), e0245532–e0245532. doi: 10.1371/journal.pone.0245532

Shulman, Z., Gitlin, A. D., Targ, S., Jankovic, M., Pasqual, G., Nussenzweig, M. C., et al. (2013). T Follicular Helper Cell Dynamics in Germinal Centers. *Science* 341 (6146), 673–677. doi: 10.1126/science.1241680

Snook Jeremy, P., Kim, C., and Williams Matthew, A. (2018). TCR Signal Strength Controls the Differentiation of CD4+ Effector and Memory T Cells. *Sci. Immunol.* 3 (25), eaas9103. doi: 10.1126/sciimmunol.aas9103

Sokal, A., Broketa, M., Barba-Spaeth, G., Meola, A., Fernández, I., Fourati, S., et al. (2022). Analysis of mRNA Vaccination-Elicited RBD-Specific Memory B Cells Reveals Strong But Incomplete Immune Escape of the SARS-CoV-2 Omicron Variant. *Immunity*. 55 (6), 1096–1104 doi: 10.1016/j.immuni.2022.04.002

Song, N., Sengupta, S., Khoruzhenko, S., Welsh, R. A., Kim, A., Kumar, M. R., et al. (2020). Multiple Genetic Programs Contribute to CD4 T Cell Memory

Differentiation and Longevity by Maintaining T Cell Quiescence. *Cell. Immunol.* 357, 104210. doi: 10.1016/j.cellimm.2020.104210

Song, S., Zhou, B., Cheng, L., Liu, W., Fan, Q., Ge, X., et al. (2022). Sequential Immunization With SARS-CoV-2 RBD Vaccine Induces Potent and Broad Neutralization Against Variants in Mice. *Virol. J.* 19 (1), 2–2. doi: 10.1186/s12985-021-01737-3

Son Young, M., Cheon In, S., Wu, Y., Li, C., Wang, Z., Gao, X., et al. (2021). Tissue-Resident CD4+ T Helper Cells Assist the Development of Protective Respiratory B and CD8+ T Cell Memory Responses. *Sci. Immunol.* 6 (55), eabb6852. doi: 10.1126/sciimmunol.abb6852

Stone, E. L., Pepper, M., Katayama, C. D., Kerdiles, Y. M., Lai, C.-Y., Emslie, E., et al. (2015). ICOS Coreceptor Signaling Inactivates the Transcription Factor FOXO1 to Promote Tfh Cell Differentiation. *Immunity* 42 (2), 239–251. doi: 10.1016/j.immuni.2015.01.017

Sun, Z., Yao, Y., You, M., Liu, J., Guo, W., Qi, Z., et al. (2021). The Kinase PDK1 is Critical for Promoting T Follicular Helper Cell Differentiation. *eLife* 10, e61406. doi: 10.7554/eLife.61406

Sweet, R. A., Lee, S. K., and Vinuesa, C. G. (2012). Developing Connections Amongst Key Cytokines and Dysregulated Germinal Centers in Autoimmunity. *Curr. Opin. Immunol.* 24 (6), 658–664. doi: 10.1016/j.coi.2012.10.003

Tan, H.-X., Esterbauer, R., Vanderven, H. A., Juno, J. A., Kent, S. J., and Wheatley, A. K. (2019). Inducible Bronchus-Associated Lymphoid Tissues (iBALT) Serve as Sites of B Cell Selection and Maturation Following Influenza Infection in Mice. *Front. Immunol.* 10. doi: 10.3389/fimmu.2019.00611

Tan, A. H.-M., Wong, S.-C., and Lam, K.-P. (2006). Regulation of Mouse Inducible Costimulator (ICOS) Expression by Fyn-NFATc2 and ERK Signaling in T Cells *. *J. Biol. Chem.* 281 (39), 28666–28678. doi: 10.1074/jbc.M604081200

Tenforde, M. W., Self, W. H., Naioti, E. A., Ginde, A. A., Douin, D. J., Olson, S. M., et al. (2021). Sustained Effectiveness of Pfizer-BioNTech and Moderna Vaccines Against COVID-19 Associated Hospitalizations Among Adults - United States, March-July 2021. *MMWR. Morbid mortal weekly Rep.* 70 (34), 1156–1162. doi: 10.15585/mmwr.mm7034e2

Thakur, V., Bhola, S., Thakur, P., Patel, S. K. S., Kulshrestha, S., Ratho, R. K., et al. (2022). Waves and Variants of SARS-CoV-2: Understanding the Causes and Effect of the COVID-19 Catastrophe. *Infection* 50 (2), 309–325. doi: 10.1007/s15010-021-01734-2

Tian, Y., and Zajac, A. J. (2016). IL-21 and T Cell Differentiation: Consider the Context. *Trends Immunol.* 37 (8), 557–568. doi: 10.1016/j.it.2016.06.001

Tsai, L. M., and Yu, D. (2014). Follicular Helper T-Cell Memory: Establishing New Frontiers During Antibody Response. *Immunol. Cell Biol.* 92 (1), 57–63. doi: 10.1038/icb.2013.68

Tubo, N. J., Pagán, A. J., Taylor, J. J., Nelson, R. W., Linehan, J. L., Ertelt, J. M., et al. (2013). Single Naive CD4+ T Cells From a Diverse Repertoire Produce Different Effector Cell Types During Infection. *Cell* 153 (4), 785–796. doi: 10.1016/j.cell.2013.04.007

Umar, D., Das, A., Gupta, S., Chattopadhyay, S., Sarkar, D., Mirji, G., et al. (2020). Febrile Temperature Change Modulates CD4 T Cell Differentiation *via* a TRPV Channel-Regulated Notch-Dependent Pathway. *Proc. Natl. Acad. Sci.* 117 (36), 22357–22366. doi: 10.1073/pnas.1922683117

V'Kovski, P., Kratzel, A., Steiner, S., Stalder, H., and Thiel, V. (2021). Coronavirus Biology and Replication: Implications for SARS-CoV-2. *Nat. Rev. Microbiol.* 19 (3), 155–170. doi: 10.1038/s41579-020-00468-6

Vacchio, M. S., Ciucci, T., Gao, Y., Watanabe, M., Balmaceno-Criss, M., McGinty, M. T., et al. (2019). A Thpok-Directed Transcriptional Circuitry Promotes Bcl6 and Maf Expression to Orchestrate T Follicular Helper Differentiation. *Immunity* 51 (3), 465–478.e466. doi: 10.1016/j.immuni.2019.06.023

Vella, L. A., Herati, R. S., and Wherry, E. J. (2017). CD4+ T Cell Differentiation in Chronic Viral Infections: The Tfh Perspective. *Trends Mol. Med.* 23 (12), 1072–1087. doi: 10.1016/j.molmed.2017.10.001

Victora, G. D., and Nussenzweig, M. C. (2012). Germinal Centers. *Annu. Rev. Immunol.* 30 (1), 429–457. doi: 10.1146/annurev-immunol-020711-075032

Vinuesa, C. G., Cook, M. C., Angelucci, C., Athanasopoulos, V., Rui, L., Hill, K. M., et al. (2005). A RING-Type Ubiquitin Ligase Family Member Required to Repress Follicular Helper T Cells and Autoimmunity. *Nature* 435 (7041), 452–458. doi: 10.1038/nature03555

Vinuesa, C. G., Linterman, M. A., Yu, D., and MacLennan, I. C. M. (2016). Follicular Helper T Cells. *Annu. Rev. Immunol.* 34 (1), 335–368. doi: 10.1146/annurev-immunol-041015-055605

Wang, X., Chen, X., Tan, J., Yue, S., Zhou, R., Xu, Y., et al. (2022a). 35B5 Antibody Potently Neutralizes SARS-CoV-2 Omicron by Disrupting the N-Glycan Switch *via* a Conserved Spike Epitope. *Cell Host Microbe* S1931-3128 (1922), 00165–2. doi: 10.1016/j.chom.2022.03.035

Wang, H., Geng, J., Wen, X., Bi, E., Kossenkov, A. V., Wolf, A. I., et al. (2014). The Transcription Factor Foxp1 is a Critical Negative Regulator of the Differentiation of Follicular Helper T Cells. *Nat. Immunol.* 15 (7), 667–675. doi: 10.1038/ni.2890

Wang, F., Hou, H., Luo, Y., Tang, G., Wu, S., Huang, M., et al. (2020). The Laboratory Tests and Host Immunity of COVID-19 Patients With Different Severity of Illness. *JCI Insight* 5 (10), e137799. doi: 10.1172/jci.insight.137799

Wang, X., Hu, A., Chen, X., Zhang, Y., Yu, F., Yue, S., et al. (2022b). A Potent Human Monoclonal Antibody With Pan-Neutralizing Activities Directly Dislocates S Trimer of SARS-CoV-2 Through Binding Both Up and Down Forms of RBD. *Signal transduction targeted Ther.* 7 (1), 114–114. doi: 10.1038/s41392-022-00954-8

Wang, H., Li, X., Kajikawa, T., Shin, J., Lim, J.-H., Kourtzelis, I., et al. (2021). Stromal Cell-Derived DEL-1 Inhibits Tfh Cell Activation and Inflammatory Arthritis. *J. Clin. Invest.* 131 (19), e150578. doi: 10.1172/JCI150578

Wang, Y., Shi, J., Yan, J., Xiao, Z., Hou, X., Lu, P., et al. (2017). Germinal-Center Development of Memory B Cells Driven by IL-9 From Follicular Helper T Cells. *Nat. Immunol.* 18 (8), 921–930. doi: 10.1038/ni.3788

Wang, Y., Tian, Q., Hao, Y., Yao, W., Lu, J., Chen, C., et al. (2022c). The Kinase Complex Mtorc2 Promotes the Longevity of Virus-Specific Memory CD4+ T Cells by Preventing Ferroptosis. *Nat. Immunol.* 23 (2), 303–317. doi: 10.1038/s41590-021-01090-1

Watanabe, M., Takagi, Y., Kotani, M., Hara, Y., Inamine, A., Hayashi, K., et al. (2008). Down-Regulation of ICOS Ligand by Interaction With ICOS Functions as a Regulatory Mechanism for Immune Responses. *J. Immunol. (Baltimore Md. 1950)* 180 (8), 5222–5234. doi: 10.4049/jimmunol.180.8.5222

Weber, J. P., Fuhrmann, F., Feist, R. K., Lahmann, A., Al Baz, M. S., Gentz, L.-J., et al. (2015). ICOS Maintains the T Follicular Helper Cell Phenotype by Down-Regulating Krüppel-Like Factor 2. *J. Exp. Med.* 212 (2), 217–233. doi: 10.1084/jem.20141432

Weber, J. P., Fuhrmann, F., and Hutloff, A. (2012). T-Follicular Helper Cells Survive as Long-Term Memory Cells. *Eur. J. Immunol.* 42 (8), 1981–1988. doi: 10.1002/eji.201242540

Wilson, C. B., Rowell, E., and Sekimata, M. (2009). Epigenetic Control of T-Helper-Cell Differentiation. *Nat. Rev. Immunol.* 9 (2), 91–105. doi: 10.1038/nri2487

Woldemeskel, B. A., Garliss, C. C., Aytenfisu, T. Y., Johnston, T. S., Beck, E. J., Dykema, A. G., et al. (2022). SARS-CoV-2 -Specific Immune Responses in Boosted Vaccine Recipients With Breakthrough Infections During the Omicron Variant Surge. *JCI Insight.* 7 (10), e159474. doi: 10.1172/jci.insight.159474

Wu, T., Shin, H. M., Moseman, E. A., Ji, Y., Huang, B., Harly, C., et al. (2015). TCF1 Is Required for the T Follicular Helper Cell Response to Viral Infection. *Cell Rep.* 12 (12), 2099–2110. doi: 10.1016/j.celrep.2015.08.049

Xu, L., Cao, Y., Xie, Z., Huang, Q., Bai, Q., Yang, X., et al. (2015). The Transcription Factor TCF-1 Initiates the Differentiation of TFH Cells During Acute Viral Infection. *Nat. Immunol.* 16 (9), 991–999. doi: 10.1038/ni.3229

Xu, H., Li, X., Liu, D., Li, J., Zhang, X., Chen, X., et al. (2013). Follicular T-Helper Cell Recruitment Governed by Bystander B Cells and ICOS-Driven Motility. *Nature* 496 (7446), 523–527. doi: 10.1038/nature12058

Xu, W., Zhao, X., Wang, X., Feng, H., Gou, M., Jin, W., et al. (2019). The Transcription Factor Tox2 Drives T Follicular Helper Cell Development *via* Regulating Chromatin Accessibility. *Immunity* 51 (5), 826–839.e825. doi: 10.1016/j.immuni.2019.10.006

Yang, K., and Chi, H. (2012). mTOR and Metabolic Pathways in T Cell Quiescence and Functional Activation. *Semin. Immunol.* 24 (6), 421–428. doi: 10.1016/j.smim.2012.12.004

Yang, J., Lin, X., Pan, Y., Wang, J., Chen, P., Huang, H., et al. (2016). Critical Roles of mTOR Complex 1 and 2 for T Follicular Helper Cell Differentiation and Germinal Center Responses. *eLife* 5, e17936. doi: 10.7554/eLife.17936

Youngblood, B., Hale, J. S., and Ahmed, R. (2013). T-Cell Memory Differentiation: Insights From Transcriptional Signatures and Epigenetics. *Immunology* 139 (3), 277–284. doi: 10.1111/imm.12074

Yu, D., Rao, S., Tsai, L. M., Lee, S. K., He, Y., Sutcliffe, E. L., et al. (2009). The Transcriptional Repressor Bcl-6 Directs T Follicular Helper Cell Lineage Commitment. *Immunity* 31 (3), 457–468. doi: 10.1016/j.immuni.2009.07.002

Zander, R., Kasmani, M. Y., Chen, Y., Topchyan, P., Shen, J., Zheng, S., et al. (2022). Tfh-Cell-Derived Interleukin 21 Sustains Effector CD8+ T Cell Responses During Chronic Viral Infection. *Immunity* 55 (3), 475–493.e475. doi: 10.1016/j.immuni.2022.01.018

Zeng, H., Cohen, S., Guy, C., Shrestha, S., Neale, G., Brown, S. A., et al. (2016). Mtorc1 and Mtorc2 Kinase Signaling and Glucose Metabolism Drive Follicular Helper T Cell Differentiation. *Immunity* 45 (3), 540–554. doi: 10.1016/j.immuni.2016.08.017

Zhou, L., Chong, M. M. W., and Littman, D. R. (2009). Plasticity of CD4+ T Cell Lineage Differentiation. *Immunity* 30 (5), 646–655. doi: 10.1016/j.immuni.2009.05.001

Zhu, J., Yamane, H., and Paul, W. E. (2010). Differentiation of Effector CD4 T Cell Populations (*). *Annu. Rev. Immunol.* 28, 445–489. doi: 10.1146/annurev-immunol-030409-101212

Zotos, D., Coquet, J. M., Zhang, Y., Light, A., D'Costa, K., Kallies, A., et al. (2010). IL-21 Regulates Germinal Center B Cell Differentiation and Proliferation Through a B Cell–Intrinsic Mechanism. *J. Exp. Med.* 207 (2), 365–378. doi: 10.1084/jem.20091777

Zuo, F., Abolhassani, H., Du, L., Piralla, A., Bertoglio, F., de Campos-Mata, L., et al. (2022). Heterologous Immunization With Inactivated Vaccine Followed by mRNA-Booster Elicits Strong Immunity Against SARS-CoV-2 Omicron Variant. *Nat. Commun.* 13 (1), 2670–2670. doi: 10.1038/s41467-022-30340-5

Conflict of Interest: The authors declare that the research was conducted in the absence of any commercial or financial relationships that could be construed as a potential conflict of interest.

frontiers | Frontiers in Cellular and Infection Microbiology

TYPE Original Research
PUBLISHED 04 August 2022
DOI 10.3389/fcimb.2022.941888

EDITED BY
Rameez Raja,
Cleveland Clinic, United States

REVIEWED BY
Smriti Parashar,
University of California, San Diego,
United States
Payel Roy,
La Jolla Institute for Immunology (LJI),
United States

*CORRESPONDENCE
Nicolas Fasel
nicolas.fasel@unil.ch
Filipa Teixeira
filipa.teixeira@unil.ch

[†]These authors have contributed equally to this work and share first authorship

SPECIALTY SECTION
This article was submitted to Virus and Host, a section of the journal Frontiers in Cellular and Infection Microbiology

RECEIVED 11 May 2022
ACCEPTED 01 July 2022
PUBLISHED 04 August 2022

CITATION
Bekkar A, Isorce N, Snäkä T, Claudinot S, Desponds C, Kopelyanskiy D, Prével F, Reverte M, Xenarios I, Fasel N and Teixeira F (2022) Dissection of the macrophage response towards infection by the *Leishmania*-viral endosymbiont duo and dynamics of the type I interferon response. *Front. Cell. Infect. Microbiol.* 12:941888. doi: 10.3389/fcimb.2022.941888

Dissection of the macrophage response towards infection by the *Leishmania*-viral endosymbiont duo and dynamics of the type I interferon response

Amel Bekkar[1†], Nathalie Isorce[1†], Tiia Snäkä[1], Stéphanie Claudinot[1], Chantal Desponds[1], Dmitry Kopelyanskiy[1], Florence Prével[1], Marta Reverte[1], Ioannis Xenarios[2,3], Nicolas Fasel[1*] and Filipa Teixeira[1*]

[1]Department of Immunobiology, University of Lausanne, Epalinges, Switzerland, [2]Agora Center, Center Hospitalier Universitaire (CHUV), Lausanne, Switzerland, [3]Center for Integrative Genomics, University of Lausanne, Lausanne, Switzerland

Leishmania RNA virus 1 (LRV1) is a double-stranded RNA virus found in some strains of the human protozoan parasite *Leishmania*, the causative agent of leishmaniasis, a neglected tropical disease. Interestingly, the presence of LRV1 inside *Leishmania* constitutes an important virulence factor that worsens the leishmaniasis outcome in a type I interferon (IFN)–dependent manner and contributes to treatment failure. Understanding how macrophages respond toward *Leishmania* alone or in combination with LRV1 as well as the role that type I IFNs may play during infection is fundamental to oversee new therapeutic strategies. To dissect the macrophage response toward infection, RNA sequencing was performed on murine wild-type and *Ifnar*-deficient bone marrow–derived macrophages infected with *Leishmania guyanensis* (*Lgy*) devoid or not of LRV1. Additionally, macrophages were treated with poly I:C (mimetic virus) or with type I IFNs. By implementing a weighted gene correlation network analysis, the groups of genes (modules) with similar expression patterns, for example, functionally related, coregulated, or the members of the same functional pathway, were identified. These modules followed patterns dependent on *Leishmania*, LRV1, or *Leishmania* exacerbated by the presence of LRV1. Not only the visualization of how individual genes were embedded to form modules but also how different modules were related to each other were observed. Thus, in the context of the observed hyperinflammatory phenotype associated to the presence of LRV1, it was noted that the biomarkers tumor-necrosis factor α (TNF-α) and the interleukin 6 (IL-6) belonged to different modules and that their regulating specific Src-family kinases were segregated oppositely. In addition, this network approach revealed the strong and sustained effect of LRV1 on the macrophage response and genes that had an early, late, or sustained impact during infection, uncovering the dynamics of the IFN response. Overall, this study contributed to shed light and dissect the intricate macrophage response toward infection by the *Leishmania*-LRV1 duo and revealed the crosstalk between modules made of coregulated genes and provided a new resource that can be further explored to study the impact of *Leishmania* on the macrophage response.

KEYWORDS

***Leishmania* RNA virus 1 (LRV1), macrophage, RNA sequencing (RNA-Seq), type I interferon (IFN), weighted gene coexpression network analysis (WGCNA), interleukin 6 (IL-6), tumor-necrosis factor alpha (TNF-α)**

Introduction

Macrophages, one of the first-line defenders of our immune system, are implicated in many processes ranging from physiological to pathological. One of such processes includes the recognition and ultimately elimination of pathogens. In order to achieve that, macrophages employ a plethora of mechanisms such as oxidative burst, inflammation, or antigen presentation (Shapouri-Moghaddam et al., 2018; Rossi and Fasel, 2018a; Ferrari, 2019; Sheu and Hoffmann, 2022; Reverte et al., 2022). However, these responses are not always straightforward nor unidirectional as pathogens use different strategies to hijack the macrophage machinery and ultimately exploit it to their advantage. This is particularly true for intracellular pathogens such as *Leishmania* that have evolved over thousands of years to counteract the microbicidal power of macrophages (Gupta et al., 2013; Rossi and Fasel, 2018a; Reverte et al., 2022).

Leishmania are medically relevant protozoan parasites that cause leishmaniasis, a neglected tropical disease that can manifest depending on the infecting species and the immune status of the host. These manifestations can range from skin ulcers to the disfiguration of the nasopharyngeal area to even potentially lethal forms if left untreated (Pearson and Anastacio de Queiroz, 1996; Scorza et al., 2017; Burza et al., 2018). Although faced with a hostile environment when phagocytosed by macrophages, *Leishmania* have evolved mechanisms to subvert the macrophage response and ultimately prevail. *Leishmania* can, for example, induce the SOCS (suppressor of cytokine signaling) proteins that are negatively regulating the JAK/STAT pathway and the cytokine release leading to the impairment of the crosstalk of the macrophage with the T cell, resulting in the decrease of interleukin 12 (IL-12) and interferon (IFN) gamma (IFN-γ) productions (Chandrakar et al., 2020). Moreover, it has been shown that *Leishmania* are able to block AIF1 (allograft inflammatory factor-1) expression in macrophages and degrade CXCL1 to inhibit the pro-inflammatory responses and the recruitment of neutrophils, respectively (Yorek et al., 2019; da Silva et al., 2021). Parasites can also inhibit the inflammasome through the upregulation of the A20 protein (Hartley et al., 2018; Zamboni and Sacks, 2019) or interfere with the oxidative stress response (Reverte et al., 2021; Reverte et al., 2022).

Leishmania RNA virus 1 (LRV1) is a double-stranded RNA (dsRNA) virus of the *Totiviridae* family living endosymbiotically in some strains of *Leishmania* (Tarr et al., 1988; Stuart et al., 1992; Zamora et al., 2000; Hartley et al., 2012). The presence of LRV1 could contribute to the exacerbation and chronicity of leishmaniasis, the development of destructive metastatic lesions, and even treatment failure (Ives et al., 2011; Cantanhede et al., 2015; Adaui et al., 2016; Bourreau et al., 2016; Hartley et al., 2016). The presence of LRV1 inside *Leishmania* results in increased macrophage survival in a mechanism dependent on Akt (Eren et al., 2016); an increased production of pro-inflammatory cytokines and chemokines such as interleukin 6 (IL-6), tumor-necrosis factor α (TNF-α), interleukin 17 (IL-17), type I IFNs (IFN-α and IFN-β) (Ives et al., 2011; Hartley et al., 2016; Rossi et al., 2017); and the inhibition of inflammasomes *via* NLRP3 (Hartley et al., 2018). This immunophenotype depends on the recognition of LRV1 by the endosomal Toll-like receptor 3 (TLR3) (Ives et al., 2011; Olivier and Zamboni, 2020) and the activation of its downstream type I IFN signaling pathways (Rossi et al., 2017). Interestingly, despite the inflammatory environment triggered by LRV1, mice are more susceptible to *Leishmania guyanensis* (*Lgy*) bearing LRV1 (from now on *Lgy*LRV1+) than to *Lgy* devoid of the virus (i.e., *Lgy*LRV1-). Interestingly, the same exacerbatory effect is observed when an exogenous virus is coadministered with *Lgy*LRV1-, resulting in an increase in parasite burden and footpad swelling (Rossi et al., 2017) underlining the importance of the systemic production of type I IFN and its signaling pathways for the exacerbation of the affliction outcome. Mice lacking *Ifnar* (*Ifnar*$^{-/-}$), the gene coding for IFNAR, the receptor of type I IFNs, exhibited a similar lesion size and parasitemia when infected with both LRV1+ and LRV1- parasites (Rossi et al., 2017). Additionally, infection with a virus even after the resolution of the *Leishmania* infection has the potential to reactivate the disease caused by *Leishmania* (Rossi et al., 2017), raising concerns on leishmaniasis control and management. Thus, viral coinfections or later exposure to any potential trigger of the type I IFN response can be considered a risk factor for leishmaniasis relapses. Despite the relevance of viral infection in the context of leishmaniasis, not many studies exist on the role of virus coinfection with *Leishmania*, with the exception perhaps of a coinfection with HIV, known to modulate and impair the adaptive immune response and can thus be considered a predictor of a worsened leishmaniasis outcome (Lindoso et al., 2016).

The advent of transcriptomics has contributed to the global comprehension of how macrophages respond toward infection, including infection by *Leishmania*. A large number of genes modulated by *Leishmania* were related to the immune response (pro- and anti-inflammatory), glycolysis, lipid metabolism, biogenesis, and phagocytosis (Fernandes et al., 2016; Aoki et al., 2017; Aoki et al., 2019; Shadab et al., 2019; Restrepo et al., 2021; Reverte et al., 2021; Salloum et al., 2021; Chaparro et al., 2022). While these studies have shed light on a plethora of mechanisms potentially perturbed by *Leishmania*, they have not explored the impact that coexposure to additional agents may have on the immune response mounted toward *Leishmania*. As mentioned above, this point is particularly relevant when macrophages are concomitantly exposed to the *Leishmania* and its endosymbiont, the LRV1 duo. Understanding how the host responds toward infection by *Leishmania* and the contribution of the presence of the virus and its downstream type I IFN response is paramount to design strategies for improving disease prevention, progression, and the outcome. To have a comprehensive and dynamic understanding of the responses mounted by the macrophage toward the *Leishmania*-LRV1 duo as well as to dissect their individual impact, their synergies or their opposing effects, an RNA sequencing (RNA-Seq) analysis was performed. Here, the different cellular pathways affected by the presence of *Leishmania* or a virus were disentangled and the genes driving those pathways were identified. In addition, the pathways exacerbated by the presence of LRV1 inside *Leishmania* that contributed to worsening the disease fallout were spotted. Interestingly, although non-pathogenic for humans, LRV1 had the potential to surpass the effect of *Leishmania* and ultimately drive the immune response of the macrophage. The dynamic and timely nature of the orchestrated macrophage response was demonstrated by the importance of the genes that had an early, late, or sustained response during infection by the *Leishmania*-LRV1 duo.

Materials and methods

Animals

Wild-type (WT; C57BL/6JOlaHsd) mice were purchased from Envigo (Gannat, France), *Ifnar*$^{-/-}$ (B6.129S2 *Ifnar1*^{tm1Agt}/Mmjax) mice were obtained from M. Aguet, Swiss Institute of Experimental Cancer Research, Epalinges, Switzerland. Mice were maintained and bred in GM500 IVC Green Line cages (Tecniplast, Buguggiate, Italy) at the specific pathogen-free (SPF) animal facility at the University of Lausanne (Epalinges site), with a relative humidity 55 ± 10%, 21 ± 2°C, and in 11/13-h dark/light cycles with *ad libitum* water (local acidified and autoclaved water) and food (Kliba Nafag or Safe). Cardboard or plastic tunnels and igloos, as well as paper tissues, were supplied as enrichment. Bone marrow was extracted from 7-week-old female WT mice (RNA-Seq dataset#1), 7- to 10-week-old female WT mice (RNA-Seq dataset#2), and 9-week- old female *Ifnar*$^{-/-}$ mice (RNA-Seq dataset#2) (Table 1). Experiments were performed according to the ethical guidelines set out by the Swiss Federal Food Safety and Veterinary Office (FSVO), and

TABLE 1 Summary table of RNA sequencing samples used for the analysis.

RNA-Seq datasets	**Dataset#2**		**Dataset#1**
Genotypes	WT	*Ifnar*$^{-/-}$ (*Ifnar1*$^{-/-}$)	WT
Ages of mice	7–10 weeks old	9 weeks old	7 weeks old
Number of mice (quality control)	4	4	5
Number of mice (RNA-Seq)	3	3	3
Conditions (treatment/infection)	Medium, *Lgy*LRV1-, *Lgy*LRV1+, poly I:C	Medium, *Lgy*LRV1-, *Lgy*LRV1+	*Lgy*LRV1-, *Lgy*LRV1+, *Lgy*LRV1- + IFN-α, *Lgy*LRV1- + IFN-β
Multiplicity of infection (MOI)	MOI 5		MOI 3
Times posttreatment/infection	8 and 24 h		

Table explaining the differences and the similarities between the two datasets of samples analyzed in this study. The factors represented are the experimental steps preceding the final sequencing of the RNA. Two different genotypes, wild type (WT) and Ifnar$^{-/-}$, at two time points p.i. (8 and 24 h) were used. Both genotypes were treated with medium, LgyLRV1+ parasites, LgyLRV1- parasites, or poly I:C. WT was treated in addition to LgyLRV1- parasites + IFN-α, or LgyLRV1- parasites + IFN-β.

procedures were approved by the Veterinary Commission of the Canton de Vaud (SCAV, Switzerland) under the authorization numbers 2113.3.

Parasites

The study was performed using lines of *Leishmania guyanensis* (MHOM/BR/78/M4147), named *Lgy*LRV1+ and *Lgy*LRV1-, bearing LRV1 or not, respectively (Kuhlmann et al., 2017). Both parasites were recovered from footpads of infected C57BL/6 mice and not kept for longer than six passages. *Leishmania* strains were cultured in a complete Schneider's medium, containing a Schneider's Drosophila Medium (Gibco, Thermo Fischer Reinach, Switzerland) supplemented with 20% heat-inactivated fetal bovine serum (FBS; Gibco), 1% penicillin–streptomycin solution (BioConcept, Allschwill, Switzerland) (i.e., 100 IU/ml and 100 µg/ml, respectively), 2% 4-(2-hydroxyethyl)-1-piperazineethanesulfonic acid (HEPES) (BioConcept) (i.e., 20 mM), hemin–folate solution (prepared from Porcine Hemin, Sigma-Aldrich and Folic Acid, Fluka) (5 and 10 µg/ml, respectively), and 6-Biopterin (Sigma-Aldrich, Buchs, Switzerland) (0.6 µg/ml). They were maintained at 26°C and diluted every week. Six-day-cultured (stationary phase) parasites were used for macrophage infection.

Bone marrow–derived macrophages

Macrophages were derived from the bone marrow of C57BL/6 mice (WT or *Ifnar*$^{-/-}$). The mice of each genotype were sacrificed, and hind leg bones were collected (both tibia and femur) and kept in the Dulbecco's modified Eagle's medium (DMEM; Gibco) on ice. The same following procedure was applied to each mouse. After cleaning the bones with 70% ethanol and the DMEM, the bone marrow was flushed out with the complete DMEM, containing DMEM, supplemented with 10% heat-inactivated FBS (Gibco), 1% penicillin–streptomycin solution (BioConcept) (i.e., 100 UI/ml and 100 µg/ml, respectively), and 1% HEPES (BioConcept) (i.e., 10 mM). The bone marrow suspension was then passed through a 40-µm cell strainer (Corning) and centrifuged for 10 min, at 1,500 rpm (453 × *g*), at 4°C. The cell pellet was resuspended with the complete DMEM medium containing 50-ng/ml recombinant mouse macrophage colony stimulating factor (M-CSF, ImmunoTools). Approximately 10 ml were distributed per Sterilin Petri Dish (Thermo Scientific), and six plates were prepared. After 3 days in culture at 37°C and 5% CO_2, 5 ml of the complete DMEM medium containing 50-ng/ml M-CSF were added per plate. The cells were differentiated into macrophages for three additional days, that is, 6 days total, at 37°C and 5% CO_2. After these 6 days, the bone marrow–derived macrophages were detached with 1X Dulbecco's phosphate-buffered saline (DPBS) (Gibco) containing 5 mM ethylenediamine tetraacetic acid (EDTA), washed and resuspended with the complete DMEM medium. The cells were then counted and adjusted to 2.6 million cells per milliliter. They were respectively plated in 12-well plates (TPP) with 1.95 million cells per well. They were finally put back in culture at 37°C and 5% CO_2 for 1 day.

Macrophage infection and treatments

The day after their plating, stationary-phase *Leishmania* promastigotes were centrifuged, washed with 1X DPBS, resuspended with a complete DMEM medium, counted, and adjusted to the concentration required. Murine bone marrow–derived macrophages (BMDMs) were infected with the *Leishmania* at multiplicity of infection (MOI) of three and five parasites per macrophage, in the first and the second RNA-Seq datasets, respectively. Cells were also alternatively treated with some synthetic TLR agonist or cotreated with recombinant murine type I IFNs. Poly I:C (HMW), a TLR3 agonist (mimicking dsRNA), was obtained from *In vivo*Gen and used at 2 µg/ml. Murine recombinant IFN-α and IFN-β were used each at 1,000 IU/ml (CellScience). *Lgy*LRV1-infected BMDMs were treated or not with type I IFNs at 6 h postinfection (p.i.). BMDMs in the complete DMEM alone were used as a control. Cells were incubated at 35°C and 5% CO_2 until 8 and 24 h p.i. or posttreatment (Table 1).

RNA isolation and selection

At 8 and 24 h posttreatment, BMDMs cultured in 12-well plates were cleared out of supernatants and lysed with 350 µl of the RLT buffer (Qiagen) supplemented with 40-mM DTT (Dithiothreitol) for RNA extraction. Plates were then frozen at -80°C until the RNA purification. The RNA samples were purified with the RNeasy Plus Mini Kit (Qiagen) following the manufacturer's instructions. Purified RNA was eluted with 30 µl of RNase-free water (Qiagen), and their RNA concentrations were measured with a spectrophotometer (NanoDrop, ThermoFisher Scientific). The quality of the RNA samples was then evaluated with a Fragment Analyzer (Agilent) at the Lausanne Genomic Technologies Facility (GTF) for both RNA-Seq datasets. For the dataset#2, the RNA quantification was performed with a fluorimetric method (Ribogreen; ThermoFisher Scientific) by the GTF according to the manufacturer recommendations, then used to prepare the RNA dilutions for the libraries. While for the dataset#1, the total integrated concentration (TIC) values given by the Fragment Analyzer were directly used to prepare the RNA dilutions for the libraries. The RNA samples diluted for the libraries were the ones that have an RNA quality number (RQN) higher than 6 (for dataset#2) and 7 (for dataset#1) and from 3 mice out of 4 and 5, respectively. The samples were diluted in 96-well plates (Labgene Scientific). Then, from these plates, the libraries and the sequencing were performed at the GTF.

RNA sequencing data processing

Purity-filtered reads were adapters and quality trimmed with Cutadapt [v. 1.8 (Martin, 2011)]. Reads matching to ribosomal RNA sequences were removed with fastq_screen (v. 0.9.3 for dataset#1 and v. 0.11.1 for dataset#2). The remaining reads were further filtered for low complexity with reaper [v. 15-065, (Davis et al., 2013)]. Reads were aligned against the Mus musculus.GRCm38.86 genome using STAR [v. 2.5.2b, (Dobin et al., 2013)] for dataset#1 and the Mus musculus.GRCm38.92 genome using STAR [v. 2.5.3a, (Dobin et al., 2013)] for dataset#2. The number of read counts per gene locus was summarized with htseq-count [v. 0.6.1 for dataset#1 and v. 0.9.1 for dataset#2, (Anders et al., 2015)] using Mus musculus.GRCm38.86 gene annotation for dataset#1 and Mus musculus.GRCm38.92 gene annotation for dataset#2. The quality of the RNA-seq data alignment was assessed using RSeQC [v. 2.3.7, (Wang et al., 2012)]. Reads were also aligned to the Mus musculus.GRCm38.86 transcriptome using STAR [v. 2.5.2b, (Dobin et al., 2013)] for dataset#1 and to the Mus musculus.GRCm38.92 transcriptome using STAR [v. 2.5.3a, (Dobin et al., 2013)] for dataset#2. The estimation of the isoform abundance was computed using RSEM [v. 1.2.31, (Li and Dewey, 2011)].

Normalization and data transformation

Statistical analysis was performed for genes independently in the software environment R. Genes with a low number of counts were filtered out according to the rule of one count(s) per million (cpm) in at least one sample. Library sizes were scaled using TMM normalization. Subsequently, the normalized counts were transformed to cpm values, and a log2 transformation was applied, by means of the function cpm with the parameter setting prior.counts = 1 [EdgeR (Robinson et al., 2010)]. For the analysis with *Ifnar*$^{-/-}$ and WT genotypes, two sets of data generated separately were merged and this to integrated WT samples treated with IFN-α and IFN-β. To check if this was possible, we plotted the distributions of the log cpm of the shared conditions between the two datasets (*Lgy*LRV1+ and *Lgy*LRV1-). The distributions had similar patterns at 8- and 24-h time points, and the different groups of conditions were well separated (Supplementary Figure S1). Given the fact that with WGCNA, we are looking at expression patterns across conditions and not individual gene differential expression, we found this sufficient to take advantage of having more experimental conditions by integrating a dataset with WT treated with IFN-α and IFN-β.

Weighted gene coexpression network analysis and downstream bioinformatics analysis

Weighted gene coexpression network analysis (WGCNA) (Langfelder and Horvath, 2008) was performed on normalized RNA-Seq data in R (package WGCNA 1.69). For each analysis, an adjacency matrix was calculated to construct a signed hybrid coexpression network using Spearman correlation. A sequence of soft-thresholding powers was tested to reach a free-topology network with a relatively low mean connectivity, and the following thresholds were chosen for each analysis: 14 for WT at 8 h p.i., 9 for WT at 24 h p.i., 7 for WT + *Ifnar*$^{-/-}$ at 8 h p.i., and 16 for WT + *Ifnar*$^{-/-}$ at 24 h p.i. A topological overlap matrix (TOM) was then calculated from the adjacency matrix, converted to distance and clustered by hierarchical clustering using average linkage clustering. Modules were identified by a dynamic tree cut with a minimum module size = 20. Module eigengenes (MEs) that are the first principal component of the module were calculated, and similar modules were merged together using an ME distance threshold of 0.08 for WT at 8 h p.i., 0 for WT at 24 h p.i., 0.18 for WT + *Ifnar*$^{-/-}$ at 8 h p.i., and 0.08 for WT + *Ifnar*$^{-/-}$ at 24 h p.i. (Supplementary Figures S2–S5). kWithin that is the intramodular connectivity and kTotal, the whole network connectivity of each gene, were calculated with the WGCNA package. The relationship of MEs with the infection status (independent variable) was assessed with a regression analysis on MEs (dependent variable) for each module separately. The WT Medium condition was used as a reference (intercept). Adjusted R-squared and *p*-values were used to assess the model performance. ME average predictions were plotted as a heatmap. Adjusted R-squared (R-squared adjusted for the number of predictors in the model) that is a statistical measure that represents the proportion of the variance for a dependent variable (expression) that is explained by an independent variable (infection groups) was calculated by fitting a linear model for each gene expression value. Gene-adjusted R-squared was then plotted against kTotal values. Gene Ontology (GO) enrichment analysis was performed for gene coexpression modules against GO categories using the topGO R package (topGO 2.26.0) (Alexa and Rahnenfuhrer, 2016) and GO database (07.2019) (Ashburner et al., 2000; Gene Ontology Consortium, 2021). Closeness centrality (CC) (Freeman, 1978) in the coexpression network was calculated for each gene at 8- and 24-h time points using the Networkx Python package (Networkx 2.5). A density map was plotted of CC at 8 h against CC at 24 h. Network visualization was performed with Cytoscape.

Results

The global network analysis of wild-type-infected macrophages highlighted modules correlated to either *Leishmania*, LRV1 or to Leishmania but further exacerbated by LRV1

To design appropriate strategies to combat leishmaniasis and understand its clinical presentations it was important to unravel the influence of *Leishmania* or LRV1 on the response mounted by the macrophage upon infection by *Lgy*LRV1+. To this end, transcriptome profiling using RNA-Seq was performed to identify global changes in the WT murine macrophage infected with *Lgy*, carrying or not LRV1, defined as LRV1+ or LRV1-, at 8 and 24 h p.i. As a control, cells were left non-infected (Medium) or treated with polyinosinic-polycytidylic acid (poly I:C), a TLR3 agonist, mimicking solely the effect of dsRNA viruses such as LRV1. Of the 36,487 genes annotated for *Mus musculus* (McGarvey et al., 2015), 12,651 and 12,594 genes were detected in this study at 8 and 24 h p.i., respectively, and used for downstream analysis as shown in Figure 1. First, a weighted gene coexpression network analysis (WGCNA) was performed. WGCNA is a systems biology approach that relies on the hypothesis that genes with similar expression patterns may be functionally related, coregulated, or members of the same pathway. Following this approach, a gene–gene similarity network was constructed allowing to identify highly correlated genes that cluster into modules. The expression profile of the module genes was summarized by the ME that is the first principal component of its expression. Upon identification of the modules a regression analysis was performed on modules eigengenes and the average prediction was calculated to identify modules that were associated with the different experimental groups (Medium, *Lgy*LRV1+, *Lgy*LRV1- and poly I:C). The intramodular (kWithin) and whole network (kTotal) connectivity were computed for each gene allowing to identify hubs (drivers). Following the WGCNA, 49 modules at 8 h and 49

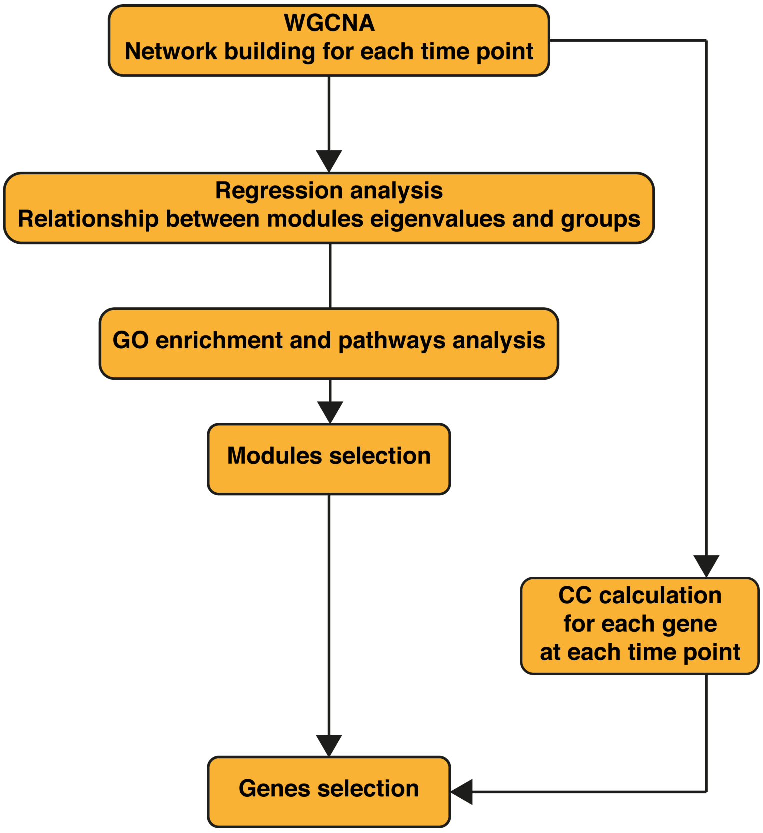

FIGURE 1
Workflow of the bioinformatics analysis. WGCNA was performed first on the wild-type (WT) samples alone, then on WT + *Ifnar*$^{-/-}$ samples merged. Regression analysis was performed on obtained modules to assess their relationship to phenotypes (infection groups). Gene Ontology (GO) enrichment was performed for each module. WT + *Ifnar*$^{-/-}$ network resulting from weighted gene correlation network analysis (WGCNA) was used to calculate the closeness centrality (CC) of genes at 8 and 24 h postinfection (p.i.).

at 24 h were defined. The different modules are represented as a heatmap based on the average predictions of the regression analysis in the different experimental groups in Figures 2A, C (*p*-values shown in Supplementary Figures S6A, B).

The blue to red scale speaks for negative to positive associations with a determined condition based on normalized enrichment scores. On top of each heatmap a dendrogram, representing the hierarchical clustering of the data, is shown. Interestingly, although *Leishmania* is the common denominator between *Lgy*LRV1+ and the *Lgy*LRV1- groups, *Lgy*LRV1- clusters correlated closer to the group left untreated (mentioned as "Medium" in Figure 2) while *Lgy*LRV1+ clusters correlated closer to the poly I:C group both at 8 and 24 h posttreatment. This observation demonstrates that the presence of LRV1 within *Leishmania* triggers a drastic macrophage response, shifting its profile closer to the response triggered solely by a virus than to that of *Leishmania* alone.

Based on the analysis of the heatmaps, the modules were defined as either *Leishmania*- or LRV1 dependent. Comparatively to the medium condition, the LRV1-modulated group encompassed modules exclusively up- or downregulated by *Lgy*LRV1+ and poly I:C but not modulated by *Leishmania* devoid of LRV1 (i.e., *Lgy*LRV1-). On the other hand, the *Leishmania*-modulated group was characterized by modules similarly regulated by *Lgy*LRV1- and *Lgy*LRV1+ comparatively to medium, but not by poly I:C. Among the 49 modules at each time point, and 5 modules were found to be associated with *Leishmania* at 8 and 24 h p.i., respectively, and 6 and 9 modules were found to be associated with the presence of LRV1 at 8 and 24 h p.i., respectively. Thus, the modules selected for further analysis due to their association with *Leishmania* were lightcyan (245 genes), grey60 (255 genes), magenta4 (70 genes), floralwhite (112 genes) at 8 h p.i. and mediumpurple3 (116 genes), green (493 genes), plum1 (134 genes), grey60 (185 genes), paleturquoise (148 genes) at 24 h p.i. The modules selected due to their association to LRV1 were blue2 (725 genes), firebrick3 (159 genes), coral3 (644 genes), navajowhite1 (130 genes), lavenderblush3 (145 genes), plum (83 genes) at 8 h p.i. and black (345 genes), skyblue3 (135 genes), lightsteelblue1 (116 genes), blue (1207 genes), brown (1137 genes), darkgrey (168 genes), red (352 genes), tan (237 genes), darkslateblue (86 genes) at 24 h p.i. Given the known exacerbatory role that LRV1 has on the leishmaniasis outcome (Ives et al., 2011; Hartley et al., 2012; Cantanhede et al., 2015; Rossi et al., 2017) another category of modules was defined as "exacerbatory". These so-called "exacerbatory" modules are, to a certain extent modified by *Lgy*LRV1-, but the presence of LRV1 in *Lgy*LRV1+ further exacerbates this response in a similar direction as that observed with the poly I:C treatment. At 8 h p.i., there were 7 "exacerbatory" modules highlighted: green (1,159 genes), orangered4 (435 genes), coral1 (744 genes), darkseagreen4 (344 genes), bisque4 (1,129 genes), darkgrey (884 genes), and mediumpurple4 (158 genes). At 24 h p.i., 6 "exacerbatory" modules: darkolivegreen (145 genes), pink (294 genes), yellow (639 genes), magenta (287 genes), brown4 (99 genes), and ivory (111 genes) were identified. (For the whole lists of genes with their module membership and their connectivity at each time point, see Supplementary Table S1).

Based on the above-mentioned selection of modules, the presence of *Leishmania* lead to a concerted modulation of 682 genes at 8 h p.i. and 1,076 genes at 24 h p.i. representing 5.4% and 8.5%, respectively, of the total genes identified. On the other hand, the presence of LRV1 impacted 1,886 genes at 8 h p.i. and 3,783 genes at 24 h p.i. representing 14.9% and 30% of the total amount of genes identified at 8 and 24 h p.i., respectively. As for the "exacerbatory" modules, they comprise a large proportion of the genes with a synchronized modulation, 4853 and 1575 genes representing 38.4% and 12.5% of the genes identified at 8 and 24 h p.i., respectively. This approach gave us a general overview of the macrophage response toward *Leishmania*, LRV1, or the combination of both agents. The results support the importance of the modulation of the macrophage response by LRV1 both at 8 and 24 h p.i.

The global network analysis of wild-type-infected macrophages highlighted key pathways associated to *Leishmania* and to LRV1

Using the WGCNA groups of genes with a similar expression were identified and classified into modules; however, to shed light into the biological processes that may be present in each of the modules selected above, a GO enrichment analysis using the topGO R package (topGO 2.26.0) (Alexa and Rahnenfuhrer, 2016) and the GO database (Ashburner et al., 2000; Gene Ontology Consortium, 2021) was performed. The aim was to identify annotated functions overrepresented in the modules. Among the biological process (BP) category of the GO terms identified, a curation of the GOs were conducted and GO terms related to either clearly different types of cells or tissues, or even to completely distinct organs or organisms were removed. The 5 most statistically significant terms (with *p*-values strictly lower than 0.01) within a module are shown in Supplementary Table S2. The fact that WGCNA analysis resulted in modules enriched for biologically important processes related to infection, including an innate immune response (found in the 8h_coral3 module) and a positive regulation of interleukin-6 production (found in the 8h_bisque4 module), suggest that these modules are a robust feature of the molecular architecture of *Leishmania* and LRV1 infection. Modules associated to *Leishmania* were enriched in terms such as the positive regulation of telomere capping, RNA secondary structure unwinding, purine deoxyribonucleotide, and glutathione metabolic process in the grey60, floralwhite, lightcyan, and magenta4 modules,

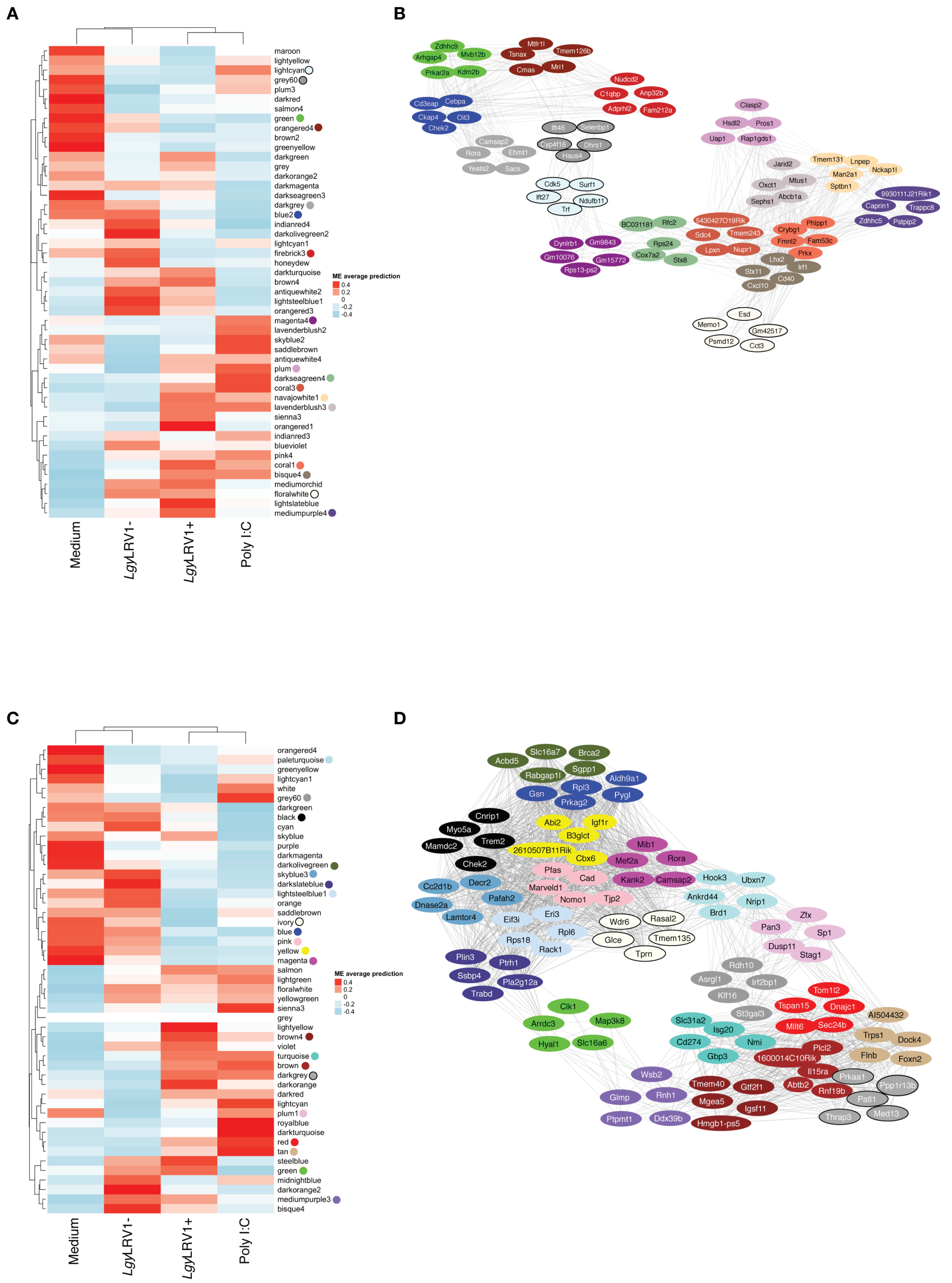

FIGURE 2

The global network analysis of WT-infected macrophages highlights modules and key pathways associated to *Leishmania* and to *Leishmania* RNA virus 1 (LRV1). **(A)** Heatmap of the average predictions of the fitted linear model on each module eigengene (ME) at the 8-h time point. **(B)** Network generated from selected modules at the 8-h time point associated with *Leishmania* infection (*Lgy*LRV1+, *Lgy*LRV1-), virus (*Lgy*LRV1+, poly I:C), and "exacerbatory" modules. Only the top five highest connected genes were selected. Node colors indicate the module color they belong to. Edges between genes indicate the correlation between genes. **(C)** Heatmap of average predictions of the fitted linear model on each ME at the 24-h time point. **(D)** Network generated from selected modules at the 24-h time point associated with *Leishmania* infection (*Lgy*LRV1+, *Lgy*LRV1-), virus (*Lgy*LRV1+, poly I:C), and "exacerbatory" modules. Only the top five highest connected genes were selected. Node colors indicate the module color they belong to. Edges between genes indicate the correlation between genes.

respectively, at 8 h p.i. (Supplementary Table S2). Moreover, at 24 h p.i., the *Leishmania*-associated modules were enriched in terms such as positive regulation of receptor internalization and asymmetric protein localization in mediumpurple3 and plum1, respectively, and the regulation of transcription, negative regulation of focal adhesion assembly, and cellular response to acid chemical in paleturquoise, grey60 and green, respectively (Supplementary Table S2). Modules associated with LRV1 at 8 h p.i. were enriched in pathways related to tRNA methylation, transcription, translation, GTPase activity, and DNA replication, in the blue2, firebrick3, navajowhite1, and lavenderblush3 modules at 8 h p.i., whereas coral3 and plum were enriched in the immune response (for example, innate immune response and a positive regulation of acute inflammatory response) and phagocytosis pathways. Comparatively, LRV1-associated modules at 24 h p.i., such as skyblue3, blue, lightsteelblue1, darkgrey, and tan, were enriched in pathways related to methylation, translation, and transcription processes, whereas the black, brown, red, tan, and darkslateblue modules were enriched in phagocytosis, cytokine production, and the oxidation–reduction process (Supplementary Table S2). On the other hand, the "exacerbatory" modules were enriched in terms such as the RNA biosynthetic process, oxidation–reduction process and mitosis-related pathways in green, orangered4 and darkseagreen4; and NF-kappaB signaling and cytokine production in coral1 and bisque4 at 8 h p.i. Furthermore, the "exacerbatory" modules at 24 h p.i. were enriched in DNA replication, transcription, and macrophage regulation in the darkolivegreen, yellow, magenta, and brown4 modules (Supplementary Table S2).

Identification of hub genes and network analysis provided insight on how the different modules may interact

In each module, the most central genes, that is, the most interconnected genes measured by their intramodular connectivity, that is, its kWithin, can be further identified as hub genes. Due to their high connectivity, hub genes are thus considered as functionally important genes that are most likely to drive the group of genes and thus the biological processes present within each module. The top 1% of genes with the highest kWithin are shown in Table 2 for each of the modules selected. In order to visualize the interaction between the *Leishmania* virus and "exacerbatory" modules, the five genes with the highest connectivity for each module (i.e., with the highest kWithin) are displayed as a network for 8 and 24 h p.i. in Figures 2B, D. The five top driver genes associated to *Leishmania* were *Ift27*, *Cdk5*, *Surf1*, *Trf*, *Ndufb11* (lightcyan), *Ift46*, *Selenbp1*, *Cyp4f16*, *Dhrs1*, *Haus4* (grey60), *Dynlrb1*, *Gm9843*, *Gm10076*, *Rps13-ps2*, *Gm15772* (magenta4), *Memo1*, *Esd*, *Gm42517*, *Psmd12*, *Cct3* (floralwhite) at 8 h p.i.; and *Ddx39b*, *Ptpmt1*, *Rnh1*, *Glmp*, *Wsb2* (mediumpurple3), *Arrdc3*, *Clk1*, *Map3k8*, *Hyal1*, *Slc16a6* (green), *Zfx*, *Sp1*, *Stag1*, *Dusp11*, *Pan3* (plum1), *St3gal3*, *Klf16*, *Asrgl1*, *Rdh10*, *Irf2bp1* (grey60), *Hook3*, *Ubxn7*, *Ankrd44*, *Brd1*, *Nrip1* (paleturquoise) at 24 h p.i. The five top driver genes inside the modules selected due to their association to LRV1 were *Cd3eap*, *Cebpa*, *Oit3*, *Ckap4*, *Chek2* (blue2), *Nudcd2*, *C1qbp*, *Anp32b*, *Fam212a*, *Adprhl2* (firebrick3), *5430427O19Rik*, *Sdc4*, *Tmem243*, *Nupr1*, *Lpxn* (coral3), *Tmem131*, *Lnpep*, *Man2a1*, *Sptbn1*, *Nckap1l* (navajowhite1), *Jarid2*, *Mtus1*, *Oxct1*, *Abcb1a*, *Sephs1* (lavenderblush3), *Clasp2*, *Pros1*, *Hsdl2*, *Uap1*, *Rap1gds1* (plum) at 8 h p.i.; and *Chek2*, *Myo5a*, *Trem2*, *Cnrip1*, *Mamdc2* (black), *Cc2d1b*, *Dnase2a*, *Decr2*, *Pafah2*, *Lamtor4* (skyblue3), *Rack1*, *Eif3i*, *Rps18*, *Eri3*, *Rpl6* (lightsteelblue1), *Pygl*, *Gsn*, *Prkag2*, *Rpl3*, *Aldh9a1* (blue), *1600014C10Rik*, *Rnf19b*, *Plcl2*, *Abtb2*, *Il15ra* (brown), *Patl1*, *Prkaa1*, *Thrap3*, *Ppp1r13b*, *Med13* (darkgrey), *Tom1l2*, *Mllt6*, *Sec24b*, *Dnajc1*, *Tspan15* (red), *Al504432*, *Trps1*, *Dock4*, *Flnb*, *Foxn2* (tan), *Plin3*, *Pla2g12a*, *Ptrh1*, *Trabd*, *Ssbp4* (darkslateblue) at 24 h p.i. For the "exacerbatory" modules, the 5 top driver genes were: *Arhgap4*, *Zdhhc9*, *Mvb12b*, *Prkar2a*, *Kdm2b* (green), *Tsnax*, *Mtfr1l*, *Tmem126b*, *Cmas*, *Mri1* (orangered4), *Phlpp1*, *Crybg1*, *Fmnl2*, *Fam53c*, *Prkx* (coral1), *BC031181*, *Rfc2*, *Rps24*, *Cox7a2*, *Stx8* (darkseagreen4), *Irf1*, *Lhx2*, *Stx11*, *Cd40*, *Cxcl10* (bisque4), *Rora*, *Camsap2*, *Ehmt1*, *Yeats2*, *Sacs* (darkgrey) and *9930111J21Rik1*, *Caprin1*, *Trappc8*, *Zdhhc5*, *Pstpip2* (mediumpurple4) at 8 h p.i.; and *Acbd5*, *Brca2*, *Slc16a7*, *Sgpp1*, *Rabgap1l* (darkolivegreen), *Nomo1*, *Marveld1*, *Pfas*, *Cad*, *Tjp2* (pink), *Igf1r*, *Abi2*, *B3glct*, *2610507B11Rik*, *Cbx6* (yellow), *Camsap2*, *Kank2*, *Mib1*, *Rora*, *Mef2a* (magenta), *Tmem40*, *Gtf2f1*, *Mgea5*, *Hmgb1-ps5*, *Igsf11* (brown4), *Glce*, *Rasal2*, *Tmem135*, *Wdr6*, *Tprn* (ivory) and *Slc31a2*, *Gpb3*, *Isg20*, *Cd274*, *Nmi* (turquoise) at 24 h p.i. (for the whole lists of genes with their module membership and their connectivity at each time point, see Supplementary Table S1).

As shown, the top five hub genes of each module were clustered diametrically, depending on whether they were either positively or negatively modulated by a given treatment as shown in Figure 2B. Interestingly, at 8 h, the connection between these two extremities was achieved by a module with an exacerbatory phenotype, the 8h_darkseagreen4, enriched in mitosis-related pathways as mentioned before (Supplementary Table S2). At 24 h, the connection between modules that were positively or negatively modulated is accomplished by two different branches. Interestingly, the connecting modules at 24 h show different modulations for either *Leishmania* (LRV1+ and LRV1-) or poly I:C (i.e., the molecule used to map virus-dependent responses). On one side, the connection was realized by the 24h_green module consisting of upregulated genes in *Leishmania*-infected macrophages but downregulated in poly I:C-treated cells. As mentioned previously, the 24h_green module was enriched in the cellular response to the acid chemical (Supplementary Table S2). On the other side, the link between modules with up- and

TABLE 2 The top 1% genes with the highest kWithin of the three groups of modules selected in WT analysis at 8 and 24 h postinfection (p.i).

Time	Group	Module	Top 1% genes
8h	*Leishmania*	lightcyan	*Ndufb11, Ift27, Surf1*
		grey60	*Cyp4f16, Ift46, Haus4*
		magenta4	*Gm9843*
		floralwhite	*Esd*
	LRV1	blue2	*Oit3, Cebpa, Ckap4, Chek2, Cd3eap, Trmt2a, Abcf3, Nat10*
		firebrick3	*Fam212a, C1qbp*
		coral3	*Nupr1, Lpxn, Sdc4, 5430427O19Rik, Tmem243, Stx18, Prpsap1*
		navajowhite1	*Lnpep, Sptbn1*
		lavenderblush3	*Sephs1, Jarid2*
		plum	*Hsdl2*
	Exacerbatory	green	*Prkar2a, Arhgap4, Kdm2b, Zdhhc9, Mvb12b, Cul7, Fads1, Adcy9, Gpd1l, Slc25a36, Manba, Slc25a16*
		orangered4	*Mtfr1l, Tmem126b, Tsnax, Cmas, Mri1*
		coral1	*Fam53c, Prkx, Crybg1, Phlpp1, Fmnl2, Ankrd50, Etv3, Ttc9c*
		darkseagreen4	*Rps24, Cox7a2, Rfc2, BC031181*
		bisque4	*Cd40, Lhx2, Stx11, Cxcl10, Irf1, Phf11b, Gnb4, Ccrl2, Rilpl1, Zufsp, March5, Sp140*
		darkgrey	*Sacs, Camsap2, Yeats2, Rora, Ehmt1, Ndst1, Chd3, Zfp652, Dnmbp*
		mediumpurple4	*Caprin1, 9930111J21Rik1*
24h	*Leishmania*	mediumpurple3	*Rnh1, Ddx39b*
		green	*Map3k8, Arrdc3, Clk1, Hyal1, Slc16a6*
		plum1	*Sp1, Dusp11*
		grey60	*Irf2bp1, Rdh10*
		paleturquoise	*Hook3, Ubxn7*
	LRV1	black	*Mamdc2, Myo5a, Cnrip1, Chek2*
		skyblue3	*Cc2d1b, Lamtor4*
		lightsteelblue1	*Rpl6, Eri3*
		blue	*Aldh9a1, Prkag2, Pygl, Rpl3, Gsn, Cd28, Aplp2, Tnfrsf21, Trim47, Fam134b, Man2a2, Sort1, Adssl1*
		brown	*Plcl2, Rnf19b, 1600014C10Rik, Il15ra, Abtb2, Lcp2, Il15, Nod1, Acsl1, Tnfaip3, Hrh2, Ctsc*
		darkgrey	*Ppp1r13b, Prkaa1*
		red	*Tspan15, Mllt6, Tom1l2, Sec24b*
		tan	*Flnb, Trps1, Dock4*
		darkslateblue	*Plin3*
	Exacerbatory	darkolivegreen	*Acbd5, Rabgap1l*
		pink	*Marveld1, Cad, Tjp2*
		yellow	*Igf1r, B3glct, Cbx6, 2610507B11Rik, Abi2, Adcy9, Grk5*
		magenta	*Rora, Mef2a, Kank2*
		brown4	*Gtf2f1*
		ivory	*Wdr6, Glce*
		turquoise	*Slc31a2, Gpb3, Isg20, Cd274, Nmi, Ogfr, Parp10, H2-Q5, Nr1h3, AW112010, Phf11b, Phf11a, Igtp, Bambi-ps1*

downregulated genes was achieved by the 24h_grey60 and 24h_plum1 showing both the downregulation of genes associated with *Leishmania* but being either upregulated or non-modulated by poly I:C. As mentioned previously, the 24h_grey60 module was enriched in genes implicated in the negative regulation of focal adhesion assembly and the 24h_plum1 in asymmetric protein localization (Supplementary Table S2). The topology of the networks represented by the five top genes from each module suggested the existence of a dependency between the different cascades triggered by *Leishmania* and LRV1 infection.

The global network analysis of wild-type-infected macrophages highlighted modules with highly connected genes that explained most of the variance of the data (highly adjusted R-squared)

Following the approach described above four, six, and seven modules were found associated to *Leishmania*, LRV1, and the combination of both, respectively, at 8 h p.i., whereas five, nine, and six modules were associated to *Leishmania*, LRV1, and the combination of both, respectively, at 24 h p.i. However, in order to understand which modules had potentially the highest impact on the macrophage transcriptional response, genes were plotted according to their total connectivity (kTotal) and adjusted R-squared (Figure 3). This approach allowed us to identify core modules. Thus, the genes present at the tip of the plot belonging to the bisque4, coral1, and green modules at 8 h and brown, turquoise, red, and blue modules at 24 h were likely to be strongly affected by *Leishmania* and LRV1 infection. Interestingly, all modules at 8 h could be considered to have an exacerbatory modulation, while at 24 h, three out of the four modules were virus driven (brown, red, and blue) while turquoise was exacerbatory. This observation indicated that while at early time points, the combination of *Leishmania* and LRV1 had the highest impact on the macrophage response, this effect was mainly achieved later by the presence of LRV1, suggesting that the presence of *Leishmania* at later time points impacts the macrophage response to a much lesser extent than LRV1. Moreover, out of the seven modules present at the tip, five (8h_bisque4; 8h_coral1; 24h_brown; 24h_turquoise and 24h_red; with a total of 1,872 genes at 8 h and 2,810 genes at 24 h) were enriched in pathways associated with the immune response (Table 3), highlighting the importance of a coordinated immune response and its overall impact when macrophages were challenged by an external agent. Among these immune-enriched pathways, there were, for example, the GO terms: innate immune response, cellular responses to or the regulations of IFNs or cytokines, defense responses to virus or protozoan (Table 3), whereas the other non-immune modules present at the tip were enriched in, for example, the GO terms: RNA biosynthetic and metabolic processes, the regulation of transcription from the RNA polymerase II promoter and

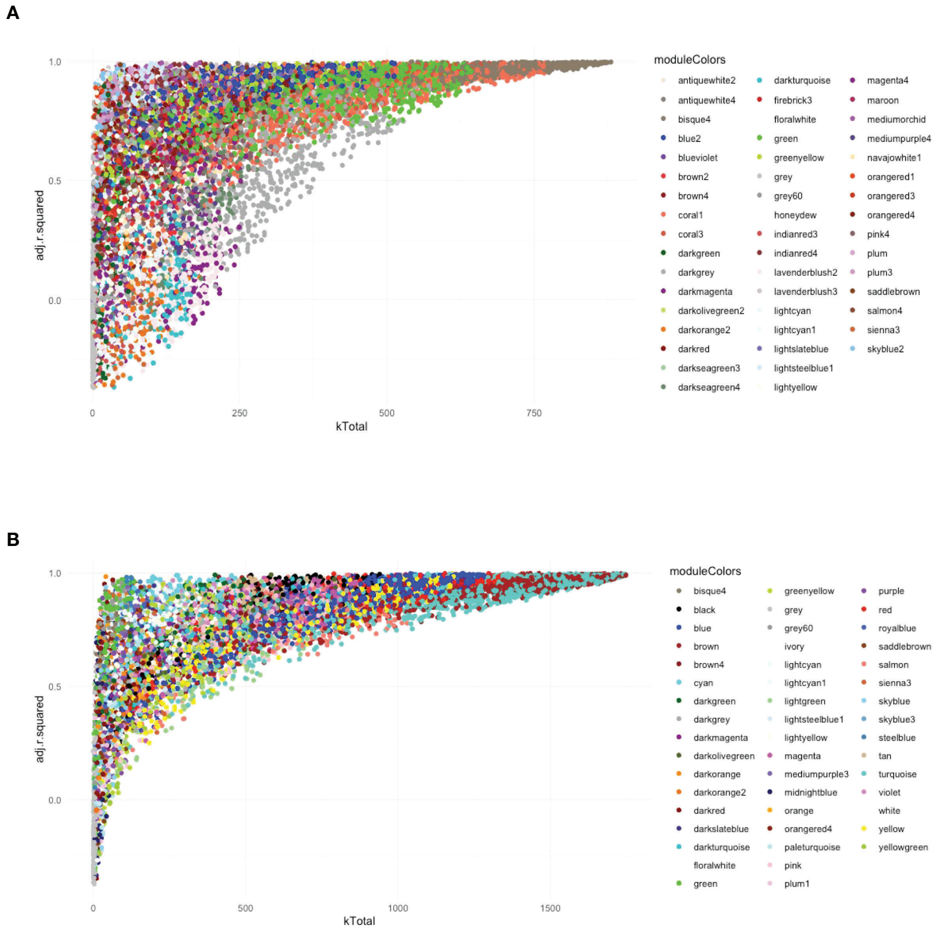

FIGURE 3
The global network analysis of WT-infected macrophages highlights modules with highly connected genes that explain most of the variance of the data (highly adjusted R-squared). **(A)** Scatter plot of kTotal (whole network connectivity) against adjusted R-squared for all genes in an 8-h network. Genes are colored according to the module (described in Figure 2) they belong to. **(B)** Scatterplot of kTotal (whole network connectivity) against adjusted R squared for all genes in the 24 h network. Genes are colored according to the module (described in Figure 2) they belong to.

TABLE 3 Examples of main Gene Ontology (GO) terms of tip modules in WT analysis (biological process "BP" category and *p*-value < 0.01) at 8 and 24 h p.i.

Time	Module	GO.ID	*p*-value	Term
8h	bisque4	GO:0071346	6.90E-15	cellular response to interferon-gamma
		GO:0035458	3.20E-14	cellular response to interferon-beta
		GO:0051607	1.06E-11	defense response to virus
		GO:0042832	7.51E-11	defense response to protozoan
		GO:0070374	4.53E-10	positive regulation of ERK1 and ERK2 cascade
		GO:0042510	5.12E-07	regulation of tyrosine phosphorylation of Stat1 protein
		GO:0032760	7.69E-07	positive regulation of tumor necrosis factor production
		GO:0050729	1.17E-06	positive regulation of inflammatory response
		GO:0045824	7.87E-06	negative regulation of innate immune response
		GO:0071222	9.11E-06	cellular response to lipopolysaccharide
		GO:0032735	9.38E-06	positive regulation of interleukin-12 production
	coral1	GO:0045087	3.79E-06	innate immune response
		GO:0006468	3.70E-04	protein phosphorylation
		GO:0007250	4.39E-04	activation of NF-kappaB-inducing kinase activity
		GO:2000637	4.39E-04	positive regulation of gene silencing by miRNA
		GO:0035329	6.52E-04	hippo signaling
		GO:0044827	6.77E-04	modulation by host of viral genome replication
	green	GO:0006298	8.05E-04	mismatch repair
		GO:0032774	1.02E-03	RNA biosynthetic process
		GO:0060828	3.22E-03	regulation of canonical Wnt signaling pathway
		GO:0019318	4.62E-03	hexose metabolic process
		GO:0051172	7.21E-03	negative regulation of nitrogen compound metabolic process
24h	brown	GO:0032755	1.42E-07	positive regulation of interleukin-6 production
		GO:0032735	2.21E-06	positive regulation of interleukin-12 production
		GO:0032760	5.16E-06	positive regulation of tumor necrosis factor production
		GO:0070374	1.68E-05	positive regulation of ERK1 and ERK2 cascade
		GO:0032496	1.71E-05	response to lipopolysaccharide
		GO:0042108	2.12E-05	positive regulation of cytokine biosynthetic process
		GO:0006954	1.69E-04	inflammatory response
		GO:0034341	2.65E-04	response to interferon-gamma
		GO:0032693	3.12E-04	negative regulation of interleukin-10 production
		GO:0051607	6.80E-04	defense response to virus
		GO:0034134	1.03E-03	Toll-like receptor 2 signaling pathway
	turquoise	GO:0035458	1.59E-13	cellular response to interferon-beta
		GO:0051607	5.89E-12	defense response to virus
		GO:0071346	2.29E-11	cellular response to interferon-gamma
		GO:0045071	8.86E-11	negative regulation of viral genome replication
		GO:0045087	5.79E-08	innate immune response
		GO:0002474	5.68E-07	antigen processing and presentation of peptide antigen *via* MHC class I
		GO:0060338	2.15E-05	regulation of type I interferon-mediated signaling pathway
		GO:0042832	3.71E-05	defense response to protozoan
		GO:0032388	6.04E-05	positive regulation of intracellular transport
		GO:0070098	1.08E-03	chemokine-mediated signaling pathway
		GO:0045824	1.38E-03	negative regulation of innate immune response
	red	GO:0000122	2.35E-04	negative regulation of transcription from RNA polymerase II promoter
		GO:0032722	5.23E-04	positive regulation of chemokine production
		GO:2000060	2.83E-03	positive regulation of protein ubiquitination involved in ubiquitin-dependent protein catabolic process
		GO:0035690	3.13E-03	cellular response to drug

(Continued)

TABLE 3 Continued

Time	Module	GO.ID	*p*-value	Term
		GO:0032755	4.38E-03	positive regulation of interleukin-6 production
	blue	GO:0055114	4.51E-06	oxidation–reduction process
		GO:0005975	1.11E-04	carbohydrate metabolic process
		GO:0008203	2.64E-04	cholesterol metabolic process
		GO:0032869	2.69E-04	cellular response to insulin stimulus
		GO:0019369	1.43E-03	arachidonic acid metabolic process

oxidation–reduction process (Table 3). These results showed how immune response–related genes shape the network topology, emphasizing its impact on the transcriptomic profile of the macrophage and highlighting the strong and sustained effect that LRV1 had on the macrophage response.

Type I interferons played a preponderant and central role in the infection mounted by macrophages toward *Lgy*LRV1+

Given the importance of the type I IFN response to the immunophenotype observed upon infection with *Lgy*LRV1+ (Rossi et al., 2017) coupled with the observation that modules containing genes with the highest kTotal and adjusted R-squared (8h_bisque4 and 24h_turquoise modules) are enriched in the cellular response to IFN-β (Figures 3A, B, Table 3) led us to further explore the systemic role of type I IFNs for gene modulation. To achieve this, a WGCNA approach was conducted in the *Ifnar* knockout macrophages (*Ifnar*$^{-/-}$). Moreover, to directly test the role of type I IFNs, two additional treatments, IFN-α and IFN-β, coadministered after 6 h post-*Lgy*LRV1-infection, were tested to specifically mimic the type I IFN response induced by the *Leishmania* virus LRV1 on the modulation of genes. The analysis generated 38 modules at 8 h p.i. and 31 modules at 24 h p.i., comprising a total of 11,442 and 11,426 genes, respectively (Figures 4A, B, *p*-values shown in Supplementary Figures S6C, D). As expected, the dendrogram displayed on top of each heatmap showed that modules representing the infection of *Ifnar*$^{-/-}$ cells with *Lgy*LRV1+ clustered closer to the modules of WT cells infected with *Lgy*LRV1-, than to the modules of WT cells infected with *Lgy*LRV1+, confirming the major impact that the recognition of type I IFNs had on the macrophages infected by *Lgy*LRV1+. At 8 h p.i. (Figure 4A), the addition of type I IFNs to *Lgy*LRV1- did not lead to a drastic effect as these groups clustered closer together with non-treated cells than with *Lgy*LRV1+. This result was not surprising as treatment with type I IFNs was only performed 6 h p.i. with *Lgy*LRV1- and thus cells were only exposed to type I IFNs for 2 h before sample collection. Nevertheless, four modules where the addition of type I IFNs showed an effect by shifting *Lgy*LRV1- closer together to *Lgy*LRV1+ and to poly I:C were identified: 8h_greenyellow (2,226 genes), 8h_mediumpurple3 (1,870 genes), 8h_firebrick4 (479 genes), and 8h_purple (424 genes). These modules contained genes whose expression was promptly modulated by type I IFNs, either exogenously added or produced in response to *Lgy*LRV1+. The heatmap for 24 h (Figure 4B) also showed the role of IFNAR in gene modulation as modules representing *Ifnar*$^{-/-}$ cells infected with *Lgy*LRV1+ clustered closer to modules representing WT infected with *Lgy*LRV1- rather than *Lgy*LRV1+. Furthermore, at 24 h, cells infected with *Lgy*LRV1- cluster together with non-treated cells. The addition of type I IFNs to *Lgy*LRV1- at 24 h leads to a new cluster further away from non-treated cells contrary to what was observed at 8 h, demonstrating the long-term effect of the type I IFN response. Modules in which the effect of type I IFNs was clearly observed were 24h_tan (579 genes), 24h_thistle2 (744 genes), 24h_thistle1 (680 genes), 24h_lightyellow (266 genes), 24h_darkturquoise (166 genes), 24h_lightsteelblue1 (1,020 genes), and 24h_magenta (1207 genes). Based on the total number of genes detected at 8 and 24 h (11,442 and 11,426, respectively), the percentages of genes modulated by type I IFNs at 8 and 24 h were 43.7% and 40.8%, respectively, showing the drastic impact that type I IFNs have on the concerted modulation of genes.

Following the approach described above, to determine and narrow down the importance of modules, the kTotal (the connectivity of the gene in the whole network) and adjusted R-squared (the proportion of the variance for expression that is explained by infection groups) of each gene were calculated at the two time points and plotted on the x-axis and y-axis, respectively (Figures 4C, D). From this analysis, two preponderant modules could explain the variance of the data at 8 h p.i. (modules with the highest kTotal and the highest adjusted R-squared, localized at the tip of the graph), namely, 8h_greenyellow and 8h_mediumpurple3 (Figure 4C), and four modules were found at the tip of the graph at 24 h p.i., namely, 24h_thistle1, 24h_thistle2, 24h_lightsteelblue1, and 24h_magenta (Figure 4D). Out of these six modules, three were enriched in pathways connected to the immune response, namely, 8h_greenyellow, 24h_thistle1, and 24h_thistle2. These modules were enriched in the following pathways: defense response to virus and protozoan and response to IFN-gamma, -beta, and -alpha; interleukin-6; and tumor necrosis factor productions, whereas the three other ones were enriched in RNA transcription and histone

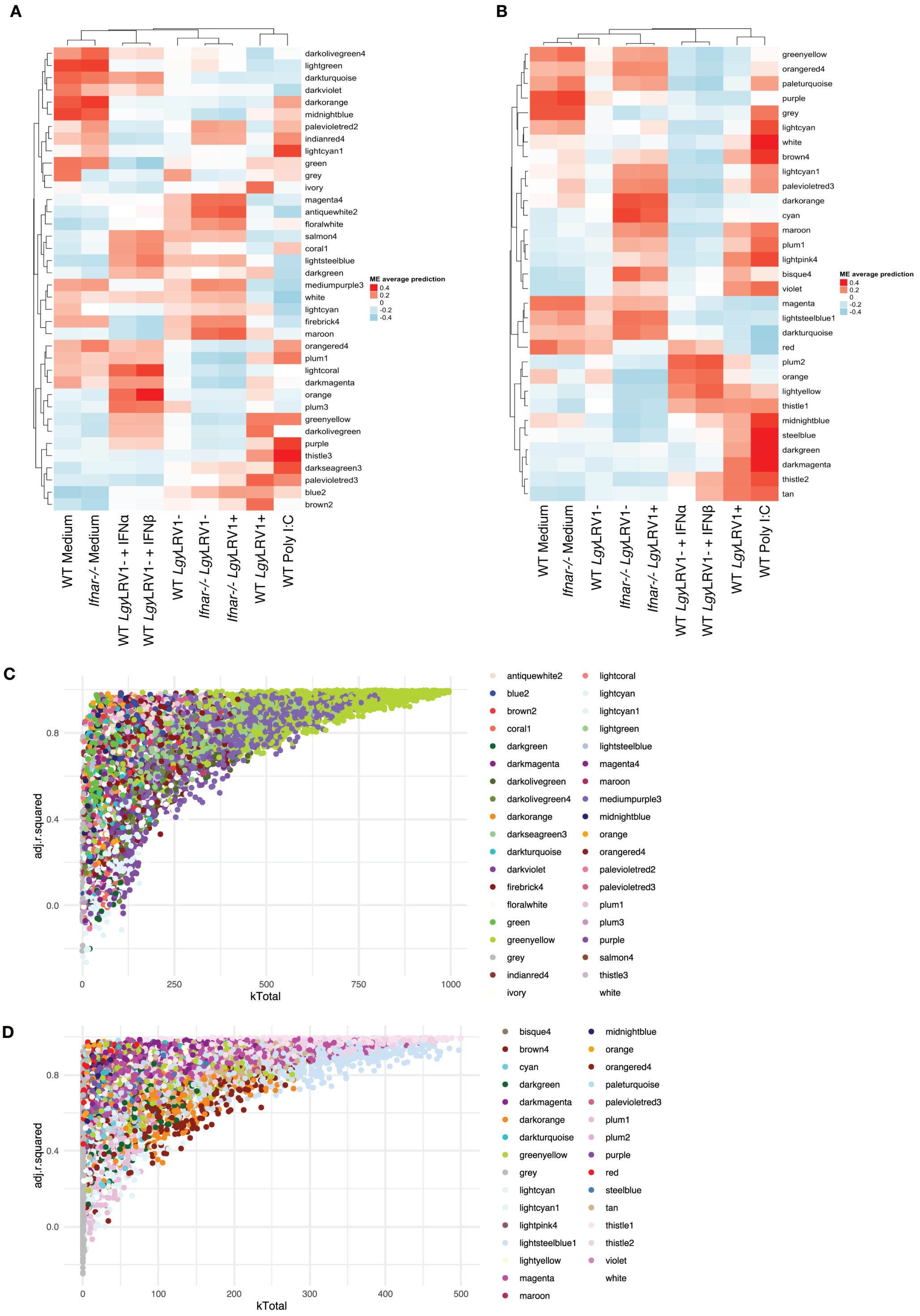

FIGURE 4

Type I IFNs play a preponderant and central role in the infection mounted by macrophages toward *Lgy*LRV1+. **(A)** Heatmap of the average predictions of the fitted linear model on each ME at the 8-h time point in WT + *Ifnar*$^{-/-}$ analysis. **(B)** Heatmap of average predictions of the fitted linear model on each ME at the 24-h time point in WT + *Ifnar*$^{-/-}$ analysis. **(C)** Scatter plot of kTotal (whole network connectivity) against adjusted R-squared for all genes in an 8-h network in WT + *Ifnar*$^{-/-}$ analysis. Genes are colored according to the module they belong to. **(D)** Scatter plot of kTotal (whole network connectivity) against adjusted R-squared for all genes in a 24-h network in WT + *Ifnar*$^{-/-}$ analysis. Genes are colored according to the module they belong to.

acetylation pathways, as well as in oxidation–reduction and metabolic processes (Supplementary Table S3). Curiously, one of the modules identified, the 8h_greenyellow module, was constituted of 2,224 genes, approximately one-fifth of all genes detected at 8 h in the RNA-Seq conducted, showing not only the importance but also the coordination of the early immune response in macrophages upon a challenge. Given the influence of hub genes in orchestrating the response of the modules, the top 1% genes with the highest kWithin of these two and four modules were examined at 8 and 24 h p.i. (Table 4). Interestingly, as examples *Cxcl11*, *Tgtp1*, and *Il27* (in the greenyellow module) at the 8-h time point; *Ifih1* and *Igtp* (in the thistle1 module), *Il15ra* and *Jak2* (in the thistle2 module) at the 24-h time point were found (Table 4) (for the whole lists of genes with their module membership and their connectivity at each time point, see Supplementary Table S1).

Overlap of highly connected modules at early and late time points uncovered the temporal dynamics of the interferon response

The greenyellow module identified at 8 h that represented a large proportion of the genes identified is also enriched in different Gos, including many related to immunity. However, at 24 h p.i., more than one module was enriched in Gos connected to immunity (Supplementary Table S3). To understand the temporal dynamics of the macrophage response, the overlap between the major module identified at 8 h and the modules identified at 24 h p.i. in the WT + *Ifnar*$^{-/-}$ analysis was evaluated. Interestingly, the upset graph (Figure 5A) showed that the 8h_greenyellow module overlapped very strongly with 24h_thistle1 and 24h_thistle2, 24h_tan, 24h_darkmagenta, and 24h_lightyellow. As previously mentioned, the striking GO terms enriched in immune-related Gos were found in 8h_greenyellow, 24h_thistle1, and 24h_thistle2. The predominant terms identified in the 8h_greenyellow module were also found at 24-h split into the 24h_thistle1 module (e.g., defense response to virus and protozoan, innate immune response, and cellular response to IFN-gamma and -beta) and 24h_thistle2 (e.g., a positive regulation of the ERK1 and ERK2 cascades, interleukin-12, and chemokine productions) (Supplementary Table S3). Intriguingly, other Gos that demonstrated a concerted modulation in 8h_greenyellow and were thus associated with initial immune responses were now split into 24h_tan (e.g., a negative regulation of the NF-kappaB transcription factor activity), 24h_darkmagenta (e.g., a positive regulation of the inflammatory response) and 24h_lightyellow (e.g., the regulation of cytokine secretion and the MyD88-dependent Toll-like receptor signaling pathway) (Supplementary Table S3 and data not shown). This latter part was interesting in terms of Gos that can be initially associated with the immune response toward invaders but were then separated. Remarkably, some other GO terms of the 8h_greenyellow module were not found significantly (p-value < 0.01) in any of the five modules cited above and identified in Figure 5A (e.g., a negative regulation of interleukin-10 production). These results pointed toward the dynamic nature of the response, being more concerted at 8 h and then split into the groups of genes with slightly different modulations and thus ending up in different modules.

To further dissect the temporal dynamic of the macrophage response toward infection, the CC of each gene in the network was calculated at 8 and 24 h p.i., then plotted on x- and y-axes, respectively. This measure allowed us to identify genes that were best placed to influence the entire network as regulators and important signal transducers. The different categories of genes regarding their position on the CC plot are shown in Figure 5B. Strikingly, there were genes with very low centrality (below 0.05) at 8 h (on the y-axis) and at 24 h (on the x-axis), 76 genes versus 1567 genes, respectively (approximately 20 times more), suggesting that these genes were essential at 24 h versus 8 h p.i., respectively. The great difference in the number of genes in these two groups showed that many central events could happen at 8 h, right at the beginning of the infection, losing its importance later on or setting the stage for the later events. At

TABLE 4 The top 1% genes with the highest kWithin of the preponderant modules that explain the variance of the data in WT + *Ifnar*$^{-/-}$ analysis at 8 and 24 h p.i.

Time point	Module	Top 1% genes
8h	greenyellow	*Tbc1d13, Mier3, Cxcl11, Tgtp1, Papd4, Snx2, Zfp319, Prpf38a, Mpp1, Hdc, Plekha2, Fbxw11, G3bp2, March5, Dync1i2, Il27, Khdrbs1, Mxd1,* *Fbxo7, Rnf31, A630012P03Rik, Gnb4, Snw1*
	mediumpurple3	*Mlec, Arrb1, Fbxo31, Scd2, Trim37, Lactb2, Ddhd2, Zfp146, Klc4, Mcm2, Rrp1b, 2410002F23Rik, Polrmt, Trmt2a, Mettl13, Nfx1, Lpin1, Rxra, Aco1*
24h	thistle1	*Ifih1, Sp110, Daxx, Samhd1, Tor1aip1, Igtp, Parp12*
	thistle2	*Rnf19b, Il15ra, Tbc1d13, Ttc9c, Peli1, Rapgef2, Jak2, Cflar*
	lightsteelblue1	*Slc25a4, Amz1, Rpl3, Zfp664, Mgst3, Gusb, Pabpc4, Smyd2, Sfxn1, Fgfr1, Mlec*
	magenta	*Ank, Aldh9a1, Adcy9, St6gal1, Man1c1, Igfbp4, Zfyve28, Klhl42, Sh3pxd2a, Prkar2a, Pygl, Deptor, B3glct*

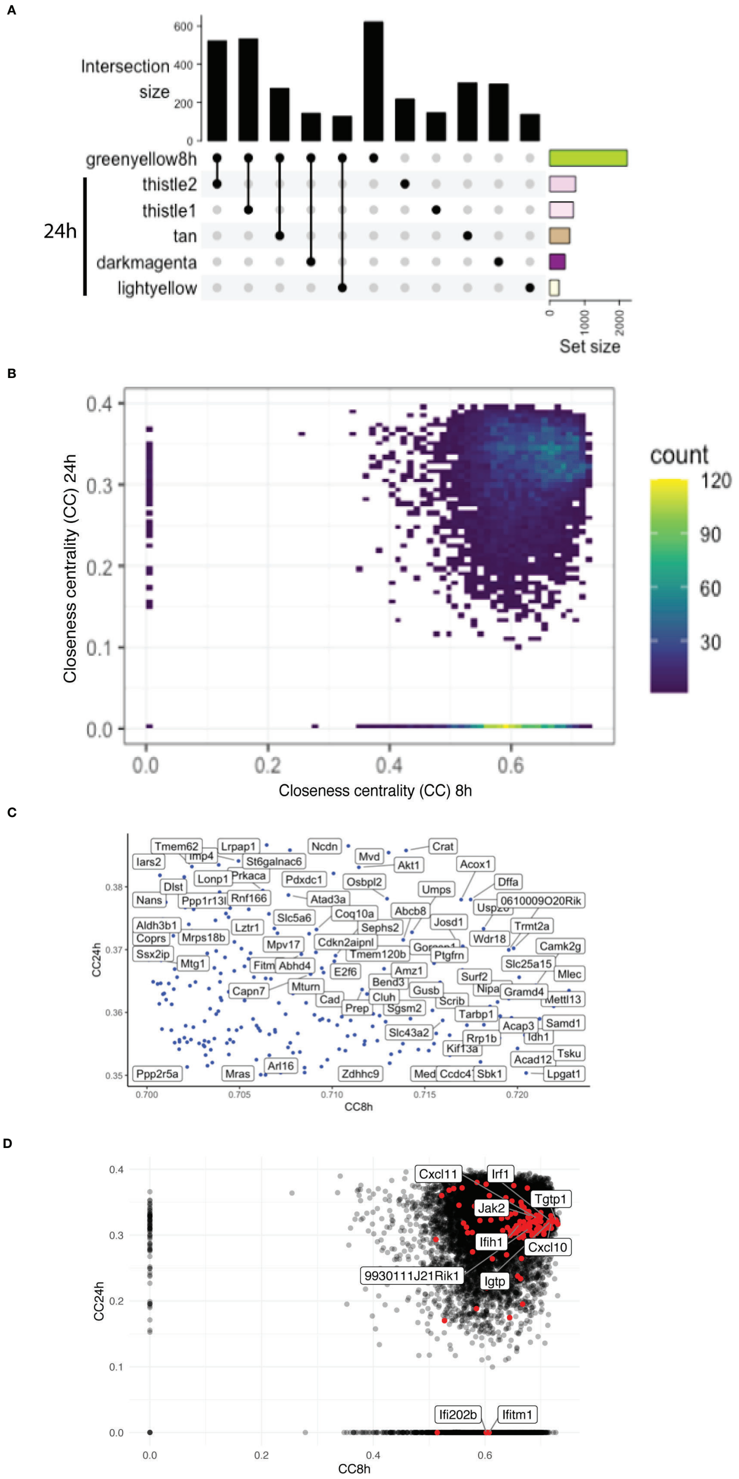

FIGURE 5
Overlap of highly connected modules at early and late time points uncovers the temporal dynamics of the interferon response. **(A)** An UpSet plot of the 8h_greenyellow module overlapping with the modules at the 24-h time point in WT + Ifnar-/- analysis. Top five overlapping modules are shown. Intersection size is shown in the y-axis. The bottom-right part shows the total module size. **(B)** Density plot of the CC of genes in the WGCNA network at 8 h (x-axis) against 24 h (y-axis) in WT + Ifnar-/- analysis. Count unit corresponds to the number of genes in each rectangle. **(C)** Zoom of the tip of the CC plot. Genes with very high centrality at both 8 and 24 h p.i. **(D)** Scatter plot of CC of genes in the WGCNA network at 8 h (x-axis) against 24 h (y-axis) in WT + Ifnar-/- analysis. Positions of ISGs are highlighted in red and the names of 10 examples are shown.

8 h, the predominant GO terms were related to the RNA polymerase II pathway such as the positive regulation of transcription and transcription initiation from the RNA polymerase II promoter (Figure 6). To sum up, 23 terms were enriched in RNA polymerase II processes in comparison to only 12 terms related to both RNA polymerase I and III pathways (for example, a positive regulation of the transcription from the RNA polymerase I promoter and RNA polymerase III promoter, respectively) (Figure 6). In contrast, no relevant GO term was found enriched in the set of 76 genes with high CC at 24 h p.i. and very low at 8 h p.i. On the CC plot, the blue-to-yellow scale (density) represents the number of genes per position. A "hotspot" with the highest density, localized on the x-axis (i.e., with very low CC at a 24-h time point), with a CC value approximately 0.6 at an 8-h time point was pinpointed. This "hotspot" of genes belonged to the 1,567 genes mentioned before (with very low centrality at 24 h p.i.).

The tip of the CC plot was defined by genes with very high centrality both at 8 and at 24 h p.i. The genes present at the tip of the CC plot belonged to the modules 8h_greenyellow, 8h_lightgreen, and most importantly 8h_mediumpurple3 (Figure 5C). As mentioned previously, this last module was globally enriched in GO terms linked to transcription, meaning that these pathways initially influenced the network the most. While there were three modules from the 8-h modules, the genes at the tip were divided into more than 10 modules from the 24-h modules (higher than four times more). For example, the tip of the CC plot included Akt1, a member of the protein kinase B family, known to be involved in macrophage survival and parasite persistence (Eren et al., 2016).

Given the high and central importance of type I IFNs in the modulation of the transcript response and the outcome of an infection by LgyLRV1+, a non-exhaustive list of genes stimulated by type I IFNs was established from the GO database and some other references and their position on the CC plot evaluated (Figure 5D). Genes from three GO terms were compiled: cellular response to IFN-alpha (GO:0035457), cellular response to IFN-beta (GO:0035458), and cellular response to type I IFN (GO:0071357). In addition, genes cited in different publications were also considered (Zhao et al., 2009; Schoggins and Rice, 2011; Rand et al., 2012; Cheon et al., 2014; Manjunath et al., 2017; Nasr et al., 2017; Pervolaraki et al., 2018; Ashley et al., 2019; Yang et al., 2020). Thus, the list comprised a total of 175 genes analyzed at 8 and 24 h p.i. in WT + *Ifnar*$^{-/-}$ analysis. Among them, 139 and 138 genes were detected at 8 and 24 h p.i., respectively. The consistency of detection between early and late time points showed a sustained induction of IFN-stimulated genes (ISGs). However, there was one gene detected at 8 h p.i. but not at 24 h p.i.: *Ifi202b* (Supplementary Table S4). The membership status of the whole list of detected genes was then investigated, and, as expected, the main modules related to immune pathways were predominant. More than half of the ISGs detected at 8 and 24 h p.i. belong to the 8h_greenyellow (96 genes) and its overlapping 24h_thistle1 and 24h_thistle2 modules (70 + 20 = 90 genes), respectively. Nevertheless, the early gene, *Ifi202b*, belonged to the 8h_blue2 module (Supplementary Table S4). To confront these ISGs to the CC analysis, the 175 genes were sought, and the detected ones are highlighted (in red in Figure 5D). The five top genes were *Myd88*, *Tgtp1*, *Mov10*, *Trim21*, and *Samhd1* showing the highest CC values at 8 h p.i. (>0.72) and *Irak1*, *Sun2*, *Ttll12*, *Mmp12*, and *Ube2g2* with the highest CC values at 24 h p.i. (>0.37) (Figure 5D, Supplementary Table S4). *Ifi202b* has a CC value of 0.60 at 8 h p.i. and is localized on the x-axis; thus, it is part of the "hotspot" already defined before (Figure 5B). Even if detected at 24 h p.i., another ISG with a very low CC value (below 0.05) at 24 h p.i. belonged to this "hotspot" and was found on the x-axis: *Ifitm1* (8h_CC value of 0.61) (Figures 5B, D, Supplementary Table S4). *Ifitm1* was part of the 8h_plum1 module, while, as expected at 24 h p.i., it was included in 24h_grey, a label reserved to genes that was not part of any module (Supplementary Table S4). Therefore, these two genes, *Ifi202b* and *Ifitm1*, seemed to be very central at the early time point, suggesting that they were both important at 8 h p.i. and not at 24 h p.i.

Discussion

Many studies have addressed, using RNA-Seq, the transcriptional changes in the macrophage response upon *Leishmania* infection (Salloum et al., 2021). Traditionally, these studies have investigated differentially expressed genes with significantly altered expression across the groups of samples. However, moving from a gene-by-gene analysis to function is very challenging. In that regard, network analysis methods, such as WGCNA, have the advantage to provide a comprehensive view at the system level. As an unsupervised algorithm, WCGNA can establish and detect the relationship between gene expression and phenotypic traits. Moreover, WGCNA has the advantage over other methods in analyzing multivariate and complex datasets (Langfelder and Horvath, 2008). Indeed, WGCNA allows to condense a large network of genes into a limited number of variables (i.e., modules). Furthermore, WGCNA permits the identification of hub genes that play a central role in driving the system of interest. While an WGCNA approach has already been conducted in the blood of patients (Gardinassi et al., 2016) and the popliteal lymph nodes of dogs (Sanz et al., 2021) infected with *L. infantum* as well as in the cutaneous lesions of *L. braziliensis*–infected patients (Christensen et al., 2016) and *L. major*–infected human dendritic cells (Zhao et al., 2019), no WGCNA investigation has been piloted on *Leishmania*-infected macrophages. Aside from being, to our knowledge, the first study where WGCNA was conducted in *Leishmania*-infected macrophages *in vitro*, this study also represents the first comprehensive transcriptional

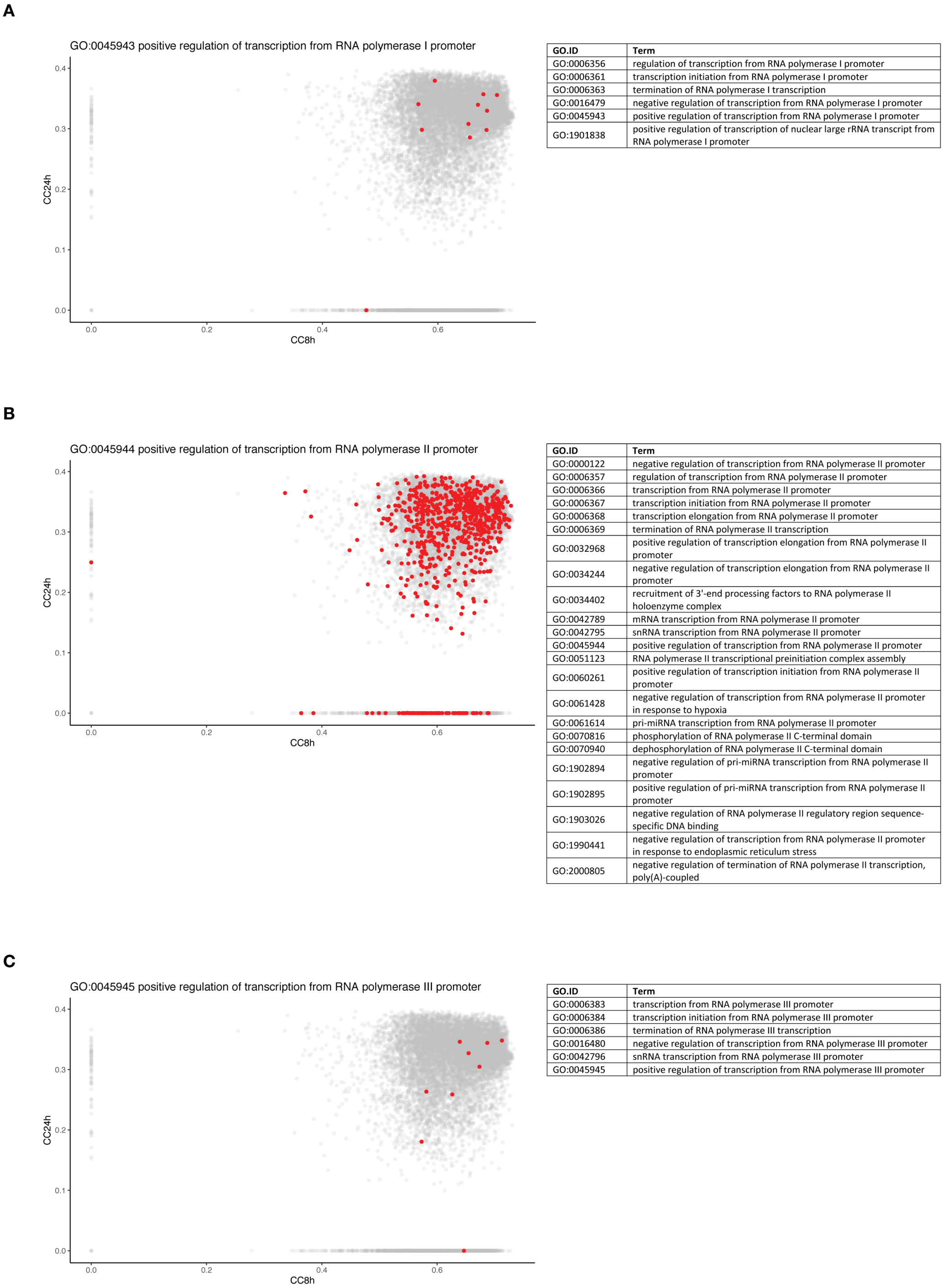

GO.ID	Term
GO:0006356	regulation of transcription from RNA polymerase I promoter
GO:0006361	transcription initiation from RNA polymerase I promoter
GO:0006363	termination of RNA polymerase I transcription
GO:0016479	negative regulation of transcription from RNA polymerase I promoter
GO:0045943	positive regulation of transcription from RNA polymerase I promoter
GO:1901838	positive regulation of transcription of nuclear large rRNA transcript from RNA polymerase I promoter

GO.ID	Term
GO:0000122	negative regulation of transcription from RNA polymerase II promoter
GO:0006357	regulation of transcription from RNA polymerase II promoter
GO:0006366	transcription from RNA polymerase II promoter
GO:0006367	transcription initiation from RNA polymerase II promoter
GO:0006368	transcription elongation from RNA polymerase II promoter
GO:0006369	termination of RNA polymerase II transcription
GO:0032968	positive regulation of transcription elongation from RNA polymerase II promoter
GO:0034244	negative regulation of transcription elongation from RNA polymerase II promoter
GO:0034402	recruitment of 3'-end processing factors to RNA polymerase II holoenzyme complex
GO:0042789	mRNA transcription from RNA polymerase II promoter
GO:0042795	snRNA transcription from RNA polymerase II promoter
GO:0045944	positive regulation of transcription from RNA polymerase II promoter
GO:0051123	RNA polymerase II transcriptional preinitiation complex assembly
GO:0060261	positive regulation of transcription initiation from RNA polymerase II promoter
GO:0061428	negative regulation of transcription from RNA polymerase II promoter in response to hypoxia
GO:0061614	pri-miRNA transcription from RNA polymerase II promoter
GO:0070816	phosphorylation of RNA polymerase II C-terminal domain
GO:0070940	dephosphorylation of RNA polymerase II C-terminal domain
GO:1902894	negative regulation of pri-miRNA transcription from RNA polymerase II promoter
GO:1902895	positive regulation of pri-miRNA transcription from RNA polymerase II promoter
GO:1903026	negative regulation of RNA polymerase II regulatory region sequence-specific DNA binding
GO:1990441	negative regulation of transcription from RNA polymerase II promoter in response to endoplasmic reticulum stress
GO:2000805	negative regulation of termination of RNA polymerase II transcription, poly(A)-coupled

GO.ID	Term
GO:0006383	transcription from RNA polymerase III promoter
GO:0006384	transcription initiation from RNA polymerase III promoter
GO:0006386	termination of RNA polymerase III transcription
GO:0016480	negative regulation of transcription from RNA polymerase III promoter
GO:0042796	snRNA transcription from RNA polymerase III promoter
GO:0045945	positive regulation of transcription from RNA polymerase III promoter

FIGURE 6
Genes from RNA polymerase II pathway are predominantly central at early time point. Density plots of the CC of genes in the WGCNA network at 8 h (x-axis) against 24 h (y-axis) in WT + *Ifnar*$^{-/-}$ analysis. Genes belonging to the examples of RNA polymerase I **(A)**, II **(B)**, and III **(C)** processes are highlighted in red. The lists of GO terms found for RNA polymerase I (Table A), II (Table B), and III (Table C) keywords are listed.

study addressing the response mounted by macrophages upon infection by *Lgy*LRV1+, thus addressing the impact the presence of LRV1 has on the macrophage response (Cantacessi et al., 2015; Salloum et al., 2021). The present WGCNA identified biologically relevant groups of transcripts, classified into modules, that were modified upon macrophage infection by *Lgy*LRV1- and *Lgy*LRV1+ after 8 or 24 h of infection. These modules were further analyzed and key pathways and hub genes associated with *Leishmania*, with LRV1 or with the exacerbatory effect of LRV1 in *Lgy*LRV1+, were identified. Additionally, the impact of type I IFNs on the transcriptional profile of macrophages upon *Lgy*LRV1+ infection was evaluated.

The major impact of LRV1 and the relevance of type I interferons

Globally, this study showed that the presence of LRV1 had a major impact in the transcriptomic profile of macrophages both at 8 and 24 h p.i. The LRV1 and the “exacerbatory” modules, that is, modules reflecting the effect of the presence of LRV1 on top of the presence of *Leishmania*, were identified and shown to represent a very considerable part of the overall transcriptomic change (representing together 53.3% and 42.5% at 8 and 24 h p.i.). The immunophenotype associated to the presence of LRV1, or to other viruses, was shown to be highly dependent on the systemic production of type I IFNs (Rossi et al., 2017; Rossi and Fasel, 2018b; Rath et al., 2019; Heirwegh et al., 2021). Although type I IFNs, such as IFN-α and IFN-β, are crucial for viral clearance, their influence during a *Leishmania* infection appears to be highly contextual. Type I IFNs have a worsening effect on the outcome of *L. guyanensis*, while in the case of *L. major*, the addition of type I IFNs promotes the resolution of infection (Hartley et al., 2014). Here, we show the massive role that the production of type I IFNs downstream of the recognition of LRV1 has at a transcriptional level influencing 43.7% and 40.8% of all transcriptional changes at 8 and 24 h p.i. Type I IFNs are produced by different cell types including macrophages and can act both in an autocrine and paracrine manner. The recognition of type I IFN by the IFNAR receptor (a complex composed of two subunits: IFNAR1 and IFNAR2) initiates a signaling cascade, leading to the expression of a vast panel of ISGs (IFN-stimulated genes) with a positive feedback loop and also direct antiviral effects (Sadler and Williams, 2008). Many studies have investigated the induction of some ISGs in response to a viral infection, for example, adenovirus, morbillivirus, retrovirus, vesiculovirus, herpesvirus, and paramyxovirus infections (Zhao et al., 2009; Manjunath et al., 2017; Nasr et al., 2017; Pervolaraki et al., 2018; Ashley et al., 2019; Yang et al., 2020). Interestingly, some of the hub genes found in the WT and WT + *Ifnar*$^{-/-}$ analyses (Figure 2, Table 4) were part of the ISGs such as *9930111J21Rik1*, *Cxcl10*, *Cxcl11*, *Ifih1*, *Igtp*, *Irf1*, *Jak2*, and *Tgtp1* in WT + *Ifnar*$^{-/-}$ analysis (Supplementary Table S4). The chemokine CXCL10 has been demonstrated to be linked to the endosymbiotic LRV1 (Ives et al., 2011; Kariyawasam et al., 2017) and the *Leishmania* evasion from the host (Antonia et al., 2019).

TNF-α and IL-6 regulation as evidence of the crosstalk between modules

Hyperinflammation is a hallmark of an *Lgy*LRV1+ infection (Ives et al., 2011). Two major mediators of inflammation contributing to this immunophenotype are the cytokines IL-6 and TNF-α. Surprisingly, these two molecules were found present in two distinct modules: IL-6 was found in the 8h_coral 3 (an LRV1-associated module), while TNF-α was found associated to the 8h_bisque4 modules (an “exacerbatory” module of WT analysis). In addition to TNF-α, CXCL10 (one of the top five hub genes), and CCL5, two chemokines also found to be the hallmarks of the inflammation caused by *Lgy*LRV1+ infection were also found to be present in the 8h_bisque4. Interestingly, even though IL-6 is not found in the 8h_bisque4, this module was shown to be enriched in the GO term “positive regulation of IL-6.” Further analysis of both 8h_bisque4 and 8h_coral3 modules revealed that the members of the Src-family kinase (SFK) were also found in these two modules. Src and Hck were also found present in the 8h_bisque 4 together with TNF-α, whereas the other members of the SFK-family such as Lyn and Lck were found present in the 8h_coral3 module, the module that contains IL-6. This specific distribution of SFK is particularly relevant since, from our previous studies, it was shown that KB-SRC4, a specific inhibitor of c-Src, blocks IL-6 but not TNF-α (Brandvold et al., 2012; Reverte et al., 2021). On the contrary, PP2, which efficiently blocks Fyn, Hck, and Lck, inhibits TNF-α but not IL-6 secretion (Hanke et al., 1996; Reverte et al., 2021). Thus, it is interesting to underline not only the relevance of SFKs in TNF-α and IL-6 secretion but also the crosstalk between two modules containing genes upregulated in *Lgy*LRV1+-infected cells. Interestingly, Csk, the kinase that regulates the intramolecular inhibition of SFKs, was also identified in the 8h_coral3 module. This module also includes important genes, such as IL-1 or IFN-γ previously associated with the presence of LRV1 (Ives et al., 2011; Hartley et al., 2016; Rossi et al., 2017; Kariyawasam et al., 2017; Castiglioni et al., 2017) as well as other genes *Il18*, *Ccl8*, *Socs 2*, *Casp3*, *Il10*, *Jun*, *Jak3*, *Bcl10*, and *Ly6e* implicated in the response to *Leishmania* infection. Overall, these data highlight a physiological and phenotypically relevant crosstalk between two different modules. Moreover, since the role of IL-6 has been considered, by Osero et al., one of the greatest oxymora in the leishmaniasis outcome due to different studies showing discordant roles (Osero et al., 2020), this crosstalk also pointed toward the relevance that a module associated in this study to an LRV1 module may contribute to the leishmaniasis outcome.

IL-15 as a possible important hub

As mentioned above, the WGCNA analysis identifies hub genes that play a central role in a given module, that is, genes most likely to influence the whole module and thus drive its enriched pathways. Among the hubs identified, one gene, found in both analyses, is *Il15ra*, encoding for the receptor of the interleukin, IL-15 (Figure 2, Table 4). This cytokine, in combination with IL-12, stimulates the cellular immune response in dogs and humans with visceral leishmaniasis (Milano et al., 2002; Costa et al., 2020). Similarly, another cytokine-related gene was observed as a driver gene but only in WT + *Ifnar*$^{-/-}$, for example, *Il27*. IL-27 is associated with resistance or susceptibility to *Leishmania* infection (Jafarzadeh et al., 2020) and to the antiviral response to several RNA viruses, such as HIV, Hepatitis C Virus (HCV), or Chikungunya Virus (CHIKV) (Valdés-López et al., 2022). Interestingly, *Il15*, *Il15ra*, *Il12a*, *Il12b*, and *Il27* genes were all present in the same "exacerbatory" module at 8 h p.i. (8h_bisque4), then separated into the 24h_brown (for *Il15* and *Il15ra*) and 24h_turquoise (for *Il12b* and *Il27*) modules, associated to LRV1 and exacerbatory phenotypes in WT analysis.

Activation of specific transcription factors in response to LRV1

Given the described importance of LRV1 in the leishmaniasis outcome, progression, relapse, and treatment failure, hub genes associated to the presence of LRV1 are of utmost interest when designing strategies to fight leishmaniasis (Hartley et al., 2014; Adaui et al., 2016; Bourreau et al., 2016; Rossi et al., 2017). Several relevant transducers and transcription factors were present in the 8h_coral3 and 8h_bisque4 modules in WT analysis (e.g., Myd88, Keap1, Tank, Ikbke, Stat1, Stat2, Irf1, Irf5, Irf7, Ets2, and Xbp1). For example, *Irf1* was part of the "exacerbatory" 8h_bisque4 module. IRF1 participates in the expression of cytokines such as CCL5 and CXCL10. The lack of IRF1 shows a dramatically exacerbated leishmaniasis disease in *L. major*–infected mice associated with a decrease of IFN-γ and IL-12 productions (Lohoff et al., 1997). IRF1 is also involved in antiviral responses against dsRNA viruses, for example, HCV (Pflugheber et al., 2002; Feng et al., 2017). Furthermore, *Igf1r* was a driver gene in WT analysis and belonged to the 24h_yellow module and the "exacerbatory" group. Similarly, the insulin-like growth factor 1 receptor (IGF1R) has previously been shown to be involved in arginase (Arg1) expression in visceral leishmaniasis (Osorio et al., 2014) and also targeted by rotaviruses, dsRNA viruses, to manipulate the PI3K/Akt pathway and block autophagy (Zhou et al., 2018). More intriguingly, several transcription factors were found among the list of these hub genes in WT analysis, such as *Sp1*. Sp1 that belonged to the 24h_plum1 is involved in the evasion mechanisms of *Leishmania*. Different species can induce the binding of Sp1 on *Il10*, *Ucp2*, and *Hdac1* promoters in macrophages, resulting in the production of the inhibitory IL-10 cytokine, the suppression of oxidative burst, and a decrease of iNOS expression, respectively (Yang et al., 2007; Basu Ball et al., 2014; Calegari-Silva et al., 2018).

Interferon-stimulated genes and temporal expression

Some studies have analyzed different time points following an infection challenge and revealed that IFN-stimulated genes (ISGs) can be temporally expressed: earlier or later, in order to specifically target and counteract different steps of the virus life cycle (Zhao et al., 2009; Manjunath et al., 2017; Nasr et al., 2017; Pervolaraki et al., 2018). The analysis of the closeness centrality of some ISGs brought two genes to the forefront, *Ifi202b* and *Ifitm1*, which were shown to be central at an 8-h time point only (Figure 5, Supplementary Table S4). Therefore, these two candidates could be decisive in the early events happening during the cellular response and could represent new targets to further investigate. On one hand, *Ifi202b*, also known as IFN-activated gene 202B and encoding for the P202 protein, belongs to the pyrin and HIN domain–containing (PYHIN) proteins, as AIM2 and IFI16 (Wang et al., 2018). In several studies, *Ifi202b* has been associated with sex differences in autoimmune diseases (Panchanathan et al., 2011; Cao et al., 2018) and this question has recently been addressed in the *Leishmania* inflammation context (Lockard et al., 2019; Snaka et al., 2022). Likewise, *Ifi202b* has been shown to be upregulated upon *L. major* footpad infection in C57BL/6 mice (Ehrchen et al., 2010) and its corresponding P202 protein to exert an inhibitory effect on the AIM2 inflammasome (Wang et al., 2018). On the other hand, Ifitm1, encoding the IFN-induced transmembrane protein 1 (IFITM1), is known to have a role in the restriction of many RNA viruses, such as HIV (Chutiwitoonchai et al., 2013) or HCV (Narayana et al., 2015).

Toward strategies to face *Leishmania*-virus coinfections and beyond

The apparent disproportional response toward a non-pathogenic element such as LRV1 has the potential to change the outcome of the infection by a pathogenic element such as *Leishmania*. Although LRV1 is only present in some strains of *Leishmania*, the results presented here can have a broader impact: the modulation of leishmaniasis by endogenous or exogenous viruses is particularly relevant as the vector of *Leishmania*, the phlebotomine sand flies, also carries phleboviruses such as Toscana virus shown previously to cause the same phenotype as the presence of LRV1 when coadministered with *Leishmania*. Additionally, the effect that virus can have go beyond LRV1 or the coadministration of phlebovirus during a sand fly bite. Mice challenged with a virus, such as LCMV, upon the resolution of *Leishmania* infection, led to a relapse of the *Leishmania* infection showing that exacerbation and the metastatic phenotype are not always linked to the presence of LRV1 (Valencia et al., 2022) but could also be related to the presence of other viruses (Rossi et al., 2017; Rath et al., 2019; Heirwegh et al., 2021). By exposing the modules and pathways affected by LRV1 as well as the hub genes responsible for driving such events, this study can contribute to the future design of strategies to deal with a *Leishmania*-viral coinfection.

The RNA-Seq data used in this manuscript are available to all communities through the website https://amelbek.shinyapps.io/fasel_lab_data/ where individual or groups of genes can be visualized in different genotypes of macrophages (as the data for this study were part of larger datasets containing additional mouse genotypes IFNAR-/-, IFNg-/-, iNOS-/-, NLRX1-/-, NOX2-/-, and PRX5-/-). The data can be downloaded for further statistical analysis. Thus, this study and these datasets also constitute a resource that can be further explored to study the impact of *Leishmania* on the macrophage response and on the importance of viral coinfections or type I IFNs and beyond in the outcome of leishmaniasis.

Data availability statement

The datasets presented in this study can be found in online repositories. The names of the repository/repositories and accession number(s) can be found below: https://www.ncbi.nlm.nih.gov/geo/, GSE201120, https://www.ncbi.nlm.nih.gov/geo/, GSE203088.

Ethics statement

The animal study was reviewed and approved by Veterinary Commission of the Canton de Vaud (SCAV, Switzerland).

Author contributions

NI, FT, TS, CD, DK, FP, and MR performed experiments. AB analyzed the data. FT, AB, and NI wrote the manuscript. FT, AB, NI, IX, and NF interpreted and discussed the data. TS, SC, IX, and NF reviewed and edited the manuscript. All authors contributed to the article and approved the submitted version.

Funding

This work was supported by the grant from the Swiss National fund for research to NF (Grant No. 310030_173180) and the grant from Foundation Pierre Mercier pour la science to FT.

Acknowledgments

The authors thank the veterinary and animal facility staff at CIIL for ensuring animal welfare and ethical standards. Library preparation, sequencing and raw data normalization were performed at the Lausanne Genomic Technologies Facility (GTF), University of Lausanne (UNIL), Switzerland (https://wp.unil.ch/gtf/). The authors specially thank the following members of the facility for their support: Leonore Wigger, Sandra Calderon, Julien Marquis, Hannes Richter, Johann Weber, Roberto Sermier, and also the former members, Sylvain Pradervand, Floriane Consales Barras and Keith Harshman. The authors thank Matteo Rossi for his help with the initiation of the study and Alexander Miesch for his precious assistance and patience in making the data available. The authors are very thankful to Slavica Masina for her critical reading.

Conflict of interest

The authors declare that the research was conducted in the absence of any commercial or financial relationships that could be construed as a potential conflict of interest.

Publisher's note

Supplementary material

The Supplementary Material for this article can be found online at: https://www.frontiersin.org/articles/10.3389/fcimb.2022.941888/full#supplementary-material

References

Adaui, V., Lye, L. F., Akopyants, N. S., Zimic, M., Llanos-Cuentas, A., Garcia, L., et al. (2016). Association of the endobiont double-stranded RNA virus LRV1 with treatment failure for human leishmaniasis caused by leishmania braziliensis in Peru and Bolivia. *J. Infect. Dis.* 213 (1), 112–121. doi: 10.1093/infdis/jiv354

Alexa, A., and Rahnenfuhrer, J. (2016). topGO: Enrichment analysis for gene ontology. r package version. *Bioconductor* 2(0). doi: 10.18129/B9.bioc.topGO

Anders, S., Pyl, P. T., and Huber, W. (2015). HTSeq–a Python framework to work with high-throughput sequencing data. *bioinformatics* 31 (2), 166–169. doi: 10.1093/bioinformatics/btu638

Antonia, A. L., Gibbs, K. D., Trahair, E. D., Pittman, K. J., Martin, A. T., Schott, B. H, et al. (2019). Pathogen evasion of chemokine response through suppression of CXCL10. *Front. Cell. Infect. Microbiol.* 9, 280–280. doi: 10.3389/fcimb.2019.00280

Aoki, J. I., Muxel, S. M., Zampieri, R.A ., Laranjeira-Silva, M. F., Muller, K. E., Nerland, A. H, et al. (2017). RNA-Seq transcriptional profiling of leishmania amazonensis reveals an arginase-dependent gene expression regulation. *PloS Negl. Trop. Dis.* 11 (10), e0006026. doi: 10.1371/journal.pntd.0006026

Aoki, J. I., Muxel, S. M., Zampieri, R. A., Muller, K. E., Nerland, A. H., and Floeter-Winter, L. M. (2019). Differential immune response modulation in early leishmania amazonensis infection of BALB/c and C57BL/6 macrophages based on transcriptome profiles. *Sci. Rep.* 9 (1), 19841. doi: 10.1038/s41598-019-56305-1

Ashburner, M., Ball, C. A., Blake, J. A., Botstein, D., Butler, H., Cherry, J. M, et al. (2000). Gene ontology: tool for the unification of biology. the gene ontology consortium. *Nat. Genet.* 25 (1), 25–29. doi: 10.1038/75556

Ashley, C. L., Abendroth, A., McSharry, B. P., and Slobedman, B. (2019). Interferon-independent innate responses to cytomegalovirus. *Front. Immunol.* 10, 2751. doi: 10.3389/fimmu.2019.02751

Basu Ball, W., Mukherjee, M., Srivastav, S., and Das, P. K. (2014). Leishmania donovani activates uncoupling protein 2 transcription to suppress mitochondrial oxidative burst through differential modulation of SREBP2, Sp1 and USF1 transcription factors. *Int. J. Biochem. Cell Biol.* 48, 66–76. doi: 10.1016/j.biocel.2014.01.004

Bourreau, E., Ginouves, M., Prevot, G., Hartley, M. A., Gangneux, J. P., Robert-Gangneux, F., et al. (2016). Presence of leishmania RNA virus 1 in leishmania guyanensis increases the risk of first-line treatment failure and symptomatic relapse. *J. Infect. Dis.* 213 (1), 105–111. doi: 10.1093/infdis/jiv355

Brandvold, K. R., Steffey, M. E., Fox, C. C., and Soellner, M. B. (2012). Development of a highly selective c-src kinase inhibitor. *ACS Chem. Biol.* 7 (8), 1393–1398. doi: 10.1021/cb300172e

Burza, S., Croft, S. L., and Boelaert, M. (2018). Leishmaniasis. *Lancet* 392 (10151), 951–970. doi: 10.1016/S0140-6736(18)31204-2

Calegari-Silva, T. C., Vivarini, Á.C., Pereira, R. d. M. S., Dias-Teixeira, K. L., Rath, C. T., Pacheco, A. S. S., et al. (2018). Leishmania amazonensis downregulates macrophage iNOS expression via histone deacetylase 1 (HDAC1): a novel parasite evasion mechanism. *Eur. J. Immunol.* 48 (7), 1188–1198. doi: 10.1002/eji.201747257

Cantacessi, C., Dantas-Torres, F., Nolan, M.J., and Otranto, D. (2015). The past, present, and future of leishmania genomics and transcriptomics. *Trends Parasitol.* 31 (3), 100–108. doi: 10.1016/j.pt.2014.12.012

Cantanhede, L. M., da Silva Junior, C. F., Ito, M. M., Felipin, K. P., Nicolete, R., Salcedo, J. M, et al. (2015). Further evidence of an association between the presence of leishmania RNA virus 1 and the mucosal manifestations in tegumentary leishmaniasis patients. *PloS Negl. Trop. Dis.* 9 (9), e0004079. doi: 10.1371/journal.pntd.0004079

Cao, Y., Wang, L., Wang, C.-Y., Ye, J., Wang, Y., Li, T., et al. (2018). Sex differences in correlation with gene expression levels between Ifi200 family genes and four sets of immune disease-relevant genes. *J. Immunol. Res.* 2018, 1290814–1290814. doi: 10.1155/2018/1290814

Castiglioni, P., Hartley, M. -A., Rossi, M., Prevel, F., Desponds, C., Utzschneider, D. T, et al. (2017). Exacerbated leishmaniasis caused by a viral endosymbiont can be prevented by immunization with its viral capsid. *PloS Negl. Trop. Dis.* 11 (1), e0005240–e0005240. doi: 10.1371/journal.pntd.0005240

Chandrakar, P., Parmar, N., Descoteaux, A., and Kar, S. (2020). Differential induction of SOCS isoforms by leishmania donovani impairs macrophage-T cell cross-talk and host defense. *J. Immunol.* 204 (3), 596–610. doi: 10.4049/jimmunol.1900412

Chaparro, V., Graber, T.E., Alain, T., and Jaramillo, M. (2022). Transcriptional profiling of macrophages reveals distinct parasite stage-driven signatures during early infection by leishmania donovani. *Sci. Rep.* 12 (1), 6369. doi: 10.1038/s41598-022-10317-6

Cheon, H., Borden, E. C., and Stark, G. R. (2014). Interferons and their stimulated genes in the tumor microenvironment. *Semin. Oncol.* 41 (2), 156–173. doi: 10.1053/j.seminoncol.2014.02.002

Christensen, S. M., Dillon, L. A., Carvalho, L. P., Passos, S., Novais, F. O., Hughitt, V. K, et al. (2016). Meta-transcriptome profiling of the human-leishmania braziliensis cutaneous lesion. *PloS Negl. Trop. Dis.* 10 (9), e0004992. doi: 10.1371/journal.pntd.0004992

Chutiwitoonchai, N., Hiyoshi, M., Hiyoshi-Yoshidomi, Y., Hashimoto, M., Tokunaga, K., and Suzu, S. (2013). Characteristics of IFITM, the newly identified IFN-inducible anti-HIV-1 family proteins. *Microbes Infect.* 15 (4), 280–290. doi: 10.1016/j.micinf.2012.12.003

Costa, S. F., Gomes, V. O., Dos Santos Maciel, M. O., Melo, L. M., Venturin, G. L., Bragato, J. P, et al. (2020). Combined in vitro IL-12 and IL-15 stimulation promotes cellular immune response in dogs with visceral leishmaniasis. *PloS Negl. Trop. Dis.* 14 (1), e0008021–e0008021. doi: 10.1371/journal.pntd.0008021

da Silva, R. L., Elizondo, D. M., Brandy, N. Z. D., Haddock, N. L., Boddie, T. A., de Oliveira, L. L, et al. (2021). Leishmania donovani infection suppresses allograft inflammatory factor-1 in monocytes and macrophages to inhibit inflammatory responses. *Sci. Rep.* 11 (1), 946. doi: 10.1038/s41598-020-79068-6

Davis, M. P. A., van Dongen, S., Abreu-Goodger, C., Bartonicek, N., and Enright, A. J. (2013). Kraken: a set of tools for quality control and analysis of high-throughput sequence data. *Methods (San Diego Calif.)* 63 (1), 41–49. doi: 10.1016/j.ymeth.2013.06.027

Dobin, A., Davis, C. A., Schlesinger, F., Drenkow, J., Zaleski, C., Jha, S, et al. (2013). STAR: ultrafast universal RNA-seq aligner. *Bioinformatics* 29 (1), 15–21. doi: 10.1093/bioinformatics/bts635

Ehrchen, J. M., Roebrock, K., Foell, D., Nippe, N., von Stebut, E., Weiss, J. M., et al. (2010). Keratinocytes determine Th1 immunity during early experimental leishmaniasis. *PloS Pathog.* 6 (4), e1000871–e1000871. doi: 10.1371/journal.ppat.1000871

Eren, R. O., Reverte, M., Rossi, M., Hartley, M. A., Castiglioni, P., Prevel, F, et al. (2016). Mammalian innate immune response to a leishmania-resident RNA virus increases macrophage survival to promote parasite persistence. *Cell Host Microbe* 20 (3), 318–328. doi: 10.1016/j.chom.2016.08.001

Feng, H., Lenarcic, E. M., Yamane, D., Wauthier, E., Mo, J., Guo, H., et al. (2017). NLRX1 promotes immediate IRF1-directed antiviral responses by limiting dsRNA-activated translational inhibition mediated by PKR. *Nat. Immunol.* 18 (12), 1299–1309. doi: 10.1038/ni.3853

Fernandes, M. C., Dillon, L. A., Belew, A. T., Bravo, H. C., Mosser, D. M., and El-Sayed, N. M.. (2016). Dual transcriptome profiling of leishmania-infected human macrophages reveals distinct reprogramming signatures. *mBio* 7 (3), 00027–ndash;16. doi: 10.1128/mBio.00027-16

Ferrari, C. K. B. (2019). "Oxidative stress and antioxidants in host defense in leishmaniasis," in *Oxidative stress in microbial diseases* (Singapore: Springer), 245–256.

Freeman, L. C. (1978). Centrality in social networks conceptual clarification. *Soc. Networks* 1 (3), 215–239. doi: 10.1016/0378-8733(78)90021-7

Gardinassi, L. G., Garcia, G. R., Costa, C. H., Costa Silva, V., and de Miranda Santos, I. K. (2016). Blood transcriptional profiling reveals immunological signatures of distinct states of infection of humans with leishmania infantum. *PloS Negl. Trop. Dis.* 10 (11), e0005123. doi: 10.1371/journal.pntd.0005123

Gene Ontology C. (2021). The gene ontology resource: enriching a GOld mine. *Nucleic Acids Res.* 49 (D1), D325–D334. doi: 10.1093/nar/gkaa1113

Gupta, G., Oghumu, S., and Satoskar, A. R. (2013). Mechanisms of immune evasion in leishmaniasis. *Adv. Appl. Microbiol.* 82, 155–184. doi: 10.1016/B978-0-12-407679-2.00005-3

Hanke, J. H., Gardner, J. P., Dow, R. L., Changelian, P. S., Brissette, W. H., Weringer, E. J, et al. (1996). Discovery of a novel, potent, and src family-selective tyrosine kinase inhibitor. study of lck- and FynT-dependent T cell activation. *J. Biol. Chem.* 271 (2), 695–701. doi: 10.1074/jbc.271.2.695

Hartley, M. A., Ronet, C., Zangger, H., Beverley, S. M., and Fasel, N. (2012). Leishmania RNA virus: when the host pays the toll. *Front. Cell. Infect. Microbiol.* 2. doi: 10.3389/fcimb.2012.00099

Hartley, M.-A., Drexler, S., Ronet, C., Beverley, S.M., and Fasel, N. (2014). The immunological, environmental, and phylogenetic perpetrators of metastatic leishmaniasis. *Trends Parasitol.* 30 (8), 412–422. doi: 10.1016/j.pt.2014.05.006

Hartley, M.-A., Bourreau, E., Rossi, M., Castiglioni, P., Eren, R. O., Prevel, F, et al. (2016). Leishmaniavirus-dependent metastatic leishmaniasis is prevented by blocking IL-17A. *PloS Pathog.* 12 (9), e1005852–e1005852. doi: 10.1371/journal.ppat.1005852

Hartley, M. A., Eren, R. O., Rossi, M., Prevel, F., Castiglioni, P., Isorce, N., et al. (2018). Leishmania guyanensis parasites block the activation of the inflammasome by inhibiting maturation of IL-1beta. *Microb. Cell* 5 (3), 137–149. doi: 10.15698/mic2018.03.619

Heirwegh, E., MacLean, E., He, J., Kamhawi, S., Sagan, S. M., and Olivier, M. (2021). Sandfly fever Sicilian virus-leishmania major co-infection modulates innate inflammatory response favoring myeloid cell infections and skin hyperinflammation. *PloS Negl. Trop. Dis.* 15 (7), e0009638. doi: 10.1371/journal.pntd.0009638

Ives, A., Ronet, C., Prevel, F., Ruzzante, G., Fuertes-Marraco, S., Schutz, F, et al. (2011). Leishmania RNA virus controls the severity of mucocutaneous leishmaniasis. *Science* 331 (6018), 775–8. doi: 10.1126/science.1199326

Jafarzadeh, A., Nemati, M., Chauhan, P., Patidar, A., Sarkar, A., Sharifi, I, et al. (2020). Interleukin-27 functional duality balances leishmania infectivity and pathogenesis. *Front. Immunol.* 11, 1573–1573. doi: 10.3389/fimmu.2020.01573

Kariyawasam, R., Grewal, J., Lau, R., Purssell, A., Valencia, B. M., Llanos-Cuentas, A, et al. (2017). Influence of leishmania RNA virus 1 on proinflammatory biomarker expression in a human macrophage model of American tegumentary leishmaniasis. *J. Infect. Dis.* 216 (7), 877–886. doi: 10.1093/infdis/jix416

Kuhlmann, F. M., Robinson, J. I., Bluemling, G. R., Ronet, C., Fasel, N., and Beverley, S. M.. (2017). Antiviral screening identifies adenosine analogs targeting the endogenous dsRNA leishmania RNA virus 1 (LRV1) pathogenicity factor. *Proc. Natl. Acad. Sci. U.S.A.* 114 (5), E811–E819. doi: 10.1073/pnas.1619114114

Langfelder, P., and Horvath, S. (2008). WGCNA: an r package for weighted correlation network analysis. *BMC Bioinf.* 9, 559. doi: 10.1186/1471-2105-9-559

Li, B., and Dewey, C. N. (2011). RSEM: accurate transcript quantification from RNA-seq data with or without a reference genome. *BMC Bioinf.* 12 (1), 323. doi: 10.1186/1471-2105-12-323

Lindoso, J. A. L., Cunha, M. A., Queiroz, I. T., and Moreira, C. H. V. (2016). Leishmaniasis-HIV coinfection: current challenges. *HIV/AIDS (Auckland N.Z.)* 8, 147–156. doi: : 10.2147/HIV.S93789

Lockard, R. D., Wilson, M. E., and Rodriguez, N. E. (2019). Sex-related differences in immune response and symptomatic manifestations to infection with leishmania species. *J. Immunol. Res.* 2019, 4103819. doi: 10.1155/2019/4103819

Lohoff, M., Ferrick, D., Mittrücker, H. -W., Duncan, G. S., Bischof, S., Röllinghoff, M, et al. (1997). Interferon regulatory factor-1 is required for a T helper 1 immune response in vivo. *Immunity* 6 (6), 681–689. doi: 10.1016/S1074-7613(00)80444-6

Manjunath, S., Mishra, B. P., Mishra, B., Sahoo, A. P., Tiwari, A. K., Rajak, K. K, et al. (2017). Comparative and temporal transcriptome analysis of peste des petits ruminants virus infected goat peripheral blood mononuclear cells. *Virus Res.* 229, 28–40. doi: 10.1016/j.virusres.2016.12.014

Martin, M. (2011). Cutadapt removes adapter sequences from high-throughput sequencing reads. *EMBnet. J.* 17 (1), 10–12. doi: 10.14806/ej.17.1.200

McGarvey, K. M., Goldfarb, T., Cox, E., Farrell, C. M., Gupta, T., Joardar, V. S, et al. (2015). Mouse genome annotation by the RefSeq project. *Mamm. Genome Off. J. Int. Mamm. Genome Soc.* 26 (9-10), 379–390. doi: 10.1007/s00335-015-9585-8

Milano, S., Di Bella, G., D'Agostino, P., Barbera, C., Caruso, R., La Rosa, M, et al. (2002). IL-15 in human visceral leishmaniasis caused by leishmania infantum. *Clin. Exp. Immunol.* 127 (2), 360–365. doi: 10.1046/j.1365-2249.2002.01749.x

Narayana, S. K., Helbig, K. J., McCartney, E. M., Eyre, N. S., Bull, R. A., Eltahla, A, et al. (2015). The interferon-induced transmembrane proteins, IFITM1, IFITM2, and IFITM3 inhibit hepatitis c virus entry. *J. Biol. Chem.* 290 (43), 25946–25959. doi: 10.1074/jbc.M115.657346

Nasr, N., Alshehri, A. A., Wright, T. K., Shahid, M., Heiner, B. M., Harman, A. N, et al. (2017). Mechanism of interferon-stimulated gene induction in HIV-1-Infected macrophages. *J. Virol.* 91 (20), e00744–17. doi: 10.1128/JVI.00744-17

Olivier, M., and Zamboni, D. S. (2020). Leishmania viannia guyanensis, LRV1 virus and extracellular vesicles: a dangerous trio influencing the faith of immune response during muco-cutaneous leishmaniasis. *Curr. Opin. Immunol.* 66, 108–113. doi: 10.1016/j.coi.2020.08.004

Osero, B. O., Aruleba, R. T., Brombacher, F., and Hurdayal, R. (2020). Unravelling the unsolved paradoxes of cytokine families in host resistance and susceptibility to leishmania infection. *Cytokine X* 2 (4), 100043. doi: 10.1016/j.cytox.2020.100043

Osorio, E. Y., Travi, B. L., da Cruz, A. M., Saldarriaga, O. A., Medina, A. A., and Melby, P. C. (2014). Growth factor and Th2 cytokine signaling pathways converge at STAT6 to promote arginase expression in progressive experimental visceral leishmaniasis. *PloS Pathog.* 10 (6), e1004165. doi: 10.1371/journal.ppat.1004165

Panchanathan, R., Duan, X., Arumugam, M., Shen, H., Liu, H., and Choubey, D.. (2011). Cell type and gender-dependent differential regulation of the p202 and Aim2 proteins: implications for the regulation of innate immune responses in SLE. *Mol. Immunol.* 49 (1-2), 273–280. doi: 10.1016/j.molimm.2011.08.022

Pearson, R. D., and Anastacio de Queiroz, S. (1996). Clinical spectrum of leishmaniasis. *Clin. Infect. Dis.* 22 (1), 1–11. doi: 10.1093/clinids/22.1.1

Pervolaraki, K., Rastgou Talemi, S., Albrecht, D., Bormann, F., Bamford, C., Mendoza, J. L, et al. (2018). Differential induction of interferon stimulated genes between type I and type III interferons is independent of interferon receptor abundance. *PloS Pathog.* 14 (11), e1007420. doi: 10.1371/journal.ppat.1007420

Pflugheber, J., Fredericksen, B., Sumpter, R. Jr., Wang, C., Ware, F., Sodora, D. L, et al. (2002). Regulation of PKR and IRF-1 during hepatitis c virus RNA replication. *Proc. Natl. Acad. Sci. United States America* 99 (7), 4650–4655. doi: 10.1073/pnas.062055699

Rand, U., Rinas, M., Schwerk, J., Nohren, G., Linnes, M., Kroger, A., et al. (2012). Multi-layered stochasticity and paracrine signal propagation shape the type-I interferon response. *Mol. Syst. Biol.* 8, 584. doi: 10.1038/msb.2012.17

Rath, C. T., Schnellrath, L. C., Damaso, C. R., de Arruda, L. B., Vasconcelos, P., Gomes, C, et al. (2019). Amazonian Phlebovirus (Bunyaviridae) potentiates the infection of leishmania (Leishmania) amazonensis: Role of the PKR/IFN1/IL-10 axis. *PloS Negl. Trop. Dis.* 13 (6), e0007500. doi: 10.1371/journal.pntd.0007500

Restrepo, C. M., Llanes, A., Herrera, L., Ellis, E., Lleonart, R., and Fernandez, P. L. (2021). Gene expression patterns associated with leishmania panamensis infection in macrophages from BALB/c and C57BL/6 mice. *PloS Negl. Trop. Dis.* 15 (2), e0009225. doi: 10.1371/journal.pntd.0009225

Reverte, M., Eren, R. O., Jha, B., Desponds, C., Snaka, T., Prevel, F, et al. (2021). The antioxidant response favors leishmania parasites survival, limits inflammation and reprograms the host cell metabolism. *PloS Pathog.* 17 (3), e1009422. doi: 10.1371/journal.ppat.1009422

Reverte, M., Snaka, T., and Fasel, N. (2022). The dangerous liaisons in the oxidative stress response to leishmania infection. *Pathogens* 11 (4), 409. doi: 10.3390/pathogens11040409

Robinson, M. D., McCarthy, D. J., and Smyth, G. K. (2010). edgeR: a bioconductor package for differential expression analysis of digital gene expression data. *Bioinf. (Oxford England)* 26 (1), 139–140. doi: 10.1093/bioinformatics/btp616

Rossi, M., Castiglioni, P., Hartley, M. A., Eren, R. O., Prevel, F., Desponds, C, et al. (2017). Type I interferons induced by endogenous or exogenous viral infections promote metastasis and relapse of leishmaniasis. *Proc. Natl. Acad. Sci. U.S.A.* 114 (19), 4987–4992. doi: 10.1073/pnas.1621447114

Rossi, M., and Fasel, N. (2018a). How to master the host immune system? leishmania parasites have the solutions! *Int. Immunol.* 30 (3), 103–111. doi: 10.1093/intimm/dxx075

Rossi, M., and Fasel, N. (2018b). The criminal association of leishmania parasites and viruses. *Curr. Opin. Microbiol.* 46, 65–72. doi: 10.1016/j.mib.2018.07.005

Sadler, A. J., and Williams, B. R. G. (2008). Interferon-inducible antiviral effectors. *Nat. Rev. Immunol.* 8 (7), 559–568. doi: 10.1038/nri2314

Salloum, T., Tokajian, S., and Hirt, R. P. (2021). Advances in understanding leishmania pathobiology: What does RNA-seq tell us? *Front. Cell Dev. Biol.* 9, 702240. doi: 10.3389/fcell.2021.702240

Sanz, C. R., Miro, G., Sevane, N., Reyes-Palomares, A., and Dunner, S. (2021). Modulation of host immune response during leishmania infantum natural infection: A whole-transcriptome analysis of the popliteal lymph nodes in dogs. *Front. Immunol.* 12, 794627. doi: 10.3389/fimmu.2021.794627

Schoggins, J. W., and Rice, C. M. (2011). Interferon-stimulated genes and their antiviral effector functions. *Curr. Opin. Virol.* 1 (6), 519–525. doi: 10.1016/j.coviro.2011.10.008

Scorza, B. M., Carvalho, E. M., and Wilson, M. E. (2017). Cutaneous manifestations of human and murine leishmaniasis. *Int. J. Mol. Sci.* 18 (6), 1296. doi: 10.3390/ijms18061296

Shadab, M., Das, S., Banerjee, A., Sinha, R., Asad, M., Kamran, M., et al. (2019). RNA-Seq revealed expression of many novel genes associated with leishmania donovani persistence and clearance in the host macrophage. *Front. Cell Infect. Microbiol.* 9, 17. doi: 10.3389/fcimb.2019.00017

Shapouri-Moghaddam, A., Mohammadian, S., Vazini, H., Taghadosi, M., Esmaeili, S. A., Mardani, F., et al. (2018). Macrophage plasticity, polarization, and function in health and disease. *J. Cell. Physiol.* 233 (9), 6425–6440. doi: 10.1002/jcp.26429

Sheu, K. M., and Hoffmann, A. (2022). Functional hallmarks of healthy macrophage responses: Their regulatory basis and disease relevance. *Annu. Rev. Immunol.* 40 (1), 295–321. doi: 10.1146/annurev-immunol-101320-031555

Snaka, T., Bekkar, A., Desponds, C., Prevel, F., Claudinot, S., Isorce, N., et al. (2022). Sex-biased control of inflammation and metabolism by a mitochondrial nod-like receptor. *Front. Immunol.* 13, 882867. doi: 10.3389/fimmu.2022.882867

Stuart, K. D., Weeks, R., Guilbride, L., and Myler, P. J. (1992). Molecular organization of leishmania RNA virus 1. *Proc. Natl. Acad. Sci. U.S.A.* 89 (18), 8596–8600. doi: 10.1073/pnas.89.18.8596

Tarr, P. I., Aline, R.F. Jr., Smiley, B. L., Scholler, J., Keithly, J., Stuart, K., et al. (1988). LR1: a candidate RNA virus of leishmania. *Proc. Natl. Acad. Sci. U.S.A.* 85 (24), 9572–9575. doi: 10.1073/pnas.85.24.9572

Valdés-López, J. F., Fernandez, G. J., and Urcuqui-Inchima, S. (2022). Synergistic effects of toll-like receptor 1/2 and toll-like receptor 3 signaling triggering interleukin 27 gene expression in chikungunya virus-infected macrophages. *Front. Cell Dev. Biol.* 10, 812110–812110. doi: 10.3389/fcell.2022.812110

Valencia, B. M., Lau, R., Kariyawasam, R., Jara, M., Ramos, A. P., Chantry, M., et al. (2022). Leishmania RNA virus-1 is similarly detected among metastatic and non-metastatic phenotypes in a prospective cohort of American tegumentary leishmaniasis. *PloS Negl. Trop. Dis.* 16 (1), e0010162. doi: 10.1371/journal.pntd.0010162

Wang, P.-H., Ye, Z. -W., Deng, J. -J., Siu, K. -L., Gao, W. -W., and Chaudhary, V. (2018). Inhibition of AIM2 inflammasome activation by a novel transcript isoform of IFI16. *EMBO Rep.* 19 (10), e45737. doi: 10.15252/embr.201845737

Wang, L., Wang, S., and Li, W. (2012). RSeQC: quality control of RNA-seq experiments. *Bioinformatics* 28 (16), 2184–2185. doi: 10.1093/bioinformatics/bts356

Yang, X., Arslan, M., Liu, X., Song, H., Du, M., Li, Y., et al. (2020). IFN-gamma establishes interferon-stimulated gene-mediated antiviral state against Newcastle disease virus in chicken fibroblasts. *Acta Biochim. Biophys. Sin. (Shanghai)* 52 (3), 268–280. doi: 10.1093/abbs/gmz158

Yang, Z., Mosser, D. M., and Zhang, X. (2007). Activation of the MAPK, ERK, following <em<Leishmania amazonensis</em< infection of macrophages. *J. Immunol.* 178 (2), 1077. doi: 10.4049/jimmunol.178.2.1077

Yorek, M. S., Poudel, B., Mazgaeen, L., Pope, R. M., Wilson, M. E., and Gurung, P. (2019). Leishmania major degrades murine CXCL1 - an immune evasion strategy. *PloS Negl. Trop. Dis.* 13 (7), e0007533. doi: 10.1371/journal.pntd.0007533

Zamboni, D. S., and Sacks, D. L. (2019). Inflammasomes and leishmania: in good times or bad, in sickness or in health. *Curr. Opin. Microbiol.* 52, 70–76. doi: 10.1016/j.mib.2019.05.005

Zamora, M., Guilbride, L., Sacks, L., and Stuart, K. (2000). Phylogenetic analysis of the 5' subterminal region of isolates of leishmania RNA virus-1. *Ann. Trop. Med. Parasitol.* 94 (2), 123–133. doi: 10.1080/00034980057464

Zhao, H., Boije, H., Granberg, F., Pettersson, U., and Svensson, C. (2009). Activation of the interferon-induced STAT pathway during an adenovirus type 12 infection. *Virology* 392 (2), 186–195. doi: 10.1016/j.virol.2009.07.006

Zhao, Y., Dang, Z., Wei, R., Gui, W., Zhang, Y., and Chong, S. (2019). The effects of CCR7 and related signaling pathways on leishmania major -infected human dendritic cells. *J. Cell. Physiol.* 234 (8), 13145–13156. doi: 10.1002/jcp.27985

Zhou, Y., Geng, P., Liu, Y., Wu, J., Qiao, H., Xie, Y., et al. (2018). Rotavirus-encoded virus-like small RNA triggers autophagy by targeting IGF1R via the PI3K/Akt/mTOR pathway. *Biochim. Biophys. Acta (BBA) - Mol. Basis Dis.* 1864 (1), 60–68. doi: 10.1016/j.bbadis.2017.09.028

frontiers | Frontiers in Cellular and Infection Microbiology

TYPE Original Research
PUBLISHED 12 August 2022
DOI 10.3389/fcimb.2022.941860

In and out: *Leishmania* metastasis by hijacking lymphatic system and migrating immune cells

Baijayanti Jha[1], Marta Reverte[1], Catherine Ronet[1,2], Florence Prevel[1], Florence D. Morgenthaler[3], Chantal Desponds[1], Lon-Fye Lye[4], Katherine L. Owens[4], Leonardo Scarpellino[1], Lalit Kumar Dubey[1,5], Amélie Sabine[6], Tatiana V. Petrova[6], Sanjiv A. Luther[1], Stephen M. Beverley[4] and Nicolas Fasel[1]*

[1]Department of Immunobiology, University of Lausanne, Epalinges, Switzerland, [2]Department of Oncology, Ludwig Institute for Cancer Research Lausanne, Lausanne University Hospital and University of Lausanne, Lausanne, Switzerland, [3]Cellular Imaging Facility, University of Lausanne, Epalinges, Switzerland, [4]Department of Molecular Microbiology, School of Medicine, Washington University, St. Louis, MO, United States, [5]Centre for Microvascular Research, John Vane Science Centre, Queen Mary University of London, London, United Kingdom, [6]Department of Oncology and Ludwig Institute for Cancer Research, University of Lausanne and Centre Hospitalier Universitaire Vaudois, Epalinges, Switzerland

OPEN ACCESS

EDITED BY
Song Yang,
Beijing Ditan Hospital, Capital Medical University, China

REVIEWED BY
Smriti Parashar,
UC San Diego Health, University of California, San Diego, United States
Paula Mello De Luca,
Oswaldo Cruz Foundation (Fiocruz), Brazil

*CORRESPONDENCE
Nicolas Fasel
nicolas.fasel@unil.ch

SPECIALTY SECTION
This article was submitted to Virus and Host, a section of the journal Frontiers in Cellular and Infection Microbiology

RECEIVED 11 May 2022
ACCEPTED 19 July 2022
PUBLISHED 12 August 2022

CITATION
Jha B, Reverte M, Ronet C, Prevel F, Morgenthaler FD, Desponds C, Lye L-F, Owens KL, Scarpellino L, Dubey LK, Sabine A, Petrova TV, Luther SA, Beverley SM and Fasel N (2022) In and out: *Leishmania* metastasis by hijacking lymphatic system and migrating immune cells. *Front. Cell. Infect. Microbiol.* 12:941860. doi: 10.3389/fcimb.2022.941860

The lymphatic system plays a crucial role in mounting immune response against intracellular pathogens, and recent studies have documented its role in facilitating tumor dissemination linked largely with cancer cells. However, in mucocutaneous leishmaniasis (MCL) caused by *Leishmania Viannia* subgenus showing infectious metastasis and resulting in severe distant secondary lesions, the route of escape of these parasites to secondary sites has not yet been investigated in detail. Our results demonstrated that when infection was associated with inflammation and additionally exacerbated by the presence of dsRNA viral endosymbiont (LRV1), lymphatic vessels could serve as efficient routes for infected cells to egress from the primary site and colonize distant organs. We challenged this hypothesis by using the intracellular *Leishmania* protozoan parasites *Leishmania guyanensis (Lgy)* associated with or without a dsRNA viral endosymbiont, exacerbating the infection and responsible for a strong inflammatory response, and favoring metastasis of the infection. We analyzed possible cargo cells and the routes of dissemination through flow cytometry, histological analysis, and *in vivo* imaging in our metastatic model to show that parasites disseminated not only intracellularly but also as free extracellular parasites using migrating immune cells, lymph nodes (LNs), and lymph vessels, and followed intricate connections of draining and non-draining lymph node to finally end up in the blood and in distant skin, causing new lesions.

KEYWORDS

lymph nodes (LNs), inflammation, dissemination, *Leishmania*, *Leishmania* RNA virus 1 (LRV1), metastasis, extracellular, free amastigotes

Introduction

Cutaneous leishmaniasis (CL) affects more than 1 million people across the globe annually, being the most common clinical form of leishmaniasis ((W.H.O), 2020). It manifests itself as self-healing skin lesions at the inoculation site of *Leishmania* parasites, which enter the human skin through the bite of a hematophagous female sand fly (Wong, 1995; Bates, 2008). Upon delivery into mammalian hosts, free-living flagellated promastigotes pass through neutrophils and invade macrophages, wherein they transform into a non-flagellated amastigote form to survive intracellularly in the phagolysosome-like organelles (Wong, 1995; Novais et al., 2009; Wynn et al., 2013; Carlsen et al., 2015; Bates, 2018). As mentioned, these protozoan parasites mainly cause cutaneous leishmaniasis (CL), but with some species, such as *Leishmania braziliensis (Lbr)* and *Leishmania guyanensis* (*Lgy*), CL primary lesions can progress to mucocutaneous leishmaniasis (MCL), a chronic inflammatory form with severe secondary lesions and destruction of nasopharyngeal tissues (Lessa et al., 2007; Hartley et al., 2014). *Lbr* and *Lgy* mainly account for most CL cases in South America, with approximately 5%–10% of such cases progressing to the more severe chronic form of the disease, resulting in mucocutaneous leishmaniasis (MCL), wherein parasites metastasize and cause severe secondary cutaneous lesions. Disseminated cutaneous leishmaniasis (DCL) is another form marked by hyper-inflammation, appearance of nodular granulomas, and numerous ulcerated skin lesions exhibiting extensive parasite migration (Hartley et al., 2012; Hartley et al., 2014). These intense symptomatic manifestations associated with several *Leishmania* species infections could be linked to the presence of *Leishmania* RNA virus 1 (LRV1) from the *Totiviridae* family, an endosymbiotic double-stranded RNA virus (dsRNA) reported to be naturally present in the cytoplasm of several *Leishmania* species, along with several other parasite species as well (Tarr et al., 1988; Ives et al., 2011; Zangger et al., 2014; Cantanhede et al., 2015).

LRV1 is a potent immunogen, recognized by endosomal TLR-3 (the dsRNA sensor) in macrophages, inducing an extensive type I interferon (IFN-I) anti-viral immune response, thus leading to a hyper-inflammatory phenotype (Ives et al., 2011; Zangger et al., 2013; Heirwegh et al., 2021). Additionally, co-infection of mice already infected with *Lgy*LRV1− with lymphocytic choriomeningitis virus (LCMV) reproduced the metastatic phenotype observed in *Lgy*LRV1+ infections, confirming the severity rendered by the LRV1 virus or other co-infecting viruses (Rossi et al., 2017; Rath et al., 2019). *Lgy*LRV1+ infections result in metastatic complications which are often associated with treatment failure and clinical relapse in patients (Adaui et al., 2016; Bourreau et al., 2016; Olivier and Zamboni, 2020). However, the mode of dissemination and the cells facilitating such extensive dissemination to distant skin leading to the formation of new metastatic lesions have not been thoroughly investigated yet. Therefore, there is an urgent need to identify the process of dissemination and potential major cargo cell type(s) transporting viable parasites from the primary site of infection to distant secondary debilitating lesion sites, for targeted therapeutic intervention to ensure the control of this disease. In this regard, the lymphatic system is of significant interest, as it is known to play key roles in the development of immune responses and has also been described to be involved in the dissemination of tumor cells to both draining lymph nodes and distant secondary sites. (Petrova and Koh, 2020; Vaahtomeri and Alitalo, 2020). Furthermore, various innate and adaptive cells of the immune system are reported to be involved in a complex interplay with each other, in different species of *Leishmania* infections, to house an effective host immune response against an invading pathogen, thereby modulating the susceptibility or resistance to such infections (Qi et al., 2001; Charmoy et al., 2010; Santos Cda et al., 2013; Yang et al., 2014; Cardoso et al., 2015; Silva-Barrios et al., 2016; Glennie et al., 2017; Novais et al., 2017; Tomiotto-Pellissier et al., 2018).

Experimentally, metastatic CL can be mimicked upon infection of the interferon gamma (IFN-γ)-deficient mice (*Ifng*$^{-/-}$) with *Lgy*-bearing LRV1 (*Lgy*LRV1+), which induces a severe metastatic phenotype (Hartley et al., 2016; Rossi et al., 2017). This metastatic mouse model is now being used to study the dissemination of the infection to secondary sites, since it validates the observation that *Lgy*LRV1+-infected patients have a high level of IL-17 but extremely low level of interferon gamma cytokine (IFN-γ) and are prone to chronic metastatic complications (Hartley et al., 2016). The model thus presents a simple yet extremely useful system for defining the different immunological determinant(s) driving leishmanial metastasis *in vivo*. Thus, in this study, we used *Lgy* parasites that may or may not be infected by LRV1, namely, *Lgy*LRV1+ and *Lgy*LRV1−, respectively, and an *in vivo* *Ifng*$^{-/-}$ mice model exhibiting infectious metastasis to investigate the mode of dissemination of *Lgy* parasites and the potential cargo cells facilitating widespread metastasis.

Materials and methods

Ethics statement

All mice experiments and animal protocols undertaken in this study were approved by the Swiss Federal Veterinary Office (SFVO), under authorization number VD 3551. Animal handling and experimental procedures were conducted with strict adherence to the ethical guidelines set by the State Ethical Committee and the SFVO for the use of laboratory animals, with regular inspection by the Department of Security and Environment of the State of Vaud, Switzerland. We managed to follow maximum experiments adhering to the set ARRIVE rules for handling laboratory animals, with proper control of animal maintenance conditions, regular behavior check, and administration of pain-relieving drugs (paracetamol/dafalgan) from the peak of infection. All these have been discussed in details in *Materials and methods*.

Laboratory animals

WT (C57BL/6) mice were purchased from Envigo (Netherlands). *Ifng*$^{-/-}$ mice and *Rag2*$^{-/-\gamma c-/-}$ transgenic mice were purchased from The Jackson Laboratory (United States). We used both male and female mice for randomization in the experimental setup, with age ranging between 8 and 16 weeks for these mice groups and median age of 12 weeks for infections and controls. Animals were treated randomly before intervention to maximize randomization and reduce bias. No wild animals were used in this study. No field-collected samples were used in this study. Different mice strains were genotyped by PCR, using KAPA Mouse Genotyping Kit (KAPA Biosystems) on tissue-isolated genomic DNA, as per provider's protocol for screening. The oligonucleotides used for genotyping were the following: *Ifng* mutant Fw, CCTTCTATCGCC TTCTTGACG; *Ifng* WT Fw, AGAAGTAAGTGGAAGGGCCCAGAAG; and *Ifng* common, AGGGAAACTGGGAGAGGAGAAATAT. All mice were maintained under a specific pathogen-free (SPF) environment, housed in micro-isolator cages, for housing, breeding, and future maintenance of the line at the animal facility of the Center of Immunity and Immunology, Lausanne, (Switzerland). Mice experiments were performed in a P2 pathogen animal facility on site (as mentioned). Food (SAFE or KLIBA NAFAG) and water (filtered local water, which is autoclaved, after acidification or Innovive Aquavive) were provided *ad libitum*. The animal facility maintained a prescribed light cycle with 11 h of darkness and 13 h of light; temperature and humidity were set at 21°C ± 2 and 55% ± 10, respectively.

Parasites and their culture

Two isogenic clones of *Lgy*, either infected with or depleted of LRV1–, namely, *Lgy*LRV1+ [LRV1^{+} *Lgy*M4147/SSU : IR2SAT-LUC(b)c3] and *Lgy*LRV1– [LRV1^{-} *Lgy*M4147/SSU : IR2SAT-LUC (b)c3], respectively, were used in this study. Both of these clones were derived from the LRV1+ parent strain, *Lgy* M4147 (MHOM/BR/75/M4147), and documented previously (Kuhlmann et al., 2017). These parasites express equivalent levels of a firefly luciferase gene, namely, "ffLUC" (5×10^{7} photons/s/10^{6} parasites), which in turn is stably integrated into the small subunit (SSU) gene of the ribosomal RNA locus (Hartley et al., 2016). Additionally, we have also used a fluorescent variant of the same parasite, namely, mCh*Lgy*LRV1+ (*Lgy*M4147 0106-9 L+ SSU : IR4BSD-LUC-mcherryc8), which has the mCherry gene integrated into the SSU, also expressing ffLUC simultaneously (Reverte et al., 2021). We also used the *Lmj* (MRHO/IR/75/ER (IR75) strain for additional controls (Noll et al., 1997; Reverte et al., 2021). *Lgy* parasites were cultured in Schneider's *Drosophila* medium (PAN$^{\text{TM}}$ BIOTECH) supplemented with 20% heat-inactivated fetal bovine serum (FBS, Gibco$^{\text{TM}}$), 1% penicillin-streptomycin (P/S) solution (Bio-Concept), 1% HEPES buffer, 0.1% hemin-folate solution (Sigma-Aldrich, Fluka), and 0.6 µg/ml of 6-Biopterin (Sigma-Aldrich). Similarly, *Lmj* parasites were cultured in Medium 199 (M199, Gibco) supplemented with 20% heat-inactivated FBS, 1% P/S solution, 1% HEPES buffer, 0.1% hemin-folate solution, and 0.6 µg/ml of 6-biopterin. Generally, these parasites were maintained as promastigotes in culture *in vitro*, at 26°C and 5% CO_2, for not more than five passages, and isolated and cultured from the WT-infected mice FP *in vivo*, to maintain their virulence, for long-term maintenance of parasite stocks. Each passage yielded stationary-phase, infectious metacyclic promastigotes after 6 days in culture, which were used directly for *in vivo* infections, diluted in Dulbecco's phosphate-buffered saline (DPBS, Gibco) at required concentrations specified later.

Reagents

Antibodies. The antibodies used in this study for various applications such as FACS, immunofluorescence/histological staining, and *in vivo* mice depletions are detailed in Supplementary Tables S1 and S2.

Mice infection and *in vivo* bioluminescence imaging and quantification

Age-matched (between 6 and 12 weeks) male and female mice were used separately for individual experiments to remove gender bias in this study. Mice were mostly infected with 1×10^{6} *Lgy* (either *Lgy*LRV1+ or *Lgy*LRV1–) stationary-phase, infectious metacyclic parasites in both hind FP subcutaneously, in 50 µl of 1× DPBS, as a fixed standard for the entire study. Following infection, changes in footpad thickness were measured weekly using a Vernier caliper, as a proxy for parasite growth and disease progression. Parasite burden was quantified in the infected mice by injecting VivoGlo D-Luciferin salt (Promega) at a concentration of 150 mg/kg, intraperitoneally (i.p.), and parasite bioluminescence produced in the mouse footpads and other visible secondary lesions (like tail and snout) were measured with *In-Vivo* Xtreme II (BRUKER) as previously described (Reverte and Fasel, 2019). Additionally, *in vivo* read out of inflammation was measured similarly by injecting Luminol sodium salt (Carbosynth) at a concentration of 200 mg/kg i.p. The infected experiment groups were imaged twice at 10 and 20 min, respectively, during late phase of chronic infection for better uptake of imaging salt in a highly metastatic condition. These acquired images were then analyzed using Molecular Imaging (MI) software (BRUKER), setting specific regions of interest (ROIs) on FP, tail, etc. and expressing the measured bioluminescence signals in units of photons per second (p/s) (Reverte and Fasel, 2019). Immunocompromised mice (*Ifng*$^{-/-}$) received constant pain-relieving medication [1g/L DAFALGAN (Upsa) diluted in drinking water], from the appearance of big primary lesions (W3–4 p.i.) till secondary lesions developed (till a maximum of W12 p.i., in case of delays) and were euthanized upon reaching any ethical limit of permitted lesion size or showing visual signs of clinical disease such as ruffled fur, inactivity, labored respiration, huddling behavior, or a loss of 20% of their original body weight.

Lymph node and lymphatic connection mapping

Groups of age-matched (6–12 weeks) male or female *Ifng*$^{-/-}$ mice were used as untreated, uninfected naive controls, alongside infected groups with *Lgy*LRV1+ parasites, at different time points (i.e., weeks 1, 2, 4, 6, 8–10) post-infection, for *in vivo* lymph node mapping using Evan's blue, as described previously (Harrell et al., 2008). Dye injections were administered with 5% Evan's Blue dye (Sigma) in 10–15 µl Hank's buffered salt solution (Gibco), delivered using a precision syringe (Hamilton, 50 µl) with a stainless-steel-made sharp, beveled RN needle (Hamilton, Germany) (Harrell et al., 2008). The dye was injected subcutaneously into both hind FP of naive and infected mice group, and subjects were anesthetized under isoflurane (2.5%) for a continuous 20 min to facilitate dye uptake by the lymphatic vessels. Then, mice were euthanized with CO_2 and dissected to locate the blue-labeled LNs of interest to assess the drained (blue) and non-drained (non-blue) LNs post-FP injection (equivalent to our infection model). While it was easier to detect the peripheral draining LNs by blue color, just after the removal of skin and fascia, deep-seated LNs like the iliac and renal LNs were visible only when the intestines were removed. Moreover, once the draining and non-draining LNs were identified, the pattern of lymphatic connection between these various LNs were mapped by injecting 2–5 µl (10 mg/ml in 1× DPBS) of the fluorescent permeability tracer fluorescein-isothiocyanate (FITC)-labeled dextran (2,000 kDa; Sigma-Aldrich) (Zheng et al., 2014; Yamaji et al., 2018) subcutaneously in the hind FP, the tip of the tail, and forelimbs of the infected mice group (*Ifng*$^{-/-}$ *Lgy*LRV1+), as described previously (Zheng et al., 2014). The apparatus and procedure of euthanasia is exactly as described for the Evan's blue mapping. Once euthanized, the mice were micro-dissected and imaged at 8× magnification (in both setups of bright light and fluorescence imaging) for 30 min with a stereomicroscope (Leica, M205FA), and acquired images were processed using LAS AF 6000 software and were processed, tiled, and stitched on Photoshop (version 21.2.0) in case of fluorescence-based images of the whole mouse, as represented in Figure 5.

Isolation of cells (from LNs, tissues, and blood) and cell count

Samples (LNs, liver, lung, kidney, heart, spleen, etc.) were mechanically processed using a McIlwain tissue homogenizer (Mickle Laboratory Engineering). They were then digested in a solution of incomplete Dulbecco's modified Eagle's medium (DMEM, Gibco$^{\text{TM}}$, without FBS) supplemented with 1 mg/ml collagenase type A (Roche, 1:100 dilution) and 25 mg/ml DNase (Sigma, 1:500 dilution), at 35°C for 15–30 min (depending upon organ size and type). For dense tissues such as FP and tail, the skin was peeled off, and tissue/lesions were separated from the bones, then processed as described, after digestion for 1 h (Regli et al., 2020). Enzyme activity was neutralized by the addition of cold complete DMEM [incomplete medium: DMEM (Gibco$^{\text{TM}}$), supplemented with 10% heat-inactivated fetal bovine serum (FBS), 1% penicillin/streptomycin, and 1% HEPES (Sigma-Aldrich)]. Cell suspension was dispersed through a 40-µm cell strainer (Falcon) to remove cell clumps and centrifuged at 500*g* for 10 min to obtain purified single-cell pellet, which may or may not be treated with erythrocyte lysis buffer (BD FACS$^{\text{TM}}$ Lysing Solution) to remove red blood cells. Meanwhile, blood samples (from infected mice and naive control) were collected in tubes containing 400 µl PBS-heparin [(Sigma-Aldrich H3149, 10,000× from (10 mg/ml)] on ice, centrifuged at 500*g* for 10 min to remove the PBS-heparin, treated immediately with 3–5ml of BD FACS$^{\text{TM}}$ Lysing Solution (1:10 diluted in deionized water from stock) for 10 min at room temperature (RT) in the dark, then washed twice with 1× DPBS and centrifuged to obtain a cleaner red blood cell (RBC)-free blood cell pellet (Regli et al., 2020).

Cell count. Once the cell suspension was prepared for each LN and tissue, cell numbers and cell viability were assessed *via* Trypan blue (Sigma-Aldrich) exclusion using an improved counting Neubauer chamber (Assistant®, catalog number 40442). This gave the absolute cell count of different organs.

Limiting dilution assay/analysis

Different LNs (PLN, ILN, iliac LN, ALN, BLN, CLN, MLN, and organs/tissues like spleen, FP, and tail) (divided into eight pieces of equal length, from the thick to the thin end, marked from T1 till T8, respectively), kidney, liver, lung, heart, and even blood were aseptically collected from infected and/or naive control groups at different time points (weeks 1, 2, 4, 6, 8–10) post-infection in cold incomplete DMEM (Gibco) on ice and further processed to obtain single-cell suspension and their absolute cell count per organ (as described in detail, previously). Then, an eightfold limiting dilution assay (in successive dilution series of 1/1, 1/2, 1/4, 1/8, 1/10, 1/100, 1/1,000, and 1/10,000 by row) with 24 technical replicates per dilution was performed on these cell suspensions in a 96-well U bottom transparent plate (Fisher Scientific) in complete Schneider's medium. These plates were then cultured at 26°C for 14–21 days, and subsequent readings were taken at 3, 6, 9, 14, 18, and 21 days in culture to monitor the presence of any *Lgy* promastigotes through microscopy. This was used to identify the infected organs at different time points of infection between different infected and control groups. Infection was annotated by a + sign for the different kinds of LNs and organs (as mentioned by abbreviations). The number of + assigned to any organ correlated to the detection of free parasites in equivalent progression of the dilution series, such that 1/1, 1/2, 1/4, 1/8, 1/10, 1/100, 1/1,000, and 1/10,000 translates to +, ++, +++, ++++, +++++, ++++++, +++++++, and ++++++++, respectively (only when minimum 12 out of 24 technical replicates showed free promastigotes). The parasite number was determined from the lowest cell concentration from which promastigotes could be grown using the ESTIMFRE software, which is based on the Poisson limit theorem as previously described (Regli et al., 2020). The corresponding heatmaps were generated using the R ComplexHeatmap package. The color gradient represented in the heatmaps is correlated to the number of + signs assigned in terms of infection in progressive dilution series through LDA for each organ, where increased color intensity corresponded to higher parasite load.

RNA isolation and RT-qPCR

LNs, FP, and tail pieces were collected from *Ifng*$^{-/-}$ mice, infected with either *Lgy*LRV1+ or *Lgy*LRV1− parasites, at weeks 1, 2, 4, 6, 8–10 p.i, and snap-frozen in liquid nitrogen. RNA isolation from these samples were facilitated by immersing them in TRI Reagent® (Molecular Research Center, Inc.) in RNAse-free tubes, adding stainless beads (Qiagen), and using Tissue Lyser system (Qiagen) for tissue disruption and homogenization. RNA was isolated through chloroform/isopropanol/ethanol phase separation, as described previously (Henn et al., 2018), following the manufacturer's description. The quality and quantity of isolated RNA were analyzed using NanoDrop™ 2000 (Thermo Fisher Scientific). cDNA was generated using SuperScript II Reverse Transcriptase (Invitrogen). LightCycler® 480 SYBR Green I Master (Roche) along with 0.5 µM primer pairs were used for performing real-time quantitative PCR (RT-qPCR) on LightCycler® 480 (Roche). Gene expression was analyzed using the threshold cycle (C_T) method $2^{-\Delta\Delta Ct}$. Data analyzed for *Leishmania Kmp11* gene expression in different organs of the infected mice were assessed using predetermined levels of *Kmp11* expression in *Lgy* parasites and normalized to the total RNA quantity of the sample (Hartley et al., 2016; Reverte et al., 2021). Primer sequence used for *Kmp11* gene were as follows: *Kmp11* Fw, GCCTGGATGAGGAGTTCAACA, and *Kmp11* Rev, GTGCTCCTTCATCTCGGG.

Immunofluorescence microscopy

Draining and non-draining LNs were carefully dissected as a whole, harvested, weighed, and fixed in 4% (wt/vol) paraformaldehyde (Fluka) in 1× DPBS at 4°C overnight (O/N), then saturated in 30% (wt/vol) sucrose (Fisher Scientific) in 1× DPBS again O/N at 4°C, before being embedded in Tissue-Tek optimum cutting temperature (OCT) compound (Sakura), and frozen in an ethanol dry ice bath. Serial longitudinal and transverse cryostat sections (8–10 µm in thickness) were collected on Superfrost/Plus glass slides (Fisher Scientific), over a span of 400 µm depth. These sections were then air-dried, fixed in ice-cold acetone for 20 min, and then rehydrated in 1× DPBS and were blocked with 1% (wt/vol) BSA (Sigma-Aldrich) supplemented with 1% normal mouse and 4% donkey serum (BIO-RAD). Various primary antibodies, in different combinations, diluted in 1× DPBS containing 1% (vol/vol) normal mouse serum and 1% (wt/vol) BSA, were added for specific immunofluorescence staining. Then, these sections were incubated O/N at 4°C. The following day, cryosections were washed at least three times in 1× DPBS, then incubated with specific fluorescently labeled secondary antibodies to detect the primary antibodies. For gp38, staining was revealed using horseradish peroxidase (HRP)-conjugated secondary reagents followed by tyramide signal amplification (Molecular Probes Kit 22) according to the manufacturer's instructions, but using a borate buffer (0.1 M in PBS; pH 8.5) for tyramide dilution. Moreover, rabbit anti-mCherry (Abcam) secondary antibody was used to detect the mCh*Lgy*LRV1+ in these infected samples, as the self-fluorescence of these parasites were quenched with 4% paraformaldehyde (PFA) fixation. Prior to mounting, sections were counter-stained for nuclei with 4′,6-diamidine-2′-phenylindole dihydrochloride (DAPI) from Molecular Probes, using ProLong anti-fade reagents (Life technologies). Stained cryo-sections were then imaged within 24–72 h post-staining and stored at 4°C in polystyrene slide box for future considerations. A detailed list of antibodies used for this study are enlisted in Supplementary Tables S1 and S2. Images were partly acquired using on an Olympus VS120-SL full slide scanner with a 20×/0.75 air objective (using Olympus OlyVIA software), at the EPFL BioImaging & Optics Platform (BIOP), or with Zeiss Axio-Imager Z1, Upright in Cellular Imaging Facility, Epalinges (using Axiovision SE64 rel 4.9.1 software). For the images acquired using the Olympus VS120-SL full slide scanner, individual images were acquired using the indicated fluorescent channels having the same exposure time employed across different samples. The images were then extracted using the VSI reader action bar [provided by the EPFL BioImaging & Optics Platform (BIOP)]. Olympus slide scanner software (OlyVIA v.2.6) was employed to directly analyze the images from different groups (naive and infected LNs) by adjusting the contrast and brightness settings, so that they are constant across different compared samples and groups, as described in detail previously (Dubey et al., 2019).

Fluorescent-activated cell sorting

All the antibody dyes and beads used for flow cytometry are detailed in Supplementary Table S1.

For flow cytometric analysis, different LNs, tissues, and blood (mentioned previously) were recovered from naive controls and *Ifng*$^{-/-}$ mCh*Lgy*LRV1+ (at different time points of infection); single-cell suspensions with respective cell counts from each organ were obtained following the procedure described in detail earlier. Briefly, in 96-well U-bottom plates, 2×10^6 cells from each organ of interest were treated for further 5 min with 5 mM EDTA in fluorescent-activated cell sorting (FACS) buffer (1× DPBS with 2% FBS) to dissociate cell clumps, then incubated with 50 µl supernatants from hybridoma 2.4G2 antibody (Miltenyi Biotec; 1g anti-FcRIII/II antibody per 10^6 cells) on ice for 20 min to block Fc receptors. Cells were then stained with optimal concentrations of specific antibodies (between 0.06 and 0.5 µg/1×10^6 cells in 50 µl of FACS buffer) in appropriate combinations, for the identification of different mouse antigens, employing fluorescein phycoerythrin (PE) or allophycocyanin or PE-Cy7, isothiocyanate (FITC), Brilliant Violet (BV421)/(BV510), APC or APC/Cy7 conjugated, or biotinylated monoclonal antibodies to CD45 (clone 104), CD11b (clone M1/70), Gr-1 (clone RB6-8C5), Ly6C (clone HK1.4), Ly6G (clone 1A8), CCR2 (clone SA203G11), CD206 (clone C068C2), MHC class II (clone M5/114.15.2), CD115 (clone T38-320), F4/80 (clone BM8), CD3e (clone 17A2), CD19 (clone D3/CD19), NK1.1 (clone PK136), and CD11c (clone N418). Plates were then incubated for 30 min at 4°C in the dark. Following incubation, the cells were washed at least three times with FACS buffer. DAPI (Molecular Probes, 1:1,000 from a stock of 10 mg/ml) was added to each sample during staining to exclude dead cells during analysis. Murine cells and fluorescent or stained parasites were then passed through the flow cytometry analyzer of either BD LSRII or BD LSR-Fortessa series (Becton Dickinson), and a minimum of 50,000 live cells were acquired (Rossi et al., 2017; Regli et al., 2020). Data were analyzed with FlowJo software (Tree Star, v10.0.6). For data analyses, a minimum of 30,000 events (cells) were evaluated at all times by back-gating from CD45+/− stained cells. The absolute number of total leukocytes or each represented cell type was quantified by multiplying the total number of cells observed by hemocytometer counting with the percentage of those individual cells (on total CD45$^+$ cells) determined by flow cytometry. The absolute number of each leukocyte subset (1A8, Ly6C, Ly6G, CD11b, and CCR2) was determined by multiplying the percentage of each gated population by the total number of CD45$^+$ cells. For the distribution of mCherry$^+$ parasites on cell-associated or non-immune cell-associated TER119$^-$CD45$^+$ immune cells, we calculated it from the point of view of the mCherry$^+$ parasites, distributing the total numbers of mCherry$^+$ parasites observed in any organ over its numbers that were either co-localized with a TER119$^-$CD45$^+$ membrane marker (thus, cell associated) or not (non-cell associated).

Imaging flow cytometry (Imaging Stream® analysis)

All the antibody dyes and beads used for imaging flow cytometry are detailed in Supplementary Table S1.

Samples were run in a two-camera, 12-channel ImageStreamX multispectral imaging flow cytometer (Amnis, Luminex Corporation) at low speed and highest magnification (60×). Instrument setup and performance tracking was performed daily using the Amnis® SpeedBead® Kit (Luminex Corporation) to verify optimal instrument performance. Cells were excited using a 405-nm laser (25 mW), a 488-nm laser (100 mW), a 561-nm yellow laser (200 mW), and a 642-nm red laser (150 mW). Only events with a brightfield area >5 µm^2 (to exclude cell debris) and non-saturating pixels were collected (as described in Hui et al., 2008). Data were acquired for a minimum of 50,000 events/sample (Regli et al., 2020).

Panel design was based on antigen expression density, fluorochrome brightness, and reagent availability in each panel for the four-laser, 12-parameter ImageStreamX. The preparation of cell suspension and staining were done exactly as described previously for regular flow-cytometric analysis and passed freshly in two panels (Panels 1 and 2), as mentioned. Panel 1 experimental samples contained images and data for brightfield (channels 1 and 9), Ly6C-FITC (channel 2), Ly6G-PE (channel 3), mCherry (for mCh*Lgy*LRV1+ parasites) (channel 4), CD11b-PECy5 (channel 5), CD206-biotin revealed with SAV-PECy7 (channel 6), DAPI (channel 7), CD45.2-BV510 (channel 8), CCR2-APC (channel 11), and F4/80-APC/Cy7 (channel 12). Panel 2 experimental samples contained images and data for brightfield (channels 1 and 9), CD19-FITC (channel 2), NK 1.1-PE (channel 3), mCherry (for mCh*Lgy*LRV1+ parasites) (channel 4), CD3-PECy5 (channel 5), CD45-PECy7 (channel 6), DAPI (channel 7), MHC II-BV510 (channel 8), CD11c-APC (channel 11), and side scatter (SSC, channel 12). Single-color controls for both panels were acquired to generate the compensation matrixes, which were applied to each panel, respectively, prior to analysis using IDEAS (Image Data Exploration and Analysis Software) 6.2 software (Amnis Corporation). Cell internalization versus non-internalization, free or sticking to the cell surface or being in clumps for parasites, was defined using the internalization of the bright parasite spots within the membrane marker mask. Calculations and analyses of cell the population were done exactly as defined under FACS studies.

Cell depletion in mice

All the antibody dyes and beads used for cell depletions are detailed in Supplementary Table S2.

To study the individual effect of different cell types on disease progress and outcome, the infected model of *Ifng*$^{-/-}$ with fluorescent parasites mCh*Lgy*LRV1+ mice (as established and documented several times previously) was subjected to three different sets of major cell depletion *in vivo*, using defined depletion antibodies (all from BioXcell) as follows:

Neutrophil depletion: To deplete neutrophils, *Ifng*$^{-/-}$ mice were injected with purified *InVivo*MAb anti-mouse Ly6G (Clone 1A8, BioXcell) (Moynihan et al., 2016; Davis Iv et al., 2019) at a dose of 0.2 mg/200 μl (in 1× DPBS) i.p., twice at 24 and 6 h, before the point of infection with *Lgy* parasites and every 48 h thereafter, continued with an equivalent dose till 2 weeks post-infection. Control groups received similar doses of purified whole rat IgG [*InVivo*MAb rat IgG2a isotype control; anti-trinitrophenol (clone 2A3)] in the same timeline as the recommended control for the depletion.

Simultaneous neutrophil and monocyte depletion [with *InVivo*MAb anti-mouse Ly6G/Ly6C (Gr-1), clone RB6-8C5, BioXcell] (Bodogai et al., 2015; Bansal et al., 2018): to facilitate GR-1+ myeloid cell depletion *in vivo*, anti-mouse Ly6G/Ly6C (Gr-1) mAb at a dose of 0.3mg/200 μl (in 1× DPBS) was administered i.p. in *Ifng*$^{-/-}$ mice, daily for 3 days prior to infection, and then continued every 48 h thereafter, with an equivalent dose till 2 weeks post-infection. Control mice received similar doses of normal rat IgG2b isotype control [*InVivo*MAb, anti-keyhole limpet hemocyanin, (LTF-2), Bioxcell] as recommended control.

Macrophage depletion [with *InVivo*MAb anti-mouse CSF1R (CD115), clone AFS989, BioXcell] (Gordon et al., 2017; Bauché et al., 2018): *Ifng*$^{-/-}$ mice were injected i.p. with anti-CSF-1R mAb (AFS98) keeping rat IgG1 isotype control (rat IgG2a isotype control; anti-trinitrophenol was clone 2A3), at doses of 0.4 mg/200 μl (in 1× DPBS) daily for 4 days from point of infection and then continued every 48 h thereafter, with an equivalent dose till 2 weeks post-infection.

Additionally, peripheral blood smears (randomly selected from the subjects of each depletion group) were examined on day 0 and weekly thereafter, for the duration of the neutrophil and RB6-8C5 depletion period. Briefly, blood was collected from the submandibular vein, smeared onto a slide, and allowed to dry. Diff-Quick was used to stain the blood smears, and at least 200 nucleated cells per slide were counted by an individual experienced in counting blood differentials. Percentages of specific cell types were determined from the total number of cells counted.

Validation of antibodies

All antibodies used in this study for different purposes enlisted above are commercially available. See the corresponding manufacturer data sheets and cited references for use (on respective webpages) for further validation and protocol for individual antibodies. They further provide information about large-scale use and validation through defined means. We followed exactly similar protocols, which were defined in close context to our kind of mice studies. All antibodies were validated before use, and the information could be made available upon further request from the corresponding author.

Further information could be found by logging into the following major sites and providing the specific information about each of the antibodies enlisted for these studies:

For BioLegend antibodies: https://www.biolegend.com/

For eBioscience antibodies: https://www.thermofisher.com/ch/en/home/lifescience/antibodies/ebioscience.html

For BioXcell antibodies: https://bxcell.com/

For R& D systems antibodies: https://www.rndsystems.com/

For anti-mCherry mouse antibody from Abcam: https://www.abcam.com/mcherry-antibody-ab167453.html

Instruments for data collection

RNA isolation mice samples were facilitated by immersing them in TRI Reagent® (Molecular Research Center, Inc.) in RNAse-free tubes, adding stainless beads (Qiagen) and using Tissue Lyser system (Qiagen) for tissue disruption and homogenization. RNA was isolated through chloroform/isopropanol/ethanol phase separation, following the manufacturer's description. The quality and quantity of isolated RNA were analyzed using NanoDrop™ 2000 (Thermo Fisher Scientific). cDNA was generated using SuperScript II Reverse Transcriptase (Invitrogen). LightCycler® 480 SYBR Green I Master (Roche) along with 0.5 μM primer pairs was used for real-time quantitative PCR (RT-qPCR) on LightCycler® 480.

For bright light and fluorescent lymphangiography, euthanized mice were micro-dissected and imaged at 8× magnification (in both setup) for 30 min with a stereomicroscope (Leica, M205FA), and the acquired images were processed using LAS AF 6000 software.

Flow cytometry data were collected using BD LSRII or the BD LSR-Fortessa series (Becton Dickinson), and a minimum of 50,000 live cells were acquired for each set of analysis. Additionally, for imaging flow cytometry, samples were run in a two-camera, 12-channel Image-StreamX multispectral imaging flow cytometer (Amnis, Luminex Corporation) at low speed and highest magnification (60×). Instrument setup and performance tracking were performed daily using the Amnis® SpeedBead® Kit (Luminex Corporation) to verify optimal instrument performance. Cells were excited using a 405-nm laser (25 mW), a 488-nm laser (100 mW), a 561-nm yellow laser (200 mW), and a 642-nm red laser (150 mW). Only events with a brightfield area >5 μm^2 (to exclude cell debris) and non-saturating pixels were collected. Data were acquired for a minimum of 50,000 events/sample. Moreover, panel design was based on antigen expression density, fluorochrome brightness, and reagent availability in each panel for the four-laser, 12-parameter ImageStreamX. Preparation of cell suspension and staining were done exactly as described for regular flow-cytometric analysis and passed freshly in two panels (Panels 1 and 2) as mentioned. Panel 1 experimental samples contained images and data for brightfield (channels 1 and 9), Ly6C-FITC (channel 2), Ly6G-PE (channel 3), mCherry (for mChLgyLRV1+ parasites) (channel 4), CD11b-PECy5 (channel 5), CD206-biotin revealed with SAV-PECy7 (channel 6), DAPI (channel 7), CD45.2-BV510 (channel 8), CCR2-APC (channel 11), and F4/80-APC/Cy7 (channel 12). Panel 2 experimental samples contained images and data for brightfield (channels 1 and 9), CD19-FITC (channel 2), NK 1.1-PE (channel 3), mCherry (for mChLgyLRV1+ parasites) (channel 4), CD3-PECy5 (channel 5), CD45-PECy7 (channel 6), DAPI (channel 7), MHC II-BV510 (channel 8), CD11c-APC (channel 11), and side scatter (SSC, channel 12). Single-color controls for both panels were acquired to generate the compensation matrixes, which were applied to each panel, respectively.

For immuno-fluorescence microscopy, images were partly acquired using an Olympus VS120-SL full slide scanner with a 20×/0.75 air objective (using Olympus OlyVIA software), at the EPFL BioImaging & Optics Platform (BIOP), or with Zeiss Axio-Imager Z1, Upright in Cellular Imaging Facility, Epalinges (using Axiovision SE64 rel 4.9.1 software). For the images acquired using the Olympus VS120-SL full slide scanner, individual images were acquired using the indicated fluorescent channels having the same exposure time employed across different samples. For *in vivo* bioluminescence imaging and quantification of parasite burden and inflammation, parasite bioluminescence produced in the mouse footpads and other visible secondary lesions (like tail and snout) were acquired with *In-Vivo* Xtreme II (Bruker).

Software used for analysis

For cell suspension prepared for each LN and tissue, cell numbers and cell viability were assessed *via* Trypan blue (Sigma-Aldrich) exclusion using an improved counting Neubauer chamber (Assistant®, catalog number: 40442). For limiting dilution assay and analysis, parasite number was determined from the lowest cell concentration from which promastigotes could be grown using the ESTIMFRE software. The corresponding heatmaps were generated using the R ComplexHeatmap package. The color gradient represented in the heatmaps are correlated to the number of + signs assigned in terms of infection in progressive dilution series through LDA for each organ, where increased color intensity corresponded to higher parasite load.

For RT-qPCR, gene expression was analyzed using the threshold cycle (CT) method $2^{-\Delta\Delta CT}$. Data analyzed for *Leishmania Kmp11* gene expression in different organs of the infected mice were assessed using predetermined levels of *Kmp11* expression in *Lgy* parasites and normalized to the total RNA quantity of the sample.

For bright light and fluorescent lymphangiography, acquired images were processed using LAS AF 6000 software along with processing, tiling, and stitching on Photoshop (version 21.2.0), in case of fluorescence-based images of whole mouse (represented in Figure 5).

For immuno-fluorescence microscopy, images were extracted using the VSI reader action bar [provided by the EPFL BioImaging & Optics Platform (BIOP)]. Olympus slide scanner software (OlyVIA v.2.6) was employed to directly analyze the images from different groups by adjusting the same contrast and brightness settings, across different groups.

For conventional FACS analysis, data were analyzed with FlowJo software (Tree Star, v10.0.6). For data analyses, a minimum of 50,000 events (cells) were evaluated at all times, by back-gating from CD45+/− stained cells. For imaging FACS, analysis was done using IDEAS (Image Data Exploration and Analysis Software) 6.2 software (Amnis Corporation).

For mice *in vivo* bioluminescence imaging and quantification of parasite burden and inflammation, acquired images were analyzed using Molecular Imaging (MI) software (Bruker), setting specific ROIs on FP, tail, etc., and expressing the measured bioluminescence signals in units of photons per second (p/s).

Additional information on calculations and gating strategy

Cell population calculation through flow cytometry

A total of 1–2 million cells were stained and collected on each measurement for both kinds of cytometer.

For conventional FACS analysis, data were analyzed with FlowJo software (Tree Star, v10.0.6). For data analyses, a minimum of 50,000 events (cells) were evaluated at all times, by back-gating from CD45+/− stained cells. The absolute number of total leukocytes or each represented cell type was quantified by multiplying the total number of cells observed by hemocytometer counting with the percentage of those individual cells (on total CD45+ cells) determined by flow cytometry. The absolute number of each leukocyte subset (for example, 1A8, Ly6C, Ly6G, CD11b and, CCR2) was determined by multiplying the percentage of each gated population by the total number of $CD45^+$ cells. For imaging FACS, analysis was done using IDEAS (Image Data Exploration and Analysis Software) 6.2 software (Amnis Corporation). Cell internalization versus non-internalization, free or sticking to cell surface or being in clumps for parasites, was defined using the internalization of the bright parasite spots within the membrane marker mask. Calculations and analyses of cell population were done exactly as defined for conventional FACS studies. For the distribution of $mCherry^+$ parasites on cell-associated or non-cell-associated $TER119^-CD45+$ immune cells, we calculated it from the point of view of the $mCherry^+$ parasites, distributing the total numbers of $mCherry^+$ parasites observed in any organ over its numbers that were either colocalized with $TER119^-CD45^+$ membrane marker (thus, cell associated) or not (non-cell-associated).

Gating strategy for Panels 1 and 2 of flow-cytometric analysis

For imaging flow cytometry (Imaging Stream® analysis), samples were run in a two-camera, 12-channel Image-StreamX multispectral imaging flow cytometer (Amnis, Luminex Corporation) at low speed and highest magnification (60×). Instrument setup and performance tracking were performed daily using the Amnis® SpeedBead® Kit (Luminex Corporation) for verifying optimal instrument performance. Cells were excited using a 405-nm laser (25 mW), a 488-nm laser (100 mW), a 561-nm yellow laser (200 mW), and a 642-nm red laser (150 mW). Only events with a brightfield area >5 µm² (to exclude cell debris) and non-saturating pixels were collected (as described in Henery et al., 2008). Data were acquired for a minimum of 50,000 events/sample. Panel design was based on antigen expression density, fluorochrome brightness, and reagent availability in each panel for the four-laser, 12-parameter ImageStreamX. Preparation of cell suspension and staining were done exactly as described previously for regular flow-cytometric analysis and passed freshly in two panels (panels 1 and 2), as mentioned. Panel 1 experimental samples contained images and data for brightfield (channels 1 and 9), Ly6C-FITC (channel 2), Ly6G-PE (channel 3), mCherry (for mCh*Lgy*LRV1+ parasites) (channel 4), CD11b-PECy5 (channel 5), CD206-biotin revealed with SAV-PECy7 (channel 6), DAPI (channel 7), CD45.2-BV510 (channel 8), CCR2-APC (channel 11), and F4/80-APC/Cy7 (channel 12). Panel 2 experimental samples contained images and data for brightfield (channels 1 and 9), CD19-FITC (channel 2), NK 1.1-PE (channel 3), mCherry (for mCh*Lgy*LRV1+ parasites) (channel 4), CD3-PECy5 (channel 5), CD45-PECy7 (channel 6), DAPI (channel 7), MHC II-BV510 (channel 8), CD11c-APC (channel 11), and side scatter (SSC, channel 12). Single-color controls for both panels were acquired to generate the compensation matrixes, which were applied to each panel, respectively, prior to analysis using IDEAS (Image Data Exploration and Analysis Software) 6.2 software (Amnis Corporation). Similar gating strategy to encompass the infections in different cell types was applied in conventional FACS as well. Thus, a representative example of gating strategy for both kinds of cytometer measurement (conventional and Amnis) is provided as auxiliary Supplementary 1, 2 in separate files (as they are too heavy in size), to define the gating strategy for panels 1 and 2, respectively.

Statistical analysis

GraphPad Prism8 [version 8.1.1(330)] was pertinently used to generate all the graphs and related statistical analysis. For single-point analysis on bar graphs, unpaired Student's test was used, while repeated-measures two-way ANOVA test was used for x/y curves, with Bonferroni's post-test correction. Significance was reached with p-values of 0.05, and p-values were represented in four ranks as * for $p < 0.05$, ** for $p < 0.01$, *** for $p < 0.001$, and **** for $p < 0.0001$. NS means non-significant statistical difference and was majorly not represented on graphs.

Results

*Lgy*LRV1+ induces a progressively severe metastatic phenotype in *Ifng*$^{-/-}$ mice

Interferon gamma (IFN-γ) is crucial for immunity against intracellular pathogens such as *Leishmania* parasites (Rossi et al., 2017), and in its absence, patients are prone to chronic metastatic complications (Hartley et al., 2016). As experimental model for the dissemination in response to an LRV1-dependent acute inflammatory stimulus, we infected groups of *Ifng*$^{-/-}$ mice in the hind FPs with either *Lgy*LRV1+ or *Lgy*LRV1−. *Ifng*$^{-/-}$ mice infected with *Lgy*LRV1+ showed a significant increase in FP lesion (Figure 1A) and parasite burden in FP (Figure 1B). Both peaked at week 4 post-infection (W4 p.i.), while the parasite burden increased progressively in the tail and remained significantly higher in the *Lgy*LRV1+ group (Figure 1C) from week 2 post-infection (W2 p.i.) till the end of infection, as compared to their *Lgy*LRV1−-infected counterparts. A detailed kinetic and comparison of parasite dissemination in *Ifng*$^{-/-}$ mice infected with either *Lgy*LRV1+ or *Lgy*LRV1− *in vivo* were documented weekly at each time point of infection with representative mice from both groups by superimposing X-ray pictures and bioluminescence of parasites expressing the LUC gene (Figure 1D). This confirmed that parasite dissemination in distant secondary organs, such as the tail (around W2 p.i.), or even in the forelimb and snout (around W8 p.i.), in the *Ifng*$^{-/-}$ *Lgy*LRV1+ group appeared much earlier as compared to the *Ifng*$^{-/-}$ *Lgy*LRV1− group, where the same phenotype appeared significantly delayed. Furthermore, the metastatic score, defined as the absolute count of the number of secondary nodules per tail, also appeared earlier and was significantly higher in the *Ifng*$^{-/-}$ *Lgy*LRV1+ group from week 7 p.i. onwards, till the end of infection (Figure 1E). Moreover, inflammation measured by myeloperoxidase activity (Eren et al., 2016; Reverte et al., 2021) was significantly higher both in the FP (Figure 1F) and in the tail (Figure 1G) of the *Ifng*$^{-/-}$ *Lgy*LRV1+ group consistently along the course of infection. We therefore confirmed and established the detailed kinetic of LRV1-associated disease exacerbation and increased metastatic outcome in *Ifng*$^{-/-}$ *Lgy*LRV1+ mice model *in vivo*, as described earlier (Hartley et al., 2016). To further validate our model of parasite dissemination and metastasis, *Ifng*$^{-/-}$ mice were infected either with the same number of *Lgy*LRV1+ parasites in lesser volume of injection (i.e., in 5 µl, for volume control) (Figure 2A) or injected with 10-fold lesser number of *Lgy*LRV1+ (1×10^5, for parasite number control) (Figure 2B). Results showed a delayed but similar final disease outcome in terms of lesion growth in footpads and metastatic score in the tail, as compared to an infection with 1×10^6 parasites/50 µl/FP (Figures 2A–C). Additionally, the levels of IL6 and IFN-γ cytokine were measured on the cell-free supernatant isolated from the primary draining lymph node (PLN) at 48 h p.i. from *Ifng*$^{-/-}$, *Ifng*$^{+/-}$, and WT (*Ifng* $^{+/+}$) mice groups, infected with *Lgy*LRV1+. Interestingly, IL6 cytokine production was equal between all the three groups and IFN-γ production was found to be equal between both *Ifng*$^{-/-}$ and WT (*Ifng*$^{+/+}$) group as compared to the negative control (*Ifng*$^{-/-}$ mice), thereby confirming the haplo-sufficiency of the IFN-γ allele *in vivo* (Figure 2D). Moreover, parasite burden was also found to be equal in the FP, PLN, ILN, and iliac LN, between the *Ifng*$^{+/-}$ and WT group and significantly lower in both these groups as compared to the *Ifng*$^{-/-}$ group, at the peak of infection (W4 p.i.) (Figure 2E). These results collectively established our model of IFN-γ-dependent infectious metastasis and *Leishmania* RNA virus (LRV1+)-associated disease exacerbation, detailing the various hallmarks of disease progression in terms of *Lgy* infection.

LRV1 induces hyper-inflammation of the draining LNs in metastatic *Ifng*$^{-/-}$ mice

LNs draining their immediate organ such as popliteal LNs (PLNs) draining FP are used to characterize the immune response to an acute inflammatory stimulus (Morton et al., 2003; Saharinen and Petrova, 2004; Angeli et al., 2006). We therefore mapped the location of different lymph nodes (LNs) in naive *Ifng*$^{-/-}$ mice by injecting 5% Evan's blue dye solution (Supplementary Figures S1A–C) for further extrapolating it to investigate the *in vivo* hubs of escaping infected cells in our infected metastatic model of FP infection (Van den Broeck et al., 2006; Harrell et al., 2007; Harrell et al., 2008). Thus, FP Evan's blue lymphatic mapping of naive *Ifng*$^{-/-}$ mice and *Ifng*$^{-/-}$ mice infected in both FP 4 weeks previously, i.e., at week 4 (W4) post-infection (p.i.) with *Lgy*LRV1+, revealed a visible blue drainage and simultaneous LRV1 exacerbated cellular increase in FP, tail, and different LNs like popliteal (PLN), inguinal (ILN), sciatic (SLN), iliac LN, axillary (ALN), and mesenteric (MLN) as compared to their *Lgy*LRV1− counterparts (Figures 3A–H). Representative stereomicroscopic images showed an evident deep blue labeling and visible increase in size of popliteal (PLN), inguinal (ILN), sciatic (SLN), iliac LN, and axillary (ALN); faint blue labeling of mesenteric (MLN) while no labeling of brachial (BLN) and cervical (CLN) in both the naive and infected groups of *Ifng*$^{-/-}$ mice. Therefore, the visible hyper-inflammation of different blue-labeled draining LNs suggested a highly active LN contribution to *Lgy* parasite metastasis *in vivo.*

LRV1 induces exacerbated parasite dissemination to lymph nodes

We therefore collected the different LNs coming from the right and left sides of *Ifng*$^{-/-}$ mice groups infected with either *Lgy*LRV1+ or *Lgy*LRV1−, along with the FP, spleen, liver, kidney, and tail (divided into eight pieces: T1–T8), and subjected their organ suspensions to an LDA. This ensured the comparison of both *Lgy*LRV1+ or *Lgy*LRV1−-infected mice groups from week 1 to 10 p.i. LDA permits the recovery and culture of free-living motile promastigote parasites, serving as a proxy to quantify the degree of infection in each tissue. The higher inflammation correlated with the progressive presence and increase in *Lgy* parasites in the culture for different organs along the course of infection. As represented by heatmaps where increased color intensity corresponds to higher parasite load, parasites were detected in the culture in a defined order, first in PLN followed by ILN, SLN, and iliac LN showing parasite presence almost at the same time but not at equivalent level (Figures 4A, B). The more distant LNs, namely, brachial and superficial cervical (BLN and CLN, respectively), spleen, and blood showed increased parasite burden only towards the late phase of chronic infection (from W4 to W6 onwards). Major infected sites, namely, FP, PLN, ILN, SLN, iliac LN, ALN, forelimb, and tail, showed significantly higher quantifiable parasite burden in the *Lgy*LRV1+ group, as compared to their *Lgy*LRV1− counterparts (Figure 4C). A schematic elucidates the time-dependent comparison of *Lgy* dissemination through LNs, between the *Ifng*$^{-/-}$ *Lgy*LRV1+ (red) and *Ifng*$^{-/-}$ *Lgy*LRV1− (blue) infection groups, for visual reference (Supplementary

Figures S2A–E). We further investigated if parasite dissemination occurred similarly in infections with other *Leishmania* species. Although we observed a similar dissemination pattern through LNs when *Ifng*$^{-/-}$ mice were infected with *L. major* (*Lmj*) (Supplementary Figure S3A), at no point were secondary debilitating lesions observed, in any distant organ like the tail, snout, or forelimb (Supplementary Figures S3B–D). This strongly suggested that the observed disseminating phenotype was not *Leishmania* species specific but that the occurrence of debilitating lesions was.

*Lgy*LRV1+ parasites disseminate through the lymphatics

Evan's blue lymphangiography confirmed the active involvement of different draining LNs due to *Lgy* infection, thereby raising questions whether lymphatic connections emanating from the site of infection could act as the major routes for the dissemination of *Lgy* parasites resulting in severely inflamed LNs and, therefore, widespread metastasis. We thus explored the major lymphatic collecting vessels through fluorescent lymphangiography in infected *Ifng*$^{-/-}$ mice (Zheng et al., 2014; Wang et al., 2015; Yamaji et al., 2018) to test this hypothesis. At defined points of infection, *Ifng*$^{-/-}$ mice infected with *Lgy*LRV1+ were injected with 5 µl of fluorescein-isothiocyanate (FITC)-labeled dextran at three different sites to visually track the existing lymphatic connections. Injection in both hind FP at week 4 post-infection (W4 p.i.) showed four major collecting vessels that emanated from the FP: route 1 (R1) with one long lymphatic connection from FP to PLN to SLN draining into the iliac LN ventrally (Figure 5A1); route 2 (R2) connecting FP directly to iliac LN; route 3 (R3) observed from iliac LN to centrally located cisterna chyli (CC), while MLN is simultaneously positive, and all these connections ultimately drained upwards into the thoracic duct; and route 4 (R4) connecting the FP to ILN to ALN to the subclavian vein (Figure 5A2). Injection at the tip of the tail at W7–W8 p.i. revealed route 5 (R5) showing the collecting vessels from the tail tip upwards to the SLN to iliac LN ventrally, which ultimately joined route 3 (R3) upwards to the thoracic duct (Figure 5B). Finally, forelimb injection documented two major lymphatic connections: route 6 (R6) connecting the forelimb to BLN to ALN to the subclavian vein and route 7 (R7) connecting the forelimb directly to ALN to the subclavian vein region (Figure 5C). The different routes of lymphatic connections along with the direction of lymph flow are detailed comprehensively in schematic diagrams for each site of reference (Supplementary Figures S4A–C). These results collectively revealed the intricate lymphatic pathways of FP drainage, which were used by *Lgy* parasites in our metastatic model as indicated by the sequence of LNs infected over time (Figure S4D). Thus, we could conclude that the lymphatic vessels could participate in the dissemination of *Lgy* infection from the primary site, which then leads to the formation of loco-regional metastases in various organs, mainly in the LNs, and lead to their large-scale distribution.

*Lgy*LRV1+ exhibits early infection of innate immune cells

Once the various routes of dissemination were established, *Ifng*$^{-/-}$ mice were infected with fluorescent mCherry-expressing *Lgy*LRV1+ parasites (mCh*Lgy*LRV1+), and FP, PLN, BLN, and tail samples were collected at 3 h, 14 h, 60 h, W1, W2, W4, and W6 p.i. Flow-cytometric analysis of each enzymatically dissociated organ determined the total number of infected (mCherry^{+}) cells for different immune cell populations (Figure 6A). Recruited neutrophils were infected first, followed by monocytes, inflammatory monocytes (expressing CCR2^{+}), and then macrophages from W1 p.i. All these cells had immigrated from the blood and got infected in cycles along the course of infection, both in FP and PLN. Although BLN showed macrophage infection only from W4 p.i., all different kinds of innate cells were infected in the tail towards the second half of infection (Figure 6A). Imaging flow cytometry on samples from *Ifng*$^{-/-}$ mice infected with mCh*Lgy*LRV1+ showed that neutrophils were the first and most abundantly increased cells in systemic circulation and varied in abundance in cycles along the course of infection, followed by monocytes, inflammatory monocytes (expressing CCR2^{+}), macrophages, and even B and T cells (Figures 6Bi, ii). However, none of these blood immune cells harbored significant parasite levels during the chronic phase of infection (Figure 6B, ii).

Extracellular mCh*Lgy*LRV1+ amastigotes stick around recruited immune cells

Remarkably, 98%–99% of mCherry^{+} *Lgy*LRV1+ parasites in the blood were observed as free amastigotes towards the latter half of infection, i.e., as non-host-cell-associated mCherry^{+} amastigotes in the TER119^{-}CD45^{-} population (Figure 6B, iv). However, approximately 1%–2% of the total parasites were also CD45^{+} immune cell associated, infecting neutrophils and monocytes in lower numbers (Figure 6B, iv7). We thus investigated whether the total mCherry fluorescence observed in different organs was due to free amastigotes (i.e., in the TER119^{-}CD45^{-} non-hematopoietic cell population) or due to infected cells (associated to TER119^{-}CD45^{+} immune cells). Our results showed that the majority of the mCherry^{+} parasite fluorescence (≥90% at each time point of infection, calculated from the parasite perspective) observed in each of the FP, PLN, CLN, and tail was due to non-immune cell-associated free amastigotes as compared to that associated with CD45^{+} cells (Figure 6C). Imaging flow cytometry also confirmed the presence of free mCherry^{+} parasites in the blood at W2, W4, and W6–W7 p.i. (Figure 6D).

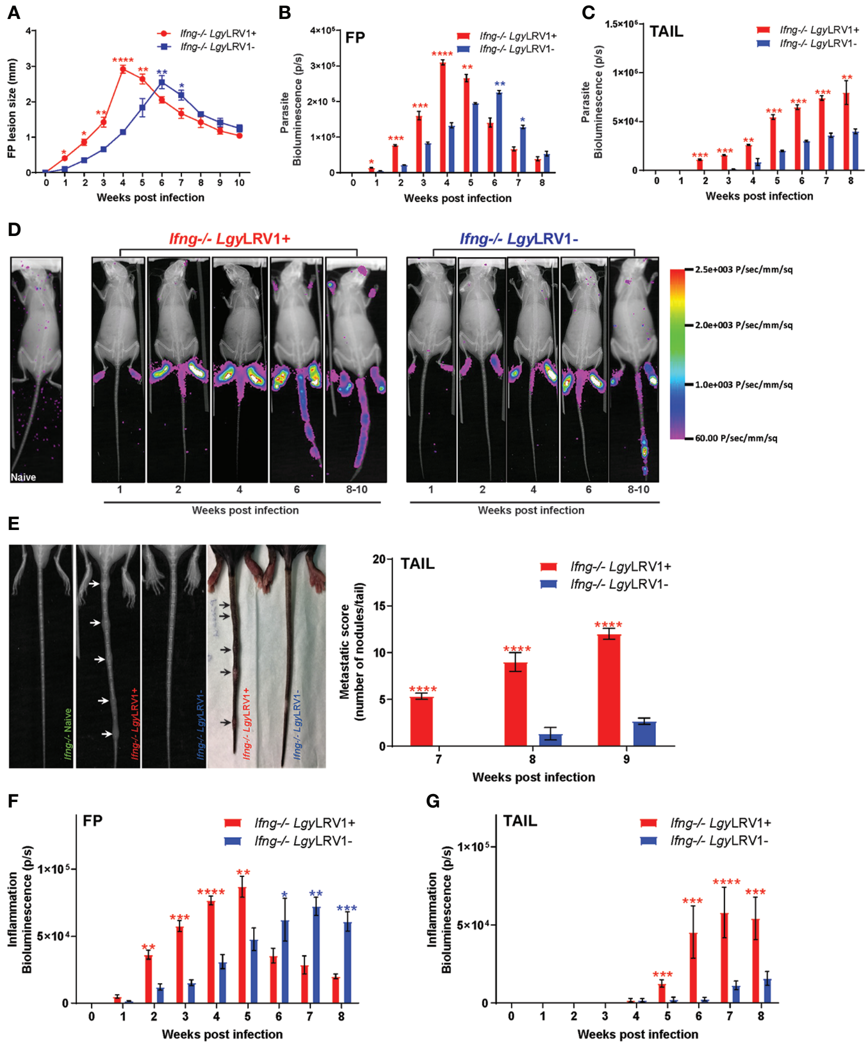

FIGURE 1

*Lgy*LRV1+ parasites induced a progressively severe metastatic phenotype in Ifng $^{-/-}$ mice. **(A–G)** Ifng$^{-/-}$ mice were infected in the hind FP with 1x10^{6} *Lgy*LRV1+ or *Lgy*LRV1- stationary-phase metacyclic promastigotes. Different proxies of disease progression were documented weekly from W1-W8 p.i, between *Lgy*LRV1+ (red) and *Lgy*LRV1- (blue) groups by measuring **(A)** FP swelling; **(B–D)** parasite burden measured in terms of parasite bio-luminescence in **(B)** FP ; **(C)** Tail ; and **(D)** representative images comparing the pattern of parasite dissemination along whole mice body between both groups with time; **(E)** x-ray pictures, along with camera pictures, showing the appearance of metastatic nodules, quantified by absolute count of the number of nodules per tail in both groups. **(F, G)** inflammation measured in terms of myeloid peroxidase activity, quantified by parasite bio-luminescence weekly in **(F)** FP and **(G)** Tail. Represented statistical data are a pool of three independent experiments whereas associated images are representative from one of these experiments of the pool, with n $\geq$ 10 mice /group/ time point. Each experiment was repeated 5 times independently with similar results. The statistics are shown as mean ± SEM with p values determined for significance, calculated at each mentioned time-point between both groups, using two-way ANOVA with Bonferroni's post-test for A-C and E-G. Stars of significance are determined as *p < 0.05; **p < 0.01; ***p < 0.001; ****p < 0.0001. Non-significant differences (ns) were not represented on the graphs while stars for significance were annotated in red if the value associated with LgyLRV1+ is > LgyLRV1–, and in blue if LgyLRV1– > LgyLRV1 +, at each time- point, for easy reference.

Imaging flow cytometry was thus further employed to understand the unexpected presence of a significantly lower number of infected cells but higher percentage of free parasites in each infected organ. Representative images revealed a significantly higher recruitment of neutrophils along with few DCs, as the first cells to arrive at the site of infection (FP) approximately 3 h p.i. While recruited neutrophils took up parasites and thus exhibited significant mCherry internalization, DCs appeared practically uninfected, and the injected mCh*LgyLRV1+* parasites mostly appeared as flagellated extracellular promastigotes in the FP of infected *Ifng*$^{-/-}$ mice at 3 h p.i (Figure 7A). Although various other immune cell types showed increase in numbers within 24 h p.i. at the site of infection, only neutrophils and various subsets of monocytes

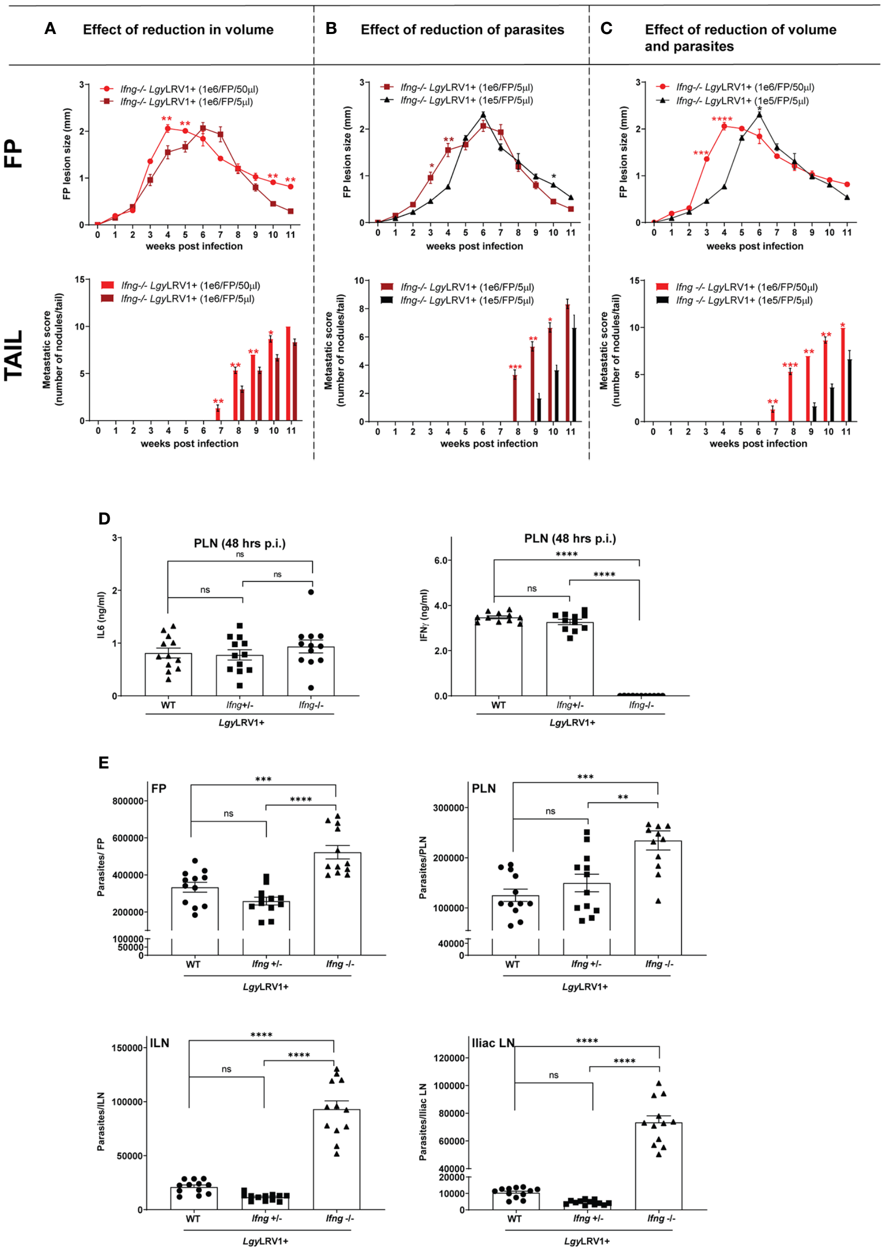

FIGURE 2

(A–C) Reduction in parasite number and volume of infection just delayed the metastatic phenotype in *Ifng*$^{-/-}$ *Lgy*LRV1+ model: *Ifng*$^{-/-}$ mice were infected in the hind FPs with different numbers of *Lgy*LRV1+ stationary-phase metacyclic promastigotes, in different volumes as defined by group. Proxies of disease progression in terms of FP lesions (in mm) and metastatic outcome on TAIL were documented weekly, along the course of infection, between **(A)** group infected with 1x10^{6} parasites/FP in 50 µl versus group infected with 1x10^{6} parasites/FP in 5 µl, **(B)** group infected with 1x10^{6} parasites/FP in 5 µl versus group infected with 1x10^{5} parasites/FP in 5 µl, and **(C)** group infected with 1x10^{6} parasites/FP in 50 µl versus group infected with 1x10^{5} parasites/FP in 5 µl. **(D)** *Ifng* gene is haplo-sufficient for the production of active IFN-γ cytokine: WT, *Ifng*$^{+/-}$ and *Ifng*$^{-/-}$ mice groups were infected in the hind FP with 1x10^{6} *Lgy*LRV1+ stationary-phase metacyclic promastigotes. Cell suspension supernatants from PLN, extracted from each infected group, were measured for the secreted levels of IL-6 and IFN-γ cytokines, at 48 h p.i., by ELISA. **(E)** Both WT and *Ifng*$^{+/-}$ infected groups showed equivalent parasite burden in infected organs, at the peak of infection: WT, *Ifng*$^{+/-}$, and *Ifng*$^{-/-}$ mice groups were infected in the hind FP with 1x10^{6} *Lgy*LRV1+ stationary-phase metacyclic promastigotes. Parasite burden assessed in terms of relative RNA expression levels of parasite specific *Kmp11* gene, at week 4 p.i. in the FPs, PLN, ILN, and iliac LN, in each infected group by RT-qPCR. Data are expressed (for each set of experiments above) as mean ± SEM from a pool of three independent experiments (n=12 mice/group) and repeated independently four times with similar results, p-values determined for significance, calculated at each mentioned time point between different groups, using two-way ANOVA with Bonferroni's post-test; significance is indicated as *p < 0.05, **p < 0.01, ***p < 0.001, and ****p < 0.0001; ns, non-significant differences.

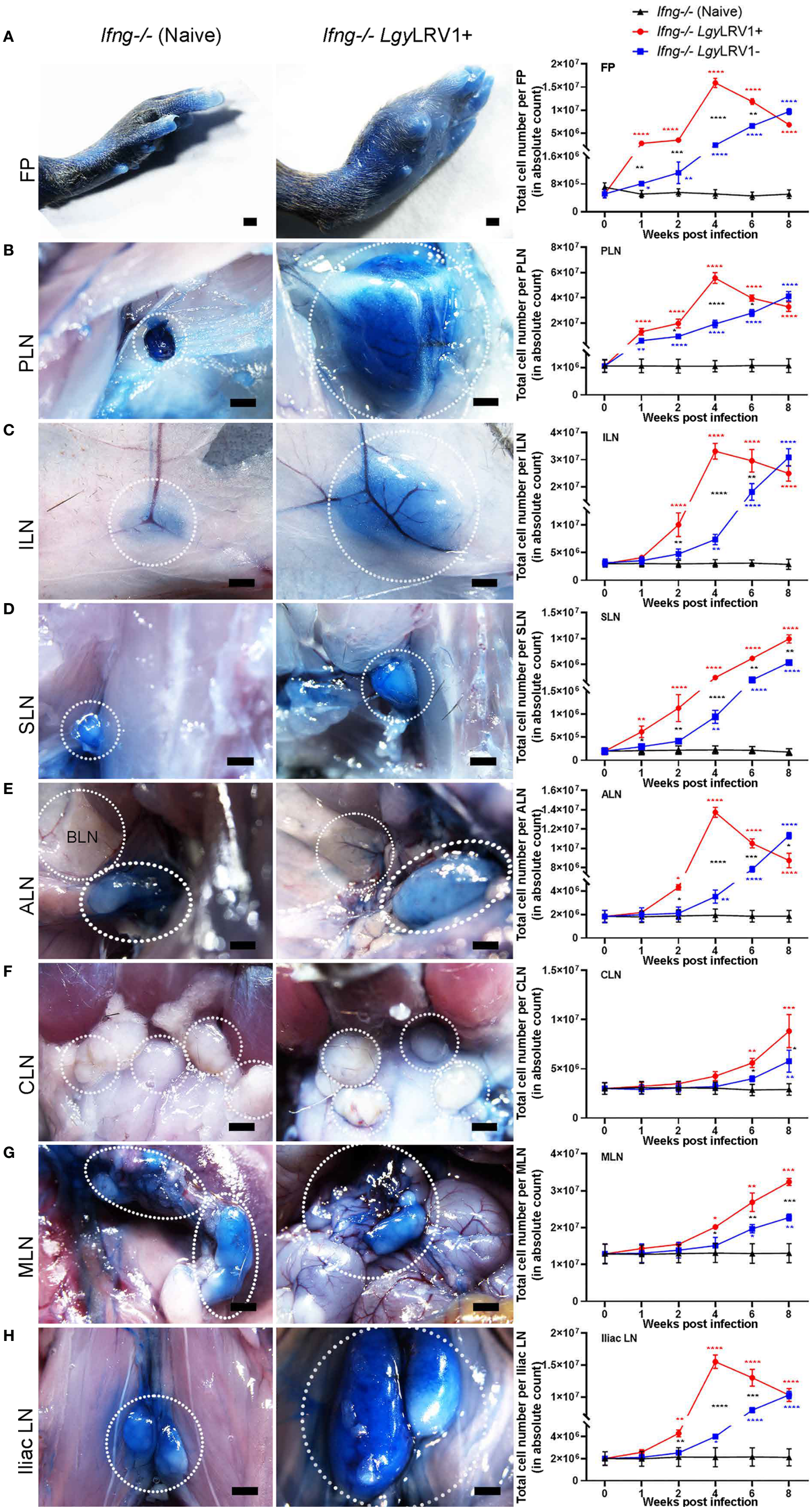

FIGURE 3 (Continued)

FIGURE 3 (Continued)
*Lgy*LRV1+ parasites triggered increased Evan's blue drainage and hyper-inflammation of draining LNs. **(A–H)** Stereomicroscopic images (scale bars: 1 mm) of the LNs were taken, after injecting 5% Evan's blue (in DPBS) for 20 min, in the hind FP of both *Ifng*$^{-/-}$ naive and *Ifng*$^{-/-}$ *Lgy*LRV1+ at week 4 p.i. (as represented in columns 1 and 2, respectively). Simultaneously, *Ifng*$^{-/-}$ mice were infected at 1x10^6/FP either with *Lgy*LRV1+ (*Ifng*$^{-/-}$ *Lgy*LRV1+ in red) or *Lgy*LRV1– (*Ifng*$^{-/-}$ *Lgy*LRV1– in blue), along with the uninfected PBS-injected control (*Ifng*$^{-/-}$ naive in black). The total number of cells in each of the three groups from W1 to W8 p.i. are represented in **(A)** FP, **(B)** PLN, **(C)** ILN, **(D)** SLN, **(E)** ALN, **(F)** CLN, **(G)** MLN, and **(H)** iliac LN in column 3. These cell counts of each organ are representative of three pooled experiment ($n \geq 18$ mice/group/time point) and repeated at least three times independently with similar results for each group. Thus, represented statistical data are a pool of three independent experiments, whereas associated images are representative from one of these experiments of the pool, with $n \geq 5$ mice/group/time point, and repeated five times with similar results. Statistics are represented as mean ± SD with p-values and significance determined by performing two-way ANOVA with Bonferroni's post-test on cell counts of each group, at each time point. Only significant points were determined as *$p < 0.05$, **$p < 0.01$, ***$p < 0.001$, and ****$p < 0.0001$, and annotated in red (*Lgy*LRV1+) and in blue (*Lgy*LRV1–), as compared to naive. Significance between *Lgy*LRV1+ and *Lgy*LRV1–, at each time point, is denoted by black asterisk.

(defined from ii to ix in Figure 7B) appeared to have internalized only a part of the parasite on site by this time. The mCh*LgyLRV1+* parasites on site appeared sequestered and more roundish, mostly existing as non-cell-associated extracellular amastigotes around the recruited immune cells (Figure 7B). Furthermore, both FP and PLN showed the maximum number of infected cells (as described previously in FACS studies, too) at W2 p.i. We indeed observed a significant amount of mCh*LgyLRV1+* parasites, either internalized by several subsets of monocytes, neutrophils, and macrophages, while a part of them stayed non-internalized around various recruited adaptive and innate cells, as extracellular amastigotes both in FP and PLN, at even W2 p.i. Collectively, we observed that mCh*LgyLRV1+* parasites were mostly distributed in three independent categories: (a) within neutrophils and, to a lesser extent, in monocytes and its various subtypes and in macrophages; (b) extracellularly around various innate and adaptive cell types; (c) majority as free/extracellular parasites or as clumps of parasites in all infected organs, as represented at 3 and 24 h p.i. in FP (Figures 7A, B) and at W2 p.i. in both FP and PLN (Figure 7C). Thus, the presence of these non-cell-associated amastigotes in various infected organs and even blood (during chronic phase of infection) pointed towards the possibility of non-cellular transport of *Lgy* parasites as well.

Extracellular mCh*Lgy*LRV1+ amastigotes disseminate *via* lymphatics to blood

Following our FACS analysis, we further assessed parasite localization in the different LNs *via* histological analysis. Immunofluorescence (IF) microscopy was performed on PLN (as the first LN shown to drain the FP), on ILN, and on iliac LN (as the two next draining LNs of FP-derived lymph), and in parallel on CLN as the non-draining negative control LN from *Ifng*$^{-/-}$ mice infected with mCh*Lgy*LRV1+ at W2 p.i. As expected, we detected mCherry$^+$ *Lgy* parasites both in the FP and PLN from infected *Ifng*$^{-/-}$ mice (W2 p.i) but not in uninfected FP and PLN from *Ifng*$^{-/-}$ mice (Supplementary Figure S5A). Additionally, collagen IV and B220 staining of the basement membrane and B-cell follicles, respectively, elucidated the different zones in each of these massively swollen, infected LNs and localized mCherry$^+$ parasites mainly within the subcapsular sinus (SCS) and medullary sinus (MS) spaces (Supplementary Figure S5B). We observed that mCh*Lgy*LRV1+ parasites decreased progressively in number from PLN to ILN and furthermore in iliac LN, as based on their distance to the FP, while being practically absent in the most distant CLN (Figures 8A–E). Subsequently, we stained these LNs for different vascular cell types. We confirmed that the *Lgy* parasites were mostly located in Lyve1$^+$ lymphatic sinus space, both in the SCS and MS of each infected LN, while the CD31$^+$ blood vessels showed a meager-to-no mCherry$^+$ co-localization at this point of infection (Figure 8A).

Infected organs are populated with extracellular mCh*Lgy*LRV1+ amastigotes

As neutrophils and fibroblastic reticular cell (FRCs) are known to be infected by *Leishmania* parasites (Bogdan et al., 2000; Hurrell et al., 2016), the FRC network and neutrophil infiltration were investigated by GP-38 and NIMP-14 staining, respectively. While FRCs showed little change in their architecture, we observed massive neutrophil recruitment that appeared to correlate with the mCherry$^+$ parasite presence in the primary drained PLN and even in the more distantly drained ILN and iliac LN, while very few neutrophils were observed in the CLN. However, most recruited neutrophils and resident FRCs were not found to be harboring mCherry+ parasites (Figure 8B). Additionally, these LNs were also stained with antibodies for other innate immune cell types. While CD11b$^+$ monocytes/macrophages and CD169$^+$ macrophages frequently showed intracellular parasite staining (Figures 8C, 9C, respectively), significantly lower numbers of CD11c$^+$ DCs harbored parasites (Figure 8C). CCR2$^+$ inflammatory monocytes were less frequent in the infected LNs and showed very low levels of infection/co-localization with the mCh*Lgy*LRV1+ parasites present within the organs, as observed earlier for neutrophils as well (Figure 8D). Moreover, both B and T cells showed no significant parasite internalization

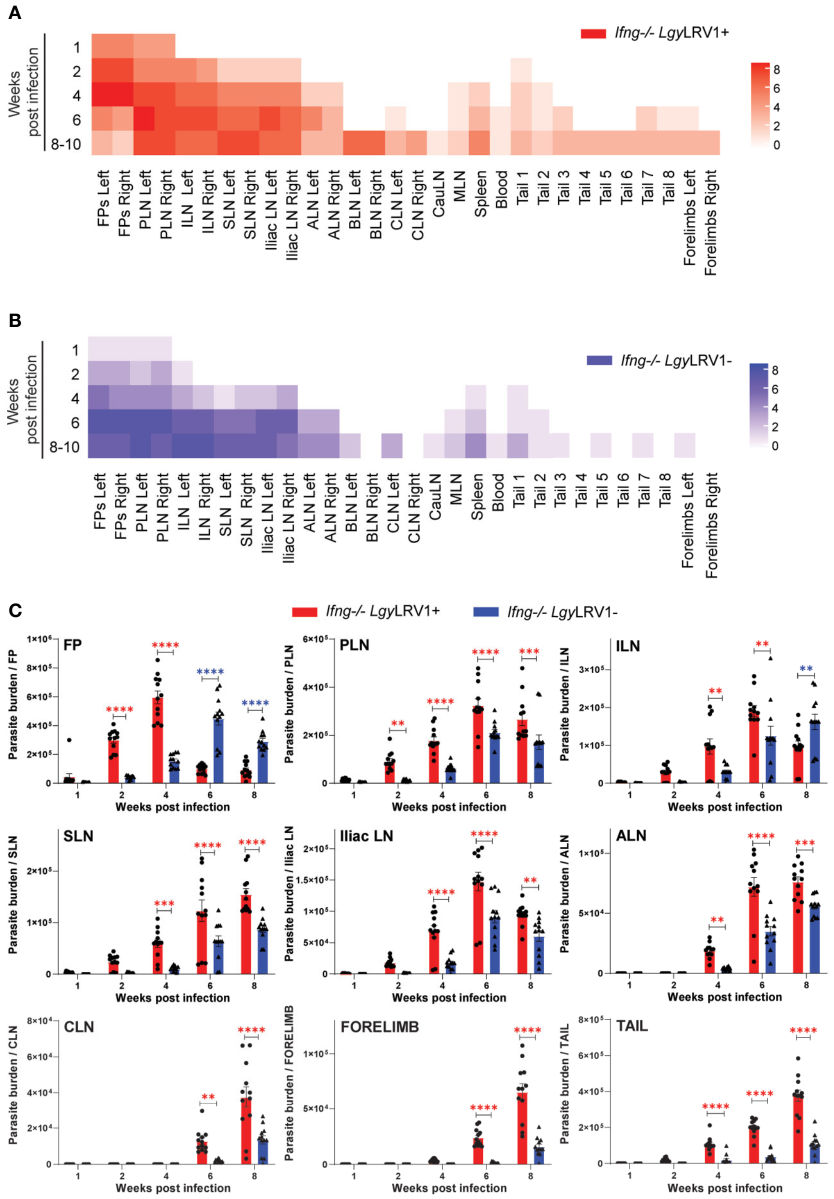

FIGURE 4

LRV1 causes exacerbated parasite dissemination through LNs into the tail. **(A, B)** Aforementioned organ suspension collected, shown as left and right, were subjected to limiting dilution analysis (LDA) from *Ifng*$^{-/-}$ mice infected in both hind FP with 1×10^6 *Lgy*LRV1+ or *Lgy*LRV1– stationary-phase metacyclic promastigotes at weeks 1, 2, 4, 6, and 8–10 p.i. Corresponding heatmaps were generated using the R ComplexHeatmap package for **(A)** *Ifng*$^{-/-}$*Lgy*LRV1+ group in red and **(B)** *Ifng*$^{-/-}$*Lgy*LRV1– group in blue. The color gradient represented in the heatmaps are correlated to the number of + signs assigned in terms of infection in progressive dilution series through LDA for each organ, where increased color intensity corresponded to higher parasite load. **(C)** Parasite burden per organ was quantified through relative RNA expression levels of parasite-specific gene *Kmp11* by RT-qPCR, in FP, PLN, ILN, SLN, iliac LN, ALN, CLN, forelimb, and tail, between *Ifng*$^{-/-}$ *Lgy*LRV1+ (red) and *Ifng*$^{-/-}$ *Lgy*LRV1– (blue). Data are representative of three independent experiment pooled, with n ≥ 4 mice/group/time point, in each experiment. All statistics represent mean ± SEM, with p-values determined by two-way ANOVA. Significance is indicated as $^{**}p < 0.01$, $^{***}p < 0.001$, and $^{****}p < 0.0001$, where they are annotated in red if the value associated with *Lgy*LRV1+ is > *Lgy*LRV1– and in blue if *Lgy*LRV1– > *Lgy*LRV1+, at each time point, for easy reference. Represented statistical data are a pool of three independent experiments, and the associated heatmap also represents the results of the pool of LDA in individual sets, with n ≥ 4 mice/group/time point, repeated at least five times independently.

but partially exhibited cell contact with mCherry$^+$ amastigotes, possibly attached to their cell surface (Figures 9A, B). Also by histology, the parasites found inside LNs appeared mostly as extracellular amastigotes. To further test this finding, a pan CD45$^+$ staining for all immune cells was performed on each of the mentioned LNs, revealing that mCh*Lgy*LRV1+ parasites

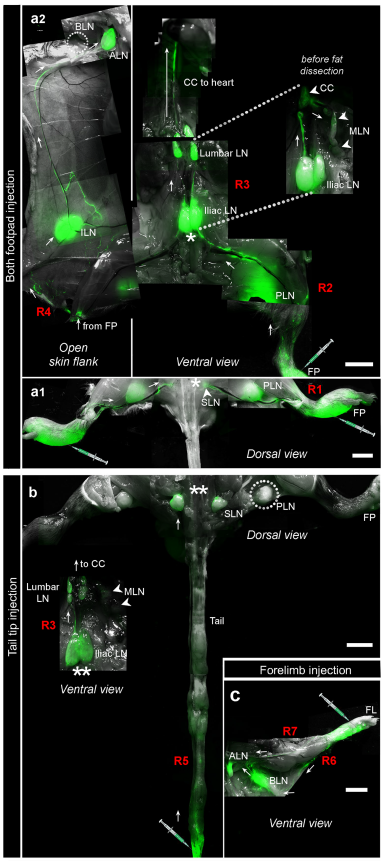

FIGURE 5
Fluorescent dextran angiography revealed lymphatic pathways of parasite dissemination. **(A–C)** *Ifng*$^{-/-}$ mice were infected in both FPs with 1×10^6 *Lgy*LRV1+, and lymphatic connections were mapped through stereomicroscopy, by injecting 5 µl of fluorescein isothiocyanate (FITC) labeled dextran (2,000 kDa) at defined sites at different time points of infection, as follows: (6) in both FP in an *Ifng*$^{-/-}$ *Lgy*LRV1+ (at week 4 p.i): a1, dorsal view of different lymphatic connections showing route R1 connecting FP to PLN to SLN to iliac ventrally, while BLN stays undrained; a2, ventral view of the lymphatic connections: revealing different routes emanating from the FP such as R2 connecting FP to iliac LN, R3 connecting iliac LN to CC to MLN to thoracic duct, and R4 connecting FP to ILN to ALN to subclavian vein. **(B)** At the tip of the tail of a metastatic *Ifng*$^{-/-}$ *Lgy*LRV1+ (at week 8 p.i) revealing route R5, which drains the tail tip upwards to the SLN to iliac LN ventrally, followed by route R3 (described above). **(C)** In both forelimbs of an *Ifng*$^{-/-}$ *Lgy*LRV1+ (at week 4 p.i) representing the lymphatic route R6, which connects the forelimb to BLN to ALN draining into the subclavian vein, and R7 connecting the forelimb drainage to ALN to the subclavian vein. Representation of different lymphatic drainage pattern observed in each group was derived by tiling several individual stereomicroscopic pictures (scale bar = 5mm). Each tilling represents one mouse from one experiment (to ensure common ends for stitching), with $n \geq 5$ mice/group/experiment, and each kind of experiment was repeated three times with similar results.

existed mainly in three forms: (a) partly internalized within the recruited immune cells; (b) partly around the immune cells, possibly in their close vicinity but not internalized; and (c) majority as non-cell associated (CD45$^-$), presumably unbound extracellular amastigotes or its clumps (Figure 8E). Furthermore, when this CD45$^+$ signal was further pushed to saturation, although it exhibited more CD45$^+$-mCherry$^+$ parasite co-localization in these staining, the overall phenotype of mCherry$^+$ parasites appearing mostly as non-immune cell-bound, extracellular amastigotes still persisted (Figure 9D).

*Lgy*LRV1+ dissemination is not solely immune cell dependent

To further assess the role of the various innate immune cells as vehicles of parasite dissemination, we performed *in vivo* depletions of the major cell types that were recruited in large numbers and also partially infected at the primary site of infection (FP) and in the first draining LN (PLN) during the early phase of infection (as previously observed through FACS studies, too). We observed that neutrophils and monocytes had limited roles in terms of parasite control, as assessed by parasite numbers in the FP and tail metastasis, while macrophage depletion led to a significant reduction in parasite numbers in the early but not late infection phase (Figures 10A, C, D, F, G, I). However, *Lgy*LRV1+ parasite dissemination still occurred even when neutrophils, neutrophils and monocytes together, or macrophages were depleted (Figures 10B, E, H). This suggested that albeit neutrophils and monocytes were significant cell type(s) to get infected during the earliest hours of infection, they were most definitely not the sole carrier(s) of *Lgy* parasites for dissemination, individually or together. However, it also signifies the commanding role of resident macrophages (and incoming monocytes) in the establishment of *Lgy* infection, thereby directly impacting disease development, its progression, and thus, its final metastatic outcome as well.

Finally, we infected *Rag2*$^{-/-}\gamma c^{-/-}$ mice (deficient in B, T, and NK cells) with *Lgy*LRV1+. These mice showed evident parasite burden in the tail, increasing significantly from W4 onwards till the end of infection (Figure 8F, tail). However, they developed significantly smaller FP lesions as compared to our metastatic *Ifng*$^{-/-}$ *Lgy*LRV1+ mice till W9 p.i. and peaked very late between W16–W21 p.i. (Figure 8F, FP). They never showed any metastatic nodules or cartilaginous destruction as observed in the *Ifng*$^{-/-}$ *Lgy*LRV1+ group even during the late phase of chronic infection (Figure 8F, tail) even if they showed extensive parasite migration to distant secondary organs such as the tail, forelimb, and snout, by W21 p.i. (Figure 8G). Thus, T, B, and NK cells were also not absolutely essential to facilitate metastatic dissemination but probably mediated disease exacerbation and tissue destruction. In conclusion, this confirmed that *Lgy* dissemination could occur even in the absence of the adaptive cells (B, T, and NK cells) (Figure 8G) or major innate cells (Figure 10) and that dissemination was not limited to the presence of any specific immune cell.

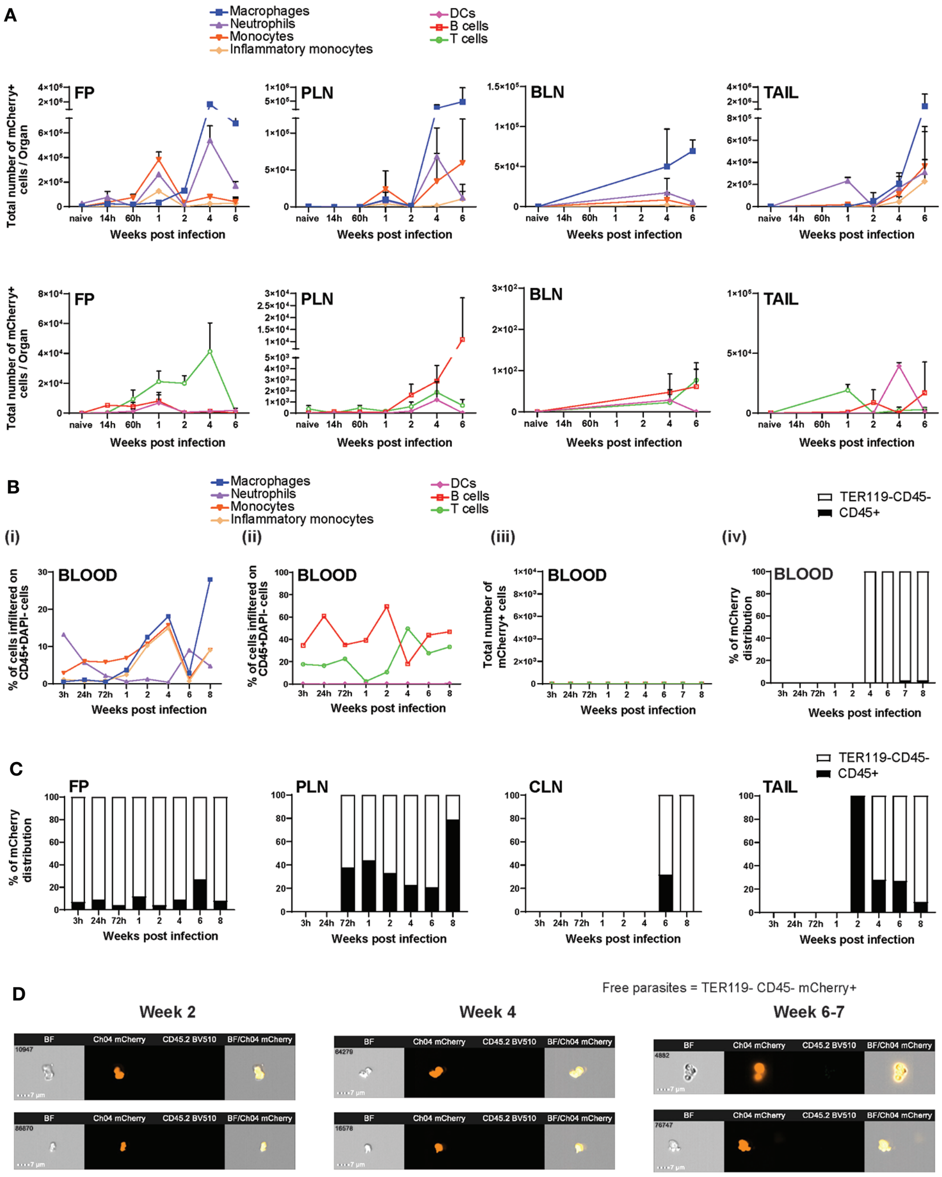

FIGURE 6

*Lgy*LRV1+ parasites existed as extracellular amastigotes in infected organs and blood. **(A–C)** *Ifng*$^{-/-}$ mice were infected in both FPs with 1x10^6 mCherry-expressing mch*Lgy*LRV1+ promastigotes. Flow cytometric analysis revealed **(A)** the total number of mCherry$^+$ cells of each cell type (defined below) in FP, PLN, BLN, and tail at W1, W2, W4, and W6 p.i. **(Bi, ii)** Percentage of infiltration of each cell type in the blood at 3 h, 24 h, 72 h, W1, W2, W4, W6, and W8 p.i. showing **(i)** neutrophils, monocytes, macrophage, and inflammatory monocytes; **(ii)** T cells, B cells, and DCs; **(iii)** total number of mCherry$^+$ cells of each cell type; (iv) distribution of total mCherry observed in the blood on its CD45$^+$ or TER119$^-$CD45$^-$ cells. **(C)** Distribution of total mCherry observed in FP, PLN, CLN, and tail over their respective CD45$^+$ or TER119$^-$CD45$^-$ cells. **(D)** Representative images taken by imaging flow cytometry show mch*Lgy*LRV1+ amastigotes in the blood of *Ifng*$^{-/-}$ *Lgy*LRV1+-infected mice, at W2, W4, and W6–W7 p.i. Corresponding samples from naive *Ifng*$^{-/-}$ mice (injected with PBS) were passed to set the baseline of increase for panel **(A)** (as negative control), while the data represented in panels **(B, C)** are already normalized to their naive values. Represented cell populations were defined by specific cell surface markers as follows: neutrophils (CD45$^+$CD11b$^+$Ly6G$^+$), macrophages (CD45$^+$CD11b$^+$F4/80$^+$), monocytes (CD45$^+$CD11b$^+$Ly6C$^+$), inflammatory monocytes (CD45$^+$CD11b$^+$Ly6C$^+$CCR2$^+$), T cells (CD45$^+$CD3$^+$), B cells (CD45$^+$CD19$^+$), DCs (CD45$^+$CD11b$^+$CD11c$^+$MHCII$^+$), and free parasites (TER119$^-$CD45$^-$mCherry$^+$). Represented statistical data are a pool of three independent experiments, whereas associated images are representative of one out of three or more independent experiments, with n ≥ 4 mice/group/time point. The statistics are given as mean ± SEM.

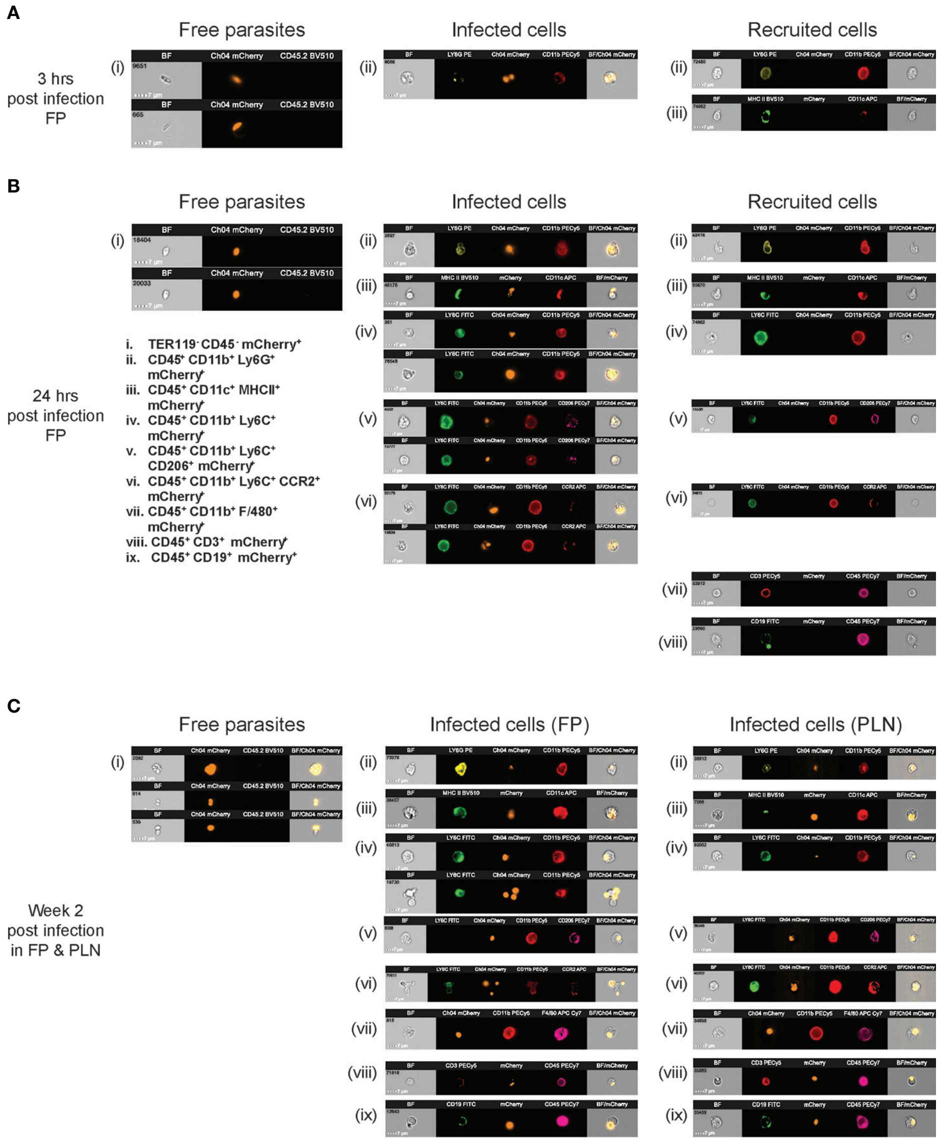

FIGURE 7
Within infected organs, *Lgy*LRV1+ mostly appeared as extracellular parasites, bound to the surface of immune cells and also as free-floating amastigotes. **(A–C)** *Ifng*$^{-/-}$ mice were infected in the hind both FP with 1x10^6 mCherry-expressing metacyclic mCh*Lgy*LRV1+ promastigotes. Sets of five mice were euthanized at 3 h, 24 h, and W2 p.i., to collect FP and PLN, which were then homogenized and digested, and different kinds of cell contents were analyzed by imaging flow cytometry (as detailed in the *Materials and methods*). Different states of association of mCh*Lgy*LRV1+ parasites with respect to the infiltrated immune cells were defined as "infected" (parasites internalized by CD45$^+$ immune cell or stuck to their surface), "recruited" (non-infected, infiltrated CD45$^+$ immune cells), and as "free" (extracellular mCherry$^+$ parasites, not bound or internalized by any CD45$^+$ immune cells). Representative images (scale, 7 µm) of **(A, B)** recruited/infected individual immune cells and free parasites are thus illustrated in **(A)** FP at 3 h p.i. **(B)** FP at 24 h p.i., and only free parasites and infected cells in **(C)** FP and PLN at W2 p.i. Individual immune cell populations were defined by specific marker sets as follows: neutrophils (CD45$^+$CD11b$^+$Ly6G$^+$), DCs (CD45$^+$CD11b$^+$CD11c$^+$MHCII$^+$), classical monocytes (CD45$^+$CD11b$^+$Ly6C$^+$), resident mannose receptor monocytes (CD45+CD11b+CD206$^+$Ly6C+), inflammatory monocytes of CCR2 origin (CD45$^+$CD11b$^+$Ly6c$^+$CCR2$^+$), macrophages (CD45$^+$CD11b$^+$F4/80$^+$), T cells (CD45$^+$CD3$^+$), B cells (CD45$^+$CD19$^+$), free parasites (DAPI$^-$TER119$^-$CD45$^-$mCherry$^+$), while each of their infected counterparts were associated with an additional mCherry$^+$ signal, as defined in the figure corroboratively. Free parasites were defined as TER119$^-$CD45$^-$mCherry$^+$ non-immune cell-associated, extracellular amastigotes. Images are representative of the pool of three independent imaging experiments, with n $\geq$ 5 mice/group/time point.

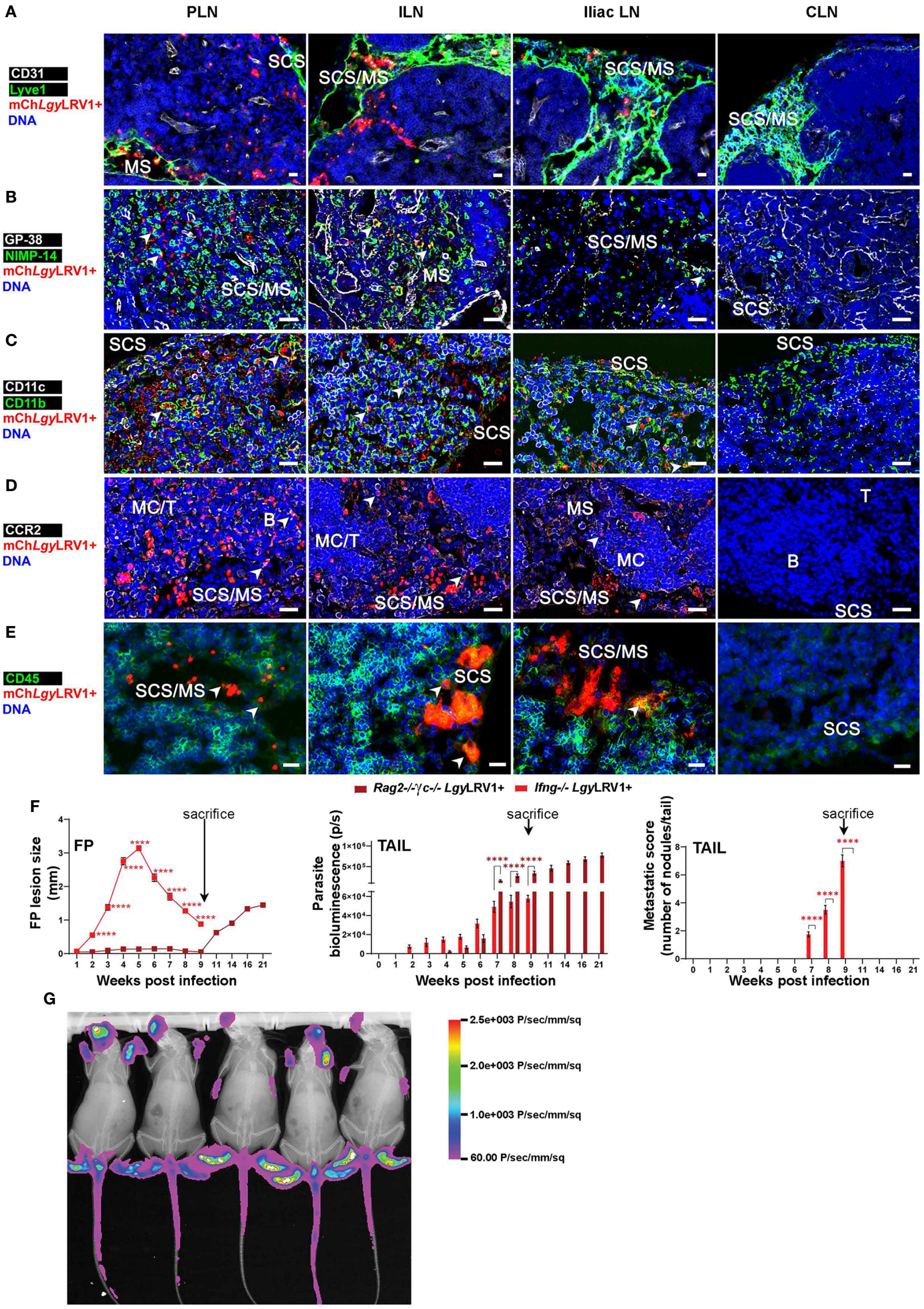

FIGURE 8

*Lgy*LRV1+ parasites dissemination was not dependent on a single immune cell type. **(A–E)** *Ifng*$^{-/-}$ mice were infected in both FPs with 1x10^{6} mch*Lgy*LRV1+ promastigotes and euthanized at W2 p.i. to recover PLN, ILN, iliac LN, and CLN for OCT embedding. Cryostat sections of 8–10µm of each of these LNs were subjected to anti-mCherry and DAPI (DNA) staining along with: **(A)** CD31 and Lyve-1, staining the blood vessels and lymphatic vessels, respectively; **(B)** GP-38 and NIMP-14 for staining fibroblastic reticular cells (FRCs) and neutrophils, respectively; **(C)** CD11c and CD11b for staining DCs and macrophages, respectively; **(D)** CCR2 staining inflammatory monocytes; and **(E)** CD45, as a pan marker for staining the myeloid immune cells. Data are representative of two to three experiments with at least two mice and six LNs/mouse. SCS, sub-capsular sinus; B/T, B-/T-cell zone in LNs; MC/MS/IL, medullary cord/medullary sinus/intranodal lymphatics, respectively (scale bars, 20 µm). **(F, G)** Groups of *Rag2*$^{-/-}\gamma c^{-/-}$ and *Ifng*$^{-/-}$ mice were infected in both FPs with 1x10^{6} *Lgy*LRV1+ promastigotes: **(F)** several measures of disease progression like FP swelling, parasite bioluminescence in tail, and metastatic score in tail were documented in each group along W1–W21 p.i. **(G)** Representative X-ray image nested with bioluminescent *Lgy*LRV1+ migration in *Rag2*$^{-/-}\gamma c^{-/-}$ mice at W21 p.i. Represented statistical data **(F,G)** are a pool of four independent experiments, whereas associated images **(A–E)** are representative from one of these experiments of the pool, repeated four times with similar results; n ≥ 6 mice/group/time point. Statistics are given as mean ± SEM, with p-values determined by two-way ANOVA. Significance is indicated as ****$p < 0.0001$.

Discussion

Our study presented a multi-component model of parasite dissemination associated with infectious inflammation, which allowed us to demonstrate inflammation-associated metastatic spread from the site of parasite entry in the skin. Conclusively, our data presented a detailed murine model of metastatic CL that documented the dynamics of early myeloid cell recruitment and their role in the large-scale dissemination of *Lgy* parasites through lymphatics. We identified LNs as major reservoirs of *Lgy* infection and defined extensive routes of their lymphatic drainage in addition to what has been previously described (Harrell et al., 2007; Harrell et al., 2008; Zheng et al., 2014; Wang et al., 2015; Yamaji et al., 2018). While parasite quantification clearly pointed towards LNs failing as efficient firewalls to stop the extensive *Lgy* spread, we established that macrophages on site play most significant roles both in the maintenance and in the resolution of infection, thereby impacting dissemination and overall disease outcome. Albeit heavily infected sites showed a significant presence of non-immune cell-associated extracellular amastigotes, a similar phenotype in the lymphatic SCS of infected LNs and a similar observation through imaging FACS further consolidated our hypothesis that *Lgy* dissemination occurred partly by cell association and also as free amastigotes through the lymph entering the systemic circulation. Thus, parasite dissemination was favored by migrating infected myeloid cells along with extracellular amastigotes sticking to their cell surfaces and amastigote clumps from different draining LNs, moving to the circulatory system. Several immuno-histological studies in clinically affected dogs with different *Leishmania* strains have reported a similar presence of amastigotes, suggestive of hematogenous dissemination of the parasite and tropism for the skin (Solano-Gallego et al., 2004; Mohebali et al., 2011; Ordeix et al., 2017). Remarkably, the presence of a large number of free amastigotes has been described across multiple clinical cases of HIV co-infection with different *Leishmania* strains (Puig and Pradinaud, 2003; Parmentier et al., 2016; Henn et al., 2018) along with free virulent amastigotes for active dissemination (Rosazza et al., 2020). Histopathological studies in humans infected with *Leishmania infantum* have also revealed the presence of free amastigotes in draining LNs and skin (Cobo et al., 2016). Thus, the presence of extracellular amastigotes in draining LNs and blood as observed in our *Ifng*$^{-/-}$ mice is not a singular event and even supports recent studies on the mode of dissemination of *S. pyogenes* bacteria, thereby suggesting that infection in *Ifng*$^{-/-}$ mice could be a very useful model system to study pathogen dissemination in various host–pathogen setup (Bogdan et al., 2000; Puig and Pradinaud, 2003; Solano-Gallego et al., 2004; Mohebali et al., 2011; Cobo et al., 2016; Ordeix et al., 2017; Henn et al., 2018; Rosazza et al., 2020; Siggins et al., 2020).

Although we cannot definitively exclude the possibility that the presence of extracellular amastigotes could be due to a local burst of heavily infected macrophages, observation of sustained numbers of extracellular parasites in blood performed through imaging flow cytometry, showing viable mCherry^{+} amastigotes, strongly favors our proposed hypothesis of parasites dissemination partly as non-cell=bound, extracellular amastigotes. *Lgy* parasites could then be flushed by the blood to selective niches for further metastases, such as to the skin for subsequent transmission by the sand fly. Additionally, complement receptors mediators or proteins (secreted by macrophages or fibroblasts) are upregulated in response to IFN-γ. The surge in complement pathway activity enhances opsonic uptake of extracellular pathogen *via* receptor mediated phagocytosis. So we probably cannot exclude a role of the complement system and that less parasites were internalized as the complement pathway was probably impaired in our model system due to the lack of IFN-γ. This would require further investigation. Additionally, the depletions of major upregulated cell types known to be host cells for *Leishmania*, could not totally block *Lgy* metastatic spread, thereby confirming that none of these heavily trafficked myeloid cells acted as the sole carrier for *Lgy* intracellular transport. While we also do not deny that such exacerbated phenotype observed could be directly associated with our unique *Ifng*$^{-/-}$ model, the metastatic outcome in *Rag2*$^{-/-}$*γc*$^{-/-}$ *Lgy*LRV1+ infection established that the pro-inflammatory immune response mediated by adaptive cells lead to tissue degradation during chronic infection. Interestingly, dissemination without the formation of debilitating lesions was also observed in *Ifng*$^{-/-}$ mice infected with *Lmj*, thereby suggesting that dissemination and lesion formation were two distinct processes. In our model, dissemination occurred with different *Leishmania* species, but lesion formation was species specific as observed in MCL patients and possibly linked to the activity of adaptive cells or hyper-inflammation as described in MCL patients infected with *L. braziliensis* exhibiting CD8^{+}T cell-mediated disease pathology (Cardoso et al., 2015; Novais et al., 2017). It also showed that *Leishmania* (*Viannia*) parasites could use different modes of transport and model the lymphatic system to cause secondary lesions and reach transmission sites. Additionally, our data cohesively established the exacerbation rendered by LRV1 in association with *Lgy* parasites, wherein their absence evidently delayed and lowered the overall disease outcome. Collectively, our results suggest that LNs should not be seen only as the site for mediating antigen-specific adaptive response through the egress of specific activated lymphocytes but also as a local canvas supporting parasite capture, multiplication, and dissemination. We therefore concluded that LRV1 could possibly impact cell retention of draining LN, which directly affect the parasite dissemination apart from increased myeloid cell and

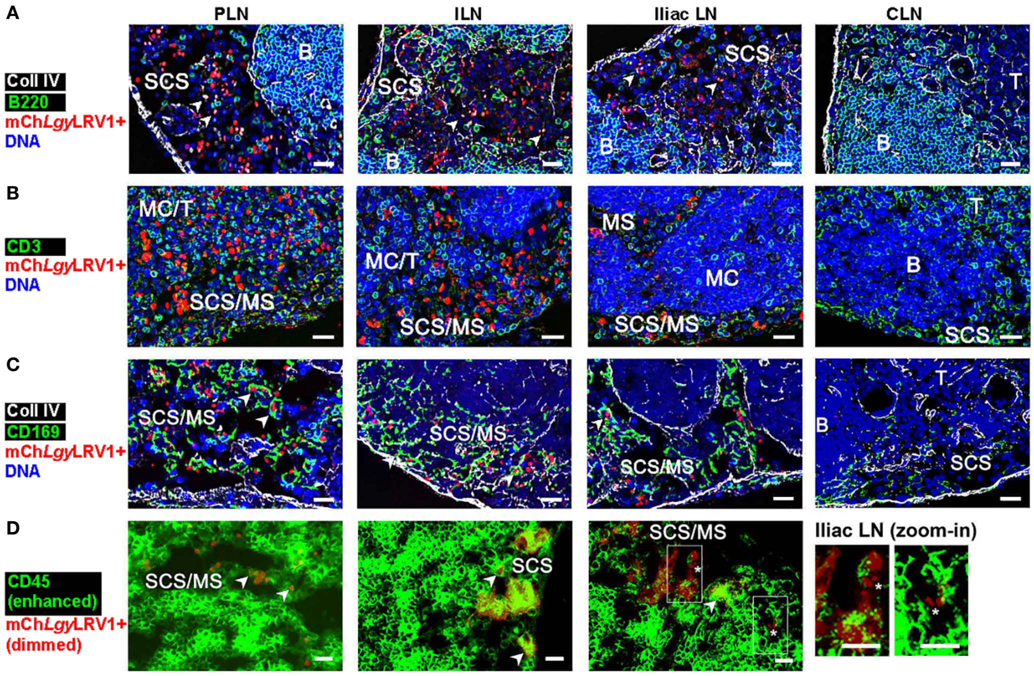

FIGURE 9
*Lgy*LRV1+ existed as extracellular amastigotes, showing little co-localization with most immune cells on site. **(A–C)** *Ifng*$^{-/-}$ mice were infected in hind FPs with 1x10^{6} mch*Lgy*LRV1+ promastigotes and euthanized at W2 p.i. to recover different LNs for OCT embedding. Cryostat sections of 8–10 µm from infected PLN, ILN, iliac LN, and CLN (as negative control) were stained with DAPI (for DNA) and anti-mCherry (for mCh*Lgy*LRV1+ parasites) labels and stained simultaneously for **(A)** B220 and collagen IV (Coll IV) antibodies for staining B cells and the basement membrane of vessels and its conduits, respectively; **(B)** CD3^{+} antibody for staining myeloid T cells; **(C)** Coll IV and CD169 antibodies for staining basement membrane of vessels and LN resident macrophages, respectively. Representative images were obtained from the slide scanner (scale bar, 20 µm). **(D)** Cryostat sections of 8–10 µm from infected LNs—PLN, ILN, and iliac LN—were subjected to CD45 and anti-mCherry antibodies for histological staining of all myeloid immune cells and mch*Lgy*LRV1+ parasites, respectively. CD45 signal was pushed to saturation (enhanced) while simultaneously dimming the mCherry signal to check if free mCherry^{+} extracellular amastigotes were still observed. These free amastigotes are pointed by white asterisk and also represented in a zoom-in section of iliac LN additionally. Representative images were obtained using Zeiss Axiovision (scale bar, 20 µm). White arrowheads represent co-localized mCherry+ *Lgy*LRV1+ with respectively mentioned cell markers. All data are representative of a pool of two to three experiments with $n \geq 2$ mice/group and six LNs/mouse. SCS, sub-capsular sinus; B/T, B-/T-cell zone in LNs; MC/MS/IL, medullary chord/medullary sinus/intranodal lymphatics, respectively.

extracellular amastigote trafficking through the lymphatics. Thus, our proposed model of overall *Lgy* dissemination in metastatic CL has been represented by a schematic diagram for visual reference (Figure 11).

Data availability and Reporting Guidelines

Sample size determination: Sample size used in this this study were not predetermined based on any statistical methods. They were rather chosen based on previous experimental experience, prior studies that showed significant effects with similar sample sizes and standards in the field. This included repetition of any designed experiment at least three independent times or more with similar results/trends, with at least 4-5 number of biological replicates for each condition. For assays in which variability is commonly high, we typically used n>5 while for assays which show low variability, we used n<5 sometimes.

Randomization: Animals were treated randomly before intervention, division for different experiments, tissue collection, and analysis. No formal randomization method such as random number generation were used to assign animals in experimental set ups. However, samples were treated randomly for several ex vivo measures like RT-qPCR or LDA processing and for various *in vitro* experiments.

Criteria of inclusion/exclusion: We did not exclude any data from consideration during analysis of individual experiments. However, while pooling experiments, expected variability in mice studies were defined to exclude outliers, all surgical or accidental deaths were excluded from the analyses. This exclusion was pre-established. Data from contaminated samples were also excluded. This exclusion was pre-established.

Blinding: Investigators were not blinded during the course of experimental follow up or treatment. Blinding during collections

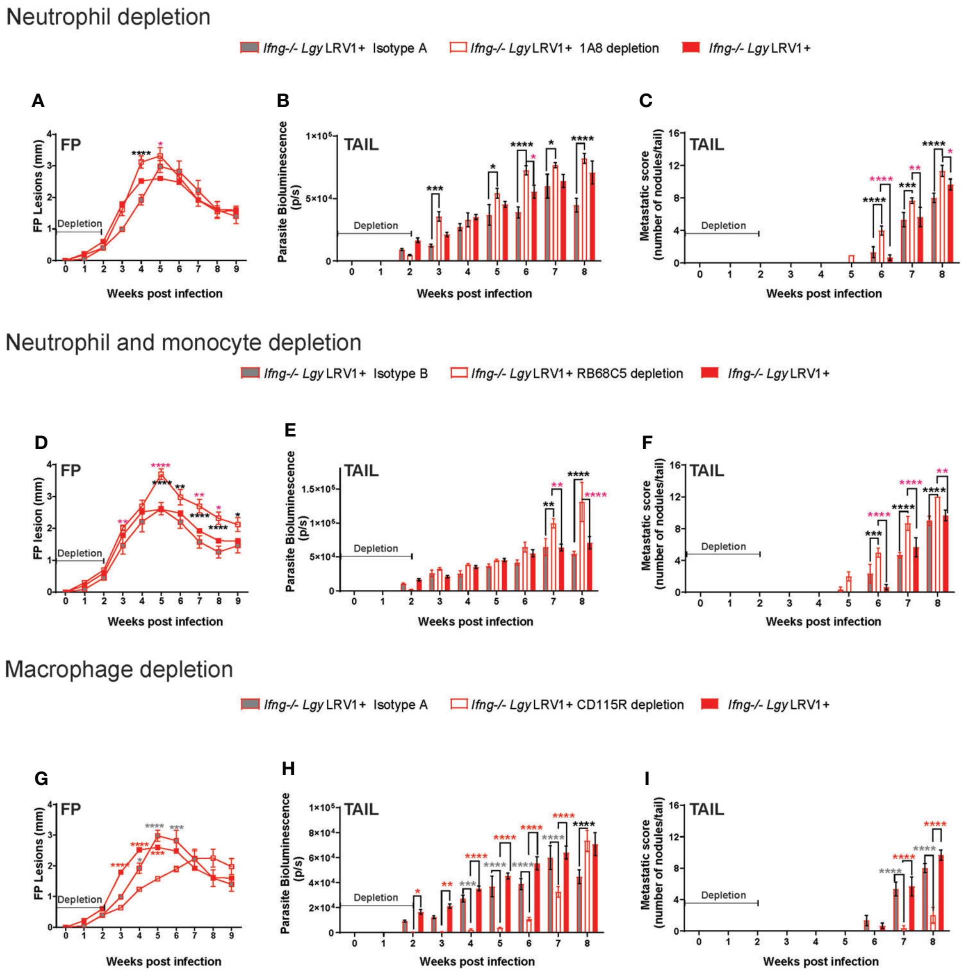

FIGURE 10

*Lgy*LRV1+ dissemination was not dependent on any particular innate cell type *in vivo*. **(A–C)** Individual groups of six *Ifng*$^{-/-}$ mice were depleted prior to infection for: **(A)** neutrophils, using anti- Ly6G monoclonal antibody (mAb), **(B)** monocytes and neutrophils together, using RB6-8C5 mAb, and **(c)** macrophages, using anti-CD11R mAb, treating additional *Ifng*$^{-/-}$ mice groups with either isotype A or B mAb as their respective treatment controls (suggested as per manufacturer's protocol). *Ifng*$^{-/-}$ mice (injected with only DPBS) were simultaneously maintained as undepleted control for comparing all depletions. Depletion regime for each mAb is detailed in *Materials and methods*. Each group was then infected in both FPs with 1x10^{6} *Lgy*LRV1+ promastigotes. Individual depletion in each group was continued till 2 weeks p.i. The following measures of disease progression were documented weekly from W1 to W8 p.i.: **(A,D,G)** FP swelling, i.e., proxy of parasite growth; **(B,E,H)** parasite bioluminescence in the tail, i.e., measure of parasite dissemination, and **(C,F,I)** metastatic score, i.e., measure of systemic debilitating metastases, as a result of **(A–C)** neutrophils/PMN depletion, **(D–F)** RB6-8C5/simultaneous monocyte and neutrophil depletion, and **(G–I)** CD115R/macrophage depletion. All statistical data are representative of a pool of four independent experiments, whereas associated images are representative from one of these experiments of the pool with n ≥ 6 mice/group/time point. Statistics, p values and significance are exactly as described for Figure 8. Asterisks of significance are in black when the value associated with the depletion group > the isotype treated (isotype A/B) group, gray when isotype A/B > depletions, red when *Lgy*LRV1+(only) > depletions, and magenta when depletions is > *Lgy*LRV1+(only) for easy visual reference.

were not needed because the conditions were well controlled. However, mice samples were processed ex vivo by technicians without any prior judgement or interpretation. The person performing several sample preparations for immunofluorescence imaging were unaware of the sample identity and collaboration across labs were carried out without giving prior expectations and were confirmed later with similar results.

Replication of experiments: It is provided in the respective Figure legend of each of the given Figure. All attempts at replication were successful with similar results/trends, across multiple experiments. All experiments included sufficient sample size, taking into account the expected variability when performing mice studies. The number of independent experiments, biological replicates for each Figure is indicated

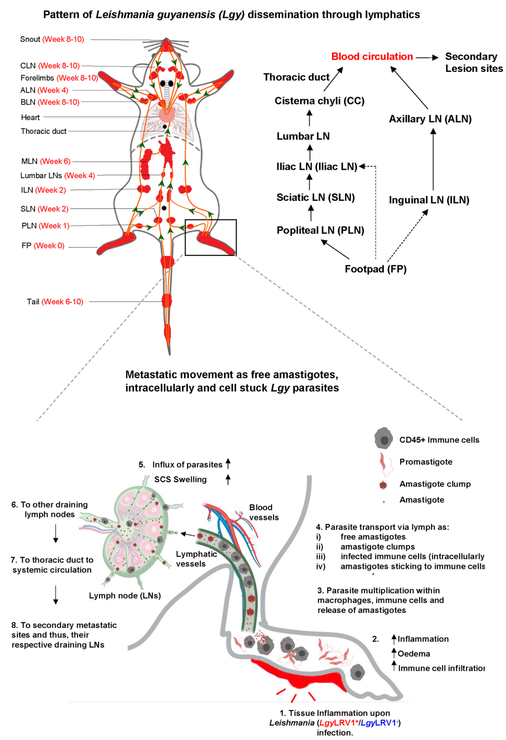

FIGURE 11
Overall model of dissemination and metastasis of *Lgy* parasites through lymphatics. Representative schematic diagram proposes the model of systemic dissemination of *Lgy* parasites, through sequential infection of mentioned draining LNs following different lymphatic routes, thereby gaining access to the systemic circulation for widespread metastasis in infected *Ifng*$^{-/-}$ mouse. The diagram summarizes stepwise events following an FP infection with either *Lgy*LRV1+ or *Lgy*LRV1– metacyclic promastigotes, leading to (1) hyper-inflammation of the infection site, causing the (2) recruitment of various CD45^{+} immune cells that exacerbates the disease. (3) Infection of recruited neutrophils, macrophages, and other immune cells facilitates the transformation and multiplication of amastigotes (from the promastigotes form) within these cells by simple division, which then ruptures to release free amastigotes. (4) Amastigotes move freely or in clumps, either infecting or getting stuck to the surface of different moving immune cells additionally to enter the draining LNs *via* lymph. (5) Influx of amastigotes causes hyper-inflammation of SCS in draining LNs, leading to further exacerbation. (6) Efferent lymphatic collecting vessels carry these parasites (in all four described forms) to infect other draining LNs sequentially in a similar manner. (7) All lymphatic collecting vessels ultimately join the thoracic duct, thereby draining *Lgy* parasites to systemic circulation, which can then (8) disseminate them further to favorable sites for continued multiplication, thereby facilitating large-scale metastases and causing secondary debilitating lesions. Although *Lgy*LRV1– infection displayed a significantly delayed disease phenotype, the sequence of disease progression followed exactly similar pattern of dissemination described.

in the Figure legend itself. Many data show the aggregation of several independent experiments, while few data like immunofluorescence images and LDA, are from a representative experiment. In case of such representative experiments, the number of independent experiments that reproduced the finding is also indicated in the Figure legends and support conclusions drawn in this report.

ARRIVE rules adherence: Although we stuck to following the prescribed ARRIVE rules to the closest possible in our animal studies, we didn't officially define it during licensing.

Software availability: All software used for analysis are commercially available and detailed in the "software used for analysis" section, under "methods" section below.

All datasets generated and analyzed are available in the main text or the Supplementary Materials; raw sources could be accessible upon request from the corresponding author.

Data availability statement

The raw data supporting the conclusions of this article will be made available by the authors, without undue reservation.

Ethics statement

The animal study was reviewed and approved by Swiss Federal Veterinary Office (SFVO).

Author contributions

Conceptualization: BJ and NF. Methodology: BJ, TP, SL, and NF. Investigation: BJ, CR, MR, FP, FM, LD, CD, AS, LS, SL, and NF. Resources: SL, L-FL, KO, SB, and NF. Writing—original draft: BJ and NF. Writing—review and editing: BJ, NF, SL, TP, AS, and SB. Funding: NF and SB. All authors read and approved the final manuscript.

Funding

This work is funded by grants from the Swiss National fund for research (http://www.snf.ch/en/Pages/default.aspx) (No. 310030_173180, NF) and the National Institutes of Health (NIH, https://www.nih.gov/) (R01AI-31078 and R01AI-30222-02, SB).

Acknowledgments

We would like to thank Dr. Luigi Bozzo (Cellular Imaging Facility, CHUV); J.-C. Stehle and Janine Horlbeck (Mouse Pathology Facility); and Dr. Francisco Sala de Oyanguren, Dr. Romain Bedel, and Dr. A. Wilson (Flow Cytometry Facility) for the technical assistance. We also thank Dr. Amel Bekkar for generating the heatmaps using R, Dr. Slavica Masina for critically assessing the manuscript, and Prof. Jean-Daniel Tissot for his support.

Conflict of interest

The authors declare that the research was conducted in the absence of any commercial or financial relationships that could be construed as a potential conflict of interest.

Publisher's note

Supplementary material

The Supplementary Material for this article can be found online at: https://www.frontiersin.org/articles/10.3389/fcimb.2022.941860/full#supplementary-material

References

(W.H.O) (2020) *Leishmaniasis*. Available at: https://www.who.int/news-room/fact-sheets/detail/leishmaniasis.

Adaui, V., Lye, L.-F., Akopyants, N. S., Zimic, M., Llanos-Cuentas, A., Garcia, L., et al. (2016). Association of the endobiont double-stranded RNA virus LRV1 with treatment failure for human leishmaniasis caused by leishmania braziliensis in Peru and Bolivia. *J. Infect. Dis.* 213 (1), 112–121. doi: 10.1093/infdis/jiv354

Angeli, V., Ginhoux, F., Llodrà, J., Quemeneur, L., Frenette, P. S., Skobe, M., et al. (2006). B cell-driven lymphangiogenesis in inflamed lymph nodes enhances dendritic cell mobilization. *Immunity* 24 (2), 203–215. doi: 10.1016/j.immuni.2006.01.003

Bansal, S., Yajjala, V. K., Bauer, C., and Sun, K. (2018). IL-1 signaling prevents alveolar macrophage depletion during influenza and streptococcus pneumoniae coinfection. *J. Immunol.* 200 (4), 1425–1433. doi: 10.4049/jimmunol.1700210

Bates, P. A. (2008). Leishmania sand fly interaction: progress and challenges. *Curr. Opin. Microbiol.* 11 (4), 340–344. doi: 10.1016/j.mib.2008.06.003

Bates, P. A. (2018). Revising leishmania's life cycle. *Nat. Microbiol.* 3 (5), 529–530. doi: 10.1038/s41564-018-0154-2

Bauché, D., Joyce-Shaikh, B., Jain, R., Grein, J., Ku, K. S., Blumenschein, W. M., et al. (2018). LAG3+ regulatory T cells restrain interleukin-23-Producing CX3CR1 + gut-resident macrophages during group 3 innate lymphoid cell-driven colitis. *Immunity* 49 (2), 342–352.e345. doi: 10.1016/j.immuni.2018.07.007

Bodogai, M., Moritoh, K., Lee-Chang, C., Hollander, C. M., Sherman-Baust, C. A., Wersto, R. P., et al. (2015). Immunosuppressive and prometastatic functions of myeloid-derived suppressive cells rely upon education from tumor-associated b cells. *Cancer Res.* 75 (17), 3456–3465. doi: 10.1158/0008-5472.Can-14-3077

Bogdan, C., Donhauser, N., Döring, R., Röllinghoff, M., Diefenbach, A., and Rittig, M. G. (2000). Fibroblasts as host cells in latent leishmaniosis. *J. Exp. Med.* 191 (12), 2121–2130. doi: 10.1084/jem.191.12.2121

Bourreau, E., Ginouves, M., Prévot, G., Hartley, M.-A., Gangneux, J.-P., Robert-Gangneux, F., et al. (2016). Presence of leishmania RNA virus 1 in leishmania guyanensis increases the risk of first-line treatment failure and symptomatic relapse. *J. Infect. Dis.* 213 (1), 105–111. doi: 10.1093/infdis/jiv355

Cantanhede, L. M., da Silva Junior, C. F., Ito, M. M., Felipin, K. P., Nicolete, R., Salcedo, J. M., et al. (2015). Further evidence of an association between the presence of leishmania RNA virus 1 and the mucosal manifestations in tegumentary leishmaniasis patients. *PloS Negl. Trop. Dis.* 9 (9), e0004079. doi: 10.1371/journal.pntd.0004079

Cardoso, T. M., Machado, Á., Costa, D. L., Carvalho, L. P., Queiroz, A., Machado, P., et al. (2015). Protective and pathological functions of CD8+ T cells in leishmania braziliensis infection. *Infect. Immun.* 83 (3), 898–906. doi: 10.1128/IAI.02404-14

Carlsen, E. D., Liang, Y., Shelite, T. R., Walker, D. H., Melby, P. C., and Soong, L. (2015). Permissive and protective roles for neutrophils in leishmaniasis. *Clin. Exp. Immunol.* 182 (2), 109–118. doi: 10.1111/cei.12674

Charmoy, M., Auderset, F., Allenbach, C., and Tacchini-Cottier, F. (2010). The prominent role of neutrophils during the initial phase of infection by leishmania parasites. *J. Biomed. Biotechnol.* 2010, 719361. doi: 10.1155/2010/719361

Cobo, F., Rodríguez-Granger, J., Gómez-Camarasa, C., Sampedro, A., Aliaga–Martínez, L., Navarro, J. M., et al. (2016). Localized mucosal leishmaniasis caused by leishmania infantum mimicking cancer in the rhinolaryngeal region. *Int. J. Infect. Dis.* 50, 54–56. doi: 10.1016/j.ijid.2016.08.003

Davis Iv, R. W., Snyder, E., Miller, J., Carter, S., Houser, C., Klampatsa, A., et al. (2019). Luminol chemiluminescence reports photodynamic therapy-generated neutrophil activity *In vivo* and serves as a biomarker of therapeutic efficacy. *Photochem. Photobiol.* 95 (1), 430–438. doi: 10.1111/php.13040

Dubey, L. K., Ludewig, B., Luther, S. A., and Harris, N. L. (2019). IL-4Rα-Expressing b cells are required for CXCL13 production by fibroblastic reticular cells. *Cell Rep.* 27 (8), 2442–2458.e2445. doi: 10.1016/j.celrep.2019.04.079

Eren, R. O., Reverte, M., Rossi, M., Hartley, M.-A., Castiglioni, P., Prevel, F., et al. (2016). Mammalian innate immune response to a leishmania-resident RNA virus increases macrophage survival to promote parasite persistence. *Cell Host Microbe* 20 (3), 318–328. doi: 10.1016/j.chom.2016.08.001

Glennie, N. D., Volk, S. W., and Scott, P. (2017). Skin-resident CD4+ T cells protect against leishmania major by recruiting and activating inflammatory monocytes. *PloS Pathog.* 13 (4), e1006349. doi: 10.1371/journal.ppat.1006349

Gordon, S. R., Maute, R. L., Dulken, B. W., Hutter, G., George, B. M., McCracken, M. N., et al. (2017). PD-1 expression by tumour-associated macrophages inhibits phagocytosis and tumour immunity. *Nature* 545 (7655), 495–499. doi: 10.1038/nature22396

Harrell, M. I., Iritani, B. M., and Ruddell, A. (2007). Tumor-induced sentinel lymph node lymphangiogenesis and increased lymph flow precede melanoma metastasis. *Am. J. Pathol.* 170 (2), 774–786. doi: 10.2353/ajpath.2007.060761

Harrell, M. I., Iritani, B. M., and Ruddell, A. (2008). Lymph node mapping in the mouse. *J. Immunol. Methods* 332 (1-2), 170–174. doi: 10.1016/j.jim.2007.11.012

Hartley, M.-A., Bourreau, E., Rossi, M., Castiglioni, P., Eren, R. O., Prevel, F., et al. (2016). Leishmaniavirus-dependent metastatic leishmaniasis is prevented by blocking IL-17A. *PloS Pathog.* 12 (9), e1005852. doi: 10.1371/journal.ppat.1005852

Hartley, M.-A., Drexler, S., Ronet, C., Beverley, S. M., and Fasel, N. (2014). The immunological, environmental, and phylogenetic perpetrators of metastatic leishmaniasis. *Trends Parasitol.* 30 (8), 412–422. doi: 10.1016/j.pt.2014.05.006

Hartley, M.-A., Ronet, C., Zangger, H., Beverley, S., and Fasel, N. (2012). Leishmania RNA virus: when the host pays the toll. *Front. Cell. Infect. Microbiol.* 2 (99). doi: 10.3389/fcimb.2012.00099

Heirwegh, E., MacLean, E., He, J., Kamhawi, S., Sagan, S. M., and Olivier, M. (2021). Sandfly fever Sicilian virus-leishmania major co-infection modulates innate inflammatory response favoring myeloid cell infections and skin hyperinflammation. *PloS Negl. Trop. Dis.* 15 (7), e0009638. doi: 10.1371/journal.pntd.0009638

Henn, G., Ramos, J. A. N., Colares, J. K. B., Mendes, L. P., Silveira, J. G. C., Lima, A. A. F., et al. (2018). Is visceral leishmaniasis the same in HIV-coinfected adults? *Braz. J. Infect. Dis.* 22 (2), 92–98. doi: 10.1016/j.bjid.2018.03.001

Hui, H., Fuller, K. A., Erber, W. N., and Linden, M. D.. (2017). Imaging flow cytometry in the assessment of leukocyte-platelet aggregates.*Methods* 112, 45-54. doi: 10.1016/j.ymeth.2016.10.002

Hurrell, B. P., Regli, I. B., and Tacchini-Cottier, F. (2016). Different leishmania species drive distinct neutrophil functions. *Trends Parasitol.* 32 (5), 392–401. doi: 10.1016/j.pt.2016.02.003

Ives, A., Ronet, C., Prevel, F., Ruzzante, G., Fuertes-Marraco, S., Schutz, F., et al. (2011). Leishmania RNA virus controls the severity of mucocutaneous leishmaniasis. *Sci. (New York N.Y.)* 331 (6018), 775–778. doi: 10.1126/science.1199326

Kuhlmann, F. M., Robinson, J. I., Bluemling, G. R., Ronet, C., Fasel, N., and Beverley, S. M. (2017). Antiviral screening identifies adenosine analogs targeting the endogenous dsRNA leishmania RNA virus 1 (LRV1) pathogenicity factor. *Proc. Natl. Acad. Sci. U.S.A.* 114 (5), E811–E819. doi: 10.1073/pnas.1619114114

Lessa, M. M., Lessa, H. A., Castro, T. W., Oliveira, A., Scherifer, A., Machado, P., et al. (2007). Mucosal leishmaniasis: epidemiological and clinical aspects. *Braz. J. Otorhinolaryngol.* 73 (6), 843–847. doi: 10.1016/S1808-8694(15)31181-2

Mohebali, M., Malmasi, A., Hajjaran, H., Jamshidi, S., Akhoundi, B., Rezaei, M., et al. (2011). Disseminated leishmaniasis caused by leishmania tropica in a puppy from karaj, central Iran. *Iranian J. Parasitol.* 6 (2), 69–73.

Morton, D. L., Hoon, D. S. B., Cochran, A. J., Turner, R. R., Essner, R., Takeuchi, H., et al. (2003). Lymphatic mapping and sentinel lymphadenectomy for early-stage melanoma: therapeutic utility and implications of nodal microanatomy and molecular staging for improving the accuracy of detection of nodal micrometastases. *Ann. Surg.* 238 (4), 538–550. doi: 10.1097/01.sla.0000086543.45557.cb

Moynihan, K. D., Opel, C. F., Szeto, G. L., Tzeng, A., Zhu, E. F., Engreitz, J. M., et al. (2016). Eradication of large established tumors in mice by combination immunotherapy that engages innate and adaptive immune responses. *Nat. Med.* 22 (12), 1402–1410. doi: 10.1038/nm.4200

Noll, T. M., Desponds, C., Belli, S. I., Glaser, T. A., and Fasel, N. J. (1997). Histone H1 expression varies during the leishmania major life cycle. *Mol. Biochem. Parasitol.* 84 (2), 215–227. doi: 10.1016/s0166-6851(96)02801-0

Novais, F. O., Carvalho, A. M., Clark, M. L., Carvalho, L. P., Beiting, D. P., Brodsky, I. E., et al. (2017). CD8+ T cell cytotoxicity mediates pathology in the skin by inflammasome activation and IL-1β production. *PloS Pathog.* 13 (2), e1006196. doi: 10.1371/journal.ppat.1006196

Novais, F. O., Santiago, R. C., Bafica, A., Khouri, R., Afonso, L., Borges, V. M., et al. (2009). Neutrophils and macrophages cooperate in host resistance against leishmania braziliensis infection. *J. Immunol.* 183 (12), 8088–8098. doi: 10.4049/jimmunol.0803720

Olivier, M., and Zamboni, D. S. (2020). Leishmania viannia guyanensis, LRV1 virus and extracellular vesicles: a dangerous trio influencing the faith of immune response during muco-cutaneous leishmaniasis. *Curr. Opin. Immunol.* 66, 108–113. doi: 10.1016/j.coi.2020.08.004

Ordeix, L., Dalmau, A., Osso, M., Llull, J., Montserrat-Sangrà, S., and Solano-Gallego, L. (2017). Histological and parasitological distinctive findings in clinically-lesioned and normal-looking skin of dogs with different clinical stages of leishmaniosis. *Parasites Vectors* 10, 4–5. doi: 10.1186/s13071-017-2051-6

Parmentier, L., Cusini, A., Müller, N., Zangger, H., Hartley, M.-A., Desponds, C., et al. (2016). Severe cutaneous leishmaniasis in a human immunodeficiency virus patient coinfected with leishmania braziliensis and its endosymbiotic virus. *Am. J. Trop. Med. Hyg.* 94 (4), 840–843. doi: 10.4269/ajtmh.15-0803

Petrova, T. V., and Koh, G. Y. (2020). Biological functions of lymphatic vessels. *Science* 369 (6500), eaax4063. doi: 10.1126/science.aax4063

Puig, L., and Pradinaud, R. (2003). Leishmania and HIV co-infection: dermatological manifestations. *Ann. Trop. Med. Parasitol.* 97 (sup1), 107–114. doi: 10.1179/000349803225002589

Qi, H., Popov, V., and Soong, L. (2001). Leishmania amazonensis-dendritic cell interactions *In vitro* and the priming of parasite-specific CD4+ T cells *In vivo*. *J. Immunol.* 167 (8), 4534–4542. doi: 10.4049/jimmunol.167.8.4534

Rath, C. T., Schnellrath, L. C., Damaso, C. R., de Arruda, L. B., Vasconcelos, P., Gomes, C., et al. (2019). Amazonian Phlebovirus (Bunyaviridae) potentiates the infection of leishmania (Leishmania) amazonensis: Role of the PKR/IFN1/IL-10 axis. *PloS Negl. Trop. Dis.* 13 (6), e0007500. doi: 10.1371/journal.pntd.0007500

Regli, I. B., Passelli, K., Martínez-Salazar, B., Amore, J., Hurrell, B. P., Müller, A. J., et al. (2020). TLR7 sensing by neutrophils is critical for the control of cutaneous leishmaniasis. *Cell Rep.* 31 (10), 107746. doi: 10.1016/j.celrep.2020.107746

Reverte, M., Eren, R. O., Jha, B., Desponds, C., Snäkä, T., Prevel, F., et al. (2021). The antioxidant response favors leishmania parasites survival, limits inflammation and reprograms the host cell metabolism. *PloS Pathog.* 17 (3), e1009422. doi: 10.1371/journal.ppat.1009422

Reverte, M., and Fasel, N. (2019). Leishmania parasite quantification by bioluminescence in murine models. *Bio-protocol* 9 (22), e3431. doi: 10.21769/BioProtoc.3431

Rosazza, T., Lecoeur, H., Blisnick, T., Moya-Nilges, M., Pescher, P., Bastin, P., et al. (2021). Dynamic high-content imaging reveals surface exposure of virulent leishmania amastigotes in infected macrophages undergoing pyroptosis. *J Cell Science* 34 (5). doi: 10.1242/jcs.242776

Rossi, M., Castiglioni, P., Hartley, M.-A., Eren, R. O., Prével, F., Desponds, C., et al. (2017). Type I interferons induced by endogenous or exogenous viral infections promote metastasis and relapse of leishmaniasis. *Proc. Natl. Acad. Sci.* 114 (19), 4987–4992. doi: 10.1073/pnas.1621447114

Saharinen, P., and Petrova, T. V. (2004). Molecular regulation of lymphangiogenesis. *Ann. New York Acad. Sci.* 1014, 76–87. doi: 10.1196/annals.1294.008

Santos Cda, S., Boaventura, V., Ribeiro Cardoso, C., Tavares, N., Lordelo, M. J., Noronha, A., et al. (2013). CD8(+) granzyme b(+)-mediated tissue injury vs. CD4(+)IFNγ(+)-mediated parasite killing in human cutaneous leishmaniasis. *J. Invest. Dermatol.* 133 (6), 1533–1540. doi: 10.1038/jid.2013.4

Siggins, M. K., Lynskey, N. N., Lamb, L. E., Johnson, L. A., Huse, K. K., Pearson, M., et al. (2020). Extracellular bacterial lymphatic metastasis drives streptococcus pyogenes systemic infection. *Nat. Commun.* 11 (1), 4697. doi: 10.1038/s41467-020-18454-0

Silva-Barrios, S., Smans, M., Duerr, C. U., Qureshi, S. T., Fritz, J. H., Descoteaux, A., et al. (2016). Innate immune b cell activation by leishmania donovani exacerbates disease and mediates hypergammaglobulinemia. *Cell Rep.* 15 (11), 2427–2437. doi: 10.1016/j.celrep.2016.05.028

Solano-Gallego, L., Fernández-Bellon, H., Morell, P., Fondevila, D., Alberola, J., Ramis, A., et al. (2004). Histological and immunohistochemical study of clinically normal skin of leishmania infantum-infected dogs. *J. Comp. Pathol.* 130 (1), 7–12. doi: 10.1016/s0021-9975(03)00063-x

Tarr, P. I., Aline, R. F.Jr., Smiley, B. L., Scholler, J., Keithly, J., and Stuart, K. (1988). LR1: a candidate RNA virus of leishmania. *Proc. Natl. Acad. Sci. United States America* 85 (24), 9572–9575. doi: 10.1073/pnas.85.24.9572

Tomiotto-Pellissier, F., Bortoleti, B., Assolini, J. P., Gonçalves, M. D., Carloto, A. C. M., Miranda-Sapla, M. M., et al. (2018). Macrophage polarization in leishmaniasis: Broadening horizons. *Front. Immunol.* 9 (2529). doi: 10.3389/fimmu.2018.02529

Vaahtomeri, K., and Alitalo, K. (2020). Lymphatic vessels in tumor dissemination versus immunotherapy. *Cancer Res.* 80 (17), 3463–3465. doi: 10.1158/0008-5472.Can-20-0156

Van den Broeck, W., Derore, A., and Simoens, P. (2006). Anatomy and nomenclature of murine lymph nodes: Descriptive study and nomenclatory standardization in BALB/cAnNCrl mice. *J. Immunol. Methods* 312 (1), 12–19. doi: 10.1016/j.jim.2006.01.022

Wang, Y., Lang, L., Huang, P., Wang, Z., Jacobson, O., Kiesewetter, D. O., et al. (2015). *In vivo* albumin labeling and lymphatic imaging. *Proc. Natl. Acad. Sci.* 112 (1), 208–213. doi: 10.1073/pnas.1414821112

Wong, A. K.-C. (1995). Molecular genetics of the parasitic protozoan leishmania. *Biochem. Cell Biol.* 73 (5-6), 235–240. doi: 10.1139/o95-028

Wynn, T. A., Chawla, A., and Pollard, J. W. (2013). Macrophage biology in development, homeostasis and disease. *Nature* 496 (7446), 445–455. doi: 10.1038/nature12034

Yamaji, Y., Akita, S., Akita, H., Miura, N., Gomi, M., Manabe, I., et al. (2018). Development of a mouse model for the visual and quantitative assessment of lymphatic trafficking and function by *in vivo* imaging. *Sci. Rep.* 8 (1), 5921. doi: 10.1038/s41598-018-23693-9

Yang, J., Zhang, L., Yu, C., Yang, X.-F., and Wang, H. (2014). Monocyte and macrophage differentiation: circulation inflammatory monocyte as biomarker for inflammatory diseases. *biomark. Res.* 2 (1), 1. doi: 10.1186/2050-7771-2-1

Zangger, H., Hailu, A., Desponds, C., Lye, L. F., Akopyants, N. S., Dobson, D. E., et al. (2014). Leishmania aethiopica field isolates bearing an endosymbiontic dsRNA virus induce pro-inflammatory cytokine response. *PloS Negl. Trop. Dis.* 8 (4), e2836. doi: 10.1371/journal.pntd.0002836

Zangger, H., Ronet, C., Desponds, C., Kuhlmann, F. M., Robinson, J., Hartley, M.-A., et al. (2013). Detection of leishmania RNA virus in leishmania parasites. *PloS Negl. Trop. Dis.* 7 (1), e2006. doi: 10.1371/journal.pntd.0002006

Zheng, W., Nurmi, H., Appak, S., Sabine, A., Bovay, E., Korhonen, E. A., et al. (2014). Angiopoietin 2 regulates the transformation and integrity of lymphatic endothelial cell junctions. *Genes Dev.* 28 (14), 1592–1603. doi: 10.1101/gad.237677.114

Glossary

Aa	amino acids
Ab(s)	antibody(-ies)
ADCL	anergic diffused cutaneous leishmaniasis
AIDS	acquires immunodeficiency syndrome
APC(s)	antigen-presenting cell(s)
ALN(s)	axillary lymph node(s)
ATP	adenosine triphosphate
B	B-cell zone (in lymph nodes)
B cell(s)	B lymphocyte(s)
BMDM	bone marrow-derived macrophage
BLN(s)	brachial lymph node(s)
Bp (bp)	base pair
CAM	cellular adhesion molecule
CC	cisterna chylae
CD	cluster of differentiation
CD169	lymph node resident macrophages
CLN(s)	superficial cervical lymph node(s)
CLR	c-type lectin receptor
CTR	C-terminal region
DAMP	danger-associated molecular pattern
DAPI	4′
6-diamidino-2-phenylindole	
DC(s)	dendritic cell(s)
DLN(s)	draining lymph node(s)
DKO	double knock-out
DNA	deoxyribonucleic acid
DL	disseminated cutaneous leishmaniasis
dsRNA	double-stranded RNA
ER	endoplasmic reticulum
EB	Evan's blue
ELISA	enzyme-linked immunosorbent assay
FACS	fluorescence-activated cell sorting
FBS	fetal bovine serum
FDA	Food and Drug Administration
FL	forelimb
FLI	forelimbs injection
FITC	fluorescein isothiocyanate
FP(s)	footpad(s)
Gp63	63 kDa surface glycoprotein of <italic>Leishmania;</italic> gl
ganglion lymphatic	
GST	glutathione <italic>S</italic>-transferase
H	hour (majorly post-infection)
H2O2	hydrogen peroxide
HEPES	N-(2-hydroxyethyl) piperazine-N′-2 ethane sulfonic acid
H2O2	hydrogen peroxide
HIV	human immunodeficiency virus
IF	immunofluorescence

(Continued)

Continued

IFN	interferon
IFNGR	IFN gamma receptor
IL	Interleukin
ILN(s)	inguinal lymph node(s)
ILC LN(s)	iliac lymph node(s)
Infl. Monos	inflammatory monocytes
i.p.	intraperitoneal
i.v.	intravenous
iNOS	inducible nitric oxide synthase
iPSC	induced pluripotent stem cell
kDa	kilo Dalton
Kg	kilogram
L. <italic>Leishmania;</italic> LCL	localized cutaneous leishmaniasis
LDA	limiting dilution assay
LCMV	lymphocytic choriomeningitis virus
LFP	left footpad
LPG	lipophosphoglycan
<italic>Lmj	Leishmania major;</italic>
LPS	lipopolysaccharide
LN(s)	lymph node(s)
LRR	leucine-rich repeat
LRV	<italic>Leishmania</italic> RNA virus
MAb	monoclonal antibody
MC	medullary chord
Macros	macrophages
MHC	major histocompatibility complex
MPO	myeloid peroxidase
qRT-PCR	quantitative real-time polymerase chain reaction
ψm	mitochondrial membrane potential
MLV	multilamellar vesicle
mM	millimolar
mRNA	messenger ribonucleic acid
MCL	mucocutaneous leishmaniasis
MEF	mouse embryonic fibroblast
MLN(s)	mesenteric lymph node(s)
Monos	monocytes
MS	medullary sinus
MYA	millions of years ago
MyD88	myeloid differentiation response protein 88
NaN3	modium azide
NaNO2	modium nitrite
NK cells	natural killer cells
NO	nitric oxide
O2-	superoxide
O3	ozone
PAMP	pathogen-associated molecular pattern
P.I./p.i.	post-infection
PBS	phosphate-buffered saline
PC	phosphatidylcholine'
PCR	polymerase chain reaction

(Continued)

Continued

PE	phycoerythrin
PKDL	postkala-azar-dermal leishmaniasis
PLN(s)	popliteal lymph node(s)
PRR	pathogen recognition receptor
PRX	peroxiredoxin
PV	parasitophorous vacuole
R (1,2,3,4,5,6,7)	route (1,2,3,4,5,6,7)
RDRP	RNA-dependent RNA polymerase
RFP	right footpad
ROS	reactive oxygen species
RNS	reactive nitrogen species
s.c	sub-cutaneous
S.D	standard deviation
SE	standard error
SCS	sub-capsular sinus
SOD	superoxide dismutase
SLN(s)	sciatic lymph node(s)
ssRNA	single-stranded RNA
T	T-cell zone (in lymph nodes)
T cell(s)	T lymphocyte(s)
TDR	Research and Training in Tropical Diseases
TEMED	NNN¢N¢-tetramethylethylene-diamine
TG	tegumentary leishmaniasis
TGF-β	transforming growth factor beta
Th	T helper
TIR	Toll/IL-1 receptor
TLR	Toll-like receptor
TNF-α	tumor necrosis factor alpha
TTI	tail tip injection
TNFR	TNF receptor
TOSV	Toscana virus
TRAF	TNFR-associated factor
TRIF	TIR domain-containing adapter inducing IFN beta
VL	visceral leishmaniasis
OH	hydroxyl
W/WK	week
WHO	World health Organization
Wt	weight

Frontiers in Cellular and Infection Microbiology

TYPE Original Research
PUBLISHED 12 August 2022
DOI 10.3389/fcimb.2022.941078

EDITED BY
Rameez Raja,
Cleveland Clinic, United States

REVIEWED BY
Asif Amin Dar,
Children's Hospital of Philadelphia,
United States
Showkat A. Dar,
National Institutes of Health (NIH),
United States

*CORRESPONDENCE
Xiaoyan Zhang
zhangxiaoyan@fudan.edu.cn
Jianqing Xu
xujianqing@fudan.edu.cn

†These authors have contributed equally to this work

SPECIALTY SECTION
This article was submitted to
Virus and Host,
a section of the journal
Frontiers in Cellular and
Infection Microbiology

RECEIVED 11 May 2022
ACCEPTED 13 July 2022
PUBLISHED 12 August 2022

CITATION
Zhu C, Zhang M, Fu W, He Y, Yang Y, Zhang L, Yuan S, Jiang L, Xu J and Zhang X (2022) Comparison of H7N9 and H9N2 influenza infections in mouse model unravels the importance of early innate immune response in host protection.
Front. Cell. Infect. Microbiol. 12:941078.
doi: 10.3389/fcimb.2022.941078

Comparison of H7N9 and H9N2 influenza infections in mouse model unravels the importance of early innate immune response in host protection

Cuisong Zhu[1,2†], Miaomiao Zhang[1†], Weihui Fu[1†], Yongquan He[3†], Yu Yang[4], Linxia Zhang[1], Songhua Yuan[1], Lang Jiang[1], Jianqing Xu[1,2*] and Xiaoyan Zhang[1,2*]

[1]Department of Scientific Research, Shanghai Public Health Clinical Center, Shanghai, China, [2]Department of Pathology, Institute of Clinical Science and Shanghai Key Laboratory of Organ Transplantation, Shanghai, China, [3]Human Disease Genes Key Laboratory of Sichuan Province and Institute of Laboratory Medicine,Sichuan Academy of Medical Sciences and Sichuan Provincial People's Hospital, University of Electronic Science and Technology of China, Chengdu, China, [4]Department of Pathology, Fudan University Shanghai Cancer Center, Shanghai, China

The outcome of infection with influenza A virus is determined by a complex virus-host interaction. A new H7N9 virus of avian origin crossed the species barrier to infect humans, causing high mortality and emerged as a potential pandemic threat. The mechanisms underlying the virulence and pathogenicity of H7N9 virus remains elusive. H7N9 virus originated from a genetic assortment that involved the avian H9N2 virus, which was the donor of the six internal genes. Unlike the H7N9 virus, the H9N2 virus caused only mild phenotype in infected mice. In this study, we used the mouse infection model to dissect the difference in the host response between the H7N9 and H9N2 viruses. Through analyzing transcriptomics of infected lungs, we surprisingly found that the H9N2 infection elicited an earlier induction of innate immunity than H7N9 infection. This finding was further corroborated by an immunohistochemical study demonstrating earlier recruitment of macrophage to the H9N2-infected lung than the H7N9-infected lung, which could occur as early as 6 hours post infection. In contrast, H7N9 infection was characterized by a late, strong lung CD8+ T cell response that is more robust than H9N2 infection. The different pattern of immune response may underlie more severe lung pathology caused by H7N9 infection compared to H9N2 infection. Finally, we could show that co-infection of the H9N2 virus protected mice from the challenge of both H7N9 and PR8 viruses, thereby strengthening the importance of the induction of an early innate immunity in the host's defense against influenza infection. Collectively, our study unraveled a previously unidentified difference in host response between H7N9 and H9N2 infection and shed new insight on how virus-host interaction shapes the *in vivo* outcome of influenza infection.

KEYWORDS

H7N9, H9N2, pathological characteristics, C57BL/6 mice, lung

Introduction

Since the first virus strain was identified in 1930s, influenza A viruses (IAVs) continue to pose a threat to humans. The IAV challenge, at least in part, stems from the fact that multiple hosts exist, including a variety of avian species, pigs, and humans, and new viruses can emerge from reassortment when two or more viruses infect the same cell. Normally the species barriers would prevent IAV's spillover from animal to human. However, such a barrier could be broken, resulting in human exposure to new viruses to which they do not have immunity, and consequently can lead to high mortality and even a pandemic if the virus evolves into acquiring human-to-human transmission ability. Most recently, a case was found in a novel avian IAV of H7N9 subtype (abbreviated as H7N9 throughout this paper), which was first reported to cause severe human respiratory infection with high fatality rate in Shanghai and Anhui Province, China, in March 2013 (Gao et al., 2013; Wang et al., 2017). Phylogenetic analysis revealed that H7N9 is a reassortment virus having hemagglutinin (HA) and neuraminidase (NA) genes derived from Eurasian avian influenza viruses (AIVs) and six internal genes from avian H9N2 genotypes (Ku et al., 2014). The death rate of H7N9-infected patients is as high as 40% (Wang et al., 2017; Wu et al., 2020), whereas H9N2 infections only cause mild symptoms in humans (Song and Qin, 2020). Recent research has also indicated a high level of genetic compatibility between H9N2 and H7N9 viruses, raising the likelihood that there could be continuous reassortment between H7N9 and H9N2 viruses co-circulated in poultry and that internal gene replacement could convert the H9N2 virus into a new threat to public health (Pu et al., 2015; Zhang et al., 2020).

The immune response of the host, comprised of two arms, innate immunity and adaptive immunity, is crucial in determining disease pathogenesis caused by viral infection and is the basis for the development of control strategies (Koutsakos et al., 2019). While a potent immune response is essential for effective viral inhibition, it must be fine-tuned, as an excessive and/or prolonged inflammatory response has been correlated to exacerbation of tissue damage both in human and animal models. This double-edged effect was clearly demonstrated in the case of H5N1 virus, which like H7N9, is of avian origin and causes severe clinical manifestation with a high mortality rate. H5N1 infections were associated with dysregulated elevation of proinflammatory cytokines, referred to as a cytokine storm, which is widely regarded as the major cause of widespread pulmonary tissue damage associated with H5N1 infection (Kash et al., 2006; Wu et al., 2020).

There have been several published studies on the characterization of H7N9 virus in mice. These studies revealed that H7N9 virus caused more severe phenotype than H9N2 virus and seasonal H3N2 influenza virus, which correlates to increased infectivity and elevated induction of proinflammatory cytokines (Belser et al., 2013; Mok et al., 2013; Meliopoulos et al., 2014; Bi et al., 2015). Of interest, the host response and the outcome of infection also varied with the mouse strain used, as C57BL/6 mice exhibited more severe phenotype than BALB/c mice, which was accompanied by a different profile of proinflammatory cytokines (Zhao et al., 2014). It was found that H7N9 infection induced significant elevation of proinflammatory cytokines at a level higher than the duck-derived H9N2 virus and the H9N2 virus of avian origin, but lower compared to that induced by the H5N1 infection (Mok et al., 2013). Thus, despite causing similar morbidity and mortality in humans, H7N9 and H5N1 may differ in the disease-causing mechanisms.

Our group has adopted a comparative approach to understanding the mechanisms underlying mammalian adaptation and pathogenesis of the H7N9 virus using H9N2 as a counterpart. Through performing bulk transcriptomic profiling of lung tissues from virus-infected mice, we recently identified IFN-κ as one of the earliest Type I IFNs induced by the H9N2 infection whereas this early induction was not featured in response to H7N9 infection (He et al., 2020). This finding prompted us to further dissect the difference between the host immune response in the H7N9 infection and the H9N2 infection using the mouse model; the results of such exploration are presented here.

Materials and methods

Viruses

A/Shanghai/4664T/2013(SH/4664) H7N9 virus (Genbank accession number: KC853225.1-KC853232.1) was conserved at a Biosafety Level 3 (BSL3) lab at Shanghai Public Clinical Center. A/Chicken/Shanghai/F/98 (CK/F98) H9N2 virus (Genbank accession number: AY253750.1-AY253756.1, AY743216.1) was conserved at Shanghai Veterinary Research Institute, Chinese Academic of Agricultural Sciences.

Animal studies

Eight- to ten-week-old female C57BL/6 mice (B&K Universal Group Limited, Shanghai, China) were maintained under specific pathogen-free conditions at the animal facilities of Shanghai Public Health Clinical Center. For the animal study comparing virulence of H7N9 versus H9N2, mice were randomly grouped, anesthetized *via* intraperitoneal injection of ketamine (100mg/kg), and then intranasally inoculated with a dose of 1×10^6 EID50 (50% egg infectious dose) virus, or PBS in a volume of 50μl. The infected mice, where indicated, were divided into subgroups for different analyses; for the assessment of morbidity and mortality, the mice were monitored for survival and body weight changes over a 14-day observation period. Mice with 30% or more body weight loss were recorded dead and humanely euthanized. For the co-infection experiment, mice were intranasally inoculated with $1x10^4$ TCID50 of H7N9/PR8, or $1.7x10^7$ EID50 of H9N2, or both viruses in a 50μl volume. All the animal-related experiments were carried out in a BSL3 facility at Shanghai Public Clinical Center. This study was performed in accordance with Home Office guidelines and were approved by the Shanghai Public Health Center Local Ethical Committee.

Histopathological and immunohistochemical staining

Mice were sacrificed at 6 hours, day 1, day 2, day 3, and day 7 after the virus challenge for collection of lung tissues. Lung tissues were fixed with 4% paraformaldehyde and then embedded in paraffin. Five-micrometer sections were cut and stained with H&E. The pathology scores were calculated following a methodology we previously published (He et al., 2020). For immunohistochemical (IHC) assays, paraffin sections of the lung were de-waxed and then subjected to heat treatment in citrate buffer, followed by quenching of endogenous peroxidase activity using 0.3% H2O2 in methanol. Sections were blocked for 1 hour (hr) with Fc Receptor Blocker and then incubated overnight at 4°C with F4/80 antibody (CST No.70076, 1:500). Antibody binding was detected using ZSGB System reagents (ZSGB, Beijing). After counterstaining with haematoxylin, the slides were incubated with CD4-specific antibody (Abcam No. ab183685, 1:1000) and CD8-specific antibody (LSBio No.LS-C43572, 1:200), and multiplexed immunofluorescence staining was then performed using Opal 7-color Manual IHC Kit (Akoya,USA). The stained slides were scanned by TissueFAXS 200 (TissueGnostics). The acquired images were analyzed by Strata Quest software to assess the number of F4/80+, CD4+, CD8+ cell and the inflammatory infiltration areas.

Extraction of total RNA and microarray analysis

Each lung from the H7N9/H9N2 infected mice was mechanically and ultrasonically homogenized at 4°C in 1.2ml RNAzol (MRC, OH, USA). Total RNA was extracted from homogenized tissue according to the protocol supplied by the manufacturer. The resulting RNA preparations were analyzed on a 2100 Bioanalyzer (Agilent Technologies, Waldbronn, Germany) to ensure quality and integrity. For microarray hybridization, 500ng of RNA were applied to Cy3-labelling reaction using the one-color Quick Amp Labelling protocol and the labeled cDNAs were hybridized to Agilent's mouse 8 x 60 k microarrays followed by detection using the Agilent Scanner G2505C (Agilent Technologies). The microarray data were analyzed by RBR embedded in Excel and cluster analyses were performed using MEGA5. The microarray data were deposited in Gene Expression Omnibus (GEO) under accession number GSE142709.

Quantitative RT-PCR

Total RNA was isolated from homogenized lung tissue using an RNA isolation kit (Qiagen, Valencia, CA). Reverse transcription was performed using oligo (dT) primer and the Reverse Transcription System (Promega, Madison, WI), and SYBR green-based real-time PCR was performed on the resulting cDNAs using Mastercycler reprealplex real-time PCR system (Eppendorf, Germany). The data were analyzed by the REALPLEX2.2 software. The gene-specific primers used in this study were: mCXCL10: F-5'-GGTCTGAGTCCTCGCTCAAG-3', R-5'-GTCGCACCTCCACATAGCTT-3'; mIL1β: F-5'-GAAATGCCACCTTTTGACAGTG-3', R-5'-CTGGATGCTCTCATCAGGACA-3'; mIL6: F-5'-CTGCAAGAGACTTCCATCCAG-3', R-5'-AGTGGTATAGACAGGTCTGTTGG-3'; mTNFα: F-5'-CATCTTCTCAAAATTCGAGTGACAA-3', R-5'-TGGGAGTAGACAAGGTACAACCC-3'; mGAPDH: F-5'-TGGCCTTCCGTGTTCCTAC-3', R-5'-GAGTTGCTGTTGAAGTCGCA-3'.

Lung viral titer determination and RNA *in situ* hybridization

Lung viral titer determinations, using 9-day-old embryonated eggs, were performed following our published procedure (Zhang et al., 2020). For analyzing viral RNA expression in the lung section by RNA *in situ* hybridization, we chose viral nucleoprotein (NP) RNA as target RNA for detection because of its high expression in infected cells and high conservation among different virus strains. An NP-specific probe, namely Probe-NP, is customized to target 236-1367 region of the NP gene of the influenza virus A/Shanghai/1/2013 (H7N9) (GenBank: KF609528.1). Sequence comparison confirmed that the targeted NP gene sequence is highly conserved in the H9N2 virus. The preparation of slides and RNA *in situ* hybridization using RNAscope reagents (Advanced Cell Diagnostics) were performed as described previously (He et al., 2020).

Statistical analysis

All the statistical analyses were performed using the GraphPad Prism 5 software (GraphPad Software, Inc. La Jolla, CA, USA). Data were expressed as mean ± SEM. One-way analysis of variance (ANOVA) test was applied when comparing more than two groups. A *P* value of ≤ 0.05 was considered statistically significant

Results

Comparison of the virulence of the H7N9 and H9N2 viruses in C57BL/6 mice

We used a mouse infection model to compare the virulence of the H7N9 virus versus the H9N2 virus. To this end, C57BL/6 mice were intranasally inoculated with PBS (mock) or a dose of 1 $\times 10^6$ EID50 of either the H7N9 or H9N2 virus, and monitored over a period of 14 days for survival and weight loss. Part of the group was subjected to lung viral load determination at 4-days post infection (dpi) by titration in embryonated eggs. The H7N9 challenged group showed a sustained weight loss starting from 1 dpi, whereas the H9N2 challenged group experienced a moderate weight decrease during the first 7 days and regained weight afterwards (Figure 1A). Accordingly, all the H7N9 infected mice died before 7 dpi whereas the H9N2 group all survived to the end of the observation period (Figure 1B). The average lung viral titer measured at 4 dpi for H9N2 group was approximately 20-fold lower than that of the H7N9 group (8.32 $\times 10^4$ EID50/g versus 1.78 $\times 10^6$ EID50/g) (Figure 1C).

To further observe the progression of virus infection, we employed RNA *in situ* hybridization technology (RNAscope) to assess the dynamic distribution of virus-infected cells, indicated by the presence of viral NP RNA, in the lung. Cells positive for NP RNA (NP-positive cells) could be detected in both bronchi and alveoli of the lung section from H7N9 infected mice 6 hours post infection (0.25 dpi) and saw a marked increase in the number over 1-3 dpi, followed by a sharp decline observed at 7 dpi. The number of NP-positive lung cells were significantly lower in samples from the H9N2 group, compared to those of H7N9 group at all time points until becoming undetectable at 7dpi (Figure 1D). Thus, the RANscope data were consistent overall with lung viral titer measurements, confirming higher replication capacity of the H7N9 virus than the H9N2 virus. Collectively, these results demonstrated that the H7N9 virus was more virulent than the H9N2 virus in C57BL/6 mice.

Comparative analysis of gene expression dynamics in the lungs of infected mice

To gain insight into host responses against the H7N9 and H9N2 viruses, we performed a microarray-based profiling of RNA extracted from lung tissues collected at a series of time points post virus challenge from H7N9- and H9N2-infected mice. Our initial analysis of this data revealed a significant

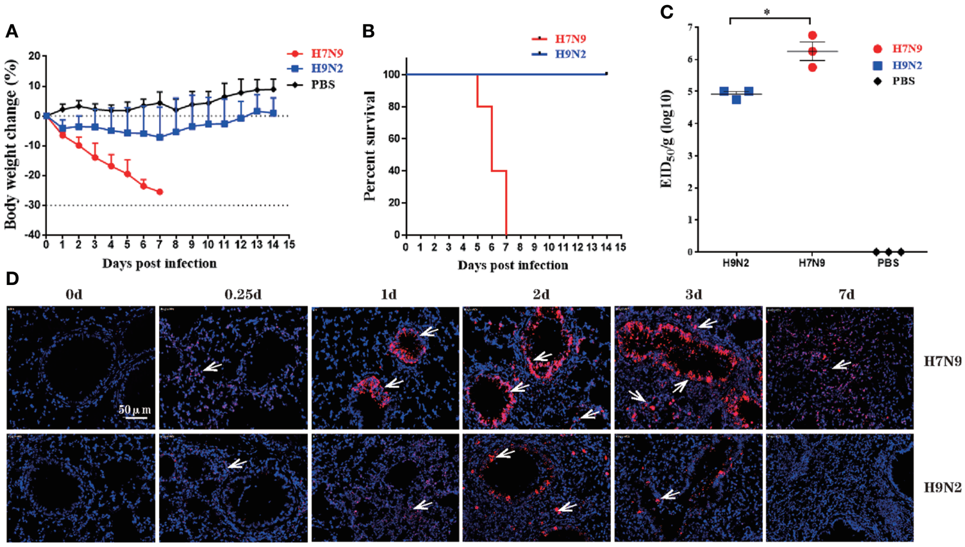

FIGURE 1
H7N9 virus is more virulent than H9N2 virus in C57BL/6 mice. Mice were intranasally inoculated with a single dose of 10^6 EID_{50} of the H7N9 virus or the H9N2 virus. **(A)** Weight loss during a 14-day observation period. **(B)** Survival curve during a 14-day-observation period. Mice that lost >30% of their pre-inoculated weight were regarded as dead and euthanized. **(C)** Virus titers in mice lungs, as determined by EID_{50} using MDCK cells. **(D)** Representative images of RNAscope *in situ* hybridization (ISH) showing virus NP expression in lung. Each red dot represents a single NP RNA molecule, further indicated by white arrow, with nuclei counterstained by DAPI. Data are expressed as mean ± SEM.*$P < 0.05$ by one-way ANOVA.

difference between H9N2 and H7N9 infection in the induction of one type I interferon, namely IFN-κ, which was then demonstrated as a broad inhibitor of influenza replication *via* the IFNAR-MAPK-Fos-CHD6 axis (He et al., 2020). We further utilized this data to interrogate other aspects of immune response in the lung by focusing on genes indicative of immune status. The analyses revealed that relative to H7N9 infection, H9N2 infection was characterized by an earlier induction of immune response in the lung, as evidenced by prompt induction of interferon-induced genes and proinflammatory cytokines with key roles in the host's response to influenza infection, including IL-10, IL-12β, MCP1, IL-1β, IL-6, and TNF-α, which occurred as early as 0.25 dpi (Figures 2A, B). Conversely, despite later initiation, the H7N9 infection-induced upregulation of proinflammatory cytokines appeared to be generally more sustainable with higher peak value as compared to that associated with H9N2 infection. These findings were further verified by measurements of representative cytokines/chemokines and ISGs using quantitative RT-PCR (Figures 2C, D). Interestingly, the earlier induction by H9N2 infection did not occur to IFN-β, which rather showed more upregulation in response to H7N9 infection, sharply rising to a peak at 1 dpi from a base level of 0.25 dpi and then dropping precipitously. The uncoupling between IFN-β and ISGs is consistent with the early ISG response to H9N2 infection and may be mediated by IFN-κ (Figure 2B). Thus, even with a lower viral replication, the H9N2 virus was able to induce an antiviral/inflammatory state in the infected lung faster than H7N9 virus, which might contribute to a better host protection.

Comparative analysis of lung pathology and immune cell infiltration

Next, we evaluated the lung pathology and immune cell infiltration during the course of infection. The degree of lung tissue injury was assessed using HE staining. The pulmonary pathological changes of mice infected with H7N9 were severe at 3 dpi and continued to worsen until death; the main injuries were characterized by massive red blood cell exudation and serious bronchial and bronchiolar damage (Figure 3A, upper panel). In contrast, the histopathology changes in the lung of H9N2-infected mice included alveolar wall thickening and inflammatory cell infiltration, which were most evident at 2 dpi. During subsequent days, although the injury of the lung tissue persisted, the inflammatory infiltration was reduced and consequently, the red blood cell exudation was significantly reduced at 7 dpi (Figure 3A). The progression of lung damage was further appraised by a pathological score curve, verifying that additional severe lung pathology was induced by the H7N9 infection compared to H9N2 infection at both 3 dpi and 7 dpi (Figure 3B).

The immune cell infiltration was assessed by immunohistochemical staining, focusing on two important

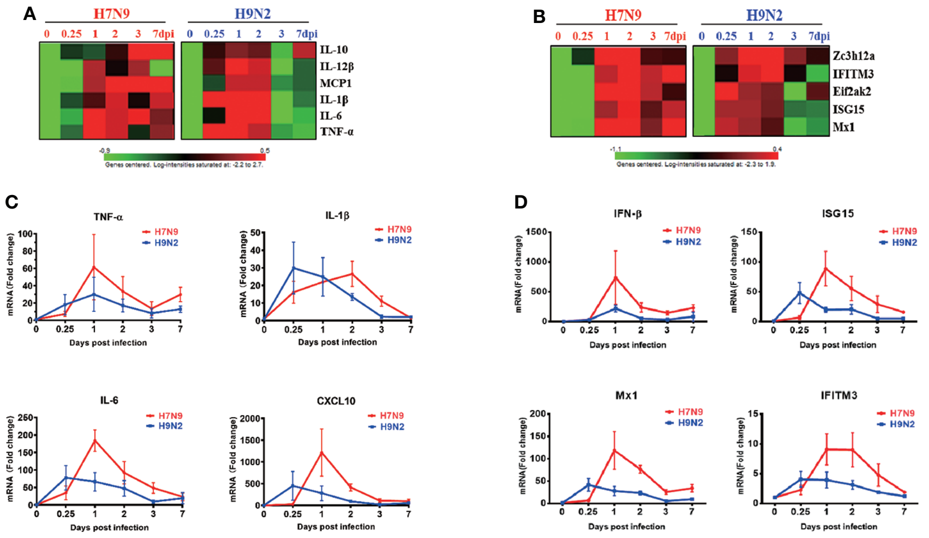

FIGURE 2
Comparative analysis of gene expression dynamics in the lungs of infected mice. Total RNA of lung tissues harvested at 0,0.25,1,2,3,7 dpi from H7N9- or H9N2-infected mice were subjected to microarray-based transcriptome analysis. The microarray data were used for analyzing the expression of proinflammatory cytokines and anti-viral ISGs, expressed as heatmaps of relative gene expression after normalization to the value of mock-infected mice **(A, B)**. Real-time RT-PCR was performed to validate the microarray analysis (n=3 per time point), with the results shown respectively for cytokines **(C)** and anti-viral ISGs **(D)**.

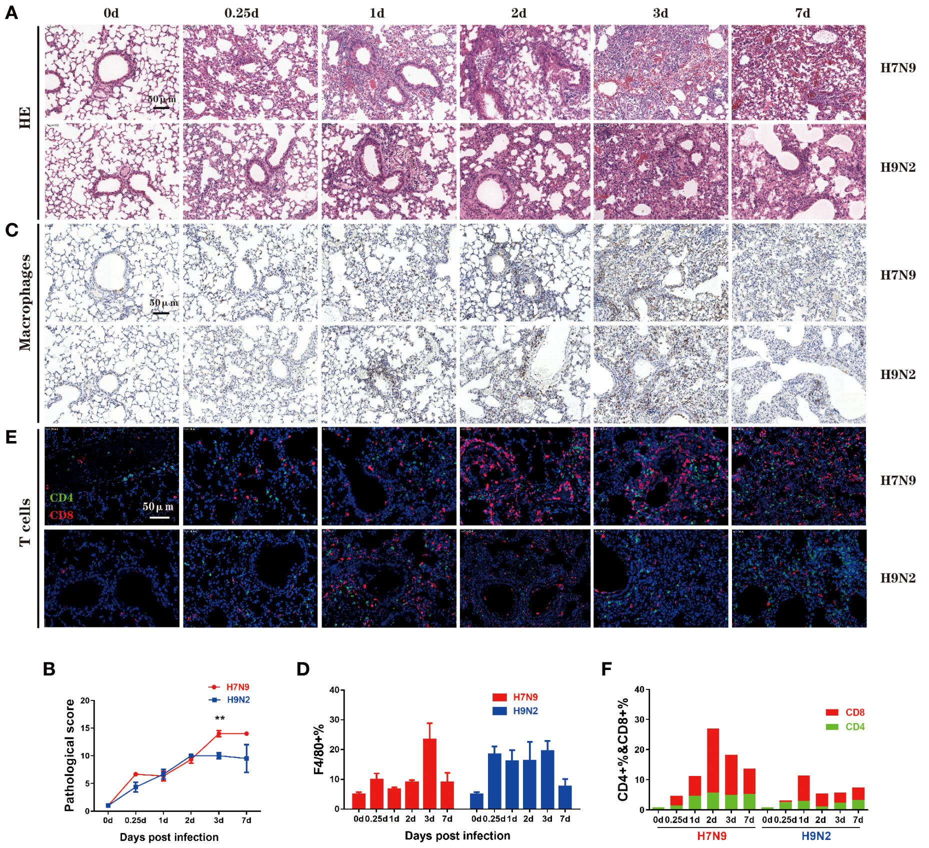

FIGURE 3
Comparative analysis of lung pathology and immune cell infiltration. **(A)** Lung tissue harvested at 0,0.25,1,2,3, and 7 dpi. from mice that had been infected H7N9 or H9N2 avian influenza virus was stained with H&E. **(B)** Quantified pathological scores derived from the calculation of lung histology data. **(C)** Immuno-histochemical detection of total macrophages in the lung sections by staining with anti-F4/80 antibody, with nuclei counterstained by hematoxylin. Brown signals indicate detected macrophages. **(D)** Summation data of the measurements of lung macrophages. **(E)** Immunofluorescence detection of CD4+ plus CD8+ T cells in the lung sections by sequential staining with anti-CD4 and anti-CD8 antibodies, with nuclei counterstained by DAPI. Red and green signals indicate detected CD8+ and CD4+ T cells, respectively. **(F)** Summation data of the measurements of CD4+ and CD8+ T cells in the lung. n=3 mice for each group per time point. $^{**}P < 0.01$ by unpaired t test.

immune cell types, namely macrophage and T cell. Macrophages play multiple functions in antiviral immune responses, including antigen recognition and secretion of interferons. After H7N9 infection, the frequency of lung macrophages moderately increased within 2 dpi before climbing to a peak level at 3 dpi which was significantly higher than the pre-infection (normal) level, and then underwent a sharp decline by 7 dpi (Figures 3C, D). In contrast, a substantial increase in the frequency of lung macrophages was observed after H9N2 infection by 0.25 dpi, which was maintained through 3 dpi before rapidly disappearing by 7 dpi (Figures 3C, D). Thus, H9N2 infection triggers a lung macrophage response more promptly than H7N9 infection, which is in accordance with the above bulky lung transcriptomics analysis revealing very early induction of interferon and proinflammatory cytokines by the H9N2 infection that did not occur with the H7N9 infection.

As one of the two arms of the adaptive immunity, T cells are critical for virus clearance. Previous analyses of human H7N9 patients indicated an early robust CD8+ T cell response is closely correlated with rapid recovery (Wang et al., 2015), whereas CD4+ T cells can directly contribute to viral clearance by cytokine secretion and provide help for B cells and CD8+ T cells (Kervevan and Chakrabarti, 2021). Our measurement identified 1dpi as a demarcation point of the two phases according to the difference between H7N9 and H9N2 infections in terms of lung CD8+ T cell response. Before 1 dpi, no significant difference appeared between the H7N9 and H9N2 infection. In fact, H9N2 induced the highest frequency of lung CD8+ T cells at 1 dpi over the course of infection, which was comparable to or even higher than that shown by H7N9 infection at the same time point. After 1 dpi, H7N9 infection was characterized by an elevation of induced CD8+T cell response, which was not observed with H9N2 infection. The CD8+ T cell response induced by H7N9 infection reached a peak level at 2 dpi and then gradually decreased afterwards, with the level at 7 dpi being still higher than the peak level observed with the H9N2 infection. The H7N9 infection was also associated with a generally stronger CD4+ T cell response than the H9N2 infection. Interestingly, this response did not have the dynamic feature of the lung CD8+ T cell response, showing a relatively stable level up to 7 dpi since showing a clear upregulation between 0.25-1 dpi (Figures 3E, F). Collectively, these immuno-histochemical studies highlighted a marked difference between H7N9 and H9N2 infections in eliciting lung macrophage and CD8+ T cell response in terms of both the timing and magnitude.

An experimental utilization of H9N2 raised early innate immunity to protect against heterologous influenza challenge

To evaluate the importance of induction of early immune response in host protection, we designed a mouse co-infection study, in which the H9N2-induced early immunity was imposed against lethal H7N9 infection or PR8 infection. To this end, the mice were intranasally challenged with 1 x 10^4 TCID50 of either H7N9 or PR8 virus, alone or in mixture with 1.7 x 10^7 EID50 of H9N2 virus, and subsequently monitored for survival and weight loss (Figure 4A). Compared to the animal group with a single H7N9 infection, that all died within 9 days post challenge, a majority of the experimental group receiving the mixed infection survived at the end of the 14-day observation period (Figure 4B). This H9N2-mediated protective effect was also reflected in weight loss curves (Figure 4C). A protection was also observed in the co-administration of PR8 virus with the H9N2 virus for challenging mice; the infected animals exhibited better survival than those infected with PR8 and they also showed significantly better weight gain from 9 dpi, despite displaying more weight loss in the earlier period (Figures 4D, E). Collectively, these results further support our view that early innate immunity, once activated/primed, could afford the host a more effective antiviral defense against invading influenza viruses.

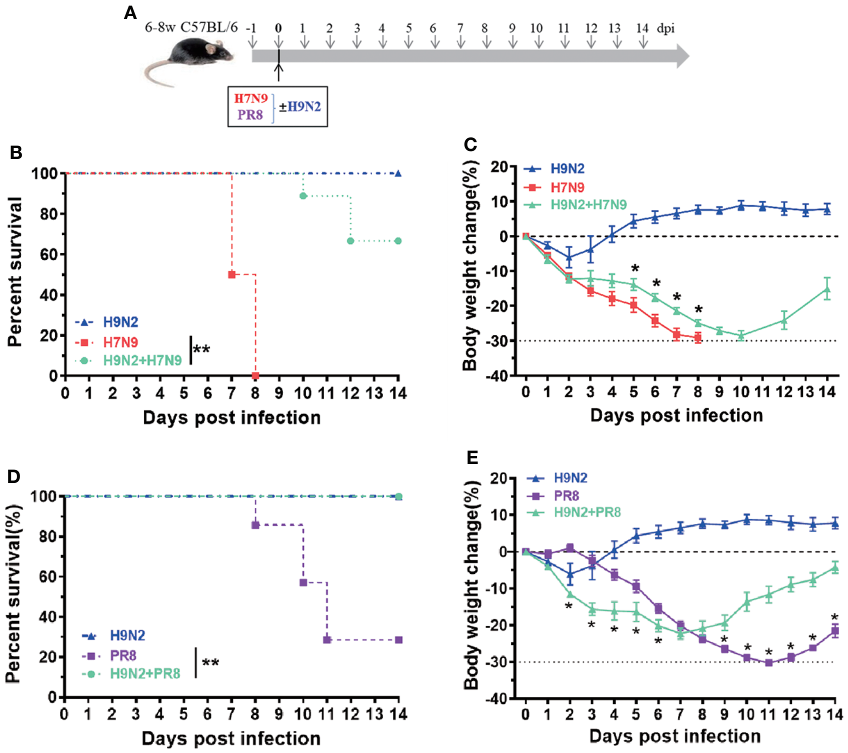

FIGURE 4
An experimental utilization of H9N2-raised early innate immunity to protect against heterologous influenza challenge. **(A)** The schematic diagram of a co-infection experiment. **(B, C)** Comparison of survival **(B)** and body weigh change **(C)** among mice infected with H7N9 alone, H9N2 alone, or a combination of H7N9 and H9N2. **(D, E)** Comparison of survival **(D)** and body weigh change **(E)** among mice infected with PR8 alone, H9N2 alone, or a combination of PR8 and H9N2. n=7-10 for each group, Data are expressed as mean ± SEM. *$P < 0.05$ by t test for body weight change at indicated time point between H7N9/PR8 infected group and H7N9/PR8+H9N2 co-infected groups. **$P < 0.01$ by Log-rank (Mantel-Cox) test for survival analysis.

Discussion

In this study, we compared the H7N9 and H9N2 influenza infections in the mouse model. We observed that, with the same challenging dose, H7N9 infection caused complete lethality before day 8 while the H9N2-infected group only initially exhibited mild weight loss before regaining normal weights and attaining full recovery by day 7. Such a difference in the outcome of infection was correlated to higher lung viral titers associated with the H7N9 infection compared to the H9N2 infection. Microarray-based analyses of gene expression in the lung surprisingly revealed an early induction of innate immunity by the H9N2 infection relative to the H7N9 infection, evidenced by the upregulation of ISGs, immune cell markers and proinflammatory genes. In accordance with this finding, we further showed that macrophages were recruited to the lung of H9N2-infected mice as early as 6 hrs post infection while the clear enrichment of macrophage in the lung was only observed for H7N9 infection on day 3. The lung macrophage response for both infections were subdued by day 7. In contrast, the H7N9-infected lung exhibited a more robust CD8+ T cell response than the H9N2-infected lung, peaking at day 2 and declining afterwards. The different pattern of immune response may correspond with the H7N9 infection which produced more severe lung pathology than the H9N2 infection. Finally, we could show that co-infection of the H9N2 virus led to an effective protection against both H7N9 and PR8 viruses, thereby strengthening the importance of an early innate immunity in the host's defense against influenza infection. Collectively, our study unraveled a previously unidentified difference in the host's response between the H7N9 and H9N2 infections: the H9N2 infection triggered an earlier innate immunity in the lung than the H7N9 infection. We proposed that such early engagement of host innate immunity, along with intrinsic weak infectivity in mammalian cells, permits an effective control of H9N2 in infected mice. It is tempting to speculate that the H7N9 virus evolves a strategy to avoid triggering early immune response and thus allows more effective virus propagation in the lung until the later arrival of adaptive immunity, which consequently contributes to lung pathogenicity as a collateral effect of viral clearance.

The study presented here is distinguished from previous mouse studies on H7N9 infection in that our analyses covered very early time points post infection starting from 6 dpi., which were previously neglected. Such an expanded investigation led us to a surprising finding that, relative to the H7N9 infection, the H9N2 infection triggered an early, while transient, innate immune response in infected lung in terms of both interferon-mediated antiviral signaling and the production of proinflammatory cytokines. We further corroborated this finding by demonstrating earlier recruitment of macrophages in the H9N2-infected lung compared to the H7N9-infected lung. In fact, we have used our microarray data to assess the expression dynamics of two monocyte-expressing chemokine receptors, namely CCR2 and CXCR4, which play key roles in mobilizing monocytes into lung in response to their respective ligand, CCL2 (MCP-1) and CXCL12. The analyses revealed that, compared to the H7N9 infection, the H9N2 infection induced an earlier induction of both CCR2 and CXCR4 transcripts, similar to that of CCL2 (Figure 2A) in the lung (data not shown). Thus, these findings, in line with the notion that the CCL2-CCR2 axis drives the lung migration of monocyte, supported the infiltrated monocytes as one if not the only source of macrophage accumulation in the lung responding to H9N2 infection. A major limitation of this study is that we had not measured the abundance of neutrophiles, which have well documented roles in influenza-induced pathogenicity (Camp and Jonsson, 2017; George et al., 2021), as well as innate immune cells other than macrophage in the H7N9/H9N2-infected lungs and BAL fluids. Our analysis of lung transcriptomics did suggest a potential early lung enrichment of neutrophiles in response to H9N2 infection, evidenced by CXCR2, the main receptor mediating the lung migration of neutrophils during influenza infection, and three major neutrophil-attracting chemokines, namely CCL3, CXCL-1, and CXCL2, which all exhibited a pattern consistent with an early induction by H9N2 infection compared to H7N9 infection (data not shown). The illustration of the complete landscape of changes in innate immune response to H9N2 versus H9N2, as well as the dissection of the functional contributions of individual immune cell types to such response, clearly warrant future investigation.

We also probed the dynamics of the T cell immune response reacting to H9N2 and H7N9 infections. The results showed a more robust CD8+ T cell response in the lung induced by the H7N9 infection than H9N2 infection. Importantly, for the H7N9 infection, such T cell response showed a pattern of gradual increase with a peak attained on day 2 post infection. Our previous studies of hospitalized H7N9 patients revealed the virus resolution and survival depends on a diversity of response mechanisms, wherein an early prominent H7N9-specific CD8(+) T-cell responses is translated into a shorter discharge time and increased survival. This rapid CD8(+) T cell response is potentially derived from cross-reactive memory T cells deposited by prior influenza exposure (Wang et al., 2015). Utilizing a sequential infection mouse model, we have recently demonstrated that lung-resident influenza-specific CD8+ T cells are promptly activated and secrete IFN-γ in response to influenza re-exposure, thereby establishing a tissue-wide antiviral state for effective viral inhibition (Jiang et al., 2022). In the current study, the mice were naïve to influenza and thus the increased number of CD8+ T cells in the H7N9-infected lung must be due to recruitment of circulating CD8+ T cells. Whether such strong T cell response, which occurred at relatively late time points after infection, functions in viral clearance, contributes to the lung histopathology, or both remains an open question and we speculate the dual effects would be more likely. In this regard, the measurement of the functionality of CD8+ T cells, as well as the assessment of their possible redistribution among different tissue compartments, will be informative to further define the role of a primary T cell response in the anti-H7N9 host immunity. They are definitely worthy of future investigation.

Finally, we performed a co-infection experiment to examine our hypothesis that the elicitation of an early innate immunity is critical for protection against influenza virus infection. We could show that co-inoculation of H9N2 did not enhance the lethality and pathogenicity of the host, but rather reduced the pathogenicity of H7N9 infection. An even better protective effect was observed with the PR8 virus. The lesser efficacy of H9N2-mediated protection against H7N9 versus PR8 might be due to a relatively higher replicative capacity of the H7N9 virus. Given that H7N9 and PR8 viruses express very different HA and NA surface proteins, the ability of H9N2 co-infection to protect mice against the challenge of a heterologous influenza virus is consistent with a mechanism primarily mediated by innate immunity, as we proposed. Taken together, we think that the lesser pathogenicity of H9N2 in the mouse model has dual mechanism: first, it is intrinsically attenuated when infecting mammalian cells and our previous study has pinpointed such defect to the lack of mammalian adaptation of its internal genes, most likely its polymerases genes (Zhang et al., 2020); secondly, it triggers an earlier innate immune response in infected lung as compared to H7N9, resulting in more effective viral inhibition.

In summary, we presented here a comparative analysis of immune responses to the H7N9 virus versus the H9N2 virus. This analysis, together with a following demonstration of the protection against H7N9 and PR8 challenge by H9N2 co-infection, brings a new perspective to the interaction between host immunity and influenza evasion. That is, the induction of early innate immune response, as seen with in H9N2 infection but absent in H7N9 infection, is the first but also potentially a primary step toward an effective viral inhibition. Without this step, adaptive immunity could be responsible for viral clearance; however, a sustained CD8+ T cell response may leave the host at higher risk of lung immunopathology. There are some important questions warranting future investigation. For example, what is the mechanism mediating H7N9's escape from trigging an early innate immune response? Is there any specific viral factor involved? An equally important question is to identify the pathogen-associated molecular pattern (PAMP) pathway(s) responsible for the detection of H9N2 infection. It should be noted that the importance of such a pathway would not be unraveled in the case of H7N9, where a viral evasion mechanism might evolve. Furthermore, is avoiding early innate immunity a general mechanism utilized by other influenza viruses that cause severe diseases? Conversely, a comparative measurement of pulmonary specific compliance and the composition of bronchoalveolar fluid is a worthy effort that has the potential to provide new clues into the H7N9-caused lung pathology and the underlying causes. These future investigations would certainly help us further understand the complex host-influenza interactions, thereby providing a new theoretical basis for development of new therapeutics for treatment of influenza-related human diseases.

Data availability statement

The original contributions presented in the study are included in the article/supplementary material. Further inquiries can be directed to the corresponding author/s.

Ethics statement

The animal study was reviewed and approved by Shanghai Public Health Center Local Ethical Committee.

Author contributions

XZ and JX conceived and designed this project and supervised the experiments. CZ and YY performed the IHC and IF experiments. WF performed extraction of total RNA and microarray analysis. MZ performed virus titer determination. YH, LZ, SY and LJ performed the *in vivo* experiments. All authors contributed to the article and approved the submitted version.

Funding

This work was supported by the National Natural Science Foundation of China (81672018,82071788, 82101846) , the Intramural Funding from Shanghai Public Health Clinical Center (KY-GW-2019-16, KY-GW-2021-03), Shanghai Science and Technology Program (20Y11900500), and Sichuan Science and Technology Program (2021YFS0404 and 2021ZYD0082).

Acknowledgments

We thank Professor Zejun Li of Shanghai Veterinary Research Institute, Chinese Academic of Agricultural Sciences for providing virus.

Conflict of interest

The authors declare that the research was conducted in the absence of any commercial or financial relationships that could be construed as a potential conflict of interest.

Publisher's note

References

Belser, J. A., Gustin, K. M., Pearce, M. B., Maines, T. R., Zeng, H., Pappas, C., et al (2013). Pathogenesis and transmission of avian influenza a (H7N9) virus in ferrets and mice. *Nature* 501, 556–559. doi: 10.1038/nature12391

Bi, Y. H., Xie, Q., Zhang, S., Li, Y., Xiao, H. X., Jin, T., et al (2015). Assessment of the internal genes of influenza a (H7N9) virus contributing to high pathogenicity in mice. *J. Virol.* 89, 2–13. doi: 10.1128/JVI.02390-14

Camp, J. V., and Jonsson, C. B. (2017). A role for neutrophils in viral respiratory disease. *Front. Immunol.* 8, 550. doi: 10.3389/fimmu.2017.00550

Gao, R. B., Cao, B., Hu, Y. W., Feng, Z. J., Wang, D. Y., Hu, W. F., et al (2013). Human infection with a novel avian-origin influenza a (H7N9) virus. *N. Engl. J. Med.* 368, 1888–1897. doi: 10.1056/NEJMoa1304459

George, S. T., Lai, J., Ma, J., Stacey, H. D., Miller, M. S., and Mullarkey, C. E. (2021). Neutrophils and influenza: A thin line between helpful and harmful. *Vaccines (Basel)* 9, 597. doi: 10.3390/vaccines9060597

He, Y. Q., Fu, W. H., Cao, K. L., He, Q., Ding, X. Q., Chen, J., et al (2020). IFN-γ suppresses the replication of influenza a viruses through the IFNAR-MAPK-Fos-CHD6 axis. *Sci. Signal.* 13, eaaz3381. doi: 10.1126/scisignal.aaz3381

Jiang, L., Liu, L., Zhang, M. M., Zhang, L. X., Zhu, C. S., He, Q., et al (2022). Prompt antiviral action of pulmonary CD8+ TRM cells is mediated by rapid IFN-γ induction and its downstream ISGs in the lung. *Front. Immunol.* 13, 839455. doi: 10.3389/fimmu.2022.839455

Kash, J. C., Tumpey, T. M., Proll, S. C., Carter, V., Perwitasari, O., Thomas, M. J., et al (2006). Genomic analysis of increased host immune and cell death responses induced by 1918 influenza virus. *Nature* 443, 578–581. doi: 10.1038/nature05181

Kervevan, J., and Chakrabarti, L. A. (2021). Role of CD4+ T cells in the control of viral infections: recent advances and open questions. *Int. J. Mol. Sci.* 22, 523. doi: 10.3390/ijms22020523

Koutsakos, M., Kedzierska, K., and Subbarao, K. (2019). Immune responses to vian influenza viruses. *J. Immunol.* 202, 382–391. doi: 10.4049/jimmunol.1801070

Ku, K. B., Park, E. H., Yum, J., Kim, H. M., Kang, Y. M., Kim, J. C., et al (2014). Transmissibility of novel H7N9 and H9N2 avian influenza viruses between chickens and ferrets. *Virology* 450-451, 316–323. doi: 10.1016/j.virol.2013.12.022

Meliopoulos, V. A., Karlsson, E. A., Kercher, L., Cline, T., Freiden, P., Duan, S., et al (2014). Human H7N9 and H5N1 influenza viruses differ in induction of cytokines and tissue tropism. *J. Virol.* 88, 12982–12991. doi: 10.1128/JVI.01571-14

Mok, C. K. P., Lee, H. H. Y., Chan, M. C. W., Sia, S. F., Lestra, M., Nicholls, J. M., et al (2013). Pathogenicity of the novel A/H7N9 influenza virus in mice. *mBio* 4, e00362–e00313. doi: 10.1128/mBio.00362-13

Pu, J., Wang, S. G., Yin, Y. B., Zhang, G. Z., Carter, R. A., Wang, J. L., et al (2015). Evolution of the H9N2 influenza genotype that facilitated the genesis of the novel H7N9 virus. *Proc. Natl. Acad. Sci. U.S.A.* 112, 548–553. doi: 10.1073/pnas.1422456112

Song, W. J., and Qin, K. (2020). Human-infecting influenza a (H9N2) virus: A forgotten potential pandemic strain? *Zoonoses Public Health* 67, 203–212. doi: 10.1111/zph.12685

Wang, X. L., Jiang, H., Wu, P., Uyeki, T. U., Feng, L. Z., Lai, S. J., et al (2017). Evolving epidemiology of human infections with avian influenza A(H7N9) virus across five epidemic waves in mainland China, 2013–17: an epidemiological study of laboratory-confirmed case series. *Lancet Infect. Dis.* 17, 822–832. doi: 10.1016/S1473-3099(17)30323-7

Wang, Z. F., Wan, Y. M., Qiu, C. L., Quiñones-Parra, S., Zhu, Z. Q., Loh, L., et al (2015). Recovery from severe H7N9 disease is associated with diverse response mechanisms dominated by $CD8^+$ T cells. *Nat. Commun.* 6, 6833. doi: 10.1038/ncomms7833

Wu, X. X., Xiao, L. L., and Li, L. J. (2020). Research progress on human infection with avian influenza H7N9. *Front. Med.* 14, 8–20. doi: 10.1007/s11684-020-0739-z

Wu, X. X., Zhao, L. Z., Tang, S. J., Weng, T. H., Wu, W. G., Yao, S. H., et al (2020). Novel pathogenic characteristics of highly pathogenic avian influenza virus H7N9: viraemia and extrapulmonary infection. *Emerg. Microbes Infect.* 9, 962–975. doi: 10.1080/22221751.2020.1754135

Zhang, M. M., Zhao, C., Chen, H. J., Teng, Q. Y., Jiang, L., Feng, D. B., et al (2020). Internal gene cassette from a human-origin H7N9 influenza virus promotes the pathogenicity of H9N2 avian influenza virus in mice. *Front. Microbiol.* 2211, 1441. doi: 10.3389/fmicb.2020.01441

Zhao, G. Y., Liu, C. F., Kou, Z. H., Gao, T. T., Pan, T., Wu, X. H., et al (2014). Differences in the pathogenicity and inflammatory responses induced by avian influenza A/H7N9 virus infection in BALB/c and C57BL/6 mouse models. *PLoS One* 9, e92987. doi: 10.1371/journal.pone.0092987

Frontiers in Cellular and Infection Microbiology

TYPE Original Research
PUBLISHED 09 September 2022
DOI 10.3389/fcimb.2022.951383

OPEN ACCESS

EDITED BY
Laura Patricia Mendoza,
Universidad Nacional de Asunción, Paraguay

REVIEWED BY
Adriana Delfraro,
Universidad de la República, Uruguay
Victor Daniel Miron,
Carol Davila University of Medicine and Pharmacy, Romania

*CORRESPONDENCE
Paúl Cárdenas
pacardenas@usfq.edu.ec

SPECIALTY SECTION
This article was submitted to Virus and Host, a section of the journal Frontiers in Cellular and Infection Microbiology

RECEIVED 23 May 2022
ACCEPTED 22 August 2022
PUBLISHED 09 September 2022

CITATION
Guevara R, Prado-Vivar B, Márquez S, Muñoz EB, Carvajal M, Guadalupe JJ, Becerra-Wong M, Proaño S, Bayas-Rea R, Coloma J, Grunauer M, Trueba G, Rojas-Silva P, Barragán V and Cárdenas P (2022) Occurrence of SARS-CoV-2 reinfections at regular intervals in Ecuador.
Front. Cell. Infect. Microbiol. 12:951383.
doi: 10.3389/fcimb.2022.951383

Occurrence of SARS-CoV-2 reinfections at regular intervals in Ecuador

Rommel Guevara[1], Belén Prado-Vivar[1], Sully Márquez[1], Erika B. Muñoz[1], Mateo Carvajal[1], Juan José Guadalupe[2], Mónica Becerra-Wong[1], Stefanie Proaño[1], Rosa Bayas-Rea[1], Josefina Coloma[3], Michelle Grunauer[4], Gabriel Trueba[1], Patricio Rojas-Silva[1], Verónica Barragán[1] and Paúl Cárdenas[1]*

[1]Instituto de Microbiología, Universidad San Francisco de Quito USFQ, Quito, Ecuador, [2]Laboratorio de Biotecnología Vegetal, Universidad San Francisco de Quito USFQ, Quito, Ecuador, [3]Division of Infectious Diseases and Vaccinology, School of Public Health, University of California Berkeley, Berkeley, CA, United States, [4]Escuela de Medicina, Universidad San Francisco de Quito USFQ, Quito, Ecuador

SARS-CoV-2 reinfection is defined as a new infection with a different virus variant in an individual who has already recovered from a previous episode of COVID-19. The first case of reinfection in the world was described in August 2020, since then, reinfections have increased over time and their incidence has fluctuated with specific SARS-CoV-2 variant waves. Initially, reinfections were estimated to represent less than 1% of total COVID-19 infections. With the advent of the Omicron variant, reinfections became more frequent, representing up to 10% of cases (based on data from developed countries). The frequency of reinfections in Latin America has been scarcely reported. The current study shows that in Ecuador, the frequency of reinfections has increased 10-fold following the introduction of Omicron, after 22 months of surveillance in a single center of COVID-19 diagnostics. Suspected reinfections were identified retrospectively from a database of RT-qPCR-positive patients. Cases were confirmed by sequencing viral genomes from the first and second infections using the ONT MinION platform. Monthly surveillance showed that the main incidence peaks of reinfections were reached within four to five months, coinciding with the increase of COVID-19 cases in the country, suggesting that the emergence of reinfections is related to higher exposure to the virus during outbreaks. This study performed the longest monitoring of SARS-CoV-2 reinfections, showing an occurrence at regular intervals of 4-5 months and confirming a greater propensity of Omicron to cause reinfections.

KEYWORDS

COVID-19, reinfection, genomic epidemiology, sequencing, SARS-CoV-2

Introduction

The outbreak of COVID-19 was declared a public health emergency of international concern in March 2020 by the World Health Organization (WHO), more than two years later the pandemic has not been fully controlled as emerging variants keep producing epidemic waves (Wise, 2022). The high evolutive rate of SARS-CoV-2 (Tay et al., 2022) contributes to the emergence of fitter variants with increased transmissibility and greater ability to partially evade immune protection acquired through natural infection or vaccination (Hu et al., 2022). Given that around half of the world's population is estimated to have been infected with COVID-19 at least once (Barber et al., 2022), the next epidemic waves are expected to be caused primarily by reinfections. SARS-CoV-2 reinfection is defined as a new infection with a different viral variant in individuals who have already recovered from a previous episode of COVID-19 (Yahav et al., 2021). The lack of sequencing technologies to confirm reinfections, mainly in low-income countries, could mask the real impact of reinfections globally, making it difficult to elucidate its risk factors and ways to prevent it in the face of future variants.

The first case of SARS-CoV-2 reinfection sequence-confirmed was reported in Hong Kong in August 2020 (To et al., 2020) and since then several cases were reported worldwide leading to scientific efforts to reinfection scrutiny. Multiple protocols were proposed to identify suspected cases and to rule out the persistence or relapse of early infecting variants. The Pan American Health Organization (PAHO) defined a suspected case of SARS-CoV-2 reinfection as a symptomatic individual with a positive test after 45 days since the prior infection or 90 days if was asymptomatic, and suggested the confirmation of the case based on laboratory evidence (sequencing of both viral variants) or epidemiological data (negative test between events) (PAHO, 2020). Early estimates from the USA, UK, Denmark, and Qatar reported a low frequency of SARS-CoV-2 reinfections, accounting for less than 1% of total infections (Abu-Raddad et al., 2021; Hall et al., 2021; Hansen et al., 2021; Harvey et al., 2021). After the arrival of the Omicron variant in late 2021, the frequency of reinfections increased to about 10% of total infections (Bastard et al., 2022; Pulliam et al., 2022). Nevertheless, these proportions were mainly estimated in high-income countries and the situation in other countries remained elusive.

Latin America was one of the most affected regions during the COVID-19 pandemic, mainly driven by a deficient public health system coupled with socioeconomic problems in its population (Bakker, 2021). The first confirmed case of SARS-CoV-2 reinfection in this region was reported in July 2020 in Ecuador (Prado-Vivar et al., 2021) followed by other reports in different countries (Díaz et al., 2021; Fonseca et al., 2021; Ramírez et al., 2021). However, most of these reports were isolated cases that do not allow elucidation of the frequency of reinfections and the impact of emerging variants. This study describes SARS-CoV-2 reinfection cases identified retrospectively in Ecuador after 22 months of surveillance. Suspected cases were identified based on the PAHO guidelines (PAHO, 2020) with some modifications to include possible reinfections occurring in less than 45 days, meanwhile, the confirmation of the case was done by sequencing SARS-CoV-2 genomes from the first and second infection using the ONT MinION platform. This study performs the most extended follow-up of SARS-CoV-2 reinfections in a low-income country and contributes to the global effort of genomic surveillance of emerging variants that could help clarify the leading causes of reinfections and understand the dynamics of COVID-19 epidemic waves.

Materials and methods

Sample collection and diagnostics

Samples included in the study were collected from clinics and hospitals in different provinces of Ecuador and tested at the diagnostic center of the Microbiology Institute of Universidad San Francisco de Quito (IM-USFQ) from May 2020 to February 2022. Demographic and clinical information for each patient was retrieved at the same time as sample collection and was derived to IM-USFQ. Specimens were oropharyngeal, or nasopharyngeal swabs taken from symptomatic and asymptomatic patients. Swabs were collected in a 1.5 mL sterile tube with 1X DNA/RNA Shield (Zymo, USA) which inactivates the virus and preserves its genomic material. Samples were immediately transported to the laboratory at room temperature in a sealed container. The diagnosis of SARS-CoV-2 was based on RT-qPCR using one of the following kits: the Veri-Q PCR 316 kit (MiCo BioMed, South Korea), the LightMix® SarbecoV E-gene kit (TIB Molbiol, Germany), or the Allplex™ 2019-nCoV Assay (Seegene, South Korea). The cycle threshold (Ct) value to identify positive results was based on manufacturers' instructions. Positive samples were sequenced as described below.

Selection of patients and ethical considerations

Identification of suspected reinfections was performed retrospectively and based on PAHO recommendations (PAHO, 2020) with some modifications. The process is represented in a flow chart in Figure 1. The IM-USFQ database of RT-qPCR test was used, which compiled every test processed by this diagnostic center since May 2020. Patients who

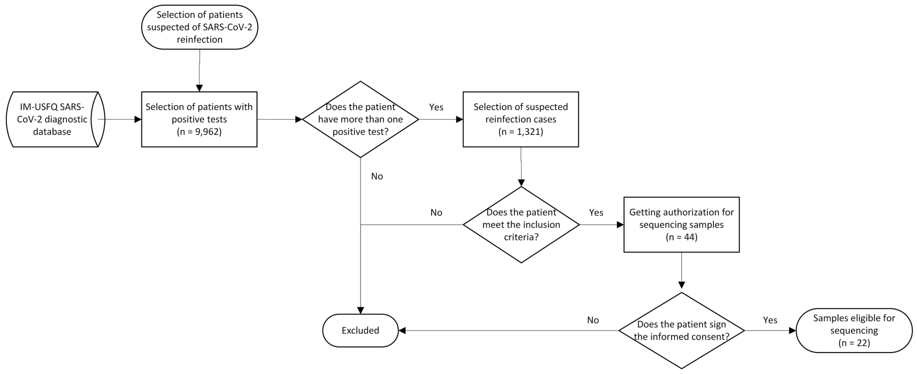

FIGURE 1
Flow chart for the selection of suspected reinfections. The database includes tests performed at IM-USFQ from May 2020 to February 2022. Suspected cases were identified retrospectively, first by patients who reported more than one positive test, and then by the compliance with inclusion criteria: at least 45 days between infections, or less if the Ct revealed a higher viral load in the reinfection. From the 44 patients who accomplished inclusion criteria, 22 were considered for sequencing.

have more than one positive test were selected and defined as suspected reinfection based on inclusion criteria that consider people with an interval of more than 45 days between infections, and to prevent exclusion of reinfections occurring in less time, were included those cases where the second test showed evidence of higher viral loads by a lower Ct-value than the first test. This study also includes a reinfected patient previously reported by the IM-USFQ (Prado-Vivar et al., 2021). Patients suspected of reinfection were reached to get their informed consent to sequence their samples and include their data in the study, which was managed anonymously through the assignation of identification codes. Demographic data were included, as well as the available clinical records, which differed for each patient depending on the care center of origin. Symptoms were classified as mild, moderate, or severe according to the WHO criteria (WHO, 2020). This study is part of a country-wide project that aims to monitor the SARS-CoV-2 variants in Ecuador which were approved by the Bioethics Committee of Universidad San Francisco de Quito (CEISH No. P2020-022IN) and by the Ministerio de Salud del Ecuador (MSP-CGDES-2020-0121-O).

SARS-CoV-2 whole-genome sequencing

The RNA extraction, cDNA preparation, and sequencing were done as described previously by (Prado-Vivar et al., 2021). Briefly, the Quick RNA viral w/zymo-Spin IC (Zymo, USA) kit was used for RNA extraction. Retro-transcription to cDNA was carried out in line with the ARTIC network protocol (Quick, 2020). The cDNA obtained was stored at 4°C for the next step. A long-read sequencing approach through MinION$^{\text{TM}}$ (Oxford Nanopore Technologies, UK) was used following the ARTIC network protocol (Quick, 2020) specific for SARS-CoV-2 sequencing. In brief, target enrichment was performed using multiplex-PCR, with primer schemes V1 and V3 (Quick, 2020; Tyson et al., 2020), over the cDNA previously prepared. Amplification was assessed by agarose gel electrophoresis and the product was quantified using the Qubit dsDNA HS assay kit (Invitrogen, USA). After normalization, the library was prepared following manufacturer instructions by using the Native Barcoding Kit (EXP-NBD196) with the Ligation Sequencing Kit (SQK-LSK-109). The genomic library was loaded into a MinION flow cell (FLO-MIN106D). The sequencing was programmed in the software MinKNOW v22.03.4 with fast basecalling, demultiplexing, and adapter removal enabled. The real-time monitoring of the sequencing process was carried out using the RAMPART software v1.2.0 (Rambaut, 2020). After sequencing, the Medaka v1.6.0 algorithm was used for variant calling and to create consensus sequences mapped against the Wuhan-Hu-1 reference genome (NC_045512.2). Consensus sequence quality was assessed by Nextclade v1.14.0 parameters (clades.nextstrain.org) and were uploaded to the GISAID repository (gisaid.org).

Data and phylogenetic analysis

Clades and linages assignments were performed using Nextclade and Pangolin COVID-19 Lineage Assigner v4.0.5 (pangolin.cog-uk.io), respectively. Nextclade was used to identify nucleotide mutations and amino acid substitutions on each sequence relative to the reference genome. A phylogenetic tree was built to ensure that paired viral sequences from each reinfection had a different immediate ancestor. The Wuhan-Hu-1 reference genome (GenBank accession: MN908947.3) was included for rooting the phylogram. These sequences were aligned along with reinfection sequences using MAFFT online program (Katoh et al., 2019). Finally, the phylogram was estimated by the Maximum Likelihood method under a GTR nucleotide substitution model and 1000 bootstrap replicates using IQ-TREE online tool (hiv.lanl.gov/content/sequence/IQTREE/iqtree.html). The phylogram figure was obtained and annotated using the iTOL v6.5.2 (Letunic and Bork, 2021). Statistical analysis was done in RStudio v2022.02.1 with the package descriptr (Hebbali, 2020). The confidence interval (CI) of incidences was estimated by Wald's test with continuity correction. The variation of symptoms and Ct-value between first and second infections were assessed with the McNemar's Chi-squared test with continuity correction, where symptoms were categorized as moderate or mild/asymptomatic, and Ct-values as < 30 or > 30. A p-value < 0.05 was considered statistically significant.

Results

Suspected reinfection cases

From May 2020 to February 2022, the IM-USFQ diagnostic database registered 9,962 patients with at least one positive RT-qPCR test for SARS-CoV-2; 1,321 of them (13.26%) had more than one positive sample, and from this subset suspected reinfection cases were selected. 44 patients (0.44% [95% CI 0.32-0.60]) met the inclusion criteria (Figure 1) and their demographic data is shown in Table S1. 28 (64%) were male patients, their average age was 36 years old (median 34.5; range 19-57), and the mean interval between infections was 237 days (median 226; IQR 90-318). 15 patients (34%) were not vaccinated during reinfection, whereas five (11%) had the first dose, 19 (43%) had the second dose, and four (9%) had the booster dose. Most patients were from Quito, the capital city of Ecuador, eight were from Manta in the Coastal region, and two were from the Amazon region (Tena and Nueva Loja). Clinical records were not available for all patients, however, none had severe symptomatology in either the first and second infection, and 13 out 25 reported milder or any symptoms during reinfection. Neither the variation of symptoms and Ct-values between the first and second reinfection were considered statistically significant ($p > 0.05$).

Figure 2 shows suspected reinfections identified during each month of surveillance. The first case was identified in June 2020, whereas the latter was in February 2022 (panel A), detecting at least one case in 13 out of the 22 months of surveillance. The figure also shows the proportion of suspected reinfections in relation to the total positive tests processed each month (Panel B), showing the highest point of incidence in August 2021 (8.70%), followed by January 2022 (2.52%), February 2022 (1.92%), and December 2021 (1.08%).

Genomic sequencing of SARS-CoV-2

Informed consents were obtained for 22 out of 44 patients suspected of SARS-CoV-2 reinfection (Figure 1). Samples from 19 patients were successfully sequenced, including 11 patients with paired samples from their first and second infection, and eight patients only with the second infection sample. Clades and lineages assigned to each genome are shown in Table S2, together with amino acid substitutions and the GISAID accession number. Isolates from 2020 were assigned as common variants, whereas variants from 2021 and 2022 were classified as variants of interest (VOI) and variants of concern (VOC) (Figure 3). All the reinfecting variants from January and February 2022 were classified as Omicron. The incidence of reinfections during the Omicron period (since December 2021) was 2.45% (95% CI 1.63-3.66), whereas in the pre-Omicron period it was 0.21% (95% CI 0.13-0.34). In the paired samples, the reinfecting virus variant was from a different clade and/or lineage than the first infecting virus variant. This was confirmed by the phylogenetic tree where none of the reinfecting variants shares an immediate ancestor with the first infecting virus variant (Figure 4). These results confirm the reinfections of 11 patients out of 44 suspected cases (25%). Only four of them presented more severe symptoms during reinfections, and none reported significant clinical sequelae.

Discussion

Suspected reinfections of SARS-CoV-2 were retrospectively identified in the period from May 2020 to February 2022, with 11 cases confirmed by sequencing of the infecting variants. The incidence of suspected reinfections increased by 10-fold after the introduction of the Omicron variant. Monthly surveillance showed that the proportion of reinfections detected was higher at regular intervals of four to five months. This study reports a 22 month-period surveillance of SARS-CoV-2 reinfections, where COVID-19 infection was detected by RT-qPCR.

SARS-CoV-2 is an RNA virus with an unexpectedly high rate of evolution (Tay et al., 2022), which has contributed to the continuous emergence of more virulent variants and the surge of several epidemic waves since the onset of the COVID-19 pandemic. The first cases of reinfections by SARS-CoV-2 confirmed the ability of the virus to partially evade the immune protection previously acquired by natural infection, as has been seen with other closely related viruses (Edridge et al., 2020). Early reports estimated a low frequency of reinfections (less than 0.70%) regarding to the total of newly infected individuals (Abu-Raddad et al., 2021; Hall et al., 2021; Hansen et al., 2021; Harvey et al., 2021), however, based on short periods of surveillance and lacking confirmation of reinfection by sequencing approaches. After 20 months of follow-up (during the pre-Omicron period), our study confirms the low rate of

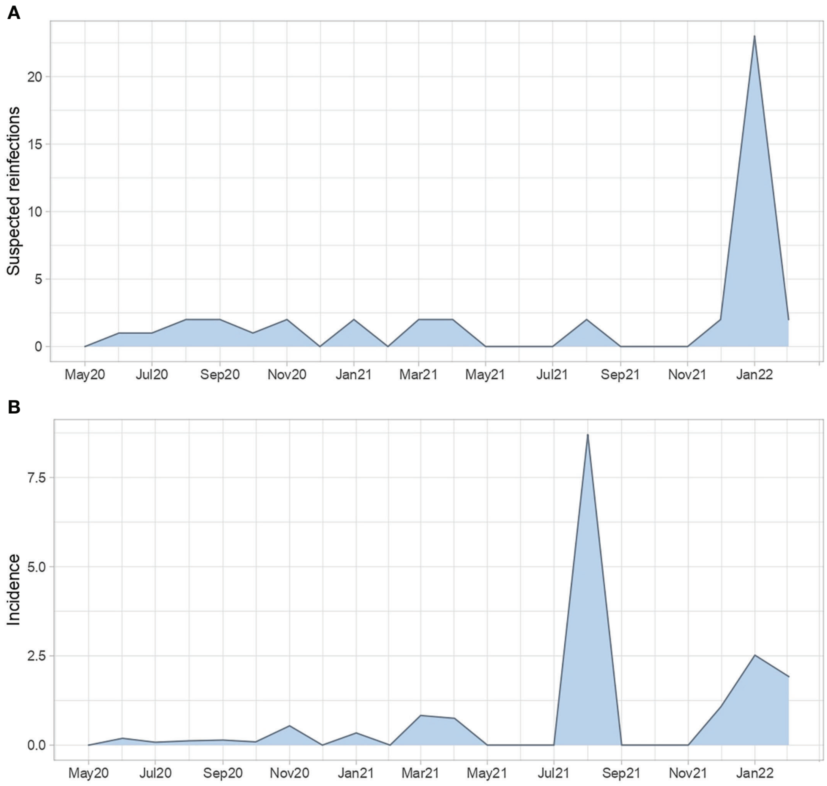

FIGURE 2
Monthly surveillance of reinfections. Suspected cases identified each month within the 22 months period **(A)** and the corresponding incidence regarding the total SARS-CoV-2 positive tests **(B)**.

reinfections, with an incidence of 0.21% of suspected cases and only four events confirmed by sequencing, were any reinfecting variant shared an immediate ancestor with the prior infecting variant (Figure 4). Nevertheless, the arrival of the Omicron variant marked a turning point regarding the frequency of reinfections detected, not seen before for other VOCs, with a 10-fold increase in the proportion of cases (Bastard et al., 2022; Nunes et al., 2022; Pulliam et al., 2022). This characteristic of Omicron is attributed to the more than 30 mutations identified in this variant, mainly in the RBD of the Spike protein and together with insertions and deletions (Akkız, 2022), that confer an increased ability to evade immune protection, including that acquired by vaccination (Bazargan et al., 2022). As expected, the incidence of suspected reinfections detected in Ecuador in this study increased to 2.45% during the Omicron period, and sequencing confirmed that the reinfecting variants were from this clade (Figure 3). Although not all samples could be sequenced, it is expected that they were also Omicron, considering that by early January 2022 this was the dominant variant in Ecuador (covariants.org/per-country). Despite we were able to only confirm 11 reinfections out of 44 suspected cases other events could be misdiagnosed, because is estimated that half of COVID-19 infections remains asymptomatic (Cohen et al., 2022).

The COVID-19 pandemic has been evolving dynamically due to the surge of multiple waves of infections related to the emergence of more virulent variants of SARS-CoV-2. South America has been one of the most affected regions in the world, driven by a precarious healthcare system and aggravated by the late arrival of vaccines. The first case in Ecuador was reported in February 2020, followed by the surge of the first wave of infections in April 2020, with the city of Guayaquil, the country's main port, as the first epicenter of the pandemic (Gutierrez et al., 2021). Quito, the capital city of Ecuador, overtook Guayaquil as the epicenter of cases between June and July 2020, and precisely at that time the IM-USFQ detected the first suspected case of SARS-CoV-2 reinfection (Figure 2). Since then, we observed an increase in the rate of cases in November 2020 (0.54%), April 2021 (0.75%), August 2021 (8.70%), and January 2022 (2.52%) (Figure 2). All of these months were identified as periods of ongoing waves of infections in the country, possibly driven by the relaxation of biosafety measures during holidays such as the Day of the Dead and the Holy Week celebrated in November and April, respectively, or by the surge of fitter variants such as Delta and Omicron during August 2021 and January 2022, respectively (MSP, 2022; MSP,

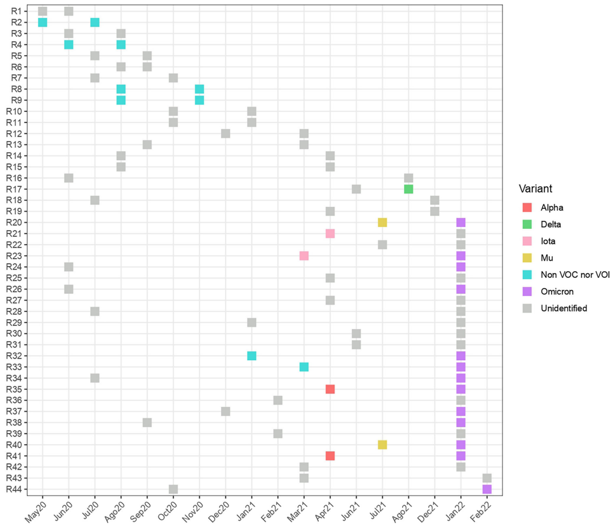

FIGURE 3
Timing of reinfections and variants identified. Plot of the first and second infection detected for each patient (y-axis) over the 22-month surveillance period (x-axis). Each identified variant is represented in different colors.

2021). This evidence suggests that the increase in the rate of suspected reinfections may be driven by waves of infections, where augmented exposure to SARS-CoV-2 could increase the risk of becoming reinfected. Our results further show the occurrence of the highest frequencies of suspected reinfections at regular intervals of four to five months (Figure 2), in agreement with the dynamics observed for the emergence of waves of infections in different countries during the COVID-19 pandemic (Callaway, 2022). This predictable behavior may be useful to prevent future surges of infections considering that at least half of the world's population has already been infected by SARS-CoV-2 (Barber et al., 2022) but remains susceptible to reinfections.

A waning immunity, either naturally induced or vaccine-induced, could also explain the occurrence of higher reinfection rates on a regular basis. Early reports suggested that the duration of protection from naturally induced immunity could be at least six months (Biobank UK, 2021; Lumley et al., 2021), close to the 5-month interval observed in this study between the highest rates of suspected reinfections in unvaccinated population (before May 2021) (Figure 2). On the other hand, the application of vaccines strengthened the immune response in

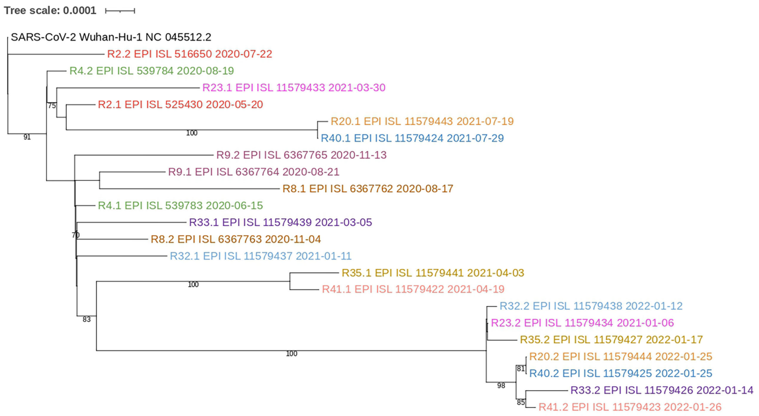

FIGURE 4
Phylogram of paired sequences. Only paired consensus sequences were used and rooted to the Wuhan-Hu's SARS-CoV-2 reference genome. Each pair is represented in different colors. Bootstraps equal to or above 70 are shown.

both naïve and convalescent individuals, inducing in the latter the so-called "hybrid immunity" that is expected to last longer (Pilz et al., 2022). In Ecuador, the vaccination program started late, immunizing most of the population since May 2021. This study identified suspected reinfections in vaccinated individuals since August 2021 (Table S1), but in persons with half-basic vaccination schemes, and subsequently most cases were in persons with basic schemes completed four months prior to reinfection. This evidence confirms the vulnerability of individuals without completed vaccination schemes and boosters, and suggests a shorter duration of the hybrid immunity, however, as we did not measure the seropositivity of reinfected patients, more evidence is needed.

As SARS-CoV-2 reinfections continue to occur, questions arise about the consequences of this event. Recent evidence suggests that reinfections increase the risk of death, hospitalization, and negative effects in the pulmonary and extrapulmonary systems, proportionally depending on the number of reinfections in the patient (Al-Aly et al., 2022). This reinforces the need of reinfections monitoring, which has been done according to different guidelines proposed by the PAHO, the Center for Disease Control and Prevention (CDC, 2020), and the European CDC (ECDC, 2021), all of them agreeing that most reinfections occur after 60 days since the prior infection (CDC, 2020; PAHO, 2020; ECDC, 2021). Nevertheless, there are reports of sequence-confirmed reinfections by common variants occurring in less than 45 days (Lee et al., 2020; Rani et al., 2021; Tillett et al., 2021) and in less than 60 days by the Omicron variant, mainly in young and unvaccinated individuals (Nevejan et al., 2022). Our inclusion criteria included cases with intervals of 45 days or less if there was evidence of increased viral load (lower Ct-value), however, only one case was identified with an interval of 34 days that could not be confirmed by sequencing (Table S1). In fact, most of the suspected cases occurred after a 90-days interval, in agreement with the guidelines mentioned before. Other parameters could be useful for the identification reinfections, such as variation in symptoms and Ct-values between first and second infections. The latter was proposed by other studies showing a significant difference in Ct-values between paired samples (Ringlander et al., 2021) and supporting its use as marker to differentiate reinfections from persistence (Julian et al., 2021). Nevertheless, our results show no significant variation in either symptoms or Ct-values and cannot support their use as markers of reinfections, even because Ct-values depends on external factors such as the time elapsed since the onset of symptoms. Despite the lack in the clinical records of all patients, none reported severe symptomology during reinfection, including those sequence-confirmed cases, which was expected due to the immunity protection acquired after the prior infection and reinforced by vaccination. However, more evidence is needed to confirm these outcomes in other age groups more susceptible to severe illness and sequelae.

This study has some limitations. Since the IM-USFQ mainly received samples from Quito, with less representation of other cities in Ecuador, results cannot be extrapolated to the whole country. Also, results did not reflect the situation of the whole population because our database was mainly composed of immunocompetent adults and working individuals. We lack the complete clinical records of surveilled patients, as this information was collected by other institutions. Additionally, we did not confirm all reinfections by sequencing because we cannot reach some patients or we did not recover enough RNA in their samples, possibly due to low viral titers. Finally, we were not able to characterize the neutralizing antibodies in patients, which could have been useful to explain reinfections.

Conclusion

This study reports an increased frequency of reinfections in Ecuador after the introduction of the Omicron variant and within 22 months of surveillance. The highest incidence of suspected cases was reached at regular intervals of four to five months and during ongoing outbreaks. Most cases occurred in male adults without a booster dose of the vaccine and after 90 days since the prior infection. These results show a regular dynamic in the occurrence of reinfections that could be useful in preventing future reinfections by emerging variants.

Data availability statement

The data presented in this study are deposited in the GISAID repository, and the accession numbers are found in Table S2 of Supplementary material.

Ethics statement

This study is part of a country-wide project that aims to monitor the SARS-CoV-2 variants in Ecuador which were approved by the Bioethics Committee of Universidad San Francisco de Quito (CEISH No. P2020-022IN) and by the Ministerio de Salud del Ecuador (MSP-CGDES-2020-0121-O). The patients/participants provided their written informed consent to participate in this study.

Author contributions

Conceptualization: VB and PC; methodology: RG, VB, and PC; laboratory work: RG, BP-V, SM, JG, EM, MC, MB, SP, and RB-R; software: RG, EM, MC, BP-V, and PC; analysis: RG, VB, PC, GT, and PR-S; writing – original draft: RG; writing – review and editing: VB, PC, GT, PR-S, EM, MC, and MJC; funding acquisition: PC, MG, and MJC. All authors contributed to the article and approved the submitted version.

Funding

This study was funded by the NIH supplement grant U01AI151788 through A2CARES-CREID. "RED PARA ELDESARROLLO DE INSTRUMENTOS INNOVADORES APLICADOS A LA INVESTIGACIÓN EPIDEMIOLÓ GICAEN AMÉRICA DEL SUR" through the Government of France and Instituto Pasteur Montevideo. RISE-USAID Project Ecuador.

Acknowledgments

We would like to thank the SIME hospital at USFQ and the other healthcare centers that collected samples and provided patients' data. We are thankful for the support of the SARS-CoV-2 diagnostic team at IM-USFQ. We are also grateful to the developers and contributors of open-access databases and free online bioinformatic tools.

Conflict of interest

The authors declare that the research was conducted in the absence of any commercial or financial relationships that could be construed as a potential conflict of interest.

Publisher's note

Supplementary material

The Supplementary Material for this article can be found online at: https://www.frontiersin.org/articles/10.3389/fcimb.2022.951383/full#supplementary-material

References

Abu-Raddad, L. J., Chemaitelly, H., Coyle, P., Malek, J. A., Ahmed, A. A., Mohamoud, Y. A., et al. (2021). SARS-CoV-2 SARS-CoV-2 antibody-positivity protects against reinfection for at least seven months with 95% efficacy. *EClinicalMedicine* 35:100861. doi: 10.1016/j.eclinm.2021.100861

Akkız, H. (2022). The biological functions and clinical significance of SARS-CoV-2 variants of corcern. *Front. Med.* 9. doi: 10.3389/fmed.2022.849217

Al-Aly, Z., Bowe, B., and Xie, Y. (2022). Outcomes of SARS-CoV-2 Reinfection. *Research Square*. doi: 10.21203/rs.3.rs-1749502/v1

Bakker, B. (2021) *COVID-19 in Latin America a high toll on lives and livelihoods*. Available at: http://elibrary.imf.org/view/journals/001/2021/168/001.2021.issue-168-en.xml (Accessed June 22, 2022).

Barber, R. M., Sorensen, R. J. D., Pigott, D. M., Bisignano, C., Carter, A., Amlag, J. O., et al. (2022). Estimating global, regional, and national daily and cumulative infections with SARS-CoV-2 through Nov 14, 2021: a statistical analysis. *Lancet* 399, 2351–2380. doi: 10.1016/S0140-6736(22)00484-6

Bastard, J., Taisne, B., Figoni, J., Mailles, A., Durand, J., Fayad, M., et al. (2022). Impact of the omicron variant on SARS-CoV-2 reinfections in France, march 2021 to February 2022. *Eurosurveillance* 27 (13). doi: 10.2807/1560-7917.ES.2022.27.13.2200247

Bazargan, M., Elahi, R., and Esmaeilzadeh, A. (2022). OMICRON: Virology, immunopathogenesis, and laboratory diagnosis. *J. Gene Med.* 24 (e3356). doi: 10.1002/jgm.3435

Biobank UK (2021) *SARS-CoV-2 serology study*. Available at: https://www.ukbiobank.ac.uk/media/x0nd5sul/ukb_serologystudy_report_revised_6months_jan21.pdf (Accessed August 12, 2021).

Callaway, E. (2022). Are COVID surges becoming more predictable? new omicron variants offer a hint. *Nature* 605, 204–206. doi: 10.1038/d41586-022-01240-x

CDC (2020) *Common investigation protocol for investigating suspected SARS-CoV-2 reinfection. centers for disease control and prevention*. Available at: https://www.cdc.gov/coronavirus/2019-ncov/php/reinfection.html (Accessed July 12, 2021).

Cohen, C., Kleynhans, J., von Gottberg, A., McMorrow, M. L., Wolter, N., Bhiman, J. N., et al. (2022). SARS-CoV-2 incidence, transmission, and reinfection in a rural and an urban setting: results of the PHIRST-c cohort study, south afric–21. *Lancet Infect. Dis* 22, 821–834. doi: 10.1016/S1473-3099(22)00069-X

Díaz, Y., Ortiz, A., Weeden, A., Castillo, D., González, C., Moreno, B., et al. (2021). SARS-CoV-2 reinfection with a virus harboring mutation in the spike and the nucleocapsid proteins in Panama. *Int. J. Infect. Dis.* 108, 588–591. doi: 10.1016/j.ijid.2021.06.004

ECDC (2021) *Reinfection with SARS-CoV-2: implementation of a surveillance case definition within the EU/EEA* (Stockholm: European Centre for Disease Prevention and Control). Available at: https://www.ecdc.europa.eu/sites/default/files/documents/Reinfection-with-SARSCoV2-implementation-of-a-surveillance-case-definition.pdf (Accessed July 13, 2021).

Edridge, A. W. D., Kaczorowska, J., Hoste, A. C. R., Bakker, M., Klein, M., Loens, K., et al. (2020). Seasonal coronavirus protective immunity is short-lasting. *Nat. Med.* 26, 1691–1693. doi: 10.1038/s41591-020-1083-1

Fonseca, V., de Jesus, R., Adelino, T., Reis, A. B., de Souza, B. B., Ribeiro, A. A., et al. (2021). Genomic evidence of SARS-CoV-2 reinfection case with the emerging B.1.2 variant in Brazil. *J. Infection* 83, 237–279. doi: 10.1016/j.jinf.2021.05.014

Gutierrez, B., Márquez, S., Prado-Vivar, B., Becerra-Wong, M., Guadalupe, J. J., da Silva Candido, D., et al. (2021). Genomic epidemiology of SARS-CoV-2 transmission lineages in Ecuador. *Infect. Dis. (except HIV/AIDS)*. doi: 10.1101/2021.03.31.21254685

Hall, V. J., Foulkes, S., Charlett, A., Atti, A., Monk, E. J. M., Simmons, R., et al. (2021). SARS-CoV-2 infection rates of antibody-positive compared with antibody-negative health-care workers in England: a large, multicentre, prospective cohort study (SIREN). *Lancet* 397, 1459–1469. doi: 10.1016/S0140-6736(21)00675-9

Hansen, C. H., Michlmayr, D., Gubbels, S. M., Mølbak, K., and Ethelberg, S. (2021). Assessment of protection against reinfection with SARS-CoV-2 among 4 million PCR-tested individuals in Denmark in 2020: a population-level observational study. *Lancet* 397, 1204–1212. doi: 10.1016/S0140-6736(21)00575-4

Harvey, R. A., Rassen, J. A., Kabelac, C. A., Turenne, W., Leonard, S., Klesh, R., et al. (2021). Association of SARS-CoV-2 seropositive antibody test with risk of future infection. *JAMA Intern. Med.* 181, 672. doi: 10.1001/jamainternmed.2021.0366

Hebbali, A. (2020) *Descriptr*. Available at: https://github.com/rsquaredacademy/descriptr (Accessed May 10, 2022).

Hu, J., Peng, P., Cao, X., Wu, K., Chen, J., Wang, K., et al. (2022). Increased immune escape of the new SARS-CoV-2 variant of concern omicron. *Cell Mol. Immunol.* 19, 293–295. doi: 10.1038/s41423-021-00836-z

Julian, K., Shah, N., Banjade, R., and Bhatt, D. (2021). Utility of ct values in differentiating COVID-19 reinfection versus prolonged viral shedding in an immunocompromised patient. *BMJ Case Rep.* 14, e243692. doi: 10.1136/bcr-2021-243692

Katoh, K., Rozewicki, J., and Yamada, K. D. (2019). MAFFT online service: multiple sequence alignment, interactive sequence choice and visualization. *Brief Bioinform.* 20, 1160–1166. doi: 10.1093/bib/bbx108

Lee, J.-S., Kim, S. Y., Kim, T. S., Hong, K. H., Ryoo, N.-H., Lee, J., et al. (2020). Evidence of severe acute respiratory syndrome coronavirus 2 reinfection after recovery from mild coronavirus disease 2019. *Clin. Infect. Dis* 73, e3002–e3008. doi: 10.1093/cid/ciaa1421

Letunic, I., and Bork, P. (2021). Interactive tree of life (iTOL) v5: an online tool for phylogenetic tree display and annotation. *Nucleic Acids Res.* 49, W293–W296. doi: 10.1093/nar/gkab301

Lumley, S. F., O'Donnell, D., Stoesser, N. E., Matthews, P. C., Howarth, A., Hatch, S. B., et al. (2021). Antibody status and incidence of SARS-CoV-2 infection in health care workers. *N Engl. J. Med.* 384, 533–540. doi: 10.1056/NEJMoa2034545

MSP (2021) *El Ministerio de salud pública detecta y aísla 3 nuevos casos de variante delta en pichincha. ministerio de salud pública*. Available at: https://www.salud.gob.ec/el-ministerio-de-salud-publica-detecta-y-aisla-3-nuevos-casos-de-variante-delta-en-pichincha/ (Accessed July 24, 2022).

MSP (2022) *Ecuador Registra 68 casos de Ómicron. ministerio de salud pública*. Available at: https://www.salud.gob.ec/ecuador-registra-68-casos-omicron/ (Accessed July 24, 2022).

Nevejan, L., Cuypers, L., Laenen, L., Van Loo, L., Vermeulen, F., Wollants, E., et al. (2022). Early SARS-CoV-2 reinfections within 60 days and implications for retesting policies. *Emerg. Infect. Dis.* 28, 1729–1731. doi: 10.3201/eid2808.220617

Nunes, M. C., Mbotwe-Sibanda, S., Baillie, V. L., Kwatra, G., Aguas, R., Madhi, S. A., et al. (2022). SARS-CoV-2 omicron symptomatic infections in previously infected or vaccinated south African healthcare workers. *Vaccines* 10, 459. doi: 10.3390/vaccines10030459

PAHO (2020) *Interim guidelines for detecting cases of reinfection by SARS-CoV-2*. Available at: https://www.paho.org/en/documents/interim-guidelines-detecting-cases-reinfection-sars-cov-2 (Accessed August 3, 2021).

Pilz, S., Theiler-Schwetz, V., Trummer, C., Krause, R., and Ioannidis, J. P. A. (2022). SARS-CoV-2 reinfections: Overview of efficacy and duration of natural and hybrid immunity. *Environ. Res.* 209, 112911. doi: 10.1016/j.envres.2022.112911

Prado-Vivar, B., Becerra-Wong, M., Guadalupe, J. J., Márquez, S., Gutierrez, B., Rojas-Silva, P., et al. (2021). A case of SARS-CoV-2 reinfection in Ecuador. *Lancet Infect. Dis.* 21, e142. doi: 10.1016/S1473-3099(20)30910-5

Pulliam, J. R. C., van Schalkwyk, C., Govender, N., von Gottberg, A., Cohen, C., Groome, M. J., et al. (2022). Increased risk of SARS-CoV-2 reinfection associated with emergence of omicron in south Africa. *Science* 376 (6593). doi: 10.1126/science.abn4947

Quick, J. (2020) *nCoV-2019 sequencing protocol v3 (LoCost). protocols.io*. Available at: https://www.protocols.io/view/ncov-2019-sequencing-protocol-v3-locost-bh42j8ye (Accessed June 25, 2021).

Rambaut, A. (2020) *nCoV-2019 novel coronavirus RAMPART runtime instructions. ARTIC network*. Available at: https://artic.network/ncov-2019/ncov2019-using-rampart.html (Accessed June 26, 2021).

Ramírez, J. D., Muñoz, M., Ballesteros, N., Patiño, L. H., Castañeda, S., Rincón, C. A., et al. (2021). Phylogenomic evidence of reinfection and persistence of SARS-CoV-2: First report from Colombia. *Vaccines* 9, 282. doi: 10.3390/vaccines9030282

Rani, P. R., Imran, M., Lakshmi, J. V., Jolly, B., Jain, A., Surekha, A., et al. (2021). Symptomatic reinfection of SARS-CoV-2 with spike protein variant N440K associated with immune escape. *J. Med. Virol.* 93, 4163–4165. doi: 10.1002/jmv.26997

Ringlander, J., Olausson, J., Nyström, K., Härnqvist, T., Jakobsson, H. E., and Lindh, M. (2021). Recurrent and persistent infection with SARS-CoV-2 – epidemiological data and case reports from Western swede. *Infect. Dis.* 1–8 900–907. doi: 10.1080/23744235.2021.1957143

Tay, J. H., Porter, A. F., Wirth, W., and Duchene, S. (2022). The emergence of SARS-CoV-2 variants of concern is driven by acceleration of the substitution rate. *Mol. Biol. Evol.* 39, msac013. doi: 10.1093/molbev/msac013

Tillett, R. L., Sevinsky, J. R., Hartley, P. D., Kerwin, H., Crawford, N., Gorzalski, A., et al. (2021). Genomic evidence for reinfection with SARS-CoV-2: A case study. *Lancet Infect. Dis.* 21, 52–58 73:e2946–e2951. doi: 10.1016/S1473-3099(20)30764-7

To, K. K.-W., Hung, I. F.-N., Ip, J. D., Chu, A. W.-H., Chan, W.-M., Tam, A. R., et al. (2020). Coronavirus disease 2019 (COVID-19) re-infection by a phylogenetically distinct severe acute respiratory syndrome coronavirus 2 strain confirmed by whole genome sequencing. *Clin. Infect. Dis.* 73, e2946–e2951.doi: 10.1093/cid/ciaa1275

Tyson, J., James, P., Stoddart, D., Sparks, N., Wickenhagen, A., Hall, G., et al. (2020). Improvements to the ARTIC multiplex PCR method for SARS-CoV-2 genome sequencing using nanopore. *bioRxiv [Preprint]*. doi: 10.1101/2020.09.04.283077

WHO (2020) *Clinical management of COVID-19: Interim guidance*. Available at: https://apps.who.int/iris/bitstream/handle/10665/332196/WHO-2019-nCoV-clinical-2020.5-eng.pdf (Accessed July 28, 2021).

Wise, J. (2022). Covid-19: Omicron sub variants driving new wave of infections in UK. *BMJ* 377 (1506). doi: 10.1136/bmj.o1506

Yahav, D., Yelin, D., Eckerle, I., Eberhardt, C. S., Wang, J., Cao, B., et al. (2021). Definitions for coronavirus disease 2019 reinfection, relapse and PCR re-positivity. *Clin. Microbiol. Infection* 27, 315–318. doi: 10.1016/j.cmi.2020.11.028

frontiers | Frontiers in Cellular and Infection Microbiology

TYPE Review
PUBLISHED 14 September 2022
DOI 10.3389/fcimb.2022.977799

EDITED BY
Rameez Raja,
Cleveland Clinic, United States

REVIEWED BY
Aravinthkumar Jayabalan,
Johns Hopkins University,
United States
Sathya Neelatur Sriramareddy,
Moffitt Cancer Center, United States
Muhammad Bilal Latif,
Emory University, United States

*CORRESPONDENCE
Mamta Chawla-Sarkar
chawlam70@gmail.com;
chawlasarkar.m@icmr.gov.in
Upayan Patra
patra@med.uni-frankfurt.de

†These authors have contributed
equally to this work

SPECIALTY SECTION
This article was submitted to
Virus and Host,
a section of the journal
Frontiers in Cellular and
Infection Microbiology

RECEIVED 24 June 2022
ACCEPTED 18 August 2022
PUBLISHED 14 September 2022

CITATION
Chandra P, Banerjee S, Saha P,
Chawla-Sarkar M and Patra U (2022)
Sneaking Into the Viral Safe-Houses:
Implications of Host Components in
Regulating Integrity and Dynamics of
Rotaviral Replication Factories.
Front. Cell. Infect. Microbiol. 12:977799.
doi: 10.3389/fcimb.2022.977799

Sneaking into the viral safe-houses: Implications of host components in regulating integrity and dynamics of rotaviral replication factories

Pritam Chandra[1†], Shreya Banerjee[1†], Priyanka Saha[1],
Mamta Chawla-Sarkar[1*] and Upayan Patra[2*]

[1]Division of Virology, Indian Council of Medical Research National Institute of Cholera and Enteric Diseases, Kolkata, India, [2]Institute of Biochemistry II, Faculty of Medicine, Goethe University, Frankfurt, Germany

The biology of the viral life cycle essentially includes two structural and functional entities—the viral genome and protein machinery constituting the viral arsenal and an array of host cellular components which the virus closely associates with—to ensure successful perpetuation. The obligatory requirements of the virus to selectively evade specific host cellular factors while exploiting certain others have been immensely important to provide the platform for designing host-directed antiviral therapeutics. Although the spectrum of host-virus interaction is multifaceted, host factors that particularly influence viral replication have immense therapeutic importance. During lytic proliferation, viruses usually form replication factories which are specialized subcellular structures made up of viral proteins and replicating nucleic acids. These viral niches remain distinct from the rest of the cellular milieu, but they effectively allow spatial proximity to selective host determinants. Here, we will focus on the interaction between the replication compartments of a double stranded RNA virus rotavirus (RV) and the host cellular determinants of infection. RV, a diarrheagenic virus infecting young animals and children, forms replication bodies termed viroplasms within the host cell cytoplasm. Importantly, viroplasms also serve as the site for transcription and early morphogenesis of RVs and are very dynamic in nature. Despite advances in the understanding of RV components that constitute the viroplasmic architecture, knowledge of the contribution of host determinants to viroplasm dynamicity has remained limited. Emerging evidence suggests that selective host determinants are sequestered inside or translocated adjacent to the RV viroplasms. Functional implications of such host cellular reprogramming are also ramifying—disarming the antiviral host determinants and usurping the pro-viral components to facilitate specific stages of the viral life cycle. Here, we will provide a critical update on the wide variety of host cellular pathways that have been reported to regulate the spatial and temporal dynamicity of RV viroplasms. We will also discuss the methods used so far to study the host-viroplasm interactions and emphasize on the potential host factors which can be targeted for therapeutic intervention in the future.

KEYWORDS

rotavirus, replication, viroplasms, pro-viral and antiviral host determinants, host-directed antivirals

Introduction

Rotavirus (RV), the leading cause of viral gastroenteritis among infants and children, primarily infects the enterocytes through fecal-oral transmission route. The subsequent destruction of the absorptive enteric cells and stimulation of the enteric nervous system result in clinical manifestations of RV infection in the form of profuse watery diarrhea, nausea, and vomiting (Crawford et al., 2017). A fully infectious RV is a non-enveloped triple-layered particle (TLP) with three concentric protein layers. The innermost layer contains the structural protein VP2 which ensheathes the 11 segments of rotaviral double-stranded RNA (dsRNA) genome and two other structural proteins VP1 and VP3. The middle layer comprising of trimers of VP6 connects the inner capsid with the outermost layer which is a glycoproteinaceous shell of VP7 with VP4 spikes inserted in it. Both VP4 and VP7 are required for the initial tethering and subsequent attachment of the TLPs to the host cell surface receptors (Figure 1) (Silvestri et al., 2004; Lopez and Arias, 2006; Desselberger, 2014). Following attachment, virions are endocytosed, trafficked along the endosomal pathway, and finally released in the host cell cytoplasm as partially unmasked double-layered particles (DLPs) (Figure 1) (Lopez and Arias, 2006; Arias and López, 2021). Transcriptionally potent DLPs further enable transcription with the help of VP1 in assistance with VP2 and VP3 to produce capped, non-polyadenylated, positive-sense, single stranded RNAs [(+)ssRNAs] which are subsequently translated into viral proteins [six structural (VP1-4, VP6, VP7) and six non-structural (NSP1-6)] (Figure 1). Interestingly, the newly translated non-structural proteins NSP2 and NSP5 mutually interact to form the electron-dense cytoplasmic inclusions bodies, called viroplasms (Figure 1). These polyribosome-surrounded viral niches represent the safe house for subsequent viral life cycle events such as viral genome replication, secondary transcription, and early morphogenesis. Although the exact sequence of events is far from clear, VP1 and VP3 along with the transcribed ss(+)RNAs have been shown to form a dynamic association complex where NSP2 joins and acts as an RNA chaperone involved in the pre-genomic RNA assortment. Assembly of decameric VP2 plates around the assorted VP1–VP3–(+)RNA complexes by virtue of VP2's affinity for VP1, VP3, and ssRNAs forms the innermost core shell. Subsequently, VP2-driven polymerase activity of VP1 initiates the biogenesis of (-)strand RNA (Figure 1) (Navarro et al., 2016; Papa et al., 2021). In the early stage, spherical viroplasms have liquid-like properties and are vulnerable to small aliphatic diols which can release nascent transcripts from the condensates (Geiger et al., 2021). The 11 dsRNA genome segments within the replicating progeny cores acquire a peripheral layer of VP6 to form progeny DLPs which can further amplify the replication cycle by producing secondary transcripts or may enter into the morphogenetic assembly pathway (Figure 1) (Navarro et al., 2016). The most important morphogenetic event includes the formation of the outermost shell containing VP4 and VP7 on the immature DLPs residing within viroplasms. This requires a budding step through ER-derived cellular membranes where VP6 on DLPs docks on NSP4 on ER-derived membranes along with co-recruitment of VP4 and VP7 on NSP4 (Figure 1) (Crawford et al., 2012; Trask et al., 2012; Crawford et al., 2019). The mature TLPs exit ER and finally the infected cells either through lytic mechanisms or by non-lytic secretory pathways which bypass the involvement of Golgi apparatus and lysosomes to continue successive infection cycles (Figure 1) (Musalem and Espejo, 1985; Jourdan et al., 1997; Patra et al., 2021).

Core to the fundamental biology of viral life cycle is the obligation to rely on host cellular resources while disarming the host-intrinsic antiviral defense machinery. Not surprisingly, many host components have been reported to be usurped or subverted by RV at different stages of the viral life cycle (Patra et al., 2021). Interestingly, many of such host components are redirected to RV viroplasms and interact with the viroplasmic proteins, raising the notion that RV replication niches not only serve as the safe houses for viral components but also allow selective proximity to certain host factors. Here, we will present a snapshot of various host determinants belonging to the translational and post-translational modification machinery, cytoskeletal elements, lipid droplets, RNA granules, autophagic components, DNA damage, and unfolded protein response which have been observed to associate with viroplasms and regulate their dynamicity at various stages. Interestingly, perturbing many of these host components has been proved to sensitize RV progeny yield, suggesting its important implications in designing host-directed antiviral therapeutics.

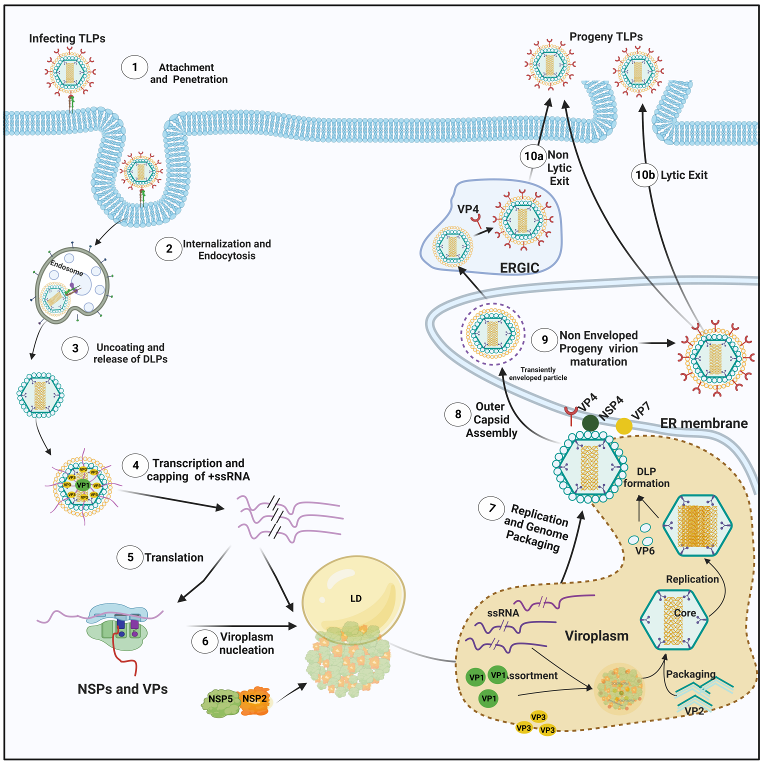

FIGURE 1
The life cycle of RV. (1) The infectious RV TLPs adhere to the specific receptors present in lipid rafts of the host cellular plasma membrane. (2) Following receptor-mediated endocytosis and trafficking along the endosomal pathway, (3) RV TLPs shed their outermost layer and release DLPs into the cytoplasm. (4) Within DLPs, viral RNAs are transcribed with VP1 acting as a polymerase to yield (+)ssRNAs that are eventually capped by another viral protein VP3. (5) Subsequently, structural and nonstructural proteins are synthesized from RV (+)ssRNAs on cellular ribosomes. (6) NSP5 and NSP2 essentially lead to the nucleation of viroplasms on host cellular lipid droplet (LD) scaffold. (7) Inside the maturing viroplasms, accumulating VP1, VP2 and VP3 participate in the viral genome replication. Within the VP2-encaged viral cores, VP2-driven polymerase activity of VP1 initiates the biogenesis of (-)ssRNAs. De novo synthesized cores acquire the VP6 layer to form the progeny DLPs. (8) The DLPs enter into the morphogenetic assembly pathway by acquiring an outer capsid which occurs by a budding step through the ER-derived cellular membrane where VP6 on DLPs docks on NSP4 on ER-derived membrane. Inside the ER, progeny particles acquire a transient envelope. (9) Subsequently, the transient envelope dissipates, NSP4 is stripped off, and the outermost VP7-VP4 layer is assembled. Alternatively, acquisition of VP4 spikes may occur on VP7-surrounded virions within the ER-Golgi intermediate compartment (ERGIC)/plasma membrane lipid raft domains (10a) before non-lytic virion release. (10b) RV progenies may also exit through lytic mechanisms. Of note, the time kinetics of RV life cycle events is dependent on many factors most important of which are the RV strains and the host cell lines used for infection as well as the multiplicity of infection. In general, in the RV permissive cell line MA104 infected with a simian RV strain SA11 at a multiplicity of infection 3, the timeline of infection is as follows: 0-4 hours post infection (hpi) includes the early life cycle events such as the viral adsorption, entry, endosomal trafficking, initiation of transcription and translation and viroplasm nucleation; 4-8 hpi includes viroplasm maturation and concurrent viral replication, secondary transcription, and initiation of the morphogenetic assembly pathway within maturing viroplasms; 8-12 hpi includes the late life cycle events such as the morphogenetic maturation and viral release.

Rotavirus viroplasms and host: An intimate association

RV viroplasms are dynamic structures that form as liquid-like, small, spherical puncta phase-separated within the host cellular cytoplasm. With the progression of infection, these inclusion bodies fuse with each other and grow bigger in size while getting fewer in number and also attain gel-like consistency (Eichwald et al., 2012; Geiger et al., 2021). The essentiality of NSP2 and NSP5 in regulating nucleation of viroplasms has been shown based on two principal lines of arguments - i) co-transfection of NSP5 and NSP2 has resulted in spherical, viroplasm-like structures (VLS) within transfected cells even in the absence other RV proteins (Fabbretti et al., 1999), and ii) loss-of-function of NSP2 and NSP5 severely affects viroplasm formation and viral progeny production (Silvestri et al., 2004; Vascotto et al., 2004; Campagna et al., 2005; Criglar et al., 2018; Papa et al., 2019; Criglar et al., 2020). Notably, apart from NSP2-induced VLS, the formation of VP2-induced VLS has also been reported under the co-transfection scenario of NSP5 with VP2 (Contin et al., 2010).

Importantly, many host cellular components have been reported to associate with RV viroplasms to regulate viroplasm formation and subsequent maturation steps, suggesting the pro-

RV significance of these host components. On the other hand, many antiviral host determinants are also sequestered within or around viroplasms whereby they are prevented from exerting their potential antiviral efficacy. In the following sections, we will describe the methods implemented so far to study host-viroplasm interactions and further elaborate on different modalities of these interaction profiles at different stages of the RV life cycle.

Methods to study host-viroplasm interactions

Staining for the viroplasmic proteins, especially NSP2 and NSP5, with antibodies and subsequent fluorescence imaging under the wide-field or confocal microscope have been the most conventional and go-to-approach for detecting RV viroplasmic puncta. Of interest, based on the affinity for two monoclonal antibodies which are generated against two different conformations of NSP2, two distinct pools of NSP2 were characterized. The dispersed NSP2 (dNSP2) remains evenly distributed in the host cellular cytoplasm whereas the viroplasmic NSP2 (vNSP2) forms distinct puncta and co-localizes with NSP5, corroborating NSP2-NSP5 containing RV inclusion bodies in the host cellular cytosol (Criglar et al., 2014). Not surprisingly, viroplasmic re-localization of many host proteins has been addressed simply by checking the microscopic localization of these proteins with respect to the localization of the viroplasmic RV proteins (Cheung et al., 2010; Zambrano et al., 2011; Criglar et al., 2018; Dhillon and Rao, 2018; Dhillon et al., 2018; Sarkar et al., 2020). Calculating the Pearson correlation coefficient has provided a quantitative assessment of these co-localization events (Dhillon and Rao, 2018; Sarkar et al., 2020). Moreover, the proximity of certain host proteins to viroplasmic proteins has also been assessed by the fluorescence resonance energy transfer (FRET) efficiency (Cheung et al., 2010). Physical interaction between host and RV viroplasmic proteins has been checked by targeted approaches such as doing co-immunoprecipitation (co-IP) coupled to immunoblot studies or through unbiased methods such as affinity-purification coupled to mass spectrometry (AP-MS) (Dhillon and Rao, 2018; Dhillon et al., 2018; Criglar et al., 2020; Sarkar et al., 2020). Sensitivity of the co-IP reactions to RNase A treatment further enabled differentiating the host-viroplasm interactions which are dependent on an intermediate scaffold of RNAs such as the viral RNAs (Dhillon and Rao, 2018; Dhillon et al., 2018). Interestingly, co-localization events observed under a microscope did not always accompany the occurrence of physical interaction identified by AP-MS or co-IP-immunoblot approach, possibly differentiating between proximity-based association and protein-protein interaction (Dhillon and Rao, 2018; Dhillon et al., 2018; Criglar et al., 2020; Sarkar et al., 2020). Indeed, some viral proteins such as NSP2 exist in two different forms. Therefore, assessing the co-localization of host proteins by vNSP2-specific antibody can only confirm the viroplasmic sequestration of host proteins. Moreover, in one particular study, the association between lipid droplets (LDs) and viroplasms has been confirmed by iodixanol density gradient centrifugation where viral dsRNAs and viroplasmic proteins co-sedimented with LD-associated proteins (Gaunt et al., 2013b).

For studying the spatial and temporal dynamicity of viroplasms, viroplasmic proteins were stained and chased over progressive infection time points in infected and fixed cells (Sarkar et al., 2020). Moreover, fusing NSP2 and NSP5 with fluorescent tags such as GFP and mCherry has also been used to study viroplasm dynamics through time-lapse video microscopy. Making stable cell lines for these wild type and different mutant reporter constructs in a trans-complementing setting where the infection is established by recombinant RV (rRV) deficient in the corresponding gene(s) has provided an ideal way to address the functionality of these viral proteins (Eichwald et al., 2012; Papa et al., 2019; Jing et al., 2021).

Host cellular contribution in the early stages of viroplasm formation

The formation of viroplasms requires not only the viroplasmic proteins NSP2 and NSP5 but also their phosphorylated forms which are primarily generated by the cellular kinases casein kinase 1α (CK1α) and casein kinase II (CKII) (Eichwald et al., 2004; Campagna et al., 2007; Criglar et al., 2018; Papa et al., 2019). Viroplasm nucleation starts with the dNSP2 which gets autophosphorylated by its intrinsic NTPase and autokinase activity and further associates with the hypophosphorylated NSP5 (26 kDa) (Figure 2). Further, CK1α co-localizes with the dNSP2-NSP5 complex and phosphorylates dNSP2 at Serine 313 (S313) residue (Figure 2). NSP5 gradually attains its hyperphosphorylated state including a priming phosphorylation at Serine 67 (S67) residue by the continued kinase activity of CK1α and/or NSP2 (Figure 2). Concurrently, the dNSP2–NSP5 complex traffics to the putative viroplasm nucleation sites, associates with LDs, and forms the vNSP2/hyperphosphorylated NSP5 complex within maturing viroplasms (Criglar et al., 2018; Papa et al., 2019). Interestingly, silencing the expression of CK1α drastically affected dNSP2-to-vNSP2 conversion and NSP5 hyperphosphorylation, leading to compromised viroplasm formation and RV progeny production (Criglar et al., 2018). Moreover, a rRV with S67A NSP5 mutation also fails to trigger NSP5 hyperphosphorylation, and proves to be defective in viroplasm assembly and infectious progeny yield (Papa et al., 2019). On a consistent note, a phosphomimetic NSP2 mutant

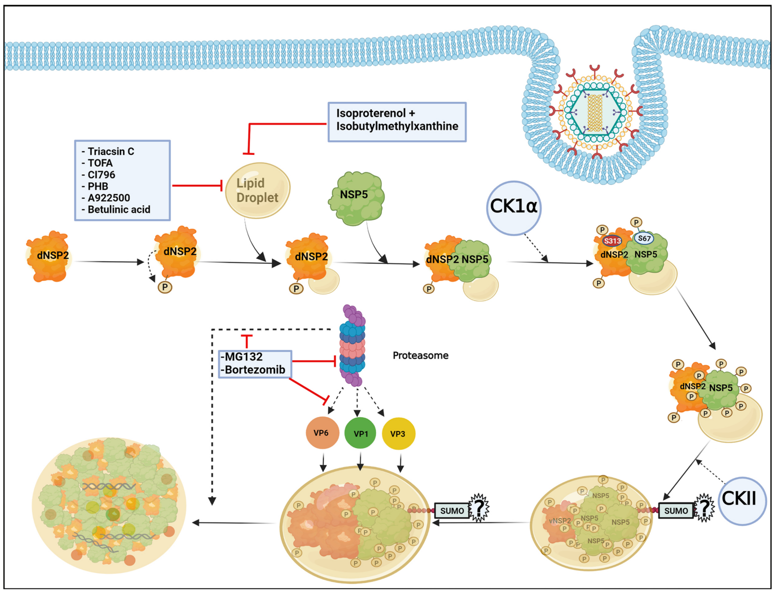

FIGURE 2
Host cellular contribution in regulating early viroplasm dynamics. Following entry to the host cell, RV NSP2, and NSP5 initiate viroplasm biogenesis. Nucleation of the viroplasm starts with the cytoplasmic, dispersed NSP2 (dNSP2) which phosphorylates itself by the intrinsic NTPase and autokinase activity. NSP2 further interacts with Lipid droplets (LDs) and hypophosphorylated NSP5. Host cellular protein CK1α localizes to viroplasms and phosphorylates NSP2 (at serine 313) and NSP5 (at serine 67). NSP5 is also phosphorylated by another host cellular kinase CKII and by the kinase activity of NSP2. Gradually, NSP5 becomes hyperphosphorylated and dNSP2 gets converted into viroplasmic NSP2 (vNSP2) through conformational changes. The size of the viroplasms and LDs continues to increase over time and the maturing viroplasms accumulate other viral proteins such as VP1, VP2, and VP6. An active ubiquitin proteasome system (UPS) is required for the early dynamics of viroplasms. Proteasome inhibition by small molecules (by MG132 and Bortezomib) leads to smaller viroplasmic size and abrogated translocation of VP1, VP2, and VP6 into the viroplasms. Inhibiting LD biogenesis by targeting the enzymes of the LD synthesis pathway or promoting LD fragmentation compromises early viroplasm dynamics. Notably, SUMOylation of NSP5 at multiple lysine residues has been shown to be important for NSP5-VP2 induced viroplasm-like structure (VLS) formation. However, the importance of NSP5 SUMOylation in viroplasm formation under natural infection scenarios is questionable.

(S313D) shows delayed kinetics of viroplasm assembly (Criglar et al., 2020), corroborating host directed phosphorylation events on NSP2 and NSP5 to have crucial regulatory roles on RV viroplasm formation. In addition to CK1α, implications of CKII-mediated phosphorylation events have also been suggested for NSP5 to form higher order oligomeric complex that exists in mature viroplasms (Figure 2) (Papa et al., 2019).

In addition to phosphorylation, NSP5 has been reported to get modified by small ubiquitin-like modifier (SUMO) molecules at multiple lysine (K) residues, suggesting that the host cellular SUMO system might potentially influence the architecture and functionality of RV viroplasms (Figure 2) (Campagna et al., 2013). The exact nature of SUMO conjugation on NSP5, especially whether NSP5 undergoes multi-mono SUMOylation (single SUMO moiety attached to multiple K residues) or polySUMOylation (internally linked SUMO chain attached to a single K residue) or both, is not confirmed. A possible correlation between NSP5 phosphorylation and SUMO conjugation has been hypothesized based on the observation that the in vitro translated NSP5 SUMO mutant shows increased phosphorylation. Moreover, the mutant NSP5 fails to form VLS when co-expressed with VP2, suggesting the importance of NSP5 SUMO modification to potentially influence its interaction with VP2. On the contrary, this mutant retains its ability to interact with NSP2 as well as VP1, and forms VLS when co-expressed with NSP2. Ectopic expression of this SUMO mutant is also as potent as the wild type NSP5 in restoring infection in NSP5-depleted infected cells. Moreover, neither overexpression of SUMO isoforms or silencing of Ubc9 (one of the enzymes in the SUMO conjugation pathway) affects NSP5 phosphorylation nor SUMOylation of NSP5 gets perturbed in presence of co-expressing NSP2, VP2, or VP1, arguing against a probable correlation between NSP5 SUMOylation and phosphorylation (Campagna et al., 2013). Therefore, the question remains regarding the significance of host cellular SUMO system and SUMO conjugation in regulating RV viroplasm formation during natural infection scenario when NSP2-NSP5 interaction initiates viroplasm nucleation and SUMO isoforms are not overexpressed. Moreover, the SUMO system is mostly nuclear in localization whereas RV viroplasms are exclusively cytosolic, raising the question of where the intersection occurs in infected cells. Of interest, overexpression of SUMO isoforms and depletion of Ubc9 antagonize RV infection as a whole, indicating potential implications of SUMOylation on other parts of RV life-cycle. Indeed, other viroplasmic components (VP1, VP2, VP6, NSP2) can be covalently SUMO conjugated or can interact with SUMO in a noncovalent manner (VP1, VP2, and NSP2) (Campagna et al., 2013).

LDs are the intracellular lipid storage organelles involved in different cellular phenomena including lipid homeostasis, signal transduction, and membrane trafficking (Ohsaki et al., 2014; Crawford and Desselberger, 2016). Structurally, LDs consist of a core of triacylglycerols (TAG) and sterol which is surrounded by a phospholipid monolayer where LD-associated proteins such as adipose differentiation-related protein (ADRP) and perilipins are inserted (Kimmel et al., 2010). LDs have been shown to be usurped by RV to foster viroplasm formation during the early hours of infection in cell culture and also in the human intestinal organoid model (Cheung et al., 2010; Foulke-Abel et al., 2014; Saxena et al., 2015). Despite mechanistic details of how viroplasms interact with the LDs are lacking, conformational changes in NSP2 or NSP5 during viroplasm nucleation have been postulated to expose lipophilic residues (NSP5 possesses an amphipathic helix) of the proteins which might further be inserted into the LD membranes, thereby assembling an amphipathic complex with LDs (Criglar et al., 2018). Agreeably, stains for viroplasmic proteins merge with different lipophilic stains and co-localize with LD-associated proteins (perilipin A, phospho-perilipin, and ADRP) in infected cells (Cheung et al., 2010; Criglar et al., 2020; Criglar et al., 2022). Moreover, both perilipin1 and phospho-perilipin1 co-immunoprecipitate vNSP2, suggesting a possible interaction between NSP2 and LD proteins (Criglar et al., 2020). Interestingly, LDs were also observed to be associated with VLS formed by NSP2 and NSP5, indicating their involvement in promoting viroplasm assembly irrespective of the RV replication potency (Cheung et al., 2010). In fact, taking advantage of the delayed viroplasm dynamicity in cells infected with the rRV which has the phosphomimetic (S313D) NSP2, LD-NSP2 association was found to precede NSP2-NSP5 interaction (Figure 2) (Criglar et al., 2020). As the infection progresses, the size of both the viroplasms and LDs increase (Eichwald et al., 2012), indicating that viroplasms assemble concomitantly with LD biogenesis (Figure 2). Consequently, when RV-infected cell extracts (detergent-free) were subjected to equilibrium ultracentrifugation through iodixanol gradients, viral dsRNAs were co-sedimented with NSP5, perilipin A, and lipids that reside in LDs in the same low-density fraction, further corroborating a lasting association of LDs with RV viroplasms (Cheung et al., 2010; Gaunt et al., 2013b). In agreement with the pro-rotaviral significance of cellular LDs in regulating viroplasms, interrupting LD homeostasis with small molecules heavily antagonized viroplasm formation and viral progeny production. Several enzymes belonging to the neutral lipid biosynthetic pathway [such as long-chain acyl-CoA synthetase (ACSL), acetyl-CoA carboxylase 1 (ACC-1), fatty acid synthase (FASN) complex, diacylglycerol acyltransferases (DGAT1, DGAT2), acyl-coenzyme A (CoA):cholesterol acyltransferases (ACAT1 and ACAT2)] have been proved to be anti-RV targets for intervention by small molecules [ACSL by triacsin C, ACC-1 by 5-(tetradecyloxy)-2-furoic acid (TOFA), FASN by C75, DGAT by A922500 or betulinic acid, and ACAT by CI-976 or PHB] (Figure 2). Notably, TOFA also interfered with the assembly step of RV outer capsid, showing drug synergism with C75 (Cheung et al., 2010; Kim et al., 2012; Gaunt et al., 2013a; Crawford and Desselberger, 2016). Moreover, LD fragmentation (by a combination of isoproterenol + isobutylmethylxanthine) antagonized RV replication and RV-induced cytopathy (Figure 2) (Cheung et al., 2010).

Among the other host determinants which contribute to the early viroplasm dynamics, implications of ubiquitin proteasome system (UPS) have been cited (Figure 2). UPS enables the turnover of proteins via proteolytic ubiquitylation coupled to proteasomal degradation and therefore is an important component of cellular proteostasis. A functional UPS is required for effective RV replication as proteasome inhibition significantly reduced viral protein and RNA levels as well as viral progeny yield (Contin et al., 2011; López et al., 2011). Mechanistically, proteasome inhibition by small molecules (such as MG132 and Bortezomib) and RNA interference (RNAi) (targeting components of the UPS) heavily sensitized the formation of viroplasms (Figure 2). A time-of-addition study showed that treatment with proteasome inhibitors resulted in stunted viroplasm assembly in the form of smaller viroplasms, suggesting the importance of functional proteasome in regulating early viroplasm dynamics (Contin et al., 2011). Moreover, proteasome inhibition also led to the failure of VP1, VP2, and VP6 to be effectively incorporated into the poorly formed viroplasmic puncta (Figure 2), justifying compromised genome replication and progeny yield of RV (López et al., 2011). Of interest, sensitivity to UPS inhibition was only evident for viroplasms formed during natural infection, but not for VLS which are formed upon co-expression of NSP5 with NSP2 or VP2. Similarly, overexpressed VP1 and VP6 did not fail to co-localize with VLS in presence of proteasome inhibitors, suggesting the relevance of UPS for actively replicating RV with dynamic viroplasmic architecture (Contin et al., 2011).

Host cellular contribution in viroplasm maturation and dynamicity

In addition to viroplasm nucleation, growth and maturation of these viral structures also require host cellular assistance. Confocal microscopy showed that viroplasms are dynamic structures where small nucleating puncta fuse with each other to form smaller number of bigger aggregates which subsequently gather in the perinuclear space during the course of infection (Figure 3) (Eichwald et al., 2012). Importantly, to achieve such dynamicity, RV usurps the host microtubular network which consists of heterodimers of α- and β-tubulin, and regulates the intracellular transport of organelles and macromolecules. Two types of molecular motors, dyneins, and kinesins are the chief mediators of this microtubule-mediated intracellular transport. RV NSP2, but not NSP5, interacts with tubulin dimers via its positively charged grooves to sequester tubulins inside viroplasms, resulting in a sharp decrease in cytoplasmic tubulin concentration and co-localization of viroplasms with microtubule granules (Martin et al., 2010). As a result, microtubule depolymerization takes place, possibly disrupting the host cellular trafficking processes. Counterintuitively, actively replicating RV has been shown to trigger prolonged intra-S phase retention of the host cells (Glück et al., 2017) and utilizes the stabilized microtubular structures for maintenance and maturation of the viroplasms (Figure 3). Stabilization of microtubules was enabled by the increased acetylation of tubulin which embeds the viroplasms. Microtubule depolymerizing drug Nocodazole blocks viroplasm growth and peri-nuclear fusion without hampering the nucleation step (Figure 3) (Eichwald et al., 2012). In addition to microtubules, viroplasm maturation and perinuclear re-localization are also governed by kinesin protein of the Eg5 family and are therefore sensitive to an allosteric inhibitor of the Eg5 kinesin, monastrol (Figure 3) (Eichwald et al., 2012). A recent report has also indicated the requirement of a microtubule-associated dynein transport system for rotaviral propagation (Jing et al., 2021). The dynein transport apparatus is associated with viroplasm formation at both early and late stages of RV life cycle. RV viroplasms are found to co-localize with the dynein intermediate chain (DIC) and physical interaction was also evidenced between RV NSP2 and DIC (Figure 3). Viroplasms exploit dynein to avail the retrograde transport to move along the microtubules. This subsequently facilitates the fusion of two small viroplasms into a bigger one, which further promotes viral progeny replication. DIC inhibition by RNAi and by small molecules such as dynapyrazole-A attenuated both the size and number of viroplasms, leading to curtailed viral progeny synthesis (Figure 3) (Jing et al., 2021).

The dynamicity of RV viroplasms has recently been shown to be influenced by the host cellular DNA damage response (DDR) factors. DDR is primarily a nuclear phenomenon where sensing of damage on the DNA by a group of proteins called sensors is followed by transducing the damage signal via another group of proteins named transducers to the effectors which either repair the damage while arresting the cell cycle or induce cellular demise by apoptosis (Bartek and Lukas, 2001; Luftig, 2014). Actively replicating RV was found to trigger activation of

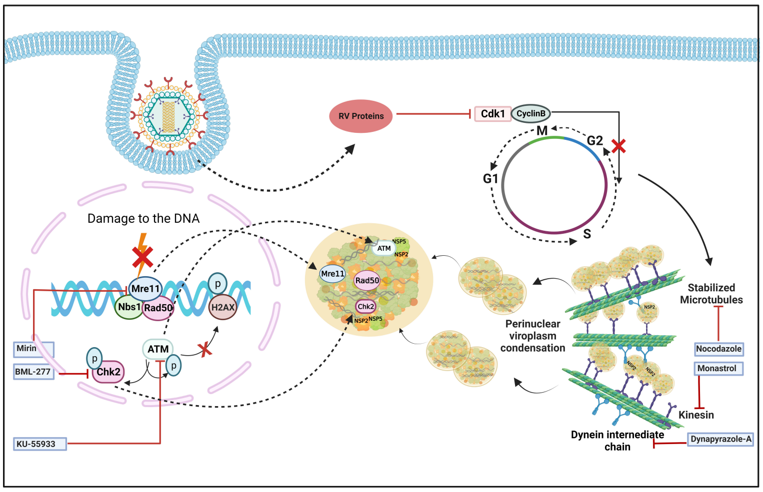

FIGURE 3
Host cellular contribution in regulating viroplasm condensation and maturation. RV blocks mitotic entry of the host cell cycle by prolonging intra S-phase retention. This is enabled by the depletion of cyclin B1 and subsequent inhibition of the Cdk1-cyclin B1 complex by multiple RV proteins. Inhibition of mitotic entry ensures the preservation of hyperacetylated and stabilized microtubular structures which along with the kinesin motor protein Eg5 and dynein facilitate viroplasmic condensation and peri-nuclear relocalization. Targeting microtubule, Eg5 kinesin, and dynein intermediate chain by small molecules nocodazole, monastrol, and dynapyrazole-A respectively, impairs viroplasm dynamics. RV also activates MRN-ATM-Chk2 branch of DDR during infection in absence of nuclear DNA damage and λ-H2AX positive nuclear foci. Moreover, MRN components, ATM and Chk2 relocate to the cytoplasm and co-localize with viroplasms. Targeting Mre11, ATM, and Chk2 by small molecule inhibitors Mirin, KU55933, and BML-277, respectively, antagonize RV replication. KU55933 and BML-277 prevent viroplasm condensation and maturation.

the damage sensor complex Mre11-Rad50-Nbs1 (MRN) followed by stimulation of the transducer kinase ATM and its downstream effector Chk2 (Figure 3) (Sarkar et al., 2020). Interestingly, induction of the MRN-ATM-Chk2 pathway during RV infection neither depends on the occurrence of nuclear DNA damage nor leads to the formation of damage-induced canonical nuclear foci (Figure 3), indicating a non-canonical response in the infected cells. Moreover, components of the MRN complex as well as ATM and Chk2 were reported to get relocated from nucleus to cytoplasm and to co-localize with RV viroplasms (Figure 3). ATM and Chk2 were also found to interact with the viroplasmic RV proteins NSP2 and NSP5 under infection scenario. Inhibiting Mre11, ATM, and Chk2 by small molecules Mirin, KU55933, and BML-277, respectively, antagonized RV progeny yield. Chasing viroplasms with ATM and Chk2 inhibitors in a time-of-addition study revealed that the ATM-Chk2 pathway is important for the fusion and maturation of viroplasms and subsequent viral propagation (Figure 3). Agreeably, nucleation of viroplasmic puncta and disintegration of already formed viroplasms were not sensitized by inhibition of this pathway. Of interest, co-expressing NSP2 and NSP5 could mimic neither the activation of the MRN-ATM-Chk2 pathway nor the cytosolic relocation and viroplasmic sequestration of MRN components, ATM, and Chk2 (Sarkar et al., 2020). The molecular rationale behind usurping a branch of DDR in a skewed, non-canonical way in favour of facilitated viroplasm fusion and productive viral perpetuation is still an open question.

Sequestering host components within viroplasms to prevent their canonical functions

RV viroplasms have recently been shown to form as phase-separated macromolecular condensates within the host cellular cytoplasm (Geiger et al., 2021). Interestingly, eukaryotic cells also possess membrane-less organelles such as processing bodies (P bodies) and stress granules (SGs) which represent phase-separated cytoplasmic condensates. These dynamic mRNA-protein inclusion foci are involved in the cellular RNA surveillance. Partitioning of eukaryotic mRNA between polysomes, SGs, and PBs/GW-bodies has been reported to dictate the fate of mRNA population by governing the rate of mRNA translation and mRNA repression/degradation/decay which further regulate gene expression (Reineke and Lloyd, 2013; Riggs et al., 2020). RV infection triggers host cellular translational arrest which may lead to activated host RNA surveillance that might have potentially deleterious effects on unrestricted translation of viral mRNAs on cellular polysomes. Interestingly, RV has been shown to prevent the formation of canonical P body and SG condensates (Figure 4) (Montero et al., 2008; Bhowmick et al., 2015; Green and Pelkmans, 2016; Dhillon and Rao, 2018; Oceguera et al., 2018). Mechanistically, this is enabled by the degradation of selective PB/SG components and by the re-organization of the granular components to different subcellular locations (Figure 4) (Montero et al., 2008; Bhowmick et al., 2015; Dhillon and Rao, 2018; Oceguera et al., 2018). Many P body (DDX6, Lsm1, Caf1, PARN, XRN1, DCP1a, DCP1b), GW body (AGO2), and SG proteins (ADAR1, CPEB, eIF2α, 4EBP1, PKR, Staufen1) have been shown to get re-located to RV viroplasmic puncta, thereby constituting a "molecular triage" (Figure 4). Moreover, some of these components also interact with the viroplasmic proteins NSP2, NSP5, and VP6 either via an intermediate RNA scaffold or independent of the viral RNAs (Figure 4) (Dhillon and Rao, 2018). The significance of viroplasmic sequestration of each of these individual proteins during RV infection awaits further mechanistic studies. Of importance, some of these relocated proteins such as the decapping complex components DDX6, XRN1, DCP1a, DCP1b showed partial and transient association with viroplasms (Bhowmick et al., 2015; Dhillon and Rao, 2018). The most notable example is AGO2 which undergoes degradation during the early hours of infection but is rescued later on and relocates to the viroplasmic niche (Figure 4) (Dhillon and Rao, 2018; Mukhopadhyay et al., 2019b). It is interesting to mention here that some of the re-located cytosolic mRNA surveillance proteins such as PKR, Staufen1, and ADAR1 have dsRNA binding domains (Saunders and Barber, 2003). ADAR1 has the property of introducing hypermutation within mRNA (RNA editing) and/or suppression of PKR. During RV infection, the presence of dsRNA, possibly of viral origin, has been detected beyond the viroplasmic confinement in the host cellular cytosol (Rojas et al., 2010; Zhu et al., 2017), and dsRNA-dependent PKR activation has been shown to contribute to eukaryotic initiation factor 2α (eIF2α) phosphorylation, leading to host translational repression (Rojas et al., 2010). Therefore, confining ADAR1 near viroplasms might facilitate PKR activation by the cytoplasmic dsRNA pool; however, viroplasmic sequestration of PKR and eIF2α has also been evidenced at late hours of infection (Dhillon and Rao, 2018). More direct involvement of ADAR1 in fostering RV replication becomes evident when depleting ADAR1 reduces RV progeny yield and overexpressing ADAR1 elevates RV titre (Dhillon and Rao, 2018). Other cytosolic RNA quality control pathways such as the Staufen mediated mRNA decay (SMD) and non-sense mediated mRNA decay (NMD) are also averted by RV, possibly by disarming Staufen-1 within viroplasmic confinement and degrading UPF1, the chief effector RNA helicase involved in both SMD and NMD, by the viroplasmic protein NSP5 (Dhillon and Rao, 2018; Sarkar et al., 2022). Unlike ADAR1, RNAi-mediated silencing of many SG/P body proteins resulted in increased viroplasmic protein (NSP2, NSP5, VP6) expressions and enhanced infectious progeny yield, indicating the antiviral importance of these host cellular determinants. Consistently, ectopic overexpression of some of these potentially antiviral host

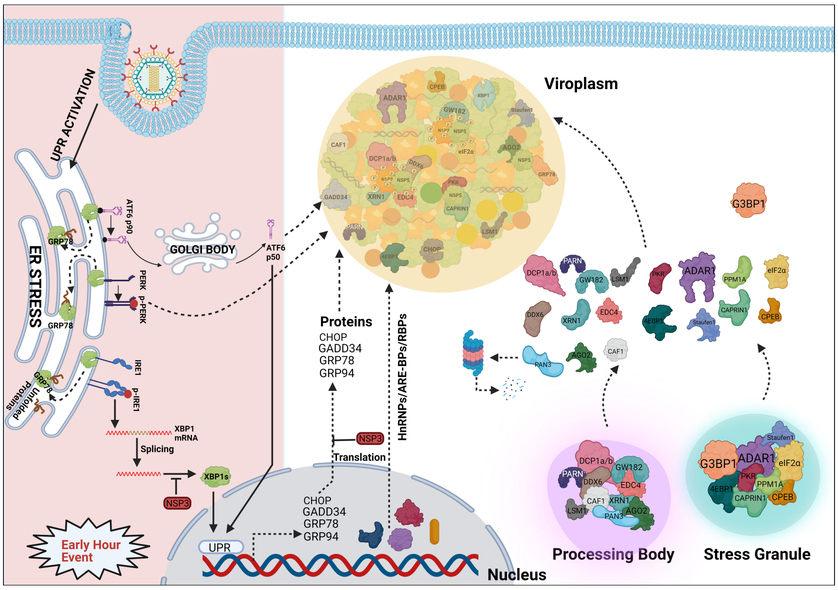

FIGURE 4
Sequestration of different host components into viroplasmic condensates. RV dismantles P bodies and SGs during infection. Many of the SG (ADAR1, eIF2α, Caprin1, PKR, Staufen1, CPEB, 4EBP) and P body (DDX6, Lsm1, Caf1, PARN, XRN1, DCP1a, DCP1b) components relocate to viroplasms at least transiently or partially and interact with viroplasmic proteins. Additionally, many hnRNPs and ARE-BPs are re-located from the nucleus to the cytosol, get sequestered within viroplasms, and interact with NSP2 and NSP5 within RV infected cells. Many relocated RBPs are also absorbed by the viral transcripts. Accumulation of misfolded proteins in the ER leads to uncoupling of GRP78 from UPR sensors, resulting in activation of the three branches of UPR-the ATF6 pathway, the PERK-dependent pathway, and the IRE1-based signalling. During early hours of infection, RV activates the ATF6 and IRE1 branches of the UPR. Following dissociation from GRP78, the transcriptionally inactive fragment of ATF6 (ATF6p90) is translocated to the Golgi apparatus where it is cleaved into the transcriptionally active fragment (ATF6p50) which is further transported to the nucleus to trans-activate UPR elements (CHOP, GADD34, GRP78 and GRP94). Despite initial activation of the ATF6 branch of UPR, RV inhibits transcription of UPR elements by sequestering the ATF6p50 fragment into viroplasms. Moreover, activation of the IRE1 pathway includes dimerized and autophosphorylated IRE1 (p-IRE1) to trigger splicing of xbp1 mRNA (xbp1u) to generate a spliced variant (xbp1s). However, further translation of the xbp1s is prevented as a result of the host translational inhibition mediated by RV-NSP3. Release of PERK from GRP78 leads to homo-dimerization and phosphorylation of PERK; however, RV sequesters p-PERK in the viroplasms inhibiting further activation. Additionally, RV blocks the potential antiviral effects of UPR by inhibiting the translation of ER stress responsive genes and by re-locating many UPR effector proteins (CHOP, GADD34, GRP78, GRP94) near/within viroplasms at the late hours of infection.

proteins (G3BP1, Caprin, Dcp1a, Caf1) resulted in reduced rotaviral titer (Dhillon and Rao, 2018).

Several heterogeneous nuclear ribonucleoproteins (hnRNPs) such as hnRNP C1/C2, D, E, F/H, I, K/J, L, and U have been reported to undergo cytosolic relocalization and viroplasmic sequestration in RV infected cells (Figure 4) (Dhillon et al., 2018). Moreover, these relocated hnRNPs have been found to interact with the viroplasmic RV proteins NSP2 and NSP5 in absence of any intermediate RNA scaffold (Figure 4). Interestingly, similar to the relocated DDR components, these translocation events were not observed in NSP2-NSP5 co-transfected cells, suggesting the involvement of active viral replication and other RV proteins. The significance of such relocation, however, is far from clear (Dhillon et al., 2018). Given that hnRNPs represent a huge family of RNA-binding proteins (RBPs), one hypothesis might be that this relocation and sequestration are stochastic. According to this view, all these RBPs are inherently nucleocytoplasmic shuttling proteins and can be recruited to the RV RNAs because of a general "sponging" effect (Oceguera et al., 2018). Indeed, RV mRNAs present 57 to 68% A + U content with UU, UA, and AU sequences being uniformly distributed along the mRNA length, suggesting the possibility of absorbing re-located AU-rich element binding proteins (ARE-BPs) (Figure 4) (Dhillon et al., 2018). On a consistent note, the nucleus-to-cytosolic shuttling of some RBPs was found to be sensitive to viral RNA depletion (Oceguera et al., 2018). hnRNPs and ARE-BPs are involved in numerous aspects of nucleic acid metabolism including mRNA stabilization, alternative splicing, transportation of mRNAs from the nucleus to the cytoplasm, transcriptional and translational regulation, and maturation of the pre-mRNA (Geuens et al., 2016), making them a target for usurpation or subversion by many viruses (Valente and Goff, 2006; Rozovics et al., 2012; Cathcart et al., 2013; Pingale et al., 2020). However, direct implications of host cellular RBPs in specifically modulating RV genome replication, transcription, and translation are yet to be addressed. Nonetheless, significance from the viral perspective is evident as RNAi-mediated silencing and plasmid-based overexpression of HuR, hnRNP D, hnRNP I, and hnRNP K led to diminished and increased progeny virus production, respectively. Other components (G3BP1, TIA1, and hnRNP C1) showed antiviral potency as their down-regulation facilitated RV infection and ectopic overexpression antagonized progeny virus yield (Dhillon et al., 2018). Moreover, for some of the hnRNPs, overexpression or silencing only sensitized modulation of selective RV viroplasmic protein levels, suggesting the possibility that hnRNPs might be exploited by RV in a highly selective manner such as regulating translation of specific viral mRNAs (Dhillon et al., 2018).

In addition to RBPs and hnRNPs, many effector proteins of the unfolded protein response (UPR) pathway such as PKR-like ER kinase (PERK), C/EBP homologous protein (CHOP), Growth arrest and DNA damage-inducible protein (GADD34), activating transcription factor 4 (ATF4), and ATF6 have been observed to get re-localized to or near viroplasms at late hours of RV infection (Figure 4) (Zambrano et al., 2011). In RV infected cells, host translation is stagnated partially because of PKR-mediated eIF2α phosphorylation and evidence of activated UPR has been found (Figure 4) (Montero et al., 2008; Rojas et al., 2010; Trujillo-Alonso et al., 2011). UPR effectively allows cellular protein homeostasis by preventing the stress-induced accumulation of misfolded proteins within ER. This is enabled by reducing the global translation rate and upregulating the synthesis of selective, stress-responsive transcription factors which further trans-activate UPR-responsive genes such as chaperones or pro-apoptotic factors (Hetz and Papa, 2018). Acutely replicating virus might inadvertently trigger host cellular ER stress leading to activation of the UPR which may heavily antagonize viral replication (Mehrbod et al., 2019). Indeed, the antiviral importance of CHOP as a pro-apoptotic factor has been evidenced (Medigeshi et al., 2007; Kim et al., 2009; Turpin et al., 2021). Moreover, GADD34 has been shown to recruit protein phosphatase 1 (PP1) leading to PP1-mediated dephosphorylation of eIF2α which initiates host cellular translation (Dalet et al., 2017). Therefore, viroplasmic sequestration of these UPR effectors might be an evasive strategy adopted by RV to avoid the potentially deleterious effects of UPR-dependent antiviral host responses. Of note, viroplasmic sequestration of UPR proteins comes as a secondary safeguard against UPR as the primary defense mechanism includes a translational block of these UPR transcripts by the RV non-structural protein NSP3 (Figure 4) (Trujillo-Alonso et al., 2011).

Several reports from independent research groups have now demonstrated that host cellular proteins with canonical nuclear annotations and functionality undergo cytosolic re-localization and sequestration within or around viroplasms, suggesting the likelihood of dysregulated nucleocytoplasmic transport during RV infection (Dhillon and Rao, 2018; Dhillon et al., 2018; Sarkar et al., 2020). This dysregulation is not a stochastic phenomenon as DAPI staining ensured nuclear integrity and the translocation events are found to be specific but not a non-selective exodus. Interestingly, changes in the sub-cellular levels of nucleocytoplasmic transport factors have also been observed in RV-infected cells as infection triggered time point-dependent increase of Exportin1, Importin-β, Ran in cytosolic fractions and reduction of Transportin1 in nuclear fractions. Moreover, all these shuttling factors were shown to co-localize with viroplasms and co-IP studies confirmed interactions between Exportin1 and NSP5 as well as between NSP2 and importin-β, Ran (Dhillon et al., 2018). However, whether these nucleocytoplasmic transport factors are involved in directly regulating sub-cellular partitioning of proteins in RV-infected cells is yet to be addressed.

Host cellular contribution in the late stages of viroplasm dynamics

Similar to RBPs and hnRNPs, many ER chaperones have been reported to be redistributed within or around viroplasmic puncta and interact with specific viroplasmic proteins in RV infected cells (Figure 5) (Maruri-Avidal et al., 2008). RV replicates within the host cellular cytoplasm and neither alters the ER membrane morphology nor harnesses the ER resident molecular chaperones for genome replication, questing the implications of such re-programming (Ravindran et al., 2016). More precisely, glucose regulatory protein 94 (GRP94) and 78 (GRP78) have been observed to co-localize with viroplasms (Figure 4). For GRP94, RV infection was shown to enhance its protein level and an interaction has been revealed with NSP5, NSP4 as well as VP7). However, transient knockdown of GRP94 did not lower virus infection (Xu et al., 1998; Maruri-Avidal et al., 2008), questioning the relevance of GRP94's viroplasmic localization. Interaction of GRP78 was found with VP4, VP7 and depletion of this chaperone compromised the production of infectious viral progeny, suggesting its importance in the assembly of mature RV particles (Maruri-Avidal et al., 2008; Zambrano et al., 2011). Other ER chaperones such as Erp57, Calreticulin, and protein disulfide isomerase (PDI) have also been found to get relocated to the proximity of viroplasms in RV infected cells (Figure 5). Erp57 depletion did not sensitize RV infection. However, for both PDI and Calreticulin, interaction with VP7 and NSP4 (only for PDI) was observed and both of them positively control the formation of disulfide bonds on VP7 residing on TLPs, justifying compromised yield of infectious progeny in absence of them (Maruri-Avidal et al., 2008; Zambrano et al., 2011). Of relevance, caspase8-dependent co-translocation of Erp57 and Calreticulin from ER to plasma membrane leading to immunogenic cell death (ICD) has been reported for several viruses (Panaretakis et al., 2009; Galluzzi et al., 2010). As caspase8 activation occurs in the late hours of

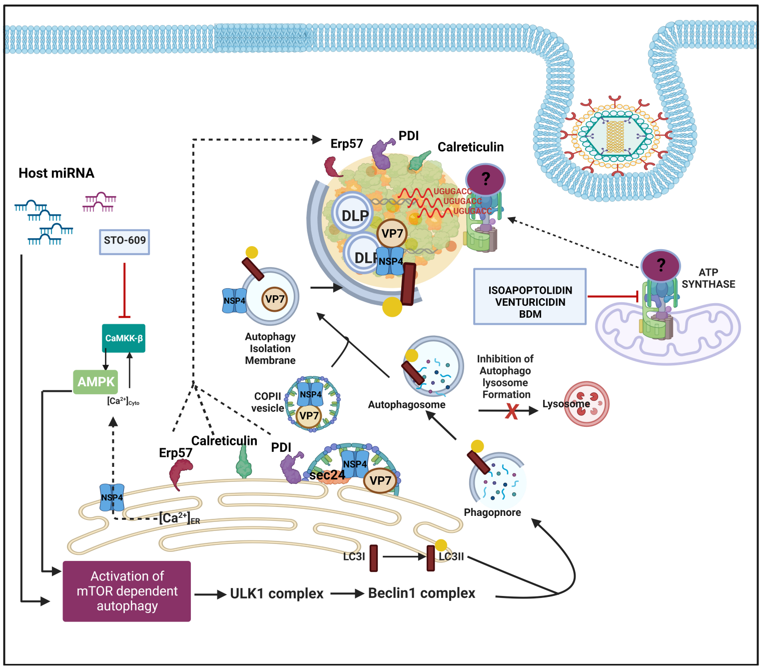

FIGURE 5
Host cellular contribution in the later events of viroplasm dynamics. Many ER chaperone proteins such as Erp57, PDI, and Calreticulin translocate near RV viroplasms. PDI and Calreticulin foster RV morphogenesis. In RV infected cells, mTOR inhibition and the autophagic signalling are induced by host microRNA-dependent mechanism and also via NSP4-Ca2+-Calmodulin-CaMKKβ-AMPK pathway. Overall, mTOR restriction causes de-repression of the ULK1 complex which subsequently forms phagophore through Beclin1 complex activation and LC3 II lipidation. However, autophagosomes are prevented from lysosomal targeting in RV infected cells; instead, they are utilized for carrying the RV proteins NSP4 and VP7 coming out with the ER-derived COP-II vesicles to maturing progeny virions within viroplasms, thereby aiding in outer capsid assembly. Inhibiting CaMKKβ by STO-609 abrogates the presence of NSP4 and VP7 to reside surrounding autophagosome-engulfed viroplasms, leading to curtailed RV progeny yield. Other host contributors which aid in the RV morphogenesis within viroplasms are subunits (ATP5B, ATP5A1, ATP5O) of the mitochondrial ATP synthase holoenzyme that re-locate to viroplasms and interact with the 3′ UTR consensus of RV RNAs (5′-UGUGACC-3′). Potential involvement of an intermediate protein has been speculated to facilitate the ATP synthase-RV RNA 3′ UTR association. Chemical inhibitors targeting ATP synthase such as Isoapoptolidin, Venturicidin, and BDM antagonize RV progeny yield.

RV infected cells (Martin-Latil et al., 2007; Mukhopadhyay et al., 2022), viroplasmic sequestration of these two chaperones might also provide an active strategy adopted by RV to evade ICD.

Another recent study demonstrated a high-affinity interaction between ATP5B, a core subunit of the mitochondrial ATP synthase, and Group A RV 3′ untranslated region (UTR) consensus (5′-UGUGACC-3′) (Ren et al., 2019). Confocal microscopy affirmed co-localization of ATP5B with the RV 3′ UTR probe within viroplasms of RV infected cells (Figure 5). In addition to ATP5B, two other subunits of the ATP synthase complex, ATP5A1, and ATP5O, were also identified as bonafide RV 3′ UTR interactors (Figure 5). The functional significance of such cellular ATPase machinery redistribution from mitochondria to RV viroplasms has remained elusive. ATP5B depletion through RNAi or chemical inhibition (by isoapoptolidin, venturicidin, BDM) heavily restricted RV progeny yield by sensitizing late stage of RV life cycle events such as viral genome assembly (Figure 5). Therefore, ATPase-driven energy might be critical to foster viral genome packaging. However, the failure of ATP5B to shift the mobility of RV 3′ UTR consensus in an electrophoretic mobility shift assay implies a possible indirect interaction through the involvement of intermediate candidates such as VP1 which accumulates during infection and also has a high affinity for the consensus (Ren et al., 2019).

Host cellular autophagic machinery has been proved to be crucial for DLPs within viroplasms to initiate their morphogenesis (Crawford et al., 2012; Crawford et al., 2019). Macroautophagy is a host cellular catabolic process whereby cargos such as damaged organelles, long-lived proteins, and intracellular pathogens are encaged by double-membrane-bound vesicles called autophagosomes and subsequently channeled through an elaborate intracellular membrane trafficking pathway to lysosomes for degradation of the engulfed contents. In RV infected cells, autophagy is induced; however, the autophagic isolation membranes have been reported to be hijacked from being directed to the canonical lysosomal degradation pathway to ultimately facilitate ER-to-viroplasm transportation of viral proteins NSP4 and VP7 for the production of progeny TLPs (Figure 5) (Crawford et al., 2012; Crawford et al., 2019). Agreeably, inhibition of autophagy sensitized RV replication and progeny yield (Crawford et al., 2012; Arnoldi et al., 2014; Mukhopadhyay et al., 2019a). More precisely, the presence of NSP4 and VP7 to reside around autophagosome-engulfed viroplasms was proved to be heavily sensitive to autophagosome inhibition (Crawford et al., 2012). A recent study has revealed the mechanistic detailing of how ER-derived autophagy isolation membranes are redirected in Coat protein complex II (COPII) vesicles from Golgi-apparatus (which are the canonical destination of ER-derived COPII vesicles) to DLPs within viroplasms. In brief, NSP4 exits the ER in COPII vesicles by interacting with the COPII cargo binding protein Sec24. Subsequently, the COPII vesicles are hijacked by the RV-induced LC3 II positive autophagic membranes possibly via the NSP4-LC3 interaction, and the NSP4/LC3 II-containing membranes get redirected to viroplasms (Figure 5). COPII vesicle protein Sec31 was reported to interact with both NSP2 and NSP5; however, its exact function in viroplasms has remained unaddressed (Dhillon et al., 2018). Interfering with the COPII vesicle formation/release from ER (either by inhibiting Sar1, a small GTPase regulating the initiation of COPII vesicle formation, through overexpression of its dominant-negative GDP-restricted form or by RNAi-mediated silencing of CK-II which phosphorylates Sec31, an outer coat protein around COPII vesicle) abrogated NSP4 translocation around viroplasms, leading to reduced production of infectious TLPs (Crawford et al., 2019).

Concluding remarks

RV viroplasms are phase-separated inclusion bodies within the host cellular cytosol where local concentrations for many viral components are high enough to facilitate RV biological processes such as viral genome replication, transcription, and early morphogenesis. They also serve as the safe house for the viral dsRNA population which would otherwise have triggered antiviral host responses. During RV infection, replicative or transcriptive viral dsRNA intermediates may succumb to processing by the host cellular RNAi machinery, yielding virus-derived small interfering RNAs (viRNAs) which might potentially direct viral RNA cleavage and attenuated viral replication. As a countermeasure, RV was found to trigger proteasomal degradation of AGO2, the catalytic effector of the siRNA-mediated RNAi in mammalian cells, during the early hours of infection, leading to the loss-of functionality of siRNA-based RNAi (Mukhopadhyay et al., 2019b). Going by the notion of viroplasms serving as a safe-house for RV RNAs is also the observation that RNAi-based silencing of NSP1 and NSP3 expression did not sensitize RV genome replication and virion assembly as a whole (Silvestri et al., 2004; Montero et al., 2006). This can be explained by the presence of two distinct and non-exchangeable pools of (+)RNAs—one siRNA-sensitive pool directing translation and the other siRNA-resistant pool guiding dsRNA synthesis— within infected cells. Therefore, the RV (+)RNAs which are used as templates for dsRNA synthesis have most likely originated from the transcriptionally active DLPs within viroplasms. This also partially justifies the poor incorporation of exogenously transfected viral (+)RNAs into the viral safe-houses of infected cells (Silvestri et al., 2004).

Similar to the viral components, viroplasm-associated host proteome is also selective. In most cases, manipulating with the viroplasm associated host components resulted in alteration in the RV progeny yield, vouching for the significance of these host factors in RV infection. However, given that RV life cycle is a multi-step, sequential process where every step depends on the successful completion of the preceding step, the multi-faceted host-viroplasm interaction dynamics have to be interpreted with utmost caution. For example, interfering with the viral entry or other events associated with the initial unmasking of the TLPs may reduce the number of viroplasms formed and promote delayed viroplasm kinetics simply because of the reduced initial viral load. This has to be differentiated from the instances where viral entry is not impeded but viroplasm nucleation is inhibited because of the interference with certain other host determinants such as CK1α, proteasome or LDs (Cheung et al., 2010; Contin et al., 2011; Criglar et al., 2018). Similarly, perturbation of the cytoskeletal network and MRN-ATM-Chk2 branch of the DDR did not sensitize viroplasm nucleation but compromised subsequent viroplasm maturation steps (Eichwald et al., 2012; Sarkar et al., 2020). Interestingly, all these perturbations culminated in the reduction of viral progeny yield despite targeting viroplasm dynamics at different stages. On another cautionary note, the sensitivity of viroplasms in response to a host-targeted small molecule might also be because of a direct effect of the small molecule on viral proteins and viroplasmic architecture and independent of the host target itself. Viroplasmic destabilization observed in presence of RNA polymerase III inhibitor ML-60218 occurs independent of the polymerase inhibitory activity of the small molecule but as a result of the inhibitor's direct effect on the oligomeric assembly of VP6 trimers (Eichwald et al., 2018). Therefore, the importance of the host factors in regulating viroplasm dynamics needs to be ascertained with more targeted, complementary approaches such as RNAi-based loss-of-functions (Contin et al., 2011; López et al., 2011; Sarkar et al., 2020), clonal overexpression-based gain-of-functions, or loss-of-target sensitivity assay (where removing the host target by secondary means abolishes the activity of the small molecule on RV) (Patra et al., 2019). For most viroplasm-relocated host proteins, the exact molecular mechanism behind the relocation and the exact significance of such redistribution are not dissected, opening many avenues for future research. With the advent of rRVs and proximity-based labelling approaches such as biotinylation, it would be interesting to address the differential composition of host proteome that associate with RV viroplasms at different stages of the RV life cycle.

Author contributions

PC, SB, PS, UP wrote the manuscript. PC, SB, PS prepared the figures. MC-S and UP edited the manuscript. MC-S provided critical suggestions. All the authors approve the final version of the manuscript.

Funding

MCS and PC are supported by ICMR. SB and PS are receiving fellowship from UGC and DST respectively.

Acknowledgments

We acknowledge the contributions of all the research personnel whose rigorous scientific works on host-rotavirus interaction enriched this review. We also acknowledge the research contribution of those scientists whose works were relevant yet exempted from this review because of space constraints. All current members of the Division of virology, ICMR-NICED, Kolkata are deeply acknowledged for their critical evaluation of the manuscript. The contribution of BioRender (through a paid subscription) is also acknowledged for preparing the figures used in the manuscript.

Conflict of interest

The authors declare that the research was conducted in the absence of any commercial or financial relationships that could be construed as a potential conflict of interest.

Publisher's note

References

Arias, C. F., and López, S. (2021). Rotavirus cell entry: Not so simple after all. *Curr. Opin. Virol* 48, 42–48. doi: 10.1016/j.coviro.2021.03.011

Arnoldi, F., De Lorenzo, G., Mano, M., Schraner, E. M., Wild, P., Eichwald, C., et al. (2014). Rotavirus increases levels of lipidated LC3 supporting accumulation of infectious progeny virus without inducing autophagosome formation. *PLoS One* 9 (4), e95197. doi: 10.1371/journal.pone.0095197

Bartek, J., and Lukas, J. (2001). Mammalian G1- and s-phase checkpoints in response to DNA damage. *Curr. Opin. Cell Biol.* 13 (6), 738–747. doi: 10.1016/s0955-0674(00)00280-5

Bhowmick, R., Mukherjee, A., Patra, U., and Chawla-Sarkar, M. (2015). Rotavirus disrupts cytoplasmic p bodies during infection. *Virus Res.* 210, 344–354. doi: 10.1016/j.virusres.2015.09.001

Campagna, M., Budini, M., Arnoldi, F., Desselberger, U., Allende, J. E., and Burrone, O. R. (2007). Impaired hyperphosphorylation of rotavirus NSP5 in cells depleted of casein kinase 1alpha is associated with the formation of viroplasms with altered morphology and a moderate decrease in virus replication. *J. Gen. Virol.* 88 (Pt 10), 2800–2810. doi: 10.1099/vir.0.82922-0

Campagna, M., Eichwald, C., Vascotto, F., and Burrone, O. R. (2005). RNA Interference of rotavirus segment 11 mRNA reveals the essential role of NSP5 in the virus replicative cycle. *J. Gen. Virol.* 86 (Pt 5), 1481–1487. doi: 10.1099/vir.0.80598-0

Campagna, M., Marcos-Villar, L., Arnoldi, F., de la Cruz-Herrera, C. F., Gallego, P., González-Santamaría, J., et al. (2013). Rotavirus viroplasm proteins interact with the cellular SUMOylation system: implications for viroplasm-like structure formation. *J. Virol.* 87 (2), 807–817. doi: 10.1128/JVI.01578-12

Cathcart, A. L., Rozovics, J. M., and Semler, B. L. (2013). Cellular mRNA decay protein AUF1 negatively regulates enterovirus and human rhinovirus infections. *J. Virol* 87 (19), 10423–10434. doi: 10.1128/JVI.01049-13

Cheung, W., Gill, M., Esposito, A., Kaminski, C. F., Courousse, N., Chwetzoff, S., et al. (2010). Rotaviruses associate with cellular lipid droplet components to replicate in viroplasms, and compounds disrupting or blocking lipid droplets inhibit viroplasm formation and viral replication. *J. Virol.* 84 (13), 6782–6798. doi: 10.1128/JVI.01757-09

Contin, R., Arnoldi, F., Campagna, M., and Burrone, O. R. (2010). Rotavirus NSP5 orchestrates recruitment of viroplasmic proteins. *J. Gen. Virol.* 91 (Pt 7), 1782–1793. doi: 10.1099/vir.0.019133-0

Contin, R., Arnoldi, F., Mano, M., and Burrone, O. R. (2011). Rotavirus replication requires a functional proteasome for effective assembly of viroplasms. *J. Virol.* 85 (6), 2781–2792. doi: 10.1128/JVI.01631-10

Crawford, S. E., Criglar, J. M., Liu, Z., Broughman, J. R., and Estes, M. K. (2019). COPII vesicle transport is required for rotavirus NSP4 interaction with the autophagy protein LC3 II and trafficking to viroplasms. *J. Virol.* 94 (1), e01341–e01319. doi: 10.1128/JVI.01341-19

Crawford, S. E., and Desselberger, U. (2016). Lipid droplets form complexes with viroplasms and are crucial for rotavirus replication. *Curr. Opin. Virol.* 19, 11–15. doi: 10.1016/j.coviro.2016.05.008

Crawford, S. E., Hyser, J. M., Utama, B., and Estes, M. K. (2012). Autophagy hijacked through viroporin-activated calcium/calmodulin-dependent kinase kinase-β signaling is required for rotavirus replication. *Proc. Natl. Acad. Sci. U. S. A.* 109 (50), E3405–E3413. doi: 10.1073/pnas.1216539109

Crawford, S. E., Ramani, S., Tate, J. E., Parashar, U. D., Svensson, L., Hagbom, M., et al. (2017). Rotavirus infection. *Nat. Rev. Dis. Primers* 3, 17083. doi: 10.1038/nrdp.2017.83

Criglar, J. M., Anish, R., Hu, L., Crawford, S. E., Sankaran, B., Prasad, B., et al. (2018). Phosphorylation cascade regulates the formation and maturation of rotaviral replication factories. *Proc. Natl. Acad. Sci. U.S.A.* 115 (51), E12015–E12023. doi: 10.1073/pnas.1717944115

Criglar, J. M., Crawford, S. E., Zhao, B., Smith, H. G., Stossi, F., and Estes, M. K. (2020). A genetically engineered rotavirus NSP2 phosphorylation mutant impaired in viroplasm formation and replication shows an early interaction between vNSP2 and cellular lipid droplets. *J. Virol.* 94 (15), e00972–e00920. doi: 10.1128/JVI.00972-20

Criglar, J. M., Estes, M. K., and Crawford, S. E. (2022). Rotavirus-induced lipid droplet biogenesis is critical for virus replication. *Front. Physiol.* 13. doi: 10.3389/fphys.2022.836870

Criglar, J. M., Hu, L., Crawford, S. E., Hyser, J. M., Broughman, J. R., Prasad, B. V., et al. (2014). A novel form of rotavirus NSP2 and phosphorylation-dependent NSP2-NSP5 interactions are associated with viroplasm assembly. *J. Virol.* 88 (2), 786–798. doi: 10.1128/JVI.03022-13

Dalet, A., Argüello, R. J., Combes, A., Spinelli, L., Jaeger, S., Fallet, M., et al. (2017). Protein synthesis inhibition and GADD34 control IFN-β heterogeneous expression in response to dsRNA. *EMBO J.* 36 (6), 761–782. doi: 10.15252/embj.201695000

Desselberger, U. (2014). Rotaviruses. *Virus Res.* 190, 75–96. doi: 10.1016/j.virusres.2014.06.016

Dhillon, P., and Rao, C. D. (2018). Rotavirus induces formation of remodeled stress granules and p bodies and their sequestration in viroplasms to promote progeny virus production. *J. Virol.* 92 (24), e01363–e01318. doi: 10.1128/JVI.01363-18

Dhillon, P., Tandra, V. N., Chorghade, S. G., Namsa, N. D., Sahoo, L., and Rao, C. D. (2018). Cytoplasmic relocalization and colocalization with viroplasms of host cell proteins, and their role in rotavirus infection. *J. Virol.* 92 (15), e00612–e00618. doi: 10.1128/JVI.00612-18

Eichwald, C., Arnoldi, F., Laimbacher, A. S., Schraner, E. M., Fraefel, C., Wild, P., et al. (2012). Rotavirus viroplasm fusion and perinuclear localization are dynamic processes requiring stabilized microtubules. *PLoS One* 7 (10), e47947. doi: 10.1371/journal.pone.0047947

Eichwald, C., De Lorenzo, G., Schraner, E. M., Papa, G., Bollati, M., Swuec, P., et al. (2018). Identification of a small molecule that compromises the structural integrity of viroplasms and rotavirus double-layered particles. *J. Virol* 92 (3), e01943–e01917. doi: 10.1128/JVI.01943-17

Eichwald, C., Jacob, G., Muszynski, B., Allende, J. E., and Burrone, O. R. (2004). Uncoupling substrate and activation functions of rotavirus NSP5: phosphorylation of ser-67 by casein kinase 1 is essential for hyperphosphorylation. *Proc. Natl. Acad. Sci. U.S.A.* 101 (46), 16304–16309. doi: 10.1073/pnas.0406691101

Fabbretti, E., Afrikanova, I., Vascotto, F., and Burrone, O. R. (1999). Two non-structural rotavirus proteins, NSP2 and NSP5, form viroplasm-like structures *in vivo*. *J. Gen. Virol.* 80 (Pt 2), 333–339. doi: 10.1099/0022-1317-80-2-333

Foulke-Abel, J., In, J., Kovbasnjuk, O., Zachos, N. C., Ettayebi, K., Blutt, S. E., et al. (2014). Human enteroids as an ex-vivo model of host-pathogen interactions in the gastrointestinal tract. *Exp. Biol. Med. (Maywood N.J.)* 239 (9), 1124–1134. doi: 10.1177/1535370214529398

Galluzzi, L., Kepp, O., Morselli, E., Vitale, I., Senovilla, L., Pinti, M., et al. (2010). Viral strategies for the evasion of immunogenic cell death. *J. Internal Med.* 267 (5), 526–542. doi: 10.1111/j.1365-2796.2010.02223.x

Gaunt, E. R., Cheung, W., Richards, J. E., Lever, A., and Desselberger, U. (2013a). Inhibition of rotavirus replication by downregulation of fatty acid synthesis. *J. Gen. Virol.* 94 (Pt 6), 1310–1317. doi: 10.1099/vir.0.050146-0

Gaunt, E. R., Zhang, Q., Cheung, W., Wakelam, M., Lever, A., and Desselberger, U. (2013b). Lipidome analysis of rotavirus-infected cells confirms the close interaction of lipid droplets with viroplasms. *J. Gen. Virol.* 94 (Pt 7), 1576–1586. doi: 10.1099/vir.0.049635-0

Geiger, F., Acker, J., Papa, G., Wang, X., Arter, W. E., Saar, K. L., et al. (2021). Liquid-liquid phase separation underpins the formation of replication factories in rotaviruses. *EMBO J.* 40 (21), e107711. doi: 10.15252/embj.2021107711

Geuens, T., Bouhy, D., and Timmerman, V. (2016). The hnRNP family: insights into their role in health and disease. *Hum. Genet.* 135 (8), 851–867. doi: 10.1007/s00439-016-1683-5

Glück, S., Buttafuoco, A., Meier, A. F., Arnoldi, F., Vogt, B., Schraner, E. M., et al. (2017). Rotavirus replication is correlated with S/G2 interphase arrest of the host cell cycle. *PLoS One* 12 (6), e0179607. doi: 10.1371/journal.pone.0179607

Green, V. A., and Pelkmans, L. (2016). A systems survey of progressive host-cell reorganization during rotavirus infection. *Cell Host Microbe* 20 (1), 107–120. doi: 10.1016/j.chom.2016.06.005

Hetz, C., and Papa, F. R. (2018). The unfolded protein response and cell fate control. *Mol. Cell* 69 (2), 169–181. doi: 10.1016/j.molcel.2017.06.017

Jing, Z., Shi, H., Chen, J., Shi, D., Liu, J., Guo, L., et al. (2021). Rotavirus viroplasm biogenesis involves microtubule-based dynein transport mediated by an interaction between NSP2 and dynein intermediate chain. *J. Virol.* 95 (21), e0124621. doi: 10.1128/JVI.01246-21

Jourdan, N., Maurice, M., Delautier, D., Quero, A. M., Servin, A. L., and Trugnan, G. (1997). Rotavirus is released from the apical surface of cultured human intestinal cells through nonconventional vesicular transport that bypasses the golgi apparatus. *J. Virol* 71 (11), 8268–8278. doi: 10.1128/jvi.71.11.8268-8278.1997

Kim, Y., George, D., Prior, A. M., Prasain, K., Hao, S., Le, D. D., et al. (2012). Novel triacsin c analogs as potential antivirals against rotavirus infections. *Eur. J. Medicinal Chem.* 50, 311–318. doi: 10.1016/j.ejmech.2012.02.010

Kimmel, A. R., Brasaemle, D. L., McAndrews-Hill, M., Sztalryd, C., and Londos, C. (2010). Adoption of PERILIPIN as a unifying nomenclature for the mammalian PAT-family of intracellular lipid storage droplet proteins. *J. Lipid Res.* 51 (3), 468–471. doi: 10.1194/jlr.R000034

Kim, H., Tu, H. C., Ren, D., Takeuchi, O., Jeffers, J. R., Zambetti, G. P., et al. (2009). Stepwise activation of BAX and BAK by tBID, BIM, and PUMA initiates mitochondrial apoptosis. *Mol. Cell.* 36 (3), 487–499. doi: 10.1016/j.molcel.2009.09.030

Lopez, S., and Arias, C. F. (2006). Early steps in rotavirus cell entry. *Reoviruses: Entry Assembly Morphogenesis.* 309, 39–66. doi: 10.1007/3-540-30773-7_2

López, T., Silva-Ayala, D., López, S., and Arias, C. F. (2011). Replication of the rotavirus genome requires an active ubiquitin-proteasome system. *J. Virol.* 85 (22), 11964–11971. doi: 10.1128/JVI.05286-11

Luftig, M. A. (2014). Viruses and the DNA damage response: Activation and antagonism. *Annu. Rev. Virol.* 1 (1), 605–625. doi: 10.1146/annurev-virology-031413-085548

Martin, D., Duarte, M., Lepault, J., and Poncet, D. (2010). Sequestration of free tubulin molecules by the viral protein NSP2 induces microtubule depolymerization during rotavirus infection. *J. Virol.* 84 (5), 2522–2532. doi: 10.1128/JVI.01883-09

Martin-Latil, S., Mousson, L., Autret, A., Colbère-Garapin, F., and Blondel, B. (2007). Bax is activated during rotavirus-induced apoptosis through the mitochondrial pathway. *J. Virol.* 81 (9), 4457–4464. doi: 10.1128/JVI.02344-06

Maruri-Avidal, L., López, S., and Arias, C. F. (2008). Endoplasmic reticulum chaperones are involved in the morphogenesis of rotavirus infectious particles. *J. Virol.* 82 (11), 5368–5380. doi: 10.1128/JVI.02751-07

Medigeshi, G. R., Lancaster, A. M., Hirsch, A. J., Briese, T., Lipkin, W. I., Defilippis, V., et al. (2007). West Nile Virus infection activates the unfolded protein response, leading to CHOP induction and apoptosis. *J. Virol.* 81, 10849–10860. doi: 10.1128/JVI.01151-07

Mehrbod, P., Ande, S. R., Alizadeh, J., Rahimizadeh, S., Shariati, A., Malek, H., et al. (2019). The roles of apoptosis, autophagy and unfolded protein response in arbovirus, influenza virus, and HIV infections. *Virulence* 10 (1), 376–413. doi: 10.1080/21505594.2019.1605803

Montero, H., Arias, C. F., and Lopez, S. (2006). Rotavirus nonstructural protein NSP3 is not required for viral protein synthesis. *J. Virol.* 80 (18), 9031–9038. doi: 10.1128/JVI.00437-06

Montero, H., Rojas, M., Arias, C. F., and López, S. (2008). Rotavirus infection induces the phosphorylation of eIF2alpha but prevents the formation of stress granules. *J. Virol.* 82 (3), 1496–1504. doi: 10.1128/JVI.01779-07

Mukhopadhyay, U., Chanda, S., Patra, U., Mukherjee, A., Komoto, S., and Chawla-Sarkar, M. (2019b). Biphasic regulation of RNA interference during rotavirus infection by modulation of Argonaute2. *Cell. Microbiol.* 21 (12), e13101. doi: 10.1111/cmi.13101

Mukhopadhyay, U., Chanda, S., Patra, U., Mukherjee, A., Rana, S., Mukherjee, A., et al. (2019a). Synchronized orchestration of miR-99b and let-7g positively regulates rotavirus infection by modulating autophagy. *Sci. Rep.* 9 (1), 1318. doi: 10.1038/s41598-018-38473-8

Mukhopadhyay, U., Patra, U., Chandra, P., Saha, P., Gope, A., Dutta, M., et al. (2022). Rotavirus activates MLKL-mediated host cellular necroptosis concomitantly with apoptosis to facilitate dissemination of viral progeny. *Mol. Microbiol.* 117 (4), 818–836. doi: 10.1111/mmi.14874

Musalem, C., and Espejo, R. T. (1985). Release of progeny virus from cells infected with simian rotavirus SA11. *J. Gen. Virol* 66 (12), 2715–2724. doi: 10.1099/0022-1317-66-12-2715

Navarro, A., Williamson, L., Angel, M., and Patton, J. T. (2016). Rotavirus replication and reverse genetics. *InViral Gastroenteritis*, 121–143. doi: 10.1016/B978-0-12-802241-2.00007-9

Oceguera, A., Peralta, A. V., Martínez-Delgado, G., Arias, C. F., and López, S. (2018). Rotavirus RNAs sponge host cell RNA binding proteins and interfere with their subcellular localization. *Virology* 525, 96–105. doi: 10.1016/j.virol.2018.09.013

Ohsaki, Y., Suzuki, M., and Fujimoto, T. (2014). Open questions in lipid droplet biology. *Chem. Biol.* 21 (1), 86–96. doi: 10.1016/j.chembiol.2013.08.009

Panaretakis, T., Kepp, O., Brockmeier, U., Tesniere, A., Bjorklund, A. C., Chapman, D. C., et al. (2009). Mechanisms of pre-apoptotic calreticulin exposure in immunogenic cell death. *EMBO J.* 28 (5), 578–590. doi: 10.1038/emboj.2009.1

Papa, G., Borodavka, A., and Desselberger, U. (2021). Viroplasms: assembly and functions of rotavirus replication factories. *Viruses.* 13 (7), 1349. doi: 10.3390/v13071349

Papa, G., Venditti, L., Arnoldi, F., Schraner, E. M., Potgieter, C., Borodavka, A., et al. (2019). Recombinant rotaviruses rescued by reverse genetics reveal the role of NSP5 hyperphosphorylation in the assembly of viral factories. *J. Virol.* 94 (1), e01110–e01119. doi: 10.1128/JVI.01110-19

Patra, U., Mukhopadhyay, U., Mukherjee, A., Dutta, S., and Chawla-Sarkar, M. (2021). Treading a HOSTile path: Mapping the dynamic landscape of host cell-rotavirus interactions to explore novel host-directed curative dimensions. *Virulence* 12 (1), 1022–1062. doi: 10.1080/21505594.2021.1903198

Patra, U., Mukhopadhyay, U., Sarkar, R., Mukherjee, A., and Chawla-Sarkar, M. (2019). RA-839, a selective agonist of Nrf2/ARE pathway, exerts potent anti-rotaviral efficacy *in vitro*. *Antiviral Res.* 161, 53–62. doi: 10.1016/j.antiviral.2018.11.009

Pingale, K. D., Kanade, G. D., and Karpe, Y. A. (2020). Heterogeneous nuclear ribonucleoproteins participate in hepatitis e virus (HEV) replication. *J. Mol. Biol.* 432, 2369–2387. doi: 10.1016/j.jmb.2020.02.025

Ravindran, M. S., Bagchi, P., Cunningham, C. N., and Tsai, B. (2016). Opportunistic intruders: how viruses orchestrate ER functions to infect cells. *Nat. Rev. Microbiol.* 14 (7), 407–420. doi: 10.1038/nrmicro.2016.60

Reineke, L. C., and Lloyd, R. E. (2013). Diversion of stress granules and p-bodies during viral infection. *Virology* 436 (2), 255–267. doi: 10.1016/j.virol.2012.11.017

Ren, L., Ding, S., Song, Y., Li, B., Ramanathan, M., Co, J., et al. (2019). Profiling of rotavirus 3'UTR-binding proteins reveals the ATP synthase subunit ATP5B as a host factor that supports late-stage virus replication. *J. Biol. Chem.* 294 (15), 5993–6006. doi: 10.1074/jbc.RA118.006004

Riggs, C. L., Kedersha, N., Ivanov, P., and Anderson, P. (2020). Mammalian stress granules and p bodies at a glance. *J. Cell Sci.* 133 (16), jcs242487. doi: 10.1242/jcs.242487

Rojas, M., Arias, C. F., and López, S. (2010). Protein kinase r is responsible for the phosphorylation of eIF2alpha in rotavirus infection. *J. Virol.* 84 (20), 10457–10466. doi: 10.1128/JVI.00625-10

Rozovics, J. M., Chase, A. J., Cathcart, A. L., Chou, W., Gershon, P. D., Palusa, S., et al. (2012). Picornavirus modification of a host mRNA decay protein. *mBio* 3, e00431–e00412. doi: 10.1128/mBio.00431-12

Sarkar, R., Banerjee, S., Mukherjee, A., and Chawla-Sarkar, M. (2022). Rotaviral nonstructural protein 5 (NSP5) promotes proteasomal degradation of up-frameshift protein 1 (UPF1), a principal mediator of nonsense-mediated mRNA decay (NMD) pathway, to facilitate infection. *Cell. Signalling.* 89, 110180. doi: 10.1016/j.cellsig.2021.110180

Sarkar, R., Patra, U., Lo, M., Mukherjee, A., Biswas, A., and Chawla-Sarkar, M. (2020). Rotavirus activates a noncanonical ATM-Chk2 branch of DNA damage response during infection to positively regulate viroplasm dynamics. *Cell. Microbiol.* 22 (3), e13149. doi: 10.1111/cmi.13149

Saunders, L. R., and Barber, G. N. (2003). The dsRNA binding protein family: critical roles, diverse cellular functions. *FASEB J.* 17 (9), 961–983. doi: 10.1096/fj.02-0958rev

Saxena, K., Blutt, S. E., Ettayebi, K., Zeng, X. L., Broughman, J. R., Crawford, S. E., et al. (2015). Human intestinal enteroids: a new model to study human rotavirus infection, host restriction, and pathophysiology. *J. Virol.* 90 (1), 43–56. doi: 10.1128/JVI.01930-15

Silvestri, L. S., Taraporewala, Z. F., and Patton, J. T. (2004). Rotavirus replication: plus-sense templates for double-stranded RNA synthesis are made in viroplasms. *J. Virol.* 78 (14), 7763–7774. doi: 10.1128/JVI.78.14.7763-7774.2004

Trask, S. D., McDonald, S. M., and Patton, J. T. (2012). Structural insights into the coupling of virion assembly and rotavirus replication. *Nat. Rev. Microbiol.* 10 (3), 165–177. doi: 10.1038/nrmicro2673

Trujillo-Alonso, V., Maruri-Avidal, L., Arias, C. F., and López, S. (2011). Rotavirus infection induces the unfolded protein response of the cell and controls it through the nonstructural protein NSP3. *J. Virol.* 85 (23), 12594–12604. doi: 10.1128/JVI.05620-11

Turpin, J., El-Safadi, D., Lebeau, G., Frumence, E., Desprès, P., Viranaïcken, W., et al. (2021). CHOP pro-apoptotic transcriptional program in response to ER stress is hacked by zika virus. *Int. J. Mol. Sci.* 22 (7), 3750. doi: 10.3390/ijms22073750

Valente, S. T., and Goff, S. P. (2006). Inhibition of HIV-1 gene expression by a fragment of hnRNP U. *Mol. Cell.* 23 (4), 597–605. doi: 10.1016/j.molcel.2006.07.021

Vascotto, F., Campagna, M., Visintin, M., Cattaneo, A., and Burrone, O. R. (2004). Effects of intrabodies specific for rotavirus NSP5 during the virus replicative cycle. *J. Gen. Virol.* 85 (Pt 11), 3285–3290. doi: 10.1099/vir.0.80075-0

Xu, A., Bellamy, A. R., and Taylor, J. A. (1998). BiP (GRP78) and endoplasmin (GRP94) are induced following rotavirus infection and bind transiently to an endoplasmic reticulum-localized virion component. *J. Virol* 72 (12), 9865–9872. doi: 10.1128/JVI.72.12.9865-9872.1998

Zambrano, J. L., Ettayebi, K., Maaty, W. S., Faunce, N. R., Bothner, B., and Hardy, M. E. (2011). Rotavirus infection activates the UPR but modulates its activity. *Virol. J.* 8, 359. doi: 10.1186/1743-422X-8-359

Zhu, S., Ding, S., Wang, P., Wei, Z., Pan, W., Palm, N. W., et al. (2017). Nlrp9b inflammasome restricts rotavirus infection in intestinal epithelial cells. *Nature.* 546 (7660), 667–670. doi: 10.1038/nature22967

frontiers | Frontiers in Cellular and Infection Microbiology

TYPE Original Research
PUBLISHED 17 October 2022
DOI 10.3389/fcimb.2022.949036

Superior antiviral activity of IFNβ in genital HSV-1 infection

Yasmin Schmitz[1†], Mara Schwerdtfeger[1†], Jaana Westmeier[1], Elisabeth Littwitz-Salomon[1], Mira Alt[2], Leonie Brochhagen[2], Adalbert Krawczyk[2] and Kathrin Sutter[1*]

[1]Institute for Virology, University Medicine Essen, University of Duisburg-Essen, Essen, Germany, [2]Department of Infectious Diseases, West German Centre of Infectious Diseases, University Medicine Essen, Essen, Germany

Type I interferons (IFNs) present the first line of defense against viral infections, providing antiviral, immunomodulatory and antiproliferative effects. The type I IFN family contains 12 IFNα subtypes and IFNβ, and although they share the same receptor, they are classified as non-redundant, capable to induce a variety of different IFN-stimulated genes. However, the biological impact of individual subtypes remains controversial. Recent data propose a subtype-specificity of type I IFNs revealing unique effector functions for different viruses and thus expanding the implications for IFNα-based antiviral immunotherapies. Despite extensive research, drug-resistant infections with herpes simplex virus type 1 (HSV-1), which is the common agent of recurrent orogenital lesions, are still lacking a protective or curing therapeutic. However, due to the risk of generalized infections in immunocompromised hosts as well as the increasing incidence of resistance to conventional antiherpetic agents, HSV infections raise major health concerns. Based on their pleiotropic effector functions, the application of type I IFNs represents a promising approach to inhibit HSV-1 replication, to improve host immunity and to further elucidate their qualitative differences. Here, selective IFNα subtypes and IFNβ were evaluated for their therapeutic potential in genital HSV-1 infections. Respective *in vivo* studies in mice revealed subtype-specific differences in the reduction of local viral loads. IFNβ had the strongest antiviral efficacy against genital HSV-1 infection in mice, whereas IFNα1, IFNα4, and IFNα11 had no impact on viral loads. Based on flow cytometric analyses of underlying immune responses at local and peripheral sites, these differences could be further assigned to specific modulations of the antiviral immunity early during HSV-1 infection. IFNβ led to enhanced systemic cytokine secretion and elevated cytotoxic responses, which negatively correlated with viral loads in the vaginal tract. These data provide further insights into the diversity of type I IFN effector functions and their impact on the immunological control of HSV-1 infections.

KEYWORDS

type I IFNs, IFNβ, herpes simplex virus-1, HSV infection, immunotherapy

Check for updates

OPEN ACCESS

EDITED BY
Santiago Guerrero,
Universidad Internacional
del Ecuador, Ecuador

REVIEWED BY
Serena Bernacchi,
UPR9002 Architecture et Réactivité
de l' arN, France
Gill Diamond,
University of Louisville, United States
Anil Pant,
Texas A&M University, United States

*CORRESPONDENCE
Kathrin Sutter
Kathrin.sutter@uk-essen.de

†These authors have contributed
equally to this work and share
first authorship

SPECIALTY SECTION
This article was submitted to
Virus and Host,
a section of the journal
Frontiers in Cellular and
Infection Microbiology

RECEIVED 20 May 2022
ACCEPTED 22 September 2022
PUBLISHED 17 October 2022

CITATION
Schmitz Y, Schwerdtfeger M,
Westmeier J, Littwitz-Salomon E,
Alt M, Brochhagen L, Krawczyk A and
Sutter K (2022) Superior antiviral
activity of IFNβ in genital
HSV-1 infection.
Front. Cell. Infect. Microbiol. 12:949036.
doi: 10.3389/fcimb.2022.949036

Introduction

As key mediators of the innate immunity, type I IFNs hold crucial functions for the defense against viral infections, by modulating a variety of cellular responses like proliferation, apoptosis or immune regulation and the establishment of an antiviral state. In humans, the type I IFN family comprises 17 functional genes for IFNβ, IFNϵ, IFNκ, IFNω and 13 IFNα subtypes (Freaney et al., 2014). Thereby, the sequence identity among type I IFNs constitutes not more than 30 %, resulting in specific activities and tissue distributions for individual subtypes (Chen et al., 2004; Thomas et al., 2011). Despite the high genetic and corresponding structural conservation of IFNα subtypes (Wittling et al., 2020), each subtype though is encoded by a single gene, assuming them to be non-redundant. Consistent with this postulation, differing antiviral and immunomodulatory activities for IFNα subtypes have been observed (Lavender et al., 2016; Dickow et al., 2019; Guo et al., 2020; Chen et al., 2021; Schuhenn et al., 2022). However, the complex system of type I IFN responses and their regulation is still not completely resolved.

The clinical administration of IFNα2 presented a potent strategy in the treatment of chronic hepatitis B virus (HBV) and hepatitis C virus (HCV) for more than three decades (Scott and Perry, 2002; Rong and Perelson, 2010; Woo et al., 2017; Ye et al., 2021). However, the biological role of individual type I IFN subtypes is mostly unresolved. In this regard, recent studies could reveal subtype-specific differences in the antiviral efficacy among type I IFNs, resulting in varying IFN-stimulated gene (ISG) expression patterns and corresponding effector functions for certain viruses.

According to this subtype-specificity, the therapeutic application of exogenous type I IFNs has regained importance as potential treatment strategy for further viruses. In this concern, HSV-1 still constitutes a major challenge of latent viral infections. Among the family of *Herpesviridae*, HSV-1 is the most frequently represented herpesvirus in humans with a worldwide seroprevalence of approx. 67 % in adults, characterized by recurrent, self-limiting lesions at oral and genital sites (Whitley and Roizman, 2001; Looker and Garnett, 2005; Fatahzadeh and Schwartz, 2007; James et al., 2020). HSV-1 presents a unique lifestyle, which is characterized by alternating phases of lytic replication and lifelong latency in sensory neurons of predominantly trigeminal ganglia (Bearer et al., 2000; Theil et al., 2003). Both primary infection and periodic reactivation from latency usually lead to formation of painful, mucocutaneous vesicles or ulcers, that crust over and heal without scarring, commonly known as *herpes labialis* or *herpes genitalis* (Spruance et al., 1977; Corey et al., 1983). Nevertheless, HSV infections can expand to further sites including liver, lung or the central nervous system, thus developing a fulminant course with in part life-threatening complications, especially in newborns and immunocompromised patients (Kimberlin, 2004; Herget et al., 2005). Until today the treatment of HSV infections still presents a major public health issue. In fact, several antiherpetic agents are commercially available. However, their efficacy is restricted to local skin lesions without reaching viral clearance and it is further limited by an increasing incidence of resistant virus mutants (Perry and Faulds, 1996; Danve-Szatanek et al., 2004; Lebrun-Vignes et al., 2007; Hammer et al., 2018; Álvarez et al., 2020).

In HSV infections, type I IFNs are known to have a crucial impact on the interplay of host defense and immune evasion, thus presenting promising candidates for antiviral treatment strategies. Following virus recognition by different pathogen-recognition receptors (Kurt-Jones et al., 2017), the production and release of endogenous type I IFNs results in a broad stimulation of several host immune cells, thus promoting the establishment of an antiherpetic environment (Hervas-Stubbs et al., 2011; Mesev et al., 2019). During acute infection, especially innate natural killer (NK) cell effector functions are stimulated by type I IFNs. Corresponding to the overall cytotoxic and cytolytic activity of NK cells in viral infections (Caligiuri, 2008), in particular their secretion of IFNγ seems to have a major impact on HSV control (Gill et al., 2011). Later during infection, type I IFN activities influence T cells with the induction of cytokine secreting CD4$^+$ T cells and the stimulation of Granzyme B (GzmB) and IFNγ expression by cytotoxic CD8$^+$ T cells (Daheshia et al., 1999; Liu et al., 2000; Carr and Noisakran, 2002; Knickelbein et al., 2008; Vahed et al., 2019). Besides their immunomodulatory effects, type I IFNs directly impede the replication of HSV (Austin et al., 2005; Carr et al., 2005). However, the induced immune responses are not able to prevent virus spreading and subsequent establishment of latency. Hence, HSV is predicted to hijack the host's immune system by specific escape mechanisms, most likely due to downregulation of type I IFN signaling.

Despite these evasion mechanisms, type I IFNs still present promising candidates for HSV treatment, assuming the application of additional, extrinsic type I IFN subtypes to reinvigorate the activity of endogenous IFNs. Several *in vivo* and *in vitro* studies reported HSV-specific preventive and therapeutic effects of human and murine type I IFN subtypes, leading to a reduction in viral titers and recurrence events as well as an accelerated lesion remission, whereas local and peripheral immune responses were not investigated in detail (Jones et al., 1976; Ho, 1990; Cardamakis et al., 1998; Carr and Noisakran, 2002; Härle et al., 2002; Härle et al., 2002; Austin et al., 2006). In this regard, previous *in vivo* studies with further recombinant IFNα subtypes as well as plasmids, expressing different type I IFN genes, examined a subtype-specificity in the antiherpetic potential, thus proposing other type I IFN subtypes than human IFNα2 to be more efficient for HSV treatment (Härle et al., 2001; Austin et al., 2006; Giraldo et al., 2020).

Hence, within the present work we addressed the question whether the application of exogenous IFNα subtypes or IFNβ can overcome the HSV-specific immune restriction and show beneficial effects on the viral burden. Therefore, the therapeutic potential of selective murine type I IFNs was evaluated in an *in vivo* mouse model of genital HSV-1 infection. Respectively, the reduction of local viral loads and potential differences in the antiviral efficacy of type I IFN subtypes was elucidated. IFNβ demonstrated a superior anti-HSV-activity *in vivo* compared to the other tested IFNα subtypes. Furthermore, treatment with IFNβ improved cytotoxic T and NK cell responses at local and peripheral sites early during HSV-1 infection, which negatively correlated with viral loads at early time points in the vaginal tract. In conclusion, we identified distinct immune cell effector functions during vaginal HSV-1 infection, which strongly correlated with the immunotherapeutic potential of murine IFNβ.

Material and methods

Cells, mice and virus

The African green monkey kidney cell line Vero and the murine fibroblast cell line NIH-3T3 were grown in Dulbecco's Modified Eagle's medium (DMEM, PAN-Biotech) supplemented with 10 % heat-inactivated fetal calf serum (FCS, Sigma-Aldrich), 100 U/mL penicillin and 100 µg/mL streptomycin (Thermo Fisher Scientific). For infection experiments cells were maintained in DMEM with 2 % FCS.

Female C57BL/6 mice were purchased from Charles River Laboratories and Envigo. Mice were at least 8 weeks of age and daily monitored for their general state of health, spontaneous behavior and body weight. Mice were kept according to the guidelines and regulations of the institutional animal care and use committee of the University of Duisburg-Essen, Germany. All procedures were performed according to the German regulations of the Society for Laboratory Animal Science (GV-SOLAS) and the European Health Law of the Federation of Laboratory Animal Science Associations (FELASA). The corresponding protocol was approved by the North Rhine-Westphalia State Agency for Nature, Environment and Consumer Protection (LANUV). All efforts were made to minimize suffering.

Wild-type virus strain HSV-1 F was propagated and titrated on Vero cell monolayers. Infectious titers were determined by Vero cell-based HSV plaque assay as described below and calculated as 50 % tissue culture infectious doses $TCID_{50}$/mL.

Vaginal HSV-1 infections

To increase the susceptibility for genital HSV challenge, mice were pre-treated with Sayana® medroxyprogesterone acetate (Pfizer) prior to intravaginal infection, thus inducing and prolonging their diestrus state. At least 7 days before infection, mice were intraperitoneally (i.p.) injected with 2.5 mg Sayana® diluted in phosphate-buffered saline (PBS, Thermo Fisher Scientific). On the day of infection, mice were anesthetized by i.p. injection with 50 mg/kg ketamine and 8 mg/kg xylazine. Subsequently, the vaginal mucosa was cleaned with a sterile cotton swab and infected with 1×10^7 $TCID_{50}$/20 µL of HSV-1 F diluted in PBS or 20 µL of PBS for naive control mice. To allow the inoculum to infect, the vaginal opening was temporarily closed with EPIGLU® skin glue (Meyer-Haake Medical Innovations).

In vitro HSV-1 infection and type I IFN stimulation

NIH-3T3 cells were seeded into 24-well plates in 10 % DMEM to reach a confluency of 80-90 % the next day. Six hours later, cells were stimulated with 1000 U/mL murine IFNα subtypes or IFNβ. The next day, cultivation medium of cells was replaced by 2 % DMEM and cells were infected with 5×10^5 $TCID_{50}$/mL of HSV-1 F. Finally, after incubation for additional 2 days at 37 °C, virus-containing supernatants were collected for further determination of infectious titers as described below.

Determination of infectious titers by HSV plaque assay

NIH-3T3 cells and Vero cells were grown in a 96-well format to reach a confluency of 80-90 % the next day. Next day, murine vaginal lavage liquids were serially diluted ($1:10^3$-$1:10^{10}$) on Vero cells in six replicates. Correspondingly, titration of cell supernatants from *in vitro* infection was performed on NIH-3T3 cells ($1:10$-$1:10^{10}$). Evaluation of plaque formation was performed after incubation for 4 days (NIH-3T3 cells) or 5 days (Vero cells) at 37 °C by manual counting of plaque-containing wells under the microscope. Corresponding infectious titers were calculated as $TCID_{50}$ values according to the Spearman and Kärber algorithm (Hierholzer and Killington, 1996).

Generation of murine type I IFNs and determination of IFN concentrations

Expression of IFNα1, IFNα4, and IFNβ was performed as previously described (Gerlach et al., 2009). To produce murine IFNα11, the cell line HEK293mIFNalpha11 was cultivated as described (Bollati-Fogolin and Muller, 2005). All concentrated supernatants were tested for type I IFN activity using the murine 3T3 ISRE-Luc reporter cell line, transfected with a plasmid containing the Firefly Luciferase gene, stably integrated under control of the IFN-stimulation-response element (ISRE). After 4.5 h of type I IFN stimulation, cells were lysed and chemiluminescence was detected using the Beetle-Juice Luciferase assay Firefly (PJK). The IFN activity was calculated to the respective activity in units against commercially available recombinant mouse IFNβ and universal IFNα (PBL assay science).

In vivo type I IFN treatment and vaginal lavages

Intraperitoneal injections of murine IFNα1, IFNα4, IFNα11, or IFNβ (8000 U) were daily administered to respective mice from day 2 *post infectionem* (*p.i.*) until day 7 *p.i.* for 8-days-studies or until day 3 *p.i.* for 4-days-studies.

For verification of local viral loads, vaginal lavages were performed every second day starting on day 2 *p.i.* until the end of the study. Therefore, mice were narcotized *via* inhalation anesthesia with isoflurane, vaginal mucus was removed with sterile PBS-soaked cotton swabs and 40 µL PBS were carefully resuspended within the vaginal lumen. Vaginal lavages were frozen at -80°C until determination of infectious titers.

On day 4 *p.i.* or day 8 *p.i.*, mice were sacrificed and analyzed for local and distal immune responses.

Isolation of vaginal tract leukocytes and spleen lymphocytes

Isolation of vaginal tract leukocytes was performed as previously described with minor modifications (Jiang and Kelly, 2012). Vaginal tracts of euthanized mice were dissected from oviducts to vaginal opening and cut into fine pieces. The minced tissue was transferred into 10 mL RPMI 1640 medium (Capricorn Scientific) supplemented with 10 % FCS, 100 U/mL penicillin, 100 µg/mL streptomycin, 1 % 1 M HEPES (Thermo Fisher Scientific) and 5 µM EDTA (AppliChem), and incubated for 15 min at room temperature while constantly shaking. Afterwards, the tissue was collected *via* 70 µm cell strainers (Miltenyi Biotec), the flowthroughs were discarded and the EDTA washing step was repeated. Afterwards EDTA was washed off with EDTA-free RPMI medium and the tissue was transferred into 3 mL RPMI medium supplemented with 10 % FCS, 100 U/mL penicillin, 100 µg/mL streptomycin, 1 % 1 M HEPES and 1 µg/mL deoxyribonuclease I (DNase, AppliChem). For subsequent digestion, 2 mg/mL collagenase IV (Sigma Aldrich) was added and the tissue suspensions incubated for 1 h at 37°C while constantly shaking. This step was repeated twice and leukocyte-containing flowthroughs were collected *via* 70 µm cell strainers, stored on ice and the remaining tissue pieces were transferred into fresh RPMI-DNase plus collagenase IV media for further digestion. Finally, collected flowthroughs were pooled and centrifuged for 7 min at 300 × g and stored at 4 °C until flow cytometry staining.

For the isolation of spleen lymphocytes, dissected spleens were mechanically dispersed into 10 mL PBS. Cell suspensions were centrifuged for 7 min at 300 × g and resulting cell pellets dissolved in an appropriate volume of PBS. Until further flow cytometry staining, prepared spleen cell suspensions were stored at 4°C.

Cell surface and intracellular staining for flow cytometry

Cell surface and intracellular staining of vaginal tract leukocytes and spleen lymphocytes was performed as previously described (Zelinskyy et al., 2006; Zelinskyy et al., 2009). For the assessment of splenic cytokine secretion, spleen lymphocytes were re-stimulated with 25 ng/mL phorbol myristate acetate (PMA, Invivogen) and 0.5 µg/mL ionomycin (Invivogen) for 1 h at 37°C. Produced cytokines were afterwards retained by adding 2 µg/mL brefeldin A (BFA, BioLegend) for further 2 h at 37°C. Vaginal tract leukocytes were stained for CD3 (clone: 145-2C11), CD4 (GK1.5), CD8 (53-6.7), CD11b (M1/70), CD11c (N418), CD19 (6D5), CD62L (MEL-14), CD69 (H1.2F3), CD80 (16-10A1), Ki67 (SolA15), MHC-II (M5/114.15.2), NK1.1 (PK136), Perforin (eBioO-MAK-D) and TRAIL (TNF-related apoptosis-inducing ligand, N2B2), while staining of spleen lymphocytes was performed with antibodies targeting CD3 (145-2C11), CD4 (GK1.5), CD8 (53-6.7), CD62L (MEL-14), CD69 (H1.2F3), GzmB (clone GB11), IFNγ (AN.18.17.24), IL-2 (JES-6-5H4), Ki67 (SolA15), NK1.1, Perforin (eBioO-MAK-D), TNFα (MP6-XT22) and TRAIL (N2B2). Exclusion of dead cells was provided by fixable viability dye (FVD, Thermo Fischer Scientific). Fluorescence minus one controls were prepared for all conditions. FACS measurements were performed with BD™ LSR II; BD FACSymphony™ A5, or BD FACSCanto™ II flow cytometer (Becton Dickinson) and resulting data were analyzed using FlowJo™ software (Becton Dickinson). The gating strategy and representative dot plots are shown in Supplementary Figure 2.

Multiplex cytokine and chemokine bead arrays

Cytokine quantification of vaginal lavages from HSV-1-infected mice (4 days post infection (dpi)) was done using the customized LEGENDplex multiplex assay (BioLegend) for the detection of the following cytokines and chemokines: CCL5 (RANTES), IFNα, IFNγ, IL-10, IL-12p40, IL-12p70, IL-15, IL-18, IL-2, IL-6, TNFα, GM-CSF, CCL3 (MIP-1α), and IL-27. The assay was performed according to the provider's instructions and analyzed using the dedicated software provided by BioLegend. Data acquisition was performed on a BD LSRII flow cytometer.

Statistical analysis

Experimental data were indicated as median or mean ± SEM. Statistically significant differences compared to the first day of treatment for individual groups or between infected and IFN-treated groups were analyzed using the nonparametric Kruskal-Wallis test or the 2way ANOVA and Tukey's multiple comparison test. Statistical analyses were conducted using the GraphPad Prism software (GraphPad).

Results

IFNβ treatment led to reduced HSV-1 titers in vaginal tract

As major part of the innate immunity, type I IFNs hold a crucial impact on the control of viral infections either by direct effects on infected and neighboring cells or by modulation of associated immune cell activities (Hervas-Stubbs et al., 2011; Teijaro, 2016). Thereby, type I IFNs and especially closely related IFNα subtypes seem to hold a subtype-specificity for certain viruses (Gibbert et al., 2013; Lavender et al., 2016; Dickow et al., 2019). Type I IFN subtypes also contribute to the host defense against HSV-1, hence preventing a systemic spread of the infection. Here, we aim to decipher the underlying antiviral and immunomodulatory properties of different murine type I IFNs during HSV-1 infection as well as to identify qualitative differences between type I IFN subtypes. Murine IFNα1, IFNα4, IFNα11 and IFNβ were selected due to their previously reported antiviral potential against Friend retrovirus and HSV-2 *in vivo* (Austin et al., 2006; Gerlach et al., 2009; Gibbert et al., 2012). According to the experimental design illustrated in Figure 1A, one week prior to intravaginal infection female C57BL/6 mice were treated with medroxyprogesterone acetate in order to induce and prolong the diestrus state in mice, thus increasing their susceptibility for genital HSV challenge (Kaushic et al., 2003; Gillgrass et al., 2005). Following HSV-1 infection, mice were assigned to different IFN treatment groups, comprising daily injections of respective type I IFN subtypes from day 2 *p.i.* until day 7 *p.i.* The impact of IFN treatment was assessed by determining viral titers from vaginal lavages on days 2, 4, 6, and 8 *p.i.* On day 2 prior to IFN treatment, all mice showed similar initial viral loads (Figure 1B). Overall, a decrease of viral titers was observed on day 4 *p.i.* until day 8 *p.i.* At the end of experiments all mice had viral loads below the detection limit. Interestingly, already on day 4 *p.i.* the group of mice treated with IFNβ had more than 5400-fold lower viral titers compared to untreated controls [median $TCID_{50}$/mL: 6.27 x 10^4 (HSV-1) and 11.58 (HSV-1 + IFNβ)]. All other applied IFN subtypes did not show any significant effect on HSV-1 replication (Figure 1B), although similar antiherpetic efficacies of those IFNs were observed *in vitro* (Supplementary Figure 1). Also, treatment with very high concentrations of IFNα4 (40,000 units per application) did not significantly reduce viral loads on day 4 *p.i.* indicating that the lack of antiviral activity cannot be overcome by increasing concentrations (data not shown). These data nicely show qualitative rather than quantitative differences between the type I IFN subtypes during vaginal HSV-1 infection.

IFN treatment did not improve immune responses in spleen and vaginal tract at 8 days post HSV-1 infection

To scrutinize potential correlations of the observed reduction in viral loads and IFN-mediated differences in immune responses, splenocytes of IFN-treated and untreated HSV-1-infected mice were analyzed on day 8 *p.i.* As shown in Figure 2A, HSV-1 significantly increased the percentages of activated $CD62L^-$ splenic $CD8^+$ T cells, whereas daily applications of IFNβ significantly reduced these frequencies. All other tested IFNs had no significant effect on the activation of T cells. Frequencies of activated $CD69^+$ NK cells were not increased in HSV-1-infected animals, but the treatment solely with IFNβ significantly elevated frequencies of $CD69^+$ NK cells. In contrast, frequencies of activated $CD62L^-$ $CD8^+$ T cells expressing the death receptor ligand TRAIL (Figure 2B) and IFNγ (Figure 2C) slightly increased upon IFNβ immunotherapy, but this effect was not significant. Furthermore, proportions of TRAIL-expressing $CD4^+$ T cells and NK cells were elevatedupon IFNβ treatment in comparison to untreated, HSV-1-infected mice (Supplementary Figure 3). Treatment of uninfected mice with IFNβ did not modulate immune responses as detected for IFNβ-treated HSV-1-infected mice (Figure 2A; Supplementary Figure 3). Again, application of IFNα1, α4, or α11 did not markedly affect immune responses in the spleen (Supplementary Figure 3).

To further dissect the immunomodulatory effects of type I IFNs on local immune responses at the vaginal tract, vaginal lymphocytes were isolated on day 8 *p.i.* and respective cell subsets were examined for their activation and effector functions. No significant effects on activation or effector functions of NK cells (Figure 3, Supplementary Figure 3G), T cells (Figure 3, Supplementary Figure 3G), B cells (data not shown), or dendritic cells (DCs, data not shown) were observed in the vaginal tract of type I IFN-treated mice compared to untreated, infected mice. Only frequencies of Perforin-expressing $CD8^+$ T cells were significantly enhanced after IFNα11-therapy; however, this treatment had no significant effect on virus control (Figure 1B). Taken together, compared to solely HSV-1-infected mice, type I IFN treatment had no remarkable effect on T and NK cells in the spleen and vaginal tract at day 8 post HSV-1 infection.

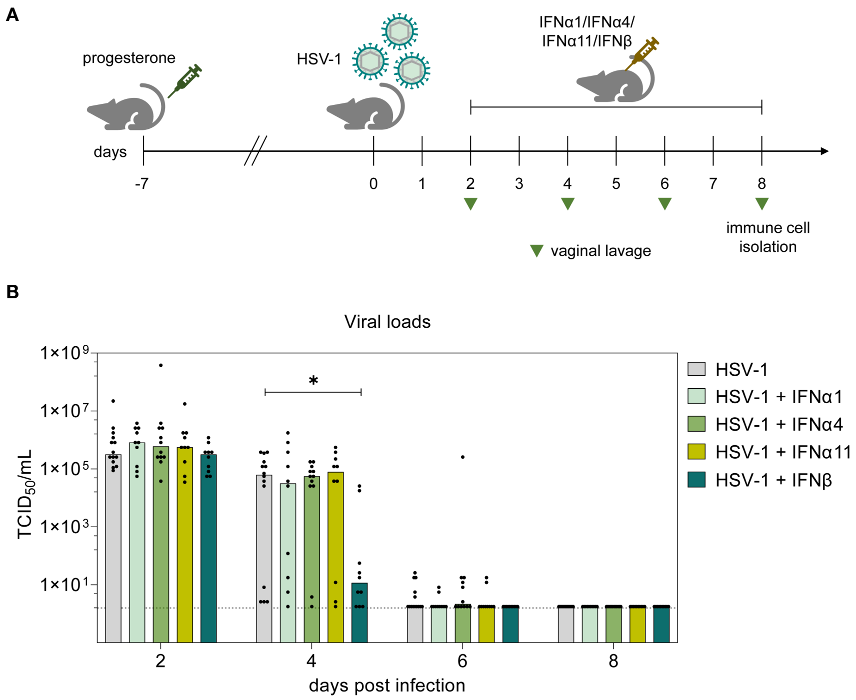

FIGURE 1
Antiviral activity of type I IFNs during vaginal HSV-1 infection on day 8 *p.i.* **(A)** Experimental setup for the *in vivo* assessment of type I IFN activities in genital HSV-1 infections. Female C57BL/6 mice were pretreated with 2.5 mg medroxyprogesterone acetate one week before infection. For intravaginal infection, mice were inoculated with 1×10^7 TCID$_{50}$ of HSV-1 F or left uninfected (naive control). Infected mice were assigned to different treatment groups (IFNα1, IFNα4, IFNα11, IFNβ) receiving daily injections of respective murine type I IFN subtypes (8000 U) for six consecutive days starting on day 2 *p.i.* or left untreated (HSV-1). From day 2 *p.i.* until day 8 *p.i.*, liquids from vaginal tract lavages were collected every second day for determination of viral loads, shown by light green triangles. After 8 days, spleens and vaginal tracts were isolated for further analysis of immune responses. **(B)** Viral titers of vaginal lavages were determined by endpoint dilution assay. Bars indicate the median virus titer of each group (HSV-1 n = 14 mice, HSV-1 + IFNα1 n = 10 mice, HSV-1 + IFNα4 n = 12 mice, HSV-1 + IFNα11 n = 10 mice, HSV-1 + IFNβ n = 10 mice). Dashed line marks the detection limit. Statistical analyses were conducted with the nonparametric Kruskal-Wallis test. Statistical significance between individual study groups is represented by $^*P < 0.05$.

Frequencies in TRAIL-expressing immune cells negatively correlated with viral loads at 4 dpi

Initial evaluation of different murine type I IFNs as potential therapeutics for genital HSV-1 infections revealed a faster reduction of local viral loads following IFNβ treatment (Figure 1B). On day 8 *p.i.*, only minor immunomodulatory effects of IFNβ were detectable in the spleen, but not within the vaginal tract, the local site of infection. Thus, we further assessed the respective modulations of local and systemic immune responses after IFNβ treatment at an earlier timepoint during HSV-1 infection, when the virus is still replicating within the vaginal tract. We therefore infected female mice with HSV-1 and treated these mice on days 2 and 3 *p.i.* with IFNβ according to the previous experiments (Figure 1A). On day 4 *p.i.*, when IFNβ treatment induced a significant reduction in viral loads (Figure 1B), mice were sacrificed and viral loads as well as splenic and local immune responses in the vaginal tract were determined. Again, we observed a strong reduction in viral loads on day 4 *p.i.* (Figure 4A). Furthermore, we also analyzed 14 different cytokines and chemokines in the vaginal lavages at 4 dpi. As depicted in Figure 4B, IL-27 was not induced during HSV-1 infection, whereas all other tested cytokines and chemokines were induced during HSV-1 infection (mean fold change (FC) between 1.7 for IL-15 and 420.8 for CCL5 relative to naive mice). Mice treated with IFNβ showed reduced levels of CCL5, CCL3, IL12p40, IFNγ, and IL-6 compared to untreated, HSV-1-infected mice, suggesting that either the reduced viral titers in IFNβ-treated mice or IFNβ itself inhibited inflammation within the vaginal tract.

To further scrutinize whether the treatment with IFNβ also modulates immune cell functions apart from its direct antiviral activity, we analyzed innate and adaptive immune cell responses in the spleen. As depicted in Figure 5A, treatment with IFNβ significantly reduced the frequencies of activated CD8$^+$ T cells, which is comparable to the previous results on day 8 *p.i.*

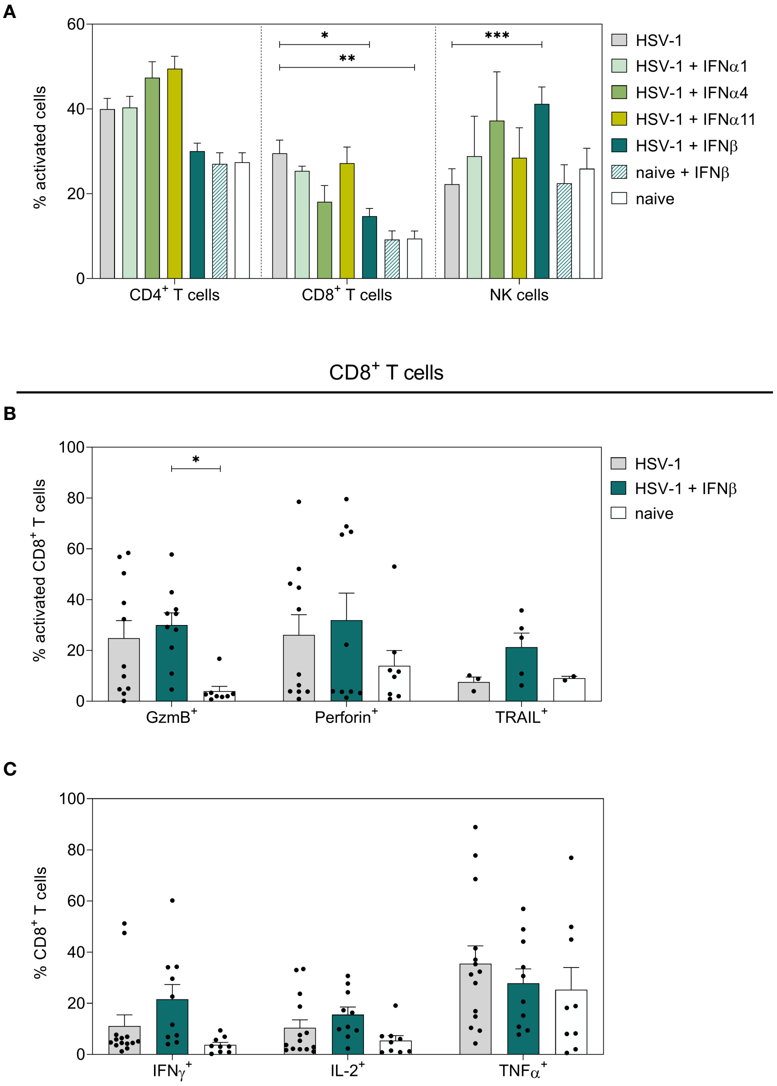

FIGURE 2
Peripheral immune responses in the spleen on day 8 post HSV-1 infection. Female C57BL/6 mice were infected with 1x10^7 $TCID_{50}$ of HSV-1 F for eight days or left uninfected (naive control). Mice were treated with 8000 U of murine IFNα1, IFNα4, IFNα11, and IFNβ for six consecutive days starting on day 2 *p.i.* or left untreated (HSV-1). On day 8 *p.i.*, splenic lymphocytes were isolated from dissected spleens. For flow cytometric analysis, isolated cells were subsequently stained for respective cell surface and intracellular markers. **(A)** Frequencies of activated $CD4^+$ T cells, $CD8^+$ T cells, and NK cells as well as **(B)** respective percentage of cytotoxic $CD8^+$ T cells and **(C)** cytokine-secreting $CD8^+$ T cells are shown. Data points represent individual mice; bars indicate the mean values ± SEM for each group (HSV-1 *n* = 3-14 mice, HSV-1 + IFNα1 *n* = 5 mice, HSV-1 + IFNα4 *n* = 3-5 mice, HSV-1 + IFNα11 *n* = 6-8 mice, HSV-1 + IFNβ *n* = 5-10 mice, naive + IFNβ *n* = 4 mice, naive *n* = 2-9 mice). Statistical analyses were conducted *via* 2way ANOVA and Tukey's multiple comparison test. Statistically significant differences among all study groups are depicted by *$P < 0.05$, **$P < 0.01$, ***$P < 0.001$.

(Figure 2A). Interestingly, already early during HSV-1 infection, percentages of cytotoxic $CD8^+$ T cells expressing GzmB or TRAIL were significantly elevated after IFNβ treatment compared to untreated controls (Figures 5B, D), whereas no effects on splenic cytotoxic and cytokine-producing $CD4^+$ T cells or NK cells were found at that time point (Figures 5B-D; Supplementary Figure 4).

Next, we also determined IFNβ-mediated effects on local immune responses in the vaginal tract. Corresponding to 8 dpi, no changes in the percentages of activated T cells or NK cells in the vaginal tract were observed earlier (Figure 6A); however, a strong increase in frequencies of cytotoxic $CD4^+$ T cells and NK cells ($TRAIL^+$) was detected (Figure 6C). No changes in cytotoxic $CD8^+$ T cells could be observed upon IFNβ

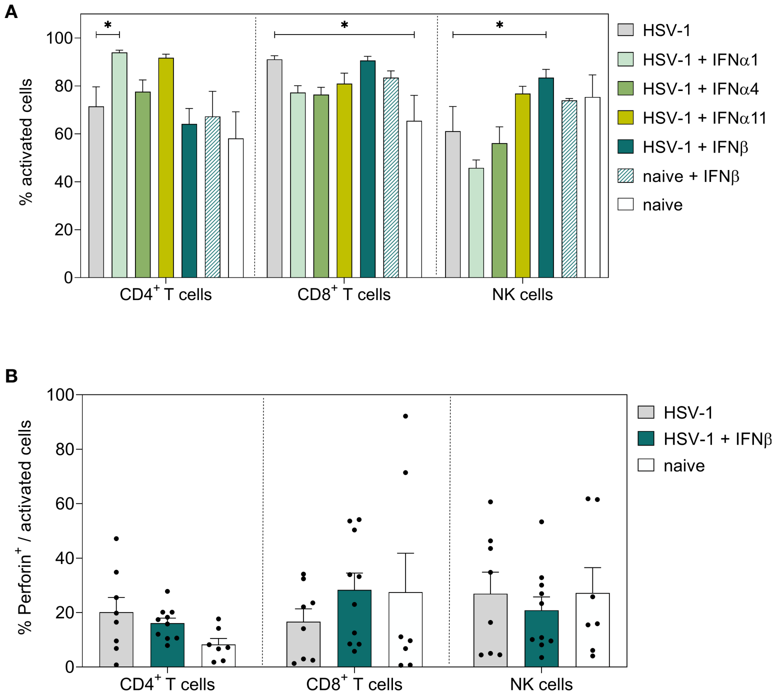

FIGURE 3
Local immune responses in the vaginal tract on day 8 post HSV-1 infection. Female C57BL/6 mice were infected with 1x10^7 $TCID_{50}$ of HSV-1 F for eight days or left uninfected (naive control). Mice were treated with 8000 U of murine IFNα1, IFNα4, IFNα11, and IFNβ for six consecutive days starting on day 2 *p.i.* or left untreated (HSV-1). On day 8 *p.i.*, vaginal lymphocytes were isolated from dissected vaginal tracts. For flow cytometric analysis, isolated cells were subsequently stained for respective cell surface and intracellular markers. **(A)** Frequencies of activated $CD4^+$ T cells, $CD8^+$ T cells, and NK cells and **(B)** percentage of respective Perforin-expressing, activated cell populations are shown. Data points represent individual mice; bars indicate the mean values ± SEM for each group (HSV-1 *n* = 8 mice, HSV-1 + IFNα1 *n* = 10 mice, HSV-1 + IFNα4 *n* = 10 mice, HSV-1 + IFNα11 *n* = 5 mice HSV-1 + IFNβ *n* = 10 mice, naive + IFNβ *n* = 4 mice, naive *n* = 7 mice). Statistical analyses were conducted *via* 2way ANOVA and Tukey's multiple comparison test. Statistically significant differences compared to the HSV-1 group are depicted by $^*P < 0.05$.

stimulation. Moreover, the overall frequencies of $CD8^+$ T cells at that early time point were rather low (Figure 6B, C and data not shown). Also, B cell and DC responses in the vaginal tract were not affected by IFNβ treatment in comparison to untreated HSV-1-infected mice (data not shown). In Figure 4 we recognized separate patterns in the viral loads with 7 out of 28 mice in the IFNβ-treated group still showing high viral loads, whereas 6 out of 35 mice in the untreated group had low viral loads. Thus, we determined if those mice with high viral loads after IFNβ treatment failed to induce an efficient immune response at 4 dpi in the vaginal tract. We observed a negative correlation of the percentage of TRAIL-expressing $CD4^+$ T cells and NK cells with viral loads, indicating that lower frequencies of TRAIL-expressing cells might drive higher viral loads (Figures 6D, E).

In conclusion, we demonstrated that IFNβ strongly reduced HSV-1 viral titers in the vaginal tract, which was not observed after treatment with IFNα1, IFNα4, or IFNα11. In addition to its direct antiviral activity, IFNβ strongly increased cytotoxic T and NK cell responses in the spleen and in the vaginal tract early during HSV-1 infection. Importantly, elevated frequencies of TRAIL-expressing NK and $CD4^+$ T cells are required for early viral control.

Discussion

Herpes simplex virus infections are usually associated with self-limiting, orofacial or genital lesions. However, they present an increasing incidence of resistance to conventional treatment agents, thus constituting a major health problem especially for immunocompromised hosts, who easily develop life-threatening sequelae due to resistant virus strains (Stránská et al., 2005; Fatahzadeh and Schwartz, 2007; Sauerbrei et al., 2011). Additionally, neither a prophylactic vaccine nor a curing therapeutic is available so far. Thereby, previous attempts for the development of new antiviral agents have been mainly hampered by the complexity of HSV-specific immune

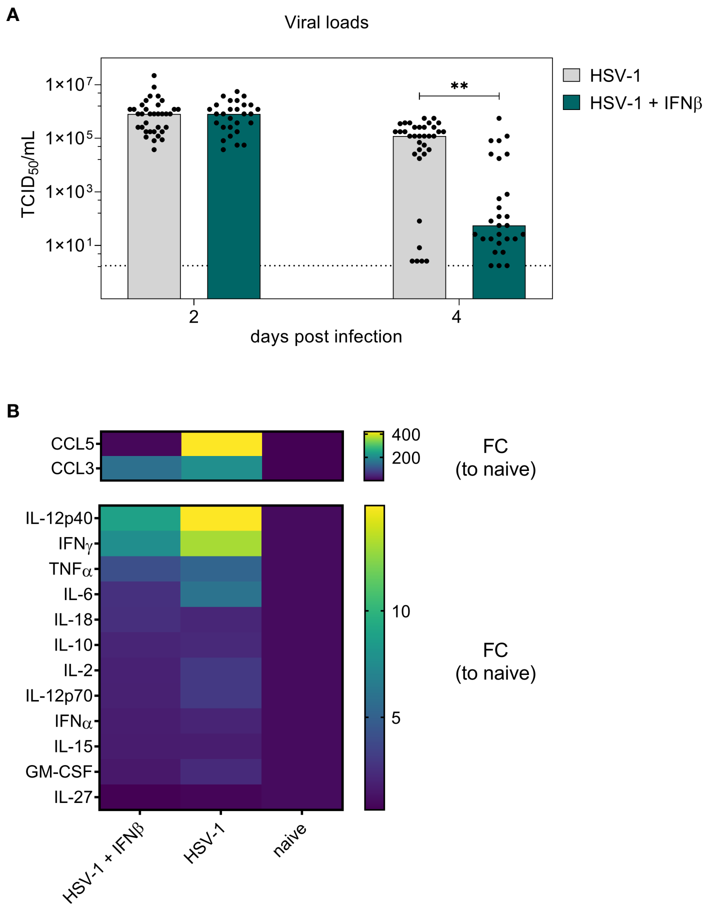

FIGURE 4
Early antiviral activity of IFNβ on day 4 post vaginal HSV-1 infection. Female C57BL/6 mice were infected with 1×10^7 $TCID_{50}$ of HSV-1 F for four days or left uninfected (naive control). Mice were treated with 8000 U of murine IFNβ for two consecutive days starting on day 2 *p.i.* or left untreated (HSV-1). On day 2 *p.i.* and day 4 *p.i.*, liquids from vaginal tract lavages were collected for determination of viral loads. After 4 days, spleens and vaginal tracts were isolated for further analysis of immune responses. **(A)** Viral titers of vaginal lavages were determined by endpoint dilution assay. Bars indicate the median virus titer of each group (HSV-1 *n* = 35 mice, HSV-1 + IFNβ *n* = 28 mice). Dashed line represents the detection limit. Statistically significant differences of mean HSV-1 + IFNβ titers compared to the initial viral load in infected mice were analyzed with the nonparametric Kruskal-Wallis test and are depicted by $^{**}P < 0.01$. **(B)** Fold change (FC) of CCL5 (RANTES), IFNα, IFNγ, IL-10, IL-12p40, IL-12p70, IL-15, IL-18, IL-2, IL-6, TNFα, GM-CSF, CCL3 (MIP-1α), and IL-27 expression of vaginal lavages from HSV-1-infected mice untreated or IFNβ-treated relative to naive mice. Mean values normalized to naive mice from 10 (HSV-1), 13 (HSV-1 + IFNβ), and 5 (naive) mice are shown.

responses, assuming the induction of both innate as well as adaptive immunity to be required for sufficient long-term protection (Koelle and Corey, 2008; Belshe et al., 2012).

In this regard, type I IFNs are known to induce a broad spectrum of cellular responses, including antiviral, immunomodulatory and antiproliferative activities to control viral infections. As part of the innate immunity, they activate early immune responses, but also modulate and regulate adaptive immune cell functions (Hervas-Stubbs et al., 2011; Teijaro, 2016). During HSV-1 and HSV-2 infections several type I IFN-related activities have been identified, which promote the impairment of viral replication and the establishment of an antiherpetic environment (Danastas et al., 2020; Feng et al., 2021). Conversely, HSV has been verified to specifically circumvent the type I IFN system by interfering with respective signaling events, thus assuring the development of latency and further reactivation (Koelle and Corey, 2008; Xu et al., 2019; Danastas et al., 2020).

Concerning this close interplay of immunity and viral evasion strategies, the question arises whether additional, exogenous type I IFNs can counteract the HSV-specific evasion and further enhance the properties of endogenously produced type I IFNs. In our study, we selected 4 different type I IFN subtypes (IFNα1, IFNα4, IFNα11, and IFNβ) and applied them therapeutically to HSV-1-infected mice. The treatment started at 2 dpi, when the vaginal infection was already established and viral loads peaked. Only exogenous application of IFNβ resulted in significantly reduced viral titers, whereas

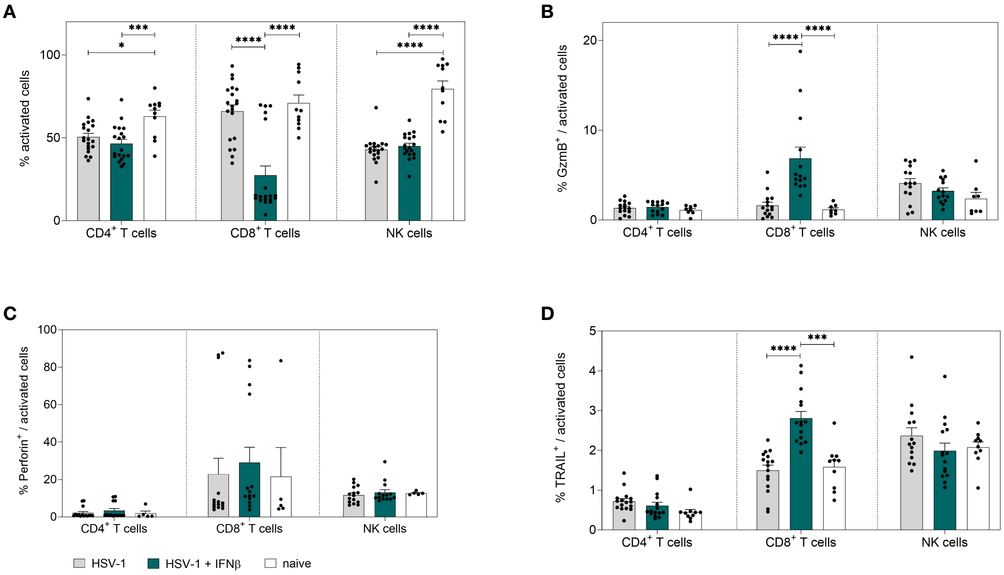

FIGURE 5
Peripheral immune responses in the spleen on day 4 post HSV-1 infection. Female C57BL/6 mice were infected with 1x10^7 $TCID_{50}$ of HSV-1 F for four days or left uninfected (naive control). Mice were treated with 8000 U of murine IFNβ for two consecutive days starting on day 2 *p.i.* or left untreated (HSV-1). On day 4 *p.i.*, splenic lymphocytes were isolated from dissected spleens. For flow cytometric analysis, isolated cells were stained for respective cell surface and intracellular markers. **(A)** Frequencies of activated CD4$^+$ T cells, CD8$^+$ T cells and NK cells as well as frequencies of **(B)** GzmB$^+$, **(C)** Perforin$^+$ and **(D)** TRAIL$^+$ activated cell subsets are shown. Data points represent individual mice. Bars indicate the mean values ± SEM for each group (HSV-1 *n* = 14-20 mice, HSV-1 + IFNβ *n* = 14-19 mice, naive *n* = 5-11 mice). Statistically significant differences among all study groups were analyzed with the 2way ANOVA and Tukey's multiple comparison test and are depicted by $^*P < 0.05$, $^{***}P < 0.001$, $^{****}P < 0.0001$.

treatment with IFNα1, IFNα4, or IFNα11 had no effect on viral replication (Figure 1B). So far, clinical trials evaluating the treatment of oral and genital HSV infections with the clinically approved human IFNα2 could already reveal an antiviral efficacy of exogenous type I IFN leading to decreased symptom duration and severity as well as a reduction of recurrence incidence, but without reaching complete prevention of infection and latency (Jones et al., 1976; Kuhls et al., 1986; Ho, 1990; Cardamakis et al., 1998). In this regard, previous *in vivo* studies with recombinant type I IFN subtypes as well as plasmids expressing different type I IFN genes examined a subtype-specific antiherpetic potential, thus assuming other type I IFN subtypes than human IFNα2 to be more efficient for HSV-1 and HSV-2 treatment (Härle et al., 2001; Austin et al., 2006; Giraldo et al., 2020). Hence, within the present study different type I IFN subtypes were assessed for their therapeutic potential in genital HSV-1 infections *via* a murine *in vivo* model, thereby focusing not only on the overall antiviral efficacy, but also on potential qualitative subtype-specific differences in underlying immune responses. In general, we observed an antiherpetic activity of IFNα1, IFNα2, IFNα4, IFNα5, IFNα6, IFNα9, IFNα11 and IFNβ *in vitro* (Supplementary Figure 1). Interestingly, those IFNα subtypes, which significantly reduced viral replication around 10-fold *in vitro* (IFNα1, IFNα4, and IFNα11), did not inhibit viral replication *in vivo* (Figure 1B) and their immunomodulatory potency during HSV-1 infection was rather low (Figures 2A, 3A and Supplementary Figure 3). In contrast, IFNβ with the lowest antiviral activity against HSV-1 *in vitro* strongly reduced viral loads already after two IFN doses *in vivo*, suggesting that apart from its direct antiviral effect, IFN-regulated immune responses are required for efficient HSV-1 control. Additionally, in the *in vitro* experiments type I IFNs were added before virus infection, that cells become alerted towards an antiviral state and antiviral effectors can be transcribed or even translated prior to viral infection. In the *in vivo* experiments, we added the IFNs when HSV-1 infection was already established suggesting the timing of the IFN treatment might also influence the antiviral effect of IFNs. Others reported similar direct antiviral activities in L929 cells transfected with different murine type I IFN transgenes, but they observed the strongest reduction *in vitro* with IFNβ and IFNα4 as most effective IFNs against HSV-1 (Härle et al., 2002). In addition, *in vivo* evaluation of these transgenes verified an increased reduction in the HSV-2 dependent mortality for IFNα1 and IFNβ (Härle et al., 2002). Interestingly, it was also reported that IFNγ, which has a very low antiviral activity against HSV-1 (Harle et al., 2002), synergizes with IFNα and IFNβ to control HSV-1 infection *in vitro* and pre-treatment with IFNβ and IFNγ

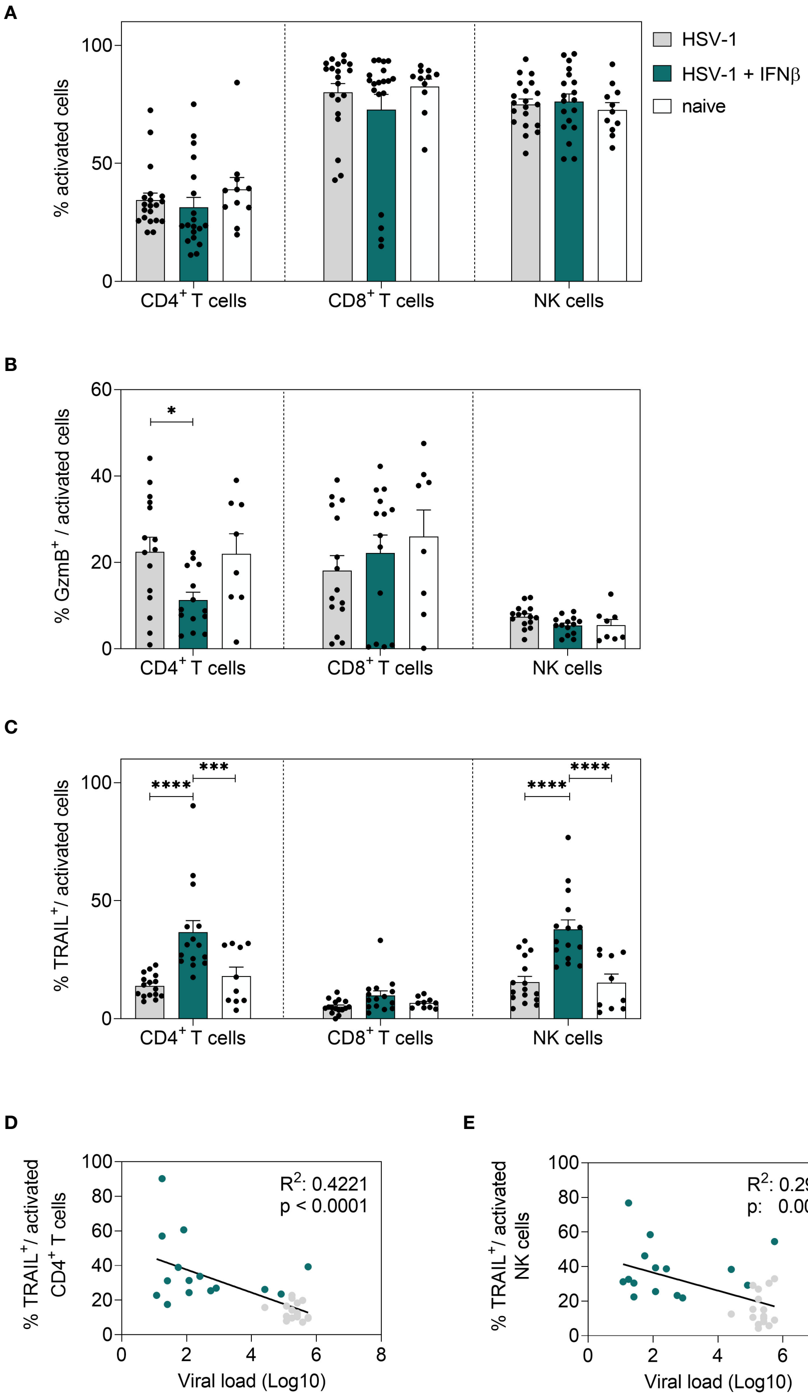

FIGURE 6
Local immune responses in the vaginal tract on day 4 post HSV-1 infection. Female C57BL/6 mice were infected with 1x10^7 TCID$_{50}$ of HSV-1 F for four days or left uninfected (naive control). Mice were treated with 8000 U of murine IFNβ for two consecutive days starting on day 2 *p.i.* or left untreated (HSV-1). On day 4 *p.i.*, vaginal leukocytes were isolated from dissected vaginal tracts. For flow cytometric analysis, isolated cells were subsequently stained for respective cell surface and intracellular markers. **(A)** Frequencies of activated CD4$^+$ T cells, CD8$^+$ T cells and NK cells, frequencies of **(B)** GzmB$^+$ and **(C)** TRAIL$^+$ activated cell subsets are shown. Data points represent individual mice. Bars indicate the mean values ± SEM for each group (HSV-1 *n* = 15-20 mice, HSV-1 + IFNβ *n* = 14-19 mice, naive *n* = 8-11 mice). Statistically significant differences among all study groups were analyzed with the 2way ANOVA and Tukey's multiple comparison test and are depicted by $^*P < 0.05$, $^{***}P < 0.001$, $^{****}P < 0.0001$. Correlation of frequencies of TRAIL$^+$ activated CD4$^+$ T cells **(D)** or frequencies of TRAIL$^+$ activated NK cells **(E)** and the viral loads (Log10) at 4 dpi of IFNβ-treated, HSV-1-infected (teal dots) and untreated, HSV-1-infected (grey dots) mice. Data points represent individual mice. Statistically significant differences among all study groups were analyzed with simple linear regression.

reduced the numbers of latent HSV-1 genomes in ocular HSV-1 infection *in vivo* (Sainz and Halford, 2002). These data suggest, that IFNγ, which is mainly produced by T cells markedly improves type I IFN-mediated control of HSV-1. In our study we did not detect a significant increase in IFNγ expressing T or NK cells (Figure 2C; Supplementary Figures 3A, C, E; Supplementary Figure 4A), although we observed an induction of IFNγ in the vaginal lavages at 4 dpi which might be produced by other important immune cell subsets within vaginal tract like granulocytes, monocytes, or macrophages. Other important members of the type I IFN family (IFNϵ, IFNκ) were already characterized during viral infections like HSV-1/2, Zika virus or human papillomavirus (HPV) in the vaginal tract (Reiser et al., 2011; Fung et al., 2013; Habiger et al., 2016; Woodby et al., 2018; Mungin et al., 2022) or in HSV-1-infected keratinocytes (Li et al., 2020; Kalke et al., 2022). Mice deficient in IFNϵ, which is constitutively expressed by epithelial cells in the female reproductive tract, were highly susceptible to HSV-2 (Fung et al., 2013).

Although we saw a direct antiviral effect of IFNα1, IFNα4, and IFNα11 *in vitro*, we did not observe any antiviral effect of these IFNα subtypes *in vivo*. In this concern, type I IFNs are also known to hold additional proviral functions either by downregulating protective immune responses or by excessive stimulation of inflammatory signals including pro-inflammatory cytokines like IFNγ, IL-6, IL-9, and granulocyte-colony stimulating factor (G-CSF) as well as chemoattractants like Eotaxin, IFNγ-induced protein 10 (IP-10), monocyte chemoattractant protein 1 (MCP-1) and macrophage inflammatory protein 1β (MIP-1β) (Davidson et al., 2014; Cheng et al., 2017). Here, we observed reduced levels of pro-inflammatory cytokines upon IFNβ-stimulation (Figure 4B), which might be either directly downregulated by IFNβ or the reduced viral loads have not triggered an inflammatory state in the female reproductive tract.

Nevertheless, analysis of viral loads alone does not confer an adequate comprehension of the antiherpetic potency of type I IFN subtypes and the here observed differences between subtypes. Therefore, the corresponding local immunity of vaginal tracts as well as systemic responses in spleens were further analyzed on days 4 and 8 *p.i.*, aiming to decipher the activation or effector functions of different cell types. From previous studies of the HSV-induced immunity it is known that a variety of cell types like NK or T cells are involved, relying on fine-tuned interactions *via* cytokines, chemokines, or co-stimulatory molecules (Chew et al., 2009; Truong et al., 2019). NK cells represent the predominant cell population of the innate immunity, that mediates cytotoxic and cytolytic attacks without prior antigen exposure, hence playing an important role for numerous viral infections. In this concern, NK cell-depletion-studies in HSV-1-infected mice could further reinforce the indispensable role of NK cells for the HSV-specific immunity resulting in increased viral loads and mortality of depleted mice (Habu et al., 1984; Nandakumar et al., 2008). Furthermore, they also reported that IFN treatment of HSV-1-infected mice increased the survival, which was not the case in NK cell-depleted mice (Habu et al., 1984), and the treatment with a mixture of type I IFNs strongly improved NK cell cytotoxicity. As typical effector cells of the adaptive immunity, CD8$^+$ T cells are characterized by an extensive expansion as well as differentiation into either cytotoxic or suppressive cell subsets. Following cross-priming with DCs, CD8$^+$ T cells were reported to interfere with the replication of HSV-1 and HSV-2 by releasing different cytokines or cytotoxic molecules and further evolve special memory functions which are assumed to contribute to a protective immunity (Shin et al., 2016; Vahed et al., 2019). Besides CD8$^+$ T cells, also CD4$^+$ T cells are detected during HSV infection. CD4$^+$ T cells are predominantly known for their regulatory or helper functions, thereby indirectly influencing the host defense. CD4$^+$ T cells were observed to hold cytotoxic activities and mediate the release of certain cytokines during HSV infections (Yasukawa et al., 1991). It was previously reported that *in vivo* treatment with plasmids encoding *IFNA1*, local and distal CD4$^+$ and CD8$^+$ T cell effector functions are required to antagonize ocular HSV-1 infections (Noisakran and Carr, 2000) and CD8$^+$ T cells are important for HSV-2 control (Austin et al., 2006), whereas IFNα1 treatment had no effect on NK cell cytotoxicity (Härle et al., 2001). Comprehensive and detailed investigations on IFN-mediated immune responses during vaginal HSV-1 infection are still lacking. The present study of genital HSV-1 infections could verify the induction of NK cell as well as CD4$^+$ and CD8$^+$ T cell immune responses following IFNβ treatment at both local and peripheral sites (Figures 3, 5, 6; Supplementary Figures 2–4). Here late infection time points, where local virus replication was already absent, were characterized by a significant increase of activated NK cells, but in turn also by suppression of activated CD8$^+$ T cells as well as the expression of cytokines and cytotoxic molecules. In contrast at very early time points during infection, treatment with IFNβ could elevate those cytotoxic effector functions for CD4$^+$ T cells and NK cells especially at the vaginal tract, thereby negatively correlating with the superior reduction of local viral loads in IFNβ-treated mice. Hence, these findings implicate a pivotal role of the early, local cytotoxicity mediated by IFNβ-stimulated NK and T cell populations for sufficient HSV-1 control. Correspondingly, previous studies on genital HSV-2 infections have also reported a particular upregulation of IL-15 within the genital mucosa (Figure 4B), that was closely associated with an enhanced activation of cytotoxic NK cells, thus supporting the indispensable role of NK cell responses for HSV immunity (Gill et al., 2011).

The variance among the different type I IFN subtypes tested in this study is in accordance with the concept of qualitative differences among type I IFNs (Lavender et al., 2016; Dickow et al., 2019; Guo et al., 2020; Chen et al., 2021; Schuhenn et al., 2022). Each subtype was assessed for its antiviral efficacies and these differences were due to induction of specific local and systemic immune responses, that altered HSV-1-induced immunity. In this concern, it would be revelatory to decipher specific properties of the remaining type I IFN subtypes as well as potential synergistic effects of certain subtypes which possibly contribute to a protective HSV-1 immunity. Furthermore, longitudinal studies to evaluate their long-term efficacy for recurrent infections as well as their impact on latency establishment have to be further validated.

Data availability statement

The original contributions presented in the study are included in the article/Supplementary Material. Further inquiries can be directed to the corresponding author.

Ethics statement

The animal study was reviewed and approved by North Rhine-Westphalia State Agency for Nature, Environment and Consumer Protection (LANUV).

Author contributions

KS and AK conceived the study. YS and MS substantially contributed to the acquisition and analysis of the data. JW, ELS, MA and LB provided reagents and performed experiments. KS wrote the original manuscript and all authors edited and approved the final manuscript.

Funding

This work was supported by the DFG RTG 1949 to KS. We acknowledge support by the Open Access Publication Fund of the University of Duisburg-Essen.

Conflict of interest

The authors declare that the research was conducted in the absence of any commercial or financial relationships that could be construed as a potential conflict of interest.

Publisher's note

Supplementary material

The Supplementary Material for this article can be found online at: https://www.frontiersin.org/articles/10.3389/fcimb.2022.949036/full#supplementary-material

References

Álvarez, D. M., Castillo, E., Duarte, L. F., Arriagada, J., Corrales, N., Farías, M. A., et al. (2020). Current antivirals and novel botanical molecules interfering with herpes simplex virus infection. *Front. Microbiol.* 11, 139. doi: 10.3389/fmicb.2020.00139

Austin, B. A., James, C. M., Härle, P., and Carr, D. J. (2006). Direct application of plasmid DNA containing type I interferon transgenes to vaginal mucosa inhibits HSV-2 mediated mortality. *Biol. Proced Online* 8, 55–62. doi: 10.1251/bpo118

Austin, B. A., James, C., Silverman, R. H., and Carr, D. J. (2005). Critical role for the oligoadenylate synthetase/RNase l pathway in response to IFN-beta during acute ocular herpes simplex virus type 1 infection. *J. Immunol.* 175, 1100–1106. doi: 10.4049/jimmunol.175.2.1100

Bearer, E. L., Breakefield, X. O., Schuback, D., Reese, T. S., and LaVail, J. H. (2000). Retrograde axonal transport of herpes simplex virus: evidence for a single mechanism and a role for tegument. *Proc. Natl. Acad. Sci. U.S.A.* 97, 8146–8150. doi: 10.1073/pnas.97.14.8146

Belshe, R. B., Leone, P. A., Bernstein, D. I., Wald, A., Levin, M. J., Stapleton, J. T., et al. (2012). Efficacy results of a trial of a herpes simplex vaccine. *N Engl. J. Med.* 366, 34–43. doi: 10.1056/NEJMoa1103151

Bollati-Fogolin, M., and Muller, W. (2005). Virus free, cell-based assay for the quantification of murine type I interferons. *J. Immunol. Methods* 306, 169–175. doi: 10.1016/j.jim.2005.08.005

Caligiuri, M. A. (2008). Human natural killer cells. *Blood* 112, 461–469. doi: 10.1182/blood-2007-09-077438

Cardamakis, E., Relakis, K., Kotoulas, I. G., Michopoulos, J., Metallinos, K., Mantouvalos, H., et al. (1998). Treatment of recurrent genital herpes with interferon alpha-2alpha. *Gynecol. Obstet. Invest.* 46, 54–57. doi: 10.1159/000009998

Carr, D. J., and Noisakran, S. (2002). The antiviral efficacy of the murine alpha-1 interferon transgene against ocular herpes simplex virus type 1 requires the presence of CD4(+), alpha/beta T-cell receptor-positive T lymphocytes with the capacity to produce gamma interferon. *J. Virol.* 76, 9398–9406. doi: 10.1128/JVI.76.18.9398-9406.2002

Carr, D. J., Tomanek, L., Silverman, R. H., Campbell, I. L., and Williams, B. R. (2005). RNA-Dependent protein kinase is required for alpha-1 interferon transgene-induced resistance to genital herpes simplex virus type 2. *J. Virol.* 79, 9341–9345. doi: 10.1128/JVI.79.14.9341-9345.2005

Chen, J., Baig, E., and Fish, E. N. (2004). Diversity and relatedness among the type I interferons. *J. Interferon Cytokine Res.* 24, 687–698. doi: 10.1089/jir.2004.24.687

Cheng, L., Yu, H., Li, G., Li, F., Ma, J., Li, J., et al. (2017). Type I interferons suppress viral replication but contribute to T cell depletion and dysfunction during chronic HIV-1 infection. *JCI Insight* 2: e94366. doi: 10.1172/jci.insight.94366

Chen, J., Li, Y., Lai, F., Wang, Y., Sutter, K., Dittmer, U., et al. (2021). Functional comparison of interferon-α subtypes reveals potent hepatitis b virus suppression by a concerted action of interferon-α and interferon-γ signaling. *Hepatology* 73, 486–502. doi: 10.1002/hep.31282

Chew, T., Taylor, K. E., and Mossman, K. L. (2009). Innate and adaptive immune responses to herpes simplex virus. *Viruses* 1, 979–1002. doi: 10.3390/v1030979

Corey, L., Adams, H. G., Brown, Z. A., and Holmes, K. K. (1983). Genital herpes simplex virus infections: clinical manifestations, course, and complications. *Ann. Intern. Med.* 98, 958–972. doi: 10.7326/0003-4819-98-6-958

Daheshia, M., Deshpande, S., Chun, S., Kuklin, N. A., and Rouse, B. T. (1999). Resistance to herpetic stromal keratitis in immunized b-cell-deficient mice. *Virology* 257, 168–176. doi: 10.1006/viro.1999.9613

Danastas, K., Miranda-Saksena, M., and Cunningham, A. L. (2020). Herpes simplex virus type 1 interactions with the interferon system. *Int. J. Mol. Sci.* 21: 5150. doi: 10.3390/ijms21145150

Danve-Szatanek, C., Aymard, M., Thouvenot, D., Morfin, F., Agius, G., Bertin, I., et al. (2004). Surveillance network for herpes simplex virus resistance to antiviral drugs: 3-year follow-up. *J. Clin. Microbiol.* 42, 242–249. doi: 10.1128/JCM.42.1.242-249.2004

Davidson, S., Crotta, S., McCabe, T. M., and Wack, A. (2014). Pathogenic potential of interferon αβ in acute influenza infection. *Nat. Commun.* 5, 3864. doi: 10.1038/ncomms4864

Dickow, J., Francois, S., Kaiserling, R. L., Malyshkina, A., Drexler, I., Westendorf, A. M., et al. (2019). Diverse immunomodulatory effects of individual IFNα subtypes on virus-specific CD8(+) T cell responses. *Front. Immunol.* 10, 2255. doi: 10.3389/fimmu.2019.02255

Fatahzadeh, M., and Schwartz, R. A. (2007). Human herpes simplex virus infections: epidemiology, pathogenesis, symptomatology, diagnosis, and management. *J. Am. Acad. Dermatol.* 57, 737–763. doi: 10.1016/j.jaad.2007.06.027

Feng, E., Balint, E., Vahedi, F., and Ashkar, A. A. (2021). Immunoregulatory functions of interferons during genital HSV-2 infection. *Front. Immunol.* 12. doi: 10.3389/fimmu.2021.724618

Freaney, J. E., Zhang, Q., Yigit, E., Kim, R., Widom, J., Wang, J. P., et al. (2014). High-density nucleosome occupancy map of human chromosome 9p21-22 reveals chromatin organization of the type I interferon gene cluster. *J. Interferon Cytokine Res.* 34, 676–685. doi: 10.1089/jir.2013.0118

Fung, K. Y., Mangan, N. E., Cumming, H., Horvat, J. C., Mayall, J. R., Stifter, S. A., et al. (2013). Interferon-epsilon protects the female reproductive tract from viral and bacterial infection. *Science* 339, 1088–1092. doi: 10.1126/science.1233321

Gerlach, N., Gibbert, K., Alter, C., Nair, S., Zelinskyy, G., James, C. M., et al. (2009). Anti-retroviral effects of type I IFN subtypes *in vivo*. *Eur. J. Immunol.* 39, 136–146. doi: 10.1002/eji.200838311

Gibbert, K., Joedicke, J. J., Meryk, A., Trilling, M., Francois, S., Duppach, J., et al. (2012). Interferon-alpha subtype 11 activates NK cells and enables control of retroviral infection. *PloS Pathog.* 8, e1002868. doi: 10.1371/journal.ppat.1002868

Gibbert, K., Schlaak, J., Yang, D., and Dittmer, U. (2013). IFN-alpha subtypes: distinct biological activities in anti-viral therapy. *Br. J. Pharmacol.* 168, 1048–1058. doi: 10.1111/bph.12010

Gill, N., Chenoweth, M. J., Verdu, E. F., and Ashkar, A. A. (2011). NK cells require type I IFN receptor for antiviral responses during genital HSV-2 infection. *Cell Immunol.* 269, 29–37. doi: 10.1016/j.cellimm.2011.03.007

Gillgrass, A. E., Fernandez, S. A., Rosenthal, K. L., and Kaushic, C. (2005). Estradiol regulates susceptibility following primary exposure to genital herpes simplex virus type 2, while progesterone induces inflammation. *J. Virol.* 79, 3107–3116. doi: 10.1128/JVI.79.5.3107-3116.2005

Giraldo, D., Wilcox, D. R., and Longnecker, R. (2020). The innate immune response to herpes simplex virus 1 infection is dampened in the newborn brain and can be modulated by exogenous interferon beta to improve survival. *mBio* 11: e00921–20. doi: 10.1128/mBio.00921-20

Guo, K., Shen, G., Kibbie, J., Gonzalez, T., Dillon, S. M., Smith, H. A., et al. (2020). Qualitative differences between the IFNα subtypes and IFNβ influence chronic mucosal HIV-1 pathogenesis. *PloS Pathog.* 16, e1008986. doi: 10.1371/journal.ppat.1008986

Habiger, C., Jager, G., Walter, M., Iftner, T., and Stubenrauch, F. (2016). Interferon kappa inhibits human papillomavirus 31 transcription by inducing Sp100 proteins. *J. Virol.* 90, 694–704. doi: 10.1128/JVI.02137-15

Habu, S., Akamatsu, K., Tamaoki, N., and Okumura, K. (1984). *In vivo* significance of NK cell on resistance against virus (HSV-1) infections in mice. *J. Immunol.* 133, 2743–2747. doi: 0022-1767/84/ 1335-2743$02.00/0

Hammer, K. D. P., Dietz, J., Lo, T. S., and Johnson, E. M. (2018). A systematic review on the efficacy of topical acyclovir, penciclovir, and docosanol for the treatment of herpes simplex labialis. *EMJ Dermatol.* 6, 118–123.

Härle, P., Cull, V., Agbaga, M. P., Silverman, R., Williams, B. R., James, C., et al. (2002). Differential effect of murine alpha/beta interferon transgenes on antagonization of herpes simplex virus type 1 replication. *J. Virol.* 76, 6558–6567. doi: 10.1128/JVI.76.13.6558-6567.2002

Härle, P., Cull, V., Guo, L., Papin, J., Lawson, C., and Carr, D. J. (2002). Transient transfection of mouse fibroblasts with type I interferon transgenes provides various degrees of protection against herpes simplex virus infection. *Antiviral Res.* 56, 39–49. doi: 10.1016/S0166-3542(02)00093-1

Härle, P., Noisakran, S., and Carr, D. J. (2001). The application of a plasmid DNA encoding IFN-alpha 1 postinfection enhances cumulative survival of herpes simplex virus type 2 vaginally infected mice. *J. Immunol.* 166, 1803–1812. doi: 10.4049/jimmunol.166.3.1803

Harle, P., Sainz, B.Jr., Carr, D. J., and Halford, W. P. (2002). The immediate-early protein, ICP0, is essential for the resistance of herpes simplex virus to interferon-alpha/beta. *Virology* 293, 295–304. doi: 10.1006/viro.2001.1280

Herget, G. W., Riede, U. N., Schmitt-Gräff, A., Lübbert, M., Neumann-Haefelin, D., and Köhler, G. (2005). Generalized herpes simplex virus infection in an immunocompromised patient–report of a case and review of the literature. *Pathol. Res. Pract.* 201, 123–129. doi: 10.1016/j.prp.2004.12.003

Hervas-Stubbs, S., Perez-Gracia, J. L., Rouzaut, A., Sanmamed, M. F., Le Bon, A., and Melero, I. (2011). Direct effects of type I interferons on cells of the immune system. *Clin. Cancer Res.* 17, 2619–2627. doi: 10.1158/1078-0432.CCR-10-1114

Hierholzer, J. C., and Killington, R. A. (1996). Virus isolation and quantitation. *Virol. Methods Man*, Chapter 2: 25–46. doi: 10.1016/B978-012465330-6/50003-8

Ho, M. (1990). Interferon as an agent against herpes simplex virus. *J. Invest. Dermatol.* 95, 158s–160s. doi: 10.1111/1523-1747.ep12875164

James, C., Harfouche, M., Welton, N. J., Turner, K. M., Abu-Raddad, L. J., Gottlieb, S. L., et al. (2020). Herpes simplex virus: global infection prevalence and incidence estimates, 2016. *Bull. World Health Organ* 98, 315–329. doi: 10.2471/BLT.19.237149

Jiang, J., and Kelly, K. A. (2012). Isolation of lymphocytes from mouse genital tract mucosa. *J. Vis. Exp.* 67:e4391. doi: 10.3791/4391

Jones, B. R., Coster, D. J., Falcon, M. G., and Cantell, K. (1976). Topical therapy of ulcerative herpetic keratitis with human interferon. *Lancet* 2, 128. doi: 10.1016/S0140-6736(76)92850-6

Kalke, K., Lund, L. M., Nyman, M. C., Levanova, A. A., Urtti, A., Poranen, M. M., et al. (2022). Swarms of chemically modified antiviral siRNA targeting herpes simplex virus infection in human corneal epithelial cells. *PloS Pathog.* 18, e1010688. doi: 10.1371/journal.ppat.1010688

Kaushic, C., Ashkar, A. A., Reid, L. A., and Rosenthal, K. L. (2003). Progesterone increases susceptibility and decreases immune responses to genital herpes infection. *J. Virol.* 77, 4558–4565. doi: 10.1128/JVI.77.8.4558-4565.2003

Kimberlin, D. W. (2004). Neonatal herpes simplex infection. *Clin. Microbiol. Rev.* 17, 1–13. doi: 10.1128/CMR.17.1.1-13.2004

Knickelbein, J. E., Khanna, K. M., Yee, M. B., Baty, C. J., Kinchington, P. R., and Hendricks, R. L. (2008). Noncytotoxic lytic granule-mediated CD8+ T cell inhibition of HSV-1 reactivation from neuronal latency. *Science* 322, 268–271. doi: 10.1126/science.1164164

Koelle, D. M., and Corey, L. (2008). Herpes simplex: insights on pathogenesis and possible vaccines. *Annu. Rev. Med.* 59, 381–395. doi: 10.1146/annurev.med.59.061606.095540

Kuhls, T. L., Sacher, J., Pineda, E., Santomauro, D., Wiesmeier, E., Growdon, W. A., et al. (1986). Suppression of recurrent genital herpes simplex virus infection with recombinant alpha 2 interferon. *J. Infect. Dis.* 154, 437–442. doi: 10.1093/infdis/154.3.437

Kurt-Jones, E. A., Orzalli, M. H., and Knipe, D. M. (2017). Innate immune mechanisms and herpes simplex virus infection and disease. *Adv. Anat Embryol Cell Biol.* 223, 49–75. doi: 10.1007/978-3-319-53168-7_3

Lavender, K. J., Gibbert, K., Peterson, K. E., Van Dis, E., Francois, S., Woods, T., et al. (2016). Interferon alpha subtype-specific suppression of HIV-1 infection *in vivo*. *J. Virol.* 90, 6001–6013. doi: 10.1128/JVI.00451-16

Lebrun-Vignes, B., Bouzamondo, A., Dupuy, A., Guillaume, J. C., Lechat, P., and Chosidow, O. (2007). A meta-analysis to assess the efficacy of oral antiviral treatment to prevent genital herpes outbreaks. *J. Am. Acad. Dermatol.* 57, 238–246. doi: 10.1016/j.jaad.2007.02.008

Li, Y., Song, Y., Zhu, L., Wang, X., Richers, B., Leung, D. Y. M., et al. (2020). Interferon kappa is important for keratinocyte host defense against herpes simplex virus-1. *J. Immunol. Res.* 2020, 5084682. doi: 10.1155/2020/5084682

Liu, T., Khanna, K. M., Chen, X., Fink, D. J., and Hendricks, R. L. (2000). CD8(+) T cells can block herpes simplex virus type 1 (HSV-1) reactivation from latency in sensory neurons. *J. Exp. Med.* 191, 1459–1466. doi: 10.1084/jem.191.9.1459

Looker, K. J., and Garnett, G. P. (2005). A systematic review of the epidemiology and interaction of herpes simplex virus types 1 and 2. *Sex Transm Infect.* 81, 103–107. doi: 10.1136/sti.2004.012039

Mesev, E. V., LeDesma, R. A., Ploss, A., and Decoding type, I. (2019). And III interferon signalling during viral infection. *Nat. Microbiol.* 4, 914–924. doi: 10.1038/s41564-019-0421-x

Mungin, J. W.Jr., Chen, X., and Liu, B. (2022). Interferon epsilon signaling confers attenuated zika replication in human vaginal epithelial cells. *Pathogens* 11: 853. doi: 10.3390/pathogens11080853

Nandakumar, S., Woolard, S. N., Yuan, D., Rouse, B. T., and Kumaraguru, U. (2008). Natural killer cells as novel helpers in anti-herpes simplex virus immune response. *J. Virol.* 82, 10820–10831. doi: 10.1128/JVI.00365-08

Noisakran, S., and Carr, D. J. (2000). Plasmid DNA encoding IFN-alpha 1 antagonizes herpes simplex virus type 1 ocular infection through CD4+ and CD8+ T lymphocytes. *J. Immunol.* 164, 6435–6443. doi: 10.4049/jimmunol.164.12.6435

Perry, C. M., and Faulds, D. (1996). Valaciclovir. A review of its antiviral activity, pharmacokinetic properties and therapeutic efficacy in herpesvirus infections. *Drugs* 52, 754–772. doi: 10.2165/00003495-199652050-00009

Reiser, J., Hurst, J., Voges, M., Krauss, P., Munch, P., Iftner, T., et al. (2011). High-risk human papillomaviruses repress constitutive kappa interferon transcription *via* E6 to prevent pathogen recognition receptor and antiviral-gene expression. *J. Virol.* 85, 11372–11380. doi: 10.1128/JVI.05279-11

Rong, L., and Perelson, A. S. (2010). Treatment of hepatitis c virus infection with interferon and small molecule direct antivirals: viral kinetics and modeling. *Crit. Rev. Immunol.* 30, 131–148. doi: 10.1615/CritRevImmunol.v30.i2.30

Sainz, B.Jr., and Halford, W. P. (2002). Alpha/Beta interferon and gamma interferon synergize to inhibit the replication of herpes simplex virus type 1. *J. Virol.* 76, 11541–11550. doi: 10.1128/JVI.76.22.11541-11550.2002

Sauerbrei, A., Bohn, K., Heim, A., Hofmann, J., Weissbrich, B., Schnitzler, P., et al. (2011). Novel resistance-associated mutations of thymidine kinase and DNA polymerase genes of herpes simplex virus type 1 and type 2. *Antivir Ther.* 16, 1297–1308. doi: 10.3851/IMP1870

Schuhenn, J., Meister, T. L., Todt, D., Bracht, T., Schork, K., Billaud, J. N., et al. (2022). Differential interferon-alpha subtype induced immune signatures are associated with suppression of SARS-CoV-2 infection. *Proc. Natl. Acad. Sci. U.S.A.* 119: e2111600119. doi: 10.1073/pnas.2111600119

Scott, L. J., and Perry, C. M. (2002). Interferon-alpha-2b plus ribavirin: a review of its use in the management of chronic hepatitis c. *Drugs* 62, 507–556. doi: 10.2165/00003495-200262030-00009

Shin, H., Kumamoto, Y., Gopinath, S., and Iwasaki, A. (2016). CD301b+ dendritic cells stimulate tissue-resident memory CD8+ T cells to protect against genital HSV-2. *Nat. Commun.* 7, 13346. doi: 10.1038/ncomms13346

Spruance, S. L., Overall, J. C.Jr., Kern, E. R., Krueger, G. G., Pliam, V., and Miller, W. (1977). The natural history of recurrent herpes simplex labialis: implications for antiviral therapy. *N Engl. J. Med.* 297, 69–75. doi: 10.1056/NEJM197707142970201

Stránská, R., Schuurman, R., Nienhuis, E., Goedegebuure, I. W., Polman, M., Weel, J. F., et al. (2005). Survey of acyclovir-resistant herpes simplex virus in the Netherlands: prevalence and characterization. *J. Clin. Virol.* 32, 7–18. doi: 10.1016/j.jcv.2004.04.002

Teijaro, J. R. (2016). Type I interferons in viral control and immune regulation. *Curr. Opin. Virol.* 16, 31–40. doi: 10.1016/j.coviro.2016.01.001

Theil, D., Derfuss, T., Paripovic, I., Herberger, S., Meinl, E., Schueler, O., et al. (2003). Latent herpesvirus infection in human trigeminal ganglia causes chronic immune response. *Am. J. Pathol.* 163, 2179–2184. doi: 10.1016/S0002-9440(10)63575-4

Thomas, C., Moraga, I., Levin, D., Krutzik, P. O., Podoplelova, Y., Trejo, A., et al. (2011). Structural linkage between ligand discrimination and receptor activation by type I interferons. *Cell* 146, 621–632. doi: 10.1016/j.cell.2011.06.048

Truong, N. R., Smith, J. B., Sandgren, K. J., and Cunningham, A. L. (2019). Mechanisms of immune control of mucosal HSV infection: A guide to rational vaccine design. *Front. Immunol.* 10. doi: 10.3389/fimmu.2019.00373

Vahed, H., Agrawal, A., Srivastava, R., Prakash, S., Coulon, P. A., Roy, S., et al. (2019). Expansion/Survival cytokines, and JAK/STAT gene signatures of multifunctional herpes simplex virus-specific effector memory CD8(+) T(EM) cells are associated with asymptomatic herpes in humans. *J. Virol.* 93: e01882–18. doi: 10.1128/JVI.01882-18

Whitley, R. J., and Roizman, B. (2001). Herpes simplex virus infections. *Lancet* 357, 1513–1518. doi: 10.1016/S0140-6736(00)04638-9

Wittling, M. C., Cahalan, S. R., Levenson, E. A. , and Rabin, R. L. (2020). Shared and unique features of human interferon-beta and interferon-alpha subtypes. *Front. Immunol.* 11, 605673. doi: 10.3389/fimmu.2020.605673

Woodby, B. L., Songock, W. K., Scott, M. L., Raikhy, G., and Bodily, J. M. (2018). Induction of interferon kappa in human papillomavirus 16 infection by transforming growth factor beta-induced promoter demethylation. *J. Virol.* 92: e01714–17. doi: 10.1128/JVI.01714-17

Woo, A. S. J., Kwok, R., and Ahmed, T. (2017). Alpha-interferon treatment in hepatitis b. *Ann. Transl. Med.* 5, 159. doi: 10.21037/atm.2017.03.69

Xu, X., Zhang, Y., and Li, Q. (2019). Characteristics of herpes simplex virus infection and pathogenesis suggest a strategy for vaccine development. *Rev. Med. Virol.* 29, e2054. doi: 10.1002/rmv.2054

Yasukawa, M., Inatsuki, A., Horiuchi, T., and Kobayashi, Y. (1991). Functional heterogeneity among herpes simplex virus-specific human CD4+ T cells. *J. Immunol.* 146, 1341–1347. doi: 00ZZ-1767/91/ 1464-1341S02.00/0

Ye, J., Chen, J. , and Interferon and Hepatitis, B. (2021). Current and future perspectives. *Front. Immunol.* 12, 733364. doi: 10.3389/fimmu.2021.733364

Zelinskyy, G., Dietze, K. K., Husecken, Y. P., Schimmer, S., Nair, S., Werner, T., et al. (2009). The regulatory T-cell response during acute retroviral infection is locally defined and controls the magnitude and duration of the virus-specific cytotoxic T-cell response. *Blood* 114, 3199–3207. doi: 10.1182/blood-2009-03-208736

Zelinskyy, G., Kraft, A. R., Schimmer, S., Arndt, T., and Dittmer, U. (2006). Kinetics of CD8+ effector T cell responses and induced CD4+ regulatory T cell responses during friend retrovirus infection. *Eur. J. Immunol.* 36, 2658–2670. doi: 10.1002/eji.200636059

Frontiers in
Cellular and Infection Microbiology

Investigates how microorganisms interact with their hosts

Explores bacteria, fungi, parasites, viruses, endosymbionts, prions and all microbial pathogens as well as the microbiota and its effect on health and disease in various hosts.

Discover the latest Research Topics

See more →

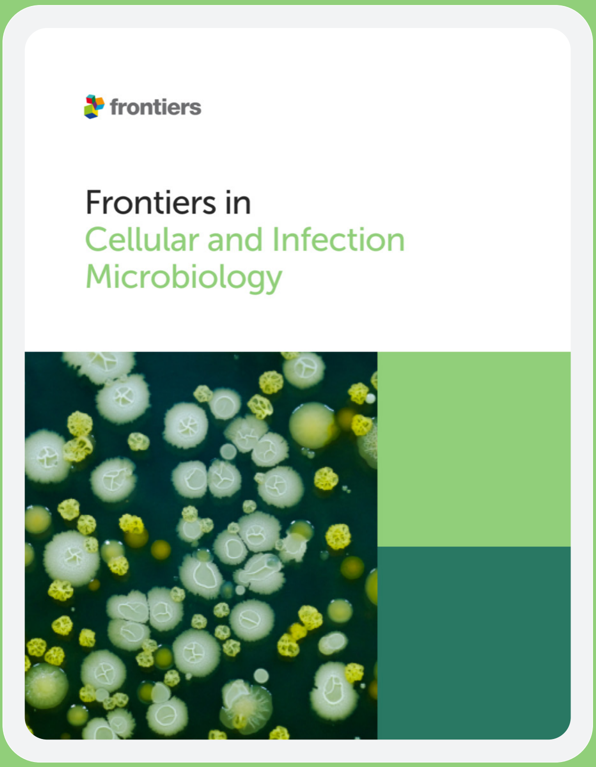

frontiers

Frontiers in
Cellular and Infection
Microbiology

Frontiers

Avenue du Tribunal-Fédéral 34
1005 Lausanne, Switzerland
frontiersin.org

Contact us

+41 (0)21 510 17 00
frontiersin.org/about/contact